Anneleen Foubert
Jean-Pierre Henriet

LECTURE NOTES IN EARTH SCIENCES

Nature and Significance of the Recent Carbonate Mound Record

The Mound Challenger Code

Springer

Lecture Notes in Earth Sciences 126

Anneleen Foubert · Jean-Pierre Henriet

Nature and Significance of the Recent Carbonate Mound Record

The Mound Challenger Code

Springer

Anneleen Foubert
Renard Centre of Marine Geology
Ghent University
Krijgslaan 281-S8
9000 Ghent
Belgium
anneleen.foubert@ees.kuleuven.be

Prof. Dr. Jean-Pierre Henriet
Renard Centre of Marine Geology
Ghent University
Krijgslaan 281-S8
9000 Ghent
Belgium
jeanpierre.henriet@ugent.be

ISSN 0930-0317
ISBN 978-3-642-00289-2 e-ISBN 978-3-642-00290-8
DOI 10.1007/978-3-642-00290-8
Springer Dordrecht Heidelberg London New York

Library of Congress Control Number: 2009921823

Cover design: Bauer, Thomas

Printed on acid-free paper

Springer is part of Springer Science+Business Media (www.springer.com)

- This Book is dedicated to my grandfather

Abstract

Carbonate mounds appear to be an important feature along the northeastern Atlantic margins. The presence of giant carbonate mounds in Porcupine Seabight, on Porcupine Bank, in Rockall Trough and on Rockall Bank, W of Ireland is already known since the nineties (Hovland et al. 1994; Henriet et al. 1998; De Mol et al. 2002; Huvenne et al. 2002, 2003; van Weering et al. 2003). These mounds have been the target of several cruises during the last decade. An exploratory cruise of R/V Belgica in 2002 off Larache (Morocco, Gulf of Cadiz) has led to the discovery of similar mound structures topping ridges and structural heights (Foubert et al. 2008). Because of their unique setting (focused fluid seepage, mud volcanoes), also the carbonate mound sites on the Moroccan margin become rapidly involved in a developing stage of focused multidisciplinary research. Scientific campaigns, industrial surveys and extensive mapping studies reveal each year new mound structures. However, the processes of mound build-up and mound nucleation are not yet completely understood. What keeps a mound growing over extended time periods? How does the biosphere interact with sedimentary fluxes to make a mound grow? On which level do palaeoclimatological and palaeoceanographic changes control mound growth? Which diagenetic processes play an important role in carbonate mound generation and how do they affect the mound?

The principal aim of the present study is twofold, focusing in a first phase on the nature of the carbonate mound record, and discussing in a second phase its significance. The nature and internal structure of one specific carbonate mound in Porcupine Seabight (SW of Ireland), i.e. Challenger Mound, is successfully unveiled. The mound is built from top to bottom of cold-water coral fragments embedded in an alternating biogenic (carbonate-rich) to terrigenous (siliciclastic) matrix. This creates a cyclicity which is considered to be driven by glacial-interglacial changes. Magnetostratigraphy and datings show that the mound started to grow between ~2.70 and ~2.50 Ma. It is nowadays in a stage of decline.

In a second phase, the significance of the carbonate mound record is discussed. The comparison of the top of Challenger Mound with another mound in Porcupine Seabight reveals that even on a regional scale, different mounds have different characteristics. Video imagery through Remotely Operated Vehicle (ROV) surveys, providing images of the surface of different carbonate mounds, substantiates the above statement. Small mound structures are occurring between the giant mounds

and “dead” mounds are flanked by “live” mounds. The carbonate mounds on the Moroccan margin occur in a different oceanographic and geological setting than the mounds along the Irish margin. So, a wide variety of mounds occur in a wide variety of settings. This calls for an appropriate classification for recent carbonate mound systems and cold-water coral reefs. The role of recent carbonate mounds, such as Challenger Mound, in the global carbonate budget is discussed and appears to be significant but not extraordinary. The way recent carbonate mounds can be seen as analogues of ancient mud mound systems is a whole study on itself. However, at first sight, some significant differences are noted.

Preface

J'ai voulu expliquer l'océanographie que j'aime
(Jean-François Minster, La Machine-océan)

"Ocean research is a lot like climbing a new route to the top of a mountain. Every time you go out to sea there's something new. I enjoy that aspect of both – the unpredictability of the mountains and the bottom of the sea. Besides, neither place is very crowded", said geologist and oceanographer Charles Davis Hollister once. I can fully endorse this statement. Climbing up a mountain or being out at sea is indeed a great feeling and the striking parallelism between both experiences is amazing. Climbing up a carbonate mound is tough but once you reach the top it is an indescribable moment of delight. Trying to look into a mound is even more difficult but the secrets that such carbonate structures hide are unbelievable and more than worth digging into this matter. I could never have experienced all these moments if I have not had a strong rope, various anchor points, and a stable platform to lead and help me during my search for the secrets behind these strange carbonate structures occurring in the deep blue. Thanks a lot to all the people who were just walking along my way, never giving up in supporting me and always giving me a pat on the back or whispering some encouragement.

In the first place, I would like to mention my supervisor and coach Prof. Dr. Jean-Pierre Henriet. His triggering enthusiasm proved infectious. Without his perseverance, carbonate mound research was not as far as it is nowadays. He prepared the way for many young scientists and involved them in the world of carbonate mound research. His support and encouragement during my research were great. Having discussions with him was sometimes intense but always more than instructive. He gave me a lot of possibilities to discover the world of carbonate mounds in all its aspects from the Arctics to Morocco, and from scientific meetings and workshops over research campaigns to classrooms.

During the last four years, I had the possibility to explore literally the whole carbonate mound world and community. I would like to acknowledge all the people who offered me a home-feeling all over the world, who supported me during hours of measurement time, and who helped in building up the extensive data set presented in this study. It has to be mentioned that this study is the result of teamwork and as

each cog has its important function in a machine, each person involved in mound research has his or her important role in unveiling the secrets of carbonate mounds.

Prof. Dr. Joseph Hus is thanked for the possibility to use the palaeomagnetic measurement infrastructure at the Geophysical Centre of the Royal Meteorological Institute in Dourbes and for his excellent support during the measurements. Dr. Veerle Cnudde introduced me in the world of computer tomographic scanning and had the patience to learn me the details of image analysis. The analytical and geochemical expertise present at the Department of Earth and Environmental Sciences at the K.U. Leuven (currently my home lab) and Prof. Dr. Rudy Swennen's profound knowledge in complex carbonate systems paved the way to start unravelling diagenetic processes in mound systems. Dr. Dierk Hebbeln offered me several times the possibility to use the excellent infrastructures available at the University Bremen (from cutting and freezing samples to extensive XRF scanning). Thanks to Prof. Dr. Tjeerd Van Weering, the XRF CORTEX scanner installed at the Netherlands Institute for Sea Research (NIOZ) could be used. Rineke Gieles helped me intensively during my stay on the Dutch island Texel, from providing nice meals to excellent support during the XRF measurements. Dr. Norbert Frank and Dr. Dominique Blamart showed me the way to the legendary caves (officially named as 'carothèque') of Gif-sur-Yvette. During the academic year 2004–2005, Erlangen University became a kind of second home place. Thanks a lot, Prof. Dr. A. Freiwald, to host me so many times at your institute specialized in carbonate research, to show me the way towards the CT-scan facilities of Siemens, and to teach me to enjoy real German barbecues. At the end of my PhD and especially last year, I got the opportunity to join a professional team of carbonate sedimentologists at the research centre CSTJF (Centre Scientifique et Technique Jean Feger) of TOTAL S.A. in Pau, France. I would like to acknowledge the whole carbonate team of TOTAL S.A. for all the stimulating discussions on reservoir-related carbonate aspects, enlarging my view on the carbonate world and triggering my enthusiasm to understand the complex relationship between diagenesis and petrophysics.

The whole scientific team and the IODP and Transocean crews aboard the R/V JOIDES Resolution on IODP Expedition Leg 307 are acknowledged. The data collected during this expedition form the key data set of this work. It was a fantastic experience to participate as palaeomagnetist in one of the biggest drilling programmes in science. In particular, Yuji Fuwa, Klayton Curtis, Margaret Hastedt and Trevor Williams are thanked for their palaeomagnetic help aboard the R/V JOIDES Resolution. Besides IODP Expedition Leg 307, a whole range of scientific expeditions was taking place during the last years with as main topic the study of carbonate mounds and cold-water coral reefs. Thanks to mound-networking, I had the possibility to participate in a lot of these expeditions. In this way, I would like to thank all the people who gave me these possibilities to broaden my horizons, and especially the scientific shipboard parties of the Géosciences 123 cruise aboard the R/V Marion Dufresne in September 2001, the Polarstern ARK/XIX3a cruise in June 2003, the GAP (SO 175) cruise aboard the R/V Sonne in December 2003, the M61/3 campaign aboard the R/V Meteor in June 2004, the Poseidon 325 expedition in July 2005 and the series of expeditions aboard the R/V Belgica in 2003, 2004, 2005, and 2006.

My port of registry during my PhD was RCMG, and I would like to thank all the inhabitants of RCMG for the nice time spend together. Deevit introduced me to the Porcupine Seabight and all kind of drift stories. Davy, my office mate during the last years, and Lieven, my previous office mate, created always a nice working atmosphere in the office and endured my endless phone calls or discussions. Peter helped me through all kind of problems at the interface between science and engineering, from swell-filtering seismic data sets over time series analysis to multibeam problems. Our "project" and "support" manager, Marc Faure, was an expert in solving (A)SAP problems, sorting out financial chaos and administrative problems and this always with a big smile. The engineers, Koen and Jeroen, were always there to sort practical things out, from sending boxes and arranging vans to the technical developments of the new ROV GENESIS. Wim solved each computer problem. The North-Sea women (Vera, Els, Kristien, and Isabelle) and former North-Sea man (Samuel) gave me useful advice concerning box coring, grain size analysis and sediment dynamics. Pieter liked intensive discussions and was supporting new ideas concerning carbonate mounds. Tist noticed each new scientific outcome and provided me with some nice references. Hans helped me with the magnetic measurements in Dourbes and his nice West-Flemish sounds will be remembered. Thanks also to Annelies, Heleen and Mieke, who did parts of their MSc work in the neighbourhood of the carbonate mounds and are nowadays still involved in ocean research. I also would like to thank all the other RCMG colleagues and the palaeo-neighbours for the nice moments and chats around the kitchen table and the great cake-and-party-hours.

While roaming around the world, I got introduced to the international "carbonate mound-clan" for young scientists, which is still growing and expanding each year. Thanks a lot Boris, Andres, Tim, Veerle, Ben, Juergen, Max, Claudia, Morten, Henk, Kai, Furu, Stephanie, Andy, Matthias, Alina, Agostina, Lydia, Stephan, Sascha, Cees, Markus, Hans, Mieke, Rory, Jaceck, Nina, Laura, Lies, and the whole bunch. I could always phone or mail you with new questions or discussion topics. Without you, mound research was not what it is nowadays! Especially, a more than "big" thank you for my "sister-soul" Veerle. She was standing behind me since the start of my work at RCMG as undergraduate until the end, was always there for nice discussions or just a chat and made it to read carefully through this PhD work by giving helpful and constructive comments. And last but not least, Andres, you started to play a major role in my life from the defense of my PhD on. More than thanks a lot to read again carefully with all your patience and eye for detail through these written pages.

Each globetrotter has its roots and I never forgot my "home-place" wherever I was crossing around. Family and friends, you can not survive without! Always there were friends to play some music, go for a climb or a mountain bike trip, have a nice chat or sit together around a party game. My two sisters, Katrien and Marjan, gave me the right "pep-talk" on the right moments. Also, Bart and recently Stan were always there. My parents and grand-parents provided a safe and cozy home-place where I was welcome at each time of the day or night. Whenever or wherever I was in troubles, they saved me from the crisis situation by arranging everything, from airport-shuttle-services to food-supply. Thanks mum, for all your presence and the

survival food packages! Thanks dad, for having tried to understand what I was doing during the last years and for giving me your positive and constructive criticism from a professional teacher's viewpoint. Godfather and granddad pepe, I appreciated it enormously that you were more than interested in my research work and that I could always come to see you for a serious talk: gratias ago vos! This book is dedicated to you.

Finally, I would like to emphasize that this work is far away from being complete. There are still a lot of questions left and many points can be discussed. However, I would be most delighted if the present volume stimulates further discussions and opens some new perspectives in the wide field of carbonate mound research.

Leuven, Belgium Anneleen Foubert

Acknowledgment

This work is the PhD Thesis of Anneleen Foubert, defended May 15th, 2007 at Ghent University, Belgium, under the supervision of Prof. J.-P. Henriet. FWO-Flanders is sincerely acknowledged for funding this PhD work, and therefore raising the anchor of this research project focusing on carbonate mounds. The results obtained during this study frame within the FWO GeNesis, ESF Euromargins MoundForce, ESF EuroDiversity MiCROSYSTEMS, EU FP5 EURODOM and EU FP6 HERMES programmes. The IODP Expedition 307 scientific party is gratefully acknowledged.

Trevor Williams, Lamont-Doherty Earth Observatory, Palisades, New York, USA; Akihiro Kano, Department of Earth and Planetary Systems Science, Hiroshima University, Japan; Timothy Ferdelman, Max Planck Institute of Marine Microbiology, Bremen, Germany; Jean-Pierre Henriet, Universiteit Gent, Belgium; Kohei Abe, University of Tsukuba, Japan; Miriam S. Andres, Rosenstiel School of Marine and Atmospheric Science, University of Miami, Florida, USA – Current affiliation: Chevron, San Ramon, California, USA; Morten Bjerager, University of Copenhagen, Copenhagen, Denmark – Current affiliation: Geological Survey of Denmark and Greenland (GEUS), Copenhagen, Denmark; Emily L. Browning, University of Massachusetts, Amherst, USA; Barry A. Cragg, Cardiff University, UK; Ben De Mol, Universitat de Barcelona, Spain; Boris Dorschel, University College Cork, Ireland; ∗Anneleen Foubert, Universiteit Gent, Belgium – Current affiliation: Department of Earth and Environmental Sciences, Katholieke Universiteit Leuven, Belgium; Tracy D. Frank, University of Nebraska, Lincoln, USA; Yuji Fuwa, Toyama University, Japan; Philippe Gaillot, Japan Agency for Marine-Earth Science and Technology (JAMSTEC), Yokohama, Japan; Jamshid J. Gharib, University of Hawaii at Manoa, Honolulu, USA; Jay M. Gregg, Oklahoma State University, Stillwater, USA; Veerle Ann Ida Huvenne, National Oceanography Centre, Southampton, UK; Philippe Léonide, Université de Provence, Marseille, France; Xianghui Li, Chengdu University of Technology, Chengdu, Peoples Republic of China; Kai Mangelsdorf, GeoForschungsZentrum Potsdam, Germany; Akiko Tanaka, Geological Survey of Japan, Tsukuba, Japan; Xavier Monteys, Geological Survey of Ireland, Dublin, Ireland; Ivana Novosel, Rice University, Houston, Texas, USA; Saburo Sakai, Japan Agency for Marine-Earth Science and Technology (JAMSTEC), Yokohama, Japan; Vladimir A. Samarkin, University of Georgia,

Athens, USA; Keiichi Sasaki, Kanazawa Gakuin University, Kanazawa Ishikawa, Japan; Arthur J. Spivack, University of Rhode Island, Narragansett, USA; Chizuru Takashima, Department of Earth and Planetary Systems Science, Hiroshima University, Japan; Jürgen Titschack, Geozentrum Nordbayern, Friedrich-Alexander-Universität Erlangen-Nürnberg, Germany. Takashima, Hiroshima University, Japan; Jürgen Titschack, Universität Erlangen-Nürnberg, Erlangen, Germany.

Leuven, Belgium — Anneleen Foubert*
Ghent, Belgium — Jean-Pierre Henriet

Contents

List of Specific Abbreviations and Units

AF	Alternating-Field
AI	Atlantic Inflow water
AMS	Anisotropy of Magnetic Susceptibility
APC	Advanced Piston Corer
ASTM	American Society for Testing and Material
AUV	Autonomous Underwater Vehicle
AWI	Alfred-Wegener-Institut für Polar- und Meeresforschung
BP	Before Present
BCR	IODP Bremen Core Repository
BHA	Bottom Hole Assembly
BIIS	British-Irish Ice-Sheets
CAT	Computer Axial Tomography
CT	Computer Tomography
DC	Direct-Current
DSDP	Deep Sea Drilling Program (former program IODP)
ENAW	Eastern North Atlantic Water
ESF	European Science Foundation
EU	European Union
Exp.	Expedition
FP	Framework Programme
GAD	Geocentric Axial Dipole
GIS	Geographical Information System
GRA	Gamma-Ray Attenuation densiometry
HE	Heinrich Events
HOV	Human Occupied Vehicle (or submersible)
IFREMER	Institut Français de Recherche pour l' Exploitation de la Mer
IGRF	International Geomagnetic Reference Field (2005)
IRD	Ice Rafted Debris
KMI	Koninklijk Meteorologisch Instituut, Belgium
LGM	Last Glacial Maximum
IRE	Ice Rafting Events
MARUM	Center for Marine Environmental Sciences, Bremen, Germany
MIS	Marine Isotopic Stages

ML	Mediterranen Lower Core
MOW	Mediterranean Outflow Water
MP	Mound Province
MPR	Mid-Pleistocene Revolution
MS	Magnetic Susceptibility
MSCL	Multi Sensor Core Logger
MST	Multi Sensor Track
MU	Mediterranean Upper Core
MV	Mud Volcano
NACW	North Atlantic Central Water
NADW	North Atlantic Deep Water
NASW	North Atlantic Superficial Water
NIOZ	Koninklijk Nederlands Instituut voor Onderzoek der Zee
NGR	Natural Gamma Ray measurement
NRM	Natural Remanent Magnetization
NSDW	Norwegian Sea Deep Water
(I)ODP	(Integrated) Ocean Drilling Program
PCA	Principal Component Analysis
PDE	Pen Duick Escarpment
PWL	P-Wave Velocity Logging
RCB	Rotary Core Barrel
RCMG	Renard Centre of Marine Geology, Gent, Belgium
ROV	Remotely Operated Vehicle
R/V	Research Vessel
SEC	Shelf Edge Current
SEM	Scanning Electron Microscope
SQUID	Superconducting Quantum Interference Device
TOBI	Towed Ocean Bottom Instrument
TWT	Two-Way Traveltime
VRM	Viscous Remanent Magnetization
XCB	Extended Core Barrel
XRD	X-Ray Diffraction
XRF	X-Ray Fluorescence

2D	two-dimensional
3D	three-dimensional
Ma	10^6 years
ka	10^3 years
dpi	dots per inch
mbsf	metres below sea-floor
cps	counts per second
psu	practical salinity units

Chapter 1
Of Mounds and Cold-Water Corals

During the last 15 years, occurrences of large mound clusters have increasingly been reported along the Northeastern Atlantic margins. These mound structures are in many cases covered with cold-water corals, suggesting an enigmatic relationship between cold-water coral growth and the development of such mounds. The growth of cold-water corals and the origin of recent deep-water carbonate mounds was a heavily debated subject during the last decade. Different theories were invoked concerning cold-water coral growth and the development of carbonate mounds. Two main schools developed to explain the origin of recent cold-water coral reefs and carbonate mounds. One school is mainly based on internal controls whereby light hydrocarbon seepage would play an important role in the initial phase of reef and mound growth (Hovland 1990, 1994, 1998; Hovland and Thomsen 1997; Henriet et al. 1998, 2001). The second school relies on the impact of external and environmental controls, such as favourable oceanographic conditions, on cold-water coral growth and so mound build-up (e.g. Freiwald et al. 1997, 1999; Freiwald and Wilson 1998; Mortensen 2000; De Mol et al. 2002; Duineveld et al. 2004; Mienis et al. 2007; Dullo et al. 2008).

A cluster of European research programmes were set up in the wake of these debates. Under the EU concerted action CORSAIRES and the EU project ENAM II (European North Atlantic Margin), the base was laid for recent mound and cold-water coral research in some well-delineated areas. Within the EU 5th framework programme, a first clustered triptych of EU projects was born: GEOMOUND, ECOMOUND and ACES, focusing respectively on the internal controls on mound build-up, on the external and environmental controls on mound development and on the Atlantic coral ecosystems. These projects teamed up to propose a major Ocean Drilling Program action: the "Modern Carbonate Mounds: Porcupine Drilling" project. In 2005, this drilling proposal turned into reality during Integrated Ocean Drilling Program (IODP) Expedition Leg 307 "Modern Carbonate Mounds: Porcupine Drilling" aboard the R/V JOIDES Resolution. Mound research was continued within the FP5 Research and Training Network EURODOM and the ESF EUROMARGINS project MOUNDFORCE (Forcing of Carbonate Mounds and Deep Water Coral Reefs along the NW European Continental Margin). Under the EU 6th framework programme, a new impetus to cold-water coral and carbonate mound research was given in the integrated research project HERMES (Hotspot

A. Foubert, J.-P. Henriet, *Nature and Significance of the Recent Carbonate Mound Record*, Lecture Notes in Earth Sciences 126, DOI 10.1007/978-3-642-00290-8_1,

Ecosystem Research on the Margins of European Seas), followed up recently under the EU 7th framework programme by HERMIONE (Hotspot Ecosystem Research and Man's Impact on European Seas). The ESF-funded EURODIVERSITY project MICROSYSTEMS, focuses on the recently discovered carbonate mounds along the Moroccan margin (see Chap. 8). The ESF EuroMARC project CARBONATE mainly compares mound structures in different margin settings (Norwegian margin, Rockall Trough, Moroccan margin and Mauretanian margin). New research initiatives are still raising, bringing European cold-water coral and mound research to a wider transatlantic community (TRACES – Trans-Atlantic Coral Ecosystem Study) and bridging gaps between the academic and the industrial world (COCARDE – Cold Water Carbonate Reservoir Systems in Deep Environments).

The phenomenon of on the one hand deep-water carbonate mound systems and on the other hand cold-water coral systems, encountered nowadays along the European and Northwest African continental margins, will be presented in this introductory chapter. The aim of this study will be framed within the light of recent mound and cold-water coral research. Relationships between the cold-water coral world and the mound world will be highlighted in the following chapters.

1.1 Recent Carbonate Mounds

1.1.1 From Ancient Mud Mounds to Recent Carbonate Mounds

A first comprehensive review about ancient carbonate mud mound systems was edited by Monty et al. (1995) as follow-up of the special symposium on "Carbonate mud mounds" organized on the International Sedimentological Congress (ISC) in 1990: "Carbonate mud mounds: their origin and evolution". A special issue focusing on mud mounds was published in 1995 in Facies (Flajs et al. 1995): "Mud mounds: a polygenetic spectrum of fine-grained carbonate build-ups". As follow-up of a theme session focusing on carbonate mounds for the 1999 Annual Meeting and Exposition of the Geological Society of America in Denver (US), a special volume was published in Sedimentology 'Carbonate mounds: sedimentation, organismal response, and diagenesis', edited by Kopaska-Merkel and Haywick. Together, the 13 papers comprising this special volume provide an important and comprehensive collection of descriptive data and interpretation of mound formation throughout the past (Kopaska-Merkel and Haywick 2001). The authors decided to use the term carbonate mound instead of mud mound, to avoid the controversial discussion about the amount of mud effectively present in such systems. At the 32nd International Geological Congress in Italy (Florence, 2004) in the session "Reef and carbonate platform sedimentation", Bourque et al. (2004) gave an updated review about ancient mud mound systems: "The mud mound system: products and processes". Vennin et al. (2007) discusses the facies of Palaeozoic reefs and bioaccumulations (including mound systems) from a wider perspective and on a global scale, while Phanerozoic reef patterns (including some specific mound systems) are reviewed

in a special SEPM (Society for Sedimentary Geology) publication (Kiessling et al. 2002). Below a brief overview is given about mud mound evolution through time, mainly based on the works of Monty et al. (1995), Bosence and Bridges (1995), and Bourque et al. (2004). For a more extensive review on ancient mound systems the reader is referred to the works mentioned above.

During the Late Precambrian, mounds are mainly microbial and constructed largely by non-calcified microbes without higher algae or fauna (Bosence and Bridges 1995). The Proterozoic experienced a development of stromatolites unique in terms of size and diversity, and interpreted as the first microbial mounds (Monty 1995). However, in the Late Precambrian, stromatolites progressively declined for reasons which are not yet fully understood, although successive glaciations may have played an important role in this decline (Monty 1995). The Late Riphean (800–700 Ma) is also marked by a most important event, i.e. the rise of calcified cyanobacteria (Knoll and Swett 1990) which, in collaboration with bacteria, played an important role in the development of mud mounds. During the Palaeozoic, especially in Cambrian and Ordovician times, microbial and biodetrital mud mounds rapidly diversify and feature a range of microbial, stromatactoid and biodetrital fabrics with abundant mound-building calcified microbes, calcified coralline and green algae and diverse Palaeozoic benthic invertebrates (Bosence and Bridges 1995). In Middle to Late Ordovician times, the increase in large skeletal metazoans such as stromatoporoids, corals (rugosa and tabulata) and bryozoans as well as higher algae paved the way for the strong development of reefs and typical stromatactoid mud mounds. Upper Ordovician carbonate mounds have been reported in the subsurface of Gotland and in the submarine areas off Gotland (central Baltic Sea, Sweden) (Bergstrom et al. 2004; Sivhed et al. 2004). Late Ordovician microbial mud mounds and Early Silurian reef constructions occur at the western margin of the Yangtze Platform (South China) (Yue and Kershaw 2003). Silurian carbonate mud mounds are also reported in the southern Sichuan Basin in Central China (Zhao et al. 2006). More well-known are the Lower Devonian Kess Kess Mounds situated in the eastern Anti-Atlas of southern Morocco (Roch 1934; Massa et al. 1965; Belka 1998; Mounji et al. 1998; Joachimski and Buggisch 1999; Peckmann et al. 1999, 2005; Aitken et al. 2002). Reefal and mud mound facies are also developed in the Lower Devonian La Vid Group at the Colle outcrops in the north-western part of Spain (Leon Province, Cantabrian zone) (Fernandez et al. 2006). The Belgian Frasnian (Upper Devonian) is famous for its carbonate mounds, known as "récifs rouges" (Bourque and Boulvain 1993; Monty 1995; Boulvain et al. 2004; Da Silva and Boulvain 2004). Waulsortian-type (Early Carboniferous) banks or build-ups are well-studied in Belgium, Ireland and the English Midlands, but are also known in North America (e.g. New Mexico), Central Asia and possibly North Africa (Dorlodot 1909; Lees and Miller 1995). One of the most distinctive features of Waulsortian banks is the occurrence of a sequence of generations of mud development (polymuds) (Lees and Miller 1995). Macro-skeletal components are mainly crinoids, bryozoans and brachiopods. The Permo-Triassic produced mud mounds of different composition, including newly evolved calcisponges, microbial crusts and sessile foraminifera coated by microbial encrustations (Pratt 1995). A decline in the

abundance and diversity of microbial mounds is recorded from the Triassic to the Cretaceous (Bosence and Bridges 1995). The Mesozoic mounds differ from their Palaeozoic ancestors in the calcified algae, rudists and corals involved in mound construction and the associated mound faunas (Bosence and Bridges 1995). From the Mid Cretaceous onwards microbial fabrics are only known as components to metazoan framework reefs, as documented by Pratt (1995), and would not be found in mud mounds (Bosence and Bridges 1995). Most Cenozoic mud mounds would be of biodetrital origin (Monty 1995), however according to Pratt (1995) microbial components might have remained significant in deeper water.

1.1.2 Occurrence and Distribution of Recent Carbonate Mounds

The discovery of actual reef and mound growth in deep-water settings set off in 1948 when Le Danois described so-called "massifs coralliens" as occurring at well-delineated locations along the European continental margins. Stetson and Squires (1962) mapped a large cluster of over 200 mounds, described as coral banks, on the outer rim of Blake Plateau, off the North American East coast in water depths of 700 to 900 m. Neumann et al. (1977) described elongate coral bioherms, called "lithoherms", in water depths of several hundred metres, axially aligned with the flow field of the Florida current. Mainly single lithoherms have been found there, but also a mound cluster 4.4 km long, 600 m wide and 150 m high (Paull et al. 2000). As the offshore oil industry steadily moved into deeper waters, more and more occurrences of large build-ups or mounds were discovered on geophysical data sets along the continental margins. The "kick-off" for the intensive study of deep-water carbonate mounds along the European Atlantic continental margins, was a paper of Hovland et al. published in 1994, which described a set of "carbonate knolls", seen on seismic profiles, in Porcupine Seabight SW of Ireland. Soon new discoveries of mounds were reported, following several industrial and scientific surveys. Nowadays different mound provinces have been mapped along the European and Northwest African continental margins (Fig. 1.1). However, just a few mound provinces have been studied in detail until now.

Giant mounds occur in Porcupine Seabight, SW of Ireland, clustered in three mound provinces (Hovland et al. 1994; Henriet et al. 1998, 2001, 2002; De Mol et al. 2002; Huvenne et al. 2002, 2003; De Cock 2005; Van Rooij et al. 2007c): (1) the Belgica Mounds occurring in water depths between 550 and 1030 m and the associated buried Enya Mounds, (2) the Hovland Mounds in water depths ranging from 400 to 1100 m and the associated buried Viking Mounds, (3) and the Magellan Mounds located in water depths around 650 m. Well-known mound provinces are noted in the Rockall Trough, which are very comparable to those in the Por-

Fig. 1.1 (continued) (**D**) Pelagia Mounds along the north-western flank of Porcupine Bank, (**E**) Logachev Mounds on the south-eastern slope of Rockall Bank, (**F**) mounds on the western Rockall Bank, (**G**) small-scaled Darwin Mounds, (**H**) small coral thickets on Galicia Bank, (**I**) mounds in El Arraiche mud volcano field (Moroccan margin), (**J**) mounds on Hatton Bank

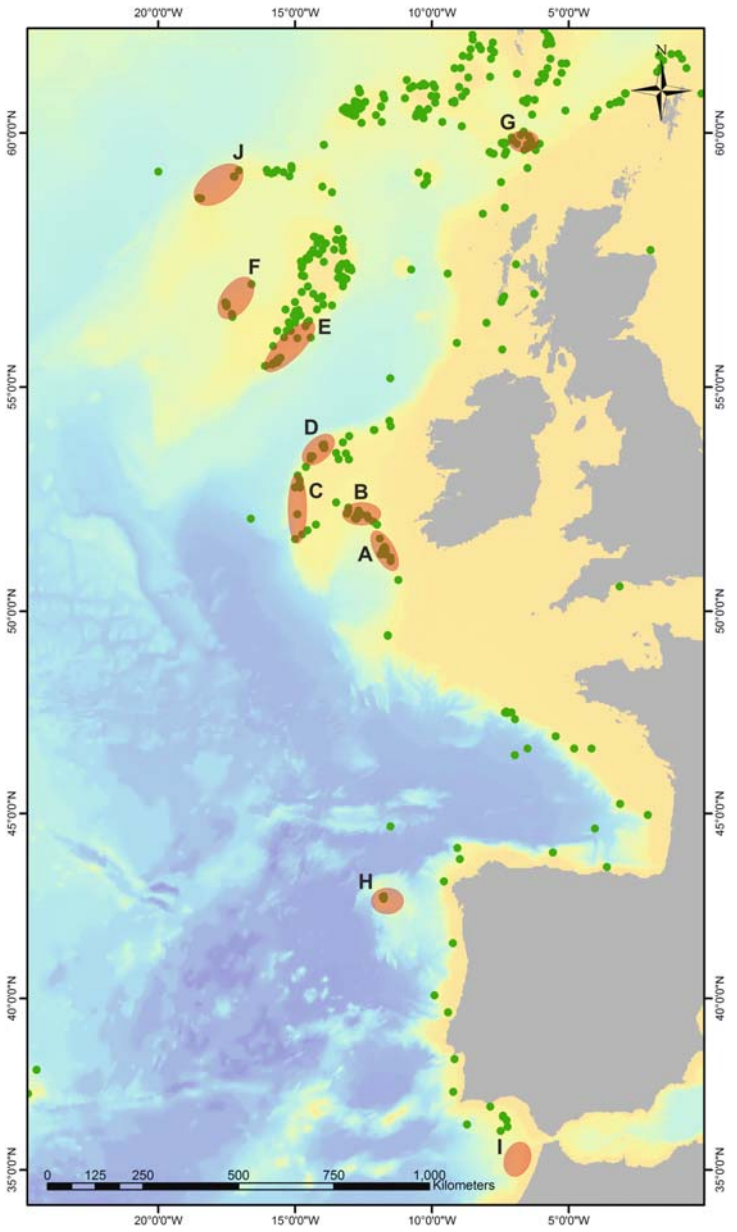

Fig. 1.1 Location of the most important carbonate mound provinces and small mound patches (*red ellipses*) and distribution of the cold-water coral species *Lophelia pertusa* (*green dots*) (http://www.searchnbn.net/hosted/ospar/ospar.html; Wisshak et al. 2006) along the European and Northwest African continental margins plotted on bathymetric map (GEBCO bathymetry). (**A**) Belgica Mound Province and associated buried Enya Mounds at the eastern margin of Porcupine Seabight, (**B**) Magellan, Hovland and Viking Mound Provinces at the northern margin of Porcupine Seabight, (**C**) Porcupine Bank Canyon Mounds at the western margin of Porcupine Bank,

cupine Seabight. Several mound groups are present on the flanks of Rockall Bank and Hatton Bank but most of them are not well studied yet (Unnithan et al. 2003; Roberts et al. 2008). Worth to mention is the mounds on the western Rockall Bank, including mounds such as the recently studied Franken Mound around 680 m water depth at the south-western slope of Rockall Bank (Wienberg et al. 2008; Ratmeyer et al. 2006). Better studied are the Logachev Mounds on the south-eastern slope of the Rockall Bank, forming a very complex and nearly continuous system of conical mounds and interconnected ridges, set between 600 and 800 m water depth (Akhmetzhanov et al. 2003; Kenyon et al. 2003; van Weering et al. 2003; Mienis et al. 2006). At the other side of the Rockall Trough, the Pelagia Mounds occur along the north-western flank of Porcupine Bank and the Porcupine Bank Canyon Mounds, at the western margin of Porcupine Bank. Both are located in water depths of ca. 800 m (Akhmetzhanov et al. 2003; Kenyon et al. 2003; van Weering et al. 2003; Wheeler et al. 2005a). Towards the north of the Rockall Trough, close to the Wyville-Thomson Ridge, another group of much smaller mound structures is observed, named the Darwin Mounds (Masson et al. 2003; Huvenne et al. 2008; Wheeler et al. 2008). Small coral thickets are present on Galicia Bank (offshore NW Spain) around 500 m water depth (Duineveld et al. 2004). Carbonate mounds and small mound patches have been also reported along the Northwestern African margins. Mound structures were discovered along the Moroccan margin in the El Arraiche mud volcano field in water depths about 600 m (Van Rensbergen et al. 2005a; Foubert et al. 2008). More to the south, carbonate mounds are mapped off Mauritania at approximately 450–550 m water depth (Colman et al. 2005) and along the Angola margin at a depth of 340 m (Le Guilloux et al. 2009).

Along the Norwegian margins different reef complexes have been described, but they do not have the same characteristics as the giant mound clusters observed at lower latitudes (Fig. 1.2). One of the largest reef complexes is the Sula Ridge Complex at 64°N measuring 14 km by 350 m with single mounds of maximum 25 m high (Freiwald et al. 2002). In the Stjernsund fjord (70°N), the Stjernsund Reef has been described, formed on the sill at the fjord entrance at a water depth of 260–235 m (Freiwald et al. 1997). Røst Reef is a reef-complex 35–40 km long, up to 3 km wide. It lies between mainly 300 and 400 m water depth in a steep and rugged part of the continental shelf break along the Norwegian margin (Fosså et al. 2005). In addition to the mentioned giant reef frameworks, much smaller reefs are reported in Norwegian and Swedish waters, f.e. Iveryggen Reef, Tisler Reef, Fjelknausene Reef, Selligrunen Reef, Fugløy Reefs, Traena Reefs, Leksa Reef, and Säcken Reef (Hovland and Mortensen 1999; Fosså et al. 2005; Ottesen et al. 2005; Wisshak et al. 2005).

It has to be mentioned that the most important metazoans associated with these recent carbonate mounds and reef frameworks are azooxanthellate colonial stone corals (Scleractinia, Anthozoa). However, the presence of Sponge reefs in the Queen Charlotte Basin (British Columbia) at water depths of 165–240 m evidence that also other organisms can play an important role in mound and reef forming processes (Conway et al. 2005). Moreover, carbonate mounds are also nowadays occurring in the Mediterranean Sea, in the western Atlantic, on the Brazilian margins, etc. . .

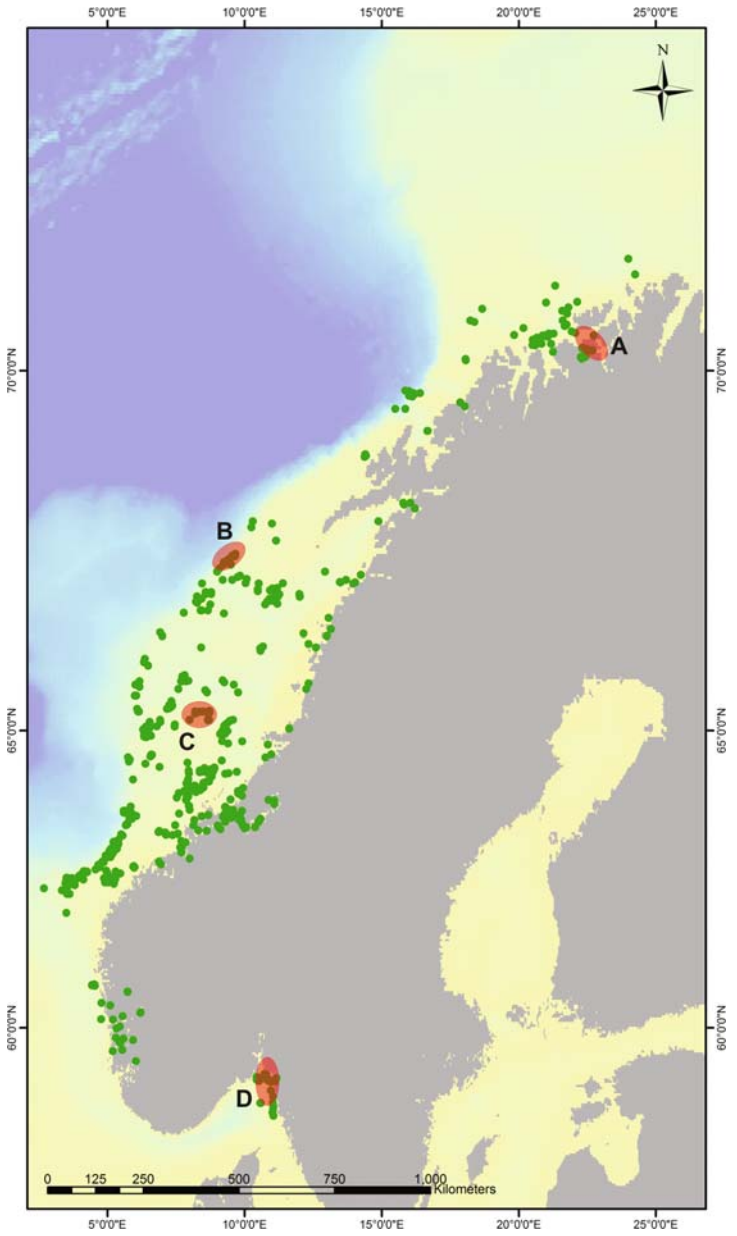

Fig. 1.2 Location of the most important cold-water coral reef frameworks (*red ellipses*) and distribution of the cold-water coral species *Lophelia pertusa* (*green dots*) (http://www.searchnbn.net/hosted/ospar/ospar.html; Wisshak et al. 2006) along the Norwegian margins plotted on GEBCO bathymetry. (**A**) Stjernsund Reef, (**B**) Røst Reef (**C**) Sula Reef Complex and, (**D**) eastern Skagerrak Reefs

but the study of those mound systems lies behind the scope of the present volume focusing on the European and Moroccan Atlantic margins.

Despite the increasing knowledge about the presence of carbonate mounds in deep-water settings, recent reviews about modern carbonate settings still barely incorporate carbonate mounds in an adequate way. An overview of the cool-water carbonate depositional realm is given by James and Clarke (1997), but they do not touch specifically the recent carbonate mounds. Flügel (2004) mentioned in his extensive review "Microfacies of Carbonate Rocks", the potential importance of recent "deep-water and cold-water coral reefs" with emphasis on the term "reef", while recent "deep-water carbonate mounds" are not mentioned. This can be due to name confusion, as discussed in Chaps. 3 and 9. It should be mentioned that cold-water coral reefs and carbonate mounds are not synonymous, and not everywhere where cold-water corals are growing, giant carbonate mounds or extensive reef frameworks are observed.

1.2 Cold-Water Corals

An extensive state-of-the-art review about cold-water corals and their associated ecosystems is given in the volume "Cold-water Corals and Ecosystems" edited by Freiwald and Roberts (2005) as follow-up of the 2nd International Symposium on Deep-Sea Corals held in Erlangen (Germany) in September 2003. Recently, two additional books were published, respectively 'Cold-Water Corals: The Biology and Geology of Deep-Sea Coral Habitats' (Roberts et al. 2009) and 'Deep-water Coral Reefs: Unique Biodoversity Hot-spots' (Hovland 2008), both emphasizing the unique habitats and the biodiversity of such reef systems. A more popular review about the subject is given in a report published by the United Nations Environment Programme (UNEP) – World Conservation Monitoring Centre (WCMC): "Cold-water Coral Reefs" (Freiwald et al. 2004). A short and summarized overview about cold-water coral ecosystems is given by Roberts et al. (2006).

The most common framework building cold-water coral species inhabiting the present deeper and colder waters of the NE Atlantic Ocean is *Lophelia pertusa* while *Madrepora oculata* is the second most reported species (e.g. Le Danois 1948; Teichert 1958; Wilson 1979a; Zibrowius 1980; Rogers 1999; Freiwald 2002) (Fig. 1.3). Other important cold-water coral species in the NE Atlantic are *Desmophyllum* spp., and *Dendrophyllia* spp. (Le Danois 1948; Zibrowius 1980).

The coral *Lophelia pertusa* is part of the functional group described as "azooxanthellate or ahermatypic scleractinian corals". They do not need symbiosis with zooxanthellate algae to survive, and hence they can occur at greater depths than the typical tropical corals, in a world where light penetration is very limited or non-existent (Teichert 1958). The azooxanthellate monotypic *Lophelia pertusa* was first described from the NE Atlantic in the mid 18th century by Linnaeus (1758) but is also reported in other works around the same time period (Pontoppidan 1755; Gunnerus 1768). The systematic taxonomic classification of the coral is given by

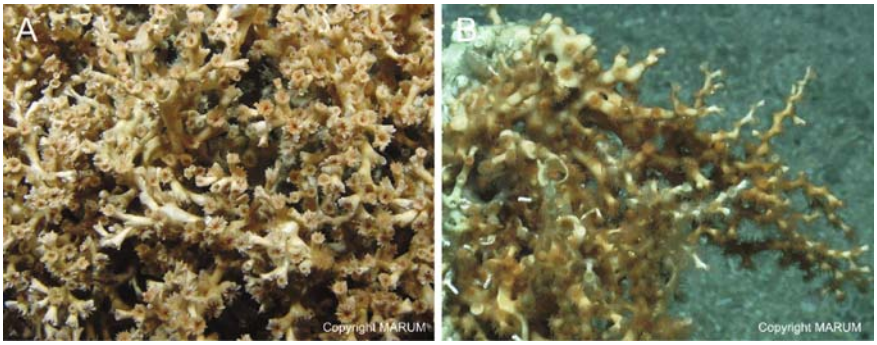

Fig. 1.3 ROV imagery visualizing the cold-water coral species *Lophelia pertusa* (**A**), and *Madrepora oculata* (**B**). Imagery copyright MARUM (University Bremen)

Zibrowius (1980). *Lophelia pertusa* forms bush-like colonies measuring several metres across and consisting of thousands of coral polyps (Fig. 1.3).

Lophelia pertusa is a cosmopolitan species and the full extent of its present geographic distribution is still unknown (Figs. 1.1 and 1.2). Overview maps have been compiled regularly since a long time (e.g. Pratje 1924; Le Danois 1948; Teichert 1958; Rogers 1999; Freiwald et al. 2004; Wisshak et al. 2006; Wheeler et al. 2007). The highest occurrence is recorded along the eastern Atlantic margin down to West Africa (Freiwald et al. 2004), but its presence is also noted in the NW Atlantic Ocean (Cairns 1979; Messing et al. 1990), Pacific Ocean (Durham 1947; Cairns 1982, 1995; Farrow and Durant 1985), Indian Ocean (Grygier 1990) and Mediterranean Sea (Zibrowius 1980). The northernmost *Lophelia* occurrence known is in the southwestern Barents Sea near Hjelmsøybank (71°21′N) (Fosså et al. 2000), while the southernmost location is the subantarctic Macquarie Ridge off New Zealand (51°S) (Cairns 1982). The shallowest occurrence of live *Lophelia pertusa* is recorded at 39 m water depth from the Trondheimsfjord, mid Norway, and the deepest from the New England seamount chain in the North Atlantic, at 3383 m, and off Morocco, at 2775 m (Zibrowius 1980). Most of the corals are found on the shelf break and the upper bathyal zone of the continental margins, although they have been reported from the slopes of seamounts, mid-ocean ridges, artificial structures and especially fjords as well (Rogers 1999). The oldest fossil *Lophelia* was found at the Gulf Coast, and dates from the Eocene (Squires 1957). Late Miocene deep-water structures built by Lophelia were found in New Zealand (Squires 1964) while from the Pliocene onwards (after the Messinian Event), *Lophelia* invaded the Mediterranean (Freiwald 1998). Its first appearance in Norwegian waters is estimated at ca. 10 ka ago (Henrich et al. 1996).

Hydrographic conditions and the geomorphology of the seabed, combined with environmental parameters such as temperature, salinity and nutrient supply, are important factors determining and limiting the distribution and growth of cold-water corals rather than specific depth ranges (Freiwald et al. 2004). *Lophelia pertusa* tolerates temperatures varying between 4 and 13°C and are restricted to depths below

the (seasonal) thermocline (Freiwald et al. 1997; Freiwald 2002). *Lophelia pertusa* tolerates salinity values from as low as 32 psu in Scandinavian fjords to at least 38.8 psu in the Ionian Sea (Strømgren 1971; Taviani et al. 2005a, 2005b). Freiwald (1998) also pointed out that the corals are often located in the depth range of the oxygen minimum zone. Recently, Dullo et al. (2008) have shown that living *Lophelia pertusa* coral reefs occur within the density envelope of sigma-theta (σ_θ) = 27.35 to 27.65 kg m^{-3}, a parameter describing the temperature and salinity conditions and thus highlighting the importance of these parameters for *Lophelia* growth. *Lophelia* corals are generally considered as suspension feeders, so it is most likely that they feed on live plankton and suspended particulate organic matter captured by the polyp tentacles (Messing et al. 1990; Jensen and Frederiksen 1992). Visual observations with a manned submersible and aquaria experiments showed that the polyps of *Lophelia pertusa* prey also upon zooplankton up to 2 cm in size (Mortensen 2001; Freiwald 2002). The quality and availability of nutrients and food particles is one of the most important factors determining the fitness of coral habitats (Freiwald et al. 2004). Cold-water corals are fueled by primary productivity in surface waters and subsequent food transport to the seabed (Duineveld et al. 2004). Growth rates of skeletal linear extension ranging from 5 (Mortensen and Rapp 1998) to 25 mm/y (Mikkelsen et al. 1982; Freiwald et al. 1997; Spiro et al. 2000) have been estimated from analysis of carbon and oxygen stable isotopes. The lifespan of *Lophelia* colonies is not yet known. Mature *Lophelia* colonies can be divided into an upper living zone and a lower dead coral framework zone (Freiwald and Wilson 1998). Through intratenticular budding daughter polyps are formed from parental polyps (Freiwald 1998): the mouth of an existing polyp stretches and constricts to form a second mouth. From there on the whole polyp divides, and a second set of tentacles is formed until the daughter polyp can develop independently. It appears that each new polyp generation coincides with the formation of a new incremental calcareous layer that is secreted around the skeleton of the older polyps belonging to the living zone only and resulting in incremental layers as observed in thin sections (Freiwald et al. 2004). Little is known about the basic sexual reproductive biology of cold-water corals but the studied cold-water corals have separate sexes (gonochoristic) and spawn their gametes in the water column for external fertilization (Waller 2005). Gametogenesis seems to be seasonally controlled for the species *Lophelia pertusa*, which might be related in the north-east Atlantic to phytodetritus fall (Waller 2005; Waller and Tyler 2005). It is thought that the larvae of deep-water scleractinians require a hard substratum for settlement to occur (Wilson 1979b; Rogers 1999). Microsatellite and ribosomal internal described spacer sequence analyses indicate that *Lophelia pertusa* is not a panmictic population in the NE Atlantic but seems to form discrete fjord and shelf populations (Le Goff-Vitry et al. 2004).

The *Lophelia* build-ups and colonies have been proven to be hotspots of biodiversity (Dons 1944; Burdon-Jones and Tambs-Lyche 1960; Jensen and Frederiksen 1992; Fosså and Mortensen 1998; Fosså et al. 2000; Rogers 1999; Freiwald et al. 2004). Mortensen and Mortensen (2004) wrote a comprehensive summary about symbiosis in deep-water corals. More than 886 species have been recorded on deep-

water corals by Rogers (1999). Mortensen and Mortensen (2004) cited more than 980 species, while within the framework of the ACES project more than 1317 species have been recorded in cold-water coral habitats (Foraminifera, Cnidaria, Polychaeta, Crustacea, Mollusca, Echinodermata, Brachiopoda, Porifera, Chordata, Hemichordata, Bryozoa, Echiurida). Beck and Freiwald (2005) identified different key-species occurring in typical cold-water coral habitats, built up a biodiversity atlas and suggested a subdivision in small-scaled coral habitats based on the high species diversity.

During the nineties, the advanced exploration of the highly diverse cold-water coral ecosystems with sophisticated camera systems, showed damage and habitat losses in most oceans of the world. Potential sources of threats to cold-water corals are well-documented in the UNEP-WCMC report "Cold-water Coral Reefs" (Freiwald et al. 2004). Human activities threaten these ecosystems in different ways: bottom trawling causes damage, hydrocarbon drilling and seabed mining has potential impacts, cable and pipeline placement can destruct cold-water coral habitats, ocean acidification may influence cold-water coral growth, and bio-prospecting and destructive scientific sampling can have a negative impact on cold-water corals. However, scientists and policy makers are aware of the problem and more and more effort is put into the conservation and protection of these biodiversity hotspots.

1.3 Aim of the Study

Carbonate mounds, observed nowadays along the Atlantic margins of Europe and Morocco, form the main study object of the presented work. This book approaches the recent carbonate mounds from a pure generic viewpoint by focusing in a first part on the nature of one specific carbonate mound. In a second part the significance of the studied mound record is discussed by looking to other carbonate mound records on a regional scale. It has to be mentioned that three previous doctoral works paved the way to make such an approach possible. De Mol (2002) gave a morphological overview of the mounds encountered in Porcupine Seabight by discussing two-dimensional high-resolution seismic data sets. Additional preliminary sample material was used to ground-truth the geophysical data sets and a model was presented to explain the origin and development of carbonate mounds. Huvenne (2003) presented and discussed a set of enigmatic, largely buried mounds, the Magellan Mound Province in the northern Porcupine Seabight, mainly based on geophysical data and with an extra emphasis on the spatial structure of this set of mounds. This full, qualitative, and where possible quantitative, description of a mound province and its surroundings gave more insights in the processes governing the mound phenomenon. Van Rooij (2004) discussed the sedimentological environment surrounding the mounds at the eastern margin of Porcupine Seabight by focusing on different Quaternary sedimentation processes.

The aim of the presented volume is in a first phase to elucidate the internal structure or the "nature" of a recent carbonate mound body: "What are the main

components of a recent carbonate mound?", "How does a recent carbonate mounds transform through early diagenetic processes?", and "How does a carbonate mound develop through time and what are the external controls on its development?". These questions will be discussed in Chaps. 3, 4, and 5, by focusing on the recently drilled Challenger Mound at the eastern margin of Porcupine Seabight, SW of Ireland (Integrated Ocean Drilling Program (IODP) Expedition Leg 307). The first results form IODP Expedition Leg 307 were published in "Proceedings of the Integrated Ocean Drilling Program, Volume 307: 'Modern Carbonate Mounds: Porcupine Drilling'" (Ferdelman et al. 2006). A first comprehensive summary of the outcome of IODP Expedition Leg 307 was presented in Eos Transactions "Cold-Water Coral Mounds Revealed". Chapter 2 frames Challenger Mound in its environmental context. Chapter 3 elucidates the internal composition of Challenger Mound. The main components of the mound are discussed and visualized by combining traditional descriptive techniques with new imaging tools. The geochemical and geophysical properties of Challenger Mound are presented in Chap. 4. Chapter 5 approaches the mound from a magnetic viewpoint to frame Challenger Mound in a magnetostratigraphic context.

In a second phase, the significance of the recent carbonate mound record is discussed, by studying other carbonate mounds in the same region and comparing on-mound records with off-mound records (Chap. 6), and by describing a new province of carbonate mounds in a completely different oceanographic and geological setting along the Moroccan margin (Chap. 8). Chapter 7 focuses on surface processes encountered nowadays at the sea-floor on top of and in between the carbonate mounds in Porcupine Seabight.

Chapter 9 summarizes the conclusions, discusses the role of Challenger Mound as a potential carbonate factory within the light of recent deep-water reef and mound settings, and touches the controversial topic of recent carbonate mounds as analogues for ancient mud mounds. The chapter is closed by a brief "look-ahead".

Chapter 2
Challenger Mound: A Case Study

The presence of giant carbonate mounds along the NE Atlantic continental margin is already known since 1994 (Hovland et al. 1994; Henriet et al. 1998; De Mol et al. 2002; Kenyon et al. 2003; van Weering et al. 2003). These mound structures have been the target of several cruises during the last decade, resulting in extensive data sets placing the carbonate mounds in their environmental and geological context. However, none of these cruises unveiled the internal structure of a carbonate mound and only the upper few metres could be sampled by gravity coring.

During IODP Expedition Leg 307 "Modern Carbonate Mounds: Porcupine Drilling" aboard the R/V JOIDES Resolution, a recent carbonate mound was drilled for the first time in history. At last, the full body of a carbonate mound could be sampled. Challenger Mound, one of the prominent elongated conical mound structures localized at the eastern margin of Porcupine Seabight SW of Ireland, was chosen as key site. The Porcupine Seabight is an amphitheatre-shaped embayment in the Atlantic Irish shelf, enclosed by four shallow platforms: Porcupine Bank on the western side, Slyne Ridge in the north, the Irish Mainland Shelf in the east and Goban Spur in the south (Fig. 2.1B). Only a relatively small opening towards the deeper North Atlantic basin is present in the southern part. Porcupine Seabight is known as the cradle of recent mound research. More than 1600 mounds are estimated to occur in this basin, mainly clustered in three well-delineated mound provinces (Fig. 2.1B): (1) the Belgica Mound Province at the eastern margin (De Mol et al. 2002), (2) the Magellan Mound Province at the northern edge of Porcupine Seabight (De Mol et al. 2002; Huvenne et al. 2002, 2003) and (3) the Hovland Mound Province immediately S to SE of the Magellan Mound Province (Hovland et al. 1994; De Mol et al. 2002). Recently, two new provinces of mainly buried mounds have been mapped in Porcupine Seabight (Fig. 2.1B): (1) a province SE of the Hovland Mound Province which can be interpreted as a south-eastern prolongation of the Hovland Mound Province, the Viking Mound Province (De Cock 2005) and (2) the Enya Mounds localized SSE of the Belgica Mound Province (Van Rooij et al. 2007c). Challenger Mound belongs to one of the sixty-six mounds encountered in the Belgica Mound Province.

In this chapter the geological evolution of Porcupine Seabight and the geomorphological and oceanographic context of the Belgica Mound Province at the eastern margin of Porcupine Seabight will be described to make the reader familiar with the

A. Foubert, J.-P. Henriet, *Nature and Significance of the Recent Carbonate Mound Record*, Lecture Notes in Earth Sciences 126, DOI 10.1007/978-3-642-00290-8_2,

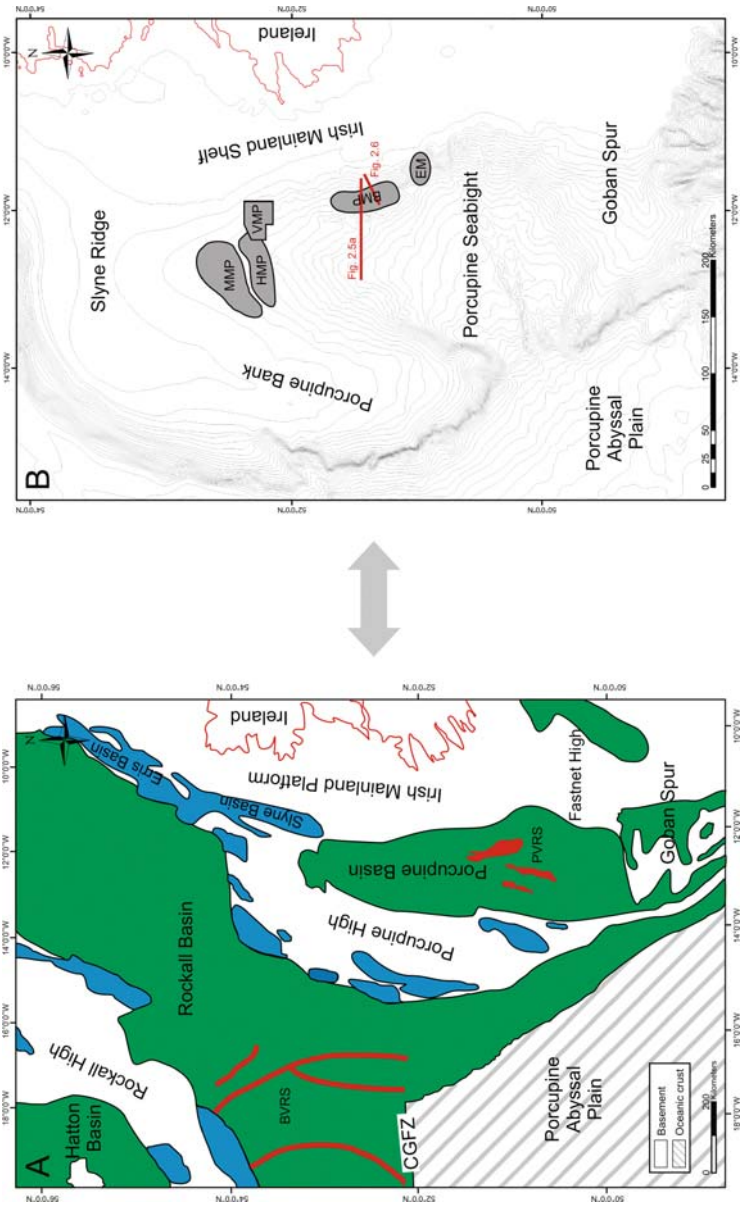

Fig. 2.1 (**A**) Distribution of sedimentary basins in the Irish Atlantic margin region (based on Naylor et al. 1999, 2002 and modified after Shannon et al. 2007). The main geological features of the region are also shown. The "perched" basins, marginal to the Rockall Basin, consisting largely of Permo-Triassic strata, are shown in *blue* while the main depocentres (largely Jurassic to Cenozoic in age) are shown in *green*. The Barra Volcanic Ridge System (BVRS) and the Porcupine Volcanic Ridge System (PVRS) are shown in *red*. CGFZ is the Charlie-Gibbs Fracture Zone. (**B**) Location map of Porcupine Seabight showing the main morphological features in the Irish Atlantic margin region. The locations of the main mound provinces are indicated by grey boxes: MMP is the Magellan Mound Province, HMP is the Hovland Mound Province, VMP is the Viking Mound Province, BMP is the Belgica Mound Province and EM are the Enya Mounds. The locations of the seismic profiles visualized on Figs. 2.5 and 2.6 are noted

environment around Challenger Mound. The primary arguments why Challenger Mound was drilled as template for other mound structures are highlighted. Finally, a technical report is given of the different IODP Holes drilled on the top and flanks of Challenger Mound and its surrounding sediments. These holes form the main study objects throughout Chaps. 3, 4, and 5.

2.1 Site Survey

2.1.1 Geological Evolution of Porcupine Basin

The Atlantic margin to the west of Ireland is underlain by a set of structurally linked sedimentary basins whose evolution extends back to the Late Palaeozoic (Shannon 1991). These basins have a complex development history involving the interplay of rift tectonics, thermal subsidence, igneous activity and oceanographic variations (Shannon et al. 2007). The main basins lying west of Ireland comprise an inner suite of relatively small, narrow, sedimentary depocentres (e.g. Slyne and Erris basins) and an outer (oceanward) set of larger under-filled deep-water basins (Porcupine and Rockall basins and Goban Spur) (Fig. 2.1A).

In the following paragraphs the tectonostratigraphic evolution of Porcupine Basin will be discussed to place the distribution of the carbonate mound provinces in Porcupine Seabight in their geological context. First, the underlying crustal structure of the basin will be shortly described. In a second paragraph, the tectono-sedimentary development will be presented with emphasis on the Neogene stratigraphy and the sedimentary and oceanographic development of the eastern margin of Porcupine Basin during the Neogene period. In the framework of the EC-funded STRATAGEM project (2000–2003) an integrated, unified stratigraphic framework and a detailed evolution model for the NW European Atlantic margin was developed, including a specific stratigraphic framework for the Porcupine and Rockall margins (Evans et al. 2005). De Mol et al. (2002) and Van Rooij et al. (2003) presented a more detailed seismostratigraphic model based on high-resolution sparker seismics for the Late Cenozoic deposits in the Belgica Mound Province on the eastern margin of Porcupine Seabight. Both models will be presented.

2.1.1.1 Crustal Structure

The basement of Porcupine Basin is composed of Precambrian and Early Palaeozoic metamorphic rocks forming continental crust (Johnson et al. 2001). The basement is often defined as pre-Hercynian (Croker and Shannon 1987). NE-SW directed trends in the Porcupine Basin are reflecting Caledonian basement inheritance (Doré et al. 1999). Doré et al. (1999) suggest that the southern part of Porcupine Basin could have been influenced by the Hercynian orogeny. However, Tate et al. (1993) states explicitly that the Main Porcupine Basin was beyond the influence of the Hercynian deformation. Porcupine Basin has undergone a complex history of crustal

attenuation but did not reach the phase of extensive rifting in Late Cretaceous and Early Cenozoic times with the development of oceanic crust, as observed to the west of Hatton Basin and south of the Charlie-Gibbs Fracture Zone (Fig. 2.1A) marking the onset of the development of the NE Atlantic Ocean. Porcupine Basin can be interpreted as a failed rift of the proto-North Atlantic Ocean (Shannon 1991). Recent deep seismic research programmes, notably RAPIDS (Rockall and Porcupine Irish Deep Seismic) 1, 2, 3, and 4 and HADES (Hatton Deep Seismic) projects, using wide-angle seismic reflection/refraction techniques, have yielded new insights in the nature, thickness and development of the crustal structure of the Porcupine and Rockall regions (Shannon et al. 1994; Hausser et al. 1995; O'Reilly et al. 1996; Mackenzie et al. 2002; Morewood et al. 2004). The wide-angle seismic data show that the crust beneath the Porcupine High (Porcupine Bank) is typically thick (25–28 km), which is interpreted as reflecting little crustal attenuation (Shannon et al. 1994). These areas have remained structurally high (close to sealevel) throughout Late Palaeozoic to Recent times (Shannon et al. 2007).

However the crust beneath the sedimentary basins is significantly thinner. Gravity modeling across the southern part of Porcupine Basin suggests that the crust thins from 28 km on the eastern margin to less than 8 km in the basin centre (Conroy and Brock 1989). Stretching factors calculated from well subsidence data in the Porcupine Basin give broadly similar results, indicating a southward increase in stretching factors (with a stretching factor ranging from 1.1 to 6) (White et al. 1992). Reston et al. (2001, 2004) suggested that the extreme crustal thinning may have resulted in the development of a zone of serpentinization, accompanied by serpentinite mud volcanism in the central and southern part of Porcupine Basin. These patterns of rapid variation in crustal thickness, interpreted as the response to a number of rifting events, are likely to have had a major effect on both the heat flow and distribution of fluid flow in the basins (Shannon et al. 2007). They also obviously influenced the sedimentary and oceanographic flux patterns of the region, leading to the development of rapidly subsiding basins adjacent to structural highs and to the location and evolution of the basin margins and their slopes (Shannon et al. 2007).

2.1.1.2 Tectono-Sedimentary Development

Seismic data suggest that about 6 km of sedimentary strata are preserved above the severely attenuated crust, interpreted as a series of stacked rift megasequences (Croker and Shannon 1987; Naylor et al. 2002). The Late Palaeozoic to Recent tectonostratigraphic framework, characterized by episodic rifting phases, each having a different extension (Shannon 1991) and resulting in a number of sub-basin depocentres (Naylor et al. 1999, 2002), is summarized in Figs. 2.2 and 2.3. Figure 2.4 frames the Late Cenozoic tectonostratigraphic evolution of Porcupine Basin within the evolution of the NE Atlantic margin.

Palaeozoic-Mesozoic Evolution

Naylor and Shannon (2005) have suggested the presence of a series of basement domains in the Porcupine region, some of which are likely to be *Lower Palaeozoic*

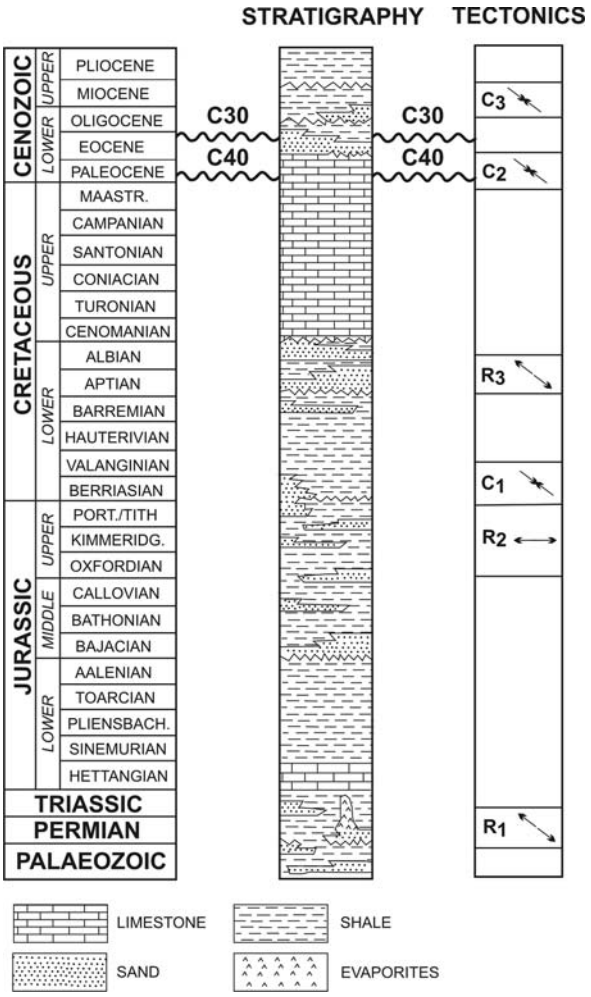

Fig. 2.2 Generalized tectonostratigraphic framework of the Porcupine region showing the major lithologies, unconformities and tectonic events of the Late Palaeozoic to Cenozoic (after Shannon et al. 2007). $R_{1–3}$ refer to the major rift phases and $C_{1–3}$ are compressive phases. The direction of extension and compression is indicated by *arrows*

or older indurate metasediments and igneous rocks, while others are *Devonian-Carboniferous* in age and contain sandstones, shales and coals. These can be interpreted as a pre-rift succession and were suggested to have influenced the location and orientation of later basins.

Permo-Triassic basins developed through much of the region, probably initially as wide extensional post-Variscan sag basins without major fault controls and later as more localized fault-controlled rifts along N-S structural fabrics in Porcupine Basin. Sandstones, shales and evaporites are the predominant lithologies (Shannon et al. 1999) (Fig. 2.2).

Early Jurassic strata are only known from the northern part of Porcupine Basin and are thought to represent a series of deep-marine shales, marls and limestones (Croker and Shannon 1987). *Middle Jurassic* strata have a widespread occurrence throughout the Porcupine Basin. The succession comprises a braided fluvial sandy

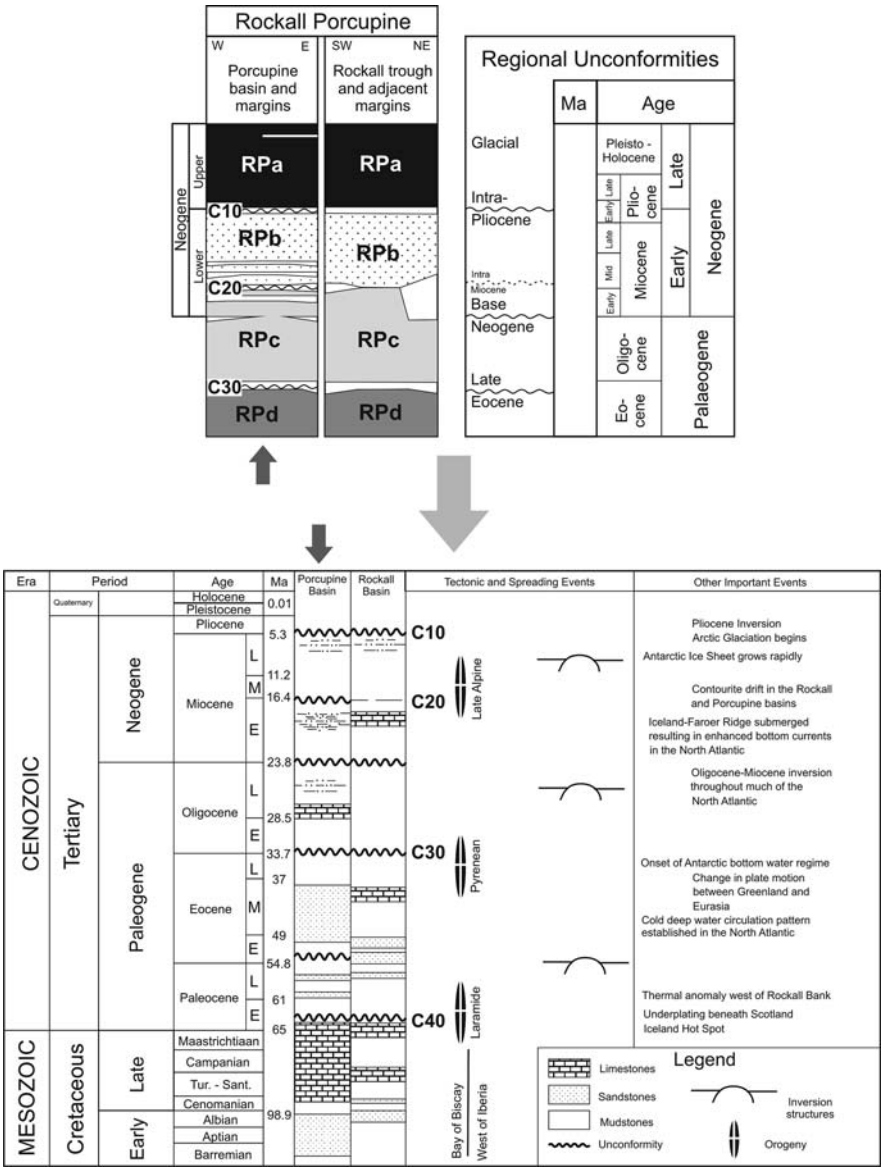

Fig. 2.3 Late Cenozoic tectonostratigraphic evolution of Porcupine Basin and Rockall Trough. *Upper panel*: Stratigraphic nomenclature (megasequences and key major and minor unconformities) for the Upper Palaeogene-Neogene strata on the Porcupine Basin and Rockall Trough Atlantic margin as defined by the STRATAGEM project (after Stoker et al. 2005). *Lower panel*: Detailed tectonostratigraphic setting of the Late Mesozoic and Cenozoic of the Porcupine and Rockall region after Shannon 2007 (modified from McDonnell and Shannon 2001)

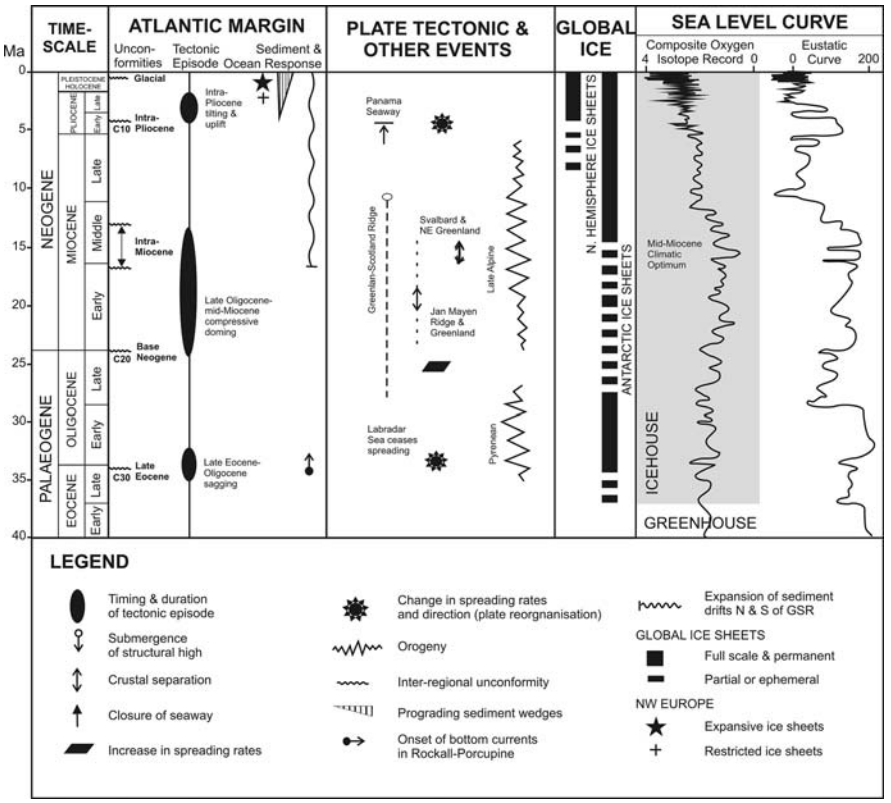

Fig. 2.4 Late Paleogene-Neogene tectonostratigraphic framework for the NW European Atlantic margin after Stoker et al. 2005

facies, interpreted by Sinclair et al. (1994) as the product of an onset warp phase of tectonism prior to major rifting (Fig. 2.2). The *Late Jurassic* strata reflect deposition of basin-edge sandy to conglomeratic alluvial fans, meandering fluvial sandy and silty sediments and deep-marine submarine sandy fans in a series of syn-rift sub-basins (Croker and Shannon 1987; MacDonald et al. 1987).

The *Early Cretaceous* succession, resting with a marked unconformity on the Jurassic strata, consists of a thick interval of muddy and silty marine strata within the centre of Porcupine Basin (Fig. 2.2). Towards the basin margin the succession is subdivided into several unconformity-bound seismic sequences that are laterally equivalent to the strata in the basin centre (Shannon et al. 2007). Syn-rift faulting waned during the Early Cretaceous but a later phase of *Aptian-Albian* rifting has been suggested to produce the deltaic sandstones seen in the northern part of Porcupine Basin (Croker and Shannon 1987; Shannon 1991). The Porcupine Volcanic Ridge System (Tate and Dobson 1988; Naylor et al. 2002) in the centre of Porcupine Basin has been interpreted as the product of extensive volcanism in Early Cretaceous times. These volcanic systems appear to have been locally reactivated with

sills and dykes in Palaeogene times. An alternative interpretation has been proposed more recently (Reston et al. 2001, 2004) that this ridge system, developed above a region of thinned continental crust, is not magmatic in origin but related to mantle serpentinization and may include mantle mud volcanism. *Late Cretaceous* chalks and marls are extensively developed, covering the whole basin and extending across the basin-bounding structural highs (Porcupine Bank) (Fig. 2.2).

Cenozoic Evolution

A Cenozoic succession, up to 4 km thick, is deposited in Porcupine Basin (McDonnell and Shannon 2001). Mapping the seismic megasequences in Porcupine Basin revealed a broad catenary shape for the Cenozoic succession (Fig. 2.5A,B) (Naylor et al. 2002). The strata dip towards the basin centre, superimposed upon a regional southerly dip towards the central part of the basin. However, the main preserved Cenozoic depocentres change in a consistent manner through time, with a southerly migration from the Palaeogene to the Neogene (Shannon et al. 2007).

A succession of sand-prone deltaics and coeval submarine fans was deposited during *Late Palaeocene* to *Eocene* times (Croker and Shannon 1987; Moore and Shannon 1992; Shannon 1992). This regressive episode was interpreted by Shannon et al. (1993) to represent the response to ridge push resulting in differential basin edge flexure, although it has also been interpreted as the result of mantle plume tectonics (White and Lovell 1997; Jones et al. 2001) (Figs. 2.2, 2.3, and 2.4).

A major facies change in *Late Eocene* times is coincident with a major *(C30) unconformity* succeeding the deposition of the Palaeocene/Eocene deltaics and submarine fans (Stoker 1997; McDonnell and Shannon 2001; Stoker et al. 2001, 2005). This unconformity is clearly observed in the centre of Porcupine Basin as a major incisional unconformity (Shannon et al. 2005) and coincides with the onset of contourite drift deposition, i.e. the Porcupine Drift, an elongate drift which is coeval with the Feni Drift (Rockall Trough) but is more subdued than the latter (McDonnell 2001; Stoker et al. 2001) (Fig. 2.5A,B). So, the unconformity marks a major change from predominantly downslope sediment transportation to mainly alongslope movement (Shannon et al. 2007). Stoker et al. (2005) suggest that the C30 unconformity results from the onset of vigorous current circulation facilitated by a rise in sealevel due to an increase in the size of the oceanic water body as a consequence of increased differential basinal subsidence (Fig. 2.4). Rapid differential subsidence coeval with the culmination of the Pyrenean orogeny (Knott et al. 1993), outstripped sedimentation to drive a rapid deepening that established the deep-water basins (Stoker et al. 2001). Porcupine Basin subsided to a point that allowed bottom currents driven by Tethyan Outflow Water to enter the basins from the south. Indeed, Ramsay et al. (1998) presented isotopic data showing that bottom current circulation patterns in the Atlantic Ocean prior to the Middle Miocene were driven by southerly derived water masses, including Tethyan Outflow Water. The Late Eocene to Oligocene onset of contourite drift accumulation in the Rockall-Porcupine area is consistent with a northward extension of activity that had been ongoing further south since the Mid Eocene (Ramsay et al. 1998; Norris et al. 2001). So, a combination of

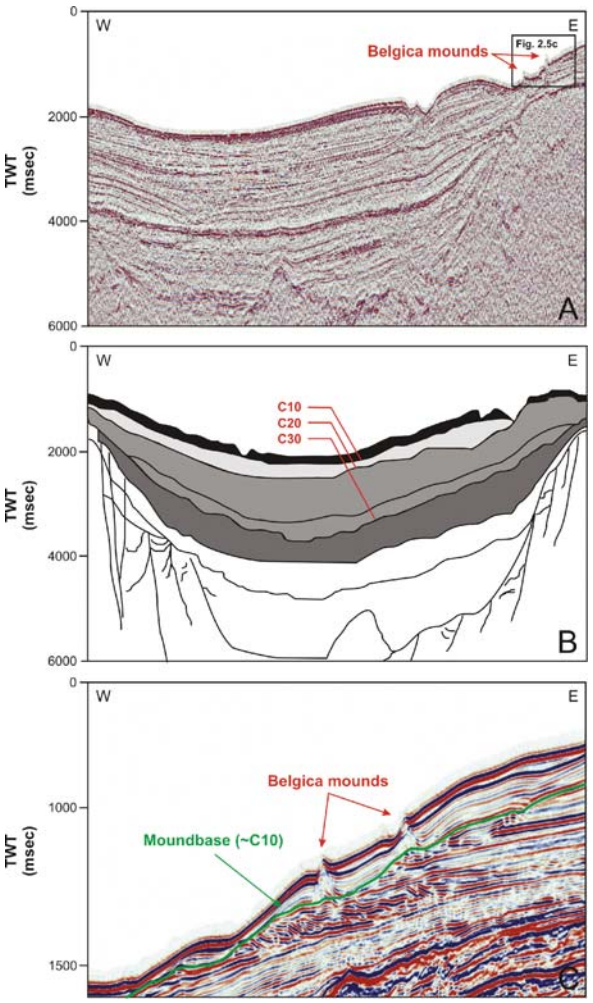

Fig. 2.5 (**A**) Seismic profile through Porcupine Basin (W-E) showing the Belgica Mound Province at the eastern margin and framing the mounds in their geological context. Location noted on Fig. 2.1B. (**B**) Interpreted geoseismic section through Porcupine Basin (W-E), focusing on the Upper Palaeogene-Neogene stratigraphy with the annotation of the unconformities (C10, C20, and, C30) as defined in the framework of the STRATAGEM project (2002, 2003) (modified after McDonnell and Shannon 2001). (**C**) Zoom in on the Belgica Mounds rooting on the same unconformity, which can be interpreted as the C10 unconformity according to McDonnell and Shannon (2001). Seismic lines provided by Petroleum Affairs Division, DCENR, Dublin

oceanographic and tectonic factors can be proposed to have been the driving forces in the formation of the C30 megasequence boundary unconformity (Shannon et al. 2005) (Figs. 2.3 and 2.4).

The *Oligocene* to *Early Miocene* drift sediments above the C30 unconformity are identified as one megasequence named *RPc* (Rockall-Porcupine) in the new STRATAGEM nomenclature (Stoker et al. 2005) (Figs. 2.3 and 2.4). The upper part of the RPc sequence consists of Upper Oligocene to lowest Miocene silty and calcareous claystones, interbedded siltstones and argillaceous limestones unconformably overlain by a Lower Miocene conglomerate (Dobson et al. 1991).

A set of unconformities, of *late Early Miocene* to *early Mid Miocene* in age, is identified in Porcupine Basin (McDonnell and Shannon 2001). The most pronounced of these unconformities is named as the *C20 unconformity* (McDonnell

and Shannon 2001; Stoker et al. 2001) (Fig. 2.5A,B). Some of these unconformities are confined to the basin margins, while one of them is correlated across the basin as an unconformity on both margins of the basin and as a correlative conformity within the basin centre. The unconformable sequence boundary is underlain by a pulsed progradational wedge, Early to Mid Miocene in age, on the eastern margin and by a coeval large composite slide feature on the western margin (Moore and Shannon 1991; Shannon et al. 2005). In common with C30 (Late Eocene), this set of unconformities is likely to be the result of the interplay of tectonism and oceanographic circulation changes (Shannon et al. 2005) (Figs. 2.3 and 2.4). Differential subsidence is interpreted as having occurred prior to the main C20 sequence boundary resulting in steep slopes and instability on the western margin, and pulsed sediment progradation due to basin margin uplift and tilting on the eastern margin (Shannon et al. 2005). The less regionally extensive unconformities are thought to reflect the effects of the tectonism associated with the differential subsidence. The observed differential subsidence is coeval with a major plate reorganization and the last pulses of the Alpine orogeny (Stoker et al. 2005) (Figs. 2.3 and 2.4).

The megasequence lying above the C20 unconformity system, named as *RPb* in the STRATAGEM nomenclature, is characterized on seismic data by a complex set of *Mid Miocene* to *Pliocene* strata with aggradational basinward-onlapping and basinward-prograding bedsets (Shannon et al. 2005) (Figs. 2.3 and 2.4). All the regional geological evidence (Stoker et al. 2001) points to the occurrence of high-energy contour-parallel currents with sediment transported by alongslope migration and deposited by accretion as contourite drifts in a deep-water setting (Shannon et al. 2005; Stoker et al. 2005). The sediment build-ups are spectacularly developed close to the basin margins (Shannon et al. 2005) and are not slump features as suggested by Roberts (1972). They show upslope progradation and their development results in the accretion of sediment wedges onto the basin margins (Shannon et al. 2005). Towards the margins of Porcupine Basin, a series of deeply eroded channel-like features are observed adjacent to the accretionary sediment build-ups. These are often spatially associated with local diachronous unconformities. Together with the overlying high-energy sediments, they can be interpreted as a contourite cut-and-fill facies. So, they clearly represent deep-water features associated with vigorous contour currents (Shannon et al. 2005). A Mid Miocene onset or acceleration of Norwegian Deep Water Overflow is proposed by Stoker et al. (2005) to explain a regional expansion in contourite drift development and accumulation above the C20 unconformity. The Early Neogene onset or acceleration of overflow of Norwegian Sea Deep Water (NSDW) is interpreted to be a consequence of a tectonic inversion in the Faroe-Shetland areas, which changed the geometry of the Wyville-Thomson Ridge complex so as to facilitate the opening of the Faroe conduit as passageway for the exchange of intermediate and deep-water masses between the Atlantic Ocean and Nordic Seas (Stoker et al. 2005; Johnson et al. 2005).

An *Early Pliocene unconformity* has been identified along the entire length of the NW European Atlantic margin (Stoker et al. 2001, 2005). McDonnell and Shannon (2001) correlated this unconformity with an unconformity of similar character in Porcupine Basin, the *C10 unconformity* (Fig. 2.5). Shannon et al. (2007) suggest

that most of the carbonate mounds in the Porcupine region appear to root on this regionally continuous sub-horizontal reflector (Fig. 2.5C).

The overlying succession is thin in the Irish offshore areas (south of 56°N), identified as *RPa,* but further north on the continental margins the succession thickens extensively in response to the development of a series of glacially influenced prograding wedges (Shannon et al. 2005) (Figs. 2.3 and 2.4). There the succession contains a pronounced internal unconformity (the glacial unconformity) of early Middle Pleistocene age. This unconformity is so far not described in Porcupine Basin. In Porcupine Basin, RPa is recognized as a seismic sequence characterized by parallel continuous to discontinuous reflectors, hummocky in character; their aggradational nature has maintained the development of the Porcupine Drift (Stoker et al. 2005). The activity of bottom currents in this sediment drift is testified by migrating sandwaves and internal erosion surfaces (Stoker et al. 2005). On the western flank of the southern Rockall Trough, DSDP Site 610 and ODP Site 980/981 proved that the RPa sequence consists of Early Pliocene to Holocene nannofossil ooze increasingly interbedded with calcareous terrigenous clay in the upper part of the section. The influx of clay and dropstones indicates that ice rafted detritus reached these sites in Late Pliocene times (Ruddiman et al. 1987; Jansen et al. 1996).

Stoker et al. (2005) attributed the formation of the intra-Pliocene boundary, dated at 4 Ma, to the uplift of onshore and shallow shelf areas accompanied by accelerated offshore subsidence which started in Early Pliocene times (Figs. 2.3 and 2.4). Late Cenozoic movements affected indeed the continental margins around the NE Atlantic (Japsen and Chalmers 2000; Praeg et al. 2005). These movements have been linked to a Late Neogene global plate reorganization (Cloetingh et al. 1990). A tilting of the margin resulted in a major seaward progradation of shelf-slope sediment wedges as well as a change in oceanographic current patterns, which combined to form the intra-Pliocene unconformity. The intra-Pleistocene glacial unconformity marks the onset of expansive, shelf-wide glaciations in NW Europe (Stoker et al. 2005). Studies of the influence of glacial processes in Porcupine Basin are scarce. The more, the shelf and slope lack the typical troughs and fans that mark the rest of the NW European continental margin (Sejrup et al. 2005). However, the onshore glacial records indicate that ice-sheets have repeatedly extended offshore (Bowen 1991; Coxon 2001; Bowen et al. 2002) and recent studies have shown that the continental margin, SW to W of Ireland, show different glacial imprints. In the northern Porcupine Seabight, iceberg scour marks are recognized at the seabed on sidescan sonar imagery at water depths of 140–500 m (Belderson et al. 1973; Pantin and Evans 1984; Kenyon 1987). Buried iceberg scour marks have also been recognized in the shallow subsurface of the northern Porcupine Basin using 3D seismic data sets (Games 2001; Mathys 2001). A channel system, the Gollum channels, is characterizing the eastern margin of Porcupine Seabight. The age of formation of the canyons is unknown but they do not appear to have been active during the present interglacial (Tudhope and Scoffin 1995; Wheeler et al. 2003). However, they may have received coarse-grained sediment supplied by glacial meltwater events (Tudhope and Scoffin 1995; Unnithan et al. 2001; Weaver et al. 2000; Wheeler et al. 2003). Studies of core sections on the eastern and northern margin of Porcupine Seabight show the

presence of ice rafted debris and glaciated sediments (Foubert et al. 2007; Van Rooij et al. 2007a). The present-day sea-floor is characterized by patches of gravel- to boulder-sized dropstones, interpreted to be of Irish provenance and of glacial (ice rafted) origin (Foubert et al. 2005a).

2.1.1.3 Seismostratigraphic Model for the Belgica Mound Province

De Mol et al. (2002), De Mol (2002), Van Rooij et al. (2003, 2007a, 2007b) and Van Rooij (2004) developed a detailed seismostratigraphic framework for the Belgica Mound Province at the eastern margin of Porcupine Seabight based on very high-resolution seismic data sets (SIG surface sparker source operating at 500 J; 0.5–1 m vertical resolution; 400–800 ms TWT penetration depth). In the next paragraphs an overview will be given of the four encountered seismic units (U1-U4), separated by three regional unconformities (RD1-RD3) (Fig. 2.6), and their link with the tectonostratigraphic framework developed within the STRATAGEM project (Evans et al. 2005; Stoker et al. 2005). All units prove to be influenced by bottom current action either during or after deposition (Van Rooij et al. 2003, 2007a).

Unit U4 is rarely observed on the high-resolution seismic profiles due to limited penetration depths but where recognized, the unit is characterized by gently dipping parallel strata with some intercalated prograding complex sigmoidal deposits

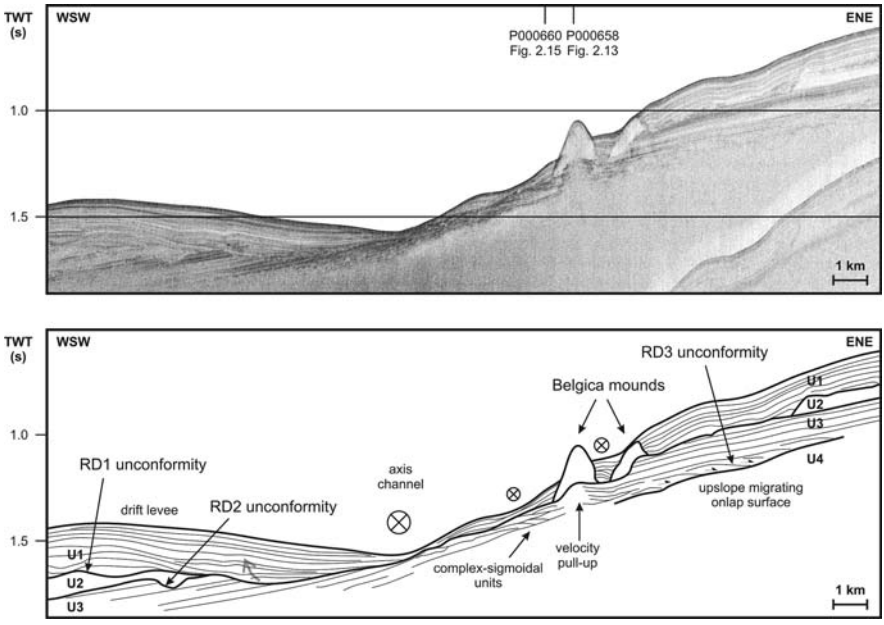

Fig. 2.6 High-resolution WSW-ENE seismic profile P980521, illustrating the general seismostratigraphic setting of the Belgica Mound Province (modified after Van Rooij 2004; Van Rooij et al. 2007a,b). The different described units and unconformities are annotated. The location of the described seismic profile is noted on Figs. 2.1b, 2.12, and 2.16

(Fig. 2.6). Seismic unit U4 is interpreted as an elongated sediment drift, which started to develop in Porcupine Seabight during Late Eocene to Early Oligocene times (Van Rooij 2004). This unit can be correlated to the lower part of megasequence RPc (Stoker et al. 2005) and the base of unit U4 can be linked with the C30 unconformity (McDonnell 2001), marking the onset of drift sedimentation probably driven by Tethyan Outflow Water in Porcupine Basin. Unit U4 is topped by the *RD3 erosive unconformity* (Fig. 2.6), interpreted by Van Rooij (2004) as caused by a general sea level fall during early Late Oligocene times attributed to the construction of ice-caps (Pearson and Jenkins 1986). However, this unconformity has to be interpreted carefully and its origin can be questioned.

Unit U3 is generally characterized by gentle basinward dipping continuous parallel strata with moderate to locally high amplitude reflections (Fig. 2.6). A clinoform pattern formed by upslope migrating sigmoidal bodies is encountered in the upper strata of unit U3, interpreted by Van Rooij et al. (2003) as buried sediment waves, associated with sediment drifts. The upper boundary of this unit is an erosional unconformity (RD2) which strongly incises the underlying strata (Fig. 2.6). The strata of *unit U3* can be correlated with the Early to Middle Miocene progradational wedge underlying the main C20 unconformity, while the *RD2 unconformity* may be linked with the Mid Miocene C20 unconformity (Shannon et al. 2005; Stoker et al. 2005; McDonnell 2001).

Unit U2 is characterized by a nearly transparent acoustic facies on top of the erosional unconformity RD2 bounding units U2 and U3 (Fig. 2.6). Only a few sets of continuous, relatively high amplitude reflectors are observed within unit U2. The nature of this transparent seismic facies suggests relatively homogeneous sediments. Following the STRATAGEM nomenclature, the strata in this unit should correlate with the Mid Miocene to Early Pliocene RPb megasequence (Shannon et al. 2005; Stoker et al. 2005; McDonnell 2001). Subsequently, a significant erosion event severely cut into these deposits, creating the *RD1 discontinuity*. Deep incisions into unit U2 created large south-north orientated ridges, which are still evident in the present-day topography (Van Rooij et al. 2003) and which formed according to De Mol et al. (2002) an ideal substrate for colonization by framework building corals which may have been the initiation of mound growth (De Mol et al. 2002). The mounds in the Belgica Mound Province on the eastern margin of Porcupine Seabight root indeed on this unconformity. Van Rooij et al. (2003) correlated the RD1 discontinuity with a regional Late Pliocene hiatus, found in the Rockall-Goban Spur transect, and interpreted the discontinuity in terms of the reintroduction of Mediterranean Outflow Water (MOW) in the NE Atlantic and the effect of glacial-interglacial events on deep-water circulation (Stow 1982; Pearson and Jenkins 1986). However, according to Shannon et al. (2005) and McDonnell (2001) and following the STRATAGEM nomenclature, the RD1 discontinuity should be correlated with the Early Pliocene (4 Ma) C10 unconformity.

Unit U1 is characterized by slightly upslope migrating wavy parallel reflectors, representing Quaternary drift deposits partly enclosing the mounds (Fig. 2.6) (Van Rooij et al. 2003). The reflectors of unit U1 onlap the mounds, suggesting that the mounds were already present before deposition of the most recent drift. Scouring and moat features around the mounds suggest that they affected the intensity of the

currents and the deposition of the enclosing sediments (De Mol et al. 2002; Van Rooij et al. 2003). Unit U1 can be correlated with megasequence RPa according to the STRATAGEM nomenclature (Evans et al. 2005; Stoker et al. 2005; Shannon et al. 2005). On the seismic profiles, the Belgica Mounds are characterized as almost acoustically transparent elevated structures with a parabolic outline (Fig. 2.6) (Van Rooij et al. 2003). Within the mounds no clear internal reflections are observed. The real shape of the mounds is masked by diffraction hyperbolae.

2.1.2 Geomorphology of the Belgica Mound Province

An extensive data set of surface information has been gathered during the last decennia on the eastern margin of Porcupine Seabight especially in the Belgica Mound Province, going from multibeam data over sidescan sonar records to video imagery and surface samples (box cores, gravity cores, Calypso piston cores, dredges, Van Veen grabs, TV-guided grabs,. . .). In this chapter a short overview and description will be given of the existing data sets, revealing the environmental and geomorphological setting of the Belgica Mounds. The results of recent mapping dives with Remoted Operated Vehicles (ROV), zooming in on small mounded structures and visualizing the different facies encountered on and between the Belgica Mounds, are discussed in detail in Chap. 7 "Surface processes". The results of surface coring are presented in Chap. 6 "The top of the record: on-mound versus off-mound".

The Belgica Mound Province is situated at the eastern margin of Porcupine Seabight between 51°10'N and 51°40'N and, 11°30'W and 11°45'W, extending over a length of 45 km and a width of 10 km (Figs. 2.1B, 2.7, and 2.8). Based on multibeam bathymetry (Beyer et al. 2003) and seismic data sets (De Mol et al. 2002) 66 mounds are described, of which 44 are outcropping and 22 are buried mounds (Figs. 2.7 and 2.8). De Mol et al. (2002) presented a first general description of the morphology of the Belgica Mounds. Beyer et al. (2003) discussed in detail the bathymetric data sets and Wheeler et al. (2007) approached the Belgica Mounds from a statistical viewpoint by comparing mound heights with mound widths, similar to the statistical study carried out by De Mol et al. (2002) on 2D seismics. De Mol et al. (2002) attributed a number to each of the Belgica Mounds, while other mounds where named throughout the years such as Thérèse Mound, Galway Mound, Poseidon Mound and Challenger Mound (Fig. 2.7).

The mounds occur in water depths between 550 and 1030 m and are bordered at their western side (downslope) by a large alongslope, N-S to NE-SW channel (Fig. 2.7). Shallow S-W trending downslope gullies feed into the N-S channel (Van Rooij et al. 2003) (Fig. 2.7). The mound shapes varies from conical, circular to NNE-SSW elongated forms, of which many seem to be aligned in several levels or sitting "en echelon" along the bathymetric contours parallel to the continental margin (Beyer et al. 2003). Most of the mounds on the slope have an exposed steep western flank that is about 20° compared to the average slope of the margin at ∼5°, while the eastern upslope side of the mound is often buried, which leads to a terrace-like margin morphology (De Mol et al. 2002; Beyer et al. 2003; Van Rooij et al.

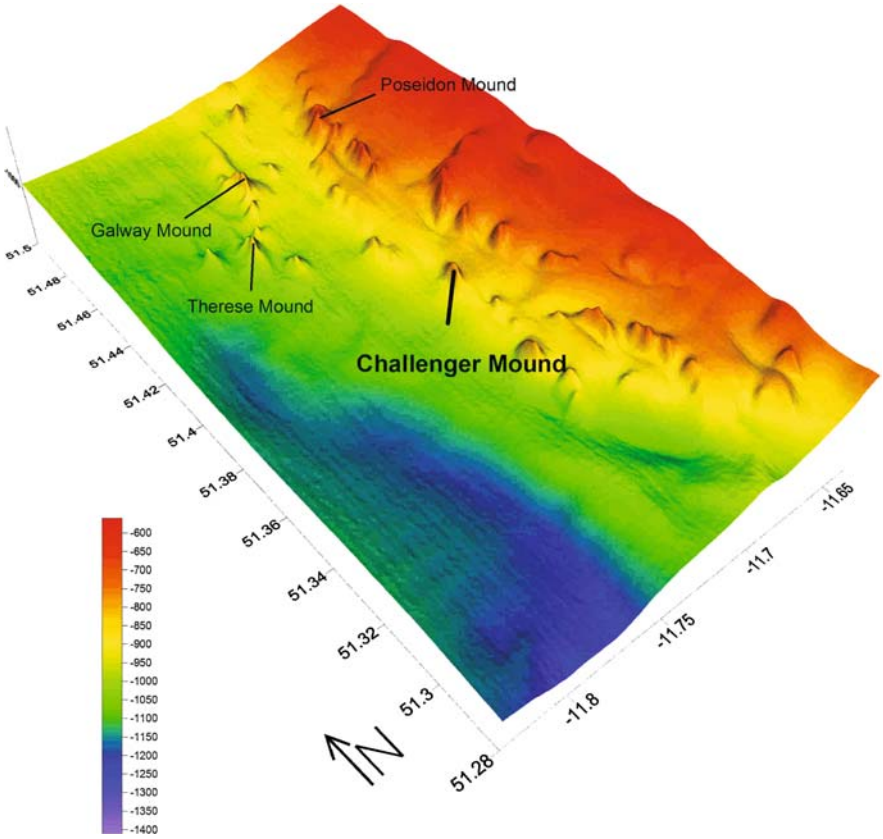

Fig. 2.7 Three-dimensional view of the outcropping Belgica Mounds based on AWI bathymetry (Beyer et al. 2003)

2003; Wheeler et al. 2007). Depressions, up to 50 m deep, often occur on the steep downslope side of some mounds and are probably the result of strong bottom currents around the mounds (Van Rooij et al. 2003). The mound widths vary from 250 to 2150 m, and the heights range from 50 to 200 m above the common mound base as defined on 2D seismic data sets (De Mol et al. 2002). Most of the mound summits occur in two main water depths: 850 and 700 m (Wheeler et al. 2007). Exposed heights of the mounds vary between 10 and 70 m (mean 40 m) on their upslope side and 40 and 160 m (mean 90 m) on their downslope side (Wheeler et al. 2007). The mean mound height protruding from the sea-floor is ~100 m. The N-S width (varying between 400 and 2000 m; mean 860 m) of the mounds has a broader range than the east-west extension (varying between 300 and 1000 m; mean 570 m) (Wheeler et al. 2007).

The Belgica Mounds and their sedimentary environment have been mapped in detail on 30 kHz TOBI (Towed Ocean Bottom Instrument) sidescan sonar records (de Haas et al. 2002; Huvenne et al. 2005) and on high-resolution 100/410 kHz

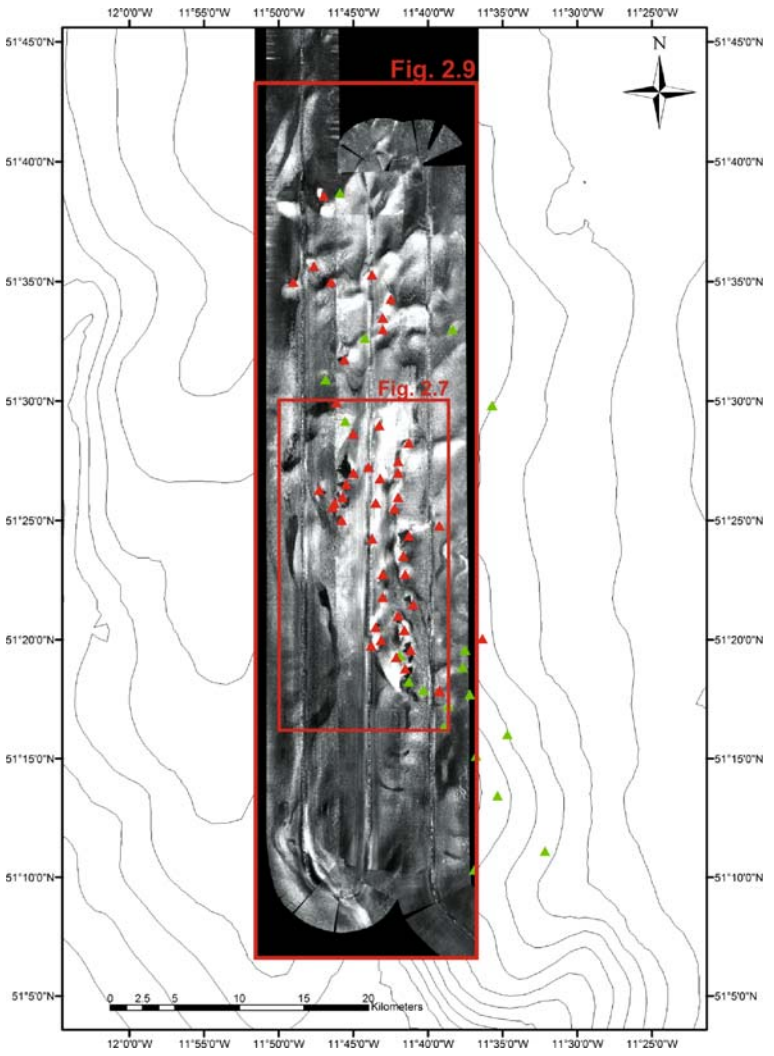

Fig. 2.8 TOBI (Towed Ocean Bottom Instrument) sidescan sonar mosaic (de Haas et al. 2002; Huvenne et al. 2005) of the Belgica Mound Province with annotation of surface mounds (*red triangles*) and buried mounds (*green triangles*)

GeoAcoustic sidescan sonar imagery (Wheeler et al. 2005b) (Fig. 2.8). These authors used existing video imagery and surface coring to ground-truth the described sidescan sonar records. Huvenne et al. (2005) identified the Belgica Mounds on the TOBI sidescan sonar imagery as having a strong backscatter signature on their flank facing the sonar and a strong acoustic shadow, reflecting their topography (Figs. 2.8 and 2.9). Small, positive high backscatter features in between the high backscatter features representing the giant mounds are interpreted as small mounded structures

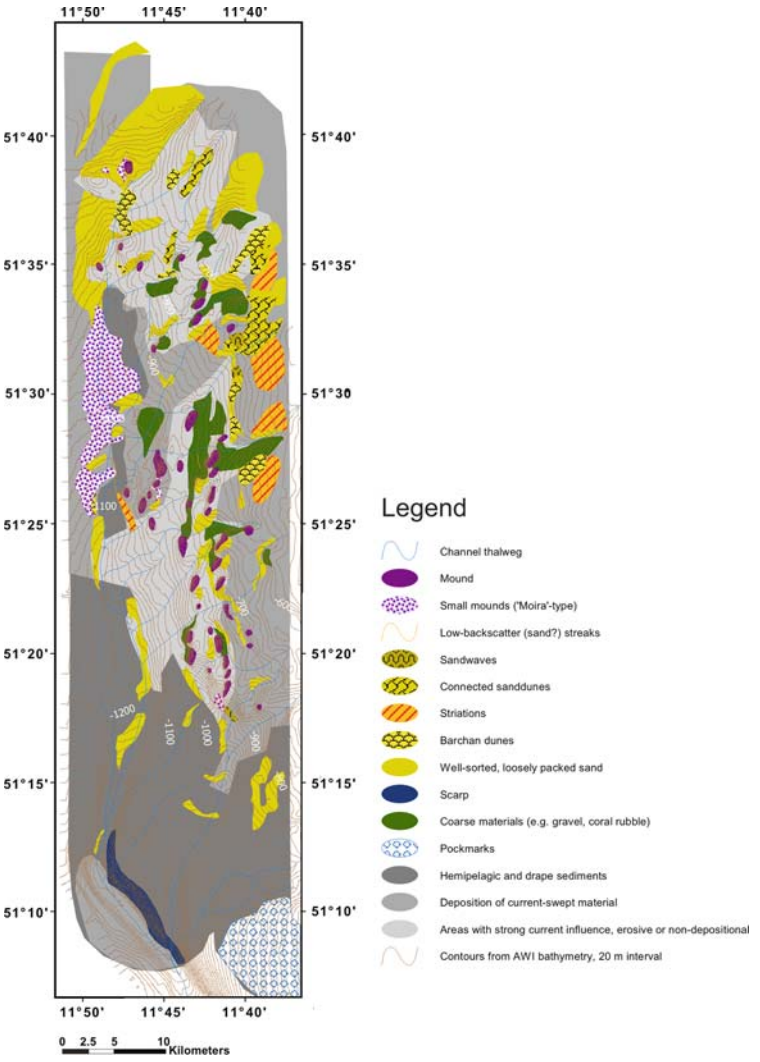

Fig. 2.9 Interpretation of the TOBI sidescan sonar mosaic in the Belgica Mound Province after Huvenne et al. 2005. AWI bathymetry is plotted on the sidescan sonar records (Beyer et al. 2003)

(Huvenne et al. 2005; Wheeler et al. 2005b; see also Chap. 7). A low backscatter facies of smooth texture is encountered south of the mounds, interpreted as a package of hemipelagic sediments (Huvenne et al. 2005) (Figs. 2.8 and 2.9). A high backscatter facies of irregular texture is mainly found in between the mounds and around the gullies and is indicative for current-swept areas where the finest fractions are winnowed from the upper sediment layer resulting in coarse, sometimes purely lag deposits (Huvenne et al. 2005). A medium backscatter facies with irregular texture occurs in the northern part of the Belgica Mound Province and east

and west of the mounds and reveals a facies with coarse material characterized by strong current effects (Figs. 2.8 and 2.9). A set of depressions south of the Belgica Mounds are interpreted as shallow pockmarks (Huvenne et al. 2005). Patches of very high backscatter between the mounds and along the north-facing slopes of the gullies represents areas with a very coarse sea-floor, consisting of gravel lags and/or dead coral rubble. Patches of very low backscatter occur at several locations and are interpreted as well sorted loosely packed sands (Figs. 2.8 and 2.9). Striations, crescent shaped forms, wavy patterns and single low backscatter streaks represent respectively current-parallel ribbons of sand, barchan dunes, sand waves and furrows, indicative of active sediment transport and even erosion or non-deposition (Huvenne et al. 2005; Wheeler et al. 2005b; Foubert et al. 2005a).

Wheeler et al. (2005b) revealed similar backscatter patterns on the high-resolution sidescan sonar records: background uniform backscatter facies representing a smooth current swept seabed surface, sediment wave facies, barchan dune facies, gravel ridge facies, sand ribbon facies, and the giant mounds themselves with some small mounded structures in between. High-resolution sidescan sonar data confirmed that the mound morphology is strongly dictated by prevailing basal current activity (Wheeler et al. 2005b). So, sidescan sonar records show that the Belgica Mounds are occurring in a very dynamic environment influenced by rather strong bottom currents.

2.1.3 Oceanographic Template

An excellent overview of the present-day oceanographic situation in Porcupine Seabight is given by White (2007). In this paragraph the different water masses and some benthic physical processes encountered nowadays at the eastern margin of Porcupine Seabight will be highlighted. For more detailed information the reader is referred to White (2007).

2.1.3.1 Water Masses

The Porcupine Seabight is mainly influenced by northward flowing Eastern North Atlantic Water (ENAW) and Mediterranean Outflow Water (MOW), with some influences from other water masses derived from the western North Atlantic (van Aken and Becker 1996). Figure 2.10 represents temperature and salinity transects across the Porcupine Seabight and the Porcupine Bank revealing the typical water mass distribution at the depth levels occupied by the carbonate mounds (White 2007). A seasonal thermocline is observed at about 50–70 m (Fig. 2.10A). At the approximate latitude for the Belgica Mound Province, warm saline water of ENAW origin, carried northwards adjacent to the NE Atlantic margin (Pollard et al. 1996), fills the upper layers down to about 600 m water depth (Fig. 2.10). A significant portion of the ENAW flow is carried by the Shelf Edge Current (SEC) that flows polewards along the continental margin (e.g. Pingree and Le Cann 1990; Huthnance 1986). Between 800 and 1000 m, MOW characterized by a high salinity core

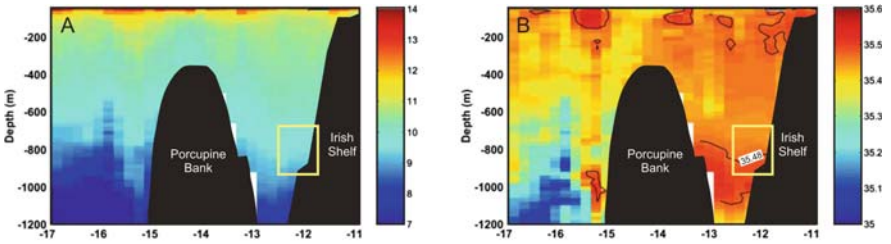

Fig. 2.10 Transect of temperature (**A**) and salinity (**B**) across the Porcupine Seabight and Porcupine Bank at 51.5°N in June 2002, taken from Mohn et al. (2002) and White (2007). A colourscale for all plots is shown on the *right*. The salinity 35.48 contour on Fig. 2.10B is shown for clarity. The yellow rectangle corresponds with the depth position of the Belgica Mounds

occupies the basin (Fig. 2.10). The upper level of MOW is associated with the permanent thermocline and matches with the mean water depth of the carbonate mound occurrences (White 2007) (Fig. 2.10).

The predominant circulation along the continental margin of the NW European shelf is directed polewards (Huthnance 1986). In the Porcupine Seabight itself, the flow is essentially cyclonic with poleward flow along the Irish shelf at the eastern margin (e.g. Pingree and Le Cann 1989, 1990). Mean residual bottom flows between 2 and 5 cm/s persist, although much stronger currents have been measured at the eastern margin of Porcupine Seabight (Pingree and Le Cann 1990; White 2007; White et al. 2007; Dorschel et al. 2007a). At the northern margin of Porcupine Seabight, the flow below 300 m water depth recirculates along the margin.

2.1.3.2 Benthic Physical Processes

Bottom current measurements in the Belgica Mound Province have shown that mean daily and maximum currents are much higher at the eastern margin than in other parts of the Seabight (Roberts et al. 2005; White 2007; White et al. 2007; Dorschel et al. 2007a). Current meter measurements at a height of 13 m above the seabed on the upper slopes of Galway Mound indicated that strong currents were present at the location with peak current speeds of over 60 cm/s (Roberts et al. 2005). The principal variability in the current record was tidal at a diurnal period with a strong spring-neap cycle (~13.6 days) (Roberts et al. 2005; White et al. 2007). The main daily currents showed a persistent daily residual flow, which varied between 5–15 cm/s, directed to the NW following the local continental slope orientation. Larger mean daily flows were associated with spring diurnal tides. The orientation of the dominant diurnal tides was approximately SW-NE (across the slope). This suggests that the mean residual current is directed along the local slope, while the strong tidal currents are directed across the slope. Dorschel et al. (2007a) revealed similar results by a current meter experiment whereby 6 current meters were deployed on the flanks and summit of Galway Mound ~120 cm above the sea-floor. These authors measured mean near-seabed residual currents between 1–7 cm/s (Fig. 2.11).

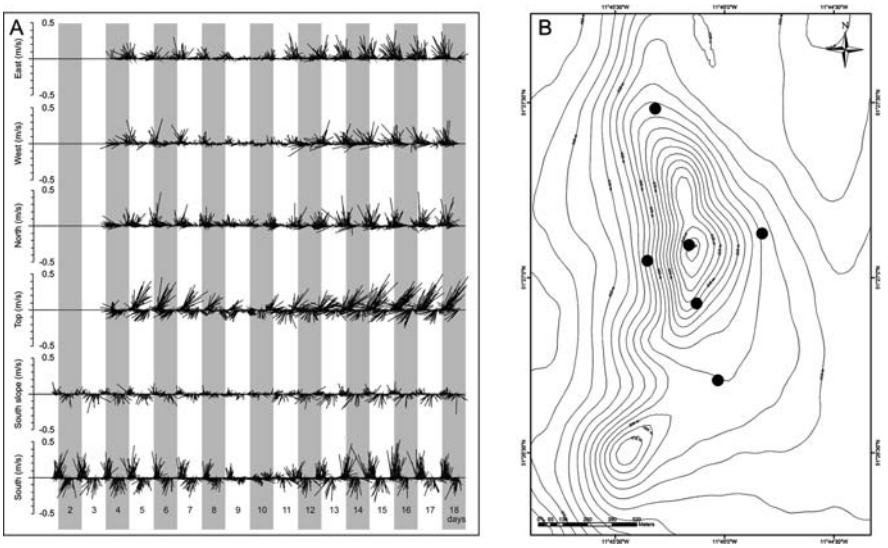

Fig. 2.11 (**A**) Current vectors, calculated from current meter measurements on the *top* and the flanks of Galway Mound, plotted against time (modified after Dorschel et al. 2007a). The numbers are days in June 2003 starting with 08.06.2003. (**B**) Position of the current meters deployed on the *top* and the flanks of Galway Mound (Dorschel et al. 2007a)

The current variability was dominated by SW-NE orientated tidal fluctuations and maximum current speeds of 51 cm/s were recorded at the summit of Galway Mound.

White (2007) and White et al. (2007) proposed two physical mechanisms responsible for the enhanced currents observed at the eastern margin of Porcupine Seabight. Internal waves are periodic oscillations in the vertical density stratification. The interaction of these internal waves with the seabed has been proposed as a way of producing enhanced bottom currents (Rice et al. 1990; White 2007). However, the cause of the high currents may not be entirely due to internal waves. Current measurements at 1000 m water depth adjacent to the Belgica Mounds have indicated that enhanced diurnal period baroclinic motions are present which dominate the current variability (White 2007). The motions will have maximum intensification where the stratification and the bottom slope are large, and the depth of the permanent thermocline is such a depth, typically 600–800 m. Most of the mounds in the Porcupine region lie close to the permanent thermocline depth. So, the relative high currents associated with the mounds at the eastern margin of Porcupine Seabight are the result of more than one dynamic process. However, White et al. (2007) suggested that the enhancement of benthic currents by resonance generation of internal waves would appear to be less significant than bottom amplification of diurnal tides in the Belgica Mound Province.

Such enhanced currents generated by benthic dynamical processes might have a secondary role in influencing the mound ecosystem, through control of food availability (White 2007). Large submerged banks, such as the Porcupine Bank, are

regions of enhanced productivity (White et al. 2005). White et al. (2005) have suggested how these banks may retain such productivity and promote the transportation of organic material to the mounds that are located along the deeper slope through downslope transport in the bottom Ekman (frictional) layer. It is the mean anticyclonic flow around the banks that promotes this downslope transport in the bottom boundary layer. White (2007) proposed that a similar process would be expected for the cyclonic flow of the slope current around Porcupine Seabight hence providing a downslope transport mechanism at all mound locations in the region. The mound regions are, therefore, regions where enhanced organic material supply might be expected.

2.2 Drilling Challenger Mound (Site U1317)

During IODP Expedition Leg 307 "Modern Carbonate Mounds: Porcupine Drilling", the scientific drilling of Challenger Mound (51°22.8'N, 11°43.1'W; 781–815 m water depth) was the central objective (Exp. 307 Scientists 2006a, d). Challenger Mound belongs to one of the 44 surface mounds encountered in the Belgica Mound Province on the eastern slope of Porcupine Seabight (Fig. 2.7).

The mound has an elongated shape with the main axis oriented in a NNE to SSW direction (Fig. 2.12). An oval plateau demarcates the summit of the mound at a water depth around ∼790 m. The mound is buried at its eastern side by drift sediments, leaving only 30–40 m of Challenger Mound exposed at this side. Its western side is characterized by a well-exposed flank, protruding 100–120 m above the seabed. The slopes of the mounds grade steeply at an angle varying between 21 and 33°. Surface observations and ROV video imagery have shown that Challenger Mound is covered with little to no live coral coverage. Surface sediments near the top of the mound consist principally of sediment clogged dead coral framework, coral rubble and other skeletal remains of various organisms (Foubert et al. 2005a; Wheeler et al. 2005b; see also Chap. 7). Shallow gravity coring (MD01-2451G) revealed that the upper on-mound sediments consist mainly of corals embedded in a carbonate-rich matrix, interspersed with occasional layers of siliciclastic material of ∼1 m thick (Foubert et al. 2007; see also Chap. 6).

The first visualization of Challenger Mound was established on high-resolution 2D seismic data (Henriet et al. 2002) (Fig. 2.13). Two of the previously described seismic units (see Sect. 2.1.1), respectively seismic unit U3 and seismic unit U1, are encountered in the environment of Challenger Mound (Fig. 2.13). Challenger Mound roots on the regional unconformity RD1 separating seismic units U3 and U1 (Van Rooij et al. 2003; Van Rooij 2004). The mound appears on seismic profiles as an almost acoustically transparent dome-shaped structure. The mound is bounded by diffraction hyperbolae originating at the summit and the flanks of the mound. Inside the mound, no internal reflectors have been recognized, indicating a uniform facies without any large acoustic impedance differences. The mound acoustic facies might also be interpreted as a loss of seismic energy due to scattering or absorption

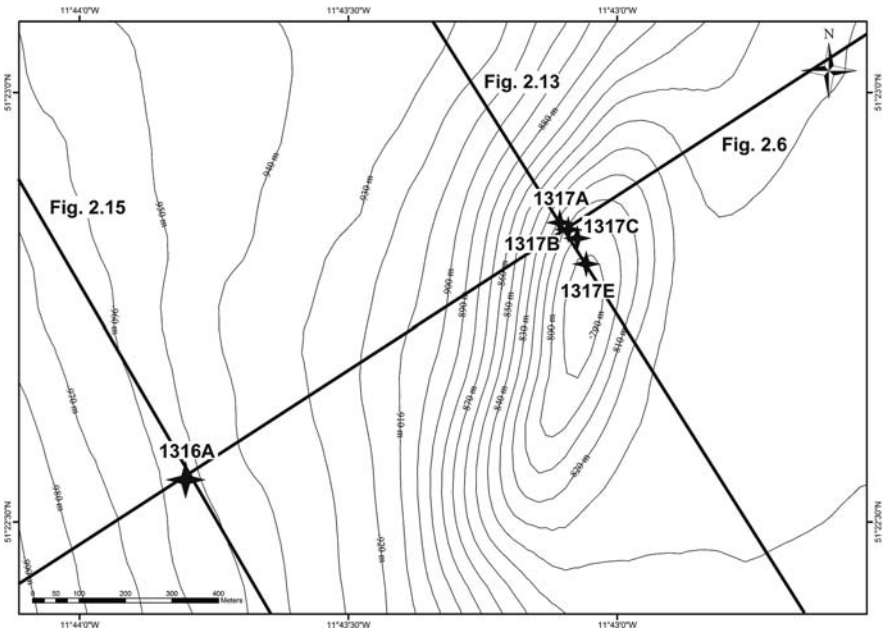

Fig. 2.12 Bathymetric map of Challenger Mound showing the location of the IODP Holes (on-mound Site U1317 and off-mound Site U1316) (*stars*) and the seismic lines visualized on Figs. 2.6, 2.13, and 2.15. Contour interval set at 10 m. Map is based on AWI bathymetry (Beyer et al. 2003)

by the rough seabed and internal structure of the mound. Analysis of velocity pull-ups of single-channel seismic indicates that the seismic facies of coral banks is homogeneous and transparent with an estimated internal velocity of 1850 ± 50 m/s (De Mol et al. 2002; Henriet et al. 2002). Such a velocity suggests a carbonate-rich sediment (velocity = 2300 m/s) intermixed with terrigenous material (velocity = 1700 m/s), as ground-truthed by the superficial sediment samples (Foubert et al. 2005a). The substratum of the mound is characterized by a set of clinoforms formed by a number of superposed sigmoid reflectors of seismic unit U3 (Fig. 2.13). These clinoforms are frequently characterized by a high-amplitude top sigmoid reflector. This seismic facies is interpreted as migrating sediment drift bodies (Van Rooij et al. 2003; De Mol et al. 2005). The high amplitude and the reversals of signal polarity of these top sigmoid reflectors indicate that these clinoforms could have contained traces of gas (Henriet et al. 2002) or a remarkable change in lithology (De Mol et al. 2005, 2007).

The main objectives to drill Challenger Mound, and in particular of interest in this study to unveil the nature and significance of the carbonate mound record, were (Exp. 307 Scientists 2006d):

- Describe the stratigraphy, lithology and diagenetic characteristics of the mound sediments to establish a principal depositional model for carbonate mounds, including the timing of key mound-building phases. This will help answer the

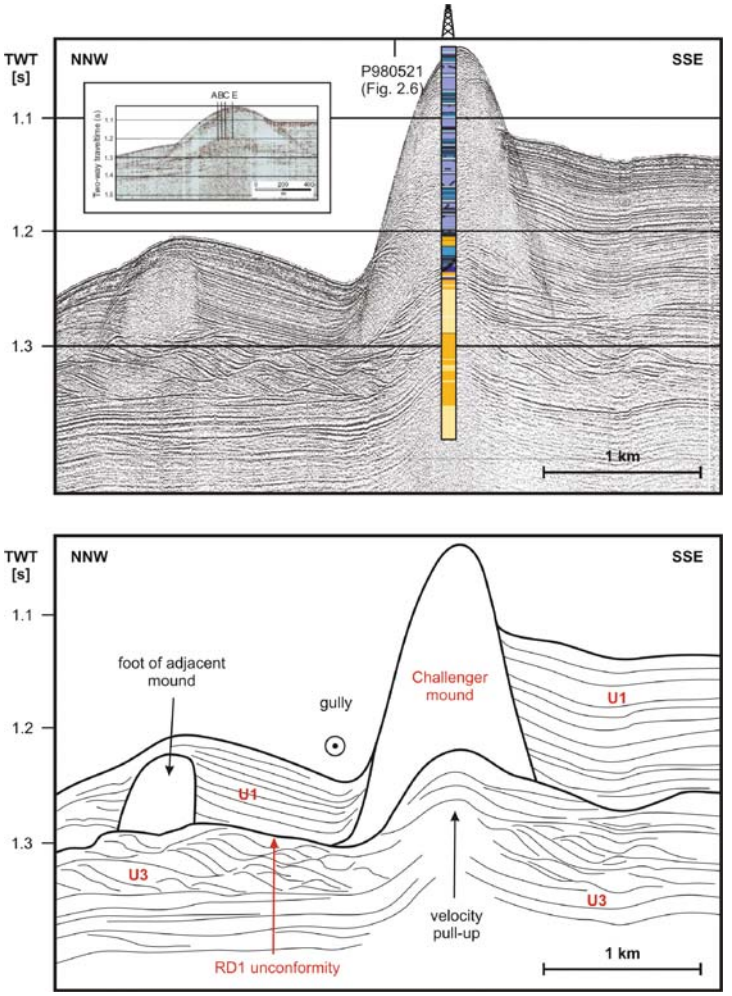

Fig. 2.13 High-resolution NNW-SSE seismic profile P000658, illustrating Challenger Mound and its environmental setting (modified after Henriet et al. 2002; Van Rooij 2004). The different described units and unconformities are annotated. The location of the described seismic profile is noted on Figs. 2.12 and 2.16. The drill location is visualized. Inset show the location of the different holes from the flank to the *top* of the mound (modified after De Mol 2002)

question whether Challenger Mound provides a present-day analog for understanding ancient mound systems.

- Define the relationship, if any, between the mound-developing events and global oceanographic events that might have formed the erosional surfaces as displayed on high-resolution seismic profiles.

Other objectives and interests to drill Challenger Mound but not highlighted in this study were (Exp. 307 Scientists 2006d):

- Establish what kind of surface the mound was built on; for instance, whether the mound base is a carbonate hardground of microbial origin and whether past geofluid migration acted as a prime trigger for mound genesis.
- Analyse microbiological profiles to define the sequence of microbial communities and geomicrobial reactions throughout the drilled sections.

It should be mentioned that no specific substrates such as hardgrounds are encountered at the mound base during the drilling process (Exp. 307 Scientists 2006d). Neither traces of hydrocarbon fluid flow or gas migration could be found (Exp. 307 Scientists 2006d). The more, it appeared that the microbiological activity in Challenger Mound is rather low (Exp. 307 Scientists 2006d). However, Webster et al. (2009) indicate a significant and active prokaryotic community both within and beneath the carbonate mound. Although total cell numbers at certain depths were lower than the global average for other subseafloor sediments and prokaryotic activities were rather low (iron and sulfate reduction, acetate oxidation, methanogenesis), they were significant enhanced compared to the surrounding reference site (Webster et al., 2009). More research is necessary to fully address these topics in their palaeoenvironmental context, what is beyond the scope of this study.

To fulfil the described objectives, five holes where drilled on the north-western shoulder of Challenger Mound, named as Site U1317 (Exp. 307 Scientists 2006d). Four of the five holes, more exactly Holes U1317A, U1317B, U1317C and U1317E respectively going from the north-western flank to the top of Challenger Mound (Figs. 2.12 and 2.13), form the main study object throughout Chaps. 3, 4, and 5. Table 2.1 represents the geographical coordinates and the technical characteristics of Holes U1317A, U1317B, U1317C and U1317E.

During IODP Expedition Leg 307, three standard coring systems were used: the advanced piston corer (APC), the extended core barrel (XCB) and the rotary core barrel (RCB). The APC is a hydraulically actuated piston corer designed to recover relatively undisturbed continuous 9.5 m long oriented core samples from very soft to firm sediments that cannot be recovered well by rotary coring (Fig. 2.14A). The APC inner core barrel is run to bottom on the coring wireline. Pump pressure is then applied to the drill pipe, which severs the shear pins and strikes the inner core barrel 9.5 m into the sediment. The inner core barrel containing the core is then retrieved by wireline. A wireline packoff at the top of the drill string permits rotation of the

Table 2.1 Geographical coordinates and technical characteristics of Holes U1317A, U1317B, U1317C and U1317E

Site/Hole	Latitude	Longitude	Water depth [mbsl]	No. of cores	Penetration [m]
1317A	51°22.848'N	11°43.108'W	815.1	18	138.8
1317B	51°22.840'N	11°43.092'W	798.0	17	148.2
1317C	51°22.830'N	11°43.076'W	791.7	18	153.0
1317E	51°22.799'N	11°43.058'W	781.1	18	158.6

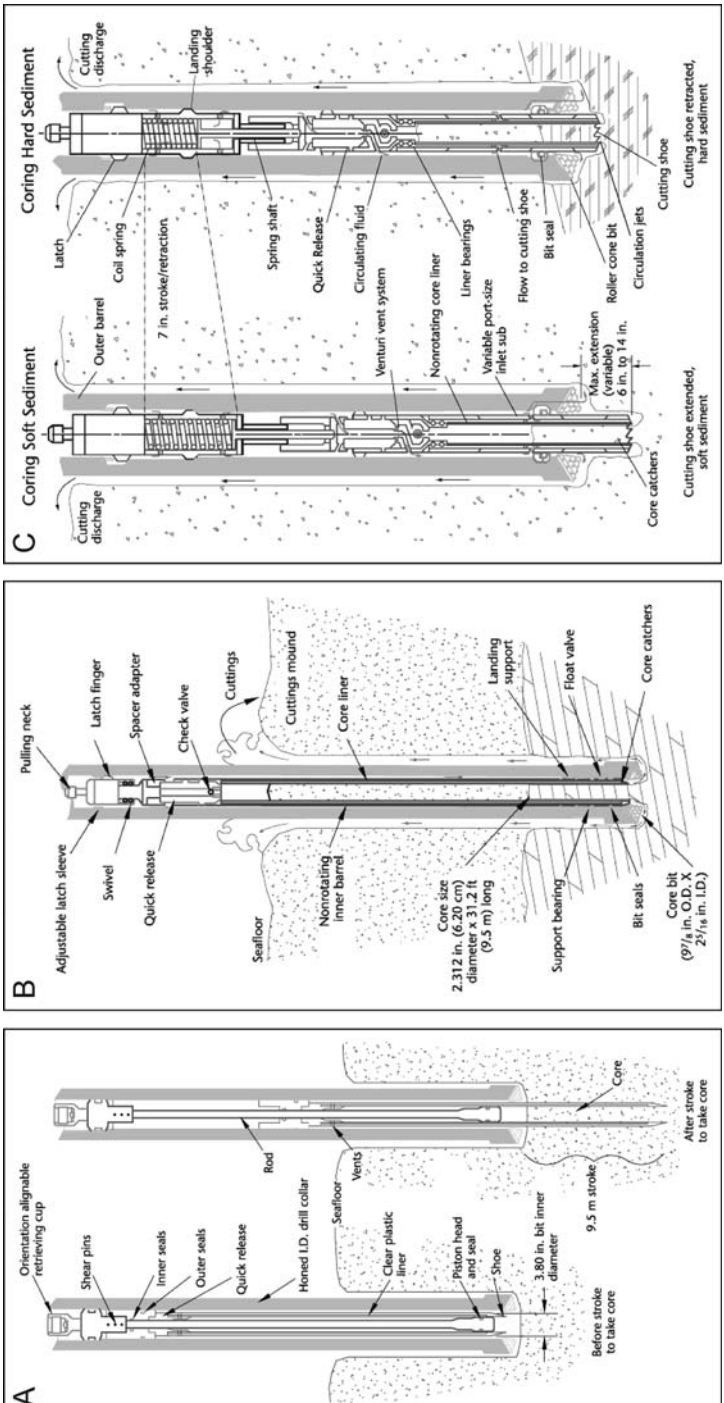

Fig. 2.14 Schematic illustrations of different coring techniques used during IODP Expedition Leg 307: (**A**) Advanced Piston Coring (APC), (**B**) Rotary Core Barrel (RCB) and (**C**) Extended Core Barrel (XCB) (after http://iodp.tamu.edu/tools/)

drill string and continued circulation while the core is retrieved. After core retrieval, the bit and bottom-hole assembly (BHA) are again advanced 9.5 m, repeating the process. The RCB is a rotary coring system designed to recover core samples from firm to hard sediments and igneous basement (Fig. 2.14B). The RCB is crucial for oceanic crustal hard rock studies. The RCB inner core barrel freely falls (and is pumped) through the drill string and latches into the RCB bottom-hole assembly (BHA). The main RCB bit trims the core. The BHA, including the bit and outer core barrel, is rotated with the drill string while bearings allow the inner core barrel to remain stationary. The inner core barrel can hold a 9.5 m core and is retrieved by wireline. The XCB coring system is used in sedimentological, climate, and palaeoceanographic studies dealing with firm sediments (Fig. 2.14C). The XCB is used to recover 9.5 m long core samples from soft to moderately hard formations. The XCB is typically deployed when the formation becomes too stiff to piston core (i.e., upon piston coring "refusal") or when it is not hard enough to permit efficient recovery with the RCB. The XCB cutting shoe extends ahead of the main bit in soft sediments but retracts into the main bit as the weight on bit increases when firm lithologies are encountered. The XCB uses the same BHA as the APC. The XCB relies on rotation of the drill string to advance the hole, and an integral cutting shoe trims the core sample at the same time. These standard coring systems and their characteristics are in detail summarized in a number of Ocean Drilling Program (ODP) technical notes (http://iodp.tamu.edu/tools/).

During IODP Expedition Leg 307, APC was mainly used to recover the mound sediments. Most cored intervals were ~9.5 m long, which is the length of a standard core barrel. Cores of ~9.5 m long were subsequently split in sections of ~1.5 m length. Drilled intervals are referred to in this study as metres below sea-floor (mbsf). Drilling deformation can occur as sediment disturbance, including the concave downward appearance of horizontal bedding, haphazard mixing of lumps of different lithologies (mainly at the top of the cores), fluidization and flow-in (Exp. 307 Scientists 2006b). The latter three disturbances can be in particular severe during XCB and RCB drilling, resulting in typical "biscuit-structures". However, such extensive deformations were filtered out during processing of the data. Throughout this study, the numbering of sites, holes, cores and samples was used following the standard IODP procedure (Exp. 307 Scientists 2006b). For example, a sample identification of 307-U1317A-1H-2, 10–12 cm, represents a sample removed from the interval between 10 and 12 cm below the top of Sect. 2, Core 1 (H designate this core was taken with APC) of Hole U1317A during Expedition 307.

Hole U1317A (51°22.848'N, 11°43.108'W) is localized at a calculated water depth of 815.1 m. Sixteen APC cores advanced to 130.80 mbsf. In a second phase, the coring assembly was switched to extended core barrel (XCB) and two XCB cores advanced an additional 8 m to a total depth in Hole U1317A of 138.80 mbsf. Hole U1317B (51°22.840'N, 11°43.092'W) is situated 23 m SE of Hole U1317A at a calculated water depth of 798 m. Sixteen APC cores advanced to 145.20 mbsf. Subsequently, the coring assembly was switched to XCB for one core, which advanced only 3 m, for a total depth of 148.20 mbsf in Hole U1317B. Hole U1317C (51°22.830'N, 11°43.076'W) is located 26 m SE of Hole U1317B at a calculated

water depth of 791.7 m. APC coring recovered seventeen APC cores advanced to a depth of 150.80 mbsf. The coring assembly was switched to XCB for one core, which advanced only 2.2 m, for a total depth in Hole U1317C of 153.00 mbsf. Hole U1317E is situated 60 m SSE of Hole U1317C at a calculated water depth of 781.1 m close to the summit of the mound. Eighteen APC cores were recovered, penetrating until a depth of 158.60 mbsf. For more detailed technical specifications of the cored holes, the reader is referred to the "Proceedings of the Integrated Ocean Drilling Program, Volume 307" (Ferdelman et al. 2006).

2.3 Drilling the Off-Mound Regions

Besides drilling Challenger Mound during IODP Expedition Leg 307 aboard the R/V JOIDES Resolution, two off-mound sites were drilled to gain information about the palaeoenvironmental setting of the surroundings of Challenger Mound (Exp. 307 Scientists 2006c,e). In this chapter both off-mound sites, Site U1316 and Site U1318 respectively located downslope and upslope of Challenger Mound, will be shortly presented.

2.3.1 Site U1316

Site U1316 (51°22.56' N, 11°43.81'W; 965 m water depth) is located in the downslope sediment deposits ~700 m south-west of Challenger Mound (Fig. 2.12). Surface sediments at Site U1316 are characterized by a patchy distribution of gravel- to boulder-sized material (interpreted as dropstones) on a rippled to unrippled sandy seabed associated with scouring features and gravel patches attesting an intensive and erosive northward-flowing bottom current regime in these areas (Foubert et al. 2005a; Wheeler et al. 2005b; see also Chap. 7). Shallow piston coring (MD01-2450) recovered 12 m of silty clay with common to abundant nannofossils (Foubert et al. 2007; see also Chap. 6). Fine to medium sandy intercalations and a few centimetre-scaled silty layers are present between the silty clays. The sediments at this site are interpreted as drift sediments (Van Rooij et al. 2003; Foubert et al. 2007; Van Rooij et al. 2007a,b; see also Chap. 7). The presence of a turbidite layer evidences a complex sedimentological and hydrodynamic environment whereby the interaction between alongslope and downslope sedimentological processes plays an important role. Only seismic units U3 and U1 are encountered at Site U1316, separated by the regional erosional unconformity RD1 (Fig. 2.15). Scouring and moat features around the mound suggest that the mound had already a substantial height before the surrounding drift sediments were deposited (Van Rooij et al. 2003).

The principal objective to drill Site U1316 during IODP Expedition Leg 307 and to incorporate the study of Site U1316 in this work was to gain insight into the history of the drift deposits at the downslope flank of Challenger Mound. Because of the close proximity of the site to Challenger Mound, the Quaternary deposits at

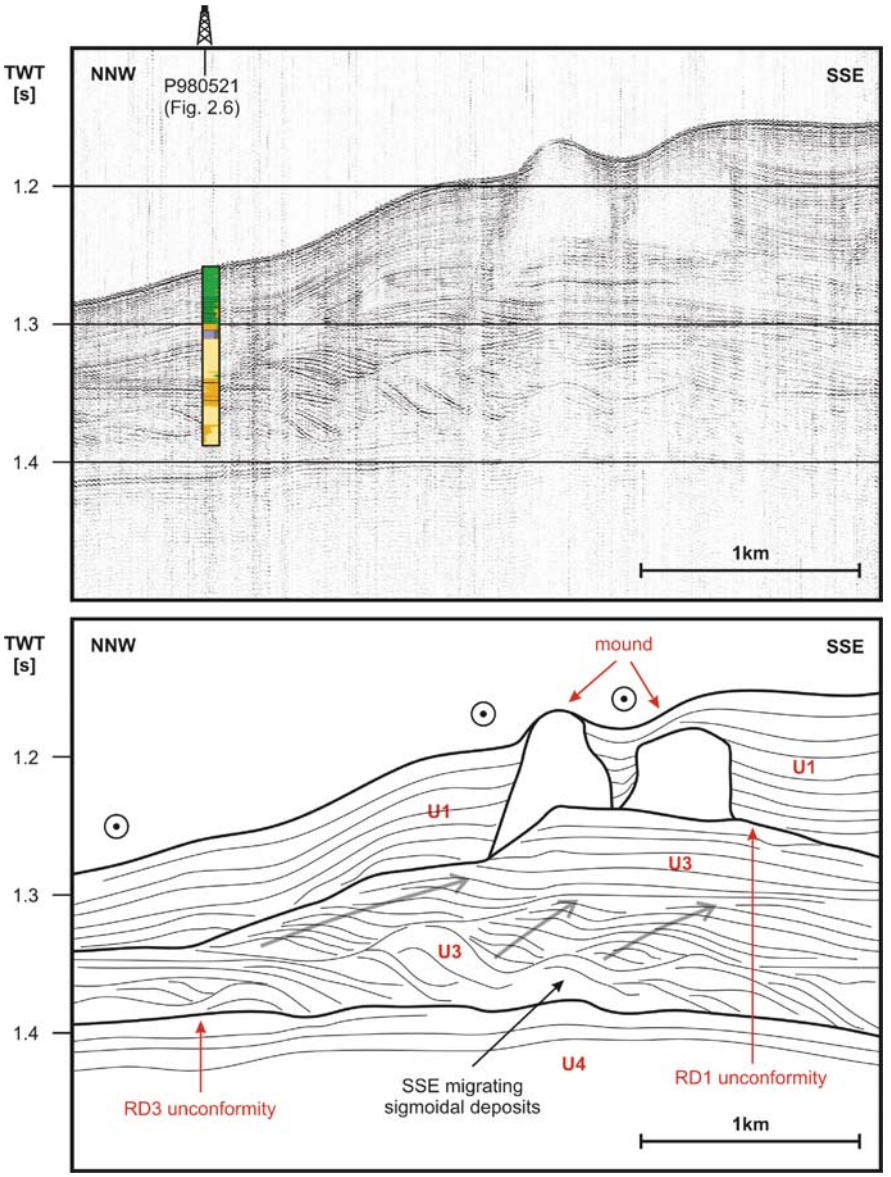

Fig. 2.15 High-resolution NNW-SSE seismic profile P000660, illustrating the downslope sediments off Challenger Mound (modified after Van Rooij 2004). The different described units and unconformities are annotated. The location of the described seismic profile is noted on Figs. 2.12 and 2.16. The drill location is visualized

Table 2.2 Geographical coordinates and technical characteristics of Holes U1316A and U1318B

Site/Hole	Latitude	Longitude	Water depth [mbsl]	No. of cores	Penetration [m]
1316A	51°22.551'N	11°43.803'W	948.4	21	134
1318B	51°26.148'N	11°33.019'W	408.8	27	244.6

Site U1316 should yield information on the development of the mound itself as well as the depositional history of the mound environment.

Three holes were drilled at Site U1316 but only Hole U1316A will be described and highlighted in this study (Fig. 2.12). Table 2.2 represents the geographical coordinates and the technical characteristics of Hole U1316A. Hole U1316A (51°22.551'N, 11°43.803'W) is located at a calculated water depth of 948.8 m. Eight APC cores advanced to 66.30 mbsf. From this depth on, the coring assembly was switched to XCB, and 13 XCB cores advanced an additional 67.7 m to a total depth of 134.00 mbsf.

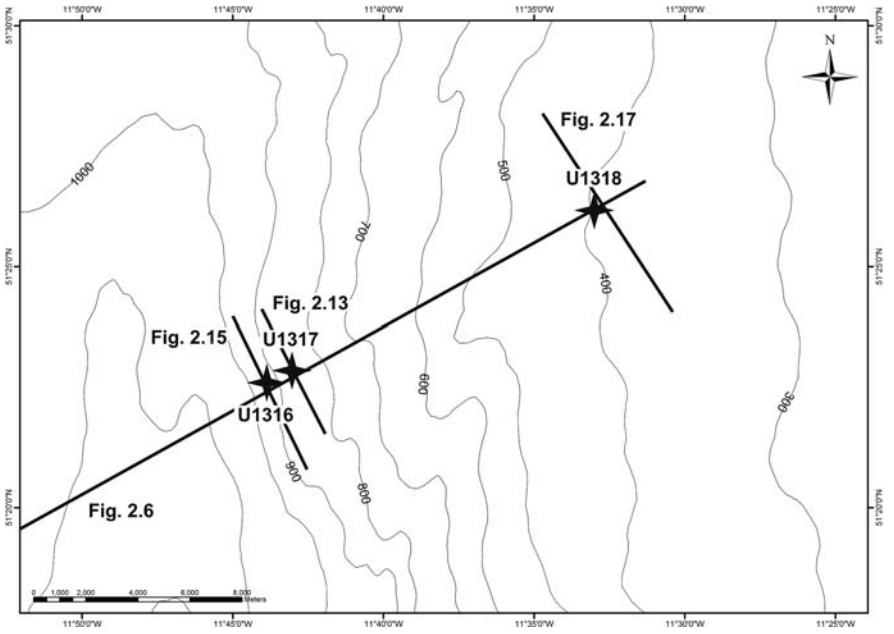

Fig. 2.16 Bathymetric map showing the location of the IODP Holes (on-mound Site U1317 and off-mound Sites U1316 and U1318) (*stars*) and the seismic lines visualized on Figs. 2.6, 2.13, 2.15, and 2.17. Contour interval set at 100 m. Map is based on GEBCO bathymetry

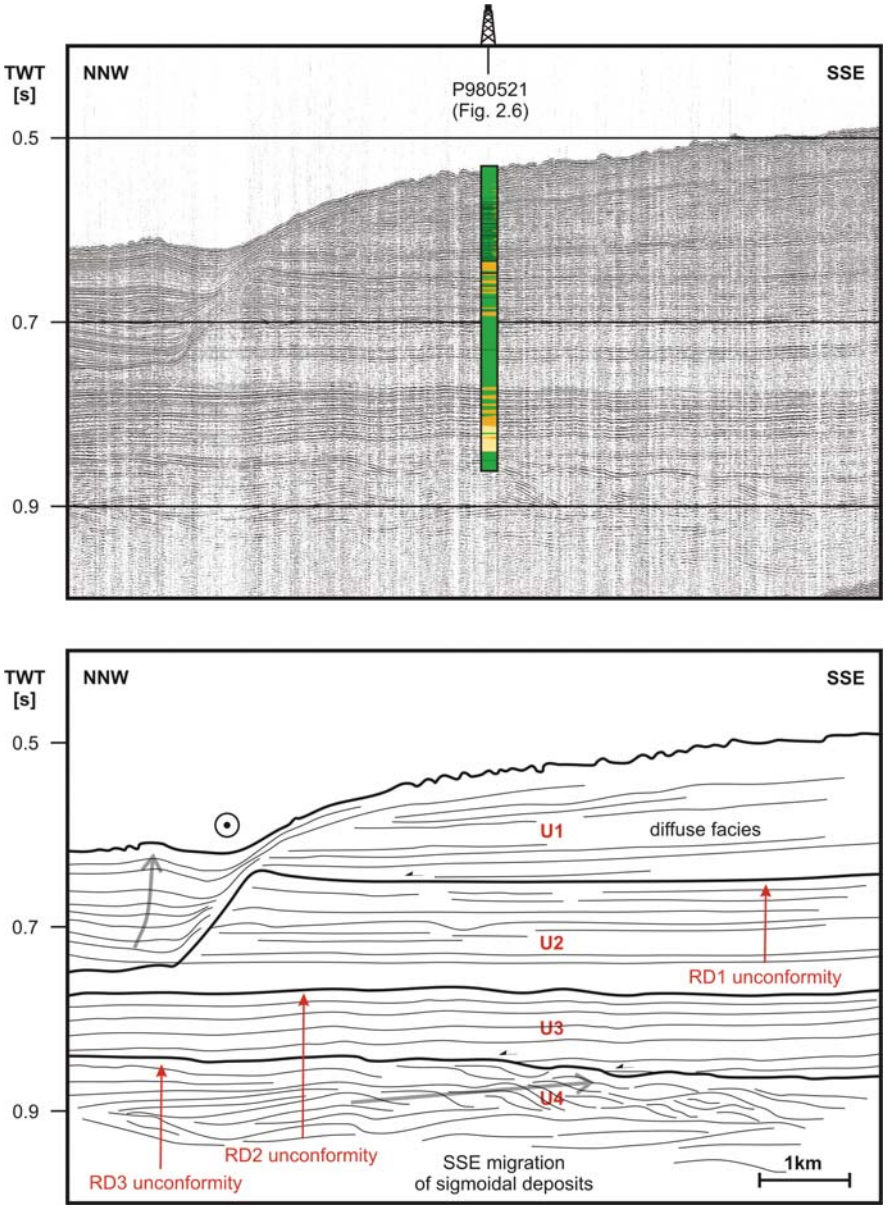

Fig. 2.17 High-resolution NNW-SSE seismic profile P010520, illustrating the upslope sediments off Challenger Mound (modified after Van Rooij 2004). The different described units and unconformities are annotated. The location of the described seismic profile is noted on Fig. 2.16. The drill location is visualized

2.3.2 Site U1318

Site U1318 (51°26.16'N, 11°33.0'W; 423 m water depth) is located 13 km NE of Challenger Mound on the south-west continental margin of Ireland (Fig. 2.16). Van Rooij et al. (2003) interpreted the sediments upslope of Challenger Mound in the neighbourhood of Site U1318 as contourite or drift deposits. Figure 2.17 represents a seismic profile through Site U1318, visualizing the three encountered seismic units U3, U2 and U1. The seismic units U1 and U2, and U2 and U3 are separated respectively by the described RD1 and RD2 disconformities (see also Sect. 2.1.1). Unit U3 is characterized by a series of parallel, continuous layers of low amplitude. At this site, the base of unit U3 is formed by a series of sigmoid-shaped bodies. Unit U2 is characterized by a nearly transparent acoustic facies on top of the erosional unconformity RD2. Only a few sets of continuous, relatively high amplitude reflectors are observed in unit U2. The uppermost seismic unit U1, characterized by slightly upslope migrating wavy parallel reflectors, represents Quaternary drift deposits (Van Rooij et al. 2003).

The principal objective to drill Site U1318 and to incorporate the study of Site U1318 in this work was to recover the sediments from the seismic units U2 and U3 to refine the palaeoenvironmental history before the onset of mound growth, or more exactly before the initiation of the growth of Challenger Mound.

Only Hole U1318B (51°26.148'N, 11°33.019'W), located at a water depth of 408.8 m, from the three Holes drilled at Site U1318 is retained in this study. The geographical coordinates and the technical characteristics of Hole U1318B are presented on Table 2.2. Fourteen APC cores advanced to 128.50 mbsf. Thirteen XCB cores advanced an additional 116.1 m to a total depth of 244.60 mbsf.

2.4 Summary

During **IODP Expedition Leg 307** aboard the **R/V JOIDES Resolution**, three sites were drilled: (1) the flanks and **top** of **Challenger Mound (Site U1317)**, (2) the sediments downslope of Challenger Mound (**Site U1316**) and (3) the sediments **upslope** of Challenger Mound (**Site U1318**). At each site, different holes were recovered from which **Holes U1317A**, **U1317B**, **U1317C**, **U1317E**, **U1316A** and **U1318B** are studied in detail throughout **Chaps. 3**, **4**, and **5.**

Challenger Mound is a 150 m high **carbonate mound** and belongs to one of the 66 carbonate mounds encountered in the **Belgica Mound Province** at the eastern margin of **Porcupine Seabight**, SW of Ireland.

Porcupine Seabight can be interpreted as a basin structure (**Porcupine Basin**) formed as a Middle to Late Jurassic failed rift of the proto-North Atlantic Ocean. The centre of the basin is filled with more than **6 km of sediment** deposited during the **Cenozoic** post-rift period. Following the **STRATAGEM** nomenclature (2002, 2003) **four megasequences RPa**, **RPb**, **RPc** and **RPd** can be distinguished separated from each other by respectively the **C10, C20**, **and C30 unconformities**

(Evans et al. 2005). Van Rooij et al. (2003, 2007a,b), Van Rooij (2004), De Mol (2002) and De Mol et al. (2002) developed a more detailed seismostratigraphic framework for the eastern margin of Porcupine Seabight. They distinguished **four seismic units** (**U1**, **U2**, **U3**, and **U4**) separated from each other by **three unconformities** (**RD1**, **RD2**, and **RD3**).

Sidescan sonar records evidence that the Belgica Mounds are occurring in a **very dynamic environment** influenced by rather strong bottom currents.

The Belgica Mounds are located within the depth range of **Mediterranean Outflow Water (MOW)**. The **mean residual current** is directed **along** the local slope (mainly **northwards**). Benthic physical processes, such as **internal waves** and **bottom intensified diurnal currents**, are responsible for **enhanced currents** at the eastern margin of Porcupine Seabight (Belgica Mound Province).

Chapter 3
Imaging

Visual information is one of the most important data sources in geosciences. Indeed, the earth and planetary sciences are founded on the direct observation of natural systems. Different visualization and imaging techniques have been developed through history, going from sketches drawn in the field, or descriptions of microscopic slides to well-advanced digital imaging systems. Technological breakthroughs made it possible to look behind microscopic and macroscopic scales and to step from a two-dimensional to a three-dimensional visualization world, producing novel ways to inspect, characterize and analyse natural materials.

Digital imaging systems make it possible to visualize a high amount of information on a high resolution in a short time-span, creating enormous and detailed data sets. So, the development of well-advanced image analysis techniques, extracting quantitative information from images captured in digital form, is necessary to cope with the enormous amount of digital data sets. Digital imaging and image analysis can be important in the palaeoenvironmental studies of sediments. A comprehensive overview of different image analysis techniques and two-dimensional imaging systems for sediments and their palaeoenvironments is presented in the book entitled "Image Analysis, Sediments and Palaeoenvironments", edited by Francus (2004). A state-of-the-art review of the applications and techniques for three-dimensional imaging of earth and planetary materials is given by Carlson (2006) and Cnudde et al. (2006).

In this chapter the mound sediments will be described and visualized in detail. Standard description techniques (analogue core description, analysis of smear slides, thin sections) and standard imaging techniques (measurement of the colour reflectance, digital pictures of the core surface) were used aboard the R/V JOIDES Resolution to identify the lithology of the mound sediments in a first phase. In a second stage, X-ray computed automated tomography (CT) was used on macro- and micro-scale in specialized shore based laboratories to visualize the mound sediments in a three-dimensional environment.

A. Foubert, J.-P. Henriet, *Nature and Significance of the Recent Carbonate Mound Record*, Lecture Notes in Earth Sciences 126, DOI 10.1007/978-3-642-00290-8_3,

3.1 Methodology

3.1.1 Shipboard Measurements

Archive half sections from the holes at Sites U1316, U1317, and U1318 were described visually and by means of smear slides at specific depths, onboard the R/V *JOIDES Resolution* during IODP Expedition Leg 307. Only Holes U1317B and U1317E were retained from lithological descriptions onboard. The coral-bearing cores posed problems for conventional coral splitting in that the wire drags coral pieces up to the core face or breaks them into fragments. Sawing unfrozen cores produced a surface layer of grime, coral fragments, and matrix that could not be scraped off without damaging the sedimentary structures (Exp. 307 Scientists 2006b). Tests carried out on coral-bearing gravity cores, collected and studied in detail in the same region before IODP Expedition Leg 307, showed that freezing the cores before splitting enhances the splitting procedure creating undamaged half sections with a clean split surface (Dorschel et al. 2005; Foubert et al. 2007). So, core sections from Holes U1317B, U1317C and U1317E were frozen before splitting. However, due to the limited freezing capacity aboard the R/V JOIDES Resolution, only Hole U1317C could be completely frozen, split and described during IODP Expedition Leg 307. Cores from Holes U1317B and U1317E were frozen and split at the IODP Gulf Coast Core Repository and described during a special description session at the IODP Bremen Core Repository. Visual core description forms were used to summarize the visual core descriptions. Cores were described according to the IODP conventions with some modifications for the typical coral-bearing sediments recovered during IODP Expedition Leg 307 (Exp. 307 Scientists 2006b). To enhance the lithological core descriptions and the descriptions of the smear slides in terms of mineralogy, X-ray diffraction analyses (XRD) were carried out aboard on bulk sediment samples at specific depth intervals. The visual core description forms were digitally stored in barrel sheets using the software “Applecore”. The barrel sheets and a description of the cores and the smearslides are presented in the “Proceedings of the Integrated Ocean Drilling Program, Volume 307” (Ferdelman et al. 2006). Only the aspects relevant for this PhD study will be highlighted in this chapter.

Colour was determined visually at first, using the Munsell Color Company (1994) colour chart. In addition, colour was measured with a Minolta CM-2002 spectrophotometer mounted on an automated track (Exp. 307 Scientists 2006b) on the cores from all the holes at Sites U1316 and U1318 and on the cores from Holes U1317A and U1317C. The measurements were carried out on a damp core surface, and clear plastic film was used to cover the core. The Minolta CM-2002 measures reflected visible light in thirty-one 10 nm wide bands ranging from 400 to 700 nm. Routine measurements were made with a resolution of 2 cm. Complete cores, core sections and specific intervals of special interest were pictured with a track-mounted Kodak DCS 460 digital camera.

3.1.2 Shore Based Measurements: X-ray Computed Tomography

X-ray computed tomography (CT) on different scales made it possible to visualize and quantify the sediments, the main framework builders and the porosity of Challenger Mound in three dimensions. Computed tomography (CT) is a technique developed in medical sciences, evolved from the traditional X-ray radiography. The mathematical principle of computed tomography (CT) was developed in the early 20th century by Radon. In the early seventies, A.M. Cormack and G.N. Hounsfield, who received in 1979 the Nobel Price for Medicine, built the first computed tomography (CT) scanner also known as the Computed Axial Tomography (CAT) scanner. Soon after the use of the first medical Computed Axial Tomography (CAT) scanners became widespread in the eighties, medical machines and protocols were adapted to address three-dimensional X-ray imaging in engineering and material sciences and in the earth and planetary sciences (Carlson 2006). Cnudde (2006), Cnudde et al. (2006), and Jacobs and Cnudde (2008) give an overview of the recent progress in X-ray CT as a geosciences tool and summarize the technical details of the use of X-ray CT in earth sciences and engineering geology.

X-ray computed tomography provides a non-destructive three-dimensional characterization of materials, creating images that map the variation of X-ray attenuation within objects. All CT devices are based on the same principle: the object is positioned between an X-ray source and X-ray detector. X-rays illuminate the object along multiple intersecting paths to measure the reduction in beam intensity (attenuation) along each of these paths. The X-ray transmission through an object is function of the composition (effective atomic number), the density and the thickness of the measured materials. For each X-ray path, the total linear attenuation coefficient is the sum of the attenuation coefficients of each element in the path. Attenuation measurements are made during a rotational motion of the sample relative to the source-detector system, which provides views of the object from multiple angles (between 0 and 360°). From these data a two-dimensional image can be reconstructed that maps the linear X-ray attenuation coefficients in the object's interior, in the plane of the X-ray beam. Such a two-dimensional image is called a "slice", which has given "tomography" its name (from the Greek "tomos", which means "slice, section") (Carlson 2006). Stacking contiguous two-dimensional slices produces a three-dimensional image, visualized by means of isosurfing, volume rendering or animation with specialized visualization software. The spatial resolution of the images depends on different factors, such as the magnification M (= ratio of the distance between source and detector over the distance between source and sample), the focal spot size of the X-ray tube, the pixel size of the detector and physical phenomena like X-ray scattering and interaction between the detector pixels. In the ideal case the resolution is determined by the pixel size of the detector divided by the magnification of the system, the best achievable spatial resolution equaling the X-ray spot size (in case of detector pixels smaller than the X-ray spot, the best resolution is equal to the pixel size of the detector) (Cnudde et al. 2006).

3.1.2.1 Medical CT Scanning

In a first stage, the medical CT scanner SOMATOM Sensation 64 from Siemens, installed at their Medical Solutions research centre in Forchheim (Germany), was used to get a general idea about the amount of coral fragments in whole-core sections. The SOMATOM Sensation 64 medical scanner uses a rotating detector-source system that revolves around the object, consisting of a STRATON 80 kW X-ray tube and Ultra Fast Ceramic (UFC) multi-row detectors (Fig. 3.1) (www.medical.siemens.com).

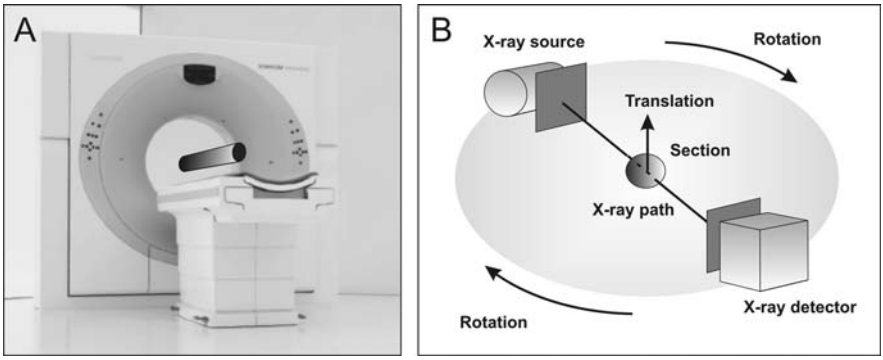

Fig. 3.1 (**A**) Picture of the Siemens SOMATOM Sensation 64 medical scanner (modified after www.medical.siemens.com). (**B**) Schematic illustration presenting the typical measure set-up used during classical medical CT scanning

In total, 17 whole-core sections were scanned from Hole U1317E (Sections 307-1317E-8H-2 to 6, 307-1317E-9H-2 to 6, 307-1317E-16H-1 to 5, and 307-1317E-17H-1 to 4) with a spatial resolution of 400 μm. Image reconstruction was carried out using the Siemens software SureView (www.medical.siemens.com) using reconstructed slice widths of 0.6 mm. Processing of the images was carried out by using the visualization software VGStudio MAX (www.volumegraphics.com) and the Siemens software SOMARIS, allowing interactive rendering and real-time 3D processing of the acquired data sets. The toolkit Morpho+, developed at the X-ray Radiography and Tomography Facility at the Institute for Nuclear Sciences from the University Ghent (UGCT) (www.ugct.ugent.be), was used for detailed three-dimensional analysis (i.e. quantification of the coral fragments) of the reconstructed volume data sets (Vlassenbroeck et al. 2007).

3.1.2.2 Micro-CT Scanning

In a second step, small-scaled structures of the mound sediments (porosity, small biogenic fragments and matrix) were visualized with a micro-CT scanner installed and developed at the X-ray Radiography and Tomography Facility at the Institute for Nuclear Sciences of the University Ghent (UGCT). Medical scanners are not suited to study objects with high resolution due to their large X-ray spot. A smaller spot can only be realized if the electron current in the X-ray tube is reduced, what is

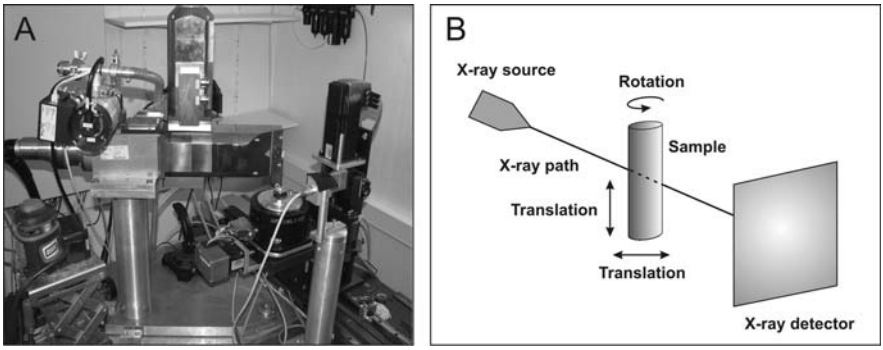

Fig. 3.2 (**A**) Picture of the set-up of the micro-CT scanner installed at the UGCT (Masschaele et al. 2007). (**B**) Schematic illustration of the set-up of a micro-CT scanner (modified after Cnudde 2006)

achieved in micro-CT scanners. Most of the micro-CT scanners use a system where the object is rotated in the X-ray beam, in contrast to medical scanners where the source-detector system is moving around the object. The micro-CT scanner set-up at the UGCT is described in detail by Masschaele et al. (2007) and presented on Fig. 3.2. During the measurements a state-of-the-art FXE-160.50 dual head open type X-ray source from Feinfocus was used with a maximum power of 150 W and a remote Rad-eye EV detector from Rad-icon (a CMOS sensor with 1024 by 512 pixels (48 μm by 48 μm)).

In total, 12 subsamples at specific depths in 12 sections from Hole U1317A were scanned with a spatial resolution of 14 μm (Sections 307-1317A-1H-3, 307-1317A-2H-3, 307-1317A-4H-4, 307-1317A-5H-3, 307-1317A-6H-3, 307-1317A-7H-3, 307-1317A-8H-3, 307-1317A-9H-3, 307-1317A-10H-3, 307-1317A-11H-3, 307-1317A-13H-3, and 307-1317A-14H-3). Subsamples were taken along the z-axis (from top to bottom) of the core sections in plastic tubes with a diameter of 10 mm and a length of 30 mm. To minimize sediment deformation and distortion by pushing the plastic tubes in the sediments, parts of the sediments were carefully cut out before. The series of radiographs provided by the micro-CT system were converted into two-dimensional cross-sections of the scanned samples by means of the reconstruction software Octopus (www.xraylab.com; Dierick et al. 2004). Three-dimensional processing of the data and volume rendering was carried out using the visualization software VGStudio MAX (www.volumegraphics.com). Morpho+ was used for detailed three-dimensional analysis (i.e. porosity analysis and quantification of bioclastic fragments) of the reconstructed volume data sets (www.ugct.ugent.be) (Vlassenbroeck et al. 2007).

3.2 Cyclic Record of the Carbonate Mound

The cores recovered on Challenger Mound (Site U1317) during IODP Expedition Leg 307 (Fig. 2.12), consist of two major sedimentological units separated from each other by a sharp firmground representing a major hiatus and identified as the

mound base (Exp. 307 Scientists 2006d). On the one hand a coral-bearing unit constitutes the mound sediments themselves, while compacted and partly cemented silt is underlying the mound sediments. In this chapter only the sediments above the mound base will be described and discussed in detail.

3.2.1 Spectral Colour Reflectance

Figure 3.3 represents the colour reflectance data (expressed as percent lightness) from Holes U1317A and U1317C, and a stack of the digital images from Holes U1317A, U1317B, U1317C and U1317E. One of the most important observations is the cyclicity noted in the digital images stacks and the colour reflectance scans. An alternation between dark green and light grey intervals is clearly observed.

Ortiz et al. (1999) has shown that diffuse spectral reflectance data can be a qualitative proxy for the percentage of carbonate content in the sediments. Indeed, by comparing the reflectance data of Hole U1317A with sediment carbonate contents determined on discrete samples (see Sect. 4.3.1), a positive correlation is observed (Fig. 3.4). Comparing the reflectance data with the geochemical properties, as discussed in Sect. 4.3, confirms the statement that varying carbonate contents play an important role in the observed cyclicity. Percent reflectance data at ODP Sites 980 through 984 in the North Atlantic Ocean show a similar systematic relationship to sediment bulk calcium carbonate content (Ortiz et al. 1999), whereby higher sediment reflectance (brightness) is associated with greater sediment bulk calcium carbonate content. In addition, sediments further to the east (ODP Sites 980/981 (Feni Drift, Rockall) and 982 (Hatton-Rockall Basin)) exhibit greater variations in percent reflectance than sediments from the west (ODP Sites 983 and 984 (Bjorn Drift)). Furthermore, most of the cycles have a saw-tooth like pattern with lightness values becoming progressively lighter from the bottom to the top followed by a rather abrupt decrease to darker values.

By examining the lithology of the opened core sections on a macroscopic scale, the mound sediments can be described as a facies of cold-water coral fragments and biogenic fragments embedded in an alternating light grey carbonate-rich matrix (Fig. 3.5) to greenish grey siliciclastic-rich matrix (Fig. 3.5). The matrix is defined as carbonate-rich when the sediments contain $>50\%$ carbonate, whereas siliciclastic sediments are defined as containing $>50\%$ siliciclastic grains (Exp. 307 Scientists 2006b). So, the carbonate/siliciclastic component ratio plays an important role in the matrix sediments responsible for the observed cyclicity in the colour reflectance records and the image stacks.

For the initial textural classification of the mound sediments, the Dunham (1962) classification of limestones was used, modified by Embry and Klovan (1971) and adapted to the carbonate sediments drilled during IODP Expedition Leg 307 (Exp. 307 Scientists 2006b) (Fig. 3.6). According to this classification scheme, the sediments can be mainly described as an unlithified floatstone with cold-water coral fragments embedded in an unlithified packstone, wackestone to mudstone matrix. In addition to the coral fragments, other biogenic fragments (such as bivalve and

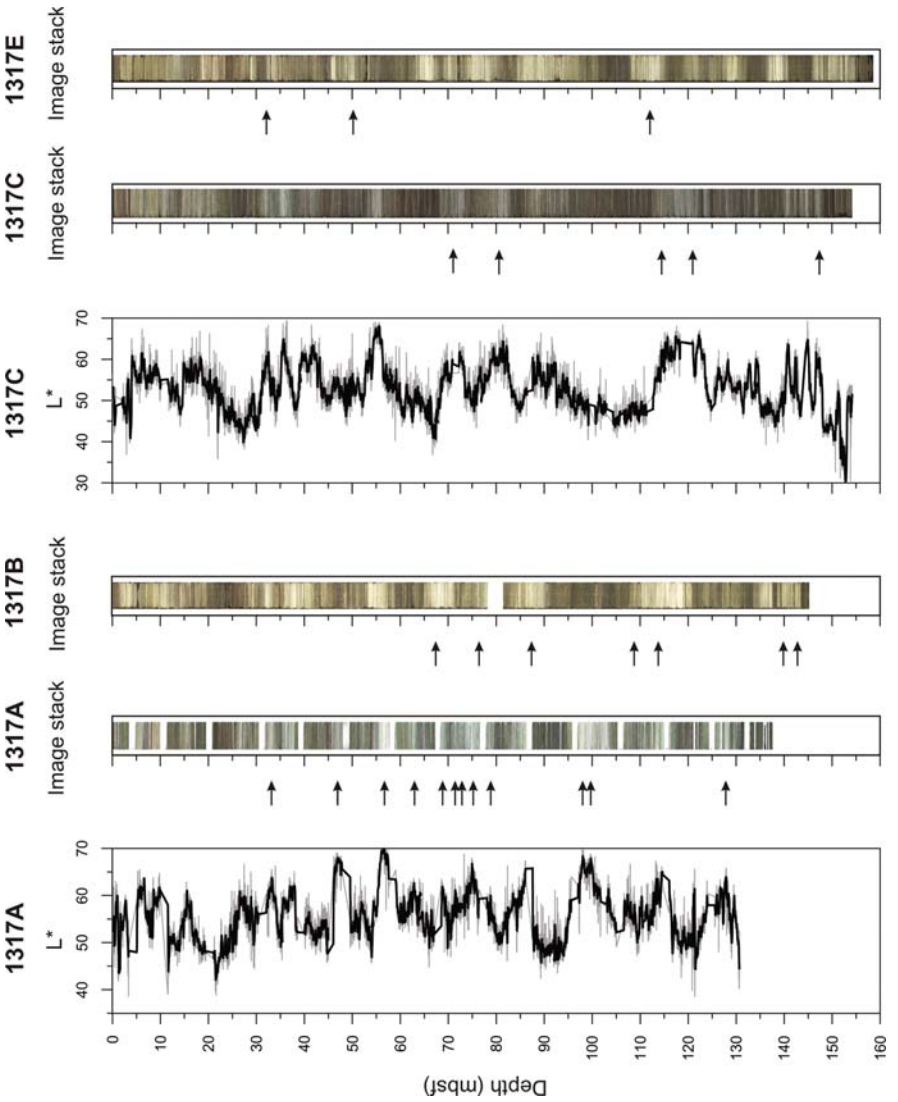

Fig. 3.3 Colour reflectance (L∗) of Holes U1317A and U1317E and image stacks of Holes U1317A, U1317B, U1317C and U1317E in function of depth (mbsf). *Arrows* indicate semi-lithified horizons. *Grey lines* represent raw records. *Black lines* represent smoothed records (7-points running mean). Note that the lightness parameters (while taking pictures) were not always the same for different holes but remained constant within the same hole

gastropod shells, echinoid spines, etc.) could be recognized macroscopically. As cold-water coral fragments are supposed to be autochthonous, the mound sediments can be better described biologically as an unlithified bafflestone with an unlithified packstone, wackestone to mudstone matrix. However, the modified Dunham

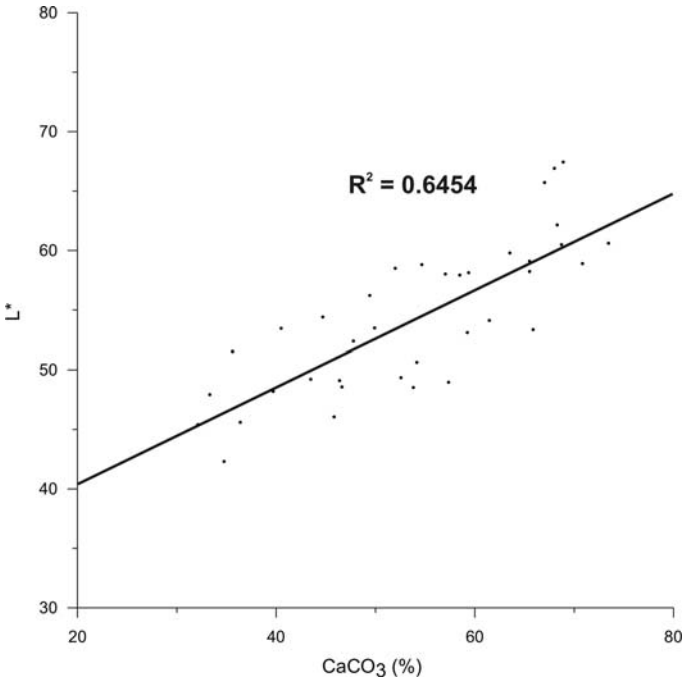

Fig. 3.4 Colour reflectance (percentage lightness L∗) in function of bulk carbonate content (percentage $CaCO_3$) determined on discrete samples from Hole U1317A

classification should be used with care because the mound sediments are composed of a mixture of carbonate and siliciclastic material. A descriptive classification system for mixed carbonate-siliciclastic rocks was proposed by Mount (1985) using four components: (1) siliciclastic sand (sand-sized quartz, feldspar, etc.), (2) non-carbonate mud (mixtures of silt and clay), (3) carbonate grains or allochems (peloids, ooids, bioclasts and intraclasts >20 μm in size) and (4) carbonate mud (or micrite, defined as <20 μm in size). The name of the sediment reflects both the dominant grain type and the most abundant antithetic component. Taking into account this classification scheme, the mound sediments can be described as an alternation between unlithified allochemic mudrock, unlithified muddy allochem limestone and unlithified muddy micrite. A disadvantage of this classification system is the term "allochem", as the cold-water coral fragments are obviously autochthonous. However, the Mount classification is adequate for the matrix sediments.

The term "unlithified" should be interpreted carefully. Most of the mound sediments are indeed "soft" and "unlithified", but some "semi-lithified" horizons less than 1 m thick are occurring in the lighter coloured intervals (Fig. 3.5). The semi-lithified identified horizons in Holes U1317A, U1317B, U1317C and U1317E are indicated by black arrows on Fig. 3.3. Coral-free intervals consisting of brown sandy

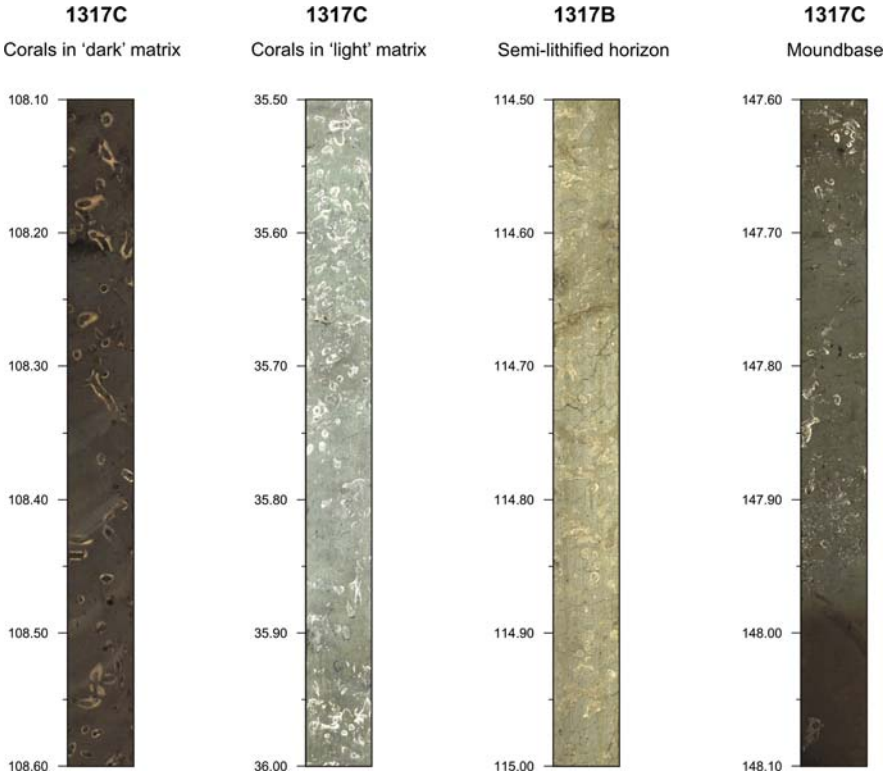

Fig. 3.5 Images representing typical lithologies encountered in the mound sediments and around the mound base

to clayey silt are rarely observed. Occasionally, larger lithoclasts such as dropstones occur. They appear to be more frequent in the topmost layers of Holes U1317C and U1317B. Erosional surfaces generally occur on top of the lighter coloured intervals. Typical burrow features are present in the semi-lithified horizons. The burrow features are filled with sediments and in many cases coated by a sub-millimetre thin fringe of pyrite. It appears that in the semi-lithified layers, the partly cemented matrix is cross-cut by surfaces that show an irregular outline and that are coated locally by a sub-millimetre thin layer of iron sulphides. The surfaces that cross-cut the marine cements can be interpreted as corrosion surfaces resulting from early post-depositional dissolution in marine-derived pore fluids (Tobin and Walker 1996). The mound base can be described as a "firmground" or "consolidated" sediment representing an erosional horizon and overlain by a basal succession of fragmented coral debris in a packstone matrix (Fig. 3.5), rather than embedding large cold-water coral fragments as observed at the centre of the mound body.

Finally, it has to be mentioned that the image stacks show an increasing thickness of the mound sediments from Hole U1317A towards Hole U1317E, so increasing from the flank to the top of the mound (Fig. 3.3).

<table>
<tr><td colspan="5">Allochthonous carbonates
original components not organically
bound during deposition</td><td colspan="2">Allochthonous
or
Autochthonous</td><td colspan="3">Autochthonous limestones
original components organically
bound during deposition</td></tr>
<tr><td colspan="5" rowspan="2">Less than 10% >2 mm components</td><td colspan="2">Greater than
10% >2 mm
components</td><td colspan="3">Boundstone</td></tr>
<tr><td colspan="2" rowspan="4">Matrix
supported</td><td rowspan="4">By
organisms
that
act
as
bafflers</td><td rowspan="4">By
organisms
that
encrust
and
bind</td><td rowspan="4">By
organisms
that
build
a rigid
framework</td></tr>
<tr><td colspan="3">Contains lime mud (<0.02 mm)</td><td>No
lime
mud</td></tr>
<tr><td colspan="2">Mud supported</td><td colspan="2" rowspan="2">Grain
supported</td></tr>
<tr><td>Less than
10%
grains
(>0.02 mm
to <2 mm)</td><td>Greater
than
10%
grains</td><td colspan="2">>2 mm
component
supported</td></tr>
<tr><td>Mudstone</td><td>Wackestone</td><td>Packstone</td><td>Grainstone</td><td>Floatstone</td><td>Rudstone</td><td>Bafflestone</td><td>Bindstone</td><td>Framestone</td></tr>
</table>

Fig. 3.6 The Dunham (1962) classification of limestones according to depositional texture, as modified by Embry and Klovan (1971) and adapted to the carbonate sediments drilled during IODP Expedition Leg 307 (Exp. 307 Scientists 2006b)

3.2.2 What's in the Matrix?

As the matrix plays an important role in the origin of the cyclic character of the reflectance records (Sect. 3.2.1) and the geophysical and geochemical records (Chap. 4), it is important to have a closer look at these matrix sediments. The matrix sediments can be divided in two categories: a biogenic (carbonate-rich) fraction versus a terrigenous (siliciclastic) fraction. The changing ratio between these two fractions is responsible for the observed cycles.

3.2.2.1 Biogenic (Carbonate-Rich) Fraction

The carbonate content from the matrix of the mound sediments is dominantly caused by calcareous nannofossil ooze of mainly coccoliths (Fig. 3.7A,B). Besides the nannofossil ooze, a high amount of micro-bioclasts are present: small fragmented cold-water coral debris, parts of small echinoderms, sponge spiculae, radiolarians, planktonic and benthic foraminifera, gastropods, bivalves and other small unidentified biogenic fragments (Fig. 3.7C–I).

Shipboard XRD analyses show the presence of calcite, aragonite and dolomite in the matrix (Fig. 3.8A). The aragonite is likely to be derived from the corals and to a lesser extent from molluscs, while the pure calcite is mainly coming from the nannofossils (coccolithophorids). A certain amount of diagenetic low-Mg calcite can not be excluded (see Chap. 4) but is limited to minor cryptocrystalline to microsparitic cements in the semi-lithified horizons. On the coccolith surfaces

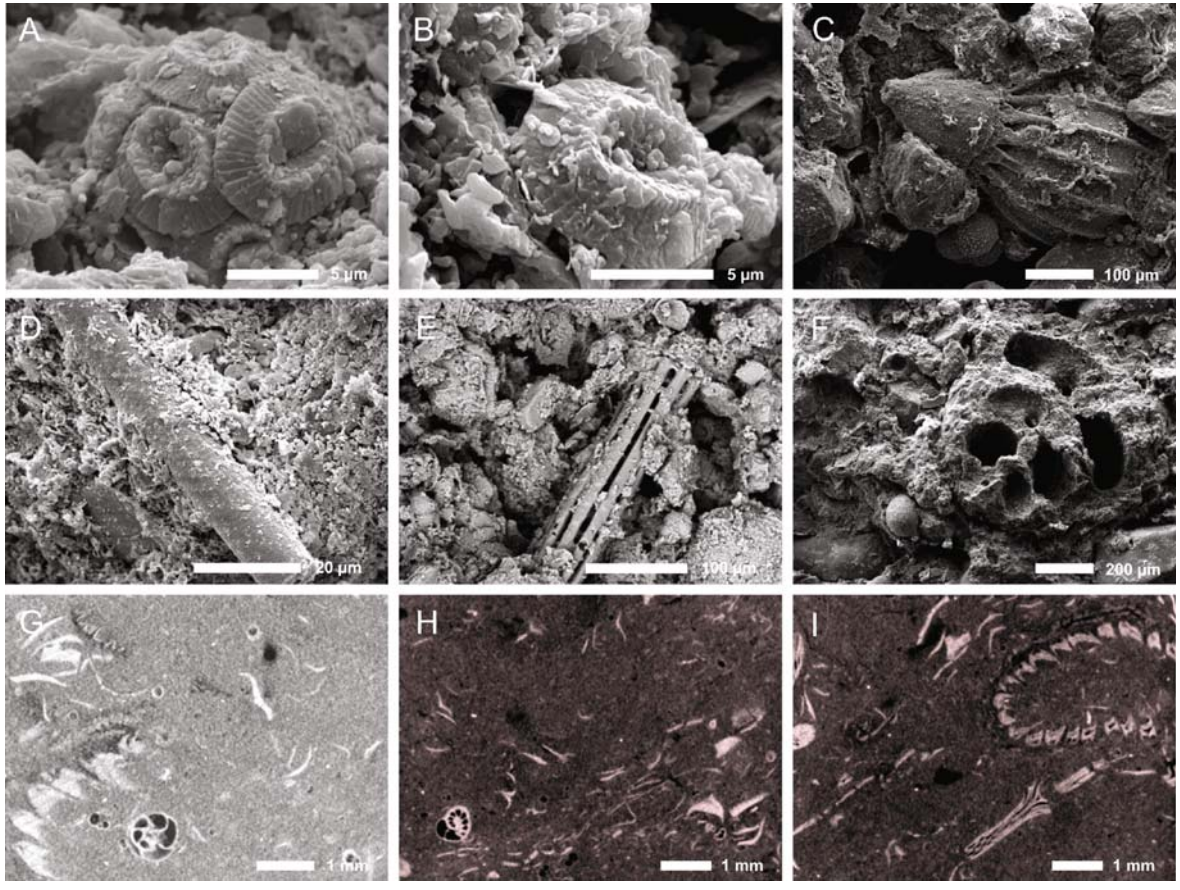

Fig. 3.7 SEM pictures (Léonide 2006; Léonide et al. 2009) (**A–F**) and μCT scans (**G–I**) from bioclasts in the mound sediments: (**A,B**) coccoliths (**C**) radiolarian (**D**) sponge spiculae (**E**) echinoid spine (**F**) foraminifera (**G–I**) foraminifera, bivalve and echinoderm fragments in micritic matrix

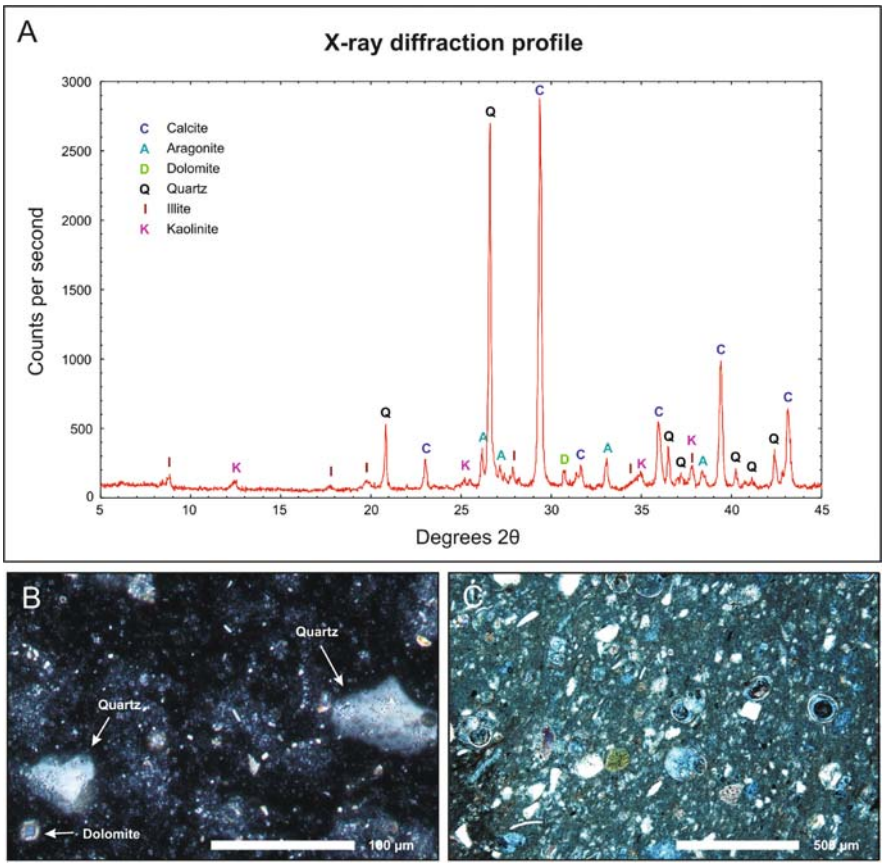

Fig. 3.8 (**A**) XRD profile from matrix sediments (Exp. 307 Scientists 2006d). (**B**) Smearslide from matrix with dominantly coccoliths and clay-sized grains and minor amounts of quartz and dolomite (Exp. 307 Scientists 2006d). (**C**) Thin section from mud matrix with forams and silt-sized quartz grains (Gregg et al. 2006)

syntaxial overgrowth of tiny calcite crystals is noted (Fig. 3.7A,B). Additionally, microsparitic rim cements are sporadically observed at the interior walls of foraminifera. The dolomite can have a detrital or diagenetic origin, but is likely to be detrital (see below).

3.2.2.2 Terrigenous (Siliciclastic) Fraction

Data from smear slides, thin sections and XRD analysis show that fine sands and silts are characterized by a dominantly quartz composition with secondary potassium feldspar and plagioclase (albite) (Fig. 3.8). Clay minerals are abundant in the mound sediments and have the same association throughout the whole mound succession, consisting dominantly of illite, kaolinite and chlorite, and a small function

of smectite (Léonide 2006; Léonide et al. 2009). Silt-sized grains of glauconite are also commonly observed. The detrital sediments can be classified as very immature, characteristic for detrital material from nearby sources. Heavy mineral grains are present in minor amounts, including zircon, tourmaline, occasional spinel, and possible rutile. Individual corroded, decimicron-sized carbonate rhombs in smear slides and minor amounts of stoichiometric dolomite in X-ray diffraction samples, suggests the presence of detrital dolomite (Fig. 3.8). It should be mentioned that Léonide (2006) and Takashima (2006) highlighted an important fraction of framboidal and monoclinic pyrite in the mound sediments, which is confirmed by detailed rock magnetic analyses in Sect. 5.3.1. This pyrite has a diagenetic origin.

3.3 Cold-Water Corals: The Framework Builders

As mentioned before, the main framework builders throughout the mound body are cold-water corals. The cold-water coral fragments are randomly orientated in the matrix and can have branch lengths up to 8 cm. The largest coral diameters were recovered from Hole U1317E, closest to the mound summit. Most of the coral fragments are identified as the species *Lophelia pertusa*. Some minor to rare occurrences of *Madrepora oculata* and *Desmophyllum cristagalli* are noted.

3.3.1 Quantification of Coral Fragments

Despite the fact that cold-water corals are observed through the whole mound body, the density and the amount of coral fragments is changing. To get an idea about the amount of cold-water corals in the core sections, two quantification techniques, based on the analysis of digital images, were developed and compared with each other.

In a first phase, corals were quantified on two-dimensional high-resolution digital images of the surface of the split core sections from Hole U1317E (Titschack et al. 2006, 2009). Quantitative analysis of digital images involves three major steps: image acquisition, image processing and image measurements (Francus 2004). It is emphasized that the quality of the image must be the best possible before any processing or quantitative measurements are undertaken. So, image acquisition is the most crucial phase. The magnification, resolution and size of the image has to be chosen in such a way that the smallest features which have to be quantified can be detected, still considering the largest feature that will be encountered and the representativity of the image with respect to the overall sample. A digital image can be described as a collection of individual, non-overlapping elements or pixels that have distinct intensities (grey scale or colour) indicating the different colour phases of the material. These pixels have a finite area. Pixels straddling a boundary effectively average the brightness levels of two regions and possess an intermediate brightness depending on how the pixels position with respect to the boundary (Russ 2002). The

resolution of the image indicates the size of the pixels, a high resolution meaning that small pixels are used. The higher the resolution and the more discerned grey levels in the image, the more accurate the boundaries between different materials can be visualized. Another important factor that has to be considered during image acquisition is the illumination: variations of the light intensity have to be kept at a minimum. To obtain high-resolution digital images, the split core sections of Hole U1317E were re-measured with a colour line scan imaging system (consisting of a custom built 3∗1024 CCD line scan imaging system) installed at the IODP Bremen Core Repository (BCR). The images have a resolution of 149 dpi (TIFF format), each picture representing split core surfaces of 150 cm long and 7.5 cm wide. To obtain quantitative information on a higher spatial resolution, the pictures were subdivided into slices of 10 cm length. The picture size and resolution were chosen in such a way that the pictures are large enough to show the typical coral distribution pattern and small enough to detect small coral fragments. In a second step, the pictures were processed with standardized filter sets in Photoshop CS to subsequently reduce noise and enhance the signal-noise ratio in the images, to manipulate the contrast/brightness levels and to convert the original pictures to greyscale pictures. After filtering the records, segmentation is one of the most critical steps in the process of transferring images into quantitative information. Image segmentation converts a grey-scale image into a two-phase black-and-white (binary) image. Segmentation of the images was carried out by a single thresholding technique using the software package AnalySIS, converting the grey-scale images into a black-and-white picture, whereby background sediments are black (0) and corals are white (1). Finally, the amount of coral fragments was determined in each picture as the percentage of white pixels, coinciding with the surface percentage of cold-water coral fragments. A total amount of 1495 surface pictures were analysed in Hole U1317E. The surface percentage of cold-water coral fragments in each picture is presented in function of the depth on Fig. 3.9.

Surface percentages are varying between 0 and 12%, with an average value of 4.5%. In total 12 cycles of sharply increasing followed by slowly decreasing coral quantity trends could be recognized from the bottom to the top of the core (Fig. 3.9). However, by comparing the image stacks with the surface percentage coral quantity no distinct correlation could be observed between the alternating darker and lighter intervals and the coral quantity cycles.

In a second phase, corals were quantified on the medical computer tomographic (CT) scans to estimate the amount of corals in whole-core sections and to check the representativeness of the two-dimensional quantitative information extracted from the digital pictures of the split core surfaces. The same steps involved in two-dimensional image analysis, have to be repeated in three-dimensional image analysis. However some substantial processing steps have to be added to convert the two-dimensional information in three dimensions. In a three-dimensional image, pixels become voxels (cubes). Image acquisition is described in detail in Sect. 3.2.1. A first adequate filtering of the images was applied during reconstruction of the images with the Siemens software SureView. The software Morpho+ was then used to quantify the amount of cold-water coral fragments on the medical scans in a

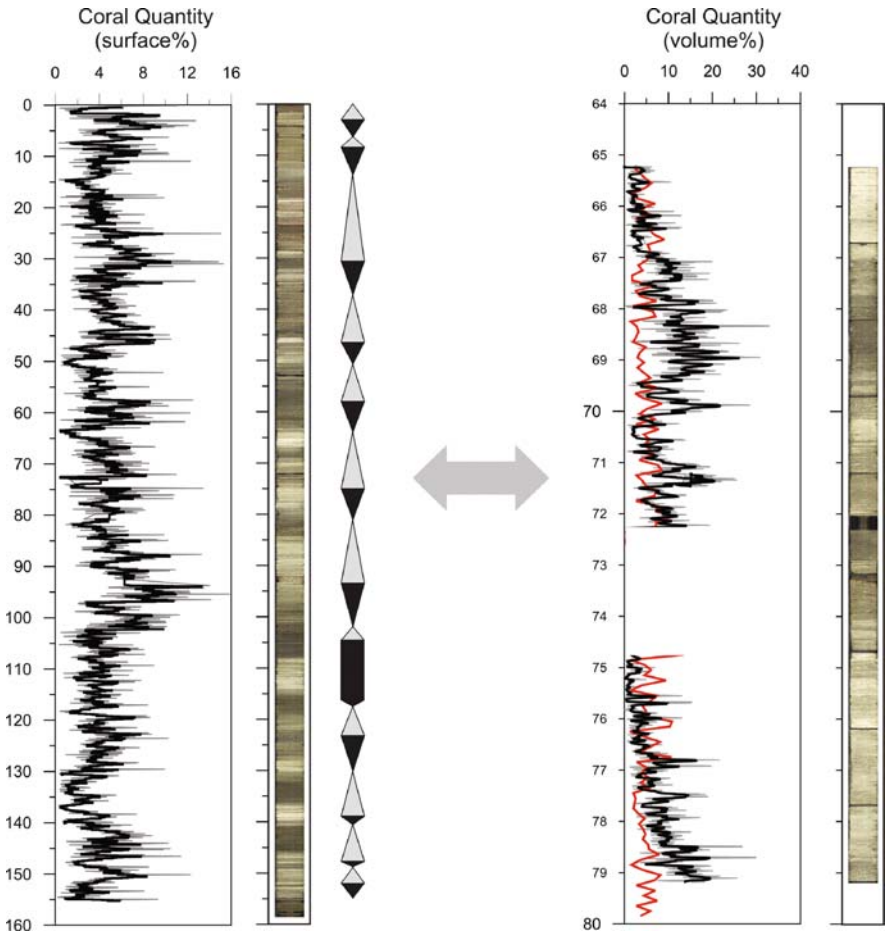

Fig. 3.9 *Left panel*: Surface percentage of coral determined on two-dimensional surface pictures of split core sections and image stack in function of depth (mbsf) for Hole U1317E (after Titschack et al. 2006, 2009). *Grey line* represents raw records. *Black line* represents smoothed record (7-points running mean). *Right panel*: Volume percentage of coral determined on medical CT scans from whole-round Sections 307-1317E-8H-2 to 6, 307-1317E-9H-2 to 4 and corresponding image stack in function of depth (mbsf). *Grey line* represents raw record. *Black line* represent smoothed record. *Red line* represents corresponding surface percentages

three-dimensional environment. Before loading the complete stack of reconstructed two-dimensional slices (TIFF-format) from a whole section in the software environment, the images were cropped in Octopus to avoid scanning artefacts, recorded at the edge of the samples and not filtered out during reconstruction of the images, to be analysed. The same volume was cropped for each analysed section, allowing quantitative comparison of the different sections. After loading the cropped slices in Morpho+, segmentation was carried out by a dual thresholding technique and an

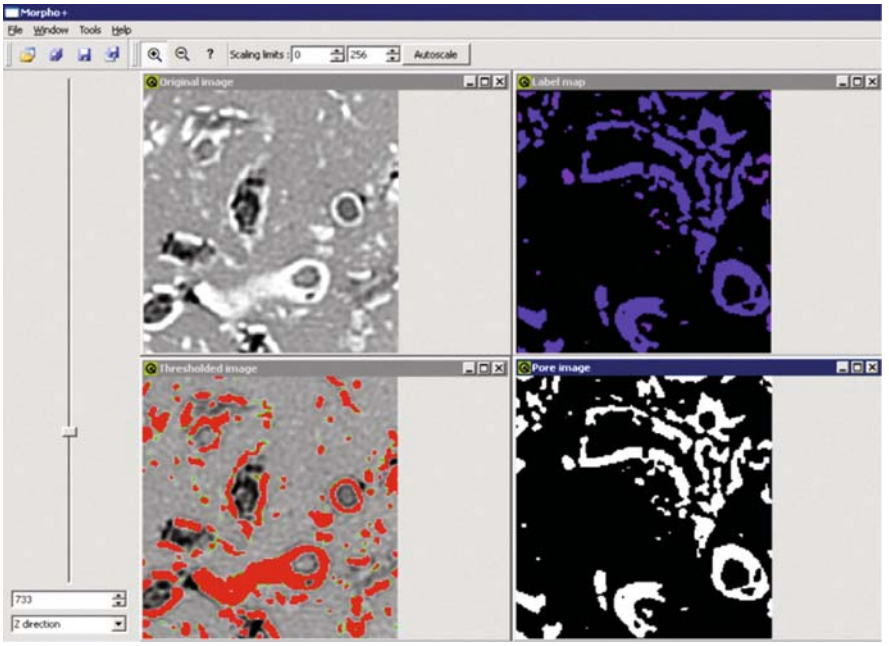

Fig. 3.10 Screenshot from Morpho+ environment representing segmentation carried by a dual thresholding technique and additional labelling operation

additional labelling operation (Fig. 3.10). A strong thresholding filtered the noise and selected the areas definitely corresponding with cold-water coral fragments, without selecting the boundaries of the fragments. Weak thresholding determined a complete delineation of all the fragments, but included some noise. The resulting segmented images combined information from both, weak and strong thresholdings to visualize the cold-water coral fragments with their corresponding boundaries. Subsequently, the data were cleaned by systematically removing isolated background and foreground pixels. The labelling step was then performed to identify subsets of the collection which are connected, resulting in a set of separated objects. Objects were labelled by attributing to each pixel (belonging to the same connected component of the input binary image) a specific grey-level value, with different values for each connected component. A set is defined as connected if each pair of its points can be joined by a path of which all the points belong to the set. After segmentation (dual thresholding and labelling), the total and partial amount of cold-water coral fragments could be calculated as volume percentage of respectively each section and each 10 slices. In a final step, each object was treated individually by calculation of the distance form. In this step the minimal distance to the border of the object is calculated for every object voxel. The distance form can be used to separate objects into an additional set of objects and to provide information about the shape and orientation of the object. In this study, a few size parameters were calculated, i.e. the equivalent diameter, which is the diameter of the sphere which

would have the same volume as an object, and the maximum opening, which is the diameter of the maximum ball which can be inscribed in the object.

Figure 3.9 represents the partial volume percentages of cold-water coral fragments in function of depth (mbsf) for Core Sections 307-1317E-8H-2 to 6, 307-1317E-9H-2 to 4. Volume percentages for these holes are varying between 0 and 26%, with an average value of 7.5% for the studied intervals. Size parameters showed that the detected coral fragments have equivalent diameters varying between 0.6 and 84 mm. The lowest equivalent diameters and maximum openings are encountered in the lightest intervals and just above the mound base, while the highest equivalent diameters and maximum openings are occurring in the darker-coloured intervals.

When dealing with image quantification, and so segmentation, it should be realized that small changes in thresholding can largely influence the results. Moreover, resolution limitations of the images can complicate segmentation. It has to be mentioned that the resolution of the CT-scanned images is lower than the resolution of the digital pictures of the split core sections, allowing detection of features up to a resolution of 400 μm on CT-scanned images compared to the possibility of the detection of features up to 170 μm on the digital pictures. On the other hand, the possibility to analyse three-dimensional volume blocks can give a more complete idea about the amount of cold-water coral fragments in the whole sections compared to the analysis of two-dimensional surface pictures. Comparing the surface percentage of cold-water coral fragments quantified on the surface pictures with the volume percentage of cold-water coral fragments quantified on CT-scanned volume blocks of each section, shows a similar background trend (Fig. 3.9), evidencing that the amount of cold-water coral fragments detected on the pictures of split core surfaces are a good relative estimation for the amount of cold-water coral fragments available in the whole section. However, the volume percentages seem to shift to slightly higher values in intervals characterized by high coral quantities compared to the surface percentages, showing that the surface percentages are quantitatively underestimating the coral quantities with a few percent in the coral-rich intervals (Fig. 3.9). It is important to mention that the coral quantity records should be interpreted with care because a dissolution effect in the lighter intervals can overprint the original coral quantity records (Sect. 3.3.2). Moreover, (dissolved) cold-water coral fragments and background sediments in lighter horizons are characterized by similar pixel values (and hence similar X-ray attenuation coefficients on CT-scan images), making it much more difficult to differentiate in an accurate way between both components. This can result in an underestimation of the amount of the original coral fragments in the lighter intervals.

3.3.2 Dissolution and Fragmentation of Coral Fragments

The preservation of the coral fragments and other large biogenic components is changing throughout the mound succession. In darker coloured intervals the preservation of the cold-water coral fragments is rather good with solid theca walls and

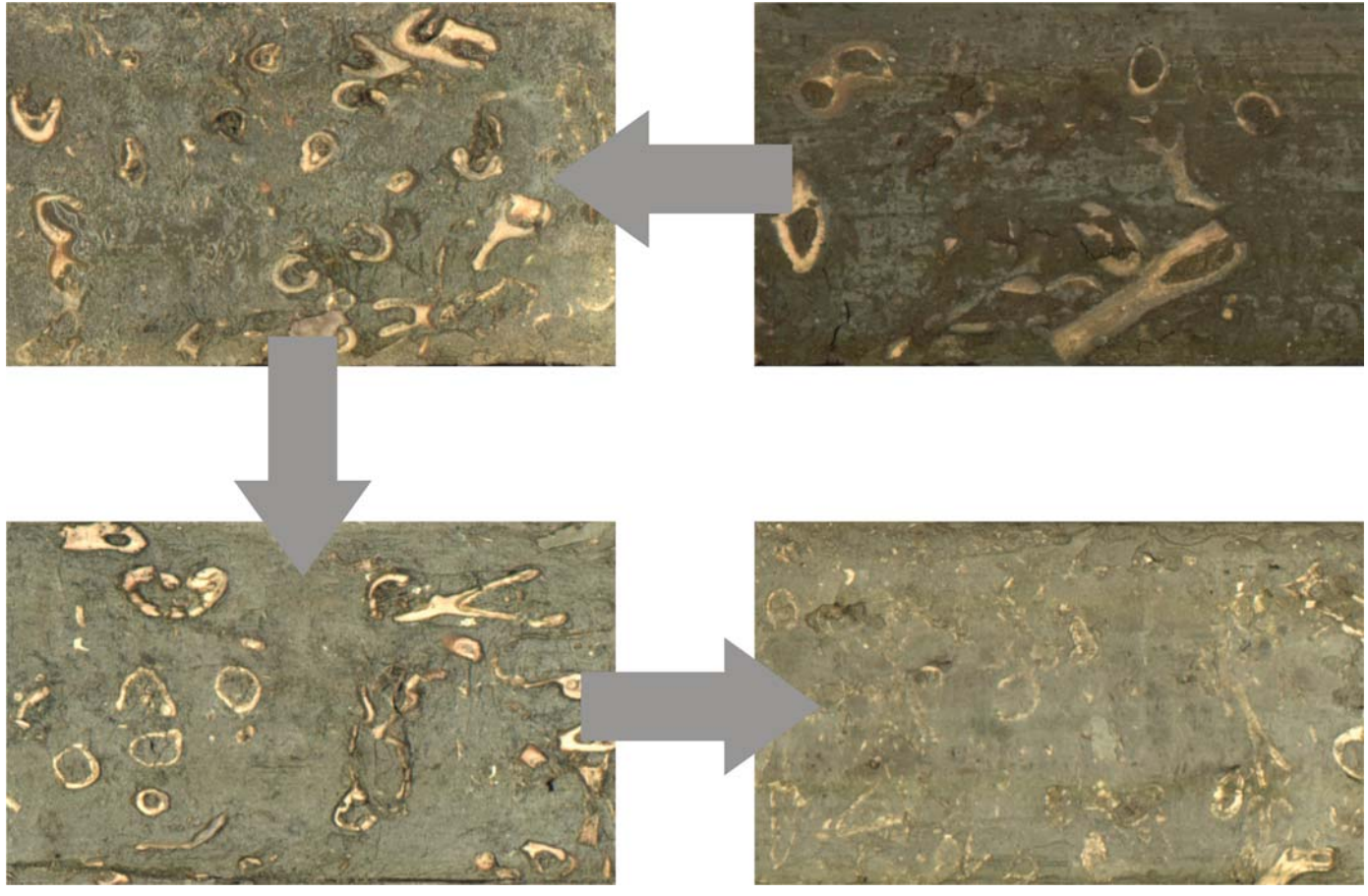

Fig. 3.11 Surface pictures presenting different stages of dissolution from well-preserved coral fragments (*upper left*) to completely dissolved coral fragments (*upper right*)

the possibility to still see the internal structure of the cold-water corals such as the lamination of the different aragonite layers (Fig. 3.11). The aragonitic skeletons in these layers did not undergo extensive dissolution. However, when the surrounding matrix is becoming lighter (∼ higher Ca-content), the corals are showing different dissolution effects (Figs. 3.11 and 3.12E). The diagenetic patterns observed in the cold-water coral fragments of Challenger Mound show that the centres of calcification are most sensitive for dissolution as (1) the small crystal sizes of these areas offer a larger reactive surface (Noe et al. 2006) and (2) bacterial and/or fungal activity utilizing the organic matter enriched between the crystals, produces a micro-environment which is undersaturated with respect to $CaCO_3$ (Titschack and Freiwald 2005). Dissolution starts at the point where the centres of calcification between outer and inner theca and those in the centre of the septa meet. Only little evidence of neomorphism or replacement by a secondary fine-crystalline neomorphic microspar of low-magnesium calcite mineralogy is noted, suggesting the production of a high moldic porosity (see Sect. 3.4). However, most of the moulds created by the dissolved coral fragment parts seem to be refilled with material from the surrounding matrix. This suggests that dissolution proceeded in soft and uncemented sediments, only leaving a faint imprint behind with a small moldic porosity and a slightly different colour and texture than the surrounding matrix. Not only corals, but also other bioclasts like molluscs underwent dissolution, leaving behind a very thin black "hair line" that may represent a relict of the periostracum. In some parts the dissolved coral fragments seems to be partly pyritized or associated with framboidal pyrite, suggesting that dissolution was accompanied or closely followed by sulphate reduction and sulphide precipitation.

In addition to dissolution, several corals show signs of extensive bioerosion. Fungal and sponge traces are quite common on the investigated cold-water coral fragments. Clionid sponges produced large borings. Large tunnel-like borings of 5–10 μm can be identified as *Orthogonum lineare* (Glaub 1994), while the round chambers with global aggregates can be identified as *Saccomorpha clava* (Radtke 1991) with the fungal sporangia still inside (Fig. 3.12A,D). These traces are typical constituents and index ichnofossils for aphotic ichnocoenoses (M. Wisshak pers. com.). Bioerosion can be an important factor in weakening the coral skeleton before chemical aragonite dissolution takes place.

Fragmentation of the coral fragments is commonly observed in the core sections (Fig. 3.12F). However, it can be questioned if the fragmentation is caused by the drilling technique, whereby coral fragments are broken during drilling or if progressive sediment accumulation gave rise to overburden stress, resulting in cracking of the skeletons. In each case, the cracking or fragmentation evidences the weakness of the coral skeletons. In addition, fragmentation can make the coral fragments more sensitive for dissolution in a second phase, as the reactive surface is bigger compared to whole coral skeletons.

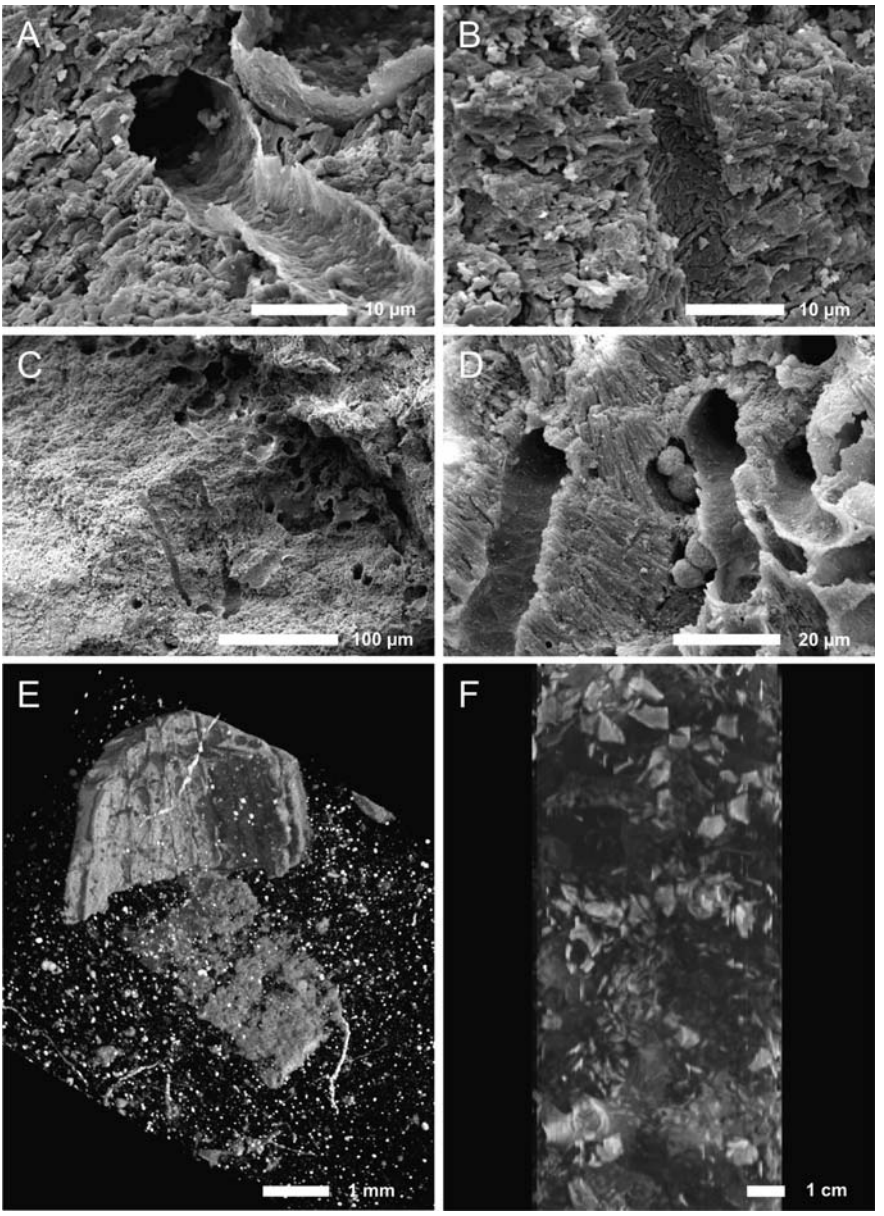

Fig. 3.12 (**A–D**) SEM pictures (Léonide 2006; Léonide et al. 2009) presenting different traces of bioerosion on the coral fragments. Tunnels of 5–10 µm are *Orthogonum lineare* (Glaub 1994) (**A,B**) and round chambers are *Saccomorpha clava* (Radtke 1991) (**C–D**). (**E**) µCT scan showing dissolution of coral fragment. (**F**) medical CT scan showing physical fragmentation of coral fragments

3.4 Porosity Analysis in Recent Carbonate Mounds

Micro-CT scanning visualized porosities and bioclasts up to a resolution of 14 μm in the mound sediments (Figs. 3.15 and 3.16). Digital image analysis of these high-resolution scans allowed quantifying the porosity and the amount of bioclasts in each sample. The software Morpho+ was used to allow identification and quantification of pores and bioclasts on well-defined volume blocks in a three-dimensional environment. For each sample, the same volume was analysed to make comparison of the different samples possible in a consistent way. The volume blocks were chosen in the inner part of the scanned samples to avoid artefacts introduced in the data sets during X-ray CT scanning and not completely filtered out during reconstruction of the images with Octopus. Beam hardening, the most frequent artefact in CT-scanning, was visible at the outer rims of the scanned samples (Fig. 3.13A). Beam hardening is caused by the fact that in a polychromatic beam X-rays with lower energy are preferentially attenuated. Due to this phenomenon, the effective attenuation coefficient of any material will diminish as the beam passes through the object and short ray paths are proportionally more attenuating than long ones (Ketcham and Carlson 2001). In reconstructed CT-images, this will artificially cause more attenuated areas near the edges of the sample and less attenuated areas in the centre. This beam hardening is especially detected in samples with cylindrical geometry, such as the samples in this study. Other artefacts that had to be taken into account while studying the reconstructed images were star artefacts (Fig. 3.13B). Star artefacts are mostly observed when very dense inclusions are present within the object. Due to scattering, randomly orientated secondary radiation is produced, which can cause noise on the reconstructed images. In some samples the high aragonite densities of the cold-water coral fragments were responsible for such star effects.

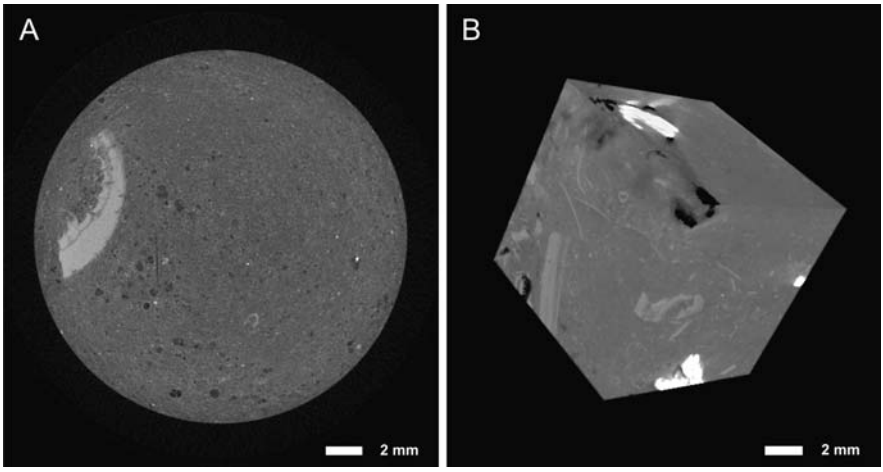

Fig. 3.13 Illustration of beam hardening at the outer margins of the μCT scans (**A**) and star effects due to the presence of dense materials like cold-water coral fragments (**B**) or small dense grains (**A**)

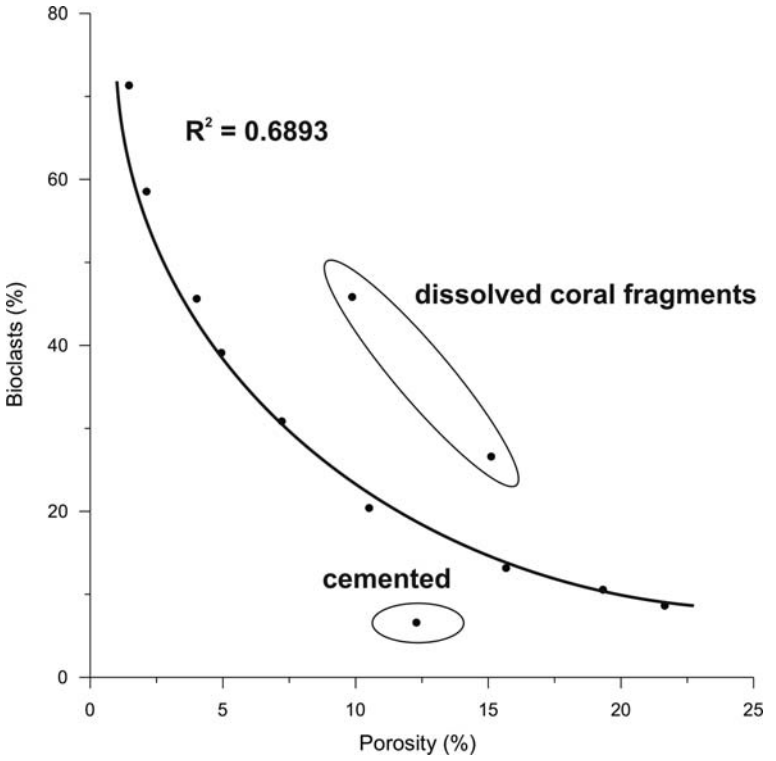

Fig. 3.14 Bivariate plot of percentage of bioclasts versus percentage porosity in the micro-CT scanned samples from Hole U1317A

The same processing steps and techniques were applied for the quantification of porosities and bioclasts in Morpho+ as described for the quantification of the coral fragments (see Sect. 3.3.1). Figure 3.14 represents the percentage of porosities versus the percentage of bioclasts for each sample. The porosities are varying between 1.46 and 21.65%. The amount of bioclasts detected in the studied volume blocks ranges from 6.60 to 71.33%. The quantified porosities are lower than the porosities calculated by moisture and density analysis (see Chap. 4) which are characterized by values varying mainly between 40 and 60%. Hence could be assumed that digital image analyses are underestimating the porosities drastically. This could be due to the resolution of the micro-CT scans whereby porosities lower than 14 μm can not be detected. We could then assume that most of the porosity is present in the fractions smaller than 14 μm, and so in the muddy matrix. Enos and Sawatsky (1981) inferred from capillary pressure curves that indeed many of the pore throats of muddy carbonate sediments are less than 1 μm in diameter after drying. The more, porosities obtained by the classical moisture and density analyses are approaching more the typical porosities calculated by Enos and Sawatsky (1981) for grainstones (range: 40–53%; mean: 44.5%), packstones (range: 45–67%; mean: 54.7%), wacke-

stones (range: 64–78%; mean: 68.0%) and very fine wackestones (range: 67–73%; mean: 70.5%) from Florida and the Bahamas. They showed that interrelationships between porosities and permeabilities in recent carbonates are largely controlled by depositional texture, particularly the amount of fine material <62 μm. The higher amount of fine and muddy material, the higher the porosities and the lower the permeabilities.

Figure 3.14 shows that there is an inverse relationship between the amount of bioclasts and the amount of porosity in the samples. The higher the amount of bioclasts, which corresponds with less muddy matrix, the lower the porosity and vice versa. Despite this relationship has to be interpreted carefully as most of the porosity is not incorporated in the porosity estimations, it can be inferred that indeed the fraction of fine and muddy material (i.e. the matrix excluding the bioclasts and cold-water coral fragments) has an important influence in increasing the porosity.

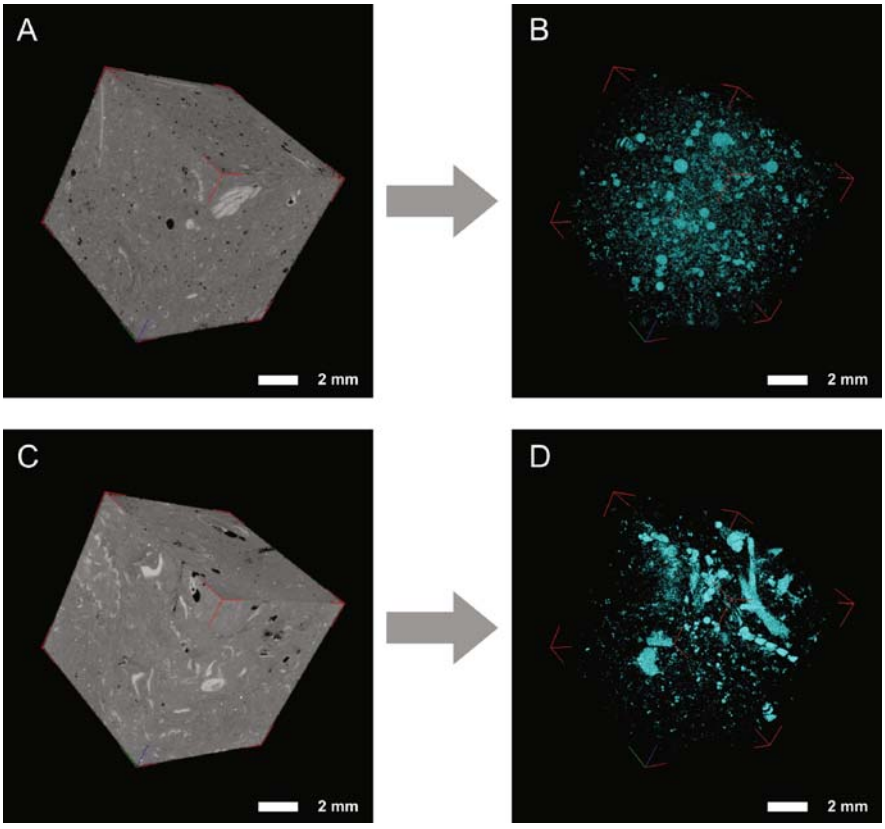

Fig. 3.15 Micro-CT scans representing bioclasts, matrix and porosities (*left panels*) and porosities (*right panels*). (**A,B**) Sample from Section 307-1317A-2H-3 representing intergranular and intragranular porosity. (**C,D**) Sample from Section 307-1317A-6H-3 visualizing intergranular and intragranular porosity

Visualizing the porosities in the scanned samples suggests that most of the porosity in the uncemented matrix is intergranular (Figs. 3.15 and 3.16). Most of the pores are really small and are not connected with each other, suggesting low permeabilities. Porous and hollow skeletons are responsible for a primary intragranular porosity beside the intergranular porosity (Fig. 3.15).

When dissolved aragonitic skeletons are present in the matrix, e.g. cold-water coral fragments, a secondary moldic porosity is created, increasing the porosity very locally around the dissolved parts of the cold-water coral fragments (Fig. 3.16A,B). The two upper isolated points on Fig. 3.14 are representing samples rich in dissolved cold-water coral fragments, which explain the slightly higher porosities in these samples. The porosity is however not that much higher, as much of moulds created by the dissolved parts of the cold-water coral fragments seem to be refilled again by the surrounding matrix. The lowermost isolated point corresponds with a sample from a semi-lithified horizon, showing that in these semi-lithified horizons

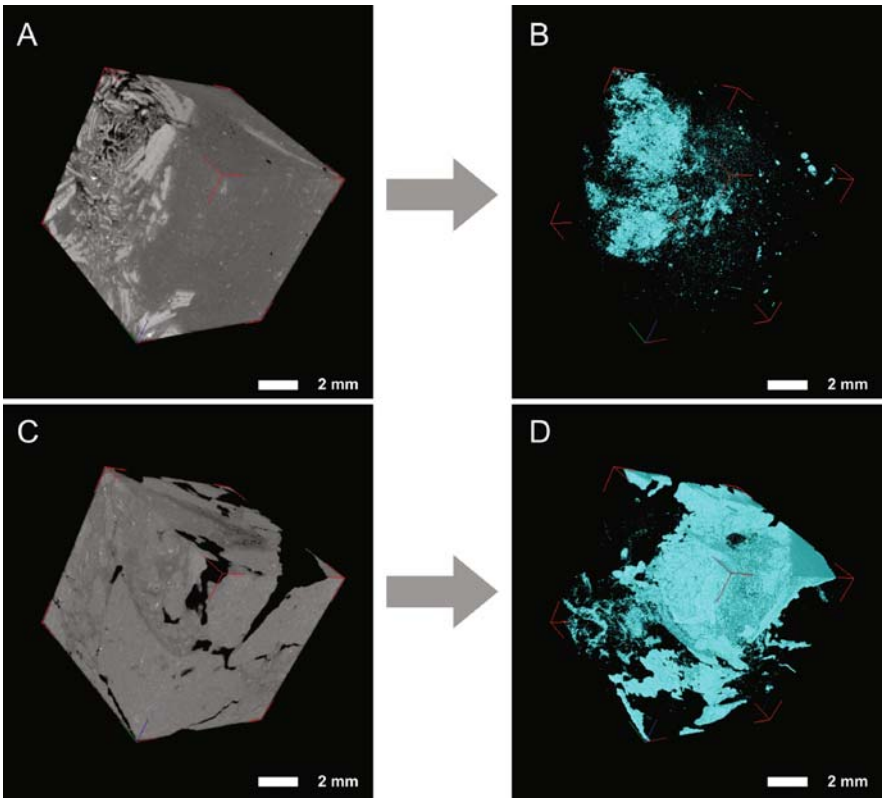

Fig. 3.16 Micro-CT scans representing bioclasts, matrix and porosities (*left panels*) and porosities (*right panels*). (**A,B**) Sample from Section 307-1317A-8H-3 showing moldic porosity around cold-water coral fragment. (**C,D**) Sample from Section 307-1317A-14H-3 visualizing secondary porosity

the porosity is decreased. Cementation lowers the porosity. Sampling these semi-lithified (or partly cemented) horizons shows that the physical characteristics of these horizons are quite different compared to the surrounding unlithified sediments. The semi-lithified horizons are much more sensitive for fracturing and brecciation, which can create a secondary porosity in this brittle material. The fractures visualized on Fig.3.16C,D are most probably introduced in the sample during sampling but it shows that during later compaction, these horizons will be excellent places for the creation of a secondary porosity. The more, the pores creating such a secondary fracture porosity are interconnected with each other, enhancing the permeability. This can explain why ancient carbonate rocks show generally a positive correlation of high porosity with high permeability (caused by a secondary porosity) compared to the inverse relationship between porosity and permeability in recent carbonate sediments (Enos and Sawatsky 1981).

3.5 Imaging the Off-Mound Records

A detailed overview of the lithology of the off-mound records is given in the "Proceedings of the Integrated Ocean Drilling Program, Volume 307" (Ferdelman et al. 2006). In the next sections a summary will be given of the encountered lithologies of the off-mound records in the upper intervals according to the lithological units defined by the Expedition 307 Scientists (2006c,e).

3.5.1 Site U1316

The lithology at Site U1316 can be divided into three main lithological units with a major unconformity and erosional surface between unit 2 and unit 3. This unconformity can be correlated with the mound base described in Sect. 3.2.1 and is overlying a heterogeneous dark green glauconitic siltstone (unit 3). Figure 3.17 represents the reflectance and the image stacks of units 1 and 2 in function of depth (mbsf) above the unconformity for Hole U1316A, which will be described in this section.

Unit 1 can be divided into two subunits, respectively subunit 1A, from 0 to 25.90 mbsf, and subunit 1B, from 25.90 to 44.40 mbsf (Fig. 3.17). Subunit 1A is dominated by a mottled greyish brown to dark greyish green silty clay to clayey silt. The sediments are partly interbedded with centimetre-thick fine sand layers that occasionally grade upwards. Bioturbation rarely occurs in this unit. Dropstones occur frequently. Fossils are generally rare and quite dispersed. At 5.90 mbsf, a very thin shell layer occurs. The base of subunit 1A is defined by an erosive boundary overlain by a 12 cm thick, graded medium to fine sand layer with up to centimetre-sized lithoclasts at the base. Subunit 1B is characterized by laminated very dark olive-grey to dark grey silty clay interbedded with fine sand layers. Lamination thickness varies from millimetre- to centimetre-scale. Dropstones occur frequently but are limited to discrete intervals. At 41.00 mbsf, a mixture of silty clay layers with a calcareous fine

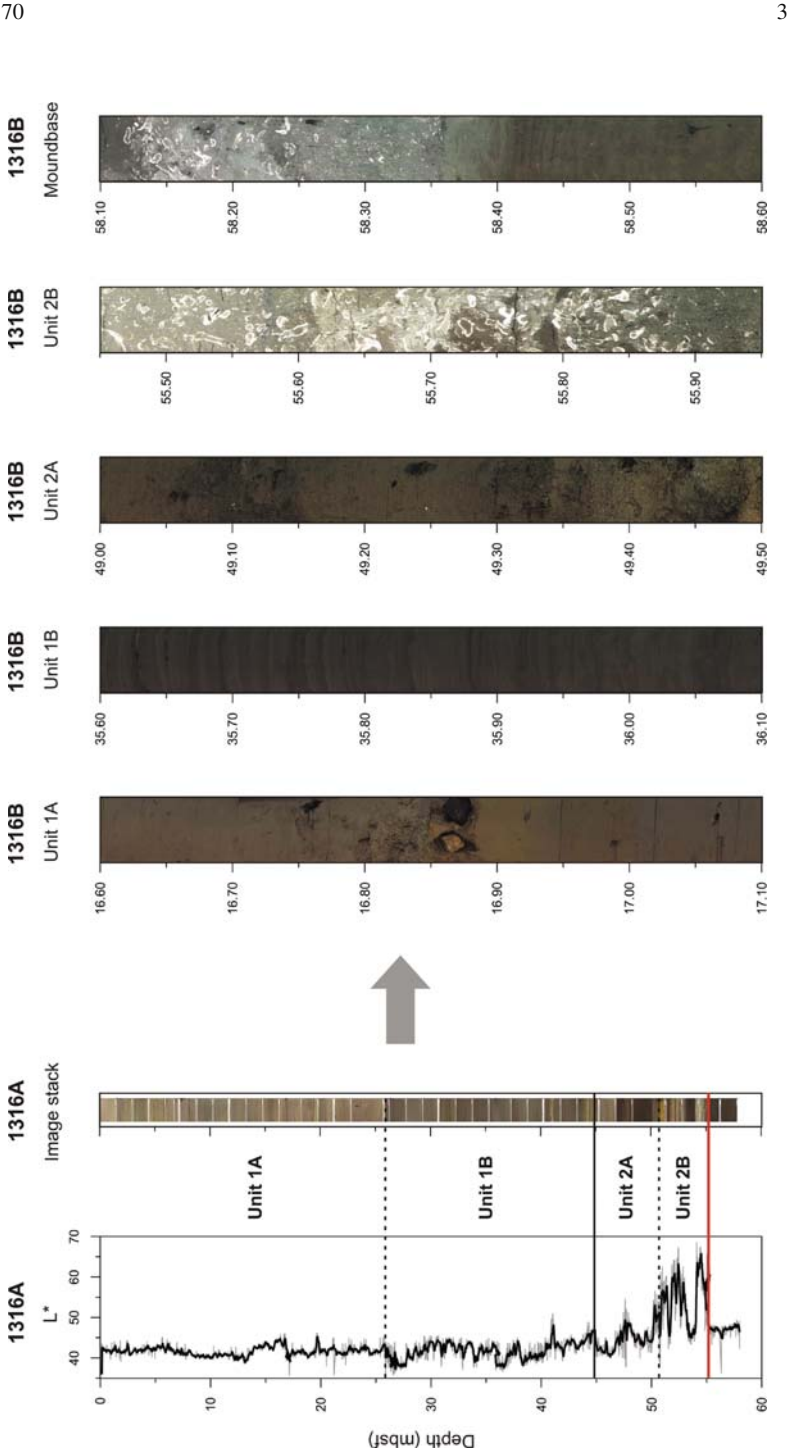

Fig. 3.17 *Left panel*: Colour reflectance (L∗), image stack and lithological units in function of depth (mbsf) of Hole U1316A. *Red horizontal line* represents the unconformity between unit 2 and unit 3. *Right panel*: images representing typical lithologies of the different lithological units and the unconformity corresponding with the mound base

to medium sand is observed. Just above this layer, a medium sand to fine gravel layer consisting of a mixture of dropstones, coral fragments and other bioclasts is present. The base of subunit 1B can be described as a small erosive boundary overlain by a fining-upward sequence of graded fine to very fine sand beds.

Unit 2 is very heterogeneous and is characterized by the presence of coral bearing layers interbedded with sands, silty sands, silt, and silty clays. A subdivision in two subunits is proposed. Subunit 2A, from 44.40 to 50.90 mbsf, is dominated by fine to medium sands and rarely intercalations of some coarser sands that grade upwards into silty clays interbedded with fine sand and silt layers. Seven small-scaled fining-upward sequences are noted with erosional contacts at their base, indicating a dynamic environment. Dropstones are common within these intervals and can range up to 3 cm in diameter. Subunit 2B is occurring from 50.90 to 55.06 mbsf and is characterized by different coral-bearing layers interbedded with siliciclastic sediments. Thicknesses of the coral-bearing layers vary between 20 and 170 cm. The coral assemblage in this interval is dominated by the species *Lophelia pertusa*. Preservation of the coral fragments is rather poor, indicating coral dissolution. The coral layers can be described as having a floatstone to rudstone texture.

It should be mentioned that no distinctive cyclic pattern is observed in the reflectance record or the image stack.

3.5.2 Site U1318

The sediments at Site U1318 can be divided in three units based on the visual description of sedimentary features and the colour reflectance data. A major unconformity, which can be correlated with the mound base at Site U1317, defines the boundary between unit 2 and unit 3. Figure 3.18 represents the colour reflectance and the image stack in function of depth (mbsf) of Hole U1318B above the erosive boundary, visualizing unit 1 and unit 2 which will be described below.

Unit 1 is dominated by an unlithified clayey succession, which can be subdivided in three lithological subunits with distinct boundaries. Subunit 1A, extending from 0 to 35.00 mbsf, is dominated by dark greyish brown to dark grey silty clays, which are partly interbedded with centimetre thick fine sand layers occasionally grading upwards. Some laminated intervals are recognized with centimetre to millimetre thick laminae consisting of light and dark greenish grey clay with very fine sand layers representing small scaled fining-upwards cycles. Bioturbation within the laminated intervals is rare, but is moderate to strong in the major part of this subunit. Dropstones are frequently found. Macrofossils are rarely observed. Black spots, interpreted as aggregations of fine iron sulphides, are common. The base of this subunit is defined by an erosive boundary overlain by a 24 cm thick fine sand to clayey silt layer. The lithology of subunit 1B, defined as the unit between 35.00 and 62.00 mbsf, comprises dark greyish brown to very dark grey silty clays that are similar to the facies of subunit 1A. In contrast to subunit 1A, dropstones are much less frequent and the laminated horizons (centimetre to millimetre scale) are occurring

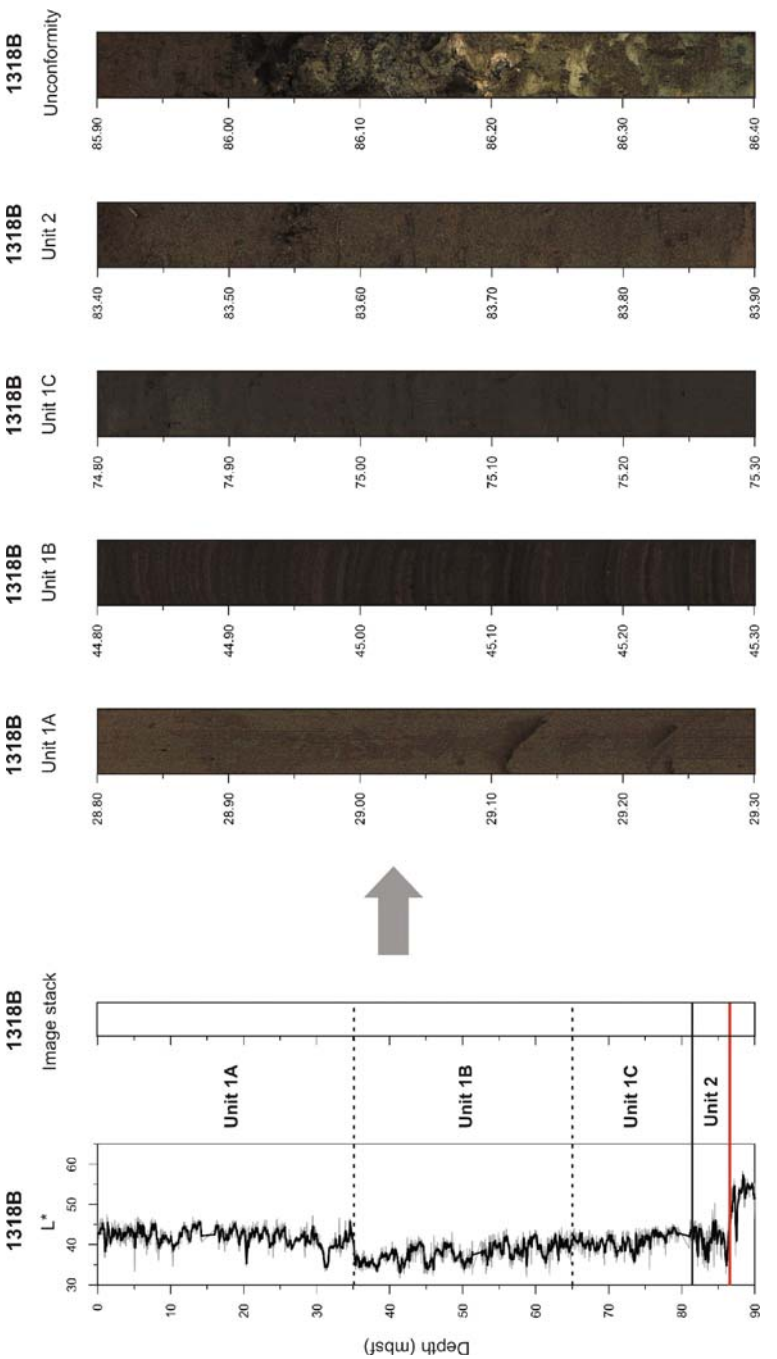

Fig. 3.18 *Left panel*: Colour reflectance (L∗), image stack and lithological units in function of depth (mbsf) of Hole U1318B. *Red horizontal line* represents the unconformity between unit 2 and unit 3. *Right panel*: images representing typical lithologies of the different lithological units and the unconformity corresponding with the mound base

throughout the whole subunit. Macrofossils are rare. The lithology of subunit 1C between 62.00 and 82.00 mbsf is characterized by alternating dark greyish brown fine sandy clay and very dark greyish brown silty clay. This subunit is distinguished from the other subunits by the presence of coarser material. Laminations of fine sand and silty clay are dominant in the middle part of subunit 1C. Dropstones are absent. The base of this subunit is marked by a sharp, erosive boundary.

Unit 2 is defined as the sediments occurring between 82.00 and 86.20 mbsf and is dominated by olive grey medium fine sand interbedded with dark yellowish brown silty clay. A gradual increase in sand indicates a coarsening upward trend throughout this unit. Lithoclasts up to 3 cm in diameter are found in both the sandy and the clayey horizons. Sand beds contain a high amount of well-preserved mollusc species and other unidentified shell fragments. The base of this subunit consist of a 5–10 cm thick bed characterized by the presence of conglomerate and black moulds, which can be interpreted as the infill from bivalves. XRD analyses show that the moulds consist of a mixture of apatite, calcite and quartz. This bed of conglomerates and black moulds are overlying the major unconformity and erosive boundary ($\sim$ mound base) between unit 2 and unit 3.

As in Hole U1316A, no cyclic pattern is observed in the reflectance record and the image stack.

3.6 Discussion

3.6.1 Western Ireland as Source for Terrigenous Material?

Rice et al. (1991) suggested that the main sediment supply zone is probably located on the Irish and Celtic shelves, whereas input from the Porcupine Bank seems to be rather limited. Gregg et al. (2006) evidenced that western Ireland can be proposed as the primary source of detrital sediments towards the Irish shelves. The Shannon River empties into the Atlantic Ocean through the Shannon estuary, on the northern boundary of County Kerry (SW Ireland), and drains a considerable portion of western Ireland. Other rivers emptying into Galway Bay (W of Ireland) very likely also contributed sediments. The detrital grains can be classified as immature and are characteristic of detrital material from nearby igneous (primarily granitic), metasedimentary, and arkosic terrains. Regions contributing detrital sediments include Early Paleozoic igneous (granitic and basic) and metasedimentary rocks as well as the Devonian age Old Red Sandstone (arkose). Lower Carboniferous dolomite outcropping in the Burrin region of County Clare (W of Ireland) is a likely source of detrital stoichiometric dolomite (Gregg pers. com.).

During glacial periods a lot of terrigenous material from the shelves may have drained towards the deeper margins of the Porcupine Seabight. Subglacial drainage networks and tunnel-valleys across Ireland and in the Irish-Celtic Sea (Warren and Ashley 1994) may have supplied sorted sediment directly to the shelf edge, to be received by slope canyons as the Gollum Channel System at the eastern margin of

the Porcupine Seabight south of 53°N. Such a channel system evidences the importance of glaciofluvial (meltwater) processes at the Irish and Celtic shelves in the contribution of sedimentary material towards the deeper margins. The presence of different glacial imprints along the northern and eastern margins of the Porcupine Seabight such as iceberg scour marks (Games 2001; Mathys 2001) and the presence of ice rafted debris (Foubert et al. 2005a, 2007; Van Rooij et al. 2007a; see also Sect. 6.2), also evidences the importance of other glacial processes, such as ice rafting, in the delivery of terrigenous material (see also Sect. 2.2.1).

3.6.2 Justification of the Name "Carbonate Mound"

In the past, different terminologies were used to describe the mounds in the Porcupine Seabight. Le Danois (1948) described the coral facies along the eastern margin of the Porcupine Seabight as "Massifs coralliens de Dingle". Hovland et al. (1994) called the structures in the Hovland Mound Province "seabed mounds", with the suggestion of a more interpretative name as "carbonate knolls" or "bioherms". Henriet et al. (1998) were initially using the term "deep-water reefs" to describe the same structures but introduced in 2001 the name "carbonate mound". De Mol (2002) discussed these different terminologies and proposed the name "coral bank" as being most adequate to describe the mounded structures in the Porcupine Seabight. Huvenne et al. (2003) suggested the name "carbonate build-up". However, the name "carbonate mound" seems to have survived and most of the recent publications refer to the mounds in the Porcupine Seabight as being "carbonate mounds" (Dorschel et al. 2005, 2007b; Foubert et al. 2005a, 2007; Rüggeberg et al. 2005, 2007; Wheeler et al. 2005b, 2007; Roberts et al. 2006). Seen the recent development in mound research whereby a mound was drilled to its base for the first time in history, the discussion to name these mounded structures in an appropriate way can be reopened.

Riding (2002) made a comprehensive review about the structure and composition of organic reefs and carbonate mud mounds, introducing a renewed classification scheme for reefs and mud mounds. This classification scheme was mainly based on the objective characteristic of the type of sedimentary support, which largely determines the sedimentary composition of the deposit. He defined "reefs" as "essentially in place calcareous deposits created by sessile organisms" and "carbonate mud mounds" as "carbonate mud-dominated deposits with topographic relief and few or no stromalites, thrombolites or in place skeletons". On their compositional and structural bases (amount of matrix versus amount of skeletons versus amount of cement), Riding (2002) recognized three main categories of organic reefs: (1) matrix-supported reefs (agglutinated microbial reefs, cluster reefs, segment reefs), (2) skeleton-supported reefs (frame reefs) and (3) cement-supported reefs (cement reefs) (Fig. 3.19).

In Challenger Mound the matrix seems to dominate on the coral skeletons, whereby the matrix is mainly characterized by the alternation between siliciclastic, terrigenous material and carbonate-rich biogenic material. The amount of cemen-

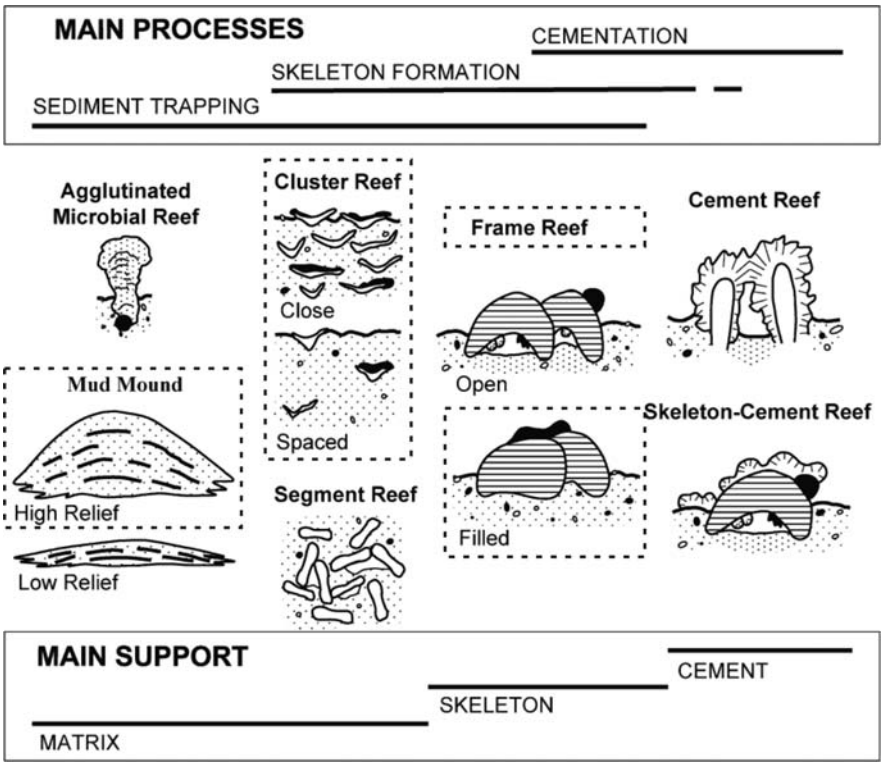

Fig. 3.19 Outline of "organic reef" and "carbonate mud mound" classification, showing main processes and structural support (after Riding 2002). *Dashed boxes* suggest appropriate names for Challenger Mound

tation is low. Following the classification of Riding (2002), taking into account the dominance of matrix compared to the amount of aragonitic skeletons and the low amount of cementation, Challenger Mound can be classified as a close to spaced "cluster reef". "Cluster reefs" are "skeletal reefs in which essentially in place skeletons are adjacent, but not in contact, resulting in matrix-support; they are characterized by relatively high matrix/skeleton ratios and low volumes of extra-skeletal early cement; sediment trapping is an important corollary of skeletal growth and cluster reef organisms are tolerant of loose sediment; absence of framework limits the topographic relief that cluster reefs can attain relative to spatial extent, and may permit bedding to develop within the reef" (Riding 2002). The last characteristic defined as "absence of framework limits the topographic relief" may argue against the interpretation of Challenger Mound as a "cluster reef". Challenger Mound has a height of 150 m, which evidences a high relief structure. In this case, the term "frame reef", defined as "skeletal reefs in which essentially in place skeletons are in contact; they are characterized by relatively high skeleton/matrix ratios; skeletal support enables them to rise themselves above the substrate independently of

cementation and particulate sedimentation; inter-skeletal spaces are penecontemporaneously occluded by surficial sediment during reef-growth" may be more appropriate. On the other hand, the relative height/width ratio of Challenger Mound is 1/10, what evidences the importance of lateral expansion. The evidence of vertical growth in certain periods, compared to horizontal expansion in other periods (Sect. 5.5.3) may also argue for an alternation in time of "cluster reefs" and "filled frame reefs". However, the importance of the matrix sediments may be underestimated in the term "frame reef". In this view, the name "high relief carbonate mud mound" defined as "thick (>5 m) carbonate mud mounds with steep marginal slopes; they can have an internal bedding and may be characterized by slumping features" may be more appropriate. The more, Riding (2002) suggested that sediment baffling whereby sediments could be localized by on-mound baffling organisms, can be an important process in the development of carbonate mud mounds. Such a baffling mechanism is evidenced in the Porcupine Seabight by the study of small, initial mounds (Foubert et al. 2005a; Wheeler et al. 2005b; Huvenne et al. 2005; see also Chap. 7).

It can be concluded that the term "carbonate mud mound" seems to be the most appropriate name for Challenger Mound; "carbonate" referring to the high amount of carbonate in the mound (~50%), "mud" referring not only to carbonate mud (nannofossil ooze in the case of Challenger Mound) but also to the terrigenous and siliciclastic components (mainly clay minerals and silt-sized quartz) and mound referring to the elevated, topographic structure. To be complete the name can be extended by "cold-water coral", resulting in "cold-water coral carbonate mud mound". For practical reasons, to avoid misunderstandings and to be coherent with the most recent publications, the term "carbonate mound" will be used throughout this study. However, readers should be aware of the vagueness of this term. The more, a "cold-water coral carbonate mud mound" can be seen as the end-member in a process whereby the interaction between sedimentation and cold-water coral growth is a crucial factor. Such an interaction can stimulate in the one case "reef growth" when cold-water coral growth prevails on sedimentation, while "cold-water coral mud mounds" will be formed when sedimentation is taking the overhand. These "cold-water coral mud mounds" can develop into "cold-water coral carbonate mud mounds" when also diagenetic carbonate precipitation is taking place as observed in the Gulf of Cadiz (Sect. 8.5.4) or when extensive biogenic sedimentation starts to dominate the system.

3.7 Summary

The Challenger Mound sediments can be described as a facies of **cold-water coral fragments** (mainly ***Lophelia pertusa*** and some minor to rare occurrences of *Madrepora oculata* and *Desmophyllum cristagalli*) and biogenic fragments embedded in an alternating light grey biogeneous (carbonate-rich) matrix to greenish grey terrigenous (siliciclastic-rich) matrix. The **terrigenous sediments** are dominated by **clay minerals** (illite, kaolinite, chlorite, and smectite) and silt-sized **quartz** with secondary potassium feldspar and plagioclase (albite). The **biogenic**

sediments are dominated by **nannofossil ooze (coccoliths)** and **micro-bioclastic fragments** (**foraminifera**, sponge spiculae, radiolarians, echinoderms, bivalves, gastropods).

Coral quantities were determined in two and three dimensions but **no distinct correlation** could be observed between the alternating darker and lighter intervals and the coral quantity cycles.

Cold-water coral fragments evidence traces of extensive **dissolution**, **bio-erosion** and **fragmentation** throughout the mound succession.

An **inverse relationship** is found between the amount of **bioclasts** and the amount of **porosity** in the samples. The higher the amount of bioclasts, which corresponds with less muddy matrix, the lower the porosity and vice versa.

Porous and hollow skeletons are responsible for a **primary intragranular porosity** beside the **intergranular porosity**. When dissolved aragonitic skeletons are present in the matrix, as cold-water coral fragments, a **secondary moldic porosity** is created, increasing the porosity very locally around the dissolved parts of the cold-water coral fragments.

The **off-mound** sediments are mainly characterized by **silty clays**, with some intercalated coarser sandy intervals. **Dropstones** are common in these sediments.

Western Ireland can be proposed as the primary source of detrital sediments towards the Irish shelves. **Fluvial transport** of sediment by the **Shannon River**, emptying into the Atlantic Ocean through the Shannon estuary, may play hereby an important role. **Glaciofluvial (meltwater) processes** at the Irish and Celtic shelves might have been important in the contribution of sedimentary material towards the deeper margins during glacial periods.

During this study the name "**carbonate mound**" will be used to refer to the studied mound structures, including Challenger Mound, in the Porcupine Seabight.

Chapter 4
Geophysical and Geochemical Core Logging

Over the past three decades, major technical and scientific advances have been made towards real-time physical and chemical characterization of deep-sea sediments (Ortiz and Rack 1999). To infer palaeoceanographic and palaeoclimatological information from physical and chemical characteristics of sediments, it is necessary to obtain the most continuous and accurate measurements possible (Röhl and Abrams 2000). Various types of core-logging systems have been developed during the last years and are able to measure continuous physical and chemical data sets down to millimetre-scale. Such a high resolution can never be obtained by standard analytical methods for discrete samples which are in addition time-consuming and expensive. Moreover, logging methods are non-destructive. Ortiz and Rack (1999) give an overview, summarize the historical details and point out the growing advantages of different geochemical and geophysical logging tools which were available at the end of the twentieth century. Nowadays, different very high-resolution sensors are combined in one logging tool to obtain as much (accurate and continuous) information as possible in a short time-span. Moreover, more and more effort is put into techniques to gain information on the spatial heterogeneity of physical properties in two- or three-dimensional space (instead of bulk (one-dimensional) measurements) (for example X-ray computer tomographic (CT) scanning techniques, see Chap. 3).

In this study, two widely applied core logging systems are used to define the chemical and physical properties characterizing uniquely the sediments of Challenger Mound and its surrounding sediments. Physical properties of rocks and sediments are indicators of composition, formation and environmental conditions of the deposits. The physical properties are logged by a multi-sensor track (MST), installed permanently on the R/V JOIDES Resolution. In soft and semi-consolidated sediment sections, physical properties data serve mostly as proxies for sediment composition, which is controlled by provenance, depositional and erosional processes, palaeoceanographic and palaeoclimatic changes, and post-depositional processes such as consolidation and early diagenesis. In consolidated sediments, diagenetic processes, including cementation and major lithological changes tend to dominate many physical properties. A major application of data collected at small sampling intervals (a few centimetres), such as magnetic susceptibility, gamma-ray density, and natural gamma radiation, is core-to-core and hole-to-hole correlation. These

A. Foubert, J.-P. Henriet, *Nature and Significance of the Recent Carbonate Mound Record*, Lecture Notes in Earth Sciences 126, DOI 10.1007/978-3-642-00290-8_4,

correlation procedures are essential for stratigraphic studies, and some of the most important ocean drilling projects are unthinkable without the high-performance acquisition of physical properties data.

Many chemical parameters are significant as they can provide palaeoclimatic and palaeoenvironmental information, complementary to geophysical data sets. Geochemical core logging with the X-ray fluorescence (XRF) core scanner is used to measure directly several parameters that are important for palaeoenvironmental interpretations, such as Ca (representing "carbonate") and Fe (representing "terrigenous" or "volcanic" material) (Röhl and Abrams 2000). XRF core logging determines in a rapid and non-destructive way the chemical composition of marine bottom sediments and gives a qualitative and quantitative (after calibration with standard geochemical analysis) overview of the relative trends in changing chemical element composition throughout the cores.

4.1 Methodology

4.1.1 Geophysical Logging

Physical core logging was carried out on whole-round cores during IODP Expedition Leg 307 with the multi-sensor track (MST), permanently installed aboard the R/V *JOIDES Resolution*. The MST is an automated core conveying and positioning system for logging core physical properties at small sampling intervals (Blum 1997). The MST system includes the following non-destructive measurements: gamma-ray attenuation densiometry (GRA), P-wave velocity logging (PWL), magnetic susceptibility logging (MSL) and natural gamma ray measurements (NGR). Magnetic susceptibility, GRA density and NGR were measured on all cores from all holes at Sites U1316, U1317, and U1318. P-wave velocities were measured only on the upper APC intervals because loss of coupling between the liner and core with XCB and RCB drilling resulted in inaccurate values (Exp. 307 Scientists 2006b). In this chapter only the geophysical properties from Holes U1317A, U1317B, U1317C, U1317E, U1316A and U1318B in the upper intervals (i.e. in the intervals localized above the mound base in Holes U1317A, U1317B, U1317C and U1317E and above the correlating unconformity in Hole U1316A and Hole U1318B) will be discussed. A detailed overview of all the geophysical properties, measured on all the holes drilled during IODP Expedition Leg 307, is given in the "Proceedings of the Integrated Ocean Drilling Program, Volume 307" (Ferdelman et al. 2006).

Magnetic susceptibility is the degree to which a material can be magnetized in an external magnetic field (see also Chap. 5). Magnetic susceptibility is used mostly as a relative proxy indicator for changes in composition that can be linked to palaeoclimate-controlled depositional processes. The high precision and sensitivity of susceptibility loggers makes this measurement extremely useful for core-to-core correlation. The physical link of magnetic susceptibility to particular sediment components, ocean or wind current strength and direction, or provenance, usually requires more detailed magnetic properties studies in a specialized shore based

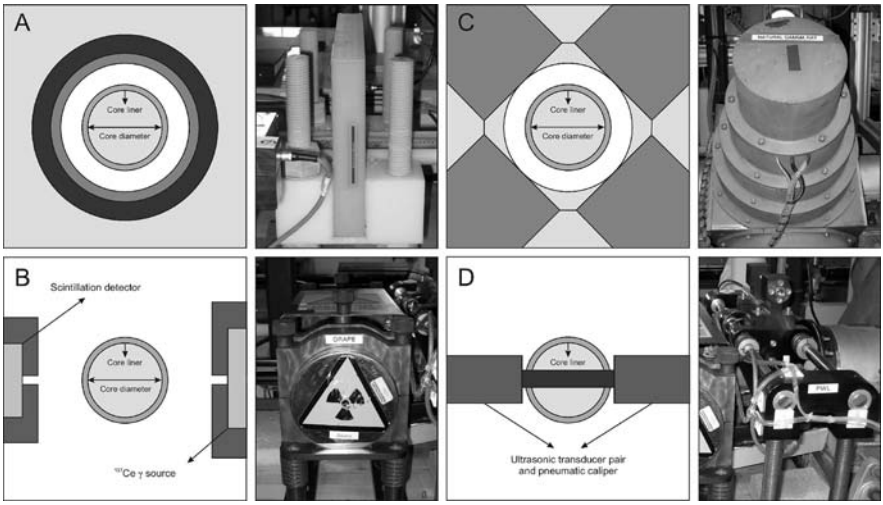

Fig. 4.1 (**A**) Schematic illustration and picture of the measurement geometry of the Bartington Model MS-2 meter integrated in the multi-sensor track (MST) for whole-core logging of the magnetic susceptibility. (**B**) Schematic illustration and picture of the measurement geometry for whole-core logging of the gamma-ray attenuation (GRA) density. (**C**) Schematic illustration and picture of the measurement geometry for whole-core logging of the natural gamma radiation (NGR). (**D**) Schematic illustration and picture of the measurement geometry for whole-core logging of the P-wave velocity (PWL). Schematic illustrations are modified after Blum 1997

laboratory (see Chap. 5). Blum (1997) gives a technical overview of the measurement of magnetic susceptibility with the MST. Magnetic susceptibility was measured using a Bartington Model MS-2 meter integrated in the MST for whole-core logging (Fig. 4.1A). The MS-2 loop sensor has an internal diameter of 80 mm, which corresponds to a coil diameter of 88 mm. It operates at a frequency of 0.565 kHz and an alternating-field (AF) intensity of 80 A/m (equivalent to 0.1 mT). Temperature drift is less than 10^{-5} SI per hour. The resolution of the loop (and so precision of the measurements) is 2×10^{-6} SI. Susceptibility values in natural, marine sediment samples over an interval of only a few metres can range from a few tens to several thousands of 10^{-6} SI units. Typically, variations are 2–3 orders of magnitude greater than the precision. This makes magnetic susceptibility one of the most precise proxies for stratigraphic changes. Accuracy is 5% (according to Bartington). Measurements were carried out on whole-round sections with a sampling resolution set at 5 cm and a frequency of 5 times per second. Such a long sampling period ensured acceptable readings for the usually low magnetic susceptibilities of carbonate sediments. Relative susceptibilities were measured, which needed to be corrected for volume variations. For a core diameter d and a coil diameter D of respectively 66 and 88 mm, the corresponding correction factor d/D is 1.48 (Blum 1997). During data reduction, the relative susceptibilities were converted to volume-normalized magnetic susceptibilities by multiplying by $1/(1.48 \times 10^5)$, or by 0.68×10^{-5} SI units.

Gamma-ray attenuation (GRA) is used to estimate the bulk density of sediments, an indicator for porosity and lithological changes (Evans 1965). This measurement is based on the principle that the ^{137}Cs attenuation, mainly by Compton scattering, of a collimated beam of gamma rays (produced by a ^{137}Cs source) passing through a known volume of sediment is related to material density (Boyce 1976). Blum (1997) summarizes the details of this method in his "Physical properties handbook". The ^{137}Cs source used transmits gamma rays at 660 KeV. A scintillation detector measures the gamma-ray beam transmitted through the core material (Fig. 4.1B). During IODP Expedition Leg 307, the measurement interval was set at 5 cm for a frequency of 5 times per second. GRA densities were corrected for the attenuation effect in high-porosity sediments using the Boyce (1976) equation (Eq. 4.1):

$$\rho = [(\rho_{bc} - \rho_{fc})(\rho_g - \rho_f)]/(\rho_{gc} - \rho_{fc}) + \rho_f \tag{4.1}$$

where ρ = corrected density, ρ_{bc} = GRA density, ρ_{fc} = fluid density calculated from gamma counts (1.128 g/cm^3), ρ_g = true grain density of quartz (2.65 g/cm3), ρ_f = true fluid density (1.024 g/cm3), and ρ_{gc} = grain density calculated from gamma counts (2.65 g/cm^3).

For Holes U1316A, U1316C, U1317A, U1318A and U1318B, GRA densities and bulk densities measured on discrete samples were compared for consistency. Moisture and density properties from discrete samples ($\sim$10 cm^3 samples from split cores) were measured at a frequency of two per section. Porosity and void ratio were calculated from phase-relation equations. Immediately after samples were collected, wet sediment mass (M_t) was measured. Samples were then placed in a convection oven for 24 h at a temperature of 105 $\pm$ 5°C. After drying, dry sediment mass (M_d) and dry sediment volume (V_d) were measured. Sample mass was determined on board with a precision of $\pm$ 0.01 g using two Scientech 202 electronic balances to compensate for the ship's motion. Volumes were determined using a helium five-chambered pycnometer with an approximate precision of $\pm$ 0.02 cm^3. The determination of water content followed the methods of the American Society for Testing and Material (ASTM) designation (D) 2216 (ASTM International 1990). The recommended equation for the water content calculation, which is the ratio of the pore fluid mass to the dry sediment mass (weight percent), is as follows (Eq. 4.2):

$$W_c(\text{wt}\%) = (M_t - M_d)/(M_d - rM_t) \tag{4.2}$$

where W_c = water content reported as a decimal ratio of percent dry weight, and r = salinity. Wet bulk density (ρ) is the density of the total sample, including pore fluid. In high-porosity sediment, bulk density was calculated using the following equation (Eq. 4.3):

$$\rho = M_t/V_t \tag{4.3}$$

where V_t is the total sample volume ($\sim$10 cm^3). Porosity (F) was calculated using the following equation (Eq. 4.4):

$$\Phi = (W_c \rho)/[(1 + W_c)\rho_w] \tag{4.4}$$

where ρ_w is the density of the pore fluid (assuming a salinity of 35‰).

Natural gamma radiation (NGR) is a useful lithologic parameter because the "primeval" emitters are at secular equilibrium; i.e., radiation at characteristic energies is constant with time (e.g., Adams and Gasparini 1970). Radioisotopes with sufficiently long life and which decay to produce an appreciable amount of gamma rays are potassium (^{40}K) with a half-life of 1.3×10^9 years, thorium (^{232}Th) with a half-life of 1.4×10^{10} years, and uranium (^{238}U) with a half-life of 4.4×10^9 years. Hence, natural gamma radiation is a product of the decay of these radioactive isotopes. Minerals that fix K, U, and Th, such as clay minerals, are the principal source of NGR. Other examples include arkosic silt and sandstones, potassium salts, bituminous and alunitic schists, phosphates, certain carbonates, some coals, and acid or acido-basic igneous rocks (Serra 1984). NGR measurements are used for three purposes: (1) correlation of core data sets in multiple holes, (2) evaluation of the clay/shale content of a formation, and (3) abundance estimates for K, U, and Th. The first, and to some degree the second, goals can be achieved by simply measuring the bulk emission (total counts) of the material. Elemental analysis is a more complex process that requires spectral data acquisition and longer sampling times, which was not achieved in the measurements during IODP Expedition Leg 307. NGR was measured using four scintillation detectors arranged at 90° to each other and perpendicular to the core as outlined by Hoppie et al. 1994 and described in detail by Blum (1997) (Fig. 4.1C). During IODP Expedition Leg 307, NGR was measured with a resolution of 5 cm on whole-round sections for a frequency of 5 times at 1 s.

The basic relationship for sonic (P-wave) velocity is (Eq. 4.5):

$$v = d/t \tag{4.5}$$

where d is the distance travelled through the material (in metres) and t is the travel time through the material (in seconds). P-wave velocity varies with the lithology, porosity, and bulk density of the material, state of stress, such as lithostatic pressure, and fabric or degree of fracturing. In marine sediments and rocks, velocity values are also controlled by the degree of consolidation and lithification, fracturing, occurrence and abundance of free gas and gas hydrate, etc. Sonic velocity can be used for estimating the depth of reflectors. Together with density measurements, sonic velocity is also used to calculate acoustic impedance, or reflection coefficients, which can be used to construct synthetic seismic profiles. The physical and technical background for the measurement of the P-wave velocity by transducers installed in a MST is given by Blum (1997). The core travels between two piezo-electric transducers mounted in epoxy and stainless-steel housings (Fig. 4.1D). The two transducers are used as a transmitter and receiver. Acoustic coupling is through an epoxy resin surface and is enhanced by a water film supplied by an automated sprinkler system. Firm contact is ensured through spring-loaded transducer housings. Two serially mounted linear variable-displacement transformers (LVDT) measure the diameter

of the core (plus liner). A hydraulic piston system displaces the transducers by several millimetres at the beginning and end of a core section log to prevent the end caps from catching on to the transducers. A 500-kHz pulse (2-μs wave period; 120 V) is produced at a repetition rate of 1 kHz. P-wave velocity was measured at 5 cm intervals (5 times during 1 s period) during IODP Expedition Leg 307. Sediments must completely fill the liner for the PWL to provide accurate results. PWL measurements were inaccurate at Site U1317 due to the high coral content in a muddy matrix. The more, drilling with XCB and RCB of the lower consolidated sediments created insufficient contact between the sediments, the core liner, and the transducers to obtain accurate measurements (Exp. 307 Scientists 2006b). However, measurements on split cores using vertically orientated transducer pairs (500 Hz) with the upper transducer pressed against the split surface and the lower pressed against the core liner, made it possible to achieve trustable P-wave velocities (PWS) for the above mentioned problematic sediments.

4.1.2 Geochemical Logging

The major chemical element composition of the cored material was analysed using the AVAATECH X-ray fluorescence (XRF) core scanner installed at the Geosciences Department of the University of Bremen (Röhl and Abrams 2000). The AVAATECH XRF core scanner is a non-destructive analysis system, developed at the Royal Netherlands Institute for Sea Research (NIOZ) and makes use of the X-ray fluorescence (XRF) technique applied directly at the surface of split sediment cores. The general method and some calibration procedures are described by Jansen et al. (1998). XRF is based on the fact that incident X-rays increase the energy level in an atom. As a result an electron from the inner shell is emitted. This vacancy is filled by an electron from an outer shell (higher energy level), which moves into the position of the emitted electron. The surplus energy detected in the fluorescent radiation, reflecting the energy difference between the shells, is element specific (Potts 1987).

The XRF core scanner is made of a cover and a core fit system, which are pneumatically activated. The central sensor unit consists of a molybdenum X-ray source (3–50 kV) and a Peltier-cooled PSI detector (KEVEX^{TM}) with a 125 μm beryllium window and a multichannel analyser with a 20 eV spectral resolution. The X-ray tube and the detector are orientated in such way that the incident beam and the detector make an angle of 45° with the surface of the sample (Fig. 4.2). The whole system is computer controlled. The system configuration (X-ray tube energy, detector sensibility) at the University of Bremen allows the analysis of elements from potassium (K, atomic number 19) to strontium (Sr, atomic number 38) (X-ray tube voltage: 20 kV). During the analysis, the measurement unit (X-ray source and detector) is moved in vertical direction, the plastic prism is lowered on the core surface (covered by a special foil) and a slit defines the dimensions of the irradiated surface. To avoid loss of energy because of scattering in air, the area of analysis is flushed by helium. The core is moved in horizontal direction.

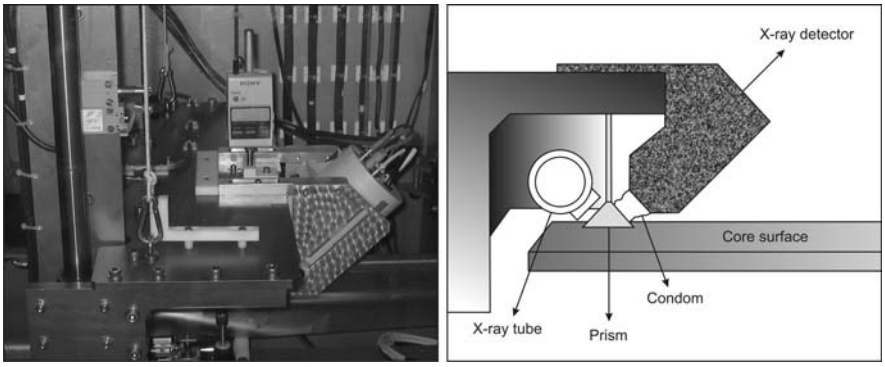

Fig. 4.2 Picture and schematic illustration of the measurement chamber of the AVAATECH XRF core scanner of the Geosciences Department of Bremen University. The X-ray tube and the detector are orientated so that the incident beam and the detector make an angle of 45° with the surface of the sample. Schematic illustration is modified after Röhl and Abrams (2000)

Element intensities (iron (Fe), calcium (Ca), potassium (K), titanium (Ti), manganese (Mn), strontium (Sr) and copper (Cu)) were analysed each 5 cm in Holes U1316A (Sections 307-U1316A-1H-1 to 307-U1316A-7H-CC), U1317E (all sections) and U1318B (Sections 307-U1318B-1H-1 to 307-U1318B-10H-CC), each measurement over an area of 1 cm^2 at the top of the archive halve sections. A resolution of 2 cm was achieved in Sections 307-1316B-7H-1 to 307-1316B-7H-5 and Section 307-1317C-7H-4, zooming in on the mound base. A 30 s count time was used for all the measurements together with an X-ray current of 0.087 mA. The acquired XRF spectrum for each measurement was processed with the KEVEX™ software Toolbox©. Background subtraction, sum-peak and escape-peak correction, deconvolution and peak integration were successively applied. The resulting data are basically element intensities in counts per second. Element concentration (e.g. in percent or parts per million) are not directly available, but by comparisons with data from standard chemical analyses from discrete samples, these counts can be converted to element concentrations (Jansen et al. 1998; Sect. 4.3.1).

4.2 Geophysical Records

4.2.1 Cyclic Record

Figures 4.3, 4.4, 4.5, and 4.6 represent the magnetic susceptibility, the bulk density (GRA) and the natural gamma radiation (NGR) in function of depth (mbsf) for Holes U1317A, U1317B, U1317C and U1317E. The colour reflectance, as discussed and described in Chap. 3, is also presented in function of depth (mbsf) for Holes U1317A (Fig. 4.3) and U1317C (Fig. 4.5). P-wave (sonic) velocity, porosity and density measurements on discrete samples are presented in function of depth

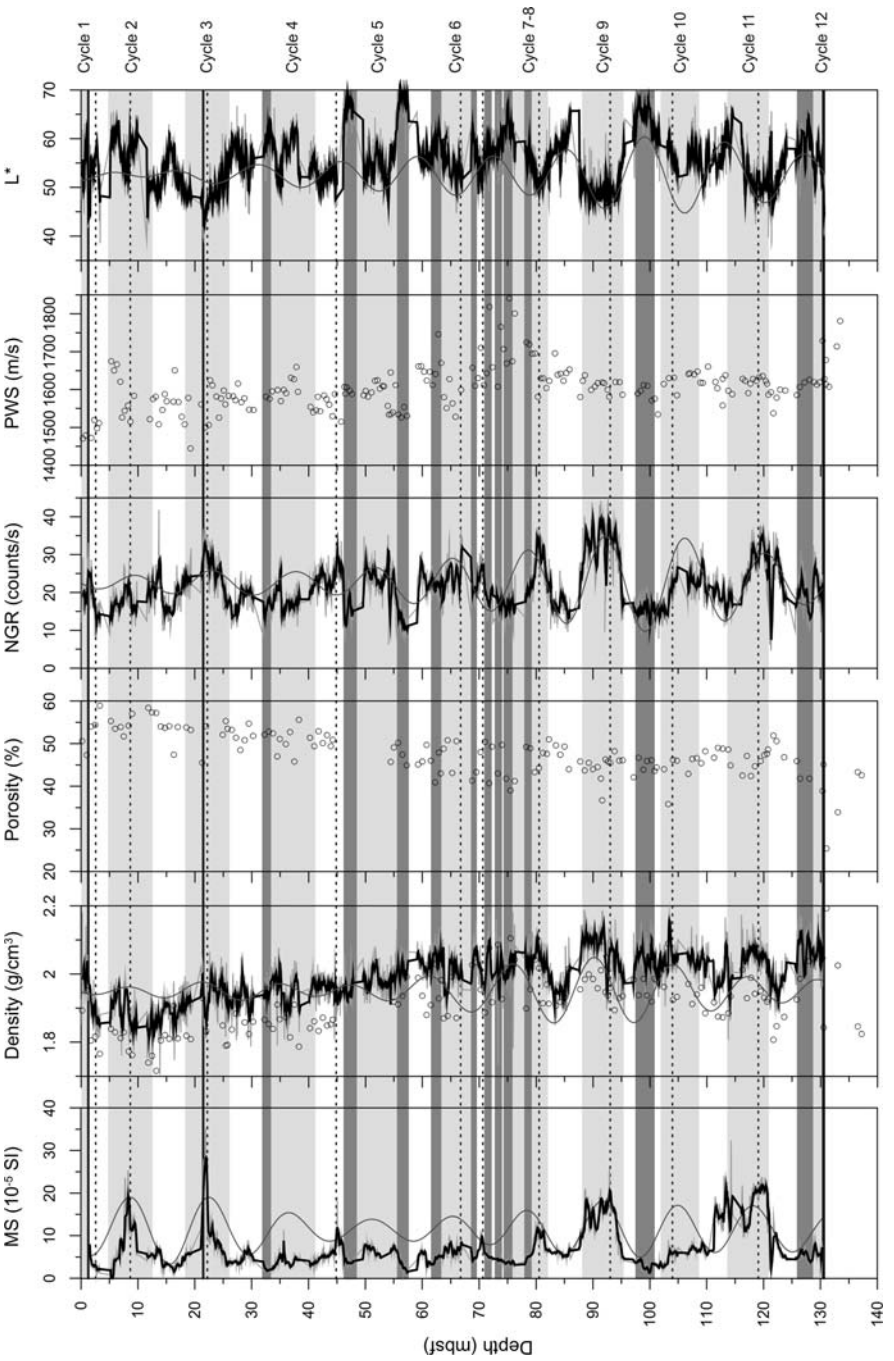

Fig. 4.3 (continued)

(mbsf) on Fig. 4.3 for Hole U1317A. All the records are respectively smoothed by a 7-points running mean (black line on Figs. 4.3, 4.4, 4.5, and 4.6) and filtered with a Gaussian filter centred at a frequency of 0.07 and a bandwidth of 0.015 to identify the different cycles (dark grey line on Figs. 4.3, 4.4, 4.5, and 4.6).

4.2.1.1 Magnetic Susceptibility

The magnetic susceptibilities for all the holes are described in detail in Sect. 5.3 (Environmental magnetism), showing that the terrigenous paramagnetic mineral fraction (mainly the clay minerals illite and chlorite) controls the susceptibility records while diamagnetic carbonate dilutes the terrigenous fraction in well-defined intervals. This alternation controls the cyclicity in the susceptibility records (light grey boxes on Figs. 4.3, 4.4, 4.5, and 4.6). Most of the cycles are characterized by a saw-tooth like pattern, i.e. a sharp increase in the susceptibility followed by a gentle decline going from the bottom to the top of each cycle. The highest susceptibilities are reached at the top of the record to fall down to the lowest values encountered in the mound core at 0.75 mbsf in Hole U1317A, 2.50 mbsf in Hole U1317B, 4.00 mbsf in Hole U1317C and 0.90 mbsf in Hole U1317E. A second sharp peak value is observed at 21.50 mbsf in Hole U1317A, 25.00 mbsf in Hole U1317B, 27.00 mbsf in Hole U1317C and 23.50 mbsf in Hole U1317E (Figs. 4.3, 4.4, 4.5, and 4.6).

4.2.1.2 Gamma Ray Attenuation Density (GRA Density)

In Hole U1317A, the GRA corrected density (g/cm^3) and density measurements on discrete samples display similar trends, indicating the reliability of the GRA corrected density measured with the MST. However, it should be mentioned that the GRA densitometer measurements are generally a bit higher than the density measurements on discrete samples (Fig. 4.3). Air trapped in the sediment-filled beakers (unconsolidated sediments) reduces the relative saturated weight and increases the relative volume measured in the pycnometer, thereby decreasing the resulting bulk density (Exp. 307 Scientists 2006b). The GRA density varies between 1.70 and 2.20 g/cm^3 throughout the mound body for all the holes (Figs. 4.3, 4.4, 4.5, and 4.6), with an average of $\sim$1.99 g/cm^3. The overall pattern shows a gradual increase in density throughout the core, going together with a general decrease in porosity (Fig. 4.3). This can be explained by the degree of compaction, whereby sediments localized deeper in the mound body are influenced by a higher degree of compaction (and thus a higher density and a lower porosity) than sediments at the surface. The average porosity is calculated to be $\sim$50% in the mound body. Density

Fig. 4.3 Geophysical properties (magnetic susceptibility (SI units), density (g/cm^3), porosity (%), NGR (counts/s), P-wave velocity (m/s) and colour reflectance (L*)) in function of depth (mbsf) for Hole U1317A. *Light grey lines* represent raw values. *Black lines* represent smoothed records (7-points running mean). *Dark grey lines* represent filtered records (Gaussian filtering centred at a frequency of 0.07 $\pm$ 0.015). Points represent measurements on discrete samples. *Light grey boxes* correspond with interpreted cycles. *Dark grey boxes* correspond with semi-lithified horizons. *Horizontal solid black lines* correspond with interpreted hiatus and the mound base. *Horizontal dashed black lines* represent correlating tiepoints

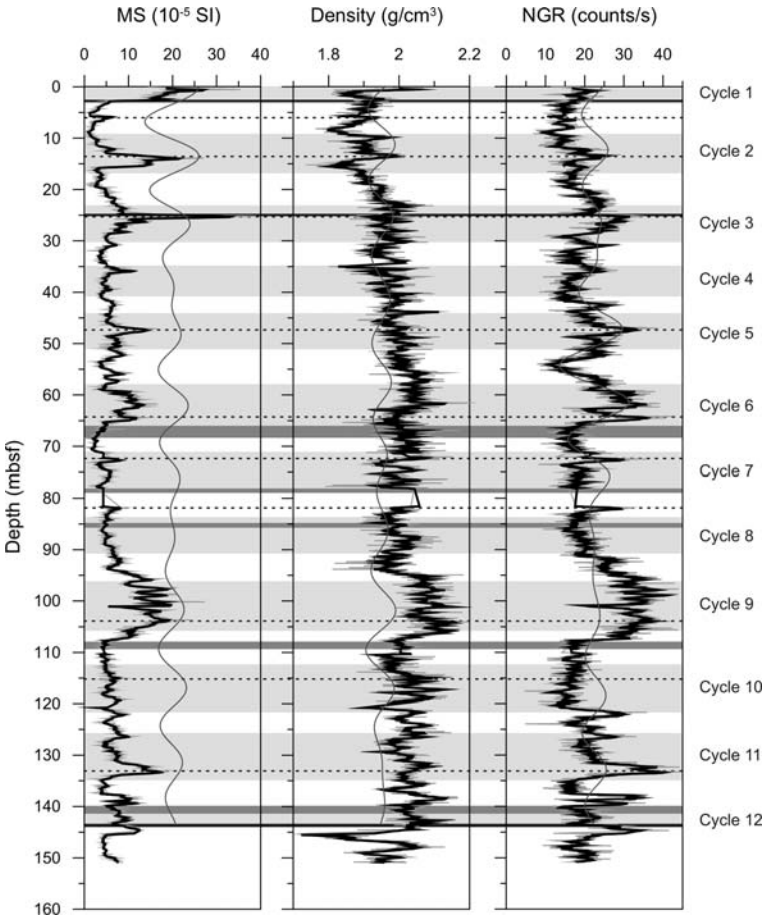

Fig. 4.4 Geophysical properties (magnetic susceptibility (SI units), density (g/cm^3), and NGR (counts/s)) in function of depth (mbsf) for Hole U1317B. *Light grey lines* represent raw values. *Black lines* represent smoothed records (7-points running mean). *Dark grey lines* represent filtered records (Gaussian filtering centred at a frequency of 0.07 $\pm$ 0.015). *Light grey boxes* correspond with interpreted cycles. *Dark grey boxes* correspond with semi-lithified horizons. *Horizontal solid black lines* correspond with interpreted hiatus and the mound base. *Horizontal dashed black lines* represent correlating tiepoints

decreases from 2.10 to 1.70–1.80 g/cm^3 in the upper ~15.00 m and increases again to 2.00 g/cm^3 around ~25.00 mbsf. Density values increase gradually to ~60.00–65.00 mbsf, remain stable until ~100.00 mbsf and decrease then again slowly towards the mound base. A similar cyclic record as noted in the magnetic susceptibility and the colour reflectance characterizes the GRA corrected density and is overprinting the general background trends (light grey boxes on Figs. 3.4, 4.4, 4.5, and 4.6). Lighter intervals, characterized by low susceptibilities, have lower densities, while darker intervals with a high susceptibility are characterized by high densities. So, it can be said that the carbonate-rich intervals have a lower density.

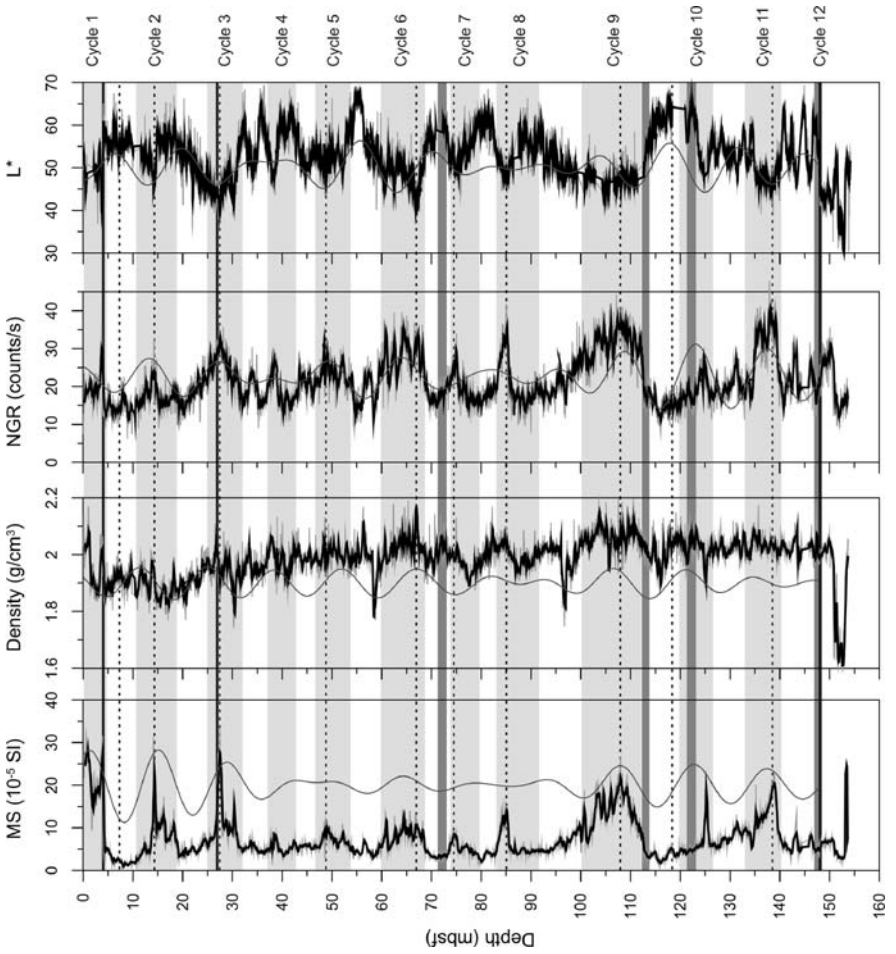

Fig. 4.5 Geophysical properties (magnetic susceptibility (SI units), density (g/cm^3), NGR (counts/s) and colour reflectance (L$*$)) in function of depth (mbsf) for Hole U1317C. *Light grey lines* represent raw values. *Black lines* represent smoothed records (7-points running mean). *Dark grey lines* represent filtered records (Gaussian filtering centred at a frequency of 0.07 ± 0.015). *Light grey boxes* correspond with interpreted cycles. *Dark grey boxes* correspond with semi-lithified horizons. *Horizontal solid black lines* correspond with interpreted hiatus and the mound base. *Horizontal dashed black lines* represent correlating tiepoints

However, it should be noted that the cyclicity noted in the GRA density record is not as pronounced as in the other geophysical records (magnetic susceptibility and NGR). Moreover, a small shift in the cycles of the GRA density compared to the cycles in susceptibility and NGR is noted. This small shift and the less pronounced cycles in the density can be explained by the presence of some more lithified (semi-lithified) layers in the carbonate-rich (lighter) intervals (Sects. 3.2.1 and 4.5.2), which have in particular an influence on the density. These small semi-lithified

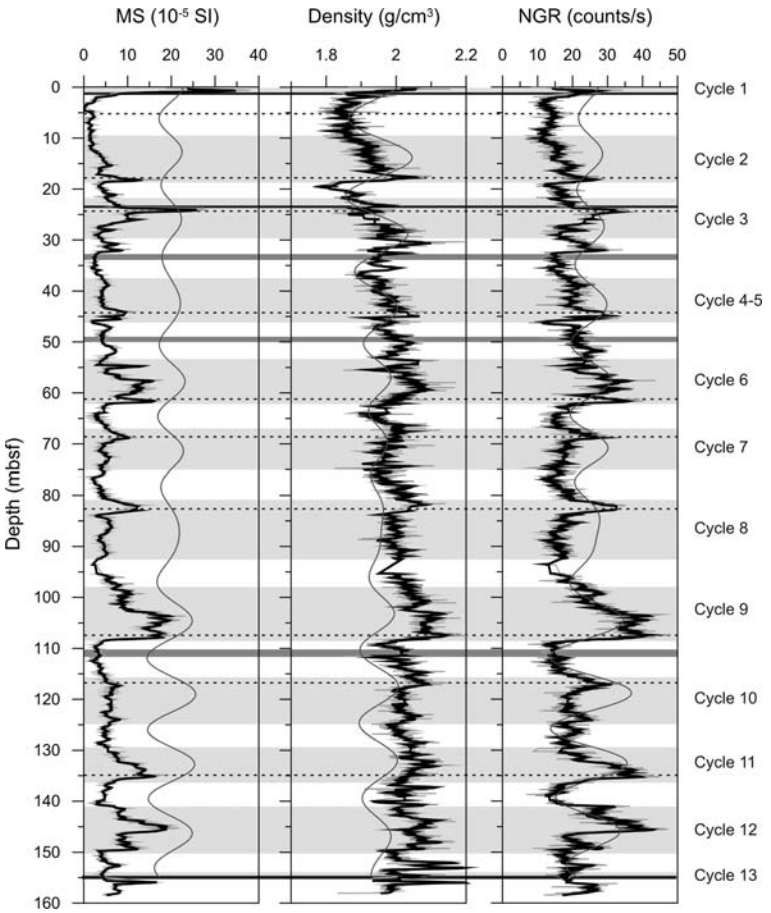

Fig. 4.6 Geophysical properties (magnetic susceptibility (SI units), density (g/cm^3), and NGR (counts/s)) in function of depth (mbsf) for Hole U1317E. *Light grey lines* represent raw values. *Black lines* represent smoothed records (7-points running mean). *Dark grey lines* represent filtered records (Gaussian filtering centred at a frequency of 0.07 ± 0.015). *Light grey boxes* correspond with interpreted cycles. *Dark grey boxes* correspond with semi-lithified horizons. *Horizontal solid black lines* correspond with interpreted hiatus and the mound base. *Horizontal dashed black lines* represent correlating tiepoints

layers are mapped in detail for Hole U1317A and are visualized on Fig. 4.3 by the dark grey boxes. The most important semi-lithified layers are also mapped in the other holes (dark grey boxes on Figs. 4.3, 4.4, and 4.5). It should be mentioned that the semi-lithified layers are occurring in these part of the cycles where the susceptibilities are reaching the lowest values and colour reflectance are reaching the highest values. Another explanation of the small shift in cycles can be the changing quantity of coral fragments, which do not have a major influence on the magnetic susceptibility and the NGR but which can influence the density records.

4.2.1.3 Natural Gamma Radiation (NGR)

The NGR varies throughout the mound body between 10.00 and 40.00 counts/s, with an average value around ~21.50 counts/s (Figs. 4.3, 4.4, 4.5, and 4.6). The upper ~20.00–25.00 mbsf are characterized by a general increasing trend. This increasing trend is continuing below ~20.00–25.00 mbsf but with a gentler slope, to decrease below ~100.00 mbsf until the mound base. The cyclic record, characterizing all the geophysical records is also overprinting the background variabilities of the NGR. The parallel trend between the NGR and the magnetic susceptibility curve in the mound body is remarkable. Just as the cycles observed in the susceptibility records, a saw-tooth like pattern is characterizing the cycles present in the NGR records. Intervals with a high susceptibility and a high GRA density correspond with a high NGR, which reflects the important contribution of clay minerals (or clayey silt) to the sediments in these intervals. In the intervals characterized with a lower susceptibility corresponding with a lower NGR, carbonate-rich material dilutes the NGR signals.

4.2.1.4 P-Wave Velocity (PWL and PWS)

PWL measurements at Site U1317 could not be used for detailed interpretation due to the high amount of artefacts in the measurements caused by the presence of coral fragments in a muddy matrix. However, there are still trends that can be derived from the PWS data collected in Hole U1317A (Fig. 4.3). Between 20.00 and 55.00 mbsf, the velocity remains constant with an average value of ± 1600 m/s. From 60.00 to 80.00 mbsf, higher velocities have been measured (up to 1800 m/s). Below 80.00 mbsf, the velocity drops again towards values averaging around 1600 m/s. The high velocity values between 60.00 and 80.00 mbsf corresponds with low NGR and low susceptibility values, characterized by carbonate-rich material. It should be noted that especially this interval corresponds with a high accumulation of semi-lithified horizons. So, the high P-wave velocities between 60.00 and 80.00 mbsf can be explained by the presence of those semi-lithified horizons (Fig. 4.3).

4.2.2 Interpretation and Correlation

A comparative study between the filtered records of Holes U1317A, U1317B, U1317C and U1317E, using the AnalySeries software package developed by Paillard et al. (1996), made it possible to define tiepoints between the different holes (Table 4.1) and to distinguish 13 different cycles numbered from 1 to 13 starting from the top of the mound towards the mound base (Figs. 4.3, 4.4, 4.5, and 4.6; Table 4.2). The definition of the tiepoints is based on peak values recorded in the smoothed records, whereas the cycles are based on the filtered records. This explains the offset between the depths of the tiepoints and the depths of the different cycles. The tiepoints and cycles were used to correlate tentatively the geophysical records from the different holes.

Table 4.1 Depths (mbsf) of the defined, correlating tiepoints in Holes U1317A, U1317B, U1317C and U1317E

Tiepoints	U1317A [mbsf]	U1317B [mbsf]	U1317C [mbsf]	U1317E [mbsf]
Tiepoint 1	2.70	5.50	7.00	5.00
Tiepoint 2	8.00	13.70	14.30	18.06
Tiepoint 3	21.65	25.30	27.35	24.00
Tiepoint 4	44.95	47.11	48.50	44.00
Tiepoint 5	66.20	64.50	67.00	61.50
Tiepoint 6	70.50	72.50	74.95	68.70
Tiepoint 7	81.00	81.81	85.00	82.00
Tiepoint 8	93.00	104.00	108.50	107.85
Tiepoint 9	104.80	115.20	118.00	116.99
Tiepoint 10	119.55	133.20	138.00	134.09

Not all the cycles are recognized in all the holes. There are some important changes in the amount of cycles going from the flank of the mound (Hole U1317A) to the top of the mound (Hole U1317E). Cycles 4 and 5 are clearly separated in Hole U1317A (Fig. 4.3) to partly merge in Holes U1317B and Hole U1317C (Figs. 4.4 and 4.5). In Hole U1317E, they seem to be completely merged and slimmed down to one cycle (Fig. 4.6). On the other hand, cycles 7 and 8 are clearly two separated cycles in Hole U1317E (Fig. 4.6). They merge partly together in Holes U1317B and U1317C (Figs. 4.4 and 4.5) to become one cycle in Hole U1317A (Fig. 4.3). So, it can be assumed that sedimentation rates were higher and that more sediment was deposited on top of the mound (Hole U1317E) between 65.00 and 97.50 mbsf resulting in cycles 7 and 8, while the opposite is true for cycles 4 and 5. Magnetostratigraphic interpretations show that cycles 7 and 8 correspond with the Réunion Subchronozone, characterized by really high sedimentation rates especially on top of the mound (Sect. 5.2.3). As discussed in detail in Sect. 5.3.3, the mound was in

Table 4.2 Depths (mbsf) of the defined, correlating cycles in Holes U1317A, U1317B, U1317C and U1317E

Cycles	U1317A [mbsf]	U1317B [mbsf]	U1317C [mbsf]	U1317E [mbsf]
Cycle 1	top	0.75	1.25	top
Cycle 2	8.25	13.00	14.70	12.95
Cycle 3	22.35	26.50	28.85	25.75
Cycle 4	35.75	37.90	40.05	42.00
Cycle 5	51.00	48.10	49.95	–
Cycle 6	66.10	62.00	63.50	58.10
Cycle 7	78.85	76.00	78.00	71.00
Cycle 8	–	88.00	94.50	90.00
Cycle 9	91.65	101.00	108.00	104.95
Cycle 10	105.90	116.25	122.85	119.00
Cycle 11	118.50	131.00	137.00	132.50
Cycle 12	moundbase	moundbase	moundbase	146.50
Cycle 13	–	–	–	moundbase

an important growth phase during this period with the highest growth rates centred at the top of the mound, boosting a vertical growth process. Cycles 4 and 5 are mainly corresponding with the Olduvai Chron, characterized by sedimentation rates increasing from the top to the flanks of the mound (Sect. 5.2.3). This suggests that the vertical growth phase centred at the top of the mound is followed by a horizontal expansion of the mound with higher growth velocities noted at the flanks of the mound compared to the top. An extra cycle 13 is recorded just above the mound base in Hole U1317E but is not present in Holes U1317A, U1317B and U1317C. This suggests that mound initiation started earlier in Hole U1317E compared to the other holes, which is confirmed by the magnetostratigraphic framework (Sect. 5.2.1).

Generally it can be concluded that the saw-tooth like cycles characterized by low values of magnetic susceptibility indicate a higher amount of carbonate-rich material (diamagnetic carbonate) and a lower amount of siliciclastic material (paramagnetic clays). NGR parallels the magnetic susceptibilities with higher values reflecting increased clay content. Intervals with higher susceptibilities and higher NGR are generally also characterized by higher densities. The P-wave velocity averages around 1600 m/s, with generally higher velocities in the carbonate-rich intervals. It can be said that the cyclic record is driven by the alternation between terrigenous clay-rich siliciclastic sediments and carbonate-dominated sediments, whereby the carbonate-rich sediments dilute the terrigenous clay-rich sediments in well-defined intervals. As discussed earlier, the small offset between the GRA density cycles and the cycles in susceptibility and NGR can be explained by the presence of semi-lithified horizons which have particularly an effect on the density, porosity and P-wave velocity. Changing coral quantities can also have an influence on the density records.

The background trends in all the geophysical records are characterized by an abrupt change around ~20.00–25.00 mbsf, corresponding with cycle 3. This change can be correlated with a lithological and erosive boundary, representing an important hiatus as discussed in Sect. 5.5.4 (Kano et al. 2007). Cycle 1 is not completely preserved in the records, but seems to be best recorded in Hole U1317C. The base of cycle 1 also corresponds with an erosive boundary. Datings in Hole U1317E and on a gravity core (MD01-2450) on top of the mound record showed that this uppermost erosive boundary also represents a hiatus (Sects. 5.5.4 and 6.4.2).

4.3 Geochemical Records

4.3.1 Cyclic Record

XRF measurements made it possible to do a semi-quantitative analysis of the major chemical elements (Fe, Ca, K, Ti, Mn, Sr and Cu) in the mound sediments of Hole U1317E. The relative variations of the major chemical elements from Hole U1317E (counts/s), the smoothed records (7-points running mean) and the filtered records (Gaussian filtering at a frequency of 0.07 and a bandwidth of 0.015) are presented in function of depth (mbsf) on Fig. 4.7. The most important elements are Ca and Fe,

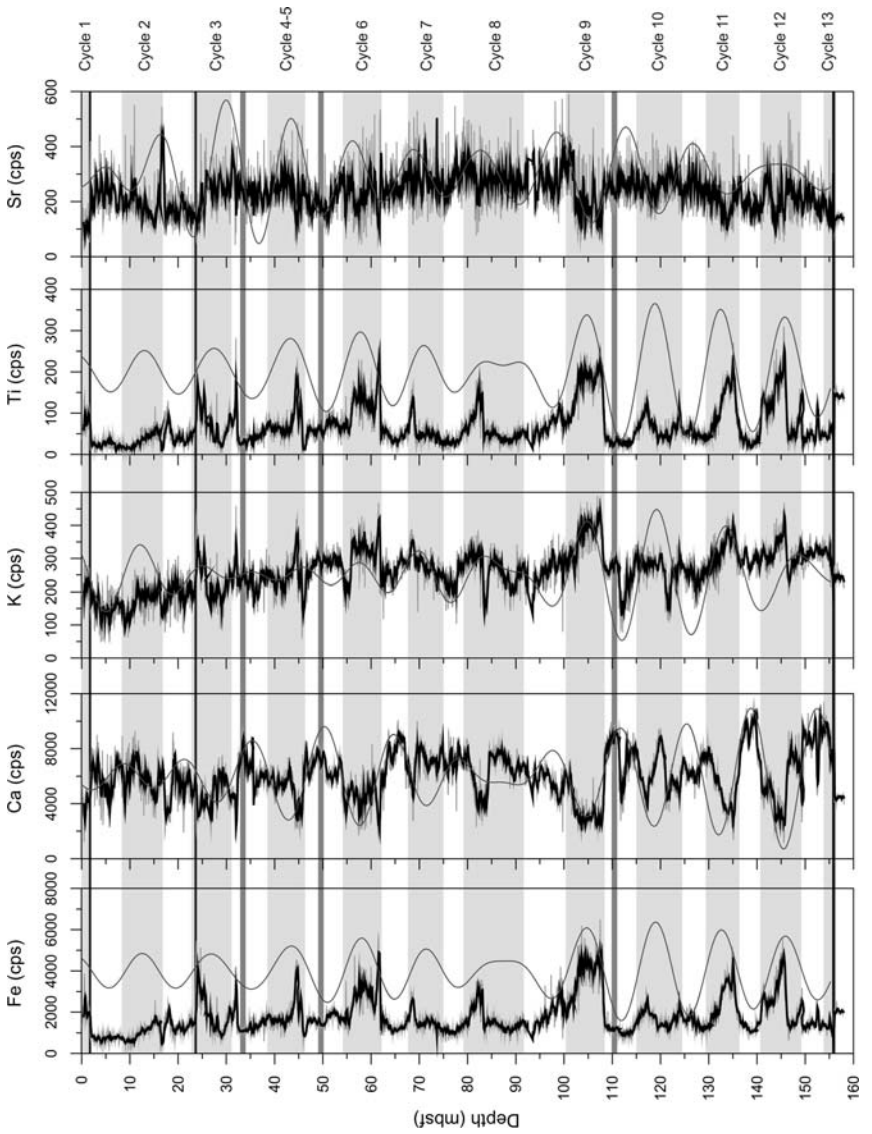

Fig. 4.7 Geochemical properties (Fe, Ca, K, Ti and Sr (counts/s)) in function of depth (mbsf) for Hole U1317E. *Light grey lines* represent raw values. *Black lines* represent smoothed records (7-points running mean). *Dark grey lines* represent filtered records (Gaussian filtering centred at a frequency of 0.07 ± 0.015). *Light grey boxes* correspond with interpreted cycles. Dark grey boxes correspond with semi-lithified horizons. *Horizontal solid black lines* correspond with interpreted hiatus and the mound base

occurring with an average of respectively 6043 counts/s and 1778 counts/s, followed by K, Sr and Ti with an average of respectively 264 counts/s, 236 counts/s and 69 counts/s. The other elements that were calculated from the spectrum (Mn, ~37 counts/s and Cu, ~33 counts/s) are close to the nominal sensitivity of the XRF core scanner and will be excluded from further analyses.

4.3.1.1 Fe, K and Ti

Fe intensities are varying between 305 and 6000 counts/s (Fig. 4.7). In the upper metre Fe counts are decreasing from 3800 to 500 counts/s. Below 1.00 mbsf, Fe intensities slightly increase until 23.50 mbsf. A second general increasing trend is observed between 23.50 and 60.00 mbsf, followed by a third increasing trend from 63.00 to 108.00 mbsf. Below 108.00 mbsf Fe count rates drop to lower values to reach maximum values between 131.00 and 136.00 mbsf, and 141.00 and 146.00 mbsf. Just below the mound base Fe intensities are around 2000 counts/s. A similar depth pattern is observed in the Ti (varying between 2 and 310 counts/s) and K (varying between 50 and 490 counts/s) intensities. The same cycles as observed in the geophysical properties and the reflectance, are overprinting the background trends in the intensities of Fe, K and Ti (grey boxes on Fig. 4.7). It should be noted that most of the cycles have a typical saw-tooth like pattern. Elements like Fe, Ti and K are related to siliciclastic components and vary directly with the terrigenous fraction of the sediment (Röhl and Abrams 2000). Probably clay minerals play hereby an important role. It should be mentioned that the influence of diagenetic Fe-rich minerals (such as pyrite) on the Fe records, can not be excluded (Sect. 5.3).

4.3.1.2 Ca and Sr

Ca count rates are varying between 1130 and 11412 counts/s and are strongly anti-correlated with Fe variations (Fig. 4.7). Ca values increase from 1200 to 8000 counts/s in the upper metre, to decrease again to 4000 counts/s at a depth of 23.50 mbsf. A second decreasing trend is observed from 23.50 mbsf on, to reach the lowest values around 60.00 mbsf. From 63.00 mbsf until a depth of 108.00 mbsf, the Ca intensities are characterized by a third decreasing trend. Below 108.00 mbsf, Ca intensities jump to slightly higher values to reach minimal count rates between 131.00 and 136.00 mbsf, and 141.00 and 146.00 mbsf. Just below the mound base Ca intensities fall back to 4000 counts/s. Again, a cyclic record is overprinting the general background trends. Comparison of shipboard carbonate data obtained from the analysis of discrete samples with measured Ca intensity variations of about 2000 to 10000 counts/s reflect carbonate contents ($CaCO_3$) varying between 20.00 and 70.00 wt.%, with an average of 49.60 wt.%. To enable determination of carbonate mass accumulation rates, discrete samples were measured for inorganic carbon content using a Coulometrics 5011 CO_2 coulometer (Exp. 307 Scientist 2006b). A total of ~10–15 mg of freeze-dried sediment was weighted and reacted with 2 N HCl. The liberated CO_2 was titrated, and the end point was determined by a photo detector. Calcium carbonate concentration, expressed as weight percent, was then

calculated from the inorganic carbon content, assuming that all released CO_2 was derived from dissolution of $CaCO_3$, by the following equation (Eq. 4.6):

$$CaCO_3(\text{wt.}\%) = 8.33 \times \text{inorganic carbon (wt\%)} \quad (4.6)$$

No correction was made for the presence of other carbonate minerals such as dolomite. Analytical uncertainty, based on repeated measurements of reagent-grade calcium carbonate, was ± 1.00%.

The Fe-intensities show an inverse relationship with the Ca values over the whole studied interval, suggesting that this site is predominantly a two-component sedimentary environment, whereby the cyclic record of the carbonate content is mainly controlled by terrigenous input. However, it should be mentioned that the record of the Ca count rates is more influenced by short-term variabilities, especially in the Ca-rich intervals, than the record of the Fe intensities. Carbonate is mainly present in the mound sediments as calcite and aragonite, whereby calcite is mainly originating from nannofossil ooze, whereas aragonite is mainly concentrated in the coral fragments (Sect. 3.2.2). However, no clear positive relationship can be found between coral quantity (volume percentages) and Ca count rates (Fig. 4.8A). On the contrary, a negative relationship can be inferred. Indeed, as discussed in Sect. 3.3.2, dissolution is occurring in the Ca-rich intervals, with preferable aragonite dissolution (dissolution of coral fragments) which can have a negative effect on the coral quantity records. On the other hand, the difficulties in detection of cold-water coral fragments in lighter intervals can influence the coral quantity records, leading to underestimation of the cold-water coral fragments in the lighter intervals. As noted in Sect. 3.2.2, the small amount of diagenetic low-magnesium calcite can not be neglected, certainly not in the semi-lithified horizons. Figure 4.7 shows that these semi-lithified horizons are corresponding with the highest Ca count rates. So, diagenesis has a secondary influence on the Ca-contents especially in the Ca-rich horizons.

Sr intensities are characterized by values between 100 and 500 counts/s. At first sight, a similar cyclic character can be observed between the Ca count rates and the Sr intensities. By looking more in detail to the Sr records, a shift between the cycles

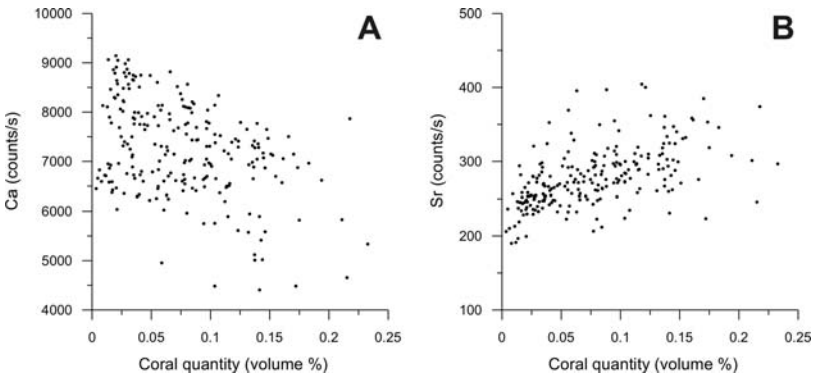

Fig. 4.8 (**A**) Ca intensities (counts/s) in function of coral quantity (vol.%). (**B**) Sr intensities (counts/s) in function of coral quantity (vol.%)

in the Sr count rates and the cycles recorded in the other geochemical parameters is observed. This suggests that a secondary cyclicity is overprinting the primary cyclicity in the Sr count rates. Sr can be an indication for the amount of aragonite in the mound core. As the aragonite in the mound sediments is mainly originating from cold-water coral fragments, Sr count rates are thus an indicator for the amount of cold-water coral fragments in the mound. Indeed, by comparing the coral quantities (volume percentages), as defined in Sect. 3.3.1, with the Sr intensities, a positive correlation can be observed (Fig. 4.8b). Dissolution of coral fragments (dissolution of aragonite) will have an important impact on the Sr contents, suggesting that diagenesis can dilute the primary cyclic record extensively.

4.3.2 Relationship with Physical Properties

The most important element intensities (Fe and Ca) can now be compared with the geophysical properties (magnetic susceptibility, GRA density and NGR) (Fig. 4.9). Fe is correlating positively with the geophysical records. In particular, the Fe intensities are correlating well with the magnetic susceptibility and the NGR, whereby higher Fe intensities correspond with higher susceptibilities and higher NGR (Fig. 4.9A,C) suggesting that the susceptibility and the NGR records are

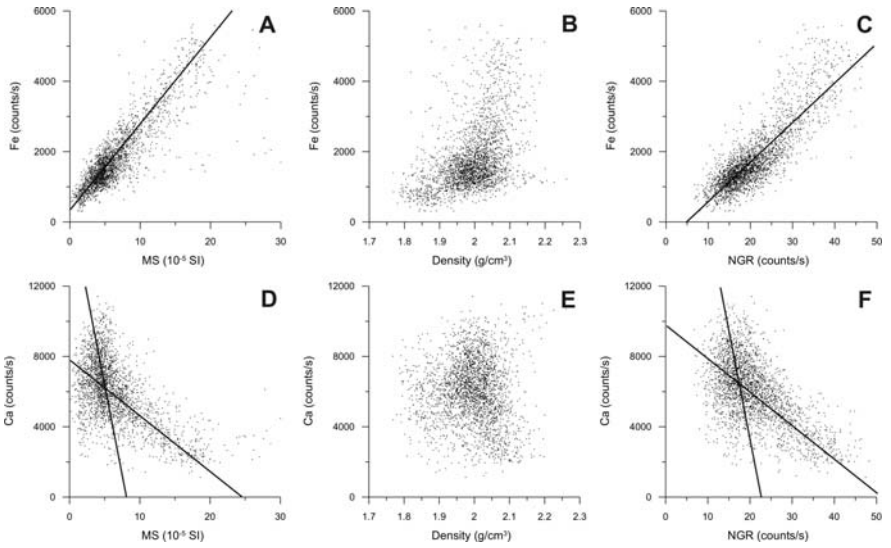

Fig. 4.9 (**A**) Fe intensities (counts/s) in function of magnetic susceptibility (10^{-5} SI units). (**B**) Fe intensities (counts/s) in function of GRA density (g/cm^3). (**C**) Fe intensities (counts/s) in function of NGR (counts/s). (**D**) Ca intensities (counts/s) in function of magnetic susceptibility (10^{-5} SI units). (**E**) Ca intensities (counts/s) in function of GRA density (g/cm^3). (**F**) Ca intensities (counts/s) in function of NGR (counts/s). *Black lines* represent trend lines but have no statistical relevance

mainly influenced by Fe-rich terrigenous clay minerals. The correlation with the GRA density is less pronounced (Fig. 4.9B) which can be explained by the fact that the density is probably influenced by the presence of semi-lithified layers formed during diagenetic processes. On the other hand changing coral quantities might influence the density records too.

Ca is negatively correlated with the presented geophysical records (Fig. 4.9D–F) but the correlation with the susceptibility and the NGR is not as pronounced as the correlations between the Fe intensities and these parameters. Two trends are recognized in the correlation plots, suggesting that the Ca records are influenced by two different processes. On the one hand, a similar trend can be inferred with a similar gradient as observed in the correlation plots of the Fe count rates with the susceptibility and the NGR but in opposite direction, suggesting that the presence of terrigenous Fe-rich material dilutes the Ca-rich intervals (or the other way around, i.e. the Ca-rich material dilutes the Fe-rich intervals). On the other hand, a second trend is observed in the Ca-rich intervals (with a steeper gradient) suggesting that diagenetic processes (i.e. dissolution of coral fragments and reprecipitation of a second carbonate phase) are influencing the Ca intensities in these intervals. A better correlation is observed between the Ca count rates and the GRA density than between the Fe intensities and the GRA densities, suggesting that both parameters (Ca count rates and GRA density) are influenced by the same mixture of processes (diagenesis and dilution by terrigenous material). This suggest that the GRA density is rather influenced by diagenetic processes (by the formation of semi-lithified layers and coral dissolution), than changing coral quantities as mentioned earlier. So, it can be concluded that the cyclicity in the geophysical records (mainly in the susceptibility and the NGR) and the cyclicity in the geochemical composition (mainly carried by the elements Fe and Ca), is driven by the alternation between intervals dominated by terrigenous clay-rich siliciclastic sediments and intervals characterized by a high amount of (biogenic) calcareous sediments. Coral dissolution and the formation of semi-lithified layers due to diagenetic processes influence the Ca intensities and the density records mainly in the Ca-rich intervals. Cold-water coral fragments are present in changing quantities in both the Ca-rich intervals and the Fe-rich intervals.

4.4 Logging the Off-Mound Records

4.4.1 Site U1316

Figures 4.10 and 4.11 represent respectively the geophysical records (magnetic susceptibility, GRA density, density measurements and porosity on discrete samples, NGR, P-wave velocity and colour reflectance) (Fig. 4.10) and the geochemical records (Fe, Ca, K, Ti, Mn, Sr) (Fig. 4.11) for Hole U1316A between 0 and 60.00 mbsf. This upper section represents the sediments above the unconformity correlating with the mound base, determined in Hole U1316A at a depth of 55.06 mbsf and corresponding with a major hiatus (Kano et al. 2007; Sect. 5.4.1). An overview of

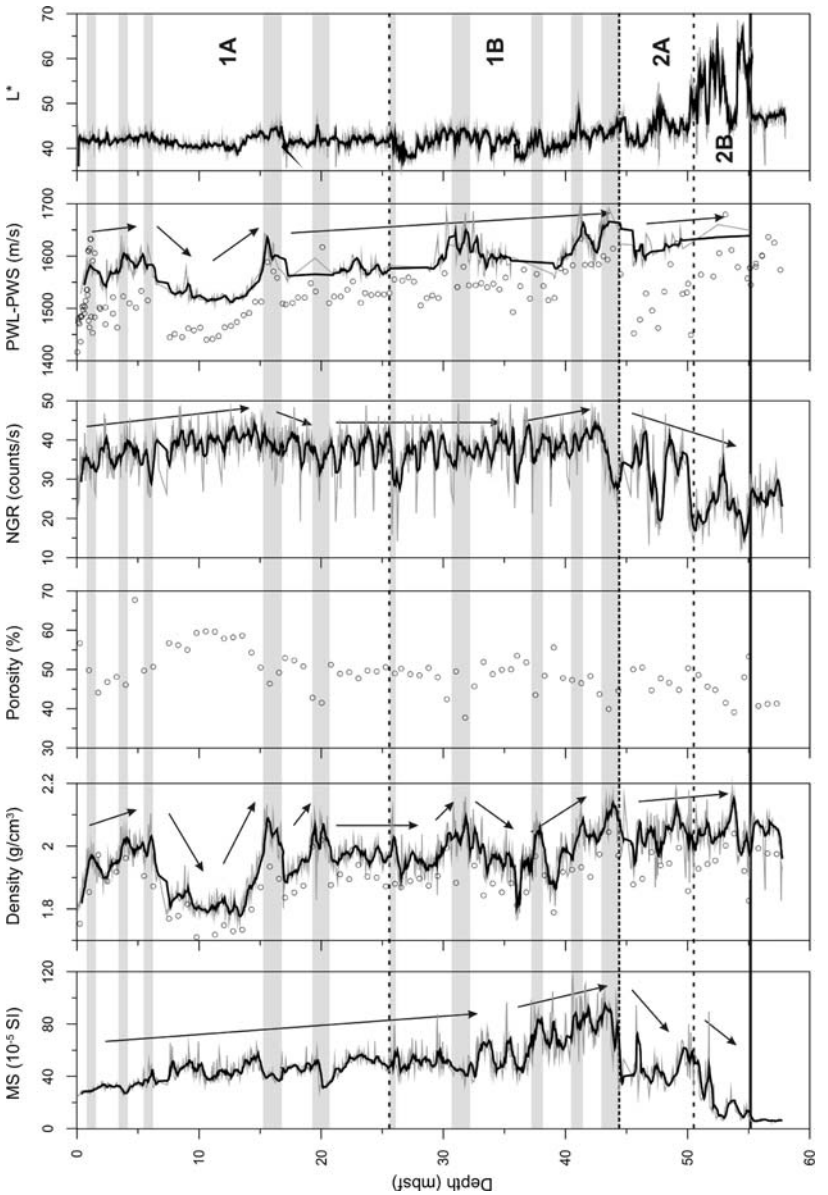

Fig. 4.10 Geophysical properties (magnetic susceptibility (SI units), density (g/cm^3), porosity (%), NGR (counts/s), P-wave velocity (m/s) and colour reflectance (L∗)) in function of depth (mbsf) for Hole U1316A. *Light grey lines* represent raw values. *Black lines* represent smoothed records (7-points running mean). Points represent measurements on discrete samples. *Light grey boxes* correspond with specific minima and maxima. *Horizontal solid black line* corresponds with the mound base. *Black arrows* represent the described trends. *Horizontal dashed black lines* and numbers represent correlating lithological units as described by the Exp. 307 Scientists (2006c) and summarized in Sect. 3.5.1

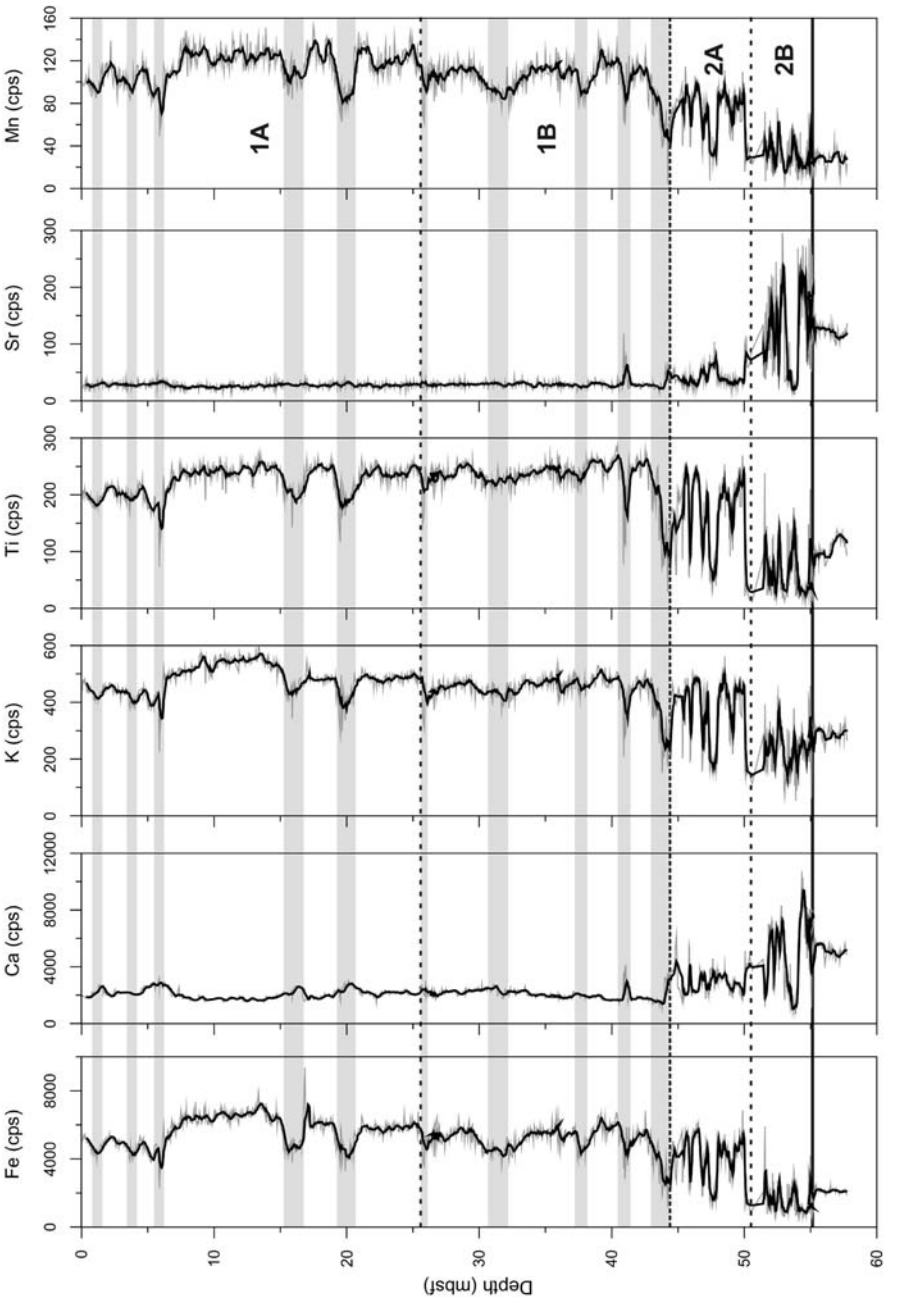

Fig. 4.11 Geochemical properties (Fe, Ca, K, Ti, Sr and Mn (counts/s)) in function of depth (mbsf) for Hole U1316A. *Light grey lines* represent raw values. *Black lines* represent smoothed records (7-points running mean). *Light grey boxes* correspond with specific minima and maxima. *Horizontal solid black line* corresponds with the mound base. *Horizontal dashed black lines* and numbers represent correlating lithological units as described by the Exp. 307 Scientists (2006c) and summarized in Sect. 3.5.1

the lithology of these upper sediments, according to the Exp. 307 Scientists (2006c), is given in Sect. 3.5.1.

4.4.1.1 Geophysical Properties

The magnetic susceptibility measurements range from 5.00×10^{-5} to 100.00×10^{-5} SI units in the studied interval (above 60.00 mbsf) (Fig. 4.10). A gradual increase until 35.00 mbsf is recorded with several saw-tooth intervals of different strength and periodicity superposed on the background trend. A break in the general increasing trend is observed at 20.00 mbsf, with a drop in susceptibility of $\sim 20.00 \times 10^{-5}$ SI units. From 35.00 to 44.00 mbsf, the magnetic susceptibility increases with a higher gradient, superimposed with cycles characterized by a shorter period and a higher variability than the saw-tooth cycles in the uppermost section. Around 44.00 mbsf the magnetic susceptibility drops sharply to $\sim 30.00 \times 10^{-5}$ SI units, followed by a more gradual reduction between 50.00 mbsf and 55.06 mbsf to reach values as low as 3.00×10^{-5} to 4.00×10^{-5} SI units. Below 55.06 mbsf, identified as the mound base, the magnetic susceptibility remains very low, varying between 3.00×10^{-5} and 10.00×10^{-5} SI units.

The GRA corrected densities and the bulk densities measured on discrete samples display parallel trends (Fig. 4.10). The densities are varying between 1.80 and 2.10 g/cm^3. The porosity, measured on discrete samples, has values between 40 and 60% and is anti-correlating with the density measurements (Fig. 4.10). Density increases in the upper 5.90 m from 1.80 to 2.00 g/cm^3. From there the values decrease to 1.70 g/cm^3 and increase again to a clear maximum (2.10 g/cm^3) at a depth of 15.50 mbsf, followed by a second maximum at a depth of 20.00 mbsf. Below 22.00 mbsf the densities remain at a constant level of 1.90 g/cm^3 to increase again at 30.00 mbsf to a maximum of 2.10 g/cm^3 at 32.00 mbsf. Between 36.00 and 44.00 mbsf, the densities increase in different cycles with maxima at 38.00, 41.00, and 44.00 mbsf. Below 44.00 mbsf, the data remain at a constant level until the mound base (55.06 mbsf), with some superimposed cycles varying around 2.00 g/cm^3.

The NGR depth curve shows an overall gradual increase in the uppermost 16.00 mbsf, characterized by high-frequency and high-amplitude variations (Fig. 4.10). Between 16.00 and 21.00 mbsf, a small decrease is recorded in the NGR, which next stays at a nearly constant level from 21.00 to 35.00 mbsf. NGR increases slightly below 35.00 mbsf to drop abruptly to lower values at 43.00 mbsf. Below 44.00 mbsf, NGR increases a bit, to decrease below 46.00 mbsf in different steps towards the mound base (55.06 mbsf). A sharp decline is observed at 50.00 mbsf.

P-wave velocities show similar patterns as the density measurements (Fig. 4.10). Velocity increases in the upper 5.90 mbsf. Below 6.00 mbsf, P-wave velocity decreases, to increase again around 12.00 mbsf, reaching a maximum at 16.00 mbsf. Between 16.00 and 44.00 mbsf, a gradual increase is observed from 1550 to 1630 m/s. The PWS data show considerable scatter and an overall increasing trend between 44.00 and 55.06 mbsf.

4.4.1.2 Geochemical Properties

Fe, Ca, K, Ti, Mn and Sr intensities (counts/s) are presented in function of the depth (mbsf) for Hole U1316A on Fig. 4.11. Fe is the most important element measured in Hole U1316A (above the mound base), varying between 500 and 8000 counts/s with an average of 2615 counts/s. Fe intensities decrease slightly in the upper 5.90 m with some local minima at 1.20, 4.00, and 5.90 mbsf. Below 6.00 mbsf Fe count rates increase to drop at 16.00 mbsf to a clear minimum, followed by a second minimum at 20.00 mbsf. Around 25.90 mbsf Fe intensities drop again to lower values to stay between 26.00 and 44.00 mbsf at a constant level with clear minima at 32.00, 38.00, 41.00, and 44.00 mbsf. Below 44.40 mbsf, Fe count rates decrease abruptly in two steps respectively between 44.40 and 50.00 mbsf and between 50.90 and 55.06 mbsf. In these lowermost intervals Fe intensities are fluctuating more intensively than the other intervals. Just below the mound base (55.06 mbsf), Fe count rates are stabilizing around 2000 counts/s, which is lower than the average Fe intensities in the uppermost intervals.

The elements K, varying between 200 and 550 counts/s with an average value of 418 counts/s, Ti, having intensities between 20 and 250 counts/s and an average value of 194 counts/s, and Mn, with count rates between 10 and 140 counts/s and an average value of 92 counts/s, are following the same trends as the Fe intensities. This suggests that the elements K, T and Mn are originating probably from the same source as the element Fe.

Ca intensities are stable above 44.00 mbsf, varying around 2054 counts/s. Some local maxima are observed at 1.20, 5.90, 16.00, 20.00, 25.90, and 41.00 mbsf. Below 44.40 mbsf, Ca count rates increase seriously to values up to 10000 counts/s just above the mound base (55.90 mbsf). Below the mound base, Ca count rates are quite high, having values around 5150 counts/s.

Sr intensities are following the same trends as the Ca intensities, with stable values averaging around 28 counts/s above 44.00 mbsf. Between 44.40 and 50.90 mbsf, Sr count rates are increasing, to increase further in a second step between 50.90 and 55.06 mbsf up to values of 250 counts/s.

4.4.1.3 Interpretation

Magnetic susceptibilities and NGR in the upper 44.00 mbsf are higher than the sediments encountered in the mound body (Sect. 4.2.1), which can be explained by the higher Fe count rates, so probably a higher amount of terrigenous clay-rich material, and lower Ca intensities, hence less dilution of the clay-rich sediments by Ca-rich material. Ca and Fe count rates are again antipodal in the upper intervals, but this is less pronounced than in the mound sediments. The density changes are more pronounced than in the mound sediments, whereas P-wave velocity seems to be a bit lower than in the mound body. Densities and P-wave velocities are following the same trends, whereby higher densities correspond with higher P-wave velocities. Magnetic susceptibility and NGR are also correlating well and with the Fe intensities, but are anti-correlating with the P-wave velocities and the densities.

The upper 44.00 mbsf correspond with lithological unit 1, as described in Sect. 3.5.1, characterized by silty clays. The increase in density, P-wave velocity and Ca intensity and the small decrease in magnetic susceptibility, NGR and Fe intensity around 5.90 mbsf correspond with a very thin shell debris layer and an interval of more silty material at these depths. Around 16.00 mbsf another maximum in density and P-wave velocity is observed as well as a small peak in Ca intensity, correlating with a minimum in magnetic susceptibility, NGR and Fe count rates. This maximum corresponds with an interval of slightly coarser material (sandy silt). Similar characteristics as observed around 16.00 mbsf in the geophysical and geochemical records are visible around 20.00 and 25.90 mbsf, which can be explained again by the presence of a coarser interval in between the homogeneous muds of lithological unit 1.

From 25.90 mbsf on, the sediments of lithological unit 1 are characterized by very dark olive-grey to dark grey silty clay, intercalated more frequently with centimetre-scaled sandy laminations ($\sim$ lithological unit 1B, Sect. 3.5.1). This explains the slightly lower NGR compared to the concave curve of NGR in the upper 25.90 mbsf ($\sim$ lithological unit 1A, Sect. 3.5.1), characterizing the high amount of clay minerals in the upper intervals. The cm- to mm-scaled laminations are responsible for the more spiky records of magnetic susceptibility below 25.90 mbsf. Small remarkable intervals are present in the records between 25.90 and 44.40 mbsf, which are most pronounced in the geochemical records. At 41.00 mbsf, a lower Fe intensity and a higher Ca intensity correspond with a deformation structure composed of a mixture of silty clay layers with a calcareous fine to medium sand. The presence of small coral rubble fragments in the upper part of this small layer can indicate that this material was slumping from the mound to the off-mound regions. The decrease in Fe count rates just above 44.40 mbsf, correlating with a decrease in NGR and a decrease in density, corresponds with an erosive unconformity overlain by a fining-upwards sequence of fine sand beds. The lower Fe intensities at respectively 32.00 and 38.00 mbsf correspond with slightly coarser (more silty) intervals, nearly not visible in the lithology. Another remarkable observation is noted between 35.00 and 44.40 mbsf in the magnetic susceptibility and the density records. Whereas between 0 and 35.00 mbsf the density and magnetic susceptibility are anti-correlating, both parameters seem to follow the same general trend between 35.00 and 44.40 mbsf. In this interval there is even some discrepancy between the magnetic susceptibility and the Fe intensities, which means that the susceptibility is probably influenced by diagenetic processes. Iron sulphides or bacterial biomineralization may have played an important role here. However, we should take into account that coarser-grained magnetic material from a different source can also be responsible for the observed changes in magnetic susceptibility. Probably the last explanation is more favourable because of the positive correlation with the GRA density in this particular interval.

The sharp drops in magnetic susceptibility, NGR and Fe intensities and the sharp increase in Ca and Sr intensities between 44.40 and 55.06 mbsf correspond with lithological unit 2 (Sect. 3.4.1), characterized by the presence of sequences containing coral fragments. The increase in carbonate content causes the decrease in magnetic susceptibility and also a gradual decrease in NGR because of the limited

clay content in these intervals. The two steps observed in the Fe, Ca and Sr intensities, with higher Fe intensities and lower Ca and Sr intensities between 44.40 and 50.90 mbsf, compared to the intensities of the same elements in the interval between 50.90 and 55.06 mbsf, can be correlated with respectively subunits 2A and 2B. Subunit 2A is characterized by intervals of siliciclastic fine to medium sands, whereas corals predominate in subunit 2B. It can be discussed if the observed coral intervals in the lowermost interval (subunit 2B) are in situ (autochthonous) or are transported by gravitational processes from the mound (allochthonous). Ca and Sr contents indicate that two major coral intervals can be distinguished. The lower Ca and Sr intensities in the upper coral interval can indicate indeed the mixing of the coral fragments with surrounding sediments, while the higher Sr contents in the lowermost intervals can indicate in situ coral fragments. However, it has been noted that diagenesis by coral dissolution can overprint the Ca and Sr records, so the hypothesis of the lower layer with in situ coral fragments and the upper layer characterized by transported coral fragments should be interpreted with caution. The mound base at 55.06 mbsf is clearly recognized in all the geophysical and geochemical parameters.

It can be concluded that the sediments in the upper intervals of Hole U1316A are dominantly terrigenous Fe- and clay-rich sediments characterized by high Fe intensities, high NGR and rather high magnetic susceptibilities. Some intercalations of coarser material are observed, characterized by higher Ca intensities, higher densities and higher P-wave velocities but lower Fe count rates, lower magnetic susceptibilities and lower NGR. The lowermost intervals are diluted by the presence of coral fragments.

4.4.2 Site U1318

Geophysical properties (magnetic susceptibility, GRA density, NGR, P-wave velocity and colour reflectance) and the major chemical element intensities (Ca, Fe, K, Ti and Mn) are presented in function of depth (mbsf) for the upper 90.00 mbsf of Hole U1318B on respectively Figs. 4.12 and 4.13. As discussed in Sect. 3.5.2 and in the cruise reports of IODP Expedition Leg 307 (Exp. 307 Scientists 2006e), these uppermost sediments in Hole U1318B correspond with the clayey succession of lithological unit 1 (from 0 to 82.00 mbsf) and the more sandy lithological unit 2 (from 82.00 to 86.20 mbsf). The base of lithological unit 2 can be correlated with the mound base representing a major hiatus (Kano et al. 2007; Louwye et al. 2008; Sect. 5.4.2).

4.4.2.1 Geophysical Properties

Magnetic susceptibilities are varying above 86.20 mbsf between 20.00×10^{-5} and 120.00×10^{-5} SI units (Fig. 4.12). Below 86.20 mbsf, susceptibilities are characterized by much lower values, averaging around 7.80×10^{-5} SI units. A gradual increase is observed in the upper 35.03 mbsf, superimposed by high-amplitude oscillations. These oscillations have a saw-tooth like pattern characterized by a sharp decrease and a gradual increase from the bottom to the top, especially at 14.50 mbsf,

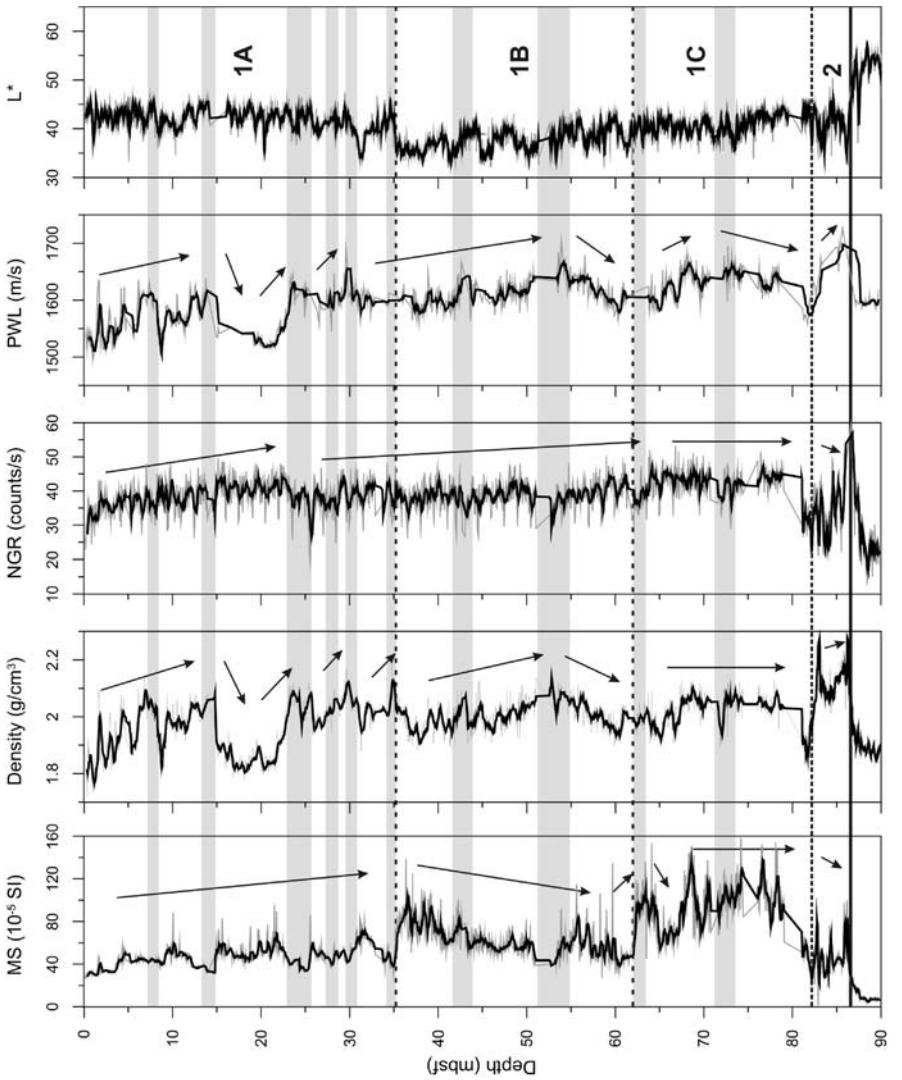

Fig. 4.12 Geophysical properties (magnetic susceptibility (SI units), density (g/cm^3), NGR (counts/s), P-wave velocity (m/s) and colour reflectance (L*)) in function of depth (mbsf) for Hole U1318B. *Light grey lines* represent raw values. *Black lines* represent smoothed records (7-points running mean). *Light grey boxes* correspond with specific minima and maxima. *Horizontal solid black line* corresponds with the mound base. *Black arrows* represent the described trends. *Horizontal dashed black lines* and numbers represent correlating lithological units as described by the Exp. 307 Scientists (2006e) and summarized in Sect. 3.5.2

25.40 mbsf and 35.03 mbsf. Below 35.03 mbsf, magnetic susceptibility gradually decreases until 52.00 mbsf, to increase again to a maximum at a depth of 55.80 mbsf. Below 55.80 mbsf, magnetic susceptibilities decrease until 62.00 mbsf, to jump

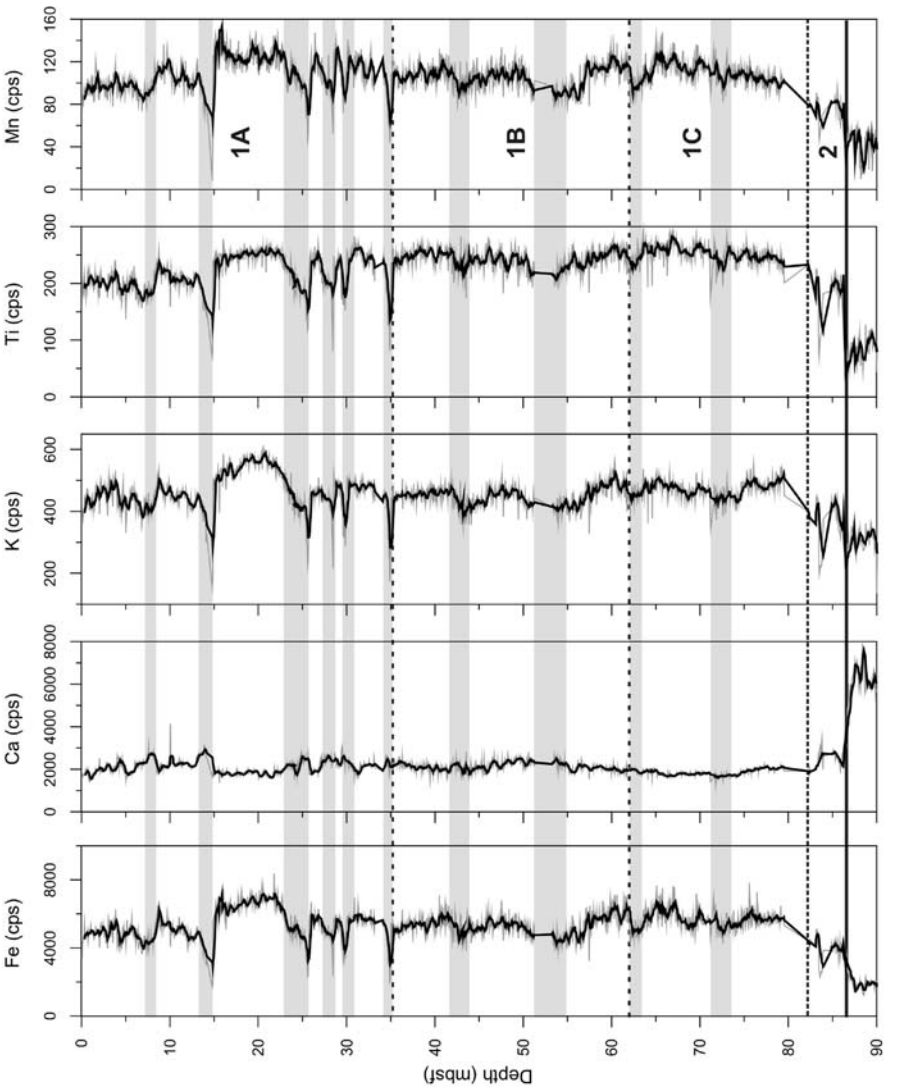

Fig. 4.13 Geochemical properties (Fe, Ca, K, Ti and Mn (counts/s)) in function of depth (mbsf) for Hole U1318B. *Light grey lines* represent raw values. *Black lines* represent smoothed records (7-points running mean). *Light grey boxes* correspond with specific minima and maxima. *Horizontal solid black line* corresponds with the mound base. *Horizontal dashed black lines* and numbers represent correlating lithological units

from these depths to the highest values encountered in the core. Between 62.00 and 82.00 mbsf, magnetic susceptibilities stay at a rather high value, to decrease to lower values between 82.00 and 86.20 mbsf. Between 35.03 and 82.00 mbsf, magnetic susceptibilities are characterized by more pronounced short-term oscillations than in the uppermost interval.

The GRA density increases gradually in the upper 14.50 mbsf from 1.70 to 2.10 g/cm^3 (Fig. 4.12). Below 14.50 mbsf, the values decrease sharply to 1.80 g/cm^3, remain low until 21.50 mbsf, and increase again in several steps to maxima at respectively 25.00, 30.00, and 35.04 mbsf. This is followed by an interval of gradual increase in density, which finally reaches a local maximum at 52.00 mbsf, followed by a minimum at 62.00 mbsf. Between 62.00 and 82.00 mbsf, densities stay at a rather constant level, to increase drastically around 82.00 mbsf reaching high values up to 2.20 g/cm^3 between 82.00 and 86.20 mbsf. Below 86.20, a major break in the density depth curve corresponds with a reduction in density from ~2.20 to 1.90 g/cm^3.

The NGR depth curve shows a gradual increasing trend from the top until 80.00 mbsf, characterized by regular and high-amplitude oscillations and values varying between 40.00 and 60.00 counts/s (Fig. 4.12). NGR decreases to lower values between 82.00 and 86.20 mbsf. Below 86.20 mbsf, NGR is falling back to values averaging around 30 counts/s.

P-wave velocities are following similar trends as the GRA densities. P-wave velocities increase irregularly in the upper 14.50 mbsf from 1500 to 1650 m/s (Fig. 4.12). Below 14.50, mbsf P-wave velocity decreases to increase again at 21.50 mbsf reaching maxima at 23.20 and 30.0 mbsf. Between 30.00 and 52.00 mbsf, the values increase slowly to decrease again between 54.00 and 62.00 mbsf. P-wave velocities slightly increase and decrease between 62.00 and 82.00 mbsf. The highest values, up to 1750 mbsf, are reached between 82.00 and 86.20 mbsf.

4.4.2.2 Geochemical Properties

From the geochemical elements measured with the XRF core scanner on Hole U1318B, the Fe intensities have the highest concentrations, characterized by values varying between 4000 and 7000 counts/s with an average value of 5385 counts/s in the uppermost sediments, i.e. sediments above 86.20 mbsf (Fig. 4.13). Fe intensities are increasing in the upper 22.00 mbsf, characterized by saw-tooth like patterns with a sharp decrease followed by a gradual increase from the bottom to the top at 8.00 and 14.50 mbsf. Below 22.00 mbsf a third saw-tooth like pattern is observed with a minimum at 25.40 mbsf. Between 25.80 and 55.80 mbsf, Fe count rates stay at a rather constant level with local minima at respectively 28.45, 29.70, 35.03, 43.55, and 54.05 mbsf. The mimima at 28.45, 29.70, and 35.03 are again characterized by a saw-tooth like pattern. However, the other minima have a more general shape. Fe count rates are rather high between 55.80 and 82.00 mbsf, characterized by lower values at 62.00 and 72.50 mbsf. An abrupt decrease is observed at 82.00 mbsf to reach values around 4000 counts/s between 82.00 and 86.20 mbsf. A second drop to values around 2000 counts/s is present just below 86.20 mbsf. K, Ti and Mn intensities are following the same trends as the Fe intensities. K count rates have values between 300 and 600 counts/s above 86.20 mbsf and an average value of 459 counts/s. Ti intensities are characterized by an average value of 232 counts/s and vary between 150 and 275 counts/s. Mn intensities are averaging around 107 counts/s having minimum values around 40 counts/s and maximum values around 140 counts/s.

Ca count rates are rather constant in the upper 82.00 mbsf, with an average value of 2063 counts/s (Fig. 4.13). Between 82.00 and 86.20 mbsf Ca values increase slightly, to jump abruptly to higher values below 86.20 mbsf. Some small-scaled local maxima are observed in the upper 30 m around 8.00, 14.50, 25.40, 28.45, and 29.70 mbsf. At 35.03 and 54.05 two other maxima can be observed. Below 55.00 mbsf, Ca intensities decrease slightly to increase again between 72.00 and 82.00 mbsf.

4.4.2.3 Interpretation

As in Hole U1316A, magnetic susceptibility and NGR are generally higher than in the mound sediments. A higher amount of terrigenous material enriched with Fe-rich clay minerals is responsible for this observation. Susceptibilities are correlating well with the Fe intensities, whereby intervals characterized by higher susceptibilities are correlating with intervals with higher Fe intensities. However, between 55.80 and 82.00 mbsf, both parameters are not coherent anymore. Probably diagenetic processes driven by the high amount of iron sulphides in this particular interval are responsible for the discrepancy between both data sets. Density, P-wave velocity and Ca intensities are anti-correlating in the uppermost intervals with the magnetic susceptibilities and the Fe count rates.

The increase in susceptibility from 0 to 35.04 mbsf is correlating with lithological unit 1A (Sect. 3.5.2), characterized by silty clays. The local minima in Fe intensities and magnetic susceptibilities characterized by a typical saw-tooth pattern at 14.50, 25.40, and 35.03 mbsf are explained as small-scaled fining-upwards intercalations of medium to coarse sands with an erosional base at these depths. These small intercalations can be interpreted as small turbidites. Also the two small jumps in Fe intensity at 28.45 and 29.70 have a typical saw-tooth pattern, representing the fining-upwards trends with an erosional base which can be interpreted as small turbidites.

From 35.04 mbsf on, the magnetic susceptibility records are characterized by frequent high-amplitude oscillations, resulting in a spiky appearance of the records. The zone between 35.04 and 82.00 mbsf can be linked with lithological units 1B and 1C (Sect. 3.5.2), characterized by silty clays to fine sandy clays with cm- to mm-thick laminated horizons, consisting of alternations of light and dark greenish grey clay with very fine sand layers, explaining the small-scaled oscillations overprinting the background trends. The minimum around 54.00 mbsf in the Fe count rates, corresponding with a minimum in susceptibility and slightly elevated Ca count rates, can be explained by the intercalation of a coarser interval. The minima around 62.00 and 72.50 mbsf can also be explained by the intercalation of sandier material. However, these minima are not corresponding with lower susceptibilities which can be explained by the dilution of the magnetic susceptibilities by diagenetic processes as explained earlier. Iron sulphides or bacterial biomineralization can play hereby an important role. Another explanation can be the presence of coarser-grained magnetic minerals in this interval, compared to the other intervals. Indeed, the highest susceptibilities between 62.00 and 82.00 mbsf are correlating with lithological unit 1C characterized by more silty and

coarser material than the upper units. So, we should take into account that the general coarser material characterizing this interval has another source than the coarser sandy intercalations corresponding with lower Fe intensities and probably coming from the upper shelves and deposited during mass wasting processes. Hence, differences in source material can also explain the discrepancy between the susceptibility and the Fe intensities in the lowermost records.

The lower susceptibility, the higher density and PWL, the lower Fe intensities and the higher Ca intensities between 82.00 and 86.20 mbsf can be correlated with lithological unit 2 (Sect. 3.5.2), characterized by fine sands interbedded with silty clays. A lot of reworked and coarse material is present in this interval, characterizing the physical and chemical records. The base of the unit consists of a conglomerate, explaining the jump in susceptibility and density just above the discontinuity at 86.20 mbsf, interpreted as the mound base and representing a major hiatus.

4.5 Discussion

4.5.1 Cyclic Record: Revealing Glacial-Interglacial Variations?

It can be questioned if the cyclic records noted in the geophysical and geochemical properties in the on-mound sediments are driven by glacial-interglacial variations. As discussed before, the alternation between Fe-rich and clay-rich terrigenous (siliciclastic) material and Ca-rich biogenic material is responsible for the cyclicity in the records, suggesting that this site is predominantly a two-component sedimentary environment, besides the in-situ coral framework.

The onset of mound growth, and hence the start of the formation of the cyclic records, coincides with the onset of the northern hemisphere glaciations (Sect. 5.5.2). Since then, the alternation between glacial and interglacial periods dominates the northern hemisphere. A comparison of the susceptibility records of Hole U1317E with the oxygen isotopic data, reveals a similar trend (Sect. 5.3.3), suggesting that intervals with a high susceptibility ("darker" intervals) corresponds with high O^{18} (‰) records evidencing of colder periods (Sect. 5.3.3). The more, Abe et al. (2006) evidenced a higher amount of cool-water foraminiferal species in the sediments characterized by a higher amount of siliciclastic and terrigenous (darker) material. Spectral analyses on the susceptibility records revealed spectral characteristics with a periodicity centred around 100 ka (see Sect. 5.3.3). After tuning the records with standard oxygen isotopic records, also the typical obliquity orbital periodicity (41 ka periods) could be visualized, characterizing the North Atlantic records since the onset of the northern hemisphere glaciations at c. 2.75 Ma and prior to the Mid-Pleistocene Revolution (MPR) (Sect. 5.5.3). These observations point to a climatic glacial-interglacial forcing of the cyclic records.

Similar cyclic alternations are noted in the Late Pliocene to Holocene sediments at ODP Sites 980/981 (Feni Drift, Rockall Trough) (Jansen et al. 1996). The sediments at Sites 980/981 have an average calcium carbonate content of ∼54%, which is similar to the average calcium carbonate content (∼50%) calcu-

lated for the mound sediments. This suggests that the rather high carbonate contents encountered on the mound are not exceptionally when compared with similar sediments deposited during the same period. Moreover, sediments at Sites 980/981 are predominantly composed of rapidly accumulated nannofossil oozes with variable amounts of clay, clayey nannofossil mixed sediments and clays with variable amounts of nannofossils and silts (Jansen et al. 1996). The main component of lithological variability occurs also at metre (at Site 980) and decimetre to metre (at Site 981) scales throughout the sediment sections in the form of distinct cyclic changes in colour that are mainly related to relative changes in the proportions of biogenic carbonate, detrital clay minerals and to a lesser extent detrital silt (Shipboard Scientific Party 1996). This suggests that indeed the amount of clay minerals play an important role in diluting the cyclic records in these periods while nannofossil ooze is the main biogenic carbonate fraction. The cyclic changes at Sites 980/981 are also attributed to distinctive glacial-interglacial changes, with distinctive higher sedimentation rates during interglacials compared to glacial rates (Jansen et al. 1996).

So, it can be assumed that glacial intervals are characterized by a high amount of Fe-rich and clay-rich terrigenous material, while during interglacials the rise in biogenic carbonate production dilutes the amount of terrigenous and siliciclastic material. As in the sediments observed at ODP Sites 980/981, the carbonate-rich interglacial sediments in Challenger Mound seem to dominate the record, compared to the Fe-rich terrigenous sediments. This was explained at Sites 980/981 by higher sedimentation rates during interglacial periods compared to glacial periods. Coccolithoforid blooms during interglacial periods may have been responsible for the creation of Ca-rich background sediments. Nowadays, mixed diatom and coccolithophorid blooms are commonly observed in the region during early April (spring blooms) (White et al. 2005). It should be mentioned that also the intervals characterized by a high amount of biogenic material still have a distinct amount of siliciclastic material. Preliminary grain size analyses show that “lighter” (Ca-rich and Fe-poor) intervals corresponding with lower susceptibilities, are characterized by coarse silts to very fine well sorted sands (terrigenous), while “darker” (Fe-rich and Ca-poor) intervals are characterized by fine to medium silts with a unimodal distribution (Huvenne et al. subm.). Hence, we can assume that there are two terrigenous fractions. On the one hand, terrigenous clay minerals play an important role in the dark, fine to medium silt-sized glacial intervals. On the other hand more coarser-grained quartz is present in the light interglacial intervals. The presence of coarser material in the interglacial intervals can bear witness of the presence of stronger bottom currents during the deposition of these units. A higher supply of terrigenous material during glacial periods is a typical process observed along the European continental margins. Certainly for the last glacial periods, this process is extensively studied (Sejrup et al. 2005). The creation of canyons and prograding wedges along the margins during extensive glaciations give evidence of the delivery of terrigenous material from the shelves towards the deeper margins. It can be supposed that during interglacials bottom current action was stronger, partly eroding the sediments deposited during glacial periods. Some authors suggest that cold-water coral growth was restricted to these interglacial periods (Dorschel et al. 2005;

Rüggeberg et al. 2007). However, until now no evidence can be found for such interglacial growth episodes in the Challenger Mound record as the corals are present throughout the whole mound in changing quantities going through the observed cyclicity (Sect. 3.3.1). Only in the uppermost sediments (upper 4 m), it has been observed that cold-water corals are restricted to interglacial periods (Sect. 6.4.2). However, as mentioned before these patterns should be interpreted with caution and further research is necessary as the coral patterns are diluted by dissolution effects (Sect. 4.5.2). It can also be supposed that corals were able to build up during interglacial periods to be filled up by terrigenous sediments during glacial periods (Dorschel et al. 2005; Rüggeberg et al. 2007).

The cycles in the mound record have a saw-tooth like pattern, characterized by a gradual decrease/increase in the Ca-rich intervals followed by an abrupt transition from the bottom to the top towards the Fe-rich terrigenous intervals. This suggests slow deglaciations and rapid glaciations, which is an opposite trend than generally observed in sediments characterized by glacial-interglacial variations (rapid deglaciations/slow glaciations). However, Maslin and Ridgwell (2005) and Lisiecki and Raymo (2007) have shown that such saw-tooth like patterns are typical for the period after the Mid-Pleistocene Revolution (MPR), while the cyclic patterns in our records are deposited before the MPR (Sect. 5.5.3). Lisiecki and Raymo (2007) suggested that glacial-interglacial cycles before the MPR have a more symmetric pattern. However, the impact of diagenesis on the records, especially in the Ca-rich units, can not be neglected (see Sect. 4.5.2) and can have an important influence on the shape of the cycles.

4.5.2 Early Diagenesis in the Mound Record

Diagenetic processes that occur prior to lithification and deep burial may profoundly affect later patterns of diagenesis in carbonate systems. Elucidating diagenetic processes in ancient systems is difficult due to overprinting late-stage diagenetic alteration. However, the sediments of Challenger Mound provide an excellent opportunity to study early diagenetic processes in a carbonate mound without the complications of burial and/or later meteoric diagenesis.

The most prominent diagenetic feature is the dissolution of cold-water coral fragments, having a major impact on the Sr records and diluting the original coral quantity records. Carbonate dissolution is a process observed in many carbonate systems from deep-water limestones (Tucker 1974; Eder 1982; Möller and Kvingan 1988) over peri-platform carbonates deposited under a few hundreds to about 1000 m water depth (Mullins et al. 1985; Dix and Mullins 1988; Malone et al. 2001) to shallow-water carbonate platforms and coral reef frameworks (Tribble 1993; Walter and Burton 1990; Walter et al. 1993; Patterson and Walter 1994). The process of chemical dissolution of calcium carbonate in unlithified carbonate sediments is determined mainly by “the degree of undersaturation” or the “saturation state” of the interstitial pore fluids (Tribble 1993; Ku et al. 1999; Sanders 2003). It has been proven that high-magnesium calcite and aragonitic bioclasts dissolve more

readily than calcitic bioclasts since aragonite is more soluble than calcite (Walter and Burton 1990; Patterson and Walter 1994). Despite the fact that there are still a lot of uncertainties with respect to near-equilibrium carbonate reaction kinetics, the saturation state of the pore waters, depending on pH, alkalinity and pCO_2, can be described as mainly affected by three elements: (1) the oxidation of organic matter and the oxidation of reaction by-products that influence calcium carbonate saturation state, by releasing/consuming chemical compounds that interact with the carbonate system (Tribble 1993; Morse and Mackenzie 1990), (2) the degree of openness of the system (Sanders 2003; Melim et al. 2002) and (3) the degree to which FeS (or other minerals) act as a sink for dissolved sulphide produced during sulphate reduction (Tribble 1993; Perry and Taylor 2006).

Oxidation of buried organic matter either by oxic respiration (Eq. 4.7) or sulphate reduction (Eq. 4.8) can alter both the pH and alkalinity of the interstitial waters and thus influence the diagenesis of carbonate minerals. Organic matter decomposition by aerobic metabolisms (oxic respiration) may generate small amounts of acidity and can be described by the following reaction path:

$$CH_2O + O_2 \rightarrow H_2O + CO_2 \leftrightarrow H^+ + HCO_3^- \tag{4.7}$$

However the upper centimetres of the sediment column are generally open and interacting with the supersaturated seawaters above. So, reaction products from aerobic oxidation alone are unlikely to build up to significant levels in order to cause aragonite dissolution in pore waters.

Sulphate reduction is another important anaerobic organic matter oxidation process in carbonate sediments:

$$SO_4^{2-} + 2CH_2O \rightarrow 2HCO^{3-} + H_2S \leftrightarrow 2HCO^{3-} + H^+ + HS^- \tag{4.8}$$

At levels <3 mM of reduced SO_4^{2-} acid generation by this reaction can lead to undersaturation of aragonite which, together with oxic respiration, can result in extensive aragonite dissolution (Walter and Burton 1990; Tribble 1993). However, at levels exceeding 3 mM of reduced SO_4^{2-}, the levels of bicarbonate released from the reactions are enough to lead to supersaturation of aragonite and precipitation of calcite (Walter and Burton 1990). However, if oxygen is introduced into sulphidic anoxic sub-environments, or if sulphide produced via sulphate reduction is transported in the oxic sediment, such as can occur within bioturbated sediments, sulphide oxidation can again generate significant acidity resulting in aragonite undersaturation and hence dissolution (Eq. 4.9).

$$2O_2 + H_2S \rightarrow SO_4^{2-} + 2H^+ \tag{4.9}$$

In general, it can be assumed that mineral saturation states decrease during oxic respiration (from release of carbonic acid) and under presence of moderate levels of sulphate reduction, and increase during extensive sulphate reduction (from increase in alkalinity).

Sanders (2003) proposed three different "layer" concepts to explain the concepts of early syn-depositional dissolution of calcium carbonate related to progressive oxidation of organic matter in neritic carbonate environments. The layer concepts differ from each other by the degree of mechanical and chemical "openness" of the system, suggesting that the openness of the system plays an important role in the spectrum of reactions of sulphate reduction (and associated reactions involving the reaction by-products), which may in one case lead to precipitation, in another to dissolution of calcium carbonate. Thus, sulphate reduction has a "double face" in early diagenesis, in one case mediating precipitation, in another case dissolution of calcium carbonate. Melim et al. (2002) proposed a similar model for dissolution of aragonite and high-Mg calcite during shallow marine burial diagenesis of platform slope limestones. In their "open-system style" model of diagenesis, carbonate is dissolved in high-permeability intervals and, by inference, is recycled to the sea. In the "closed-system style", carbonate is dissolved in muddy, low-permeability intervals, but is largely repricipitated as a microsparitic cement in the same interval.

Taking into account the above mentioned diagenetic models, a new combined model can be proposed for the extensive dissolution observed in the Ca-rich intervals of the Challenger Mound sediments. Pore water analyses in the Challenger Mound sediments show that organoclastic sulphate reduction is mainly occurring in the upper 50 m. Sulphate reduction coupled to anaerobic methane oxidation is occurring below the mound base but will not be discussed here (Exp. 307 Scientists 2006d). pH is highest at 1.4 mbsf, decreases to ~7.3 at 30–40 mbsf and remains constant at ~7.3 mbsf to the bottom of the hole (Exp. 307 Scientists 2006d). Such a profile results from the diffusion of seawater in the pore waters that are influenced by oxidation of organic carbon and buffered by carbonate phases. In the topmost layer of the mound sediments, aerobic oxidation (Eq. 4.7) lowers the pH which can result in undersaturation of aragonite. However, due to the interaction with the saturated seawaters above, it can be supposed that the pH lowering will not be that extensive to induce cold-water coral dissolution. Below this upper layer, initial organoclastic sulphate reduction may also lead to undersaturation of aragonite, building up degrees of undersaturation at which extensive aragonite dissolution can occur. The more, diffusion of reaction byproducts from anaerobic sulphate reduction (as hydrogen sulphides) towards the oxic layer, can lead to oxidation of the reaction byproducts releasing even more hydrogen ions (Eq. 4.9), hence promoting undersaturation of aragonite which, together with aerobic respiration, is able to lead to extensive dissolution also in the upper layers. Ku et al. (1999) showed that episodic reoxygenation is a major source of hydrogen ions for carbonate dissolution. Here, bioturbation can also play an important role by driving many times the same amount of sediment through a cycle of oxic to anoxic organic matter remineralization and oxidation of reaction by-products, with many reactions resulting in, or promoting undersaturation of aragonite.

Because alkalinity is increasing during extensive sulphate reduction, it is expected that at a certain point the pore waters will become oversaturated with respect to calcium carbonate. And as calcite has a lower solibility than aragonite, it is expected that low-Mg calcite with high Sr contents will be deposited. However,

compared to the high amounts of aragonite dissolution, just a minor amount of calcite cement is observed in the Challenger Mound sediments. It can be questioned why cementation is limited to some small horizons, and why the pore waters seem to stay undersaturated with respect to calcium carbonate. The presence of a permeable system can answer the question whereby through an upward flux of the interstitial pore waters, supersaturated pore waters may be recycled to the water column before substantial carbonate reprecipitation takes place. A visualization of the pore system in Sect. 3.4 has shown that the permeability in the mound sediments is rather low but that an inverse relationship can be suggested between porosity and permeability, suggesting that sediments with a higher amount of bioclastic fragments, as observed in the lighter intervals, and a lower amount of fine-grained matrix, have a lower porosity and a higher permeability. The more, grain size analyses showed that the Ca-rich intervals (with the typical dissolution patterns) are characterized by coarse silts to fine sands, while the darker layers (without substantial dissolution) are characterized by fine to medium silts (Huvenne et al. subm.). The presence of a coarser fraction can also enhance the permeability. A diffusive upward pore water flux or the pumping of fluids in moderately permeable mound sediments is modelled by Depreiter et al. (2005a). In this model a mounded feature on the seabed was subjected to rather strong peak currents, developing zones of high pressure at the lower slopes and low pressure areas at or near the summit. This pressure effect can create a fluid migration from deeper layers to the top of the structure. This model suggests that indeed an active fluid pumping system may be active in the uppermost sediments of Challenger Mound, moving supersaturated pore waters back upwards towards the sea-floor.

Some of the calcium carbonate might also be taken up by cementation of finer-grained beds, but the intervals altered with this open-system style of marine burial diagenesis are not associated with sufficient low-Mg calcitic cement to account for the amount of aragonite dissolved. Another mechanism which can be responsible for early cementation has been explained by Noe et al. (2006). These authors propose seawater as a more probable source of carbonate ions for cementation, whereby the driving mechanism of the ion supply into the sediment is a diffusion process maintained by a saturation gradient between seawater and interstitial water. Bottom currents are responsible for the diffusion that reinforces the transfer of seawater carbonate ions into the sediments, possibly supporting a pumping mechanism. However, circulating sea water to be the only source for the carbonate cement is unlikely because of the huge volume of water required to provide enough dissolved calcium carbonate for even small amounts of cementation. For a 1% reduction in porosity by cementation from waters with 200% saturation, 4000 volumes of water must pass through each bulk volume of rock (Enos and Sawatsky 1981). Neuweiler et al. (1999) proposed a process of automicrite formation via organomineralization: carbonate is precipitated on non-living organic substrates such as particulate organic matter by means of energy (ATP) deriving from bacterial metabolism. Soluble humic substances which form the largest fraction of dissolved organic carbon in seawater serve as organic substrates, while fulvic acid-like compounds controls the nucleation of marine calcite (Neuweiler et al. 2003). These mechanisms may

apply to the observed cryptocrystalline cements but should be investigated more in detail.

Another explanation for the presence of the small cemented horizons can be the fact that an open diagenetic system can suddenly be sealed by the fast deposition of a high amount of less permeable and finer material. Such a burial event will bring the original material in a state of extensive sulphate reduction, increasing the alkalinity and the degree of saturation inducing the precipitation of calcite. However, saturation indices for aragonite, calcite and dolomite derived from pore water data show that all three phases remain undersaturated thoughout much of the mound (Russel et al. 2006). This suggests that a second stage of slow cementation over substantial burial depth is unlikely to happen in the mound sediments. It appears that organic matter diagenesis and iron hydrolysis keep the whole mound system undersaturated with respect to calcite. It should be mentioned that the presence of a high amount of coccolith ooze in the matrix and the presence of clay minerals can also play a role in retarding cementation. However, more detailed research is necessary to explain these extensive dissolution versus really slow cementation processes. In each case, high dissolution rates and low cementation rates can play an important role in increasing the reservoir qualities of these recent carbonate mound systems.

The presence of a substantial amount of reactive iron oxides, present in a lot of terrigenous sediments, can alter the pore water chemistry effectively in terms of carbonate saturation, by reacting with free sulphides to form iron sulphides (Eq. 4.10).

$$3H_2S + 2\,FeOOH \rightarrow FeS_2 + FeS + 4H_2O \tag{4.10}$$

This reaction will buffer sulphide to low levels in pore waters (Raiswell 1997), thereby minimizing the potential for sulphide oxidation and acid generation. So, the formation of FeS minerals appears to exert a strong effect on the aragonite saturation state. Sedimentary environments rich in iron would tend towards aragonite oversaturation relative to iron-poor systems. Systems having very low levels of respiration will remain oversaturated with respect to aragonite. Iron-poor systems that experience an intermediate degree of net heterotrophy would tend to be corrosive to aragonite. The impacts of terrigenous Fe-rich sediment input on syn-depositional carbonate diagenesis is also evidenced by Perry and Taylor (2006), examining the impact of bauxite on the dissolution of carbonate grains in the nearshore fringing and bank-barrier reefs of Discovery Bay (midway along the north coast of Jamaica). This process of differential dissolution in Fe-rich sediments versus Fe-poor sediments can explain the differential dissolution present in the Challenger Mound sediments, with extensive dissolution observed in the Ca-rich (Fe-poor) intervals compared to the good preservation of the cold-water coral fragments in the darker intervals, which are much more Fe-rich as observed in the XRF records.

It can be concluded that even early marine diagenesis can overprint the primary environmental signals. The observed early diagenetic effects affect the geophysical and geochemical records of the mound sediments, especially the Ca and Sr count

rates, the porosities, the P-wave velocities and the densities. The highest degrees of diagenesis are occurring in the "lighter" intervals. The "darker" intervals underwent a substantially lower degree of diagenesis and seem to have kept their original environmental signature. Such an effect of differential diagenesis shows that post-depositional early alteration (diagenesis) has the potential to not only seriously distort primary environmental signals, but also to mimic primary environmental signals. The role of early diagenesis in overprinting primary environmental records has been studied extensively in the recent past to explain limestone-marl alternations in ancient carbonate systems (Munnecke and Samtleben 1996; Westphal et al. 2004; Munnecke and Westphal 2004, 2005; Westphal 2006), but until now it was not yet proven to be present in recent carbonate mound systems.

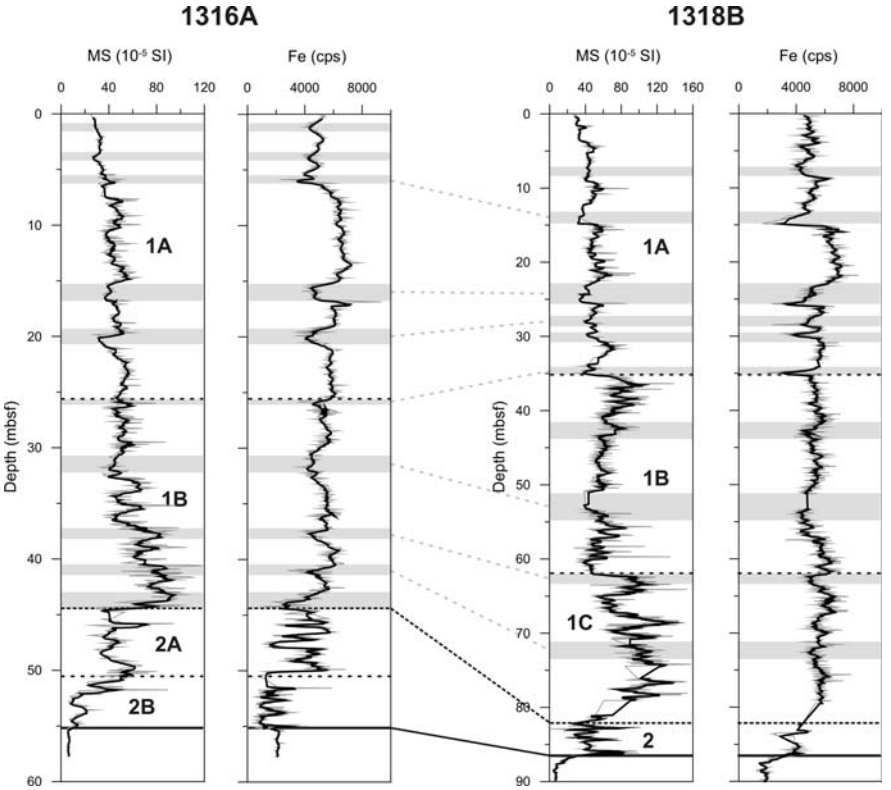

Fig. 4.14 Correlation between Hole U1316A and U1318B based on magnetic susceptibility (SI units) and Fe intensities (counts/s). *Light grey lines* represent raw values. *Black lines* represent smoothed records (7-points running mean). *Light grey boxes* and *light grey dashed lines* correspond with specific minima and maxima. *Horizontal solid black line* corresponds with the mound base. *Horizontal dashed black lines* and *numbers* represent correlating lithological units as described by the Exp. 307 Scientists (2006c,e) and summarized in Sect. 3.5.2

4.5.3 Depositional Processes in the Off-Mound Records

Comparing the geochemical and geophysical records from Hole U1316A with the records from Hole U1318B, unveils some similarities. Especially the Fe intensities and the magnetic susceptibilities from both holes correlate well (Fig. 4.14).

The saw-tooth cycles in the magnetic susceptibilities and the Fe intensies observed in the uppermost interval can be correlated from Hole U1316A to Hole U1318B: the minimum in Fe intensity at 5.90 mbsf in Hole U1316A can be correlated with the minimum in Fe intensity and magnetic susceptibility at 14.50 mbsf in Hole U1318B. The same is true for next depth couples for respectively Hole U1316A and Hole U1318B: 16.00 versus 25.40 mbsf, 20.00 versus 28.45–29.70 mbsf and 25.90 versus 35.03 mbsf. These changes in this uppermost interval can be linked with lithological units 1A from both holes. Similar correlations can be made for the intervals below respectively 25.90 and 44.40 mbsf in Hole U1316A and 35.03 and 82.00 mbsf in Hole U1318B. The minima in Fe intensities are not longer explicitly characterized by a typical saw-tooth pattern, but they can be linked between both holes: the minimum in Fe intensity around 32.00 mbsf in Hole U1316A corresponds with a similar minimum in Fe intensity around 54.05 mbsf, the minimum at 38.00 mbsf in Hole U1316A with the minimum around 62.00 mbsf in Hole U1318B and a last minimum couple in Fe intensity at Hole U1316A and Hole U1318B around respectively 41.00 mbsf and 72.50 mbsf. Finally the coral-rich units in Hole U1316A between 44.40 and 55.06 mbsf ($\sim$ lithological unit 2), could have been deposited during the same time interval as the reworked sediments between 82.00 and 86.20 in Hole U1318B ($\sim$ lithological unit 2) (for discussion see Sect. 5.5.3). The proposed tiepoints between Holes U1316A and U1318B can be discussed but more detailed magnetostratigraphic datings confirm the correlation presented on Fig. 4.14 (Sect. 5.5.3).

As explained earlier (Sect. 4.4), the observed minima in Fe intensity and magnetic susceptibility correspond with more Ca-rich sediments, slightly coarser and siltier than the surrounding clays and in the upper interval characterized by a typical fining-upwards sequence. It can be supposed that they represent small mass wasting processes like turbidites in the uppermost interval. However, the coarser intercalation in the lowermost interval can probably not be explained by simple mass wasting processes. Previous studies on the uppermost sediments in the Porcupine Seabight have evidenced the alternation between muddy contourites and sandy contourites (Foubert et al. 2007; Van Rooij et al. 2007a,b; see also Sects. 6.2 and 6.4.1). These authors suggested the onset of more vigorous bottom currents during interglacials and interstadials, possibly triggered by the sporadic reintroductions of Mediterranean Outflow Water (MOW) during warmer periods in the North Atlantic Ocean (Schönfeld and Zahn 2000) responsible for the deposition of sandy contourites. Finer, muddy contourites were deposited during glacial, colder periods characterized by quieter bottom current conditions, probably due to the absence of the erosive MOW in the glacial North Atlantic (Schönfeld and Zahn 2000). A similar alternation, with the deposition of muddy contourites during glacials and the deposition of sandy contourites during interglacials, was evidenced by Ovrebo et al.

(2006) for sediments on the slopes west of the Porcupine Bank. Hence, the lowermost coarser units can be described as sandy contourites deposited during warmer periods by alongslope transport. The finer silty intervals in between the coarser intervals, characterized by the deposition of much more material and the intercalation of dropstones (see Sect. 3.5.2), can be described as a muddy contourite facies deposited during colder periods. As the sediments above the unconformity in Holes U1316A and U1318B are dated to be deposited after the Mid-Pleistocene Revolution (MPR) (see Sect. 5.5.4) characterized by extensive and prolonged glaciations, the thick packets of muddy contouritic facies compared to the smaller intervals of coarser sediments can bear witness of these prolonged glaciations. The presence of dropstones in the fine silty sediments gives evidence of the glacial character of these sediments. They may have been deposited during ice rafting events.

However, it should be remarked that examples of sandy contourites occurring as deep-water massive sands are rare and in most cases they are interpreted as sandy debris flows. Van Rooij et al. (2007b) suggest that the interglacial sediments in the Belgica Mound Province are probably not the result of mass wasting processes. However, as suggested before, a closer observation of the upper coarser intervals learnt that they are in many cases characterized by an erosional base and that they are associated with turbiditic events. Probably a combined depositional mechanism should be proposed, whereby during warmer periods, an enhanced current regime is established by the input of MOW in the basin, triggering mass wasting processes. Due to the steered northward flow of the MOW along the eastern margin, this can result, if this current regime is established for a longer period, in the deposition of a sandy contourite. It is not sure if one or the other mechanism is prevailing, but it can be assumed that in the upper parts of cores U1316A and U1318B more erosional mass wasting processes and turbidic events are present as a result of shelf erosion during interglacial or interstadial events In the lower part of the record, shelf erosion seems to have been kept at a minimum, resulting in the deposition of more contouritic deposits during interglacials. The required sediment supply zone of the contouritic deposits can be variable. In this case several sources can be proposed, whereby the Gollum Channel system is probably the most important supply zone of sediments in glacial times (Wheeler et al. 2003). The sands deposited at the foot of the Gollum Channel system could have been remobilized during interglacial times, resulting in the deposition of coarser contourites.

The laminated horizons (centimetre to millimetre thick laminae, consisting of light and dark greenish grey clay with very fine sand layers) observed in subunits 1B at Hole U1316A and subunits 1B and 1C at Hole U1318B and influencing extensively the geophysical records by the superposition of small-scaled oscillations on the background trends, can be explained as sediment lofting from turbidity currents (Hesse and Khodabakhsh 2006). Sediment lofting is a process that occurs in density currents generated from fresh-water discharges into the sea. Settling of sediment from the top or deposition from the bottom of the flows may lower the density below that of ambient seawater, causing the currents to lift up from their substrate either in part or as a whole through buoyancy reversal (Sparks et al. 1993). Such a process can result in the deposition of fine-grained laminated sediments characterized by

a bimodal grain size distribution (Stow and Wetzel 1990; Hesse and Khodabakhsh 2006). Such a process of sediment lofting might have occurred during the extensive glacial episodes in the Porcupine Seabight.

Overall, it can be concluded that glacial deposits in the Porcupine Seabight were the result of a combination of three processes: ice rafting (vertical transport), subsequent sediment lofting (downslope transport) and contouritic deposition (alongslope transport). Currents were weaker than during interglacial periods but it appears that they were still strong enough to enable alongslope contouritic deposition. During interglacials, alongslope transport characterized by vigorous bottom currents probably dominated, but the influence of downslope transport, culminating in turbiditic events, possibly can not be neglected.

4.6 Summary

The geochemical and geophysical properties in the mound sediments revealed a **cyclic record** caused by the continuous alternation between **terrigenous** Fe-rich and clay-rich (siliciclastic) material and **biogenic** Ca-rich material, suggesting a predominantly **two-component sedimentary environment**. The cyclicity is most probably driven by the typical **glacial-interglacial changes**, characterizing the northern hemisphere during the Quaternary. A correlation between the different holes on Challenger Mound is proposed.

Early differential diagenesis overprints the primary environmental signals, with extensive **coral dissolution** and the genesis of small-scaled **semi-lithified layers** in the Ca-rich, "lighter" intervals. In particular, the Ca and Sr count rates, the P-wave velocities and the densities are influenced by the observed diagenetic patterns. The low cementation rates compared to the extensive dissolution patterns can be explained by an **open-system** diagenetic model.

The off-mound records are correlated based on their geophysical and geochemical properties. The off-mound sediments can be interpreted as drift sediments deposited mainly during extensive glaciations as **silty muddy contourites**. **Sediment lofting** from density currents generated from freshwater discharges (downslope transport) can explain the laminated horizons in the glacial silty muddy contourites. Dropstones in the glacial deposits bear witness of **ice rafting events** (vertical transport). Currents were weak during glacial periods but it appears that they were still strong enough to enable alongslope contouritic deposition. During interglacials coarser **sandy contourites** (alongslope transport) were deposited by vigorous bottom currents steered along the continental margin. However, the impact of **turbiditic currents** during interglacial and interstadial periods can not be neglected. Such turbidity currents could be initiated by the onset of an intensive current regime whereby Mediterranean Outflow Water (MOW) probably played an important role.

Chapter 5
Magnetic Record of a Carbonate Mound

The use of magnetism in the study of marine sediments started over a century ago. In their "Report on the Scientific Results of the voyage of the Challenger: Reports on Deep-Sea Deposits" (1891), John Murray and Alphonse-François Renard described already in detail the presence of magnetic particles in deep-sea sediments. Opdyke (1972) found that sediments of various lithologies cored from most parts of the deep ocean floor contain a record of the past behaviour of the earth's magnetic field, especially the sequence of reversals over at least the past 5 million years. Kent (1973) indicated that detrital remanent magnetization and post-depositional remanent magnetization are viable mechanisms of magnetization of deep-sea sediments. Detrital magnetic particles can align themselves in the direction of an applied earth magnetic field while falling through the water column, leading to a "detrital remanent magnetization". However, the magnetization of most of the sediments is formed after the particles are deposited by rotation of the magnetic grains in water-filled interstices. This so-called "post-depositional remanent magnetization" is locked into the sediment by consolidation due to either compaction or to the growth of authigenic minerals (Kent 1973). Taking into account that the past behaviour of the Earths magnetic field is well-known for the Late Cretaceous and Cenozoic periods from previous studies (Cande and Kent 1992, 1995), magnetic archives can be used for dating purposes in a discipline called "magnetostratigraphy".

Thompson et al. (1980) and Thompson and Oldfield (1986), laid the base for a relatively new discipline of geophysics named "environmental magnetism", whereby rock magnetic parameters are used to study marine, limnic and fluvial sediments, soils and atmospheric dust deposits in terms of source materials, transport mechanisms and diagenetic phenomena. The way was paved for the use of rock magnetic studies to marine sediments. Convincing correlations of oxygen isotope and calcium carbonate variations with the magnetic susceptibility signal were found by Kent (1982) and Robinson (1986). They explained this phenomenon as a cyclic dilution and enrichment of the magnetic mineral component by climatically driven changes in carbonate accumulation. Bloemendal et al. (1988) used rock magnetic parameter core logs as a direct proxy for oxygen isotope records. Mead et al. (1986) applied spectral analyses to magnetic susceptibility data sets to illustrate their relation to orbital driven periodicities. Von Dobeneck and Schmieder (1999)

A. Foubert, J.-P. Henriet, *Nature and Significance of the Recent Carbonate Mound Record*, Lecture Notes in Earth Sciences 126, DOI 10.1007/978-3-642-00290-8_5,

used different rock magnetic proxy records for orbital tuning and extended time series analyses into the super- and sub-Milankovitch bands. DeMenocal et al. (1988) found variations in bottom current activity documented in rock magnetic properties of marine sedimentary deposits. Bloemendal et al. (1992) related rock magnetic parameters to sediment sources, lithology and diagenetic processes. Maher and Thompson (1999) wrote a comprehensive overview of the relation between Quaternary climates and environmental magnetism. Frederichs et al. (1999) summarized different parameters, techniques and potentials of rock magnetic studies as a key to palaeoclimatic and palaeoceanographic changes.

Despite the fact that the record of magnetic mineral archives in deep-sea sediments is growing, magnetic experiments on carbonate-rich sediments are scarce. However, Fuller et al. (2006) have shown that palaeomagnetic records from different carbonate-rich sediments, acquired during ODP-legs in the southern ocean (Leg 182 to the Great Australian Bight, Leg 189 around Tasmania, and Leg 194 off the Great Barrier Reef on the Marion Plateau), can reveal the original magnetostratigraphy despite the reported coring overprints. In this chapter, an overview will be given of the relevance and the use of magnetic properties in the sediments of a recent carbonate mound, in particular of Challenger Mound in the Belgica Mound Province, SW of Ireland. Palaeomagnetic and rock magnetic measurements were partly carried out aboard the R/V JOIDES Resolution during IODP Expedition Leg 307 (Exp. 307 Scientists 2006b,c,d,e) and in the palaeomagnetic labs of the Geophysical Centre of Dourbes (KMI, Belgium).

5.1 Methodology

5.1.1 Shipboard Magnetic Measurements

Shipboard analyses comprised measurements of the natural remanent magnetization (NRM) before and after alternating-field (AF) demagnetization and low-field magnetic susceptibility measurements (k).

Remanence measurements and AF demagnetizations were performed using a long-core cryogenic magnetometer (2G Enterprises model 760-R), permanently installed on the *JOIDES Resolution*. This instrument is equipped with a direct-current superconducting quantum interference device (DC-SQUID) and has an inline AF demagnetizer capable of reaching peak fields up to 80 mT. The spatial resolution measured by the width at half-height of the pickup coils response is $<$10 cm for all three axes, although they sense a magnetization over a core length up to 30 cm. The magnetic moment noise level of the cryogenic magnetometer is $\sim 10^{-9}$ emu or 10^{-6} A/m for 10 cm^3 rock volume. The practical noise level, however, is affected by the magnetization of the core liner ($\sim 8 \times 10^{-6}$ A/m) and the background magnetization of the measurement tray ($\sim 1 \times 10^{-5}$ A/m).

Measurements were conducted on whole-round sections from cores of Holes U1317A, U1317B, U1317C and U1317E with a resolution of 5 cm. A comparative

test on whole-rounds and archive halves of cores from Site U1316 in the off-mound sediments showed that measuring whole-round sections does not adversely affect the measurements. On the contrary, for core sections with very weak intensities (e.g. carbonate-rich sediments), whole-round sections provide more precise information because the entire mass of material (double of the volume compared to split sections) is measured. The more, disturbance of the sediment surface resulting in irregular and assymetric cross-sections (Roberts 2006) and possible remagnetization caused by section splitting (Fuller et al. 1998) are eliminated. AF demagnetization of NRM was conducted up to 20 mT in 5 mT steps on Section 307-U1317A-1H-1, showing that a tentative characteristic remanent magnetization component could be isolated around 15 mT. Based on this demagnetization experiment (Fig. 5.1), cores from Holes U1317A, U1317B and U1317C were demagnetized at 10 and 15 mT. Cores from Hole U1317E were demagnetized at 2, 5, 7, 10, and 15 mT.

Measurements were undertaken using the standard IODP magnetic coordinate system (+x = vertical upward from the split surface of archive halves, +y = left split surface when looking upcore, and +z = downcore) (Fig. 5.2).

Full orientation was attempted using the Tensor orientation tool. The Tensor tool is rigidly mounted onto a nonmagnetic sinker bar attached to the top of the core barrel assembly. The Tensor tool consists of three mutually perpendicular magnetic field fluxgate sensors and two perpendicular gravity sensors. The information from both sets of sensors allows the azimuth and dip of the hole to be measured as well as the azimuth of the APC core.

Magnetic susceptibilities (k) were measured using a Bartington Model MS-2 meter, installed in a multi-sensor track (MST) (see Sect. 4.1.1), with an 80 mm internal diameter sensor loop (88 mm coil diameter) operating at a frequency of 565 Hz and an alternating-field of 80 A/m. Measurements were carried out on whole-round sections from Holes U1317A, U1317B, U1317C and U1317E with a sampling resolution set at 5 cm and a frequency of 5 times per second. Such a long sampling period ensured acceptable readings for the usually low magnetic susceptibilities of carbonate sediments. Relative susceptibilities were measured, which need to be corrected for volume variations. For a core diameter d and a coil diameter D of respectively 66 and 88 mm, the corresponding correction factor d/D is 1.48 (Blum 1997). During data reduction, the relative susceptibilities were converted to volume-normalized magnetic susceptibilities by multiplying by $1/(1.48 \times 10^5)$, or by 0.68×10^{-5} SI units.

5.1.2 Shore Based Magnetic Measurements

Discrete samples (7 cm^3) were taken on the working halves of each core-section in Hole U1317A (91 samples) to calibrate and evaluate shipboard measurements.

Remanence measurements and AF demagnetizations were performed on each of the cubes with a cryogenic magnetometer (2G Enterprises model 760-R) installed at the Geophysical Centre of Dourbes (KMI, Belgium) and equipped with

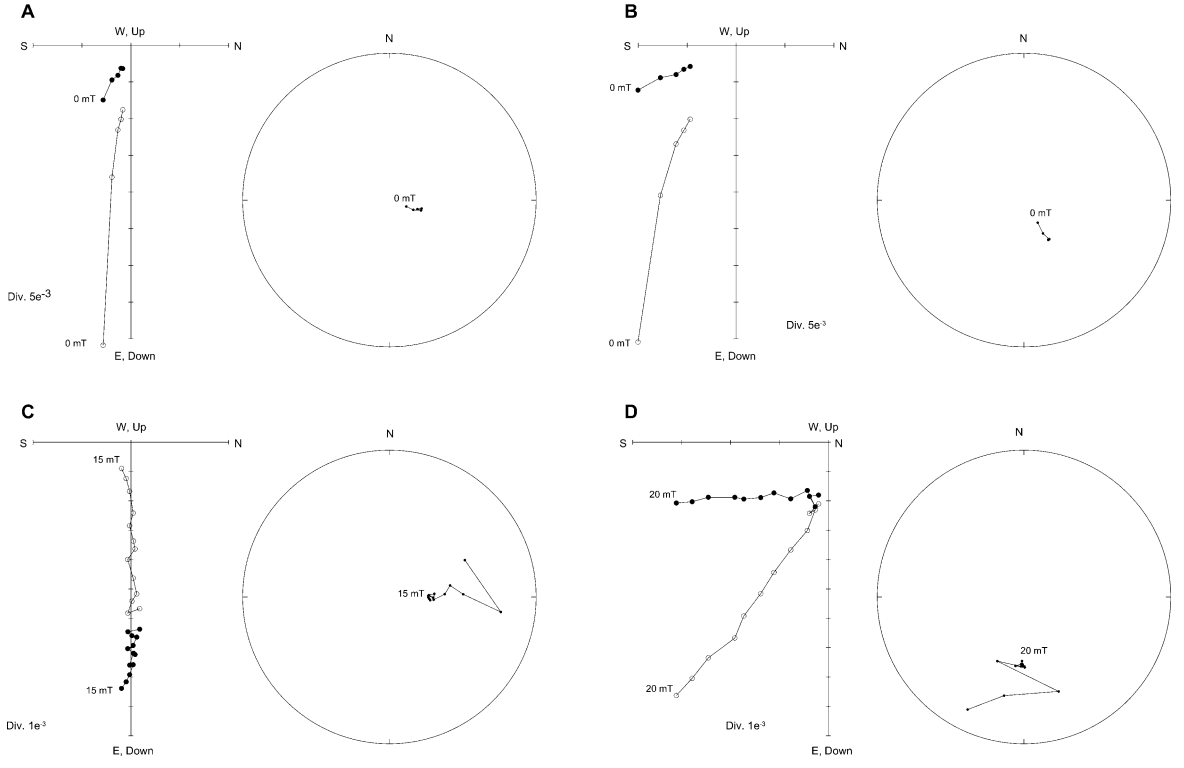

Fig. 5.1 (**A**) Stepwise AF demagnetization (5, 10, 15, and 20 mT) of Section 307-U1317A-1H1 at 0.40 mbsf. (**B**) Stepwise AF demagnetization (5, 10, 15, and 20 mT) of Section 307-U1317A-1H1 at 1.20 mbsf. (**C**) Stepwise AF demagnetization (15, 20, 25, 30, 35, 40, 45, 50, 60, 70, 80, 90, and 100 mT) of Section 307-U1317A-3H4 at 21.95 mbsf. (**D**) Stepwise AF demagnetization (20, 25, 30, 35, 40, 45, 50, 60, 70, 80, 90, and 100 mT) of Section 307-U1317A-1H1 at 0.82 mbsf. *Left panels* represent orthogonal projections of endpoints of the magnetization vector. *Open circles* = projection on vertical plane, *solid circles* = projection on horizontal plane. *Right panels* represent equal area projection of the magnetization vector during demagnetization

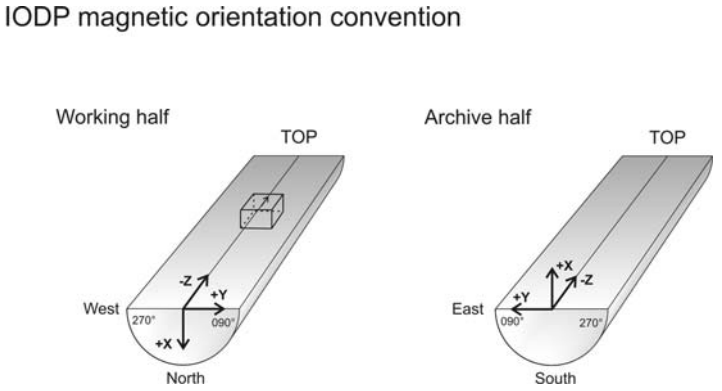

Fig. 5.2 IODP core orientation convention: +X = vertical upward from the split surface of archive halves, +Y = left split surface when looking upcore, and +Z = downcore

direct-current superconducting quantum interference device (DC-SQUID) magnetic sensors. An inline AF demagnetizer has the capability to reach peak fields up to 100 mT. The SQUID-sensors can detect magnetizations up to 10^{-12} A/m. The more precise detection limit, compared to the same instrument installed aboard the *JOIDES Resolution*, can be explained by lower interference of magnetic and electrical noise.

Demagnetization experiments on selected samples, whereby the alternating-field was driven up to 100 mT in steps of 5 mT (15–50 mT) and 10 mT (50–100 mT), learnt that the characteristic remanent component could be isolated around ~15–20 mT (Fig. 5.1). This is in coherence with shipboard experiments. Based on the demagnetization experiments, all samples were demagnetized at respectively 15, 17.5, and 20 mT. AF-demagnetization below 15 mT did not make sense because the samples were already demagnetized aboard the *JOIDES Resolution* up to 15 mT. Characteristic remanent magnetizations were calculated by the standard three-dimensional least-squares fit to palaeomagnetic vector data via principal component analysis (PCA) on respectively AF-demagnetization steps 15, 17.5, and 20 mT (Kirschvink 1980). Visualization and analysis of the palaeomagnetic data were performed in the windows-based "palaeomagnetic analysis programme", developed by Zhang and Ogg (2003).

Low-field magnetic susceptibilities (k) and the anisotropy of magnetic susceptibility (AMS) were measured with a KLY-3S Kappabridge on all individual cubes with a sensitivity of 2×10^{-8} SI. The KLY-3S Kappabridge is one of the most sensitive laboratory instruments available for the measurement of bulk magnetic susceptibilities and its anisotropy. The measurement of magnetic susceptibility is based on the change in inductance by placing a sample in a solenoid. The magnetic field is produced by a source solenoid (which is electrical charged). A coaxial solenoid detects the induced magnetization. The nature of the material in the coil system controls the inductance and causes a signal in the coaxial solenoid, in coherence with the total susceptibility of the sample. The Kappabridge consist of a Pick-Up Unit with a coil system having an inner diameter of 43 mm and operating at a frequency

of 875 Hz and a field of 300 A/m, a Control Unit and a User′s Computer. The instrument represents a fully automatic inductivity bridge and is equipped with an automatic zeroing system, automatic compensation of the thermal drift and an automatic switch of the appropriate measuring range. The measuring coils are designed as 6th-order compensated solenoids with remarkably high field homogeneity. When a field is applied in the neighbourhood of a magnetic anisotropic sample, the induced magnetization is not parallel with the applied field, resulting in anisotropy of magnetic susceptibility (AMS). In practice, three series of 64 measurements of a spinning specimen in three perpendicular directions were carried out, resulting in the determination of the minimal, intermediary and maximal susceptibility. Software SUSAR combines the measurements in three perpendicular planes plus one bulk value to create a complete susceptibility tensor. The errors in determination of this tensor are estimated using multivariate statistics.

A thermomagnetization experiment was carried out on oven-dried powders of two discrete samples in core sections 307-U1317A-3H-2 and 307-U1317A-3H-3. The susceptibility was measured in different steps (500–700 points), while heating the samples up to 650°C and subsequent cooling down to 40°C. The susceptibility measurements were carried out in air with the KLY-3S Kappabridge. Heating and cooling was controlled by a CS-3 furnace apparatus. The samples, about 0.25 cm^3 in volume, are heated electrically by a platinum element and the temperature is measured by a special platinum temperature sensor. The quasi-continuous measurement process is fully automated.

5.2 Magnetostratigraphy

5.2.1 Magnetostratigraphic Framework

The geomagnetic components at the drilling sites during the drill operations and according to the International Geomagnetic Reference Field 2005 (IGRF) are summarized in Table 5.1, showing that the present-day inclination value is about 66.30° at Hole U1317A. The geocentric axial dipole (GAD) inclinations are also

Table 5.1 Present geomagnetic components according to the International Geomagnetic Reference Field 2005 (IGRF 2005) and calculated from the geocentric axial dipole for drilling Sites U1317A, U1316A and U1318B

Site	Latitude	Longitude	IGRF 2005 D [°]	IGRF 2005 I [°]	IGRF 2005 FI [nT]	GAD I [°]
1317A	51.38	–11.72	–7.13	66.30	48438.00	68.23
1316A	51.38	–11.73	–7.14	66.31	48438.60	68.23
1318B	51.44	–11.55	–7.07	66.36	48453.20	68.27

IGRF International Geomagnetic Reference Field, *D* declination, *I* inclination, *FI* field intensity, *GAD* calculated geocentric axial dipole.

summarized in Table 6.1 (inclination = $\tan^{-1}$ [2 × tan (latitude)]), showing GAD inclinations of about 68.23° for Hole U1317A. Mean inclinations for the normal and reversed chrons at Hole U1317A are respectively 71.79° and –71.98°, showing a small offset of 3.50° from the expected GAD inclinations. Moreover, it should be noted that most of the inclination records obtained by shipboard measurements show a distinctive scattered pattern (Fig. 5.3). Despite the appropriate cleaning methods, the effects of coring on the magnetization of recovered sediments are known from the earliest days of palaeomagnetism of ocean sediments. This problem may be especially severe in carbonate-rich sediments that have low magnetic intensities (Fuller et al. 2006). The high scatter observed in the shipboard inclination data can be explained by this magnetic overprint gathered during drilling, resulting in an artificial magnetic inclination pointing downward, and by the bias and background noise (due to the motion of the ship) in the cryogenic magnetometer, which may influence the measurements. Another factor influencing the magnetic records is the presence and formation of authigenic iron sulphide minerals and the high amount of paramagnetic and diamagnetic minerals which do not have a permanent remanence compared to the small preservation of ferrimagnetic components, carriers of the natural remanent magnetization (see Sect. 5.3.4). However, after smoothing the records by a 7-points running mean, they could be used for magnetostratigraphic dating.

Combination of the characteristic magnetization directions measured on whole-round sections with the magnetization directions obtained by the standard least-squares method on discrete samples (Kirschvink 1980), made it possible to reconstruct a magnetostratigraphic framework for Hole U1317A. Magnetostratigraphic dating was possible by correlating the inclination records with the geomagnetic polarity timescale from oceanographic data collected and processed by S.J. Crowhurst (Delphi Project 2002) and modified from Cande and Kent (1995) and Funnell (1996). The magnetostratigraphic dates for the Réunion Subchronozone were modified according to Channell et al. (2003). Comparing filtered (Gaussian filtering) and smoothed (7-points running mean) susceptibility and inclination records on respectively Holes U1317A, U1317B, U1317C and U1317E, made it possible to define correlating tiepoints between the different holes (AnalySeries, Paillard et al. 1996) (see also Sect. 4.2.2) and to extrapolate the magnetostratigraphic framework defined on Hole U1317A to Holes U1317B, U1317C and U1317E (Fig. 5.3, Table 5.2). Declination data could only be corrected by Tensor tool measurements for Cores 307-U1317A-3H through 7H, Cores 307-U1317B-3H through 12H, Cores 307-U1317C-1H through 11H, and Cores 307-U1317E-3H through 15H but appeared useless for magnetostratigraphic dating.

The inclination records above 16.50 mbsf in Hole U1317A show positive values clustered around 70.00°. Similar inclination values are observed in Holes U1317B, U1317C and U1317E above respectively 15.45, 19.40, and 18.20 mbsf (Fig. 5.3). These predominantly positive polarities belong to the Brunhes Chron (C1n), which has an age younger than 0.78 Ma. Below these uppermost sections inclination values have a tendency to decrease to negative values, which indicates the transition to reversed polarities coinciding with the Matuyama Chron (C1r.1r). Sr-isotopic datings on skeletal aragonite collected from Hole U1317E and $\delta^{13}C$ records pointed out

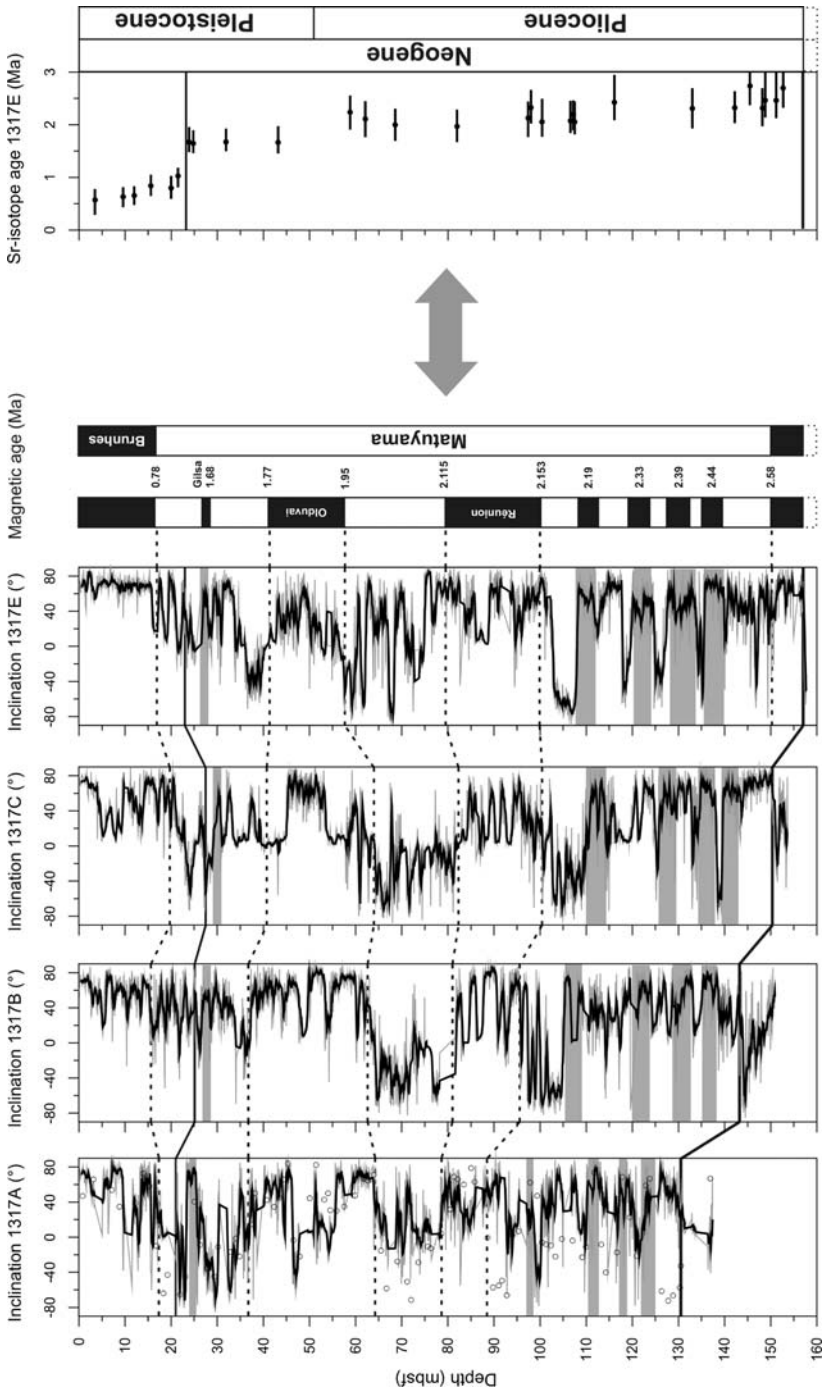

Fig. 5.3 (continued)

the presence of an important hiatus of more than 0.50 Ma (1.00–1.67 Ma) at 23.50 mbsf (Kano et al. 2007), resulting in the lack of an important part of the top of the Matuyama Chron, including the Jaramillo and the Cobb Mountain Subchrons. This hiatus, corresponding with an abrupt lithological change from carbonate-rich dominated sediments to siliciclastic-dominated sediments, could be tracked from Hole to Hole (21.00 mbsf for Hole U1317A, 25.00 mbsf for Hole U1317B and 27.00 mbsf for Hole 1317C). The observation and age determination of this hiatus was important in the interpretation of the magnetostratigraphy and the lack of this knowledge during Expedition 307, resulted in a different preliminary interpretation of the magnetic shipboard data (Exp. 307 Scientists 2006d). In Holes U1317E and U1317C a small transition towards positive inclination values just above the hiatus is observed, which can be linked with the top of the Jaramillo Chron (C1r.1n). However, the most important part of this normal polarity Chron is not present. The sediments below the hiatus are characterized by negative inclinations, corresponding with the Matuyama Chron (C1r.2r). A small excursion towards positive inclination values is observed at 24.05 mbsf in Hole 1317A, which can be correlated with the Gilsa Event (0.68 Ma). Similar excursions are observed in Holes U1317B, U1317C and U1317E at respectively 27.20, 30.00, and 27.50 mbsf. Pronounced normal polarities (positive inclinations) characterize Hole U1317A between 36.65 and 63.95 mbsf, Hole U1317B between 37.20 and 62.50 mbsf, Hole U1317C between 40.25 and 64.00 mbsf and Hole U1317E between 40.57 and 57.80 mbsf. These positive inclination values present the Olduvai Chron (1.77–1.95 Ma, C2n) and are underlain again by reversed polarities of the Matuyama Chron (C2r.1r). A second zone of positive inclinations is observed between 78.65 and 88.00 mbsf in Hole U1317A, between 80.50 and 95.50 mbsf in Hole U1317B, between 82.50 and 100.25 mbsf in Hole U1317C and between 79.25 and 99.25 mbsf in Hole U1317E and can be interpreted as the Réunion Subchron (C2r.1n). The Réunion Subchron is extensively reviewed by Channell et al. (2003) at ODP Site 981 (Feni Drift, Rockall), showing that the duration of the Réunion Subchron (38 ka) is almost four times that assumed in current geomagnetic polarity timescales. At ODP Site 981, the Réunion Subchron is recorded from the Marine Isotopic Stage (MIS) 81/82 boundary to MIS 79 as a single normal polarity zone spanning the 2.115–2.153 Ma interval (Channell et al. 2003). Considering the proximity of IODP Site U1317 to ODP Site 981, a similar time interval for the Réunion Subchron can be extrapolated to the

Fig. 5.3 *Left panel*: Inclination records at peak fields of 15 mT (*light grey line* represents raw inclination values; *black line* represents smoothed (7-points running mean) records; *dots* represent the characteristic remanent magnetizations on discrete samples calculated by the standard three-dimensional least-squares fit to palaeomagnetic vector data via principal component analyses (PCA) (Kirschvink 1980) and interpreted magnetostratigraphic framework in Holes U1317A, U1317B, U1317C and U1317E. *Horizontal solid black lines* represent respectively the interpreted hiatus and the mound base. *Horizontal dashed black lines* represent the interpreted Chrons and Subcrons. *Grey boxes* represent possible magnetic events. *Right panel*: Sr-isotopic datings on skeletal aragonite (Kano et al. 2007)

Table 5.2 Magnetostratigraphic tiepoints defined from the inclination records for Holes U1317A, U1317B, U1317C and U1317E

Chrin/Subchron/Event [Ma]	U1317A [mbsf]	U1317B [mbsf]	U1317C [mbsf]	U1317E [mbsf]
Brunhes/Matuyama (0.78)	17.00	15.45	19.40	18.20
Hiatus (1.00–1.67)	21.50	25.00	27.00	23.50
Gilsa Event (1.68)	24.05	27.20	30.00	27.50
Top Olduvai Chron (1.77)	36.65	37.20	40.25	40.75
Base Olduvai Chron (1.95)	63.95	62.50	64.00	57.80
Top Réunion Subchron (2.115)	78.65	80.50	82.50	79.25
Base Réunion Subchron (2.153)	88.00	95.50	100.25	99.25
Possible Event (2.19)	97.75 (95.70–99.25)	108.00 (105.60–109.75)	112.00 (110.25–114.40)	110.50 (108.30–112.15)
Possible Event (2.33)	111.75 (110.20–113.10)	122.00 (120.30–123.60)	128.00 (126.35–129.75)	122.50 (120.75–124.40)
Possible Event (2.39)	118.50 (117.25–119.75)	131.50 (129.75–133.25)	136 (134.00–137.75)	130 (127.75–134.00)
Possible Event “X” (2.44)	123.50 (122.40–124.50)	136.75 (135.25–138.50)	141.24 (139.75–142.75)	138.00 (136.00–139.50)
Top Gauss (2.58)	–	–	–	151.50

above described positive polarity Subchrons in Holes U1317A, U1317B, U1317C and U1317E. Below the Réunion Subchron negative inclinations from the reversed Matuyama Chron (C2r.2r) are again dominating. However some positive excursions can be noted. The positive excursions at 97.50, 111.75, 118.50, and 123.50 mbsf in Hole U1317A can be linked with magnetic events dated at respectively 2.19, 2.33, 2.39, and 2.44 Ma (Crowhurst 2002) and are also recognized in Holes U1317B, U1317C and U1317E (Fig. 5.3). The inclination values in Holes U1317A, U1317B and U1317C show no evidence of move towards positive inclination values just above the mound base. Only in Hole U1317E a transition towards positive inclination values from 151.5 mbsf on, coinciding with the transition towards the Gauss Chron (C2An.1n, 2.58 Ma) could be inferred. The mound base is characterized by an angular unconformity as observed on seismic profiles (De Mol et al. 2002; Van Rooij et al. 2003). It represents an age gap of several millions years (Kano et al. 2007) and coincides with a clear lithological change from consolidated Miocene sandy silts to Upper Pliocene-Pleistocene unconsolidated sediments, characterized by cold-water corals embedded in an alternating siliciclastic to calcareous-rich matrix. The mound base could not be clearly recognized in the inclination records of the different holes.

By comparing the absolute Sr-isotopic datings on cold-water coral fragments in Hole U1317E (Kano et al. 2007) with the magnetostratigraphic frameworks, a good correlation could be observed, confirming the magnetostratigraphy (Fig. 5.3). The correlation of biostratigraphic events, based on planktonic foraminifera present in the sediments of Hole U1317E, with the magnetostratigraphic frameworks is consistent. Plio-Pleistocene species are dominant through the mound succession, implying that the upper 18.17 mbsf of Hole U1317E should be younger than 0.65 Ma based on the appearance of the species *Globorotalia truncatrunoides,* and that the sediments between 21.17 and 59.98 mbsf have a biostratigraphic age between 0.65 and 2.09 Ma based on the appearance of the species *Globorotalia inflata* (Abe 2006). There is some discrepancy with the nannofossil datums which can be explained by the difficulties of biostratigraphic dating based on coccoliths due to the bad preservation and a high amount of reworked material (Browning pers. com.). Nevertheless the upper section, corresponding with the Brunhes Chron, is consistent with the nannofossil biostratigraphy.

5.2.2 Palaeointensity

During the past 10–15 years significant developments were noted in the possibility to obtain relative palaeointensity signals of the magnetic field from deep-sea sediments. A few reviews about palaeointensity have been published during the last years by Tauxe (1993), Jacobs (1998) and Valet (2003). Recent analyses of many records distributed over the globe provided already a lot of information to develop independent time-scales based on relative palaeo-intensities of the geomagnetic field (e.g. Valet and Meynadier 1993; Guyodo and Valet 1999; Channell et al. 2002; Channell and Raymo 2003; Yamazaki and Oda 2005; Guyodo and Valet 2006;

Lund et al. 2006). However, the reliability of these data depends on different factors, and important criteria have to be taken into account to obtain reliable relative palaeointensity records (King et al. 1983; Tauxe 1993; Constable et al. 1998; Valet 2003):

1. *The natural remanence must be carried by stable magnetite, preferably in the grain size range of about 1–15* μ*m. The portion of the natural remanent vector used for palaeointensity determination should be a single well-defined component of magnetization.*
   As described in Sect. 5.3.4, the magnetic measurements in Holes U1317A, U1317B, U1317C and U1317E are influenced by the presence of authigenic iron sulphides diluting the original magnetic records. The more, the intensities in the mound body are extremely low (10^{-4} to 10^{-6} A/m), typical for carbonate-rich sediments. The weakest intensity values are within the range of the noise level of the shipboard cryogenic magnetometer. However, we can assume there is still a fraction of magnetite carrying the natural remanence. AF-demagnetization showed that a characteristic remanent magnetization could be isolated at 15 mT for most of the samples (Sects. 5.1.1 and 5.1.2).
2. *The detrital remanence must be an excellent recorder of the geomagnetic field (Tauxe 1993). Normal and reversed polarity data should be antipodal.*
   Despite the scattered data, normal and reversed polarity data could be identified.
3. *Concentration of magnetic grains should not vary by more than about an order of magnitude.*
   The magnetic susceptibility, mirroring the concentration of magnetic grains, is characterized by rather low values varying between 0 and 40×10^{-5} SI throughout the mound body (see Sect. 5.3.1). So, the magnetic susceptibilities vary by less than an order of magnitude throughout the mound.
4. *Normalization should be done by several methods, all yielding consistent results. The selected normalizer should be the one that is best correlated with the remanence.*
   The intensity of the remanent magnetization in sediments is normally function of both alignment of magnetic grains by the geomagnetic field and concentration of the magnetic particles (Valet 2003). It is possible to extract the relative variations of the past magnetic field by normalizing the intensity records with a magnetic parameter that documents variations in magnetic concentrations. Only one possible normalizer is measured in this study, i.e. magnetic susceptibility. So no comparison between different methods is possible. However susceptibility measurements and intensity measurements show comparable relative records, indicating that the susceptibility could be an appropriate normalizer in this study. Normalization of the intensities was carried out by dividing intensities by magnetic susceptibilities for the shipboard data (Holes U1317A, U1317B, U1317C and U1317E).
5. *The estimated relative palaeofield, obtained by normalizing the NRM by some bulk parameter, can be renormalized by the mean of the entire time series, such that the relative palaeointensity is unity*.

To allow comparison of the normalized intensity records with relative intensity records from other drilling sites around the world, the records were divided by their mean. So, only relative variations are plotted.

The normalized relative palaeo-intensities (7-points running mean) for Holes U1317A, U1317B, U1317C and U1317E are visualized in function of depth (mbsf) on Fig. 5.4. A similar trend can be observed in the four holes above the hiatus defined in Sect. 6.2.1 (Fig. 5.4). The intensity values in the uppermost sections are an order of magnitude higher than the sections below. Comparison of the inclination records with the intensity records shows that the intensity values decrease to lower values at the transition between the Brunhes Chron and the Matuyama Chron. Moreover, peak values are recognized in Holes U1317A, U1317B, U1317C and U1317E which can be correlated between the holes (Fig. 5.4).

The normalized palaeointensity records from Site U1317 above the hiatus, can now be compared with well-defined palaeointensity proxies for ODP Site 980 (Feni Drift, Rockall) (Channell and Raymo. 2003) and with the Sint-800 global stack (Guyodo and Valet 1999). As the relative palaeointensity records of Site U1317, lower mean palaeointensity values for the Matuyama Chron, relative to the Brunhes Chron are recognized in the records of Site 980 (Channell and Raymo 2003). Channell and Raymo (2003) explain this effect by the presence of an uncleaned Brunhes-age viscous remanence (VRM), which is not apparent in the orthogonal projections of the demagnetization data (Fig. 5.1). Remarkable is the similarity between the relative palaeointensity values of the Brunhes Chron at Holes U1317A (1.50–17.00 mbsf), U1317B (2.50–15.45 mbsf), U1317C (4.00–19.40 mbsf), U1317E (0.90–23.50 mbsf) and the reference records, especially those of ODP Site 980 between 780 and 560 ka (Fig. 5.4). If the mentioned correlation on Fig. 5.4 is true, an important part of the sediments belonging to the top of the Brunhes Chron is missing at Site U1317 or a lot of time is represented in a few metres of sediments indicating really low sedimentation rates. As described in Chap. 2, Challenger Mound is a dead mound with no active coral-growth anymore nowadays. It can be assumed that the main growth phase stopped a long time ago and that just a small amount of sediments were deposited during the last 560 ka. Moreover, detailed studies of a gravity core taken on the upper flanks of Challenger Mound learnt that the cold-water corals and sediments at the top of this core belong to the Holocene (2100 years BP) but that a hiatus characterizes the records around 4 m (Foubert et al. 2007; see also Chap. 6). So we can assume that a second hiatus in the upper few metres is present in the IODP Holes which is, due to the IODP drilling technique, not recovered in as much detail as the previous studied gravity core (see Chap. 6). This second hiatus in the uppermost sediments can explain why rather old sediments are present close to the surface. Sr-isotopic datings on cold-water coral fragments at 3.47 mbsf in Hole U1317E revealed ages of 571 ka (Kano et al. 2007), confirming the statements above. It should be mentioned that the uppermost sediments (upper 2–3 m) are better recorded in Holes U1317A, U1317B and U1317C than in Hole U1317E. This is also observed in the geophysical and geochemical records whereby the uppermost cycle is less preserved in Hole U1317E (see Chap. 4). So it can be

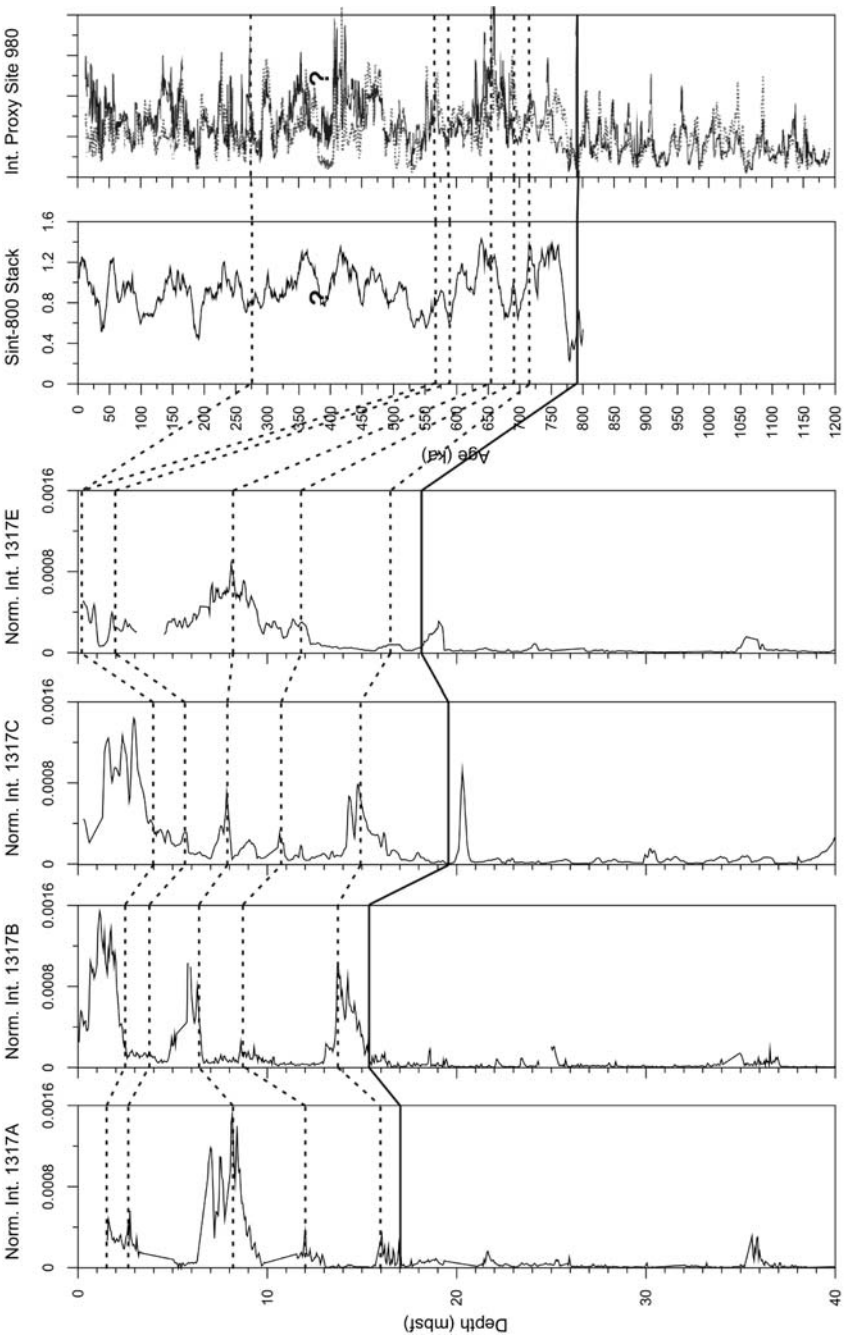

Fig. 5.4 Comparison of normalized palaeo-intensities above 40 mbsf in Holes U1317A, U1317B, U1317C and U1317E with SINT-800 Stack (Guyodo and Valet 1999) and normalized intensities of ODP Site 980 (Channell and Raymo 2003). *Horizontal dashed black lines* represent correlation lines between the holes. *Horizontal solid black line* represents Brunhes-Matuyama boundary

assumed that the sediments above the mentioned hiatus and the hiatus itself are better preserved in the holes located more at the flank of the mound.

The extremely low values in the records below 17.00 mbsf in Hole U1317A, 15.45 mbsf in Hole U1317B, 19.40 mbsf in Hole U1317C and 23.50 mbsf in Hole U1317E make the intensity values unreliable for detailed interpretation and correlation.

5.2.3 Sedimentation Rates

Based on the magnetostratigraphic tiepoints (Table 5.2), sedimentation rates can be calculated for the different Chrons observed in Holes U1317A, U1317B, U1317C and U1317E. Figure 5.5 reflects the sedimentation rates in the different holes. A similar pattern is observed in the four holes. The lowest sedimentation rates are noted above the hiatus, with an average of 4.70 cm/ka for the lower part of the Brunhes Chron (400–780 ka). The lower sedimentation rates in the uppermost sections can be explained by the fact that the mound is reaching a stage of retirement whereby the mound is not growing anymore that fast as in earlier times.

The sedimentation rates below the hiatus can be separated in three trends, whereby the highest sedimentation rates are observed during the Réunion Subchronozone. Channell et al. (2003) observed a similar effect at ODP Site

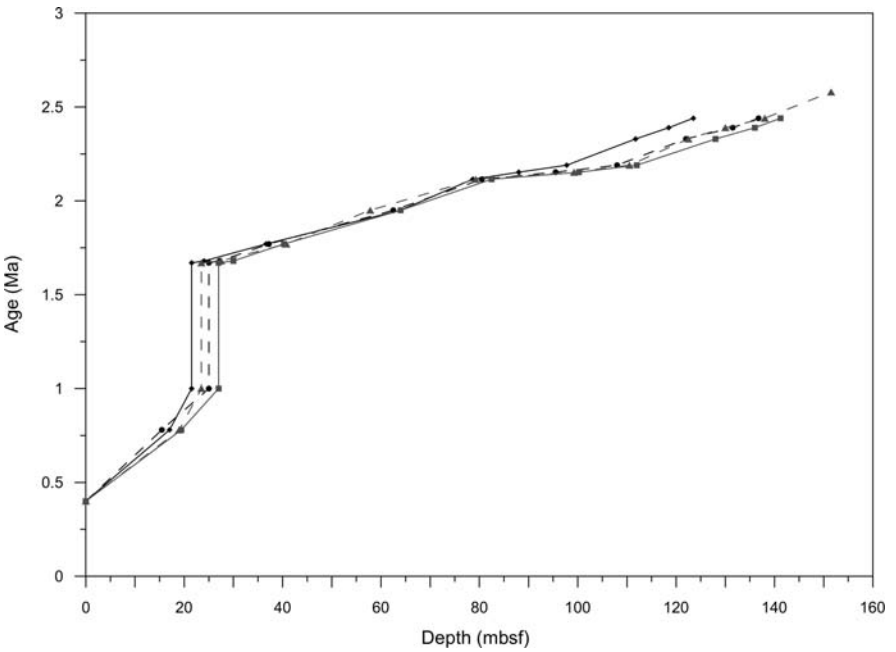

Fig. 5.5 Visualization of the sedimentation rates (age (Ma) in function of depth (mbsf)) of Holes U1317A (*black line* with *diamonds*), U1317B (*black dashed line* with *circles*), U1317C (grey line with squares), and U1317E (*grey dashed line* with *triangles*)

981 (Feni Drift, North Atlantic), whereby sedimentation rates of 18 cm/ka where reached during this period resulting in an unusually detailed record of this Subchron. The sedimentation rates for the Réunion Subchron at Site 1317 are 24.60, 39.50, 46.70, and 52.60 cm/ka for respectively Holes U1317A, U1317B, U1317C and U1317E, with an average for the four holes of 40.90 cm/ka. This is nearly four times higher than recorded above and below this Subchronozone. Remarkable is that the sedimentation rates are increasing towards the top and centre of the mound. Thus, around 2.15 Ma, the mound was in an important growth phase with the highest growth rates centred at the top of the mound, boosting a vertical growth process. The average sedimentation rates above and below this zone are respectively 12.60 and 13.60 cm/ka. Another remarkable observation is the increasing trend of the sedimentation rates going from Hole U1317E to Hole U1317A during the Olduvai Chron: 9.47 cm/ka at Hole U1317E, 13.19 cm/ka at Hole U1317C, 14.06 cm/ka at Hole U1317B and 15.20 cm/ka at Hole U1317A. This suggest that after the main growth phase of the mound, centred at the top of the mound, the mound started to expand in horizontal direction with higher growth rates at the flank of the mound compared to the top of the mound.

The generally high sedimentation rates in the mound body were responsible for the detection of short-duration geomagnetic excursions, normally not recorded in deep sea sediments, as described in Sect. 5.2.1.

5.3 Environmental Magnetism

5.3.1 Magnetic Susceptibility

The values of magnetic susceptibility are in general very low throughout the mound body. The average values are $\sim 6.00 \times 10^{-5}$ SI units with peak values up to $\sim 40.00 \times 10^{-5}$ SI units. Similar trends are observed in the four holes with distinctive peaks and cycles traceable from one hole to the other hole. The typical cycles recognized in all the geophysical and geochemical records, as discussed in Sect. 4.2.2, are clearly visible in the magnetic susceptibilities (Fig. 5.6). The relation between the susceptibility records and the other geophysical (GRA density, P-wave velocity and NGR) and geochemical (Ca, Fe, Sr, K and Ti) data sets are discussed in detail in Sects. 4.2 and 4.3. Only the most important relationships will be highlighted again in this chapter.

Bulk susceptibility measurements on discrete samples in Hole U1317A revealed similar trends as measured on whole-round core sections on board of the R/V *JOIDES Resolution* (Fig. 5.6). The average value of the mean magnetic susceptibility of the discrete samples is $\sim 4.71 \times 10^{-5}$ SI, which is a bit lower than noted for the shipboard measurements. Negative susceptibility values ($\sim -1.00 \times 10^{-5}$ SI) are only present between 3.60 and 4.35 mbsf in Hole 1317E. No negative values are encountered in the other holes.

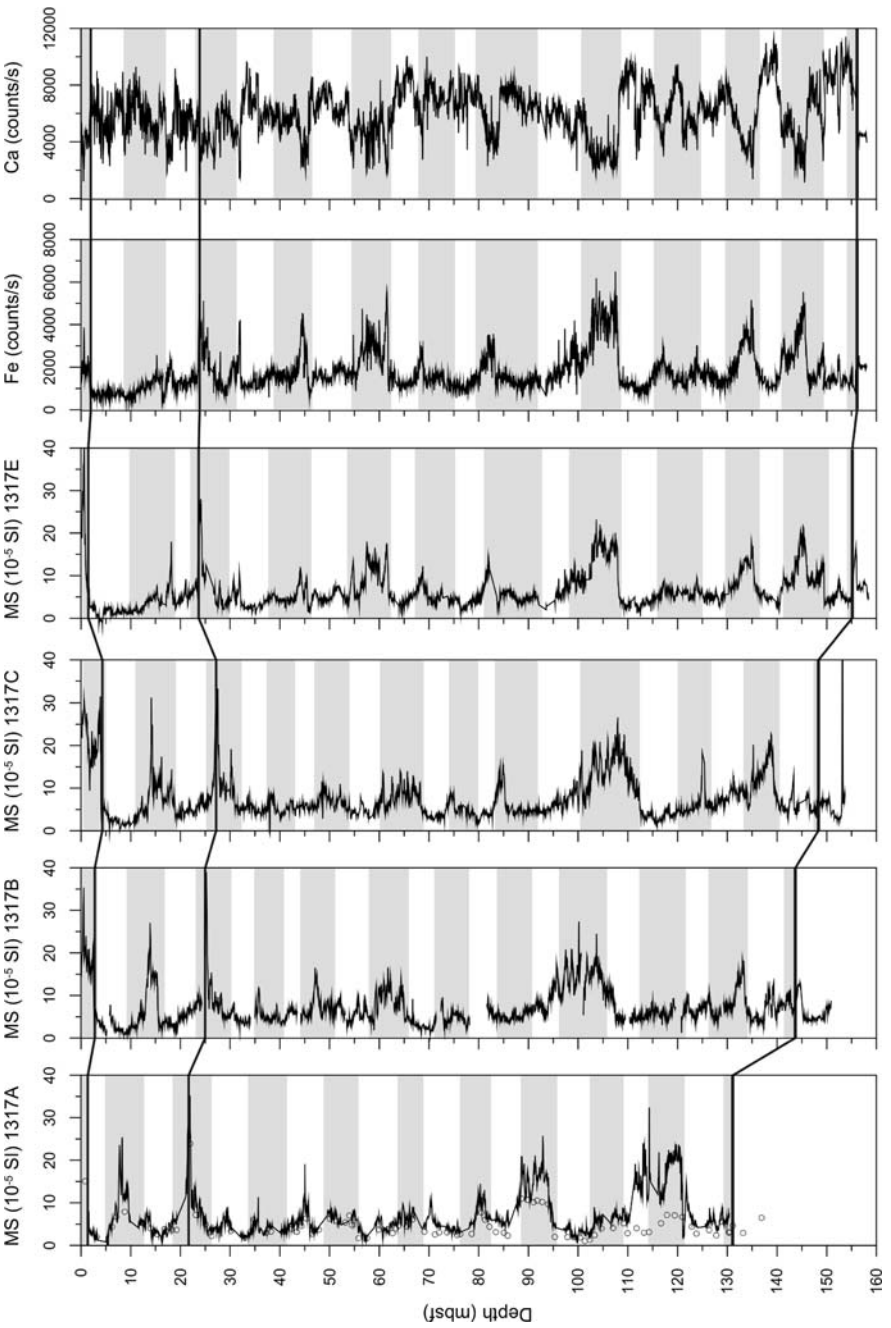

Fig. 5.6 Magnetic susceptibility (10^{-5} SI units) in function of depth (mbsf) for Holes U1317A, U1317B, U1317C, and U1317E and relative Ca and Fe intensities (counts/s) in function of depth (mbsf) for Hole U1317E. *Grey boxes* represent the cycles in the different holes as defined in Chap. 4. *White circles* represent measurements of the magnetic susceptibility on discrete samples of Hole U1317A. *Horizontal solid black lines* correspond with interpreted hiatus and the mound base

Low mean magnetic susceptibilities indicate that paramagnetic minerals probably are determining the magnetic susceptibility trends in the mound. Many minerals are paramagnetic – particularly the non-ferromagnetic iron-bearing silicates including the clays (olivines, amphiboles, pyroxenes, biotite, chlorite, mica, etc. . .) – but they do not carry a magnetic remanence (like ferromagnets) (Tarling and Hrouda 1993). The susceptibilities of paramagnetic minerals are low, typically in the order of 10^{-3} to 10^{-5} SI units, but are very uniform for different mineral species, varying only with iron content. Comparing the magnetic susceptibilities throughout the mound with the relative values of iron (Fe), measured with a XRF core scanner (see also Sect. 4.3.2), reveals a positive correlation (Fig. 5.6). XRD analyses confirm the important presence of iron-bearing clay-minerals (illite, chlorite and smectite) in the sediments of Challenger Mound (Léonide 2006; Léonide et al. 2009; see also Sect. 3.3.2). If sediments contain paramagnetic constituents and their susceptibility is less than 5.00 $\times 10^{-4}$ SI units, the paramagnetic fraction controls the susceptibility of the sediments (Tarling and Hrouda 1993). So, we can assume that the paramagnetic fraction provides the main control of the susceptibility records in Challenger Mound.

The negative susceptibilities in Hole U1317E can be explained by the presence of a small amount of diamagnetic minerals. Diamagnetic minerals all have weak negative susceptibilities, $\sim$–1.00 $\times 10^{-5}$ SI, i.e. they acquire a weak induced magnetization in a direction opposite to the applied field (Tarling and Hrouda 1993). Such minerals, which include very common ones like quartz and calcite, only become important when ferromagnetic minerals are completely absent (less than 0.0001% of the total amount of sediment) and paramagnetic minerals are virtually absent (less than 1% of the total amount of sediment). When ferromagnetic or paramagnetic minerals are present in quantities that approach or exceed these limits, the observed magnetic properties will be dominated by the ferromagnetic or paramagnetic components (Tarling and Hrouda 1993). The significant presence of paramagnetic minerals in Challenger Mound explains the rareness of negative magnetic susceptibility values despite the significant amount of the diamagnetic calcium carbonate (see Sect. 4.3) and some quartz (Léonide 2006; Léonide et al. 2009; see also Sect. 3.3.2) in the mound sediments.

It has to be mentioned that the presence of a small remanent magnetization measured in most of the samples (Sect. 5.2.1) in the mound sediments, argues for the presence of a small amount of remanence carrying minerals (ferromagnetic minerals). The ferrimagnetic mineral magnetite is mainly responsible for the natural remanent magnetization in the sediments. The presence of magnetite in the sediments of Challenger Mound is confirmed by a detailed investigation of the thermal changes of magnetic susceptibility. Figure 5.7 represents the thermomagnetic curves of a sample from Section 307-1317A-3H-3 (Fig. 5.7A,B) and a sample from Section 307-1317A-2H-3 (Fig. 5.7C,D). The heating curves for both samples have a hyperbolic shape in the initial part with a decreasing trend (Fig. 5.7B–D), indicating that the paramagnetic fraction controls indeed in a predominant way the susceptibility of the specimens at room temperature (Hrouda 1994). A sharp decrease in susceptibility from $\sim$535 to 590°C is noted, reaching minimum values up to 1.10 SI units (307-1317A-3H-3) and 0 SI units (307-1317A-2H3) at 600°C (Fig. 5.7).

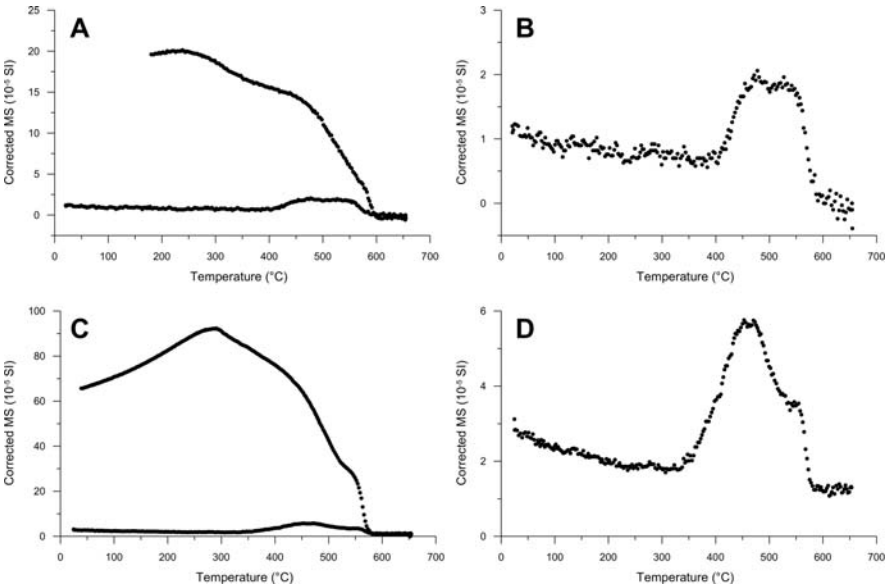

Fig. 5.7 Heating and cooling curves (magnetic susceptibility (10^{-5} SI units) in function of temperature (°C)) for samples at Section 307-1317A-2H-3 at 9.98 mbsf (**A**) and Section 307-1317A-3H-3 at 19.84 mbsf (**C**). Heating curves for samples at Section 307-1317A-2H-3 at 9.98 mbsf (**B**) and Section 307-1317A-3H-3 at 19.48 mbsf (**D**)

This temperature matches the Curie Temperature (T_c) of magnetite, which has a value of 575 to 600°C. Such observations confirm the presence of magnetite. The heating curves contain a high elevation between 400 and 600°C (Fig. 5.7). Shi et al. (2001) suggested that the susceptibility peak around 500°C in heating cycles might arise from the conversion of iron sulphides into magnetite. Traces of oxygen may be absorbed around the pyrite powder, which may oxidize pyrite (FeS_2) into magnetite (Fe_30_4) from the temperature of ~380°C onwards. More magnetite is produced with increasing temperature. The susceptibility enhancement, arising from newly formed magnetite, descends when the temperature is above 520°C. Li and Zhang (2005) proved that at higher temperatures the newly formed magnetite can combine with pyrite and/or sulphur atoms released from pyrite lattice to form pyrrhotite. Pyrite can also transform directly to pyrrhotite by desulphidation. The formation of pyrrhotite at high temperatures is expressed in the cooling curves, which have values almost an order of magnitude higher than the heating curves and a distinctive peak around 280°C, corresponding with the T_c of pyrrhotite.

The above mentioned observations suggest the presence of pyrite in the sediment samples before heating. XRD analyses and SEM observations give evidence of the presence of framboidal and monoclinic pyrite in the mound sediments (Léonide 2006; Léonide et al. 2009). Pyrite can be formed by dissolution of magnetite during sulphate reduction according to the following reaction paths (Eqs. 5.1 and 5.2) (Florindo et al. 2003):

$$SO_4^{2-} + 2CH_2O \leftrightarrow 2HCO_3^- + H_2S \tag{5.1}$$

$$3H_2S + 2FeOOH \leftrightarrow FeS_2 + FeS + 4H_2O \tag{5.2}$$

Organoclastic sulphate reduction takes place throughout the whole mound body, whereby dissolved sulphate in the pore waters is present in quantities of 27.30 mM at 1.40 mbsf to decrease to below its analytical detection limit near ~170.00–180.00 mbsf (Exp. 307 Scientists 2006). Bacterially mediated sulphate reduction can play a role in particular zones in the mound body (Exp. 307 Scientists 2006d). The diagenetic formation of paramagnetic pyrite (by dissolution of magnetite) is responsible for the small amount of original ferrimagnetic magnetite and dilutes the original magnetic signals, which explains the highly scattered records of the directions of the remanent magnetizations (Sect. 5.2.1).

The alternating domination of diamagnetic versus paramagnetic and ferrimagnetic components is responsible for the cyclic trend observed in the susceptibility records, whereby higher values correspond with a higher percentage of paramagnetic (mainly iron-rich) clay minerals (i.e. illite, chlorite and pyrite) and a small amount of the ferrimagnetic magnetite, while lower susceptibility values relate to a higher content of diamagnetic components (mainly biogenic carbonate and small amounts of quartz). The total magnetic susceptibility can be described as a function of these components (Eq. 5.3):

$$\begin{aligned}\text{Total MS} = {} & \%\text{ferrimagnetic components (magnetite)} + \\ & \%\text{paramagnetic components (clayminerals illite and chlorite} + \\ & \text{diagenetic pyrite)} + \%\text{diamagnetic components (biogenic } CaCO_3 + \text{quartz)}\end{aligned} \tag{5.3}$$

Thus, at Challenger Mound the interplay between terrigenous sedimentation (with the supply of paramagnetic Fe-rich clay minerals (mainly illite and chlorite), diamagnetic quartz and ferrimagnetic magnetite), biogenic sedimentation (diamagnetic calcium carbonate) and diagenesis (dissolution of ferrimagnetic magnetite and formation of paramagnetic pyrite) control the susceptibility records whereby at some periods terrigenous sedimentation was dominating, while in other periods biogenic sedimentation took over, diluting the terrigenous sediments and lowering the susceptibility values.

The susceptibility values of Hole U1317E can now be compared with the relative variations of the Ca-content, measured with a XRF cortex core scanner (Fig. 5.6; Sect. 4.3). This comparison indicates an inverse relationship between both parameters, whereby lower susceptibilities correspond with higher reflectance values and thus a higher carbonate-content. So, the inverse relationship confirms the observation that diamagnetic minerals, mainly biogenic carbonate, dilute the mainly paramagnetic and ferrimagnetic terrigenous fractions in well-distinct intervals and lower the susceptibility.

5.3.2 Anisotropy in Magnetic Susceptibility

In most samples the strength of magnetization induced by a weak field of constant strength depends on the orientation of the sample within the field (Tarling and Hrouda 1993). Such sediments are magnetically anisotropic. The variation of susceptibility with orientation can be described mathematically in terms of a second-rank tensor and can be visualized in three-dimensional space as a susceptibility ellipsoid with three orthogonal axes, corresponding to the maximum (K_1), intermediate (K_2) and minimum (K_3) principal susceptibilities. This ellipsoid represents the combined results of the susceptibility anisotropy produced by the shape of the magnetic grains (shape anisotropy) and/or the crystallography in a sample (crystalline anisotropy), as well as by the net alignment of the magnetic grains within the sample (Tarling and Hrouda 1993). The crystallographic control arises from the action of lattice forces on the electron-spin configurations whereby, for any given crystal, the electron spins align more easily along specific directions i.e. the magnetization acquired in an applied field is strongest in these directions.

The magnitude of the anisotropy is presented by the corrected anisotropy degree P′ (Eq. 5.4) (Jelinek 1981):

$$P' = \exp\sqrt{2[(\eta_1 - \eta_m)^2 + (\eta_2 - \eta_m)^2 + (\eta_3 - \eta_m)^2]} \tag{5.4}$$

where $\eta_1 = \ln K_1$, $\eta_2 = \ln K_2$, $\eta_3 = \ln K_3$ and $\eta_m = (\eta_1 + \eta_2 + \eta_3)/3$. Higher values of P′ represent stronger degrees of magnetic anisotropy. The shape of the anisotropy can be expressed in several ways – mainly in terms of ratios of, or differences between, the axial values such as the normalized lineation L (Eq. 5.5) and foliation F (Eq. 5.6) (Khan 1962):

$$L = (K_1 - K_2)/K_{mean} \tag{5.5}$$

$$F = (K_2 - K_3)/K_{mean} \tag{5.6}$$

Other parameters have been published that combine lineation and foliation, like the shape parameter T (Eq. 5.7) (Jelinek 1981):

$$T = [(2(\eta_2 - \eta_3))/(\eta_1 - \eta_3)] - 1 \tag{5.7}$$

Oblate (disk) shapes correspond to $0 < T < -1$, while negative values, $-1 < T < 0$ correspond to prolate (rod) shapes.

The results of the measurements of the anisotropy in magnetic susceptibility are shown on Figs. 5.8 and 5.9. Figure 5.8A represents a stereographic projection of the K_1 (maximum) and K_3 (minimum) axes of the AMS. The minimum axes of anisotropy are well-grouped perpendicular to the stratification plane, whereas the maximum axes of anisotropy are distributed mainly in the stratification plane (horizontal plane). At first sight the maximum axes seem to be randomly distributed in the stratification plane. However taking into account only the declinations of the

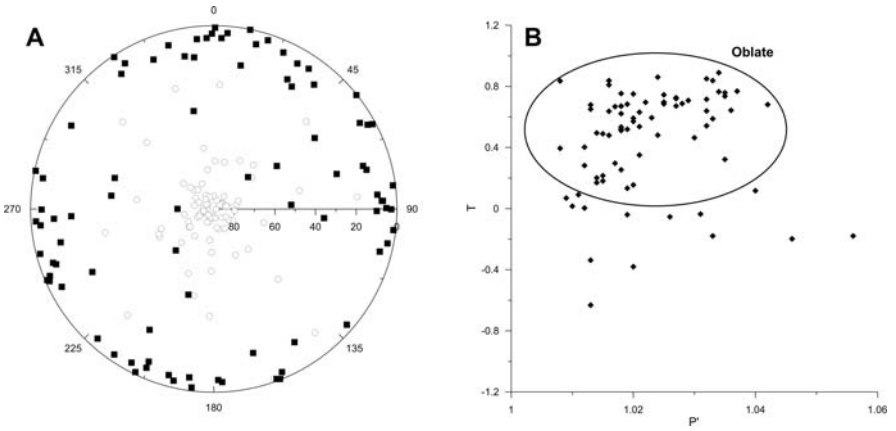

Fig. 5.8 (**A**) Stereographic projection of the K_1 (maximum) (*black squares*) and K_3 (minimum) (*white circles*) axes of the anisotropy of magnetic susceptibility (AMS). (**B**) Shape parameter T versus the corrected degree of anisotropy P′

maximum axes corrected by the Tensor Tool measurements (to obtain a true declination) and with an inclination <25°C, a S-N to SW-NE-trend can be inferred from the stereographic plot (Fig. 5.8A).

In the P′-T-graph, the fabric appears to be mainly oblate (T >0) (Fig. 5.8B). The degree of anisotropy P′ varies between 1.006 and 1.056, coinciding with values typical for drift sediments as demonstrated by Joseph et al. (1998). Joseph et al. (1998) identified a relationship between the median grain size and intensity of anisotropy (P′) with current speed (whereby both the median grain size and P′ increase as the current speed increases) and applied this relationship to distinguish different depositional environments. The Blake Outer Ridge drift sediments are characterized by a magnetic fabric P′ ranging from 1.01 to 1.05 and ellipsoid shapes that are primary oblate. These values correspond with the anisotropy in the Challenger Mound sediments. So, analysis of magnetic fabric permits differentiation between deposits resulting from random grain settling (pelagic and hemipelagic) and those resulting from ensuing transport along the sea-floor (drifts and turbidites) (Rea and Hovan 1995; Boven and Rea 1998; Joseph et al. 1998).

The degree of anisotropy P′ and shape parameters T, L and F are, jointly with a plot of the mean susceptibility, visualized in function of depth on Fig. 5.9. The degree in anisotropy P′ and the foliation F follow the small-scaled cycles observed in the magnetic susceptibility (Fig. 5.9). Peaks in degree of anisotropy can be correlated with peaks in the magnetic susceptibility. The few encountered negative values of the shape parameter T, can be correlated with lows in magnetic susceptibilities.

As the paramagnetic fractions dominates the susceptibility in the sediments of Challenger Mound (Sect. 5.3.1), the anisotropy in magnetic susceptibility may be also carried mainly by these fractions (Tarling and Hrouda 1993). As established in previous section, Fe-rich clay minerals may play hereby an important role, so the

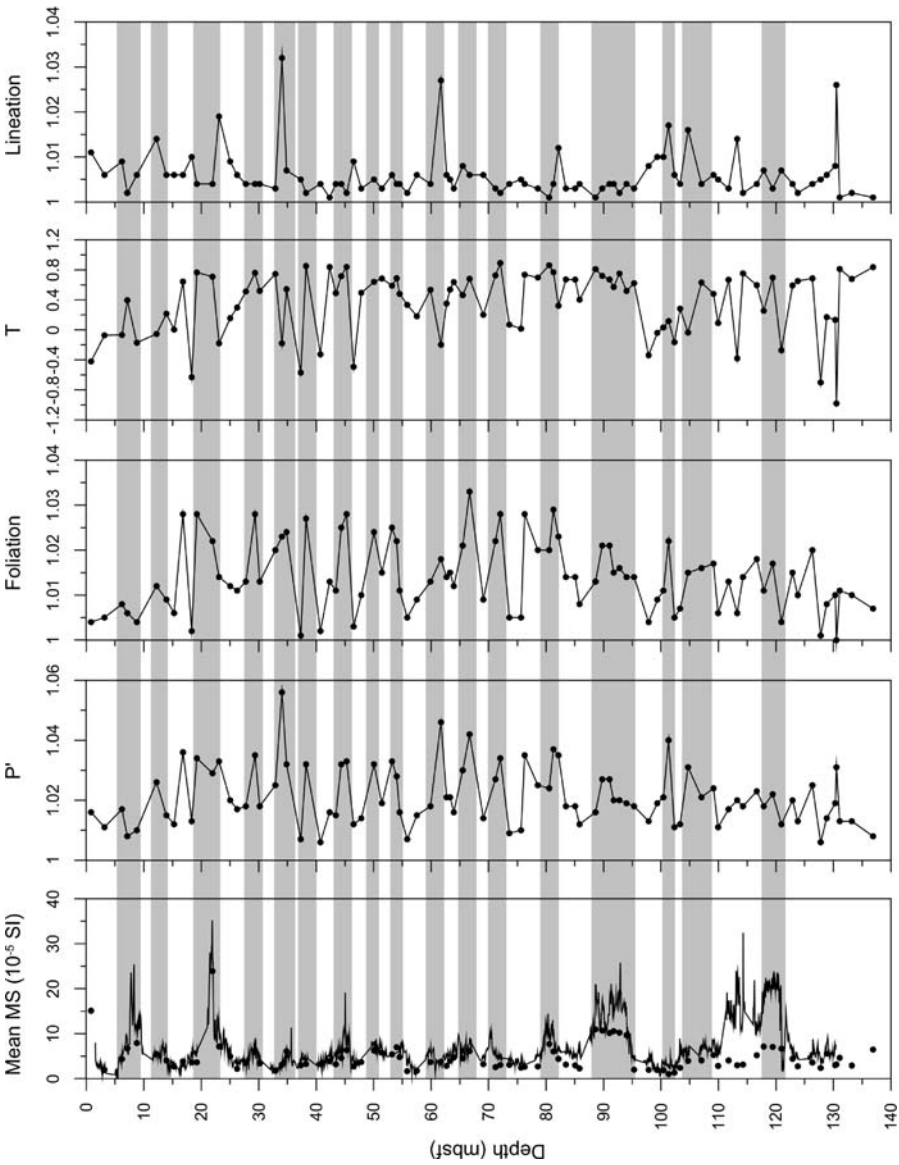

Fig. 5.9 The degree of anisotropy P′, shape parameters T, L (lineation) and F (foliation) and mean susceptibility in function of depth (mbsf) for Hole U1317A. *Grey boxes* represent correlations between the different parameters (peaks in degree of anisotropy can be correlated with peaks in the magnetic susceptibility)

anisotropy in magnetic susceptibility (AMS) might provide information about the fabric of the magnetic clay minerals. This latter is linked to the crystal lattice and is mainly oblate with the minimum axes perpendicular to the cleavage plain (Ballet et al. 1985; Borradaile and Werner 1994). So, flat-shaped clay minerals tend to orient

perpendicular to the main stress axis, that is, the vertical axis during compaction, whereas rounded sand grains do not have a preferred direction to align with. So, it appears likely that the degree of AMS is mainly a function of the matrix grain size and shape properties whereby intervals characterized with a higher content of paramagnetic clay minerals tends to have a higher degree of anisotropy.

Kissel et al. (1998) presented an attempt to relate the magnetic fabric of sediments to changes in bottom currents in the North Atlantic Ocean. However, due to the highly variable magnetic mineral content in the Challenger Mound sediments, this assumption is not straightforward and we have refrained from interpreting the AMS in terms of bottom current intensity. However, there has been another approach to investigate palaeocurrent behaviour. The anisotropy of magnetic susceptibility has been used to infer current directions. Because current force the alignment of sediment particles that result in the anisotropy of magnetic susceptibility (Rees and Woodall 1975; Taira and Lienert 1979), the direction of the long axes of the anisotropy ellipsoid can be used as an indicator of deep-current direction (Ledbetter and Ellwood 1980; Shor et al. 1984). So, the N-S to SW-NE direction of the maximum axes of the anisotropy ellipsoid postulate a N-S to SW-NE bottom current at the top of Challenger Mound (Fig. 5.8A). A general northwards bottom current is observed at the eastern flanks of the Porcupine Seabight (White 2001, 2007). Dorschel et al. (2007a) demonstrated that also on top of the mounds a general northward current is noted with some deflections at the flanks and a superimposed tidal signal (see Chap. 2). So the observed bottom current in the Porcupine Seabight coincides with current directions inferred from the AMS.

5.3.3 Time Series Analysis

As discussed in Sect. 5.3.1, the magnetic susceptibility records delineate important variations in sediment lithology. Using the magnetostratigraphic age model established in Sect. 5.2.1, it can be verified to what extent the susceptibility records mirror climatic and oceanographic changes of different duration, driven by orbital forcing. It has been demonstrated in many records of the Atlantic Ocean that Milankovitch cyclicity (1941) resulting from orbital forcing of terrigenous and biogenic sedimentation (or carbonate dissolution in deep-sea records) prevails (Robinson 1986; Von Dobeneck and Schmieder 1999; Channell et al. 2002).

Spectral analysis of the susceptibility records has been carried out with the programme AnalySeries (Paillard et al. 1996) using the widely applied Blackman-Tukey (BT) Method with a Welch-window (Blackman and Tukey 1958). It is based on the standard Fourier transform of a truncated and tapered (to suppress spectral leakage) autocovariance function. The Blackman-Tukey Method requires evenly spaced time series, so linear interpolation of the records was necessary before BT spectral analyses.

Magnetostratigraphic dating provided reliable tiepoints below the hiatus in Holes U1317A, U1317B, U1317C and U1317E. By attributing these ages to the respective magnetic susceptibility logs and by linear interpolation between the tiepoints, some

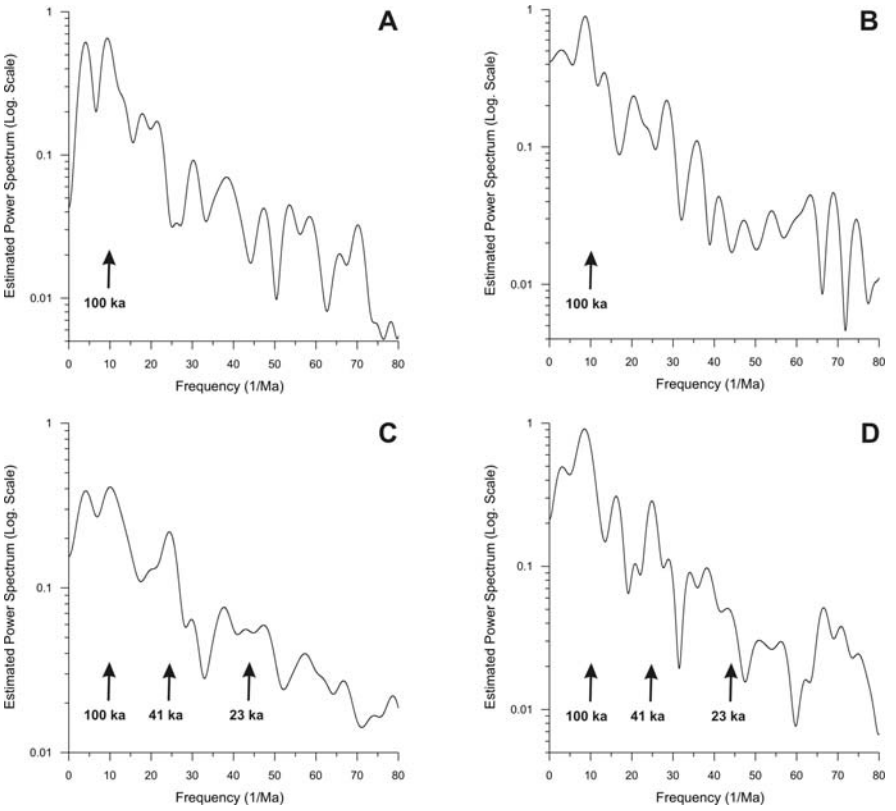

Fig. 5.10 Estimated spectra of the susceptibility signals (linear interpolated between the magnetostratigraphic tiepoints) on logarithmic scales for Holes U1317B (**A**) and U1317E (**B**). Estimated spectra of the tuned susceptibility signals (tuned with the oxygen isotope TARGET curve (Shackleton et al. 1990, 1995a,b; http://delphi.esc.cam.ac.uk/coredata)) on logarithmic scales for Holes U1317B (**C**) and U1317E (**D**)

spectral characteristics of Milankovitch cyclicity became apparent in the records between the mound base (~2.5–2.7 Ma) and the hiatus (~1.67 Ma) suggesting climatic forcing (Fig. 5.10A,B). Spectral analyses revealed Milankovitch cycles with a periodicity around 100 ka (eccentricity), suggesting that the age model based on the magnetostratigraphic tiepoints is probably not detailed enough to visualize the typical obliquity orbital periodicity resulting in glacial-interglacial cycles with a mean period of 41 ka (Imbrie et al. 1992), characterizing the North Atlantic records since the onset of the northern hemisphere glaciations at c. 2.75 Ma and prior to the Mid-Pleistocene Revolution (MPR). However, the output of a Gaussian filter centred at 0.05 ka (20 ka period) with a 0.02 ka bandpass applied to the susceptibility record can be compared with the orbital solution for obliquity and precession from Berger and Loutre (1991) (Fig. 5.11). Although the peak-to peak match is imperfect, the modulation of orbital precession is well matched by modulation of the filtered

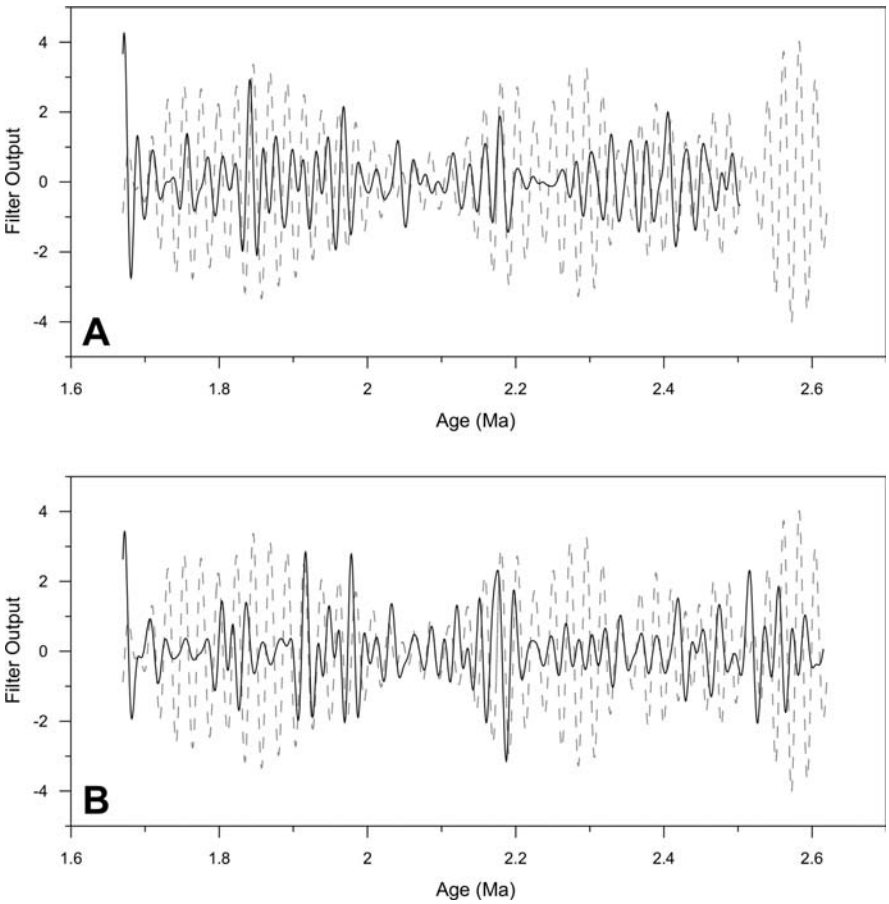

Fig. 5.11 Gaussian filter centreed at 0.05 ka (20 ka period) with a 0.02 ka bandpass applied to the susceptibility record (*solid black line*) compared with the orbital solution for obliquity and precession from Berger and Loutre (1991) (*dashed grey line*) (1991) for Holes U1317B (**A**) and U1317E (**B**).

susceptibility record. We consider that at least some of the peak-to-peak mismatch is due to noise in the susceptibility record produced by stochastic influences. For this reason, and because of unknown lag between precessional forcing and response, the classic spectral analyses should be interpreted with caution. Nonetheless, the match of the filtered susceptibility records to the astronomical solution for precession and obliquity strengthens the age model.

To check whether the age model of the magnetic susceptibility records, based on the magnetostratigraphic tiepoints, could be refined, the magnetic susceptibilities were compared with oxygen isotopic records. At Site U1317E, oxygen isotope measurements were made on benthic foraminifera, using specimens of *Cibicoides wuellerstorfi* and *C. kullenbergi* selected from the >150 μm size fractions (Abe 2006). A comparison of the susceptibility records of Hole U1317E with the oxygen

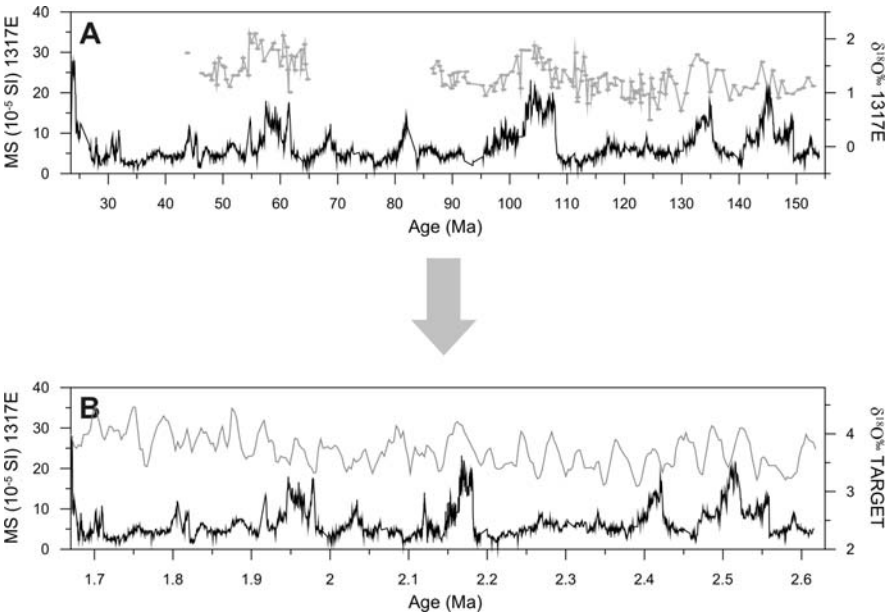

Fig. 5.12 (**A**) Comparison of the magnetic susceptibility (*black line*) with benthic δO^{18} data (*grey line*) in function of depth (mbsf) for Hole U1317E. (**B**) Comparison of magnetic susceptibility (*black line*) placed on the age model as defined from linear interpolation between the magnetostratigraphic tiepoints with the standard benthic δO^{18} TARGET curve (*grey line*) (Shackleton et al. 1990; 1995a,b)

isotopic data reveals a similar trend (Fig. 5.12A). Both records can now be compared with the chronology of Shackleton et al. (1990, 1995a,b) as defined by his reference benthic oxygen isotopic TARGET curve. The values of the benthic oxygen isotope record at Site U1317E are lower than the reference curve. It has to be mentioned that the resolution of the measured isotopic record is quite low, making it difficult to align the isotopic data with the TARGET curve. However, the resolution of the susceptibility records at Site U1317E is higher than the isotopic records, making it possible to correlate the susceptibility records with the standard reference curve (Fig. 5.12B). The close resemblance of the susceptibility record with the benthic O^{18} record indicates a linkage between global ice volume and the abundances of minerals that produces the susceptibility records in these sediments. The proposed age model for the magnetic susceptibility records can now be re-tuned by matching the susceptibility records to the standard δO^{18} curve for all the holes at Site U1317.

Spectral analyses on the retuned susceptibility records reveals distinctive peaks around frequencies of 10 and 24.4 1/Ma and a small peak around 43 1/Ma, corresponding with Milankovitch cycles with a periodicity around respectively 100 ka (eccentricity), 41 ka (obliquity) and 23 ka (precession) (Fig. 5.10C,D). So, tuning the lithological characteristics, revealed in the magnetic susceptibility, to reference curves yield a higher precision and consistency in dating the mound sediments.

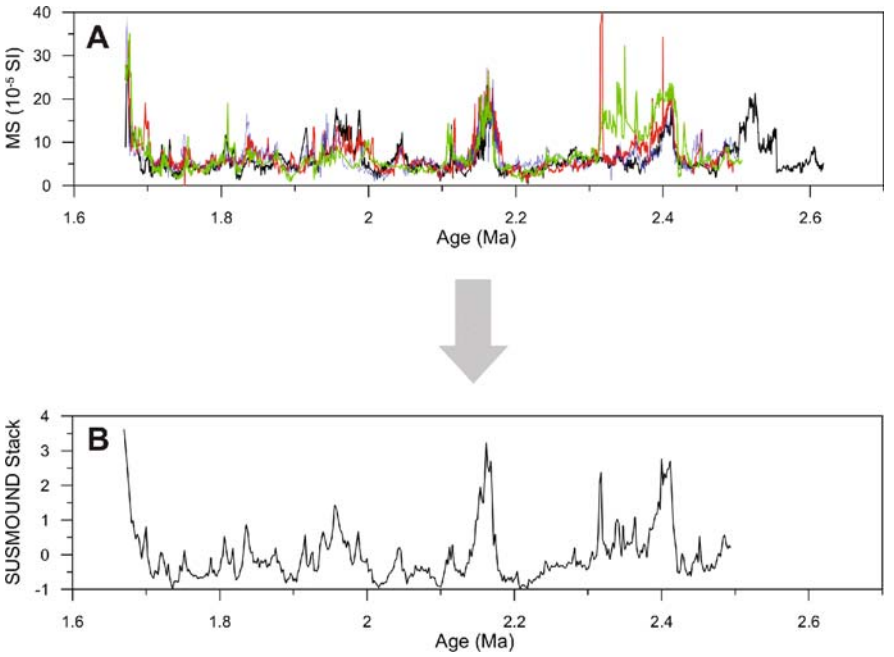

Fig. 5.13 (**A**) Magnetic susceptibility records for Holes U1317A (*green line*), U1317B (*bleu line*), U1317C (*red line*), and U1317E (*black line*) placed on an age model defined by tuning the susceptibility records with the standard benthic δO^{18} TARGET curve (Shackleton et al. 1990, 1995a,b). (**B**) SUSMOUND stack determined as an arithmetic mean of the individual normalized (subtraction of core mean and division by standard deviation), interpolated ($\delta t = 2$ ka) susceptibility records from Holes U1317A, U1317B, U1317C, and U1317E

By combining the retuned age models of the susceptibility records of Holes U1317A, U1317B, U1317C and U1317E, a susceptibility stack for the mound sediments at Site U1317 can be established (SUSMOUND) (Fig. 5.13). Because of the slightly different amplitude ranges, the SUSMOUND stack is determined as an arithmetic mean of the individual normalized and interpolated ($\delta t = 2$ ka) records from Holes U1317A, U1317B, U1317C and U1317E. The normalization has been carried out by subtraction of the core mean and division by the standard deviation.

5.4 Magnetostratigraphy in the Off-Mound Regions

5.4.1 Site U1316

Shipboard palaeomagnetic measurements have been carried out on cores from Holes U1316A, U1316B and U1316C. Alternating-field demagnetization of the natural remanent magnetization was driven up to 20 mT in 5 mT steps on Section 307-U1316A-1H-1. Based on this demagnetization experiment (Fig. 5.14A,B), the

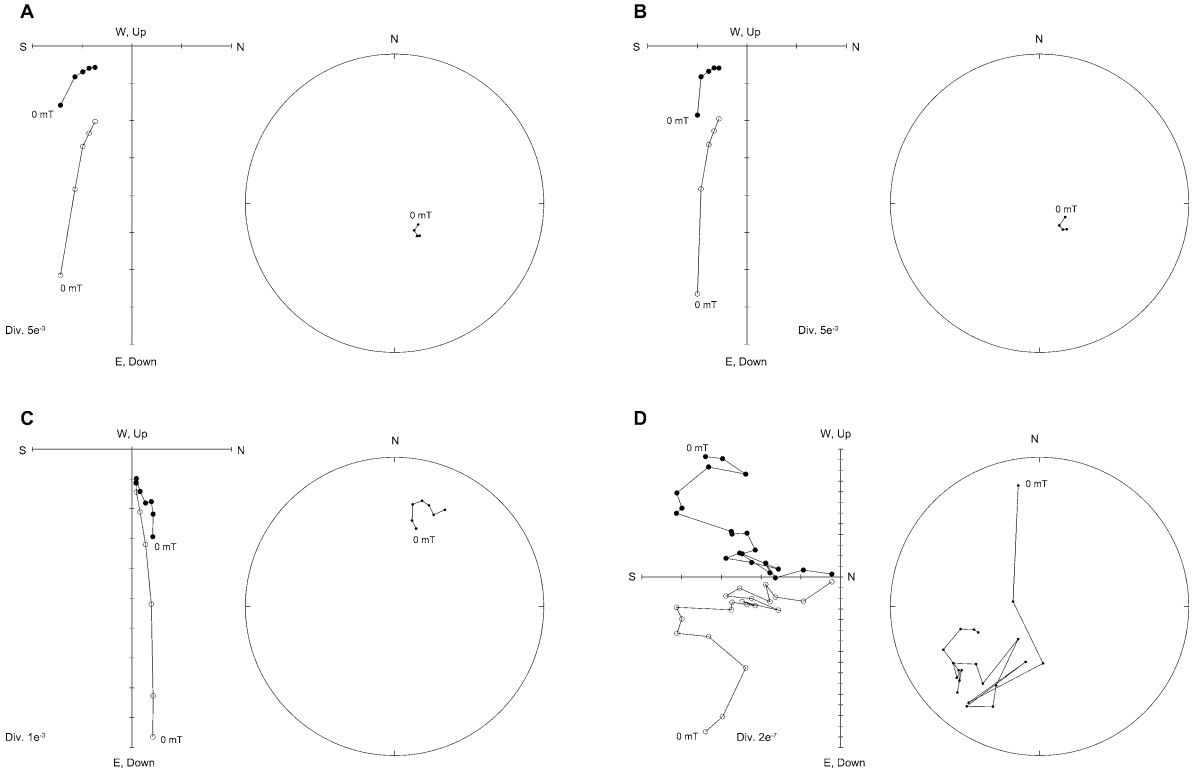

Fig. 5.14 (**A**) Stepwise AF demagnetization (5, 10, 15, and 20 mT) of Section 307-U1316A-1H1 at 0.55 mbsf. (**B**) Stepwise AF demagnetization (5, 10, 15, and 20 mT) of Section 307-U1317A-1H1 at 0.85 mbsf. (**C**) Stepwise AF demagnetization (0, 5, 10, 15, 20, and 25 mT) of Section 307-U1316A-2H5 at 13.75 mbsf. (**D**) Stepwise AF demagnetization (0, 2.5, 5, 7.5, 10, 12.5, 15, 17.5, 20, 22.5, 25, 30, 35, 40, 45, 50, 60, 70, 80, 90, and 100 mT) of Section 307-U1316A-20X1 at 119.07 mbsf. *Left panels* represent orthogonal projections of endpoints of the magnetization vector. *Open circles* = projections on vertical plane, *solid circles* = projections on horizontal plane. *Right panels* represent equal area projection of the magnetization vector during demagnetization

other sections from Site U1316 were demagnetized at 15 and 20 mT. For Holes U1316A and U1316C, NRM and magnetizations after two-step demagnetization were measured on archive halves, whereas for Hole U1316B, whole-round sections were measured. Discrete samples were taken from the working halves of Hole U1316A. Subsequent shore-based measurements were carried out on the discrete samples at the Geophysical Centre of Dourbes. Shore-based measurements showed that in the upper parts of Hole U1316A a characteristic remanent magnetization could indeed be isolated at AF demagnetizations around 15 mT (Fig. 5.14C). However, for discrete samples from the lowermost sections no stable magnetization could be obtained by AF-demagnetization (Fig. 5.14D). Hence, the lowermost sections should be interpreted carefully.

Inclination data cluster around ∼66.00° in the uppermost part and become more scattered at ∼44.40 mbsf in Hole U1316A and ∼45.20 mbsf in Hole U1316B (Fig. 5.15). The upper values are approaching the reference inclination at the study area, which is 66.31° according to the IGRF 2005 (Table 5.1), and can be interpreted as normal polarities belonging to the Brunhes Chron (<0.78 Ma). The more scattered records between 44.40 and 55.06 mbsf in Hole U1316A and 45.20 and 58.30 mbsf in Hole U1316B can be explained by the presence of cold-water coral fragments in this unit. Due to the unreliability of the lowermost sections, correlation to the geomagnetic polarity time scale was not possible below 55.06 and 58.30 mbsf in Holes U1316A and U1316B.

The magnetic intensities in Holes U1316A and U1316B reached values between 15 and 45 mA/m (20 mT intensity) in the uppermost part of the holes and slightly increased to depths of 44.40 mbsf in Hole 1316A and 45.20 mbsf in Hole 1316B (Fig. 5.16). Below these depths, intensities decreased in two steps to fall below 55.06 mbsf in Hole U1316A and 58.30 mbsf in Hole U1316B within the range of the noise level. The intensities follow the same trend as the magnetic susceptibilities (Sect. 5.3), suggesting that the concentration of magnetic minerals, magnetic mineralogy and size of magnetic minerals have a strong impact on the intensities. The impact of the geomagnetic intensity is secondary. However, the effect of the magnetic mineral concentration and composition on the intensity could be normalized by dividing the intensities by the magnetic susceptibilities. The normalized intensities above 55.06 mbsf for Hole 1316A are presented on Fig. 5.16 and can now be compared with the standard palaeointensity curve SINT-800 (Guyodo and Valet 1999) and with the palaeointensity proxies for ODP Site 980 (Channell and Raymo 2003). The normalized palaeo-intensities for this upper unit, correspond well with the reference global SINT-800 palaeointensity stack and the intensities for ODP Site 980. This correlation suggests that the unit between 0 and 45.20 mbsf has an age between 0 and 475 ka (Fig. 5.16). The uppermost metres have to be interpreted carefully as detailed dating studies in a gravity core taken at the same place as IODP Site U1316, suggest the presence of a possible hiatus, with sediments having ages older than 45 ka below the hiatus and sediments having ages around 35 ka just above the hiatus, overlain by a turbidite around 5.50 m (Foubert et al. 2007; see also Sect. 6.2.1). Geophysical and geochemical properties show around the same depth in Hole U1316A a coarser fining-upwards sequence with an erosional boundary (see Sect. 4.4.1).

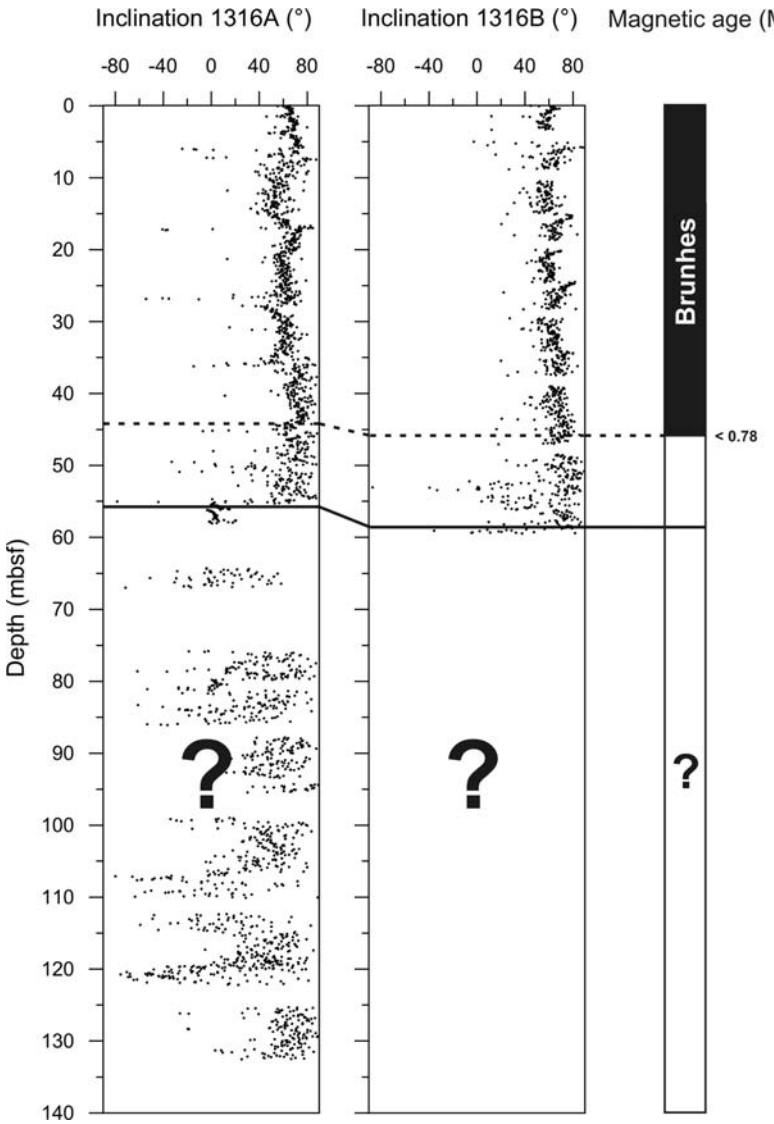

Fig. 5.15 Inclination records at peak fields of 15 mT and interpreted magnetostratigraphic framework in Holes U1316A and U1316B. *Horizontal dashed black line* represents the interpreted Brunhes Chron. *Horizontal solid black line* represents the mound base. Below this base magnetostratigraphic interpretation became impossible (no stable magnetization; Fig. 5.14D)

The extremely depleted values of the magnetic intensities and magnetic susceptibilities in the lowermost sections are greater than can be accounted for by dilution with magnetite-poor sediments and suggest that post-depositional destruction of magnetite has occurred, explaining the scattered directional data at these depths. Florindo et al. (2003) showed that dissolution of magnetite is a common feature in

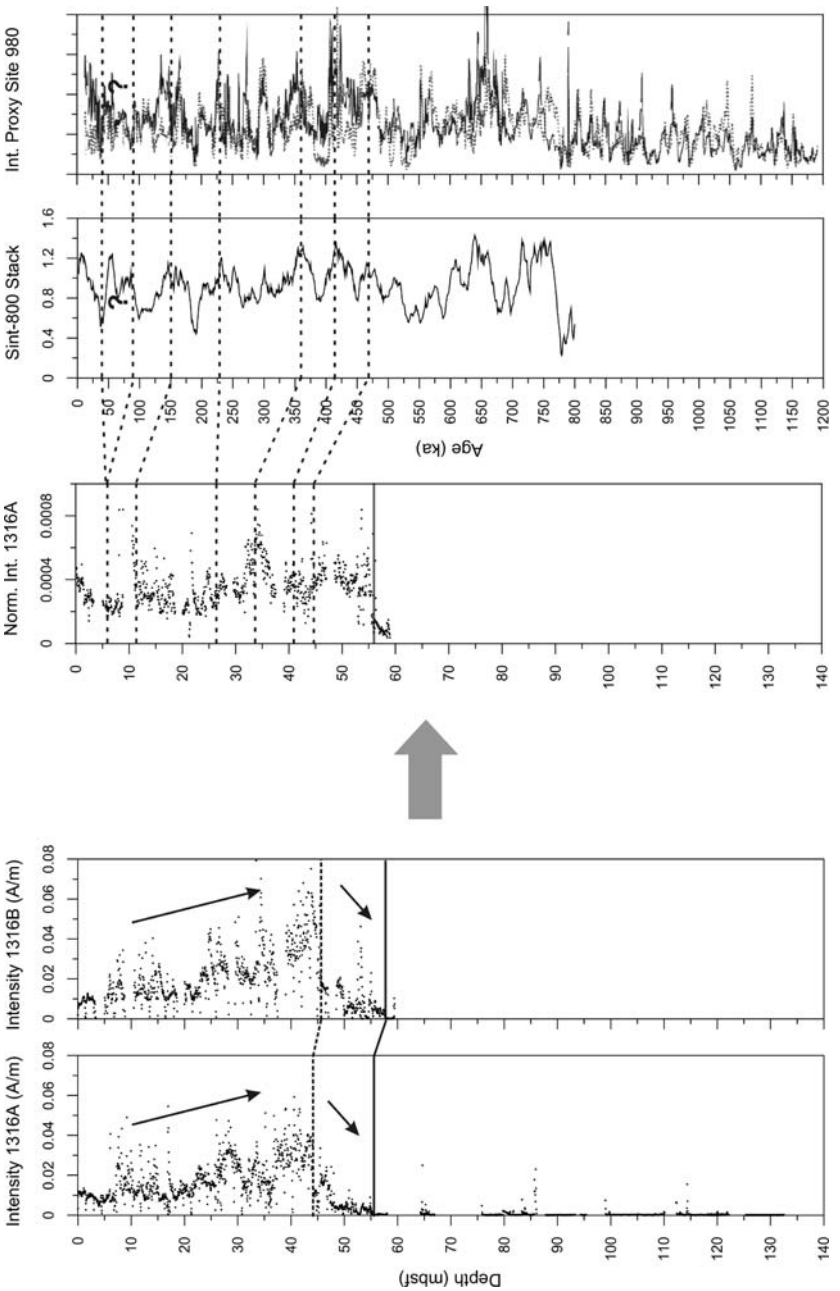

Fig. 5.16 *Left panel*: Intensities at peak fields of 15 mT for Holes U1316A and U1316B. *Right panel*: Comparison of normalized palaeo-intensities of Hole U1316A with SINT-800 Stack (Guyodo and Valet 1999) and normalized intensities of ODP Site 980 (Channell and Raymo 2003). *Horizontal dashed black lines* represent correlation lines between the holes. *Horizontal solid black line* represent the unconformity. Below this base intensities are extremely low (no stable magnetization; Fig. 5.14D)

siliceous sedimentary environments, whereby thermodynamic calculations indicate that magnetite is unstable under conditions of elevated dissolved silica concentrations (and appropriate Eh-pH conditions) and predict that magnetite will break down to produce iron-bearing smectite. Pore water analyses in the off-mound sediments indeed show an increase in silica concentrations in the lowermost sections (Exp. 307 Scientists 2006c).

Sr-isotopic datings on skeletal aragonite confirm the proposed magnetostratigraphic framework for Site U1316 (Kano et al. 2007). The clear changes in magnetic characteristics around 55.06 mbsf in Hole U1316A and 58.30 mbsf in Hole U1316B correspond with a major lithological boundary (Sect. 3.4.1), which can be correlated with the unconformity representing the mound base and representing an age gap of several million years. Sr-isotopic datings at 77.62 mbsf in Hole U1316A point out an age of 16.578 Ma (Kano et al. 2007), while at 31.20 mbsf in Hole U1316A an age is noted of about 0.429 Ma. Sr-isotopic datings in the coral-rich unit at 49.35 mbsf in Hole U1316C, correspond with an age around 2.482 Ma, suggesting that at least a part of the coral-rich units is probably in situ (see also Sects. 3.4.1 and 4.4.1). Biostratigraphic research confirms that the lowermost sections have an Early to Middle Miocene age while the upper units have a Pleistocene age (Exp. 307 Scientists 2006c).

5.4.2 Site U1318

Shipboard palaeomagnetic measurements were conducted on cores from Holes U1318A, U1318B and U1318C. Alternating-field demagnetization of natural remanent magnetization was conducted up to 20 mT in 5 mT steps on core 307-U1318A-1H. Based on this demagnetization experiment (Fig. 5.17A,B), the other sections were demagnetized at 10 and 15 mT. NRM and magnetization after two-step demagnetization were measured on archive halves. Discrete samples were taken on the working halves of cores in Hole U1318B. Shore-based measurements were carried out with the cryogenic magnetometer at the Geophysical Centre of Dourbes, confirming the isolation of the characteristic remanent magnetization for the uppermost sections around 15 mT. Obtaining stable remanent magnetizations in the lowermost sections was difficult (Fig. 5.17C). However, characteristic remanent magnetizations could be calculated by the standard three-dimensional least-squares fit to palaeomagnetic vector data via principal component analyses (PCA) on respectively AF-demagnetization steps 7.5, 10, and 12.5 mT (Kirschvink 1980).

Only the inclination data from the characteristic remanent magnetizations were retained for the interpretation of a magnetostratigraphic framework (Fig. 5.18). For Hole U1318, magnetostratigraphic dating was possible by correlating the inclination records of Holes U1318B and U1318C with the geomagnetic polarity timescale from Lourens et al. (2004) (Table 5.3). The inclination data (Fig. 5.18) cluster around $\sim 66^{\circ}$ above 82.00 and 79.90 mbsf in respectively Holes U1318B and

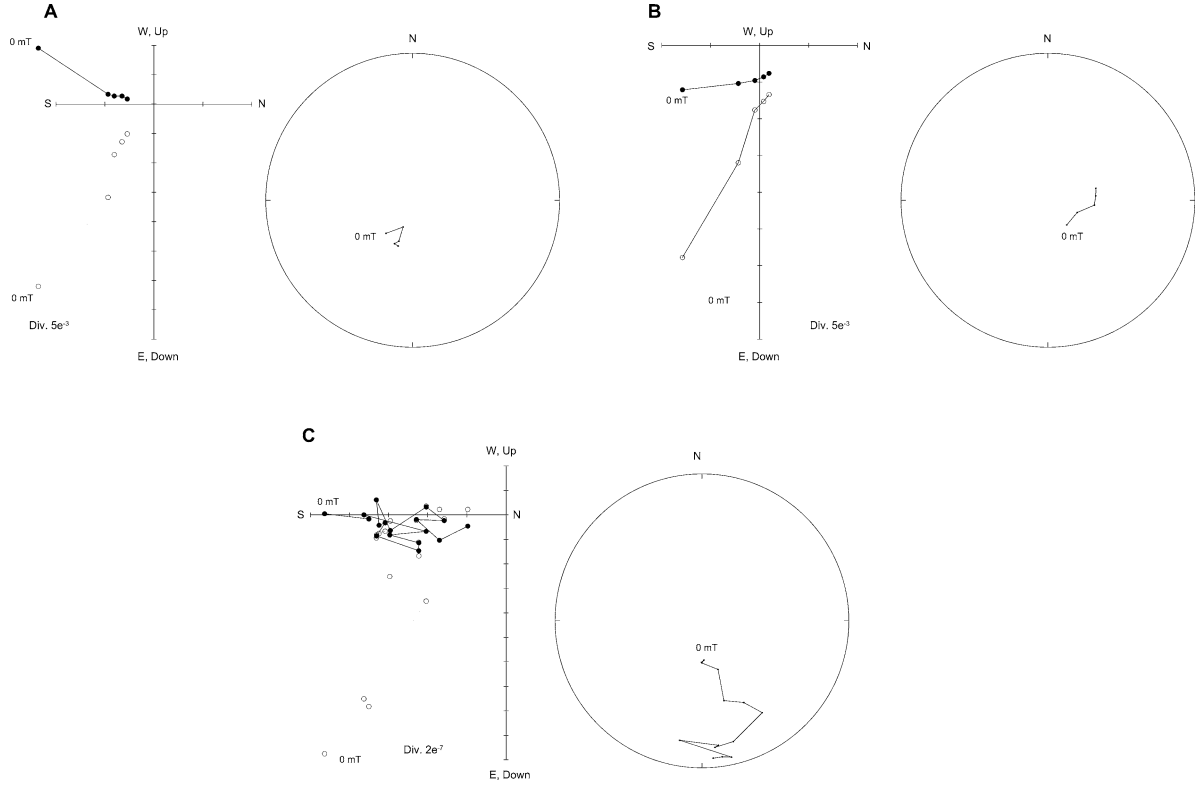

Fig. 5.17 (**A**) Stepwise AF demagnetization (5, 10, 15, and 20 mT) of Section 307-U1318A-1H1 at 0.25 mbsf. (**B**) Stepwise AF demagnetization (5, 10, 15, and 20 mT) of Section 307-U1318A-1H3 at 3.15 mbsf. (**C**) Stepwise AF demagnetization (0, 2.5, 5, 7.5, 10, 12.5, 15, 17.5, 20, 22.5, 25, 30, 35, 40, 45, and 50 mT) of Section 307-U1318B 18X5 at 164.5 mbsf. *Left panels* represent orthogonal projections of endpoints of the magnetization vector. *Open circles* = projections on vertical plane, *solid circles* = projections on horizontal plane. *Right panels* represent equal area projection of the magnetization vector during demagnetization

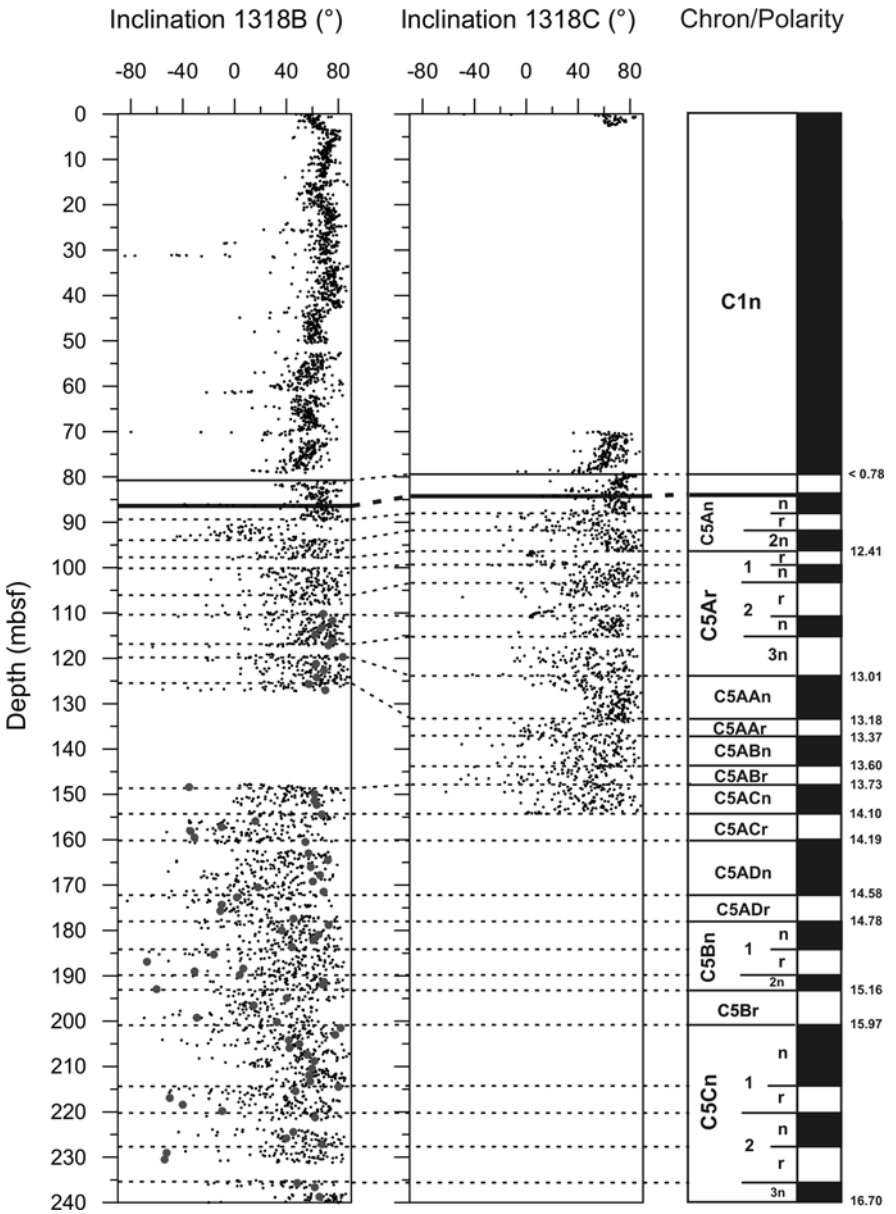

Fig. 5.18 Inclination records at peak fields of 15 mT and interpreted magnetostratigraphic framework in Holes U1318A and U1318B. *Black horizontal dashed lines* represent the interpreted Chrons and Subchrons. *Horizontal solid black line* represent the unconformity, interpreted as the mound base. *Light grey dots* represent the characteristic remanent magnetizations on discrete samples calculated by the standard three-dimensional least-squares fit to palaeomagnetic vector data via principal component analyses (PCA) (Kirschvink 1980)

Table 5.3 Magnetostratigraphic Chrons and Subchrons and corresponding ages according to Lourens et al. (2004), defined in Holes U1318B and U1318C

Normal polarity (Chron/Subchron)	Top [Ma]	Bottom [Ma]	Epoch, stage (approximate)
C1n	0.000	0.781	Pleistocene
C5An.1n	12.014	12.116	Miocene, Serravalian
C5An.2n	12.207	12.451	Miocene, Serravalian
C5Ar.1n	12.730	12.765	Miocene, Serravalian
C5Ar.2n	12.820	12.878	Miocene, Serravalian
C5AAn	13.051	13.183	Miocene, Serravalian
C5ABn	13.369	13.605	Miocene, Serravalian
C5ACn	13.734	14.095	Miocene, Serravalian
C5ADn	14.194	14.581	Miocene, Serravalian
C5Bn.1n	14.784	14.877	Miocene, Langhian
C5Bn.2n	15.032	15.160	Miocene, Langhian
C5Cn.1n	15.974	16.268	Miocene, Langhian
C5Cn.2n	16.303	16.472	Miocene, Langhian
C5Cn.3n	16.543	16.721	Miocene, Burdigalian

U1318C. Below these depths inclination data show a small shift, which can be explained by the presence of more reworked and coarser material in the intervals between 82.00 and 86.20 mbsf (Hole U1318B) and 79.90 and 84.20 mbsf (Hole U1318C). The inclinations of the uppermost sections correspond with the reference inclination of the present geomagnetic field at the drilling site, which is 66.36° according to the IGRF 2005. These positive inclinations can be interpreted as a normal polarity zone corresponding with the Brunhes Chron, which has an age <0.78 Ma. Below 86.20 and 84.20 mbsf, inclination data become more scattered (Fig. 5.18). However, a tentative magnetostratigraphic framework could be proposed for the lowermost sections based on the general inclination trends and taking into account the presence of an important unconformity and some smaller-scaled erosive boundaries. The unconformity is localized at 86.20 and 84.20 mbsf in Holes U1318B and U1318C and corresponds with the mound base unconformity, as discussed in previous chapters. Palynological analyses (Louwye et al. 2008), showed that a latest Middle Miocene age can be proposed for the sediments immediately below the unconformity. This palynological datapoint was used as a palaeomagnetic tiepoint. Figure 5.18 and Table 5.3 represent the tentative magnetostratigraphic framework, and the boundary Chron ages according to Lourens et al. (2004). The lowermost sections have an age between the Late Burdigalian (Chron C5Cn.3n; 16.7 Ma) at 240.00 mbsf and the Late Serravalian at 86.20 mbsf (C5An.1n; 12.01 Ma). The proposed magnetostratographic framework is confirmed by palynostratigraphic analyses (Louwye et al. 2008) and by Sr-isotopic datings (Kano et al. 2007).

Up to 33.00 mbsf in Hole U1318A and 35.05 mbsf in Hole U1318B, magnetic intensities are between 0.002 and 0.020 A/m (Fig. 5.19). At 33.00 mbsf in Hole

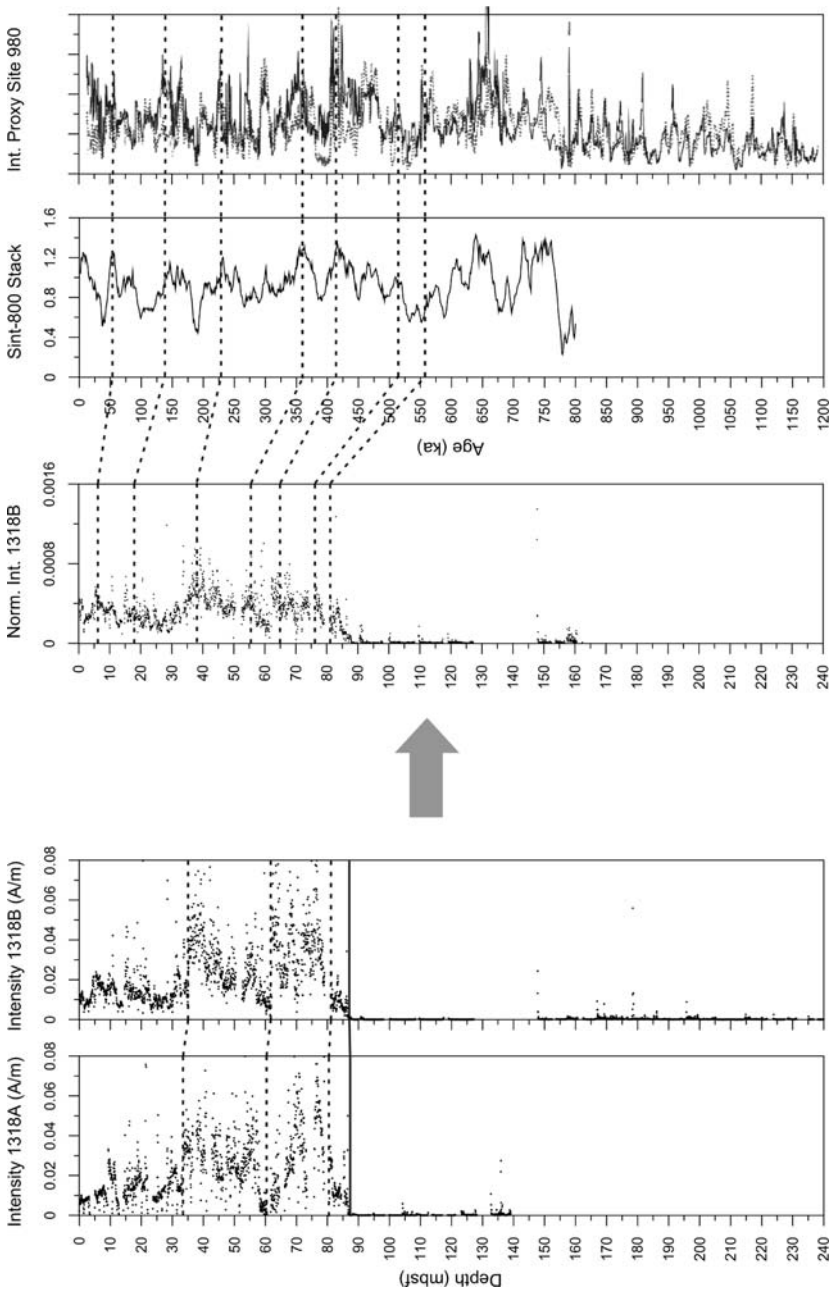

Fig. 5.19 *Left panel*: Intensities at peak fields of 15 mT for Holes U1318A and U1318B. *Right panel*: Comparison of normalized palaeo-intensities of Hole U1318B with SINT-800 Stack (Guyodo and Valet 1999) and normalized intensities of ODP Site 980 (Channell and Raymo 2003). *Black dashed horizontal lines* represent correlation lines between the holes. *Horizontal solid black line* represent the unconformity. Below this base intensities are extremely low (no stable magnetization; Fig. 5.17C)

U1318A and 35.05 mbsf in Hole U1318B, intensities show an increase to 0.03–0.04 A/m and fall to 0 A/m at 60.00–62.00 mbsf. Between 60.00 and 80.70 mbsf in Hole U1318A and between 62.00 and 82.00 mbsf in Hole U1318B, a doublet in magnetic intensity shows the highest values at Site U1318 (up to 0.07 A/m). Below 86.70 mbsf (Hole U1318A) and 86.20 mbsf (Hole U1318B) magnetic intensities drop below extremely low values of 10^{-5} A/m (Fig. 5.19). As at Site U1316, the low susceptibilities and intensities below these depths can be explained by post-depositional destruction of magnetite (Florindo et al. 2003). Similar trends are recognized in the magnetic susceptibilities (Sect. 5.3), suggesting that the concentration of magnetic minerals and magnetic mineralogy have the primary effect on the intensities; geomagnetic intensity being secondary. However, by normalizing the intensity records of Hole U1318B with the magnetic susceptibility, normalized palaeo-intensities could be obtained for the upper interval. Comparing the normalized intensities of Hole U1318B with the standard palaeointensity curve SINT-800 (Guyodo and Valet 1999) and with the palaeointensity proxies for ODP Site 980 (Channell and Raymo 2003), a correlation between these records could be proposed (Fig. 5.19). This correlation, established on Fig. 5.19, suggest that the sediments between 0 and 82.00 mbsf in Hole U1318B have an age between 0 and 550 ka.

5.5 Discussion

Based on the magnetostratigraphy described in previous sections, a general evolution model for Challenger Mound and his surrounding environment can be proposed. This evolution will be described as occurring in four phases: (1) pre-mound phase (Sect. 5.5.1), (2) mound initiation (start-up phase) (Sect. 5.5.2), (3) mound evolution (main mound growth phase) (Sect. 5.5.3) and (4) mound declination (give-up phase) (Sect. 5.5.4).

5.5.1 Pre-mound Phase

Understanding the evolution of the eastern margin of the Porcupine Seabight before the onset of extensive mound development is important as the interaction between tectonic, sedimentary and palaeoceanographic processes may have played an important role in "preparing" the margin towards an environment or habitat where cold-water corals liked to build up mounded structures. The combination of magnetostratigraphy, biostratigraphy and absolute datings on the IODP Holes, especially the holes recovered at Site U1318, made it possible to frame the pre-mound evolution of the eastern margin of Porcupine Seabight and to evaluate and interpret the unconformity interpreted as the mound base more accurate as suggested before based on high-resolution seismic data (De Mol et al. 2002; Van Rooij et al. 2003).

Palaeomagnetic and biostratigraphic data indicate a Late Burdigalian (Chron C5Cn.3n; 16.7 Ma; 240.00 mbsf) to Late Serravallian (C5An.1n; 12.01 Ma; 86.20

mbsf) age for the sediments below the unconformity at Hole U1318B. Sr isotopic datings point to slightly younger ages below the hiatus at Site U1318, but are in the same age range (Kano et al. 2007). Sr-isotopic datings at Site U1316A show ages of 16.578 Ma (77.62 mbsf) below the unconformity (Kano et al. 2007), suggesting that the unconformity is representing a bigger time hiatus at Site U1316 than at Site U1318. This evidences that the sediments (lithological unit 3) at Hole U1318 are indeed best preserved to study the evolution of the eastern margin before cold-water corals started to colonize this margin.

The lowermost sediments at Site U1318 (240.00–190.30 mbsf) have an age from Late Burdigalian to Early Langhian and can be correlated with lithological unit 3C, consisting of consolidated silty clay to fine-grained sand with a varying carbonate content of approximately 25–35 wt.% (Exp. 307 Scientists 2006e). This unit can be tentatively correlated with the upper strata of seismic unit U3 (Van Rooij et al. 2003; Van Rooij 2004) (Fig. 5.20). Based on the relative and absolute datings, a (Early to) Middle Langhian to Early Serravallian age can be attributed to the next layer of sediments (190.30–121.00 mbsf) correlating with unit 3B consisting of

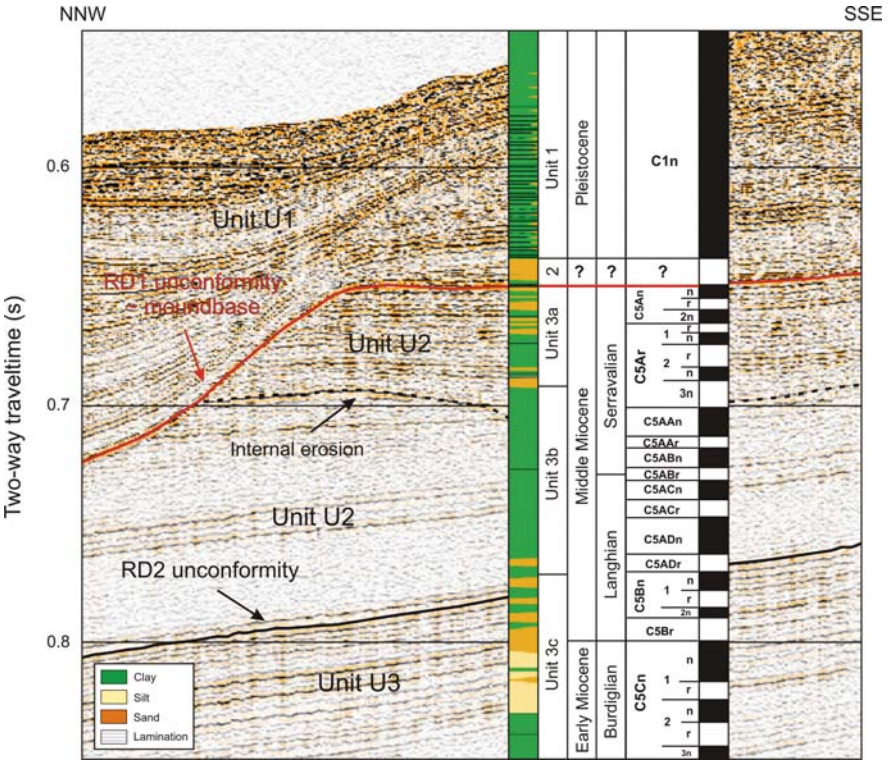

Fig. 5.20 Correlation between magnetostratigraphic time framework, lithological units as defined by Exp. 307 Scientists (2006e) and seismic units as defined by Van Rooij et al. (2003) along a N-NW to S-SE transect at Site U1318

consolidated silty clay with a carbonate content varying between 10 and 20 wt.% and abundant bioturbation (Exp. 307 Scientists 2006e). This unit can be correlated with the lowermost strata of the seismic unit U2 (Fig. 5.20).

For sediments just below the unconformity (121.00–86.20 mbsf) an age can be attributed from (Early to) Middle Serravallian to Late Serravalian corresponding with lithological unit 3A, consisting of consolidated silty clays interbedded with well-sorted fine-grained sand and carbonate contents between 27 and 50 wt.%. Lithological unit 3A is characterized by an erosive boundary at its base, separating lithological unit 3A from lithological unit 3B. This small erosive boundary is also observed on the seismic data as an internal erosional unconformity filled with a very complex facies, resembling a cut-and-fill geometry, within seismic unit U2 (Fig. 5.20). This internal erosional unconformity is not yet described as such. The uppermost sediments can be correlated with the strata of seismic unit U2 above this erosional unconformity.

The RD2 discontinuity, separating seismic units U3 and U2 and described by Van Rooij et al. (2003) as an erosive discontinuity genetically related to the introduction of Norwegian Sea Water (NSW) in the North Atlantic, most probably represents a hiatus of minor magnitude since it is not readily reflected as a major shift in the dinoflagellate cyst assemblage (Louwye et al. 2008). Also the magnetostratigraphic record does not show a major break or shift in the data. It can be suggested that the event causing the RD2 discontinuity observed on seismic profiles took place during early Middle Miocene times ($\pm$ 15 Ma) but is not as erosive as pointed out by Van Rooij et al. (2003).

Louwye et al. (2008) calculated some palaeoenvironmental indices, including parameters such as temperature, diversity, terrestrial influence and productivity signal, based on the fossil dinoflagellate cyst assemblage to interpret the records in terms of palaeoclimatic changes. These authors suggested a dominance of neritic species throughout Hole U1318B, probably transported from the shelfal areas to the deeper depositional areas, evidencing the fact that the main sediment supply zone is located on the Irish and Celtic shelves (Rice et al. 1991). Between 241.00 mbsf to approximately 144.00 mbsf, a dominance of thermophylic dinoflagellate species is encountered in Hole U1318B (Louwye et al. 2008). A sudden increase of cold-water indicating dinoflagellate cysts is observed at 139.00 mbsf, followed by a short return of warm water indicating species in the uppermost sediments below the unconformity (Louwye et al. 2008). During the Late Oligocene a warm phase set in during which the extent of the Antarctic ice-sheets reduced and the temperature of the bottom waters increased. This warming period culminated in the Middle Miocene Climatic Optimum, which is well documented in the marine and continental realm from several proxies and lasted approximately from 17.00 to 14.50 Ma (Zachos et al. 2001; Böhme 2003). A gradual cooling phase set in after 14.50 Ma and was characterized by several short-lived glaciations (Miller et al. 1998). Zachos et al. (2001) considered the astronomical forcing by long-period orbital cycles to be the driving factor behind Neogene climate changes. The lowermost units can be interpreted as deposited during the Middle Miocene Climatic Optimum. The observed drop in thermophylic dinoflagellate species at 139.00 mbsf can be paralleled with the onset

of the global, climatic cooling phase which occurred after the Middle Miocene Climatic Optimum. The relative dating (magnetostratigraphy and biostratigraphy) places the distinct cooling event at 139.00 mbsf in Chron C5ABn at approximately 13.60 Ma. The erosive event observed on the seismic profiles within seismic unit U2 and at the base of lithological unit 3A can be interpreted as caused by this climatic cooling phase coinciding with a change in the oceanographic circulation patterns characterized by the increasing influence of Norwegian Sea Deep Water (NSDW) flow in the North Atlantic. It can be supposed that the effects of the increasing influence of NSDW in the North Atlantic Ocean during Early to Middle Miocene times were not yet fully established. This can explain the minor hiatus represented by the RD2 unconformity. However, around 13.00 Ma the influence of this NSDW in the North Atlantic could have had a major impact on the sediments in PSB resulting in local erosion surfaces as the internal erosive discontinuity (Fig. 5.20). Isotopic data from DSDP Sites 116 and 610 evidences that major NSDW overflow began in the late Middle Miocene around 12.00–13.00 Ma. This was confirmed by Stoker et al. (2005) which recognized a regional expansion of contourite development after the so-called C20 discontinuity in these regions. Stoker et al. (2005) interpreted the onset and acceleration of NSDW overflow since Middle Miocene times to be a consequence of tectonic inversion in the Faroe-Shetland area, which changed the geometry of the Wyville-Thomson Ridge Complex so as to facilitate the opening of the Faroe conduit as a passageway for the exchange of intermediate and deep-water masses between the Atlantic Ocean and the Nordic Seas. It may be no coincidence that with the development of this oceanic circulation pattern, there was a progressive cooling of the northern hemisphere climate linked to the development of both northern and southern gateways (Zachos et al. 2001).

The youngest sediments below the unconformity at Site U1318 are thus of Late Serravalian age. However, it remains unknown whether the unconformity located at the top of the section, which can be correlated with the RD1 unconformity (Van Rooij et al. 2003) is precisely located at the Serravalian-Tortonian boundary or somewhere in the upper parts of the Serravallian. Louwye et al. (2008) suggested that the upper boundary of the studied section, can be correlated with the major sequence boundary Ser4/Tor1 at 10.50 Ma (Hardenbol et al. 1998). However, as mentioned before, the RD1 unconformity is a discontinuous unconformity and his lateral variability is described in earlier studies (Van Rooij et al. 2003; Van Rooij et al. 2007b). Based on the absolute and relative datings it can be suggested that the RD1 unconformity represents a hiatus of minimum 8.00 Ma as the youngest sediments below the unconformity have an age around 10.50 Ma and the oldest sediments encountered above the unconformity have an age around 2.60 Ma (for discussion see Sect. 5.5.2). It might be questioned if the erosion event responsible for such a major hiatus may have occurred at once or in several steps, which may explain the lateral variability. Praeg et al. (2005) has proven that Late Cenozoic tectonic movements affected the continental margins around the NE Atlantic in the Early Pliocene, resulting in kilometre-scale domal uplift of onshore and shallow shelf areas, coeval with accelerated offshore subsidence. These movements have been linked to a Late Neogene global plate reorganization (Cloetingh et al. 1990).

Stoker et al. (2005) correlated the C10 unconformity (interpreted as a late Early Pliocene boundary) along the NE European Atlantic margins as formed by a combination of tilting in shelf areas and submarine erosion in deep-water basins caused by a Late Neogene plate reorganization both in the Atlantic and the Pacific regions (Pollitz 1988; Cloetingh et al. 1990). It can be supposed that an epeirogenic tilting of the margins in the Late Cenozoic occurred in different phases, responsible for the lateral variability of the unconformity. However, global oceanographic changes during this period cannot be neglected. The closure of the Central American Seaway by the formation of the Isthmus of Panama in the Late Miocene to Early Pliocene resulted in the replacement of a circum-equatorial circulation pattern by an interpolar flow (Haug and Tiedemann 1998; Lear et al. 2003), resulting in the redirection of warm and saline water masses to high northern latitudes (Lear et al. 2003). This may have strengthened the formation of North Atlantic Deep Water and consequently an increase in submarine erosion along the NE Atlantic margins. The redirection of warm and saline water masses to the north might have also influenced the current patterns in Porcupine Seabight dramatically, resulting in erosion of the eastern margin. However, Stoker et al. (2005) suggested that the intensity of the current flow and submarine erosion is likely to have been enhanced by changes in the configurations of basins and the elevation of bathymetric thresholds, induced by the Early Pliocene large-scale tilting of the margin (Cloetingh et al. 1990).

5.5.2 Mound Initiation

Relative magnetostratigraphic dating and absolute datings have shown that the mound started to grow in the Late Pliocene (Gelasian) around 2.70 Ma (Gauss Chron) at Hole U1317E, i.e. the hole localized closest to the summit of Challenger Mound. The start-up phase in the holes localized more towards the flanks of Challenger Mound, seems to be a bit younger as the transition towards the Gauss Chron could not be identified anymore in these holes (Fig. 5.3). This suggests that the nucleation point for the onset of cold-water coral growth, and so mound growth can be situated below the top of Challenger Mound. More evidences for an earlier start-up phase towards the top of Challenger Mound is found in the cyclic record of the geophysical properties, whereby an extra cycle is noted just above the mound base in Hole U1317E (see Sect. 4.2.2).

It can be questioned what triggered cold-water coral growth, and so mound growth during this period. It is obvious that the start-up phase of mound growth coincides with the onset of major northern hemisphere glaciations. The onset of glaciations near 3 Ma is thought to owe to a gradual cooling trend over the last 4 Ma (Shackleton and Hall 1984; Raymo 1994; Ravelo et al. 2004), which is itself part of a longer-term trend over the last 50 Ma (Zachos et al. 2001). Marine sedimentary records of ice rafted debris and oxygen isotopic composition revealed major glacial expansions at 2.50 Ma (Shackleton et al. 1984) and 2.70 Ma (Haug et al. 1999). Mudelsee and Raymo (2005) found that northern hemisphere glaciations started as

early as 3.60 Ma and ended at 2.4 Ma. They suggest that such a long-term increase points to slow tectonic forcing such as closing of gateways or mountain building as the root cause of northern hemisphere glaciations. However the exact cause of even these well-studied transitions from a greenhouse world (Crowley 1991) to a world with periodically waxing and waning ice-sheets (Berger et al. 1984) remain unknown. Anyway, it is evidenced that the oceanographic circulation underwent major changes most probably caused by tectonic activities just before the onset of the northern hemisphere glaciations, which played an important role in Porcupine Seabight by creating the RD1 unconformity as substrate for the onset of cold-water coral growth and which may have played an important role in initial cold-water coral growth by the redirection of warm and saline water masses to the north (see Sect. 5.5.1). The introduction of the high saline Mediterranean Outflow Water in the North Atlantic Ocean during this period, might play locally in the Porcupine Seabight an important role (De Mol et al. 2002).

Freiwald et al. (1999) pointed out that cold-water corals prefer to settle on hard substratum on an elevated position where enough nutrients are available. The external input of nutrients is often regarded as one of the most important factors thriving cold-water coral growth (Freiwald et al. 1999; Mortensen 2000; Roberts et al. 2006). It should be mentioned that no specific hardgrounds, dropstones or hard substrates are observed within the IODP core sections which might have been an initial settling surface. However, the Miocene substrate can be described as consolidated silts and clays which probably was a sufficient consolidated surface for cold-water coral growth. The presence of bivalves moulds and conglomerate above the unconformity at Site U1318, suggest that also conglomerate might have been a nucleation point where cold-water corals started to settle on. However, no obvious conglomerate is found at the mound site. Anyway, it should be reminded that sampling a mound of 1.5 km in width and 150 m in height with cores of 6 cm in diameter might have missed the nucleation point of mound growth. Once the cold-water corals started to grow, a self-sustaining mechanism can keep the corals growing, as old cold-water coral framework can provide new substrate for further enhanced cold-water coral growth. Van Rooij et al. (2003) evidenced that the erosive events responsible for the creation of the RD1 unconformity left behind a topographic irregular landscapes with terraced-like features. These authors suggested that most of the mounds started to grow on a topographic irregularity or a scarp created by the RD1 erosive event, so a topographic high which may have favourized cold-water coral growth by creating micro-habitats rich in nutrients. Another factor playing an important role in mound growth is the interaction between sediments and currents (Foubert et al. 2005a; Huvenne et al. 2005; Wheeler et al. 2005b). Currents should be high enough to prevent the living polyps to be buried but should be from that sort that it allows baffling of transported sediments to make mound growth possible (Foubert et al. 2005a; Huvenne et al. 2005; see also Chap. 7). The presence of enhanced currents is thus required to keep the living polyps sediment-free. The vigorous bottom currents, responsible for the creation of the RD1 unconformity may have been sustained throughout the Pliocene and the Early Pleistocene triggering cold-water coral growth.

5.5.3 Mound Evolution

Once the initial mound building phase was set up, the mound came in an important growth episode. Relative magnetostratigraphic dating and absolute dating revealed that the mound was in an important mound growth phase between ~2.60 and ~1.60 Ma, showing that about 125 m of the mound was built in approximately 1 million year. Sedimentation rates calculated based on the magnetostratographic tiepoints, illustrate the highest mound growth rates around 2.15 Ma (~Réunion Subchronozone). Moreover, the highest sedimentation rates are during this period noted at Hole U1317E closest to the summit of the mound, suggesting that the mound was then in a vertical growth phase, while mound growth at the flank of the mounds was limited. This is also evidenced by the presence of more cycles in the geophysical properties during this period at the top of the mound, compared to the flank of the mounds. The opposite is true for the period, following up this extensive vertical mound growth phase around 2.15 Ma, characterized by a decrease in mound growth rates going from the flank of the mound to the top of the mound. This evidences that the mound started to expand in horizontal direction after 2.00 Ma, resulting in extra cycles in the geophysical properties at the flank of the mound. So, it can be suggested that the main mound growth phase can be divided in two growth episodes: (1) a vertical growth episode from 2.60 Ma until ~2.00 Ma and (2) a horizontal growth episode from ~2.00 Ma until ~1.60 Ma.

Important to note is that no sediments are encountered in the off-mound region during this main mound growth phase. This evidences the presence of vigorous bottom currents during this period preventing sedimentation in the off-mound regions. Only lithological unit 2 described in the holes at Site U1316 evidences of the presence of sediments deposited during the extensive mound growth phase. However, some of the coral-rich sediments in this interval can be autochthonous (Sect. 3.5.1). The same can be supposed for the sediments in lithological unit 2 at Site U1318, which are characterized by reworked sandy sediments and the presence of conglomerate (Sect. 3.5.2). Such a condensed unit can bear witness of the high bottom current regime during the period of mound growth, resulting in non-deposition in the off-mound regions. Moat structures around the mound, clearly observed on seismic data (Van Rooij et al. 2003), evidence also the presence of high bottom currents during mound build-up.

5.5.4 Mound Decline

Two important hiatus are noted in the uppermost mound sediments. The first one is situated around 25.00 mbsf and represents a time hiatus of more than 500 ka (~1.00–1.60 Ma), corresponding with an abrupt lithological change. A second hiatus of minor magnitude is present around 4.00 mbsf but is not recovered in as much detail in all the IODP Holes. However, a gravity core (MD01-2450) on the some location as the IODP Holes, confirm the presence of this hiatus. The age constraints on the uppermost hiatus are not that well-established, but Sr isotopic datings on the skeletons of cold-water corals revealed ages of 571 ka below the hiatus in Hole

U1317E (Kano et al. 2007), while U/Th datings showed ages older than 250 ka just below the hiatus in the gravity core (MD01-2450) (Sect. 6.4.2). The sediments just above the second hiatus belong probably to MIS 6 (Sect. 6.4.2).

Really low mound growth rates are noted above the first hiatus (25.00 mbsf), suggesting that the mound started to decline around 1.00 Ma. This seems to coincide with the onset of the Mid-Pleistocene Revolution (MPR). The Mid-Pleistocene Revolution is the term used to describe the transition between 41 and 100 ka glacial-interglacial cycles which occurred about 1 million years ago (Maslin and Ridgwell 2005). However, not only does the periodicity of glacial-interglacial cycles increase going through the MPR, but there is also an increase in the amplitude of global ice volume variations. The ice volume increase may in part be attributed to the prolonging of glacial periods and thus of ice accumulation (Maslin and Ridgwell 2005). So, the MPR could be thought of not as a transition to a new mode of glacial-interglacial cycles *per se*, but simply the point at which a more intense and prolonged glacial state and associated subsequent rapid deglaciation became possible. Lisiecki and Raymo (2007) show that the relative duration of interglacial stages decreases during the MPR. Many authors suggest this MPR as occurring in two phases (Mudelsee and Stattegger 1997). Helmke et al. (2005) evidenced such a systematic, gradual change in the sedimentation patterns of the Nordic seas region. A first distinct change occurred around 1 Ma and revealed the beginning of a shift in climate periodicity from stronger 41 ka cycles towards a dominant 100 ka cyclicity, while the most pronounced changes in the sedimentary environment occurred between 700 and 420 ka (Helmke et al. 2005). Such a two-phase evolution of the MPR may explain the two hiatus in the uppermost mound sediments, whereby the second hiatus may represent the definitive decline of Challenger Mound. The switch to more intensive glaciations might have been noxious for cold-water coral growth and mound build-up. Moreover, Raymo et al. (1990) and Ferretti et al. (2005) evidenced that the oceanographic circulation patterns were also changing during the MPR. In particular, North Atlantic Deep Water (NADW) was produced strongly during most of the period from 2.50 to 1.50 Ma ago, and after this time it was greatly weakened allowing water from the Antarctic to penetrate far northward in the Atlantic; finally, during the last 0.70 Ma these periods of weak NADW production corresponds to times of peak glaciations. This periods of weak NADW production, might have shutdown the transport of warm surface waters and vigorous MOW towards the north, which can have resulted in quieter bottom current conditions in Porcupine Seabight. Such quieter bottom current conditions where not sufficient for cold-water corals to keep their polyps any longer sediment free and to allow nutrient-rich waters reaching the zones of extensive cold-water coral growth.

Remarkable is that palaeointensity variations evidence the onset of sedimentation in the off-mound regions around 550 ka at Site U1318 and around 475 ka at Site U1316. This sudden onset of off-mound sedimentation might be a reflection of the more intensive glaciations after the MPR in Porcupine Seabight coinciding with an increase in terrigenous input from the shelves. Indeed, ice-sheets are inferred to have formed over Ireland and Britain only during the last 0.50 Ma (Bowen 1989; Bowen 1991). The more, Sejrup et al. (2005) showed that only in glacial episodes during the last 0.50 Ma ice-sheets reached the shelf edge along the whole NW

European margin. Subglacial drainage networks and tunnel-valleys across Ireland and in the Irish-Celtic Sea (Wingfield 1990; Warren and Ashley 1994) may have supplied sorted sediment directly to the shelf edge to be received by slope canyons, as the Gollum channel system, which may have become again inactive since the end of the last glaciation (Tudhope and Scoffin 1995; Unnithan et al. 2001; Weaver et al. 2000; Wheeler et al. 2003).

5.6 Summary

The interpretation of inclination records and palaeointensity records allowed building up a magnetostratigraphic framework for the mound records at Site U1317 and the off-mound sediments at Sites U1316 and U1318. A four-phase general evolution model for Challenger Mound and his surrounding environment could be proposed. During a **pre-mound phase** the eastern margin was prepared for the onset of cold-water coral growth by an erosive event, probably caused by a combination of uplifting of the continental margins and associated changes in bottom current regimes, cutting in older deposited units. A **Late Burdiglan (Chron C5Cn.3n; 16.70 Ma) to Late Serravalian (C5An.1n; 12.01 Ma)** is attributed to the sediments at Site U1318 below the unconformity deposited during the Middle Miocene Climatic Optimum and a subsequent cooling phase around 13.60 Ma. **Mound initiation** started between **∼2.50 and ∼ 2.70 Ma** at Site U1317, coinciding with the onset of the northern hemisphere glaciations. **Mound evolution** occurred in two important mound growth episodes: (1) a **vertical growth episode** from **∼2.60 Ma until ∼2.00 Ma** and (2) a **horizontal growth episode** from **∼2.00 Ma until ∼1.60 Ma**. **Mound decline** started probably around **∼1.00 Ma**. The switch towards more intense and prolonged glacial states during the Mid-Pleistocene Revolution (MPR) may have been responsible for the decline of mound growth. Extensive **off-mound sedimentation** started around the same period, respectively at **475** and **550 ka** at Sites U1316 and U1318, reflecting the more intensive glaciations after the MPR in Porcupine Seabight coinciding with an increase in terrigenous input from the shelves.

The interplay between **terrigenous sedimentation** (with the supply of paramagnetic Fe-rich clay minerals (mainly illite and chlorite), diamagnetic quartz and ferrimagnetic magnetite), **biogenic sedimentation** (diamagnetic calcium carbonate) and **diagenesis** (dissolution of ferrimagnetic magnetite and formation of paramagnetic pyrite) controls the susceptibility records. The anisotropy in magnetic susceptibility evidenced that the sediments in the mound are deposited by **northward directed currents** ensuing **alongslope transport** of sediments.

Tuning the susceptibility records to standard oxygen isotopic records, made it possible to define a **stacked susceptibility record** calibrated in age for the mound sediments (**SUSMOUND**). Spectral analysis of the susceptibility records and the tuned records revealed some **spectral characteristics** of Milankovitch cyclicity between the mound base (∼2.50–2.70 Ma) and a major hiatus present around 25.00 mbsf (∼1.67 Ma), suggesting **climatic forcing**.

Chapter 6
The Top of the Record: On-Mound and Off-Mound

Before the R/V JOIDES Resolution ever entered the Porcupine Seabight to drill Challenger Mound, the top of different mounds and their surrounding environments were already subjected to many detailed studies to unveil the top of their secrets. A systematic sampling of the top of different on-mound and off-mound records was carried out with the Calypso piston corer and the gravity corer aboard the R/V Marion Dufresne during the MD123-Géosciences campaign in September 2001. Within the EC FP5 programmes GEOMOUND and ECOMOUND these cores have been extensively studied.

In this chapter, the on-mound and adjacent off-mound records from two mound sites, respectively Challenger Mound and Mound Perseverance, localized in two different mound provinces in Porcupine Seabight, respectively the Belgica Mound Province and the Magellan Mound Province, will be discussed and compared with the long IODP records. Both provinces show nowadays clear differences in their hydrodynamic environment. This study evidences that also during the past the sedimentological environment of both provinces differ clearly, which can have an important impact on cold-water coral growth and carbonate mound development. Geophysical properties (P-wave velocity, gamma density and magnetic susceptibility), colour reflectance, X-ray imagery, medical (macro-scaled) computer tomographic (CT) scanning, geochemical XRF logging, grain size analysis, isotopic measurements ($\delta^{18}O$ and $\delta^{13}C$ measurements, and ^{14}C-dating) and U/Th dating on cold-water coral fragments are used to identify and describe the recent past sedimentation regimes and the respective palaeoceanographic and palaeoclimatological settings of both mound sites. The more, due to poor sampling of the top of the IODP records, a detailed study of the uppermost sediments sampled with other sampling gear, allows interpreting also the upper records of Challenger Mound in an adequate way.

6.1 Material and Methodology

The cores available for this comparative on-mound versus off-mound study were obtained with a Calypso piston corer (off-mound cores) and a gravity corer (on-mound cores) aboard the R/V Marion Dufresne during the MD123-Géosciences

A. Foubert, J.-P. Henriet, *Nature and Significance of the Recent Carbonate Mound Record*, Lecture Notes in Earth Sciences 126, DOI 10.1007/978-3-642-00290-8_6,

Table 6.1 Localization and characterization of the studied cores MD01-2450, MD01-2451G, MD01-2452, and MD01-2459G

Core	Recovery [m]	Depth [m]	Type	Latitude	Longitude
MD01-2450	11.97	944	Calypso	51°22′31.27″	11°43′48.71″
MD01-2451G	12.84	762	Gravity	51°22′47.99″	11°43′03.45″
MD01-2452	18.43	617	Calypso	52°19′23.78″	12°41′28.61″
MD01-2459G	10.79	610	Gravity	52°18′00.60″	13°02′51.00″

campaign (September 2001), within the framework of the EC FP5 GEOMOUND project. Two on-mound cores (MD01-2451G and MD01-2459G) and two off-mound cores (MD01-2450 and MD01-2452) have been retained for this detailed on-mound versus off-mound study (Table 6.1) (Foubert et al. 2007).

The Calypso piston core MD01-2450 has a recovery length of 11.97 m and is situated at the SW flank of Challenger Mound in the Belgica Mound Province at a water depth of 944 m, corresponding with the location of IODP Site U1316 (Fig. 6.1). Gravity core MD01-2451G with a recovery length of 12.84 m is situated on top of Challenger Mound at 762 m water depth, corresponding with the location of IODP Site U1317 (Fig. 6.1). A general description of Challenger Mound and a site survey of his near-by environment and the Belgica Mound Province are given in Chap. 2. An overview of the actual hydrodynamic surface processes and the recent appearance of the sea-floor in the Belgica Mound Province are discussed in Chap. 7. Sidescan sonar imagery and video imagery shows the presence of coarse sediments and numerous bedforms in between the mounds indicative of strong bottom currents and active sediment transport (de Haas et al. 2002; Huvenne et al. 2005; Wheeler et al. 2005b; Foubert et al. 2005a; see also Chaps. 2 and 7).

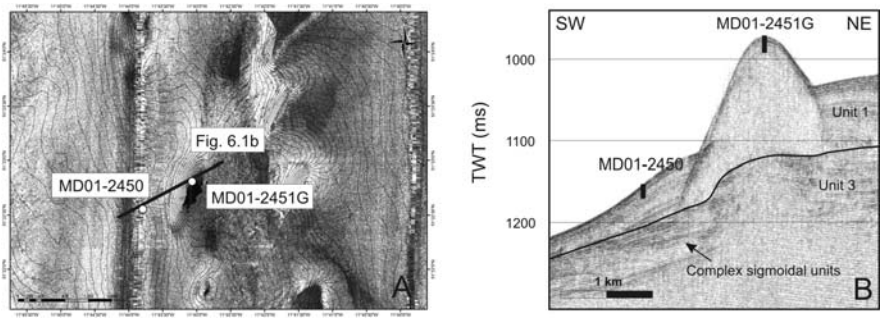

Fig. 6.1 Localization of cores MD01-2450 and MD01-2451G (Belgica Mound Province). (**A**) TOBI sidescan sonar imagery of Challenger Mound and his surroundings (de Haas et al. 2002) and detailed multibeam bathymetry (Beyer et al. 2003). Contour interval is set at 10 m. (**B**) SW-NE orientated RCMG sparker profile with localization of core sites MD01-2451G and MD01-2450 and seismic-stratigraphic features, as defined by Van Rooij et al. (2003)

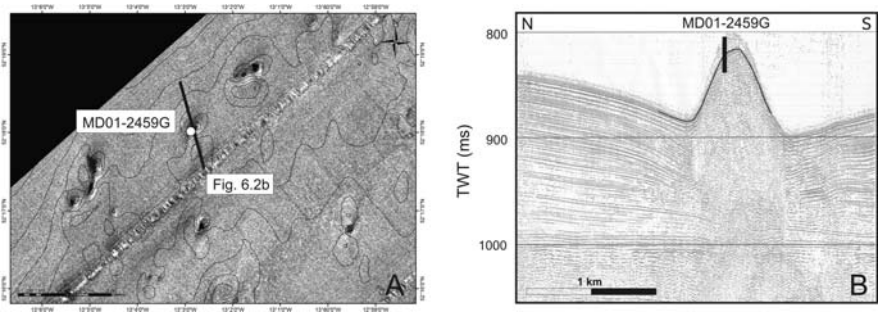

Fig. 6.2 Localization of core MD01-2459G (Magellan Mound Province). (**A**) TOBI sidescan sonar imagery of Mound Perseverance and his surroundings (de Haas et al. 2002) and GSI multibeam bathymetry. Contour interval is set at 10 m. (**B**) NNW-SSE orientated RCMG sparker profile with localization of core site

The second mound site is located within the Magellan Mound Province situated at the northern margin of the Porcupine Seabight (see Chap. 1). More specific, gravity core MD01-2459G with 10.79 m recovery length, is localized on top of Mound Perseverance at 610 m water depth (Fig. 6.2). The calypso piston core MD01-2452 has a recovery length of 18.43 m and is situated in the sediments above some buried Magellan Mounds at a water depth of 617 m (Fig. 6.3). A detailed study of the Magellan Mound Province has been performed by Huvenne et al. (2002, 2003, 2007). On TOBI sidescan sonar imagery the Magellan Mound Province appears as an area with a homogeneous acoustic facies of medium, although rather "grainy" backscatter strength (Huvenne et al. 2005), which can be linked to bioturbated muddy or silty hemipelagic sediments (Kenyon et al. 1998). The seabed has a gentler slope and a more regular appearance, without erosion or sedimentation patterns, such as bedforms, as observed in the Belgica Mound Province (Chaps. 2 and 7). Most

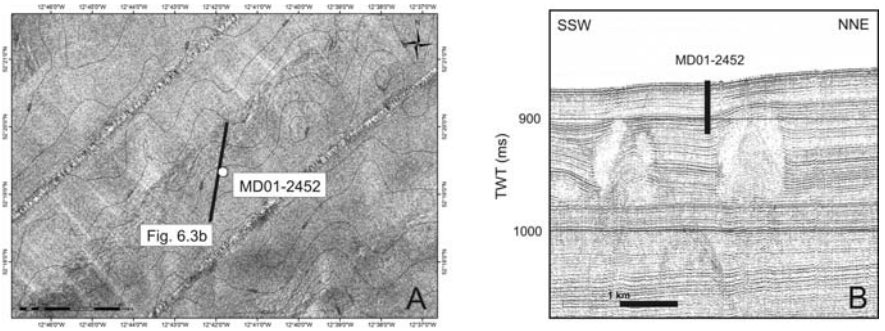

Fig. 6.3 Localization of core MD01-2452 (Magellan Mound Province). (**A**) TOBI sidescan sonar imagery of sediments above buried Magellan Mounds (de Haas et al. 2002) and GSI multibeam bathymetry. Contour interval is set at 10 m. (**B**) SSW-NNE orientated RCMG sparker profile through core site

mounds are buried under a sediment drape but some mounds (like Mound Perseverance) form clear features in the topography. Mound Perseverance is elevating about 50 m above the present-day seabed and is elongated in NNE/SSW direction. The sediments over and around the buried Magellan Mounds are characterized by a seismic unit of semi-parallel stratified reflections, sometimes abut abruptly against the mound flanks, and in other cases bent downwards creating a depression or a moat surrounding the mound (Huvenne et al. 2007).

All four cores were analysed with the GEOTEK Multi Sensor Core Logger at a resolution of 2 cm, measuring magnetic susceptibility (Bartington loop sensor MS2B), GRAPE density (Cs^{137} source with energies principally at 0.662 MeV) and P-wave velocity (P-wave "piston" transducers) on whole-round sections.

The Calypso piston cores (MD01-2452 and MD01-2450) were opened, described and photographed with a digital camera. The colour reflectance was measured with a Minolta colour spectrophotometer. The gravity cores (MD01-2451G and MD01-2459G) were at a first stage left unopened and submitted to X-ray analyses with the SCOPIX X-ray equipment installed at the University of Bordeaux (DGO, Université Bordeaux I) to estimate the coral content and the coral distribution. SCOPIX uses classical X-ray equipment (X-ray source: 160 kV, 19 mA), coupled with new radioscopy instrumentation (CCD camera 756 × 581 resolution), connected to a computer for data acquisition and processing (Migeon et al. 1999). All whole-core sections (150 cm long) were cut in two representing sections of 75 cm, in order to reduce weight of the chariot. The whole-cores were put in the chariot and parts of 10 cm were X-rayed and digitally processed and saved (Fig. 6.4). The X-ray images were then plotted in intensity grey scale logs. The density of a substance is the predominant factor determining X-ray attenuation (as in X-ray CT scanning) (Lofi and Weber 2001). In a second phase the on-mound gravity cores (MD01-2451G and MD01-2459G) were frozen and subsequently split with a diamond saw blade. The

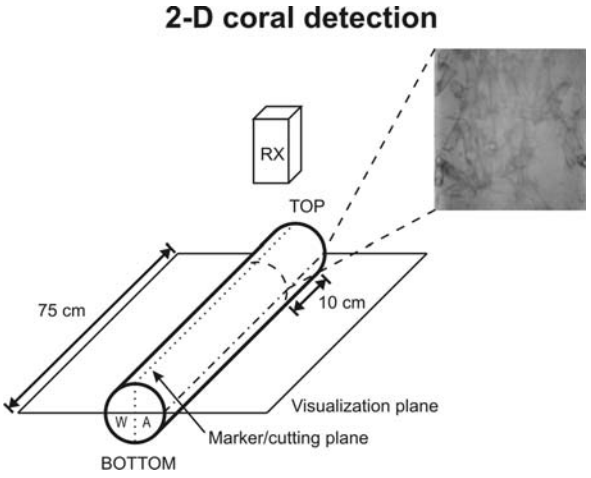

Fig. 6.4 Method of two-dimensional X-ray analyses for unopened cores containing coral fragments as used with SCOPIX (DGO, University Bordeaux I)

split core sections were described and photographed with a colour line scan camera imaging system (consisting of a custom built 3 × 1024 CCD line scan imaging system) installed at the Royal Netherlands Institute for Sea Research (NIOZ) in Texel. Detailed visualization of the coral fragments in a three-dimensional environment was realized by the medical CT-scanner SOMATOM Sensation 64 from Siemens, installed at their Medical Solutions research centre in Forchheim (Germany) (see Chap. 3).

Geochemical elemental composition of the on-mound cores (MD01-2451G and MD01-2459G) was determined with the AVAATECH XRF core scanner installed at the Royal Netherlands Institute for Sea Research (NIOZ) (www.avaatech.com). Element intensities were measured in two runs with a resolution of 1 cm. In a first run, a 30 s count time and a computer controlled forced air cooked Oxford 50 W X-ray source operating at a current of 0.15 mA and 10 kV was used to obtain accurate element intensities for the elements ranging from Al to Co. In a second run, a 30 s count time and an X-ray source operating at a current of 0.8 mA and 30 kV resulted in element intensities for the elements ranging from Zn to Zr, including the Sr count rates which can be important for the mound sediments containing cold-water coral fragments. Additional geochemical logging was carried out on the off-mound core MD01-2450 using the CORTEX XRF core scanner installed at the Geosciences Department of the University of Bremen (Röhl and Abrams 2000) (see Chap. 4). Scans were run for 30 counts at 20 kV with a resolution of 5 cm. The data from both XRF scanners were processed using the KEVEX^{TM} software Toolbox©. In this study, mainly the Ca count rates, as an indicator for the amount of carbonate in the core, the Fe count rates, as a proxy for the influx of terrigenous material, and the Sr records, as a proxy for the amount of cold-water coral fragments, will be discussed.

Grain size analyses were performed on the off-mound core MD01-2450 using the Malvern Laser Particle Sizer Mastersizer 2000 installed at the University College of Cork and are in detail described and discussed by Kozachenko (2005) and Jurkiw (2005). Only the data relevant for this comparative on-mound versus off-mound study will be highlighted in this chapter.

Stable oxygen and carbon isotopic analyses were performed on core MD01-2450 at the Isotope Lab Bremen University using a Finnigan MAT 251 mass spectrometer. About 5 individual specimens of 2 benthic foraminiferal species, *Cibicides wuelerstorfi* and *Cibicides kullenbergi,* and about 20 specimens of the planktic foraminifer *Neoglobigerina pachyderma* were selected each 10 cm. The isotopic composition of the foraminiferal tests was determined on the CO_2 gas evolved by treatment with phosphoric acid at a constant temperature of 75°C. Working standard (Burgbrohl CO_2 gas) was used for all stable isotope measurements. All $\delta^{18}O$ and $\delta^{13}C$ data have been calibrated against PDB by using the NBS 18, 19, and 20 standards and are given relative to the PDB standard. Analytical standard deviations are about ±0.07% PDB for $\delta^{18}O$ and ±0.05% PDB for $\delta^{13}C$. Isotopic measurements are in detail discussed by Jurkiw (2005). Only the data relevant for this comparative on-mound versus off-mound study will be highlighted in this chapter.

Radiocarbon datings (AMS ^{14}C), using mono-species samples (∼10 mg) of the planktonic foraminifera *Neogloboquadrina pachyderma* (either dextral or sinistral)

from the fraction between 125 and 250 μm at specific sampling depths in piston core MD01-2450, were performed at the Leibniz Laboratory for Age determinations and Isotope Research at IFM-GEOMAR (Nadeau et al. 1997). The data were corrected for ^{13}C and calibrated to kilo-years before present (ka BP) using the software Calib 4.3 (Stuiver and Reimer 1993). Radiocarbon datings were used in this chapter to test the hypothetic palaeoclimatological models based on the geochemical and geophysical measurements.

Well-selected coral species from the top of the gravity cores MD01-2451G and MD01-2459G were sampled for U/Th dating. $^{230}Th/U$ datings were measured in the Laboratoire des Sciences du Climat et de l'Environnement (LSCE) in Gif-sur-Yvette with a thermal ionization mass spectrometer Finnigan MAT262. Some of these measurements are discussed by Frank et al. (2005), but a new series of measurements has shed a new light on these first results (Frank et al. subm.) and will be presented in this chapter.

Additional foraminiferal and coccolith assemblage studies were performed on core MD01-2452 (Thierens 2005), but will not be extensively discussed in this chapter.

6.2 Off-Mound Records

The off-mound cores are studied in order to provide a tentative palaeoclimatic framework. A first palaeoclimatic framework and palaeoceanographic interpretation for the top record of the off-mound sediments in the Belgica Mound Province (MD99-2327) was already proposed and discussed by Van Rooij et al. (2007a). Taking into account these observations and observations in Late Cenozoic records of the NE Atlantic Ocean, Foubert et al. (2007) proposed an identification key for the off-mound records in the Porcupine Seabight to interpret geophysical and geochemical properties in terms of palaeoclimatological changes. Glacial-interglacial variations can be seen in the background variations of the magnetic susceptibility signals (Grousset et al. 1993; Robinson et al. 1995). Changes in magnetic susceptibility are due to changes in the concentration and the composition (grain size and/or mineralogy) of the present magnetic minerals (see Chap. 5). These variations in Late Cenozoic sediments of the NE Atlantic Ocean can be driven by changes in carbonate productivity and amount of ice rafted debris (IRD) driven by oceanographic changes triggered by climatic changes. Warmer periods have a lower susceptibility background signal, colder periods a higher. The individual maxima, with more than an order of magnitude difference compared to the background signals, can be explained by high-frequent ice rafting events (IRE) characterized by the deposition of sandy, magnetite-rich IRD (Robinson et al. 1995; Thouveny et al. 1994, 2000; Richter et al. 2001). Gamma density and P-wave velocity reflect changes in the lithology and porosity, which could be interpreted in terms of changing oceanographic and palaeoclimatic conditions. Interglacial periods within the PSB seem to be characterized by coarser material due to enhanced currents (Van Rooij

et al. 2003; 2007a,b), whereas glacial periods are characterized by the deposition of finer material witnessing of quieter deposition environments. Individual IRE corresponds to maxima in gamma density and P-wave velocity due to the abrupt increase of coarser material (IRD). However, the gamma density should be interpreted with caution because a slightly increase in the density by going downwards can be explained by compaction. Cortijo et al. (1995) have shown that the reflectance can be an estimation of the carbonate productivity and so reflection of changing oceanographic conditions due to glacial-interglacial variations. Changes in carbonate productivity are also reflected in the Ca count rates, while the Fe count rates can be used as a proxy for the amount of terrigenous material (see also Chap. 4).

Palaeoclimatological and palaeoceanographic models based on geophysical and geochemical properties only have to be interpreted with great caution as other factors (diagenesis,. . .) can overprint the original records (see Chap. 4). However, correlating the interpreted units with the isotopic curves and absolute datings (Jurkiw et al. 2005; Kozachenko 2005), confirmed the proposed palaeoclimatic frameworks and the potential use of geophysical and geochemical properties to interpret palaeoenvironmental changes.

6.2.1 MD01-2450: SW Flank of Challenger Mound

The off-mound core MD01-2450 can be divided in four units and six distinctive layers based on a comparison of the lithology with the measured geophysical and geochemical parameters (Fig. 6.5). A detailed description of the four units, respectively from the top to the base of the core, will be given in the next paragraphs to establish a palaeoclimatic framework.

6.2.1.1 Unit A (0–210 cm)

The upper part of the core (0–210 cm) consists of homogeneous structureless olive gray silty clays with common to abundant nannofossils and a few sulphide specks. The susceptibility increases slightly from the base to the top of the core, while the gamma density decreases towards the top. The decrease in gamma density can be explained by a combination of the loosely packed uppermost sediments and a lack of sandy material, which is normally expected at the present-day sea-floor (Foubert et al. 2005a; see also Chap. 7). The P-wave velocity values are not trustable in unit A due to a bad contact of the P-wave transducers with the cores during data acquisition. Ca count rates are decreasing towards the top of the unit, while Fe count rates are increasing. The lack of typical Holocene foraminiferal-rich sands in this unit, the dominant presence of fine silty clays and the tendency for higher susceptibilities, higher Fe count rates and lower Ca count rates compared to the subsequent units, form evidences that the sediments from unit A are witnessing a colder period. The maxima in gamma density and susceptibility around 50 cm can indicate the presence of IRD, and so probably the imprint of an IRE. A second maxima in gamma density is observed around 175 cm, followed by a relatively small peak

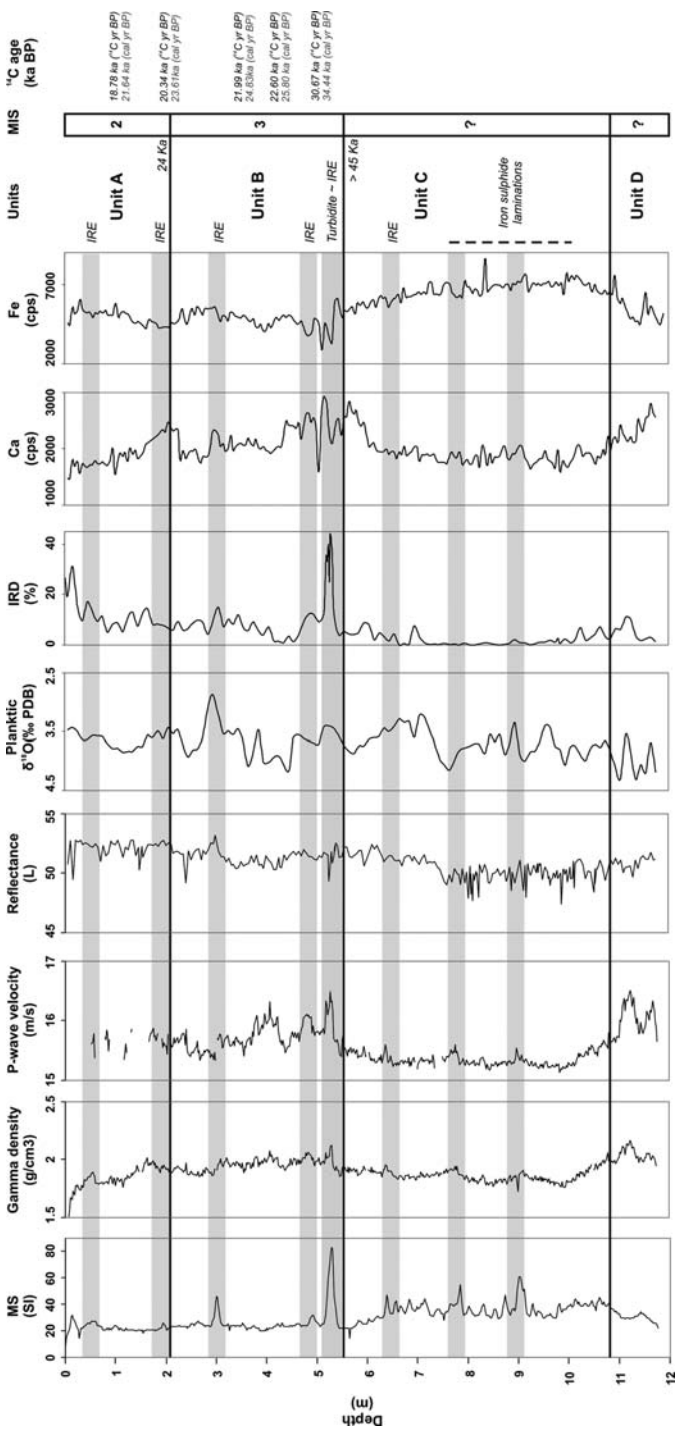

Fig. 6.5 (continued)

in susceptibility around 195 cm. The combined interpretation of both parameters suggests the presence of a second IRE between 170 and 200 cm. This second maximum is also observed in the Ca count rates, suggesting that the present IRD consists of a Ca-rich fraction. No corresponding peak is observed in the Fe count rates.

6.2.1.2 Unit B (210–540 cm)

Generally, this part of the core consists of olive grayish bioturbated silty clays with common to abundant nannofossils and few sulphide specks. Fine to medium sandy intercalations and a few centimetre-scale silt layers are present in between the silty clays. The gamma density and P-wave velocity present higher and more fluctuated values in unit B due to the pockets and intercalations of sand- and silt-sized material. Also Ca and Fe intensities are fluctuating more than in unit A. The more, Ca count rates seem to be a bit higher than in unit A, while Fe count rates seem to be a bit lower. The higher abundance of coarser material and the higher Ca count rates (and lower Fe count rates) can correspond to a slightly warmer period, taking into account the interpretations of Van Rooij et al. (2003, 2007a).

All geophysical parameters (magnetic susceptibility, gamma density, P-wave velocity and reflectance) correspond with maxima at depths around 300 and 485 cm which can be explained by the presence of IRD (visualized at 485 cm core depth by the presence of medium-sized dropstones) deposited during IRE. The second IRE in this unit features again a slightly offset in the density and P-wave velocity maxima (at 480 cm depth) from the maximum in magnetic susceptibility (at 490 cm depth). Remarkable is that the Ca count rates are also increasing in the same depth intervals, while Fe count rates are decreasing. However, as the offset observed in the density and P-wave velocity maxima, an offset can also be observed between a Ca peak at 480 cm (corresponding with the maximum in P-wave velocity) followed by a minor Fe peak at 490 cm (corresponding with the maximum in susceptibility). A similar Ca peak, followed by a minor Fe peak is observed for the maximum around 300 cm.

An important change in lithology can be observed between 510 and 540 cm core depth. Visual observations suggest a coarsening downwards trend from 510 cm on to a gravely sand layer with an erosional basal contact at 535 cm. At the same depth a distinctive peak is registered in the susceptibility, gamma density and P-wave velocity, while the reflectance corresponds with a minimum. Previous observations suggest the record of a mass event such as a turbidite. The presence of dropstones in the same interval suggests that probably a combination of an ice rafting event with a turbiditic event contributes towards the creation of the remarkable sedimentary record

Fig. 6.5 Interpretation of core MD01-2450 based on magnetic susceptibility (10^{-5} SI), gamma density (g/cm^3), P-wave velocity (m/s), reflectance (L*), Fe and Ca intensities (counts/s) and correlation with radiocarbon datings (AMS ^{14}C) (Jurkiw 2005), δ^{18}O (‰ PDB) records (Jurkiw 2005) and IRD measurements (percentage >150 μm) (Kozachenko 2005). A tentative correlation with Marine Isotopic Stages (MIS) according to Martinson et al. (1987) is proposed. *Light grey boxes* correspond with possible ice rafting events (IRE). *Dark grey box* corresponds to turbidite

at these depths. In this interval, a Ca maximum is followed by a Fe maximum. It can be assumed that the Ca maximum correspond with the IRD material, while the Fe maximum corresponds with the turbiditic material.

6.2.1.3 Unit C (540–1080 cm)

Unit C (540–1080 cm) is build up of silty clayey material, similar as in unit A, but typified by a high concentration of sulphide specks and sulphide concentrations turning into clear frequent semi-parallel sulphide-laminations (FeS) between 750 and 1050 cm. Each layer is approximately 1–2 cm in thickness and occurs with an average spacing of 1–2 cm. The higher and more irregular susceptibility signals within this unit can be explained by the high concentration of iron sulphide concretions and laminations (Thompson and Oldfield 1986; Maher and Thompson 1999; Roberts 1995). Sulphate reduction, in this case probably due to the mineralization of organic material, can lead to a pronounced overprinting or modification of the primary sediment composition by dissolution of minerals and precipitation of authigenic minerals (Berner 1970, 1984). Magnetic iron oxides (e.g. magnetite) dissolve under sulfate- and iron-reducing conditions and/or subsequent precipitation of authigenic minerals at different sediment levels may alter the magnetic signals and seriously influence the interpretation of the sedimentary magnetic record (Karlin and Levi 1983, 1985). The black colour of the laminations is expressed in the lower and irregular values of the reflectance at the corresponding depth intervals. The general background signals of the gamma density and P-wave velocity are lower than in unit B. Fe count rates are generally higher, while Ca intensities are generally lower than in unit B. Combined with the silty clayey lithology as in unit A and a general higher background value of the magnetic susceptibility, this suggest the presence of a cold period.

Around respectively 640, 780, and 900 cm parallel peaks in magnetic susceptibility, P-wave velocity and gamma density are observed, which can be explained by the presence of IRD, deposited during IRE. No correlating maxima in the Ca records are recognized, but small correlating peaks in the Fe intensities have been observed.

6.2.1.4 Unit D (1080–1180 cm)

From 1080 to 1180 cm (unit D), core MD01-2450 is composed of poorly sorted dark greyish silt with an intercalation of foram-rich fine sandy material between 1095 and 1130 cm comparable to the material as observed in box core samples and video-imagery from the present-day sea-floor (Foubert et al. 2005a). The magnetic susceptibility is low at the base of the core and slightly increases by going upwards. The gamma density and P-wave velocity are high compared to the previous described units. Ca count rates increases, while Fe intensities decreases. The similarities in lithology with the present-day situation (Holocene) as well as the rather low susceptibilities and high Ca count rates suggest the start of an interglacial

period or the last culmination of a warm period before the onset of a colder period in unit C.

6.2.2 MD01-2452: Magellan Mound Province

Core MD01-2452 shows clear variations in the background signals of the geophysical parameters, which suggest a tentative correlation with climatic changes (Fig. 6.6). Four units can be distinguished and different IRE, analogous to these observed in core MD01-2450.

6.2.2.1 Unit A (0–120 cm)

Unit A (0–120 cm) consists of fine grayish brown sand to dark grayish brown silty clay with pockets of fine sand. The top of the unit (0–20 cm) is characterized by pure foraminifera-rich sand, characteristic for the sediments found at the present-

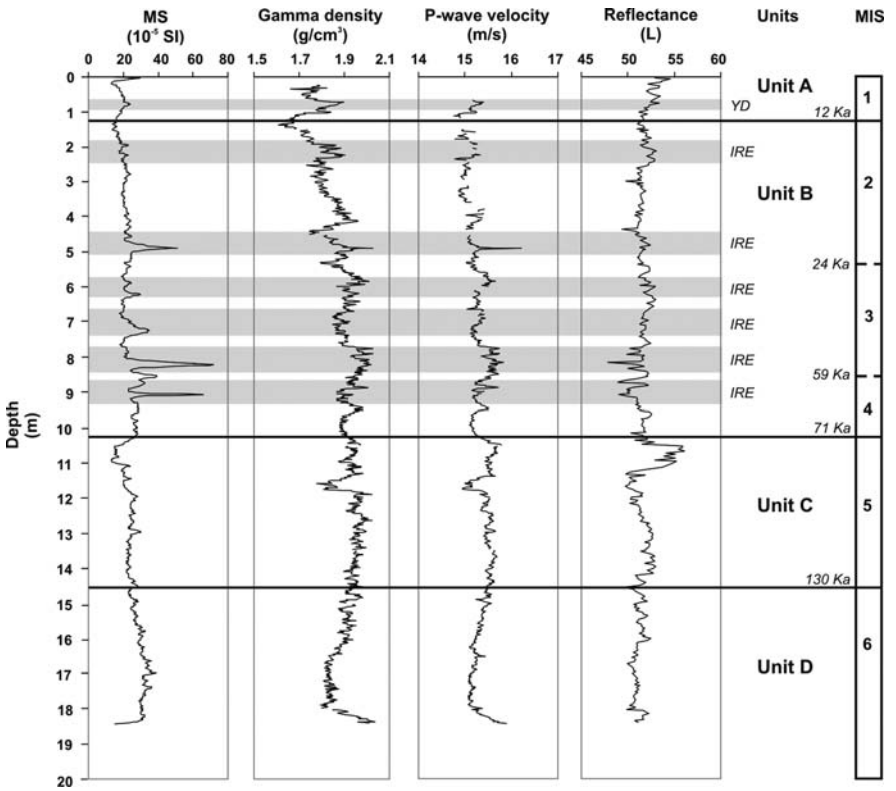

Fig. 6.6 Interpretation of core MD01-2452 based on magnetic susceptibility (10^{-5} SI), gamma density (g/cm^3), P-wave velocity (m/s) and reflectance (L*). *Grey boxes* correspond with IRE. A tentative correlation with Marine Isotopic Stages (MIS) according to Martinson et al. (1987) is proposed

day sea-floor in the Magellan Mound Province (Huvenne et al. 2005) and thus can be interpreted as pure Holocene sand. The presence of more sandy material in the uppermost unit bears witness of a warmer period. The small maximum in susceptibility, gamma density and P-wave velocity at 78 cm core depth can indicate the presence of IRD in this uppermost part of the core, probably due to a last cold meltwater induced change in the ocean–atmosphere circulation during the early stages of deglaciation towards the warmer Holocene. This event is known as the Younger Dryas (YD) cooling.

6.2.2.2 Unit B (120–1030 cm)

Unit B is composed of dark grayish brown silty clays with rare to abundant nannofossils. Few faint sulphide streaks can be observed throughout the bioturbated clays. The presence of silty clays combined with higher values of the susceptibility and lower values for reflectance in unit B compared to unit A can be explained by the presence of a record of sediments deposited during a colder period (the last glacial period). Between 540 and 878 cm slightly higher gamma densities (due to the presence of centimetre-scale layers of fine to medium sand from 812 to 870 cm) and a higher reflectance (higher carbonate content) witnesses of a warmer period within this glacial. The individual maxima (respectively around 210, 480, 600, 700, 800, and 900 cm core depth) superimposed on the background signal of the susceptibility, gamma density and P-wave velocity are the consequence of the presence of IRD, deposited during IRE. Most of these maxima show a multiple character (Fig. 6.6). Maxima in susceptibility and gamma density are preceded and/or followed by a smaller peak. Moreover, a small offset in the maximal susceptibility peak and the maximum in gamma density can be observed (e.g. IRE around 900 cm with a maximum in gamma density at 895 cm core depth and a maximum in susceptibility at 905 cm core depth). Such a multiple character and offset was also characteristic but less pronounced for the observed IRE in core MD01-2450.

6.2.2.3 Unit C (1030–1450 cm)

From 1030 to 1140 cm unit C presents light brownish gray fine to medium sized sands gradually going over between 1140 and 1450 cm in dark grayish brown bioturbated clays with faint sulphide streaks. The abrupt decrease in magnetic susceptibility and increase in reflectance are probably due to the increase in carbonate content triggered by the culmination of a warm period between 1030 and 1140 cm.

6.2.2.4 Unit D (1450–1843 cm)

Unit D (1450–1843 cm) is characterized by the typical dark grayish brown silty bioturbated clays with few faint sulphide streaks. Between 1600 and 1800 cm mm-scale silty laminae are recognized within the silty clay going over in clayey silt with scattered pockets of coarse silt at the bottom of the core. This unit is characterized by higher susceptibility values and lower density, P-wave velocity and reflectance values compared to unit C, evidencing of a colder period.

6.3 On-Mound Records

The main information about the on-mound cores was interpreted from a combination of the physical and the geochemical properties data, and the X-ray imagery. For the on-mound core MD01-2451G, additional information was provided by 3D X-ray CT-scanning. X-ray imagery allowed the identification of dead cold-water coral fragments and an estimation of the density of these fragments throughout the core sections before they were opened.

Different "radiofacies" were observed, distinguished by the coral content (Fig. 6.7): a facies with no corals but only sediment (Fig. 6.7A), a combined facies consisting of small coral and bioclastic fragments (debris) embedded in a matrix of silty sediments (Fig. 6.7B) and a facies with large coral chunks filled up by sediments (sediment filled coral framework) (Fig. 6.7C). In both last defined facies the coral skeletons are darker than the surrounding sediments, which mean that the coral chunks are denser than the sediments. A fourth facies is identified that seems to be

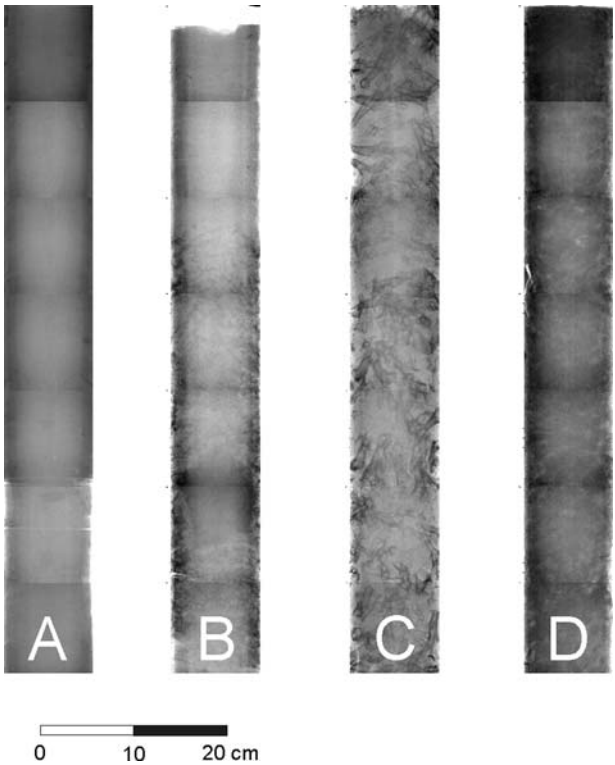

Fig. 6.7 Four different "radiofacies", based on the coral content (X-ray imagery); darker values represent denser material: (**A**) facies with no corals but only sediment, (**B**) a combined facies consisting of small coral and bioclastic fragments (debris) embedded in a matrix of silty sediments, (**C**) facies with large coral chunks filled up by sediments (sediment filled coral framework), (**D**) facies with altered and dissolved coral fragments

on first sight homogenous (Fig. 6.7D). A closer look learns that this facies is characterized by coral fragments figured on the X-ray images with a lighter colour than the surrounding sediments. So, the corals seem to be less dense than the surrounding sediment. This facies is interpreted as an altered coral-rich facies whereby corals are completely dissolved leaving skeleton footprints and carbonate-rich sediments behind.

The interpretation of the X-ray images from both studied on-mound cores are schematized on Figs. 6.8 and 6.9. Magnetic susceptibility, gamma density and chemical element intensities can be correlated with the information extracted from the X-ray images. Presented below is an overview and description of the alternating coral-rich, coral-poor and sediment-rich units and layers as observed on the X-ray imagery and their correlation with the geophysical and geochemical properties for respectively core MD01-2451G (top of Challenger Mound) and core MD01-2459G (top of Mound Perseverance).

6.3.1 MD01-2451G: Top of Challenger Mound

Based on the geophysical properties, geochemical properties (Ca, Fe and Sr intensities) and the X-ray imagery, generally two distinctive units can be recognized in core MD01-2451G (Fig. 6.8).

6.3.1.1 Unit A (0–400 cm)

The upper 400 cm of core MD01-2451G is characterized by a high-frequent alternation of three distinctive coral-rich layers and three layers with homogeneous to bioturbated or laminated sediments (Fig. 6.8). The top of the core (0–40 cm) is composed of small coral rubble debris and broken bioclastic fragments, corresponding with a declining susceptibility pattern towards the top. High Ca and Sr intensities evidence the presence of coral fragments embedded in a Ca-rich matrix.

Between 40 and 219 cm bioturbated sediments are present with some apparent dropstones from 60 to 70 cm (Fig. 6.8). The whole layer corresponds to elevated magnetic susceptibility values and Fe intensities. Sr count rates drop towards really low values, evidencing the lack of aragonite-rich material as cold-water coral fragments. The dropstone interval (60–70 cm) can be correlated with a remarkably peak in magnetic susceptibility and gamma density at the same depth level, suggesting an ice rafted origin. A correlating small peak is also recognized in the Ca count rates, suggesting the presence of Ca-rich IRD. The transition from this layer to the

Fig. 6.8 Magnetic susceptibility (10^{-5} SI), density (g/cm^3), Fe, Ca and Sr count rates (counts/s), X-ray log and image stack for core MD01-2451G in function of depth (m). Insets display detailed features of dropstones (indicated with *arrows*) and fine laminated sediments going abrupt over in the coral-rich unit B. *Grey boxes* represent possible ice rafting events (IRE). U/Th datings are noted (Frank et al. subm.)

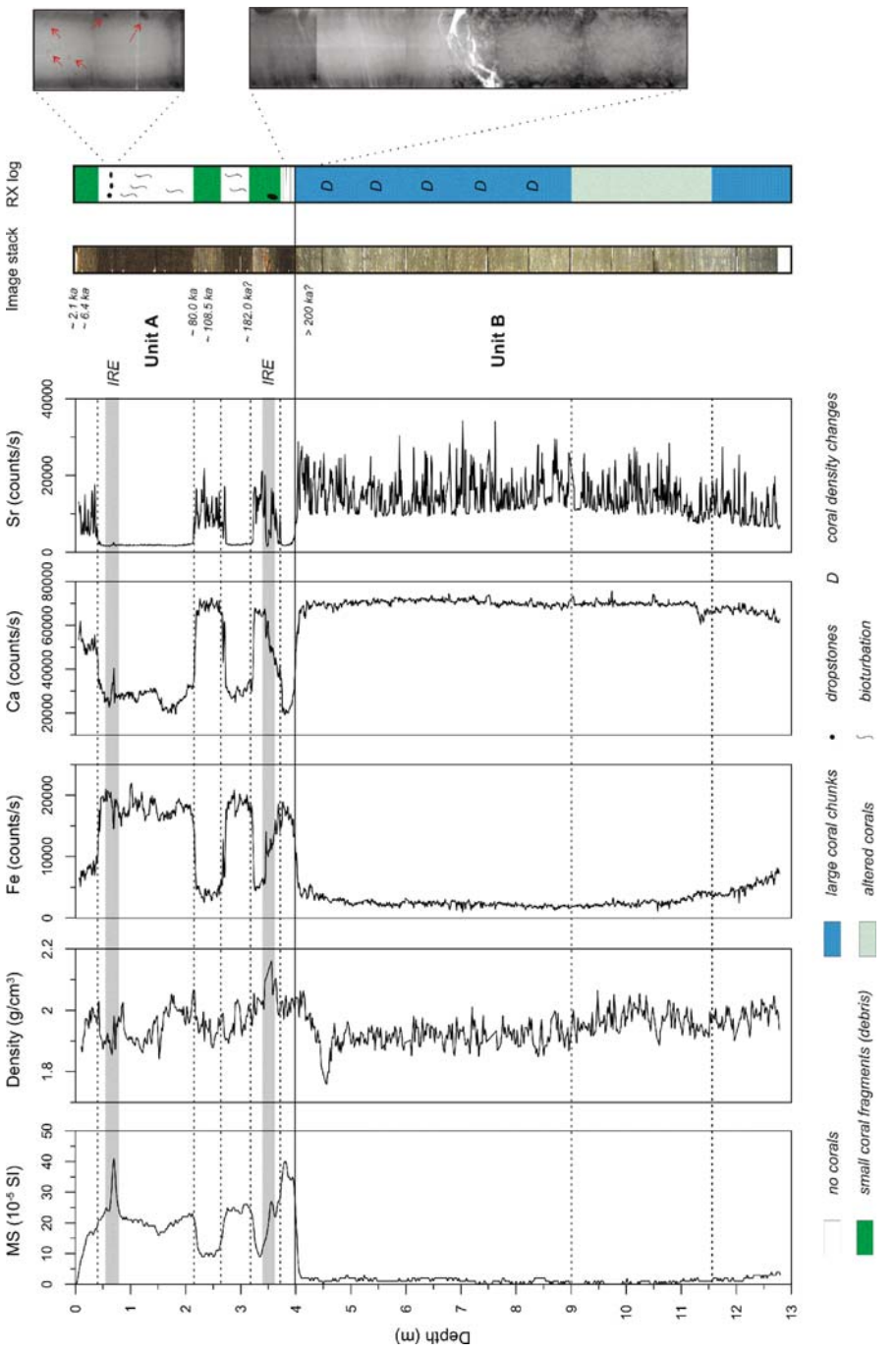

Fig. 6.8 (continued)

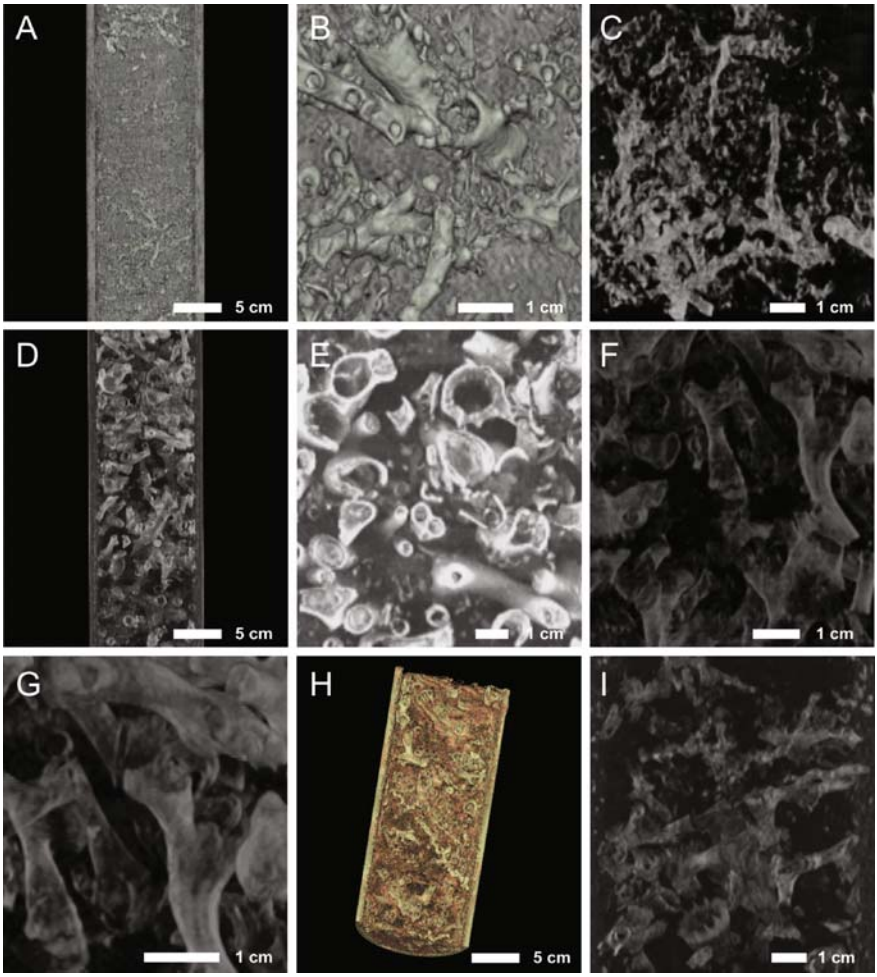

Fig. 6.9 Medical X-ray CT scan images visualizing the cold-water coral fragments of core MD01-2451G in a three-dimensional environment. (**A–C**) Cold-water coral fragments in unit A of the coral species *Madrepora oculata*. (**D–G**) Cold-water coral fragments in unit B of the coral species *Lophelia pertusa*. (**H–I**) Cold-water coral fragments in unit B of the species *Madrepora oculata*, *Lophelia pertusa* and *Desmophyllum cristagalli*

uppermost zone rich in small coral rubble fragments is rather gradual. In contrary a sharp boundary is noticed between the first sediment layer and the second layer, from 219 to 270 cm, composed of coral rubble and fragmented bioclastic material. A plateau-shaped minimum in the magnetic susceptibility record and the Fe intensities is recognized at the same depth interval, while the Ca and Sr count rates show elevated values.

From 270 to 323 cm the core is again composed of highly bioturbated sediments, correlating with high magnetic susceptibilities and high Fe count rates. As observed in the first sedimentary layer, the transition to the coral-rich layer above is gradual, while the boundary with the next coral-rich layer below is sharp. The third layer composed of coral rubble debris and small bioclastic fragments interfering with sediment occur from 323 to 375 cm. A decrease in magnetic susceptibility is noted and an increase in Ca and Sr count rates. However, a small peak in susceptibility and gamma density is observed from 350 to 356 cm and can be correlated with the presence of a big dropstone observed on the X-ray imagery. This dropstone-layer corresponds to higher Fe count rates and lower Ca count rates, suggesting that the dropstone is Fe-rich. The observed dropstone represent partly the transition zone to a finely laminated sediment layer from 375 cm until the sharp base of unit A (400 cm) and can form the fingerprints of an IRE (Fig. 6.8). The third sediment layer can be observed at the same depth levels in the geophysical parameters by elevated magnetic susceptibilities and in the geochemical records by increasing Fe intensities and decreasing Ca and Sr count rates.

So three cycles from the bottom to the top can be recognized in unit A; one cycle consisting of bioturbated or laminated sediments going gradually over in a coral-rich layer and characterized at the top by a sharp contact which corresponds with the onset of the next cycle (Fig. 6.8).

Medical X-ray CT-scanning visualized the rather small cold-water coral fragments in the coral-rich layers in a three-dimensional environment, showing the branching pattern of the cold-water coral fragments (Fig. 6.9A–C). A detailed study of the big cold-water coral fragments in a three-dimensional environment and a comparison of the three-dimensional images with sampled coral chunks allowed identification of these fragments, showing that the uppermost coral-rich layers are dominantly built up by the cold-water coral species *Madrepora oculata,* while the species *Lophelia pertusa* seem to be rare to absent.

6.3.1.2 Unit B (400–1280 cm)

The lower part of the core (400–1280 cm) is nearly completely composed of a sediment filled coral framework with a high concentration of large coral chunks changing in density throughout the unit. The shape and size of the imaged fragments in the X-ray CT scans allowed identification of the coral species (Fig. 6.8), showing that the dominant coral species is represented by *Lophelia pertusa* (Fig. 6.9D–G) with some minor occurrences of *Madrepora oculata* (Fig. 6.9H,I). This is in contrast with the uppermost intervals were the dominant cold-water coral species is *Madrepora oculata*. Extremely low values for the magnetic susceptibility are recorded in this coral-rich part of the core. The gamma density is more continue compared to unit A. Fe count rates decrease to really low values, while Ca count rates and Sr count rates are extremely high, evidencing the presence of cold-water coral fragments and Ca-rich background sediments. From 900 cm onwards, the gamma density increases to slightly higher values, with maxima around 1025 cm to decrease again until 1150 cm. A detailed look to the imaged coral fragments learns that in this small

interval the walls of the coral fragments are thinner. So, dissolution of the fragments can be responsible for the observed higher gamma density, generating denser carbonate-rich background sediments and leaving soft and dissolved coral fragments behind. Slightly lower Sr count rates in the same depth interval confirm the dissolution of cold-water coral fragments, while slightly elevated Ca intensities can evidence the generation of a matrix enriched in Ca. In the same interval the magnetic susceptibilities, still reaching values up to 3 SI above 900 cm, fall completely back to 0 SI and even negative values are recorded. This can be explained by the presence of a higher amount of diamagnetic carbonate-rich minerals in the background sediments.

Below 1150 cm, Fe count rates and magnetic susceptibilities have the tendency to increase again, while Ca count rates and Sr count rates seem to decrease, suggesting the transition towards a unit characterized by less coral fragments.

6.3.2 MD01-2459G: Top of Mound Perseverance

The combination of physical properties, geochemical properties and X-ray imagery allowed the identification of two units in core MD01-2459G (Fig. 6.10).

6.3.2.1 Unit A (0–535 cm)

The uppermost part of the core, up to 535 cm is full of big coral chunks (mainly fragments of the species *Lophelia pertusa*) in alternating quantities (Fig. 6.10). The variable gamma densities can be explained by the changing coral quantities throughout this unit. The magnetic susceptibilities are rather low with values averaging around 5 SI but higher than the unit below. Fe count rates are rather high compared to the unit below, but not that high as noted in the uppermost coral-free intervals in Challenger Mound. Ca and Sr intensities are high but lower than the unit below. The highly variable scatter in the Sr intensities can be explained by the presence of good-preserved cold-water coral fragments in Ca-poor background sediments.

6.3.2.2 Unit B (535–1079 cm)

In the lowermost part of the core (535–1079 cm) corals cannot be clearly recognized on the X-ray images, except for a small interval between 985 and 1050 cm characterized by small coral fragments. The X-ray images in this unit show a typical coral-altered facies. The magnetic susceptibility records extremely low values which can be explained by the presence of carbonate-rich sediments characterized by the presence of diamagnetic carbonate-minerals resulting in low susceptibility values (at certain depths even turning into negative values). Gamma density changes are less pronounced in this lower part of the core, probably due to the creation of a more homogeneous facies rich in carbonate. Fe intensities decrease to low values, while Ca and Sr intensities increase. The increase in Sr count rates is not that pronounced as the increase in Ca intensities and the decrease in Fe intensities.

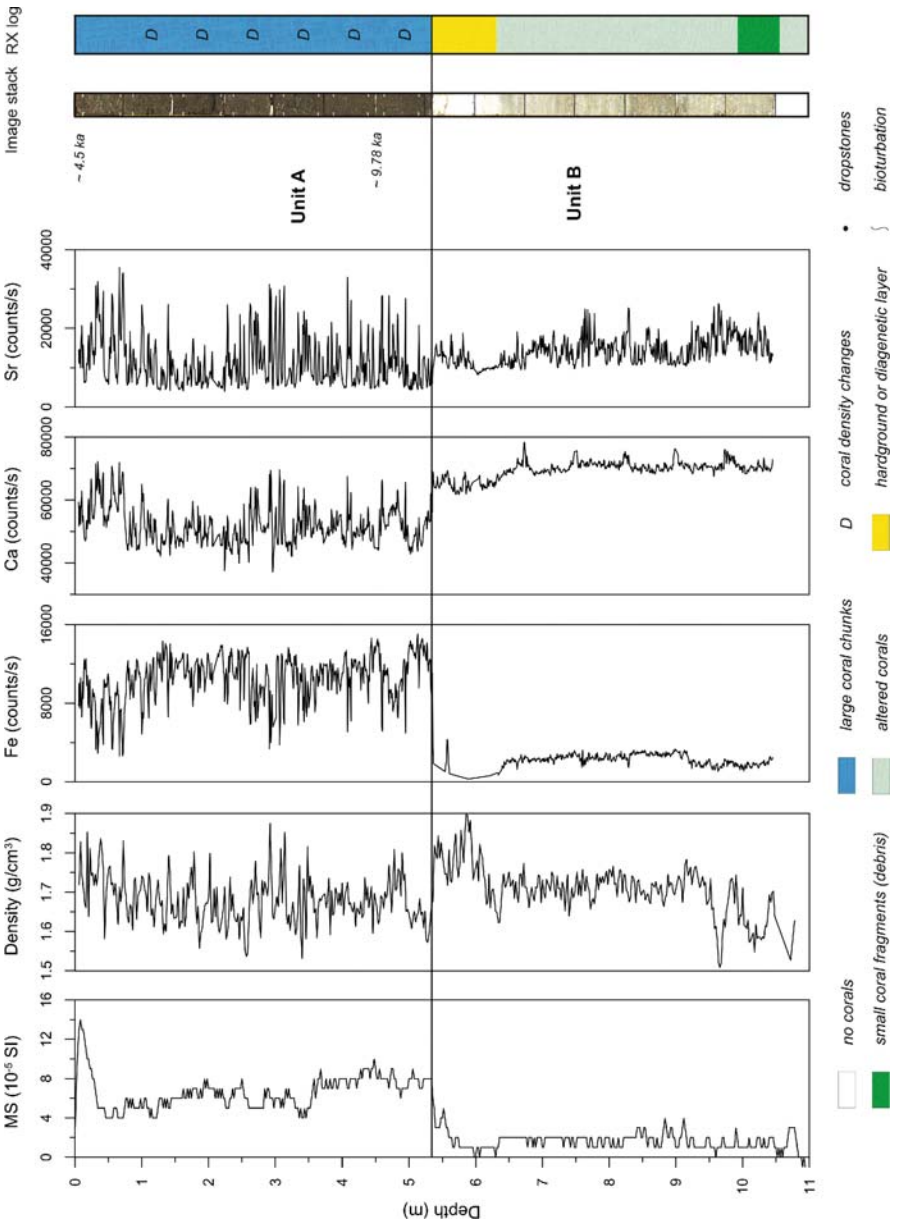

Fig. 6.10 Magnetic susceptibility (10^{-5} SI), density (g/cm^3), Fe, Ca and Sr count rates (counts/s), X-ray log and image stack for core MD01-2451G in function of depth (m). U/Th datings are noted (Frank et al. subm.)

The more, the scatter in Sr count rates is not as pronounced as in unit A, suggesting that the difference in chemical element intensities between the cold-water coral fragments and the matrix is not as pronounced as in unit A (where the background sediments are Fe-rich). Remarkable is the very high density from 535 to 600 cm corresponding with extremely high X-ray intensities, Fe count rates averaging around 0 counts/s and high Ca and Sr intensities. This interval corresponds with a lithified layer, which can be interpreted as a possible hardground or a diagenetic layer.

6.4 Discussion

6.4.1 Off-Mound Records and Palaeoenvironmental Changes

Based on the known correlation of the geophysical parameters with the isotopic record and AMS C^{14} dates of a 26 m long piston core (MD99-2327) localized in the drift sediments upslope of Challenger Mound, the different units recognized in the off-mound cores can be tentatively correlated with the marine isotopic stages (MIS) defined by Martinson et al. (1987) and recognized as such on core MD99-2327 by Van Rooij et al. (2007a). Oxygen isotopic measurements performed on both benthic (mainly *Cibicides kullenbergi*) and planktonic foraminifera (*N. pachyderma s.*) and accelerator mass spectrometry (AMS) C^{14} dates (Jurkiw 2005) confirm the proposed tentative palaeoclimatic framework of core MD01-2450 and so the potential of geophysical parameters to facilitate palaeoenvironmental interpretations in the studied area.

Unit A recognized as such in core MD01-2450 and evidencing of a colder period can be linked to MIS 2, while Unit B showing characteristics in the geophysical properties and the geochemical records of a warmer period, can be correlated with the interstadial MIS 3 (Fig. 6.5). So, the whole upper part of the core evidences of the middle and the end of the last glacial period, whereby MIS 2 corresponds with the last glacial maximum. The lack of typical foraminifera-rich sands at the top suggests that the core does not contain typical Holocene sediments. This can be due to the piston coring method were the upper sandy sediments are blown away during sampling (Skinner and McCave 2003). Alternatively, the location of the core site in an area with active hydrodynamics may also suggest that most of the Holocene sediments could have been eroded in the recent past by vigorous bottom currents. Nowadays, the presence of enhanced currents in the Belgica Mound Province is highly dependant on the interaction of ENAW and MOW responsible for the creation of internal tides and waves (White 2001, 2007; see Chap. 2).

The input of Mediterranean Outflow Water (MOW) may have played a very important role in earlier interglacial or warmer periods too (Schonfeld and Zahn 2000; Van Rooij et al. 2007a). The warmer MIS 3 ($\sim$ unit B) is characterized by the presence of a turbiditic sequence and the local presence of coarser parts in the core, evidencing of a very dynamic and unstable deposition environment during this time.

The lower part of the core, described as unit D, was characterized by the intercalation of sandy foram-rich material, typical found at the sea-floor during recent times and so witnessing of a warmer period similar to the present-day situation. Schonfeld and Zahn (2000) showed that the outflow of MOW was restricted to the Gulf of Cadiz during glacial times and did not penetrate further in the Atlantic Ocean, so the conditions for enhanced currents could not be reached, resulting in the deposition of more continuous records of finer material. The high energy associated with the deposition of a turbidite, as observed in MIS 3, can result in destruction of earlier deposited layers by subsequent turbidity currents creating a sharp erosional contact. It is not known how much material is removed during the observed turbiditic event but radiocarbon datings suggest that the material below the erosional boundary has to be older than 45 ka BP (Jurkiw 2005).

The geophysical records of core MD01-2452 carry significant indications of glacial-interglacial variations (Fig. 6.6). The upper part of the core (unit A) is interpreted as pure Holocene sand and can be correlated with MIS 1. The observations of imprints characterizing a colder period in unit B, can be linked with the last glacial period before the onset of the present Holocene, and so with MIS 2, 3, and 4 (Fig. 6.7). Unit C is characterized by the intercalation of a sandy layer but most of the unit is composed of silty clays. However, the records of the reflectance and magnetic susceptibility evidence of a warmer period which can be correlated with MIS 5. The last unit D, witnessing of colder records can be again linked with a glacial period, i.e. MIS 6. This last unit corresponds with the upper part of the seismic facies that buried most of the Magellan Mounds. So, it is assumed that most of these mounds are buried during the glacial period corresponding with MIS 6. Recent research (Huvenne et al. 2002, 2003, 2007) shows that the Magellan Mound Province bears witness of a hydrodynamically more stable environment than the Belgica Mound Province. It has to be mentioned that indeed no distinctive turbiditic sequences are recognized in the core record. Here, the climatic variations are not disturbed by mass wasting processes from the shelf and the impact of bottom currents is not that intense as in the Belgica Mound Province. The impact of MOW in the northern part of the basin is less vigour than on the eastern margin of PSB. The proposed tentative palaeoclimatic framework is confirmed by biostratigraphic research on coccoliths (Thierens 2005).

In both cores clear IRE are recognized in the last glacial period. Frequent ice rafting episodes are well known in the north-east Atlantic Ocean, called Heinrich events (HE) (Broecker et al. 1992). Heinrich layers were deposited when melting icebergs unloaded their debris en masse in the North Atlantic Ocean. The icebergs were released at the culmination of Dansgaard–Oeschger events, within the last glacial period (Bond et al. 1992). In the north-east Atlantic Ocean, in between 45°and 53°N (= Ruddiman belt (Ruddiman 1977)), these Heinrich layers are associated with a strong magnetic susceptibility signal, due to a higher fraction of IRD containing multidomain, ferrimagnetic material (magnetite) and a smaller amount of detrital carbonate and quartz (Grousset et al. 1993; Robinson et al. 1995). However, the maxima in magnetic susceptibility values, correlating with the different IRE were not that pronounced in core MD01-2450 as in core MD01-2452. The

more, the upper IRE in core MD01-2450 are associated with small maxima in Ca count rates. Core MD99-2327, located more upslope, also illustrates several IRE, characterized by a low magnetic susceptibility and associated with higher Ca count rates (Van Rooij et al. 2007a; Richter et al. 2001). Probably the mass wasting processes from the shelf and bottom currents have a great impact on the sedimentation in this part of the basin and could blur the impact of IRE. Another important factor is the origin of the IRD deposited during these IRE. Broecker et al. (1992) mentioned that the IRD, deposited during the HE in the north–east Atlantic Ocean, was mainly derived from the Precambrian gneisses of the Canadian shield with the Laurentide and Greenland ice sheets as the sole source of these events. Glaciogenic detritus from these sources often contains primary, unaltered ferrimagnetic (magnetite) minerals (Thompson and Oldfield 1986). However, more recent work has provided evidence that European ice-sheets also contribute to the story (Snoeckx et al. 1999; Grousset et al. 2000, 2001). Moreover, the described IRE in Porcupine Seabight are influenced by the proximity of the British-Irish ice-sheets (BIIS) (Van Rooij et al. 2007a). Ice rafted material derived from the European continental margin contains detrital Campanian Upper Chalk, derived from bedrock sources eroded on the Celtic shelf by the BIIS (Scourse et al. 2000) and can thus be responsible for the less pronounced signals in the magnetic susceptibility and the small peaks in Ca count rates.

The pattern described from cores MD99-2327 (Van Rooij et al. 2007a), MD01-2450 and MD01-2452 suggests a NW-ward increasing magnetic susceptibility, indicating the products of the Laurentide icebergs were losing intensity towards the Irish mainland or BIIS IRD diluted them. Remarkable is the observation of the multiple character of the IRE in both cores. Recent isotopic research revealed that Heinrich events could be characterized by three-step internal structures (Grousset et al. 2000, 2001; Snoeckx et al. 1999). During the first step, IRD derived from the European ice-sheets are released into the North Atlantic Ocean, displaying a so-called "precursor event". A second step, which may occur 1.0–1.5 ka after the start of the precursor event, is represented by a major input of Laurentide derived IRD. Finally during a last step, IRD from the European ice-sheets are accumulated. Scourse et al. (2000) observed the same for Heinrich Layer 2 in two cores on the European Goban Spur–Porcupine continental margin, with a first deposition of chalk grains, derived from the BIIS and followed by the deposition of both British and Canadian derived IRD. Scourse et al. (2000) explains this by a more rapid response of the smaller British ice-sheet on the external climatic forcing of Heinrich events. Only the real Laurentide events, and not the precursor events which contains more chalk-rich material, contains ferrimagnetic-rich IRD and are thus clearly visible in the susceptibility. This can explain the offset between peaks in the records of magnetic susceptibility, gamma density and chemical element intensities and the occurrence of a smaller peak in susceptibility before the actual maximum, whereby the first peak represents IRD from the BIIS, whereas the second peak in susceptibility corresponds with Canadian derived IRD. So, it can be concluded that the BIIS variability had an important influence on the off-mound records during glacial times. In this view, the turbiditic sequence in core MD01-2450 can be also interpreted as a product of a pre-

Last Glacial Maximum (LGM) deglaciation about 25–37 ka, which was observed by Bowen et al. (2002) and which can be responsible for a destabilization of the BIIS and subsequent small mass wasting processes.

6.4.2 On-Mound Records: Revealing Episodes of Coral Growth?

The first aim of the X-ray imagery was to describe the content of the coral cores, realized by the observation and interpretation of four different radio-facies (Fig. 6.7). A comparison of the X-ray logs with the geophysical and geochemical properties revealed a coherent correlation and made it possible to distinguish the units described in Sect. 6.3. Correlating the described units with U/Th datings on coral fragments (Frank et al. 2005, subm.) helps in defining a palaeoclimatic framework for the studied cores and postulating some mechanisms of recent mound growth in respectively the Belgica Mound Province and the Magellan Mound Province.

U/Th datings on cold-water coral fragments at the top (0 cm) of core MD01-2451G on Mound Challenger yielded an age of 2.08 ka calibrated BP (Frank et al. subm.). At 6, 27, and 31 cm U/Th datings on cold-water coral fragments revealed calibrated ages of respectively 2.95 ka BP, 5.87 BP and 6.37 to 6.42 BP (Frank et al. subm.). So, the uppermost layer of unit A can be interpreted as Holocene. The date for the top of the core suggests that the uppermost layer of Mound Challenger is apparently missing, which can be explained by strong bottom currents eroding the uppermost sediments or preventing sediment deposition. Video surveying with the ROV Victor on board of R/V Polarstern in 2003 shows that the entire coral assemblage over Challenger Mound is composed of dead coral rubble (Foubert et al. 2005a; see Chap. 7). So, Challenger Mound can be interpreted as a dead mound with no active coral growth during present times. It can be assumed that coral growth entirely stopped around 2000 years ago. The second coral layer revealed ages of about ~80.00 ka BP at 223 cm and ~108.50 ka BP at 248 cm. It can be assumed that the cold-water coral fragments in this second coral-rich layer are belonging to MIS 5, an interglacial period. U/Th dating on a cold-water coral fragment at the top of the third layer (326 cm) yielded an age of 182 ka, suggesting these corals are formed during the interstadial 6.5. The presence of a dropstone layer at the base of this coral-rich layer (350–356 cm), bears witness of an IRE suggesting the presence of glacial sediments in the unit below. The presence of dropstones (60–70 cm) in the sediment-rich layers between the first and the second coral-rich layer, evidence also the presence of IRD deposited during IRE. Such IRD is typical for sediments deposited in a glacial period. It can be assumed that the first sediment-rich and coral-free layer is correlating with the last glacial period corresponding with MIS 2, 3, and 4. The last glacial period within this region is known as one with high sedimentation rates and multiple IRE, as observed in core MD01-2450 and confirmed by Van Rooij et al. (2007a). It can be concluded that during the recent past, coral growth was restricted to interglacial and interstadial periods, while Fe-rich sedimentation prevailed during glacial times. The transitions from the interglacial (or interstadial) coral-rich layers towards the glacial coral-free sediments are rather abrupt. It has

been proven in the off-mound cores that during interglacial times enhanced bottom currents are observed in the basin, provoking higher nutrient fluxes and lower sedimentation rates, which might be the underlying reason why the corals in unit A are restricted to interglacials.

U/Th dating learns that the coral fragments in unit B are older than 200 ka calibrated BP (Frank et al. subm.). Extensive dissolution of coral fragments made it difficult to obtain accurate U/Th datings. Some datings completely failed which can be due to practical restrictions of the U/Th technique. The sharp erosive contact between unit A and unit B, learns that some material could have been eroded, resulting in a hiatus and the presence of rather old cold-water coral fragments at the top of unit B. The fine laminations observed in the sedimentary layer draped over the coral-rich unit B can be connected to a high meltwater influx and/or a turbidite event. It can be assumed that during the subsequent MIS 6 the sedimentation rates were so high that the eroded cold-water corals at the top of unit B became partly buried. However, the observation of three cycles in unit A evidences that cold-water coral growth restarted during intercalated interglacial and interstadial periods. From MIS 6 on, an interplay between siliciclastic sedimentation and cold water coral growth took place whereby in some periods sedimentation gained on coral- and mound growth, while in the next stage cold-water coral growth took again the overhand. However no healthy recovery of cold-water coral growth could be reached anymore. A shift in dominant coral species in the uppermost intervals can form an evidence for the different environmental conditions of the uppermost coral-rich layers, whereby corals had to deal with more stressing factors than in the period before. It appears that *Madrepora oculata* can survive in more stressed situations dealing with more sediment influx than the species *Lophelia pertusa*. So, it appears that changing sediment fluxes are an important factor controlling cold-water coral growth.

The upper level with a high amount of corals in core MD01-2459G on Mound Perseverance shows ages of *Lophelia* corals ranging from 4.50 ka BP at the core top to 9.78 ka BP at 4.5 m core depth, indicating a Holocene growth episode for unit A. ROV video surveying showed that actively live corals are only found at the topmost part of Mound Perseverance (Huvenne et al. 2005). The slight offset of the localization of the core from the top of the mound can explain the presence of older dead coral fragments at the top of the core. This important mound growth in a relatively short time span (85 cm/ka) shows that mound growth is accelerated when conditions are favourable. Core MD01-2452 learnt that most of the Magellan Mounds were buried during glacial MIS 6. However, Mound Perseverance seems to have survived this period of burial. No ages are available for unit B. The top of this unit is characterized by the presence of a hardground or lithified layer. Possible mechanisms for the creation of such a lithified layer are in detail discussed in Chap. 4.

The extensive Holocene growth episode in Mound Perseverance, compared to the small Holocene coral-rich layer in Mound Challenger, evidence that even in the same basin, conditions positive for cold-water coral growth and mound build-up can differ. The present-day situation in the Magellan Mound Province gives evidence of a quieter environment than the Belgica Mound Province. It can be questioned if this quieter environment is responsible for the enhanced growth episode. This is

in contradiction with the situation provoked for Challenger Mound where corals in the upper units are limited to interglacials and interstadials. This is explained by the presence of higher currents, responsible for a higher nutrient flux and a lower sedimentation rate, positive for coral-growth in stressed situations. However, the corals in the northern part of Porcupine Seabight are not in such a high sediment-stressed situation as at the eastern margin, which is much more influenced by BIIS fluctuations and mass wasting processes. This shows that cold-water corals can even survive in quiet environments as long as they keep up with sedimentation. A positive interaction between cold-water coral growth rates and sedimentation rates can result in really high mound growth rates.

6.5 Summary

The study of both **on-mound** and **off-mound** cores by means of geophysical properties and X-ray imagery in respectively the **Belgica** and the **Magellan Mound Province** reveals some **clear differences** in the **palaeoenvironmental** setting of both provinces.

Core **MD01-2450** in the sediments at the SW flank of **Challenger Mound** in the **Belgica Mound Province** bears evidence of a **very dynamic environment**, while core **MD01-2452** above the buried **Magellan Mounds** is evidencing **less energetic palaeoenvironments**.

Significant **glacial–interglacial variations** have been identified in both cores, whereby stronger bottom currents probably due to the **influence of MOW** are responsible for the record of the characteristic coarser sediments deposited during **interglacial periods**.

Ice rafting events (IRE), some of them with a poly-phased character probably due to a more rapid response of the **British-Irish ice-sheets** (BIIS) on the external climatic forcing of Heinrich Events, could easily be recognized during the last glacial period. The footprints of IRE are more pronounced in the susceptibility records going NW-ward, indicating the products of the Laurentide icebergs were losing intensity towards the Irish mainland or BIIS IRD diluted them.

Geophysical and geochemical properties could clearly be correlated with X-ray imagery for the **on-mound** cores. Alternating units of **coral-rich and coral-free sediments** are observed, as well as layers with distinct coral alteration. The core on **Mound Challenger** shows that this mound is now in a **stage of retirement (mound decline)**, whereby most of the cold-water corals were buried during MIS 6. Some **reinitiating phases of cold-water coral growth** during **interglacials** or **interstadials** occurred. The **Holocene** record dominated by coral fragments in the core on **Mound Perseverance** evidences a cold-water coral bloom during this period resulting in a **mound growth of 85 cm/ka**.

Not only during present times but also in the **past** both provinces, the **Belgica Mound Province** and the **Magellan Mound Province** show clear **differences** in their **hydrodynamical environment**, an observation that has an important impact on the interaction of **sedimentation** and **mound growth**.

Chapter 7
Surface Processes

Still in recent past, benthic sampling techniques, using box corers, Van-Veen grabs or dredges, were the most common tools for biologists and geologists to examine the surface processes occurring at the present-day sea-floor and to ground-truth geophysical data sets (sidescan sonar, multibeam,. . .). In the last decade, the increasing Remotely Operated Vehicle (ROV)-based exploration and visualization of deep-water environments revealed a large number of new insights in this underwater world.

The first developments in underwater photography took place over a century ago along the French Riviera during the 1890s by Louis Boutan (Solan et al. 2003); his efforts were nothing astonishing given the slow films and early lenses of his time (Vine 1975). Boutan also undertook the first underwater night photography using flash powder for illumination. While William Beebe took some of the first deep-sea photographs through the porthole of his "Bathysphere" at a depth of 800 m, the first remotely operated deep-sea camera was developed at Woods Hole in the late 1930s by Maurice Ewing and his associates to study depositional processes in deep-sea sediments (Ewing et al. 1946). However it was not until Harold "Doc" Edgerton adapted his new strobe for underwater housings that both shallow and deep underwater photography really took off in the 1940s and 1950s, coupled with impetus from the U.S. Department of Defense for wartime applications (Broad 1997). In the past decade, advances in optical imaging technology due to the current revolution in electronics, sensing technology and signal processing have permitted improvements and accomplishments that would have been considered impossible just one generation ago (Jaffe et al. 2001). The first tethered Remotely Operated Vehicle (ROV), named POODLE, was developed by Dimitri Rebikoff in 1953. The ROV's were in fact a reaction on the development of the Human Occupied Vehicles (HOV's), called manned submersibles. The first operational manned submersibles, the French-Belgian "FNRS III" (later on renamed as "Archimede") and the Italian "Trieste" (later on bought by the Americans) were active around the same period in 1953. The advantages of ROV's compared to HOV's (the need for substantial dedicated support vessels, limited bottom time rendering them economically ineffective and the human risk underwater), led to a more rapid development and wide-spread use of the ROV's than the HOV's. The first ROV's were developed for military applications. However the transition from military purposes towards the industrial

A. Foubert, J.-P. Henriet, *Nature and Significance of the Recent Carbonate Mound Record*, Lecture Notes in Earth Sciences 126, DOI 10.1007/978-3-642-00290-8_7,

world (offshore oil and gas exploration) in the mid-seventies was rather rapid. In the eighties and nineties ROV's made their introduction in the scientific world. Nowadays, a lot of ROV's are used by the scientific community and became a standard tool to study the ocean floors in detail. The next step in underwater exploration will be the extensive development of Autonomous Underwater Vehicles (AUV). For the moment, AUV's are increasingly being used by the military, for science and in the commercial world for survey work.

Such new ROV technologies are producing a large amount of visual data, claiming for new analytical methods, both qualitative and quantitative. In this chapter, an integrated method is presented for the study of video data specially adapted to cold-water coral environments. ROV imagery gave the possibility to look to the surface of the mounds in the Belgica Mound Province and to see which facies is dominating the sea-floor in between the mounds. The more, the combined use of a ROV system mounted with a multibeam system, provided a new technique to look behind the normal resolution of bathymetry, creating a new field of study called "micro-bathymetry". In this chapter, a micro-bathymetric data set over some small mound structures will be described, revealing some new insights in sedimentary processes, cold-water coral growth and mound growth.

7.1 Material and Methodology

An extensive data set of video imagery was collected with the ROV Victor 6000 installed aboard the R/V Polarstern during Expedition ARK/XIX3a in June 2003 (Klages et al. 2004). A reconnaissance video survey over numerous steep-flanked Belgica Mounds, from Challenger Mound over Poseidon Mound to Galway Mound, was carried out resulting in 36 h of video footage (Figs. 7.1 and 7.10). ROV Victor 6000 is a big-sized, multi-purpose ROV designed and built by IFREMER (Institut Français de Recherche pour l'Exploitation de la Mer, France) for scientific applications (Fig. 7.2A) (Opderbecke et al. 2004). For a detailed technical description of the ROV Victor 6000 the reader is referred to Michel et al. (2003). The ROV Victor 6000, depth rated for 6000 m, is equipped with various instruments to be used for scientific operations in the deep sea such as two manipulator arms (MAESTRO), seven digital cameras, a water sampler, a slurp gun and temperature sensors. The "Basic Sampling Toolsled" containing all necessary tools for adequate sampling (sediment, water, fauna), was installed under the ROV Victor 6000 during the expedition. Close to the main camera, a high-resolution digital still camera (HYTEC VSPN3000, 3 megapixels, autofocus and optical zoom) allowed taking high-quality pictures. Additionally, laser beams were placed around the main camera as scale to estimate the distance and the size of objects within the camera view field. The onboard ROV navigation sensors are: (1) RDI workhorse-600 Doppler Velocity Log (DVL), (2) IXSEA Octans fibre-optic gyrocompass and motion sensor, and (3) DIQIQUARTZ Paro-scientific depth sensor. Positioning was achieved by a "Posidonia" USBL (Ultra Short Base Line) system (Rybicki et al. 1999).

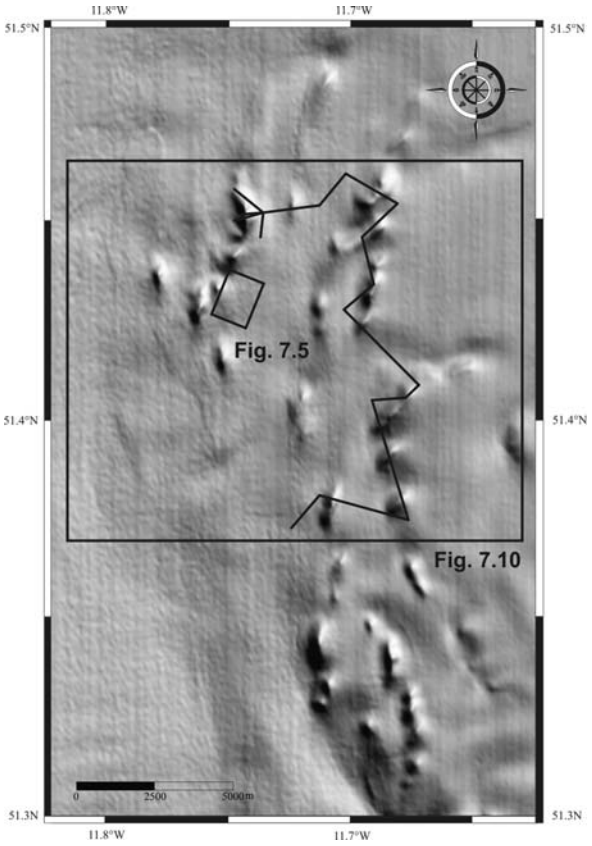

Fig. 7.1 Shaded relief map of the Belgica Mound Province with the morphological features (carbonate mounds, channels) showing the location of the ROV track over and in between the different Belgica Mounds (*black line*) and the micro-bathymetric dive (*black rectangle*). The shaded relief map is based on AWI bathymetry (Beyer et al. 2003)

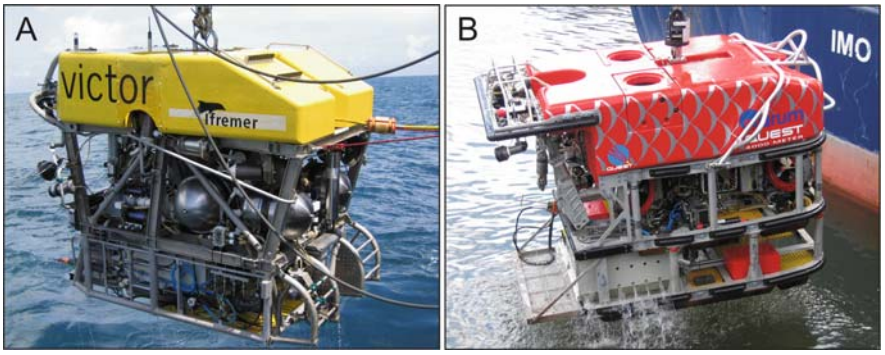

Fig. 7.2 Pictures of ROV VICTOR 6000 designed and built by IFREMER (Institut Français de Recherche pour l'Exploitation de la Mer, France) (**A**) and, ROV QUEST operated by MARUM (University Bremen, Germany) (**B**)

Additional videomaterial, collected during the CARACOLE cruise with the same robotic submersible Victor 6000 aboard the R/V Atalante in June 2001 (Olu-Le Roy et al. 2002) and during the M61/3 cruise with the ROV Quest aboard the R/V Meteor in June 2004 (Ratmeyer et al. 2006), was used to illustrate the different facies encountered on and between the Belgica Mounds. The ROV Quest is an electric commercial work-class ROV, operated by MARUM, University of Bremen (Germany) (Fig. 7.2B) (Ratmeyer et al. 2006). The robot is designed and manufactured by Alstom Schilling Robotics (ASR, Davis, USA). In contrast to the commercial model, the Bremen QUEST has been adapted for scientific deployment and for diving in water depths down to 4000 m. The ROV Quest is equipped with a RIGMASTER manipulating arm, as well as a set of other scientific tools and adaptations for adequate geological and biological sampling. The major installation is the advanced camera and lighting suite, consisting of 2.4 kW light power and 6 different video and still cameras. Quest uses a Doppler velocity log (DVL) to perform Station Keep Displacement and automatically controlled 3D positioning allowing reliable and precise positioning with accuracy within centimetre to decimetre ranges.

High-resolution swath bathymetric mapping with the ROV Victor 6000 during the R/V Polarstern expedition ARK/XIX3a in June 2003 produced a micro-bathymetric map up to a resolution of 20 cm, visualizing small-scaled mound structures (Moira Mounds) (Figs. 7.1 and 7.5). Compared to surface-borne mapping, ROV-borne micro-bathymetric mapping increases the spatial resolution of the observations (Opderbecke et al. 2004). This gives more detailed insights in the local morphology of the seabed, allowing the recognition of structures only a few centimetres in relief. During the micro-bathymetric mapping survey over the small Moira Mounds, the multi-beam echosounder system Simrad EM2000, operating at a frequency of 200 kHz and a swath width of 120°, was mounted on the Victor 6000 in a special "seabed mapping module". The maximum number of beams across wise was 111 with an angular resolution of $1.5^\circ \times 2.5^\circ$. The fly-height above the sea-floor was kept at a constant level of ~10 m. High-resolution mapping is not possible without precise navigation. The multibeam resolution (~10 cm horizontally) and the one of video mapping (~1 cm horizontally) ideally imply navigation data of the same level of accuracy. Underwater positioning, taking into account the absence of radio-electric signal transmission in seawater, is normally based on acoustic measurements with respect to reference transponders that are mounted under the vessel or moored on the sea-floor. During the ARK/XIX3a expedition, the ROV Victor 6000 was positioned with the USBL system "Posidonia", which yields a positioning accuracy of about 0.5% of the slant range (depending on the ship noise, the meteorological conditions (turbulent water around the transducers, roll, pitch and heave dynamics), and the system calibration 5-sonic velocity profile). The acoustic positioning, which is not sufficient for map construction, was completed by the inertial navigation system of the ROV Victor 6000. A 3D fibre-optic gyro and motion-sensor (Octans/Ixsea), and a Doppler Velocity Log (DVL-Workhorse600/RDI), measure the displacements of the ROV in time, starting from a given USBL-position. The integration of measurement noises lets the positioning error drifting off at a rate of less than 10m/hour. The high-resolution mapping procedures use the inertial

gyro-Doppler navigation reset on USBL-positions at given intervals (1–2 h) before or after the individual survey lines. Roll and pitch compensation was carried out with data from the Octans system, which measures these angles with an accuracy of 0.5 mrad. The vehicle depth was obtained by a DIQIQUARTZ Paro-scientific depth sensor. It has an accuracy of a few centimetres.

All the data were recorded and processed (filtering of the vehicle depth measurement, roll calibration, removal of bad pings and pitch correction) in the software package Qinsy. It has to be mentioned that some navigation errors have not been filtered out due to the complexity of the problem. The accuracy of underwater navigation in the horizontal plane and in the vertical axis is less accurate than at the surface (Opderbecke et al. 2004). Dead-reckoning induces a short term drift that builds up to a few metres during a 1 km survey line. This means that the assembly of the map will show considerable artefacts between joining survey lines. Even slight variations in the vehicle depth may cause vertical shifts which are difficult to filter out during post-processing.

Additional ground-truthing of the video data was done by systematic sampling of the different encountered facies with Van Veen grabs and giant box cores during the Polarstern ARKXIX/3a cruise in June 2003, the M61/1 and M61/3 cruises aboard the R/V Meteor in May and June 2004, and the POS314 expedition with the R/V Poseidon in August 2004.

7.2 Moira Mounds

7.2.1 What are the "Moira Mounds"?

Small-scaled mounded features were first observed east of Thérèse Mound as lumpy structures with spots of high backscatter indicative of coral colonisation on 100/410 kHz GeoAcoustic sidescan sonar imagery, collected during the RRS Discovery 248 cruise (Bett et al. 2001; Kozachenko 2005; Wheeler et al. 2005b) (Fig. 7.3A,B). Extensive 30 kHz TOBI sidescan sonar mapping showed that hundreds of such small mounds exist in the Belgica Mound Province (Fig. 7.3C) (de Haas et al. 2002; Huvenne et al. 2005). The first group of such build-ups to be identified on the sidescan sonar records was named "Moira Mounds" (Wheeler et al. in prep.). Over 250 Moira Mounds have now been identified in the Belgica Mound Province, most of them occurring in water depths between 900 and 1080 m. Lack of subsurface expression on 3.5 kHz echosounder profiles shows that they are recent features (Fig. 7.3D) (Huvenne et al. 2005; Kozachenko 2005; Wheeler et al. in prep.). No seismic evidence for buried components is observed (Huvenne et al. 2005). Sidescan sonar imagery reveals the Moira Mounds as clearly defined, high backscatter structures with slope gradients of about 15–20°, measuring between 20 and 50 m across and up to ~5 m tall (Kozachenko 2005; Wheeler et al. 2005b, in prep.). Most of the Moira Mounds are subcircular in shape, showing elongation in the direction of the dominant current flow (Wheeler et al. 2005b, in prep.).

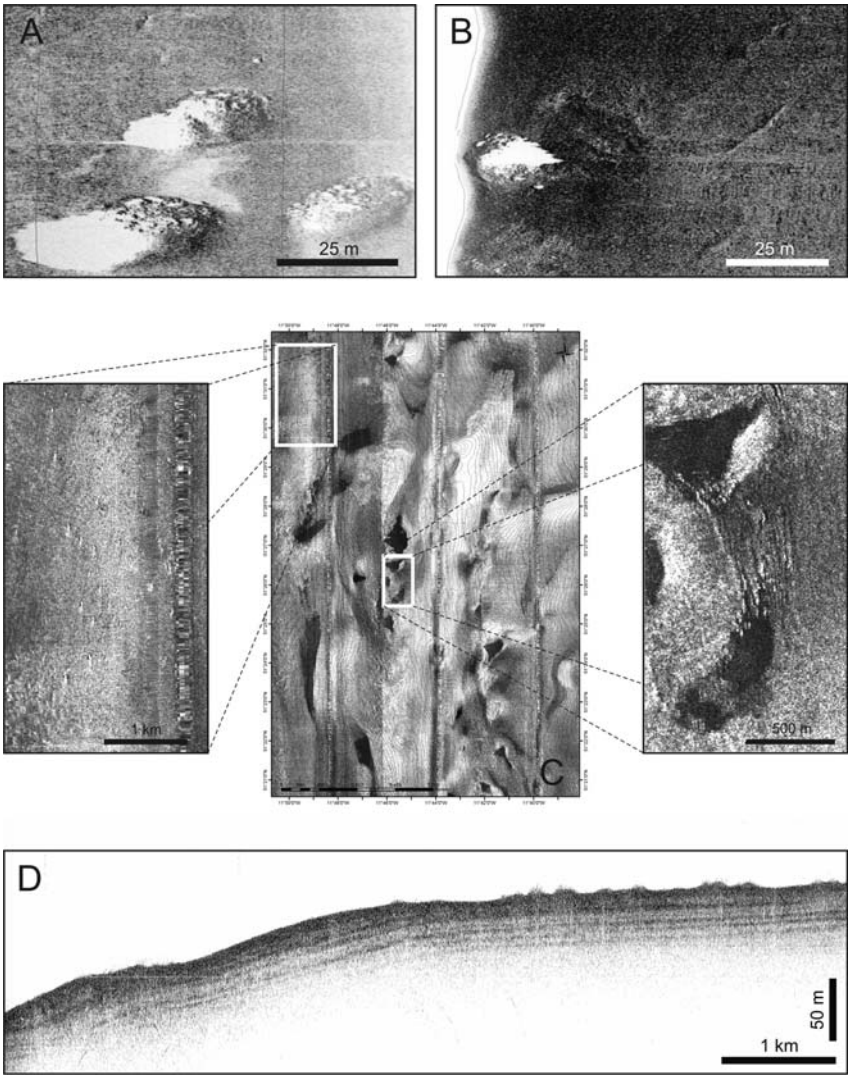

Fig. 7.3 (**A–B**) Moira Mounds visualized on 100/410 kHz GeoAcoustic sidescan sonar imagery, collected during the RRS Discovery 248 cruise (Bett et al. 2001; Kozachenko 2005; Wheeler et al. 2005b). (**C**) TOBI sidescan sonar imagery of the Belgica Mound Province (de Haas et al. 2002; Huvenne et al. 2005). Insets display the small Moira Mounds on the TOBI sidescan sonar imagery. (**D**) Detail of 3.5 kHz echosounder profile showing small positive features on the seabed, interpreted as the Moira Mounds

Some Moira Mounds possess long tail-like structures aligned in a south-north direction representing down-current sediment wave trains (Wheeler et al. 2005b). The mounds include isolated examples although the majority is clustered in groups or swarms. The mounds coexist with low (dark-toned) backscatter patches, indicative

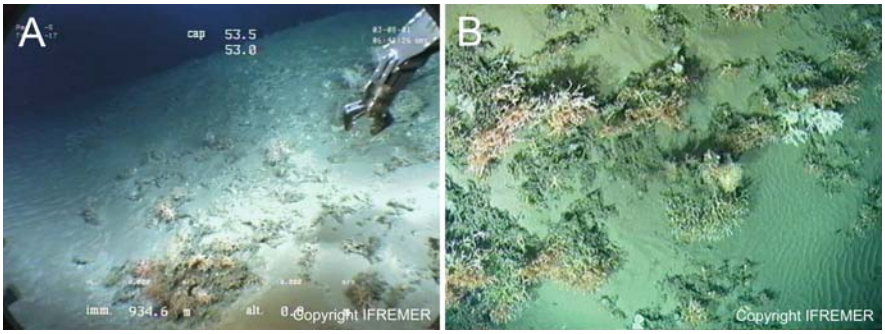

Fig. 7.4 ROV imagery visualizing the Moira Mounds. (**A**) Slope of one of the Moira Mounds with patches of live coral framework (mainly the species *Madrepora oculata*) and dead coral fragments on the flank. (**B**) Rippled sand patches in between coral thickets on the flanks of a Moira Mound

of sandy sediments, and occur on the upstream margins of sediment wave fields (Wheeler et al. 2005b, in prep.).

Video imagery reveals that the seabed in between the mounds is dominated by a rippled sand facies with occasional dropstones and odd coral patches (Huvenne et al. 2005; Wheeler et al. 2005b). Mound's flanks and mounds themselves are represented by a rippled seabed with patchy mostly alive corals, followed by dense mostly alive coral coverage with patches of rippled seabed on the mound summits (Fig. 7.4). Ground-truthing by box coring during the ARK/XIX3a expedition evidenced the presence of live coral on the top of the Moira Mounds. The corals are mainly identified as *Madrepora oculata*. However, small occurrences of the species *Lophelia pertusa* can not be excluded. The sediments of the mounds consist of well-sorted medium to coarse sand with a unimodal distribution and a mean grain size fraction of ~277 μm (Kozachenko 2005).

So, the main feature of the Moira Mounds is that they occur in areas of active sand transport on rippled sand sheets in areas of sediment wave development. A detailed study of a micro-bathymetric grid over the Moira Mounds will show the interrelationships between mounds, sediments, sedimentary structures and water mass movements in this area, characterized by active sediment transport (Foubert et al. 2005a; Sect. 7.2.2). The more, geospatial relationships between the Moira Mounds and the giant Belgica Mounds suggests that the Moira Mounds are distinct features closely associated with the contourite drifts located between the giant Belgica Mounds. It can be questioned if the Moira Mounds represent examples of initial mound growth or a very early stage of mound growth. In this view, a detailed study of these mounds may give new insights into mound genesis.

Small mounds comparable in size to the Moira Mounds have been found in the northern Rockall Trough, named the "Darwin Mounds" (Masson et al. 2003). However, Masson et al. (2003) suggested that the Darwin Mounds do not represent classical examples of carbonate mounds but are in fact coral-topped mounds, representing coral-colonized water escape structures. On the other hand, Huvenne et al. (2008) suggested that active sand transport and hydrodynamics play an important role in

the formation of the Darwin Mounds, which might imply more similarities with the Moira Mounds than thought before.

7.2.2 Micro-Bathymetric Mapping

A detailed examination of the micro-bathymetric grid (1300 × 820 m surface coverage) revealed five well-delineated zones, each of them characterized by a distinctive morphology, and some small mounded structures, the "Moira Mounds" (Figs. 7.5 and 7.6). The three most distinctive areas (zones 1, 2, and 3) were already indicated by Foubert et al. (2005a) and will be described here in detail. Due to the scarcity of ground-truthing material, the two other zones will be just shortly mentioned (zones 4 and 5).

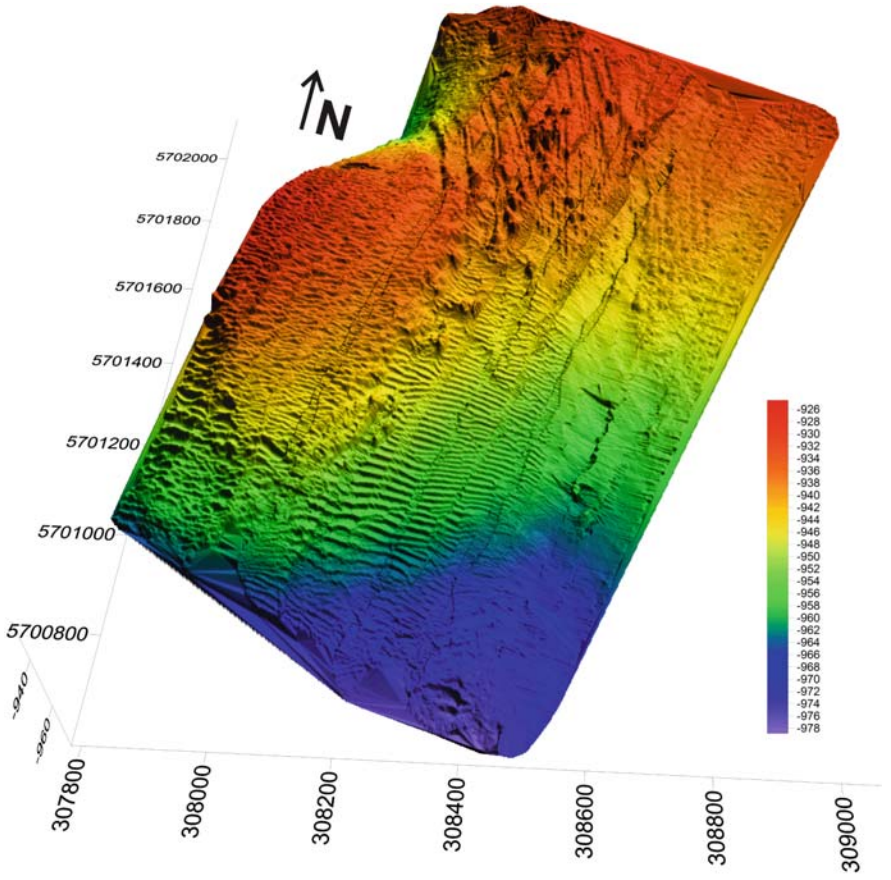

Fig. 7.5 Three-dimensional view of the micro-bathymetric grid over the Moira Mounds east of Thérèse Mound and the surrounding sedimentary environment

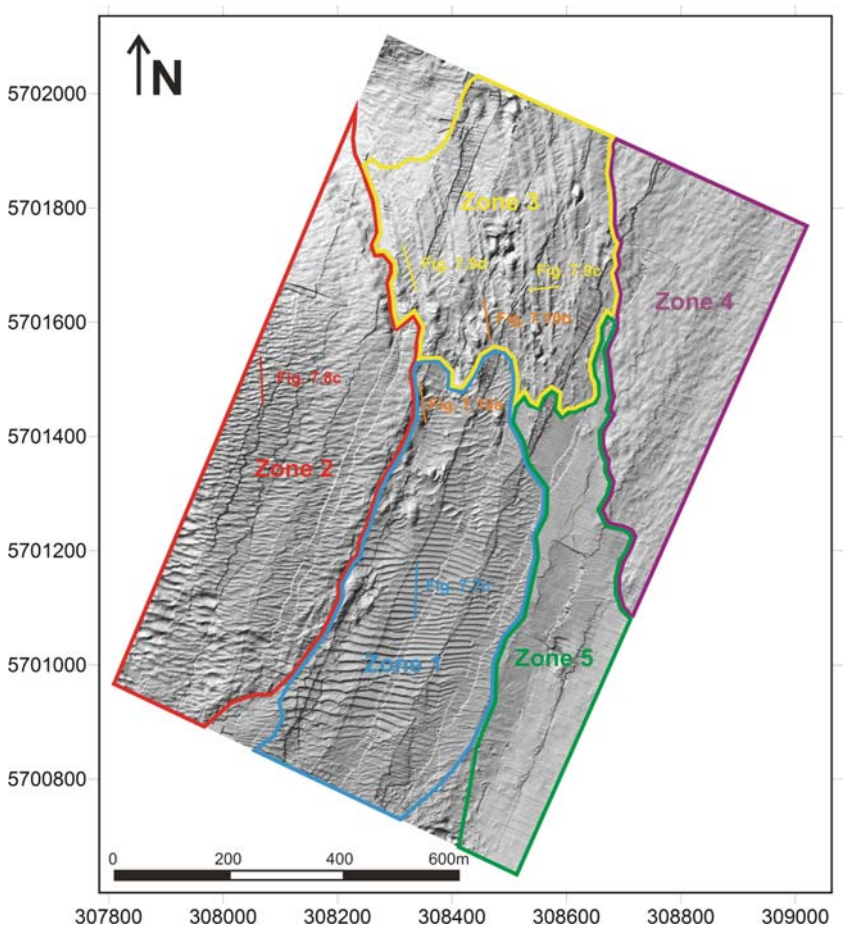

Fig. 7.6 Shaded relief map of the micro-bathymetric grid with annotation of the different studied zones and profiles through the described bedforms

7.2.2.1 Zone 1: Regular E-W Directed Sandwaves

Zone 1 is situated in the southern to middle part of the rectangular micro-bathymetric grid at water depths between 970 and 940 m (Figs. 7.5, 7.6, and 7.7). This zone is characterized on the micro-bathymetry by straight, long-crested, asymmetric, E-W aligned sediment waves with some bifurcations (Fig. 7.7A). A set of profiles, transverse orientated on the sediment waves, revealed that the bedforms have average wavelengths of ~10.06 m and average heights of ~0.50 m (Fig. 7.7C). The waves are characterized by N-ward facing long slopes with average lengths of ~5.59 m and average gradients around ~5.46°, while the S-ward facing short slopes have an average length of ~4.23 m and an average gradient of ~7.34°. These parameters allowed calculating the length to height ratio (L/H) and the symmetry index

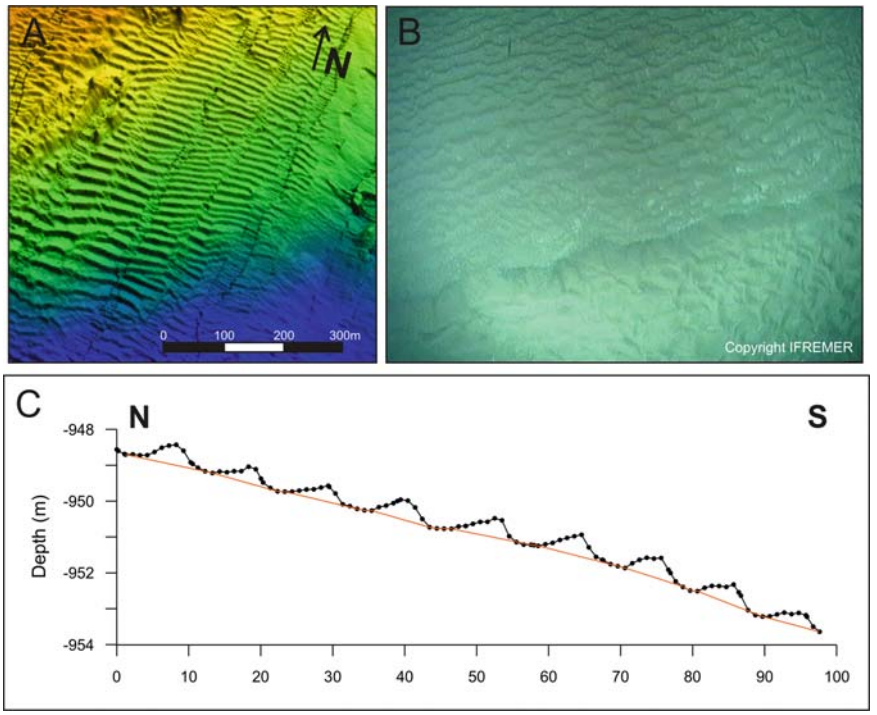

Fig. 7.7 (**A**) Zoom in on zone 1 of the micro-bathymetric grid visualizing the regular E-W directed sandwaves. (**B**) ROV video imagery showing the sandwave-pattern with superimposed ripples. Note the changing ripple patterns, probably resulting from local variations in bottom current speed and direction. (**C**) N-S profile through the sandwaves (for location see Fig. 7.6)

(SI) defined as the ratio of the long slope side versus the short slope side. The average L/H ratio is ∼18.34, while the average symmetry index is ∼1.36. However, it should be mentioned that the sediment waves in the most southern part of zone 1 have a generally lower L/H ratio and a higher symmetry index compared to the sediment waves in the northern part of zone 1. This can be explained by the decreasing availability of sandy material by going northwards, and thus upslope. Calculations of the minimum shear stress 100 cm above the seabed necessary to go over from a rippled seabed to a sandwave-dominated seabed, taking into account material with an average grain size of 277 μm, revealed minimum current velocities of 50 cm/s with a maximum limit of 120 cm/s. According to the geometrical characteristics of the observed sediment waves (average height of ∼55 cm, average wavelength of ∼10 m), the sediment waves are most probably formed under current velocities of 55–60 cm/s (Soulsby 1997).

According to Allen (1982), the sandwaves can be classified as rather symmetric. Based on their symmetry index, a ratio of 1/100 can be suggested for the steady velocity versus the maximum periodical velocity (Allen 1982). These observations suggest that the sandwaves in zone 1 are under the influence of a strong tidal

component but superposed with a small residual S-ward directed current. As pointed out in Sect. 2.1.3, the general hydrographic regime in the Belgica Mound Province is dominated by a near seabed contour following, mainly poleward directed residual current generated by tidal rectification processes (White 2007; White et al. 2007). Dorschel et al. (2007a) and White et al. (2007) evidenced the impact of bottom intensified diurnal tidal currents directed across the slope (NE-SW direction). However, S-ward directed residual currents are not measured. The small S-ward directed current deduced from the sedimentary structures in zone 1 can be explained as an effect of topographic steering whereby the generally N-ward directed currents are slowed down by going upslope. A similar effect is noted at the southern slopes of the giant Galway Mound, where a southward directed residual flow and generally low current speeds indicated a stagnant region (Dorschel et al. 2007a).

Video imagery confirms the presence of sandwaves in zone 1 characterized by a sharp drop at their S-ward facing flank and local accumulations of coarser biogenic deposits in their troughs (Fig. 7.7B). Obvious is the superposition of an asymmetrical ripple pattern with straight, elongated to linguoid ripple crests on the slopes of the sediment waves having a slightly different orientation than the sediment waves (Fig. 7.7B). The ripple patterns are changing at the different flanks of the sandwaves, probably resulting from local variations in bottom current speed and direction associated with the sediment wave topography. White biogenic accumulations are also observed in the troughs created by the ripples. This ripple pattern may be caused by the influence of tidal currents. Some scattered patches of corals (mainly of the species *Madrepora oculata*) are present on the rippled seabed but they do not appear to merge in bigger frameworks or to form mounded features in this area.

So, the bedforms in zone 1 can be interpreted as long-crested, E-W directed sandwaves shaped by a strong periodic (tidal) component but still under the influence of a small residual S-ward directed current. The formation of active sandwaves with a superimposed (tidal?) ripple pattern implies abundant sand supply and active sediment transport in this region.

7.2.2.2 Zone 2: Irregular Overgrown Waveforms

Zone 2 is localized in water depths between 950 and 925 m at the south-western edge of the micro-bathymetric grid (Figs. 7.6 and 7.8). Zone 2 is situated in slightly shallower water depths than zone 1 and corresponds with the lower flank of a little mound between the Thérèse Mound and the Galway Mound, named BEL36 according to De Mol et al. (2002). The bedforms in zone 2 have a quite irregular sinuous and in some cases an abrupt terminating shape (Fig. 7.8A). However, they seem to be aligned in the same direction (E-W) as the crests of the sediment waves in zone 1. The bedforms have an average height of ∼0.66 m and an average wavelength of ∼9.23 m (Fig. 7.8C). The long slopes have an average length of ∼4.38 m, while the shorter slopes are characterized by an average length of ∼3.46 m. The average L/H ratio is ∼13.90 and the SI index is calculated to be ∼1.30. So, the bedforms in zone 1 have similar geomorphological characteristics as the bedforms in zone 2 and are characterized by a rather low symmetry index.

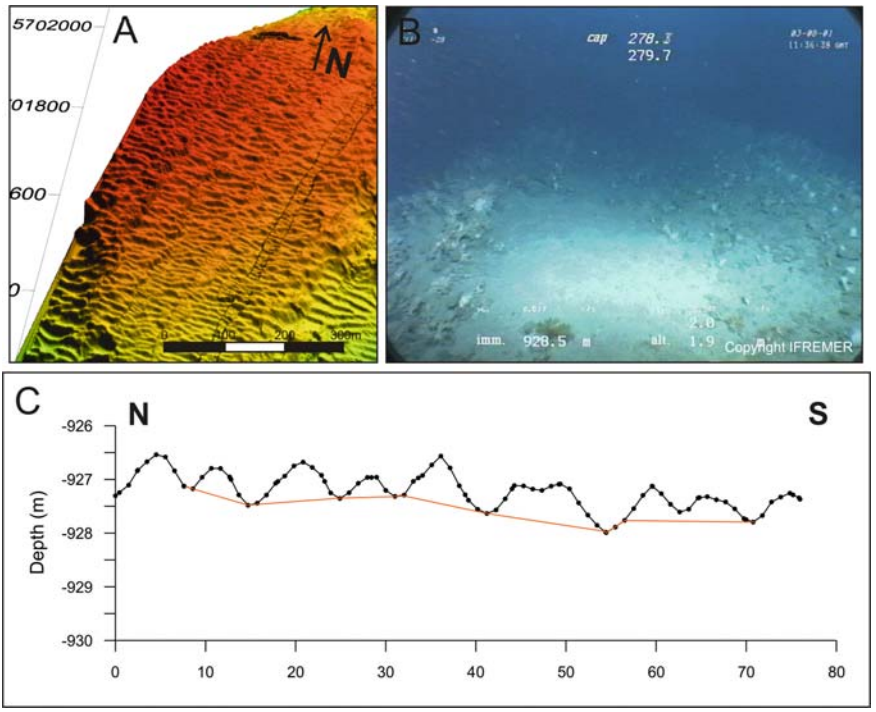

Fig. 7.8 (**A**) Zoom in on zone 2 of the micro-bathymetric grid visualizing the irregular overgrown sandwaves. (**B**) ROV video imagery showing the overgrown sandwaves. Note the preferable setting of the cold-water corals and associated fauna on the flanks and the crests of the sandwaves, while no real coral patches are observed in the troughs. (**C**) N-S profile through the overgrown sandwaves (for location see Fig. 7.6)

Video imagery revealed that the bedforms in zone 1 are covered with rather dense frameworks of dead and some patches of live cold-water corals (mainly *Madrepora oculata* and some minor occurrences of *Lophelia pertusa*) (Fig. 7.8B). Several sponge species (*Aphrocallistes* sp.) are co-occurring with the coral frameworks colonizing the bedforms. The cold-water corals seem to be preferentially settled on the crests of the bedforms and their steepest flanks facing local troughs or "stoss" sides. Some small areas characterized by irregularly spaced small-scaled current ripples are present in between the coral-patches. No coral growth is observed in the troughs between the bedforms.

The bedforms in zone 2 can be interpreted as overgrown sandwaves or coral growth forms. Due to the stabilization of the bedforms by the cold-water corals, it can be supposed that they are not mobile anymore at present times. So, they can be interpreted as relict structures. However, some small patches of ripples evidence the influence of currents and active sediment transport on a smaller scale. Similar sandwaves overgrown by cold-water corals are observed on the flanks of Thérèse Mound (De Mol et al. 2007) and on the flanks of Galway Mound (Foubert et al.

2005a; see also Sect. 7.3.2). Such overgrown sandwaves seem to be characteristic for the flanks of the mounds in the Belgica Mound Province. De Mol et al. (2005) suggest that such large sediment waves might represent an initial phase of coral bank development. Wheeler et al. (2005b) interpreted the sediment waves, based on high-resolution sidescan sonar imagery, as transgressing under different forms from the off-mound regions (as mobile sediment waves), over mound flanks (as coral-colonized sediment waves) to mound summits (as coral banks).

7.2.2.3 Zone 3: Furrows and Ridges with Straight-Crested Sandwaves

Zone 3 is situated at the north-western part of the micro-bathymetric grid at water depths around 938–940 m (Figs. 7.6 and 7.9). Zone 3 is characterized by a set of parallel furrow- and ridge-like structures on a shallow "sill" (∼940 m water depth) between BEL36 and the surrounding slope sediments (Fig. 7.9A). The lineated features have a length up to 200–250 m and are aligned in a mainly N-S to NNW-SSE direction. The average spacing between the parallel striations is 25–30 m. The "ridges" (∼ elevated structures) are generally ∼9–12 m wide and the "furrows" (∼ troughs) have widths around ∼10–14 m (Fig. 7.9C). Kozachenko (2005) interpreted the ridges as relict gravel waves. However, no extensive gravel patches are observed below the sandy top units, suggesting the interpretation of the ridges as sand ribbons. Shallow pushcores, taken with the ROV Victor 6000 during the CARACOLE cruise (Olu-Le Roy et al. 2002), evidence the presence of mainly fine silt to silty clays below a top layer consisting of 10 cm of Holocene sands. Gravity cores and box cores in the drift sediments surrounding the mounds are suggesting the same lithological pattern characterized by a small Holocene sandy top layer overlying more clayey glacial sediments (Foubert et al. 2007; Van Rooij et al. 2007a,b). Taking into account these observations, the parallel lineated features can be interpreted as caused by erosive furrows formed in the underlying glacial fine silty to silty clayey sediments.

Flood (1983) identified furrows as longitudinal bedforms which form in fine-grained, cohesive sediments of the deep-sea floor. The model of Flood (1983) for furrow initiation and development in muddy cohesive sediments suggests that furrows develop in depositional environments swept by recurring, directionally stable and episodically strong currents. Furrows are initiated when secondary circulations in the boundary layer align coarse, generally light debris in sand ribbon-like bedforms. As the coarse, light sediments move along the sea-floor, they abrade small longitudinal troughs into the muds. The grooves may fill in during intervals between strong currents events if sedimentation rates are too high. Once a furrow is established on the sea-floor, further development may be controlled by the balance between sediment deposition and erosion, where deposition occurs continuously and erosion occurs only episodically during brief periods of increased current strength. Based on the furrow cross section and the width/spacing ratio, Flood (1983) suggested a classification scheme. According to this classification scheme the furrows in zone 3 can be classified as "wide" furrows of the type "1C" characterized by a width/spacing ratio of ∼1/2–1/3. Wide furrows develop when erosion

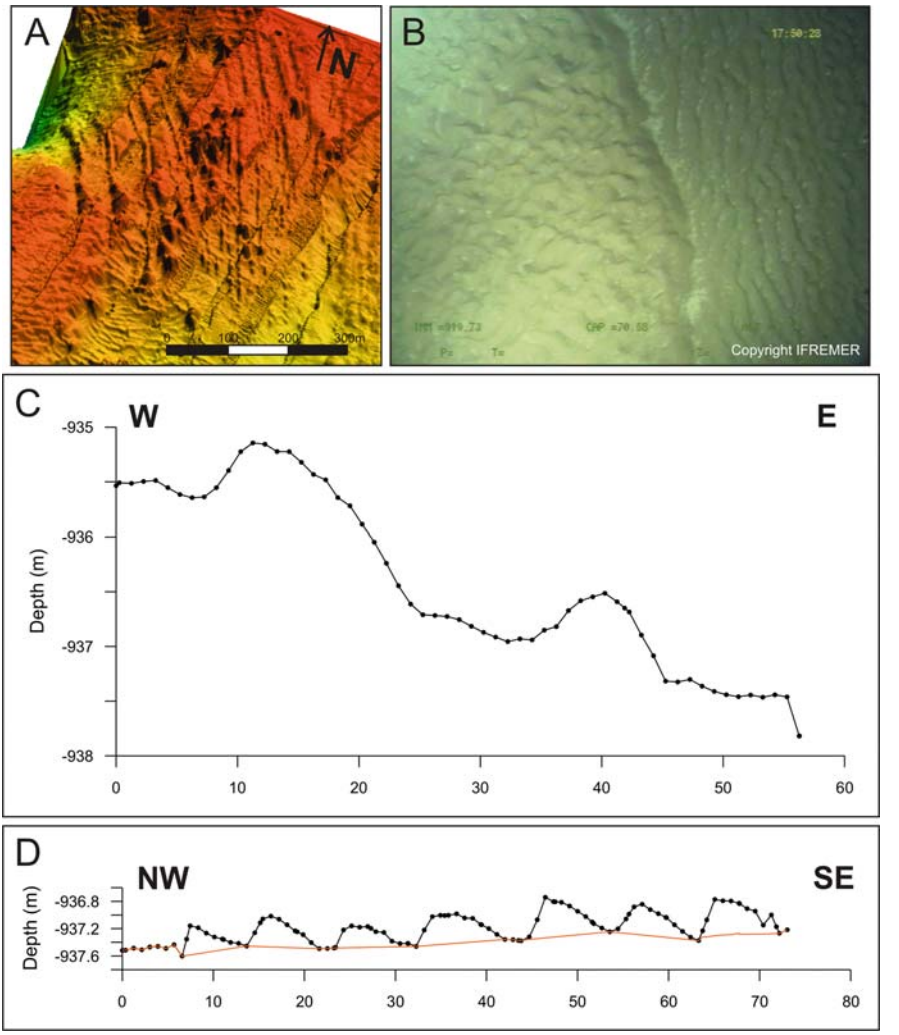

Fig. 7.9 (**A**) Zoom in on zone 3 of the micro-bathymetric grid visualizing the furrows and ridges. (**B**) ROV video imagery showing the sandwaves with superimposed ripple pattern. (**C**) W-E profile through the furrows (for location see Fig. 7.6). (**D**) NW-SE profile through the sandwaves within the furrows (for location see Fig. 7.6)

exceeds or equals deposition. Type 1 furrows are classified as furrow forms with distinct troughs, walls steeper than ∼30° and flat floors. Type 1C furrows have a more variable shape, a wider spacing and steeper walls compared to the smaller-spaced (1/5–1/15) asymmetric type 1B and the symmetric type 1A furrows. Type 1A and 1B furrows develop where directionally stable, periodically strong currents sweep areas where fine-grained sediments are accumulating. Type 1B furrows may develop their asymmetric shape as sediments accumulate around a type 1A trough.

Type 1C furrows develop under flow conditions similar to 1A and 1B, but where sedimentation and erosion balance each other, or where erosion is dominant. It should be mentioned that no single relationship exists between furrow spacing and hydrodynamic variables, although it is suggested that furrow spacing can be about two to four times the boundary layer thickness (Hollister et al. 1976). Measurements suggest that furrows may develop in a wide range of environments (Flood 1983). One end-member environment is the deep-sea where nearly unidirectional flows, only slightly modified by 1–2 cm/s tidal currents, range from 5 cm/s to greater than 20 cm/s and move along the regional bathymetric contours as observed on the Blake Outer Ridge (Jenkins and Rhines 1980). The other end-member environment can be a continental shelf where the flow is mainly tidal and currents range from 50 cm/s to often much more than 100 cm/s (Flood 1980). According to Belderson et al. (1982) features aligned in the main current direction should be formed by strong helicoidally currents up to 100–150 cm/s.

Within the furrows of zone 3, a set of transverse, SW to NE orientated, straight-crested wave-like bedforms are observed (Fig. 7.9D). The bedforms have an average height of ∼0.46 m and an average wavelength of ∼8.93 m. Their long slopes are varying around ∼6.33 m and ∼4.17°, while the short slopes are characterized by values around ∼3.04 m and ∼11.07°. An L/H ratio of ∼19.54 and a symmetry index (SI) of ∼2.79 could be calculated from the geomorphological parameters. The bedforms can be classified as sandwaves having a more pronounced asymmetry than the sandwaves in zone 1 and the overgrown sandwaves in zone 2. A ratio of 1/10 can be suggested for the steady velocity versus the maximum periodic velocity (Allen 1982), evidencing the effect of a rather strong NW-directed residual current. Minimum current velocities of 50 cm/s with an upper limit of 120 cm/s are necessary for the creation of such straight-crested asymmetric sandwaves, taking into account average grain sizes of 277 μm (Soulsby 1997). It should be mentioned that the length and the morphology of the sandwaves within the furrows is constrained by the morphology of the furrows. At some places, they seem to overrun the flanks of the furrows and the ridge-like structures flanking the furrows, suggesting that the furrows are probably formed before the onset of sandwave development.

Video imagery (Fig. 7.9B) evidences that sandy sediments are covering the furrows and the ridges associated with the furrows and that rippled structures are superposed on the described bedforms. Similar ripple patterns are observed as in zone 2 whereby the troughs are filled with coarse biogenic material. The ripple patterns may witness the tidal influence. Some of the ridges associated with the furrows seem to be colonized by patchy frameworks of cold-water corals.

It can be concluded that zone 3 is characterized by the presence of furrows, identified as type 1C furrows according to Flood (1983). These erosive furrows were responsible for the creation of the ridge-like, elevated features as observed on the micro-bathymetry. Straight-crested, SW to NE directed, asymmetric sandwaves are channelled within the furrows, evidencing the presence of a rather strong NW-directed residual current responsible for active sediment transport. The furrows are probably formed by recurring, directionally stable and episodically strong currents in the fine-grained, cohesive sediments underlying the uppermost sandy sediments.

The erosive furrows were probably developed before the onset of extensive active sand transport in the form of sandwaves, as observed nowadays. Rippled (tidal?) patterns are superposed on the observed bedforms.

7.2.2.4 Zones 4 and 5

Zone 4 is located at the north-eastern edge of the micro-bathymetric grid in water depths between 952 and 932 m. This zone seems to be characterized by a rough seabed but no distinct bedforms can be distinguished. Video imagery and box core samples confirm the presence of a rippled sandy seabed characterized by the presence of pebble to boulder-sized material, shell fragments and some well-eroded fragments of the cold-water coral species *Madrepora oculata*. Box cores revealed the presence of a muddy clayey layer below the upper coarse sandy sediments.

Zone 5 coincides with the south-eastern part of the micro-bathymetric grid, characterized by a smooth seabed and occurring in water depths between 976 and 946 m. No bedforms are observed. Sidescan sonar interpretations suggest the presence of hemipelagic drape sediments (Huvenne et al. 2005; Wheeler et al. 2005b). However, no coring or video information is available for this zone.

7.2.2.5 Mounds

At the boundary between zone 1 and zone 3, and extensively in zone 3, mounded structures are observed on the micro-bathymetric grid, i.e. the "Moira Mounds" (Figs. 7.6 and 7.10). A minor amount of mound structures are found at the boundary between zone 1 and zone 2. The micro-bathymetry confirms that the mound structures measure 30–50 m across and are up to 5 m high. They are characterized by slope gradients around $\sim 15^{\circ}$ (Fig. 7.10). Most of the mounds seem to be aligned and clustered in front of and/or on some of the ridges created by the erosive furrows as described in zone 3. Moreover, they seem to occur on the highest parts of the slopes. A detailed look to the micro-bathymetric grid and to some profiles traversing the mounds learns that the mounds are overridden by sandwaves (Fig. 7.10). The sandwaves have an average wavelength of ~ 6.35 m and a wave height averaging around ~ 0.40 m. They have similar geomorphological characteristics as the sandwaves observed within the furrows.

7.3 ROV-Imagery: New Ways of Looking to the Surface

7.3.1 Sedimentary Facies Distribution and Faunal Presence

The reconnaissance video survey with the ROV VICTOR 6000 over and in between several mounds in the Belgica Mound Province visualized different facies reflecting changes in the distribution of coral populations on mounds and mound flanks and characterizing the seabed in off-mound regions. On the basis of these

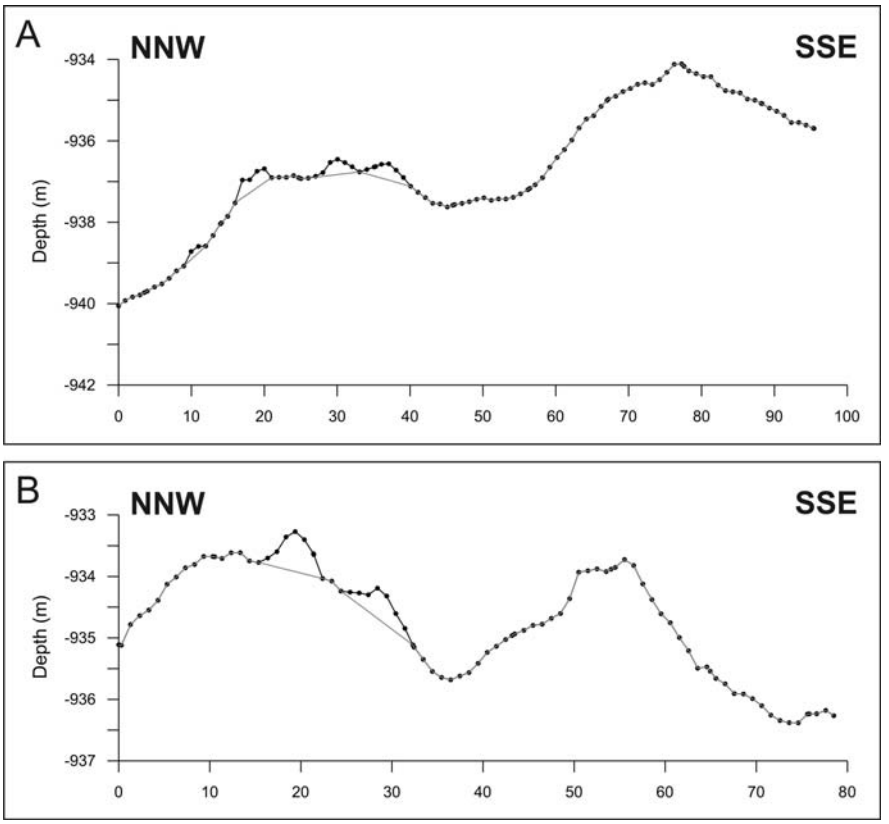

Fig. 7.10 (**A–B**) NNW-SSE profiles through the mound structures and the overrunning sandwaves (for location see Fig. 7.6)

video observations, a number of facies characteristic for the study area were derived (Fig. 7.11; Foubert et al. 2005a; Wheeler et al. 2005b). Each facies was given a colour-code and integrated within a GIS (ArcGIS 8.3), resulting in a facies-interpretation map (Fig. 7.11).

Eight mounds were video ground-truthed within the eastern area of the province (Fig. 7.11). The lack of live coral on the eastern ridge of mounds is obvious. From Challenger Mound to Poseidon Mound, the most common coral facies is the presence of sediment clogged dead corals and/or coral rubble (Fig. 7.12A). It is unclear why there is a lack of live coral here but it is presumably linked to an adverse hydrodynamic environment with respect to coral growth (for discussion see Sect. 7.4.2). Moreover, the exposed dead coral facies is confined to the western side of the mounds whereas their eastern flanks are characterized by the presence of sandy material. This corresponds with the observations of De Mol et al. (2002) and Van Rooij et al. (2003) on seismic profiles of a well-exposed western side and a buried eastern side of mounds. In several places, the coral rubble is colonized by large

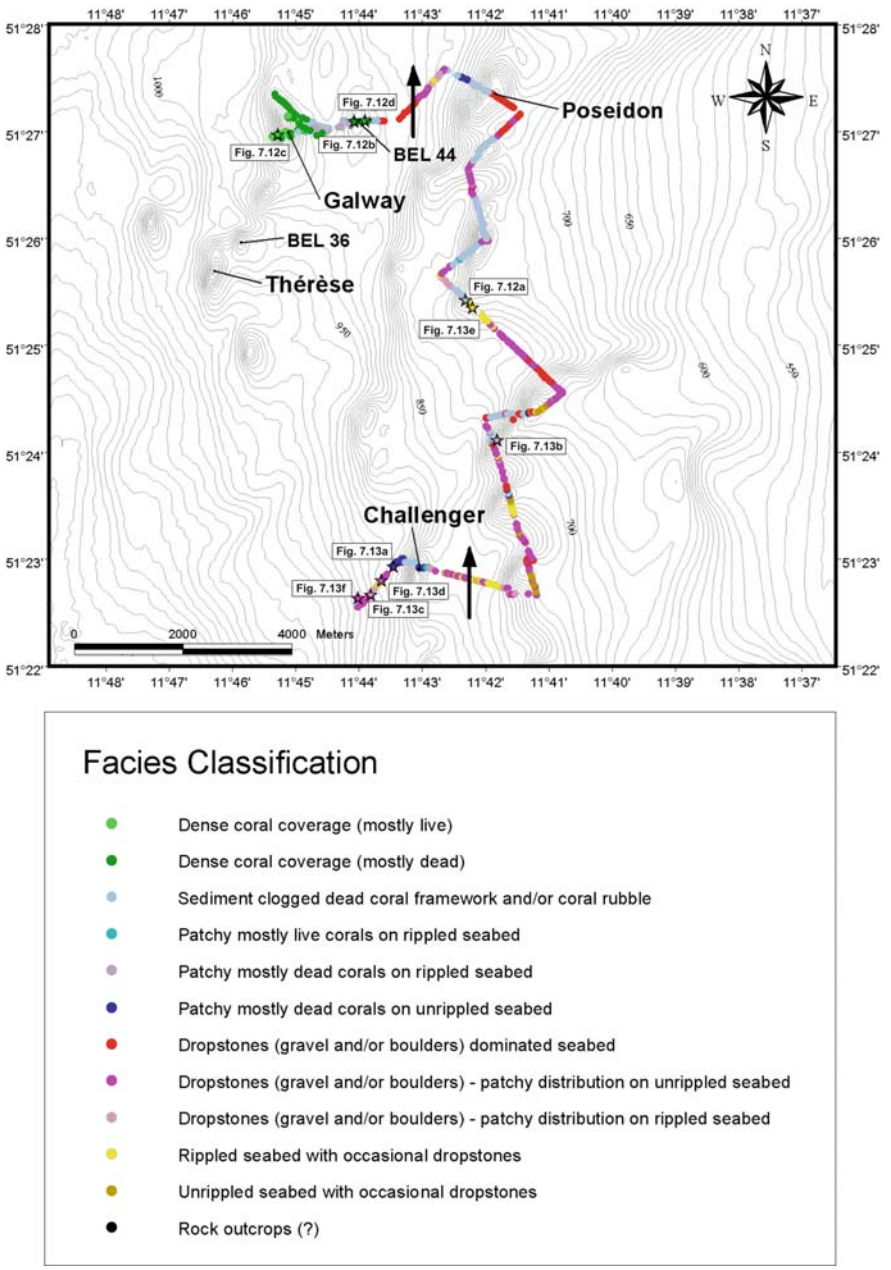

Fig. 7.11 Facies interpretation map over the Belgica Mounds plotted against bathymetric map (AWI bathymetry, Beyer et al. 2003). Contour interval is 10 m. *Black arrows* correspond with the deduced current orientations. The locations of the ROV images, visualized on Figs. 7.12, 7.13, are shown (*black stars*)

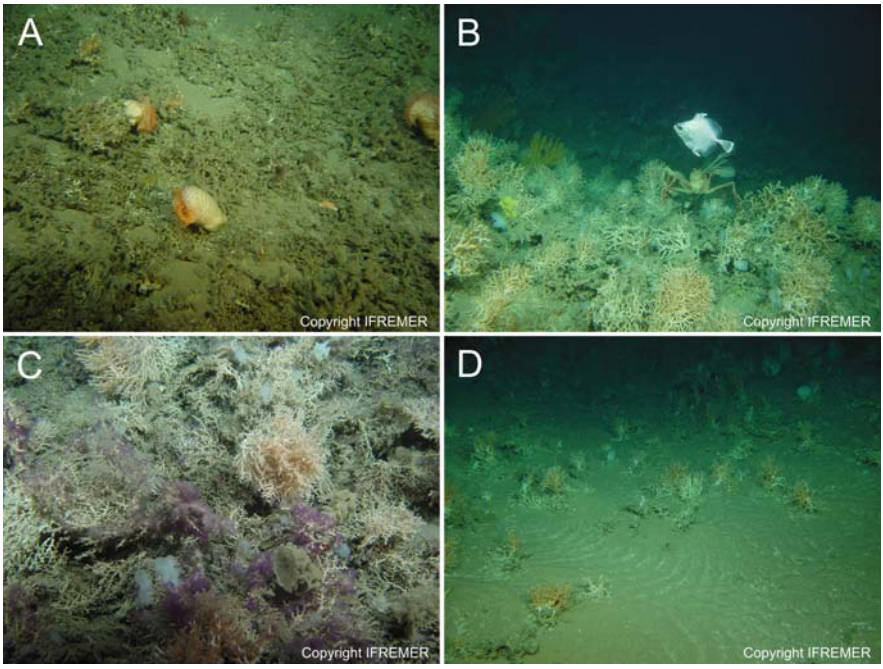

Fig. 7.12 ROV video imagery highlighting the most important facies and associated fauna encountered on the Belgica Mounds. (**A**) Coral rubble providing a firm substrate for the anemones (*Phelliactis* sp.). (**B,C**) Dense coral coverage on top of Galway Mound with a huge amount of live coral colonies (mainly *Madrepora oculata* and *Lophelia pertusa*). (**B**) *Lophelia* and *Madrepora* thickets with some gorgonians (*Acanthogorgia* sp.). In between the corals hexactinellid sponges (*Aphrocallistes* sp.) occur frequently. Common fish encountered in the Belgica Mound Province (*Neocyttus helgae*) together with a spider crab (*Paromola cuvieri*). (**C**) Living coral thicket (*Lophelia pertusa* and *Madrepora oculata*) with several *Aphrocallistes* and larger alcyonarians (*Anthothelia* sp.). (**D**) Patchy distribution of live coral (*Madrepora oculata* and *Lophelia pertusa*) on rippled sand. Several stylasterids (*Pliobothrus* sp.) are growing on the coral framework, indicating high currents

anemones (*Phelliactis* sp.) and large alcyonarians (*Anthomastus* sp.) (Fig. 7.12A). Patches of finer sediment between the dead coral frameworks are frequently inhabited by tube anemones (*Cerianthus* sp.).

In contrast to the eastern mounds, the western ridge of mounds in the Belgica Mound Province show dense coral coverage with a large percentage of live colonies of mainly *Lophelia pertusa* and *Madrepora oculata* on their summits. Dense coral coverage with a large percentage of live coral species (Fig. 7.12B,C) was encountered on Galway Mound and on the little mound (BEL 44) between Galway Mound and Poseidon Mound. The coral facies distribution pattern encountered on Galway Mound is similar to that of Thérèse Mound (also aligned in this western ridge of mounds), where a transition of dead coral and coral rubble at the base of the mounds gives way to denser live coral coverage progressing up the mound (Olu-Le Roy et al. 2002; Huvenne et al. 2005; Wheeler et al. 2005b).

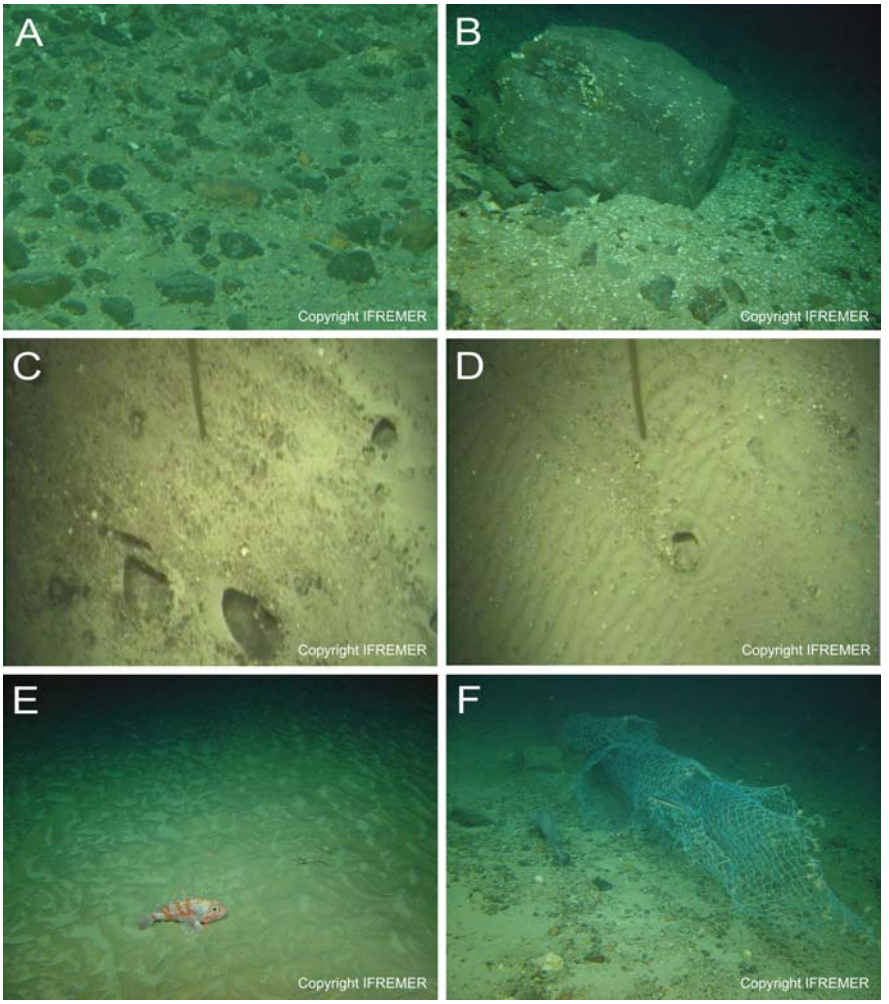

Fig. 7.13 ROV video imagery highlighting the most important facies encountered in between the coral-dominated areas. (**A)** Seabed dominated by dropstones. Stylasterids (*Pliobothrus* sp.) are settling on the dropstones. (**B)** Dropstone colonized by barnacles (*Bathylasma* sp.) on a seabed characterized by barnacle plates, dropstones and broken coral fragments. (**C)** Patchy distribution of dropstones on an unrippled seabed. Current marks are visible in the neighbourhood of dropstones with scouring and gravel patches. (**D)** Patchy distribution of dropstones on a rippled seabed. (**E)** Rippled seabed and Redfish. (**F)** Lost fishing net and lost fish *Phycis blennoides*

The seabed immediately east of Galway Mound is characterized by a patchy distribution of corals on rippled sand (Fig. 7.12D), where the presence of stylasterids (*Pliobothrus* sp.) growing on the coral framework indicates stronger currents. A clear increase of megafaunal concentrations and species on mounds with live coral coverage is noted (Fig. 7.12B,C), especially for the hexactinellid sponge

Aphrocallistes sp. and the gorgonians *Acanthogorgia* sp. and *Paramurecea placomus*. Several species of antipatharians are also represented by many colonies. Spider crabs (*Paromola cuvieri*) frequently occur in and over the coral framework. This western ridge of mounds can be interpreted as a "live" mound belt.

The presence of dropstones (gravels and/or boulders) is very common in areas between the mounds and in the channels flanking the mounds. At some locations, the seabed is dominated by dropstones (gravel and boulders), barnacle plates and broken coral fragments (Fig. 7.13A,B). In this dropstone facies, larger boulders are abundantly covered by barnacles (*Bathylasma* sp.). Beside some serpulids, encrusting sponges and bryozoans, the epifauna of these boulders is very poor. Very few boulders show prolific growth of larger sessile animals such as gorgonians, antipatharians or corals (*Madrepora oculata* or *Lophelia pertusa*). This may be due to excessive current speeds that are also responsible for the creation of the exposed dropstone facies. The presence of *Bathylasma* sp. and some stylasterids (*Pliobothrus* sp.) also indicates strong currents. Other areas are characterized by a patchy distribution of dropstones on an unrippled or rippled seabed (Fig. 7.13C,D) with scouring in front of boulders and a typical gravel patch behind (Fig. 7.13D).In this facies, the isolated dropstones are frequently colonized by encrusting sponges, barnacles (*Bathylasma* sp.) and stylasterids (*Pliobothrus* sp.). Rippled sand sheets tend to dominate the remaining seabed (Fig. 7.13E).

These observations confirm the presence of strong benthic currents in this part of the Belgica Mound Province. However, a few small patches of unrippled fine silty sand represent areas of quiescence within this region of strong bottom currents. The silty sand patches are localized on the eastern side of the mounds where sediment drift is accumulating. The orientation of current marks, scouring marks and sand ripples made it possible to deduce the orientation of the currents in some places. The overall image of the sedimentary patterns, bedform occurrences and the deduced current orientations fits very well with the general idea of a northward directed slope current. However, the impact of bottom intensified diurnal tides across the slope can not be neglected (White et al. 2007). The impact of trawl marks and even the presence of stranded fishing nets were noted (Fig. 7.13F; Grehan et al. 2003).

7.3.2 Video Mosaicing: A Quantitative Approach

In Sect. 7.3.1, a qualitative description is given from the different encountered facies in the Belgica Mound Province. However, the high amount of video information claims for more adequate and analytical quantitative techniques to study such mound and cold-water coral environments. In this chapter, an integrated method is presented for the quantitative study of video data, specially adapted to cold-water coral habitats. The proposed method is successfully tested on parts of the reconnaissance video transect between Poseidon Mound and Galway Mound collected with the ROV VICTOR 6000 during the ARKXIX/3a expedition in June 2003 (Figs. 7.11 and 7.15).

To allow quantitative analysis on video imagery, high-resolution source material has to be available. In this view, lot of attention and great care has to be paid on the acquisition of high-resolution under water video imagery. The better the source material, the better the interpretations. Three main problems have to be encountered while collecting under water imagery:

1. *Underwater positioning*
   Accurate positioning is necessary to ensure geo-referenced video material. This is not always evident in deep-sea environments. However, by using a combination of acoustic positioning and relative navigation techniques as described in Sect. 7.1, a rather accurate positioning could be achieved.
2. *Changing fields of view, different lighting conditions and distortions in the image*
   While collecting under water imagery with ROV-systems, different cameras are mounted in different positions on continuously moving vehicles flying over irregular topographic features what is resulting in continuously changing fields of camera views, different lighting conditions and distortions in the image. In order to avoid from the start strongly changing views and distortions a downward-looking (vertical) camera mounted on the ROV was used for focused mapping dives. The quantitative analyses are based on images taken by the vertical camera. Taking into account the opening angle of the camera (60°) and the optimal average height of the camera above the sea-floor (3 m), the analysed surface for each view field of the camera (or frame) is 3 m^2 resulting in a frame width of 1.732 m. It is presumed that working with an average distance over ground, the sea-floor inclination as varying factor, not exceeding 34° in the study area, can be neglected with the camera mounted in the middle of the ROV. Video footage from obliquely mounted cameras, recording high-resolution images, was used to refine the visual information recorded by the vertical mounted camera.
3. *Video imagery restricts the resolution of observations to megafauna, very few characteristic macro-fauna and well-developed seabed characteristics*
   In order to look behind the restricted resolution of video imagery, ground-truthing with giant box cores and Van Veen grabs was carried out. This allowed detailed identification of animals observed on the video footage and precise characterization of the sediment composition.

Once the data are collected, the data have to be reduced to workable units. In this study, the video data have been cut into more than 270 video sequences for quantitative analyses. Sequence selection was done based on GIS referenced navigation files. A distance of 25 m has been defined as standard length for each sequence, taking into account the small-scale changes in topography and facies in the study area (Fig. 7.14C). Each selected sequence was then processed to a video-mosaic. Special adapted software developed by Luong et al. (2006) allowed creating high-quality video mosaics filtering out light effects and distortions. Existing mosaicing techniques failed due to the non-uniform illuminated environments caused by the spotlights mounted on ROV's, necessary to illuminate dark deep-sea environments. The more, traditional image blending techniques suffered from ghosting artifacts in

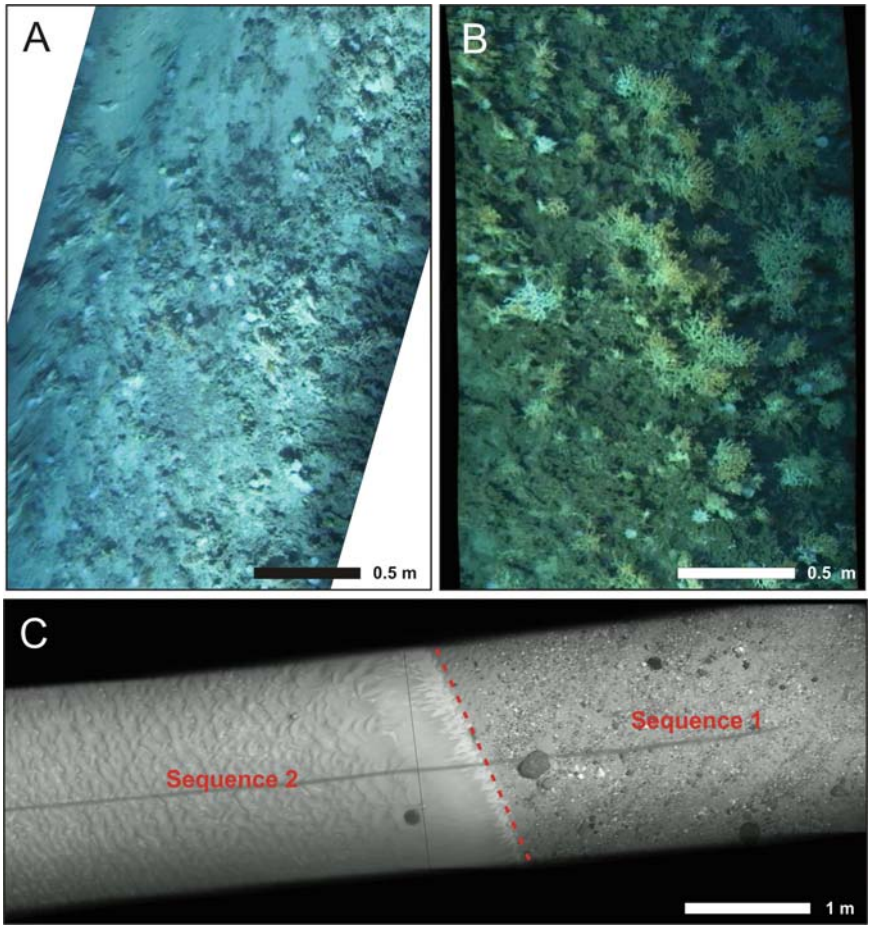

Fig. 7.14 Techniques of video mosaicing. (**A**) Video mosaic created by traditional mosaicing techniques, showing artifacts at the margins. (**B**) Video mosaic created by special developed software to filter out light effects and distortions (Luong et al. 2006). (**C**) Video mosaic showing a distinct facies transition. By cutting the video data in separate sequences, such distinct facies changes were taken into account

the presence of moving objects (f.e. fish). A new robust mosaicing algorithm tackled the problems (Luong et al. 2006) (Fig. 7.14A,B). Due to the use of GIS-integrated systems, the seabed surface corresponding to each mosaic is well known (sequence length times sequence width).

Finally different "classes" and "layers" have to be defined before the mosaics can be subjected to quantitative analysis. As the most important facies were already described during a first qualitative study (Sect. 7.3.1), the different classes and layers to quantify were based on this qualitative study. The layer-concept used in GIS environments was adapted to the cold-water coral environments and three

main layers were identified: (1) substrate, (2) bedforms, and (3) associated fauna. Each layer was subsequently subdivided in different classes. For the "substrate" layer, the following classes were defined: sand, dropstones, dead coral rubble, dead coral framework, few live coral (<5%), moderate live coral (5–50%) and abundant live coral (>50%). Within the layer "bedforms", next classes were identified: rippled sand sheets, rippled sand sheets and asymmetrical sandwaves (E-W), current-swept gravel, asymmetrical sandwaves (E-W), symmetrical sandwaves (E-W) and, symmetrical sandwaves (N-S). Only abundant associated fauna was classified: gorgonians, antipatharians and, sponges. The percentage of coverage of each identified substrate type and each kind of bedform was quantified on the videomosaics using the software analySIS, allowing semi-automated classification. Each videomosaic was then labelled according to the dominant substrate type and bedform type encountered in the video mosaic. The associated fauna was quantified using the point-count utility of the software analySIS. Species covering large surfaces were retained in the quantitative analysis with percentage of coverage for each mosaic.

The results of the quantitative analysis and the video mosaics representing the most important classes are visualized on Figs. 7.15 and 7.16. By looking to the substrate classes, it can be summarized that abundant live coral is present on the top and western flanks of Galway Mound and the small mound (BEL 44) between Galway Mound and Poseidon Mound (Figs. 7.15A and 7.16A). Moderate live coral is observed at the eastern flank of Galway Mound and BEL 44 and at the lower western flank of mound BEL 44 (Figs. 7.15A and 7.16B). At the western side of Galway Mound and between Galway Mound and mound BEL 44, few live coral patches are observed. Also at the lower western flank of Poseidon Mound some live coral patches are identified but most of its western flank is covered with dead coral rubble and dead coral framework (Figs. 7.15A and 7.16C,D). Gravel- and boulder-sized material (identified as dropstones) characterizes the sea-floor between Poseidon Mound and mound BEL 44 and the eastern flank of Poseidon Mound (Figs. 7.15A and 7.16H–J). A small sheet of rippled sands is present between Poseidon Mound and mound BEL 44 (Figs. 7.15A and 7.16I). Typical bedforms bear witness of active sediment transport in the studied regions (Fig. 7.15B). Rippled sand sheets and asymmetrical sandwaves characterize the sea-floor between Galway Mound and mound BEL 44. Current-swept gravel is mainly dominating between Poseidon Mound and mound BEL 44, evidencing stronger and more vigorous bottom currents than between Galway Mound and mound BEL 44 (Figs. 7.15B and 7.16H–J). The orientation of the bedforms indicates in both areas a generally northward directed current. Asymmetrical and symmetrical sandwaves aligned with their crests in E-W direction, overrun the eastern flank and the summit of Galway Mound and mound BEL 44 and the lower western flank of Poseidon Mound (Fig. 7.15B). In all areas the sandwaves are overgrown by dead coral rubble and/or live coral framework. Symmetrical N-S directed sandwaves are observed at the lower eastern flanks of Galway Mound and bears witness of the impact of bottom intensified diurnal tidal currents across the slope in these areas. Trawl impacts are frequently noted, especially at the eastern side of Poseidon Mound (Figs. 7.15B and 7.16 K).

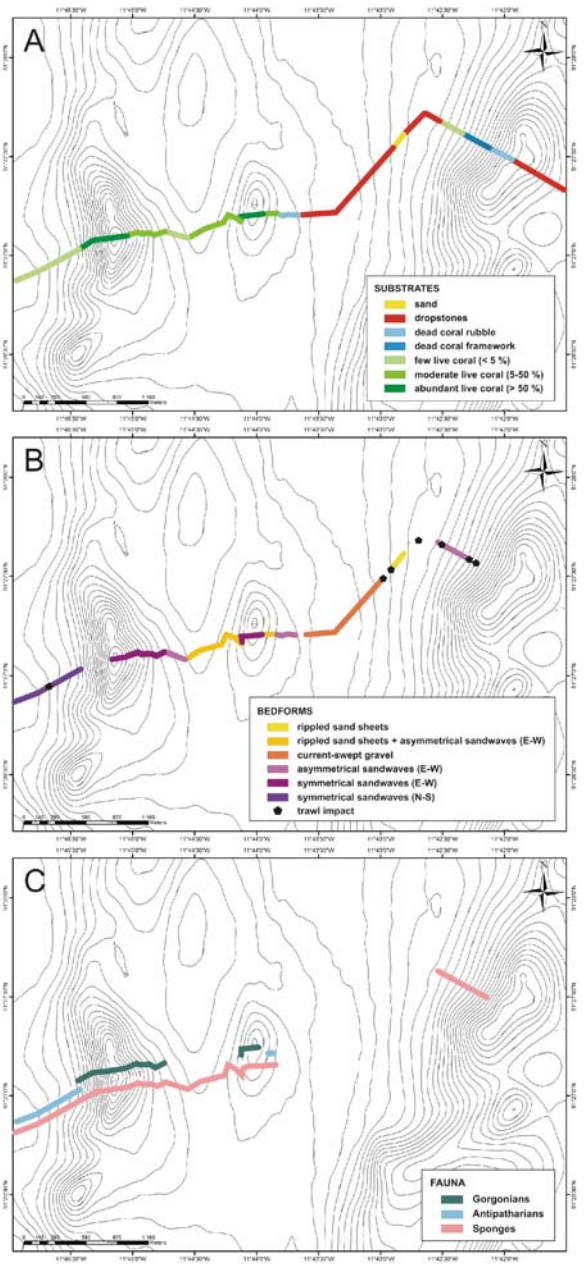

Fig. 7.15 Visualization of the defined layers and classes between Poseidon Mound and Galway Mound by integration of the video mosaics in a GIS system (ArcGIS8.3). Data are plotted against the bathymetry with contour intervals set at 10 m (AWI bathymetry, Beyer et al. 2003). (**A**) Occurrence of the classes defined in the layer substrate. (**B**) Occurrence of the classes defined in the layer bedforms. (**C**) Occurrence of the classes defined in the layer associated fauna

Most of the observed fauna is co-occurring with dead and/or live coral framework (Fig. 7.15C). Gorgonians, i.e. the species *Paramuricea placomus*, are mainly identified on the upper flanks and the summit of Galway Mound and at the summit

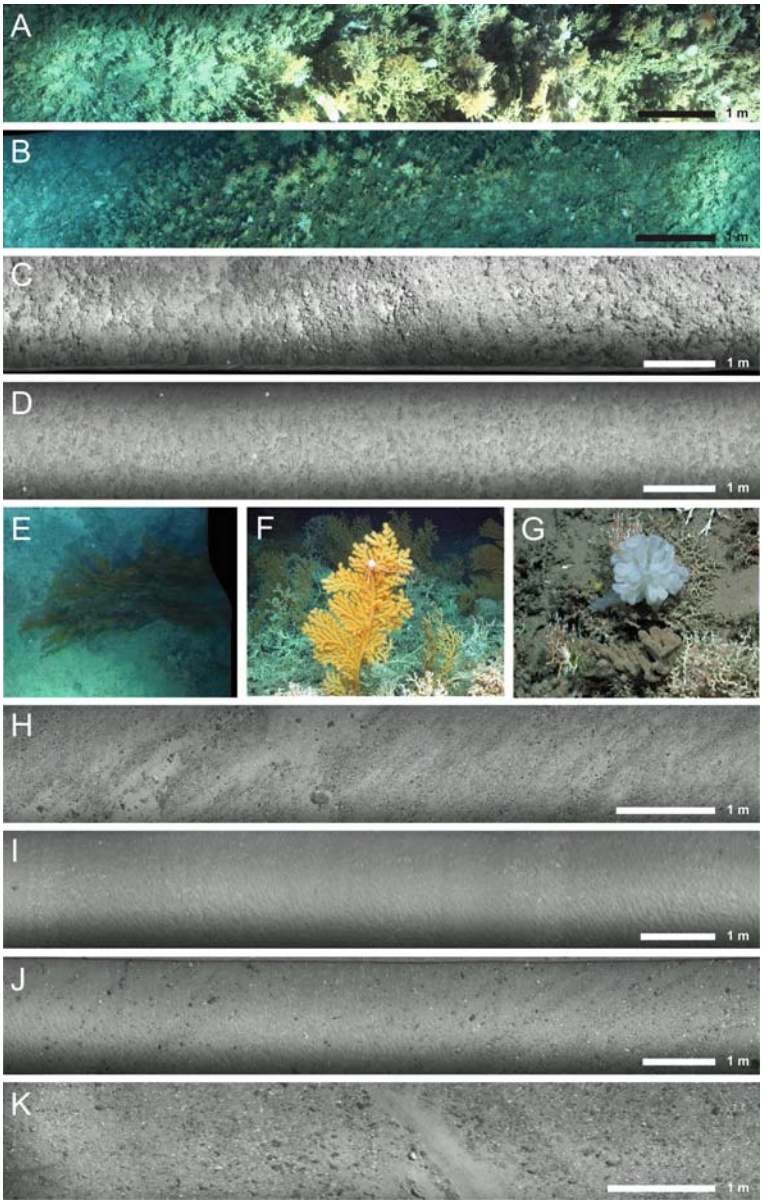

Fig. 7.16 Video mosaics and ROV video imagery visualizing substrate, bedforms and associated fauna. (**A**) Abundant live coral coverage (*Madrepora oculata* and *Lophelia pertusa*) with associated fauna. (**B**) Moderate live coral coverage (*Madrepora oculata* and *Lophelia pertusa*) and associated fauna. (**C**) Low live coral coverage but mainly dead coral framework. Sponges frequently inhabit the dead coral framework (*Aphrocallistes bocagei*). (**D**) Patchy distribution of dead coral rubble and moderate occurrence of sponges (*Aphrocallistes bocagei*) on unrippled sandy seabed. (**E**) Anthipatharian (*Leiopathes glaberrima*). (**F**) Gorgonian (*Paramuricea placomus*) with the spider crab *Chirostylus formosus*. (**G**) Sponge (A*phrocallistes bocagei*).

of the mound BEL 44 (Figs. 7.15C and 7.16E). The highest occurrences (with an average of 120 colonies each 43.3 m^2 or 2.77 colonies each m^2) are observed at the summit of the Galway Mound. The anthipatharian *Leiopathes glaberrima* is mainly occurring at the lower western flank of Galway Mound and at the upper eastern flank of mound BEL 44 (Figs. 7.15C and 7.16F). Sponges are colonizing the substrates as soon as dead or live cold-water coral framework is present. The sponge species *Aphrocallistes bocagei* was point-counted, revealing the highest occurrences at the lower eastern flank of Galway Mound (with an average of 250 specimens each 43.3 m^2 or 5.89 speciments each m^2) (Figs. 7.15C and 7.16G). As well as the species *Aphrocallistes bocagei*, as the species *Leiopathes glaberrima* seem to prefer areas characterized by strong diurnal tidal bottom currents.

The quantification of specific classes made it possible to refine the habitat and facies definitions described in Sect. 7.3.1. The contrast of, on one hand carbonate mounds with live coral coverage (Galway Mound) and on the other hand mounds covered with mainly dead cold-water coral rubble (Poseidon Mound), is highlighted and amplified by a quantitative comparison including as well sedimentological as biological parameters. Moreover the presented methodology can allow cluster analysis to redefine macro-environments. Linear correlation and stepwise regression can be used to relate benthic species and their associations to environmental variables. However, due to the testing character of this small methodological study such detailed statistical analyses were not yet carried out for the presented data.

7.4 Discussion

7.4.1 Moira Mounds: A Form of Stressed Coral Growth?

A detailed study of the micro-bathymetric grid and the corresponding video imagery confirms that the Moira Mounds are occurring in an area where the dynamic interaction between active sand transport, sedimentation and current dynamics play an important role in shaping the present-day sea-floor. It should be mentioned that the micro-bathymetric grid is a "snapshot" of the seabed, revealing the bedforms and structures of the sea-floor at the time of data collection. No repeated surveys of adequate resolution are available to check the temporal variability of the interpreted bedforms. In this study, it is assumed that most of the bedforms are formed under regular peak flow events.

Following the micro-morphological observations, an evolution model can be proposed for the development of the Moira Mounds framed in their surrounding sedimentary environment (Fig. 7.17). Currents in conjunction with moderate sediment

Fig. 7.16 (continued) (**H**) Seabed dominated by current-swept gravel with scouring features and gravel patches associated with boulder-sized material. (**I**) Rippled sand sheet. (**J**) Current-swept gravel on a rippled seabed. (**K**) Trawlmark on dropstone-dominated sea-floor. The original ROV video imagery is copyright IFREMER

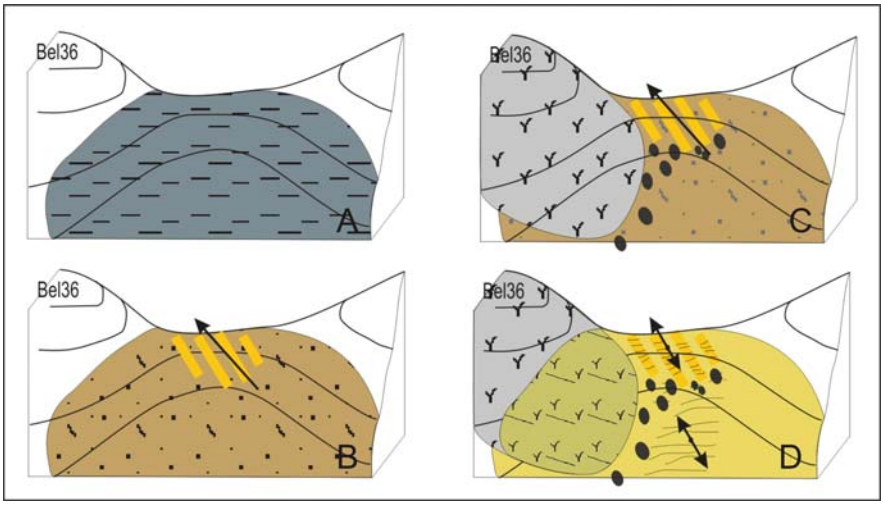

Fig. 7.17 Block diagram summarizing the depositional history for the evolution of the Moira Mounds and their surrounding sedimentary environment. (**A**) Glacial: deposition of fine cohesive sediments. (**B**) Deglaciation: onset of vigorous bottom current regime resulting in extensive erosion and scouring with the formation of type 1C furrows. (**C**) (Re)colonisation of the area by cold-water corals and the creation of small mound build-ups. (**D**) Holocene: gradual build-up of mobile sand sheets with associated ripples and sandwaves

supply and transport play hereby an important role. Extensive core-studies in the off-mound regions of the Belgica Mound Province have evidenced that glacial periods are characterized by the deposition of fine-grained material (Chap. 6; Foubert et al. 2007; Van Rooij et al. 2007a,b). It can be supposed that also in the studied micro-environment extensive cohesive fine-grained sediments where characterizing the sea-floor during the last glacial period (Fig. 7.17A). Subsequent deglaciation, reinitiated the vigorous bottom current regime typical for interglacial and interstadial periods in the Porcupine Seabight, transporting high amounts of reworked coarse material (Chap. 6; Foubert et al. 2007; Van Rooij et al. 2007a,b). On the saddle-like structure secondary circulations in the boundary layer started to align the coarse, generally light debris, transported by the strong N-ward directed bottom currents, in sand ribbon-like bedforms. As the coarse and light sediments moved along the seafloor, they abraded small longitudinal troughs into the muds, resulting in the creation of the described furrows (Fig. 7.17B). During these times, erosion was dominating on deposition. Belderson et al. (1982) suggested current speeds between 100 and 150 cm/s for the creation of longitudinal bedforms such as furrows and sand ribbons. Flood (1983) showed that furrows can be also generated by much lower current levels. However, the typical 1C furrows are witnessing periods of extensive erosion suggesting current speeds up to 100 cm/s. Such high current speeds may have prevented cold-water coral growth during erosive deglaciation events. The more, Frederiksen et al. (1992) suggest that current speeds $>$100 cm/s probably cause coral colonies to topple over having thus a negative effect on cold-water

coral growth. However, when fully interglacial conditions where established, currents waned but were still stronger than observed during quiet glacial conditions. It is exactly under these conditions that cold-water corals probably started to grow in the studied area (Fig. 7.17C). The ridge-like structures created by the furrows, could have been suitable settling substrates for cold-water corals seen their elevated position. However, it should be mentioned that not all the mounded structures are settled on the ridge-like structures. On the contrary, they seem to be in many cases clustered in front of the lineations. In each case they are localized on the highest points in the studied micro-environment, i.e. on the saddle-like structure. In this view, elevated positions, subjected to stronger currents and so enhanced food supply, may have been the most crucial factor for the cold-water corals in choosing their settlement place. As at the base of Challenger Mound, cold-water corals seem to be initiated on a regional scoured erosional surface but no hardground or hard substrate as settling substrate is observed. Again, this can form an argument for the fact that the impact of currents and sedimentation prevails on suitable settling grounds for the initiation of cold-water coral growth. An important factor which might have been the triggering mechanism to go over from cold-water coral growth to small mound build-ups is the onset of a sedimentary regime with active sand transport. Once cold-water corals gained a certain footing, the coral colonies can trap the sediments and so build up positive features for further coral development on the sea-floor. In this way, corals become elevated above the benthic-boundary layer gaining access to fast-flowing waters (with increased nutrient flux), and thus stimulating further coral growth, sand entrapment and increases in mound elevation. So, a positive feedback mechanism, whereby the coral sediment entrapment process provides support for coral colonies encouraging new coral growth can play an important role in initial mound growth. Cold-water coral thickets can be seen in this way as a kind of "micro-environment" or "permeable barrier". The thickets reduce the flow, making sediment "baffling" or sediment deposition possible, but do not block the current completely. Such a flow reduction caused by coral thickets is also evidenced by the ripple patterns that seem to disappear between the corals but are extensively formed in the open spaces within the coral forest. A positive feedback mechanism can also be proposed to explain the overgrown sandwaves observed on the flank of mound BEL 36. In this way, it is envisaged that coral colonies on the flank of mounds are encroached upon by sediment waves whose progress is retarded by the coral colonies that also trap the sand (Wheeler et al. 2005b). As on the Moira Mounds, a sediment entrapment process supports the coral colonies allowing them to grow higher. This enhanced vertical growth facilitates further sand entrapment, encouraging more growth. Overtime the sediment waves become larger and steeper with extensive coral growth on their crests and restricted or absence of coral growth in their troughs (Wheeler et al. 2005b). Nowadays, the area is characterized by extensive active sand transport, evidenced by the presence of sandwaves and rippled structures in the area, and even sandwaves overriding the small Moira Mounds (Fig. 7.17D).

It can be questioned if the presence of such extensive active coarse sand transport is positive for coral and mound growth, or if it bears witness of a process of cold-water coral growth (and their attempt to build up mound structures by sand baffling)

in a stressed environment where cold-water corals are trying to find the best and highest positions to survive. Indeed, it should be mentioned that no coarse sediment entrapment process is yet observed on the top of healthy live mounds. The more, most of the sediments on top of the giant mounds and the sediments on Challenger Mound are rather fine silty to silty clayey sediments, suggesting deposition of finer material filling the coral frameworks during slack water. Moreover, in the neighbourhood of the Moira Mounds the cold-water coral species *Madrepora oculata* seem to dominate, while *Lophelia pertusa* is dominating throughout Challenger Mound with only a change towards *Madrepora oculata* in the top layers, when the mound is in a decline phase. Sanders and Baron-Szabo (2005) suggested that the form and species of scleractinian assemblages are changing under different sedimentary environments with a clear shift towards more sediment-resistant morphs and taxa in sedimentary stressed environments. These authors marked a high sediment tolerance for small-polyped taxa, e.g. *Porites, Montipora*. Due to their small-sized coral heads, such small-polyped corals probably reject sediment more effective than large specimens of lower convexity. The dominance of the small-polyped species *Madrepora oculata* may witness the presence of a higher sediment stress caused by the vigorous contouritic drift sedimentation characterizing the Belgica Mound regions nowadays. So, Moira-like mound build-ups in a sandy contouritic environment may represent stressed forms of cold-water coral growth trying to keep up with active sand transport. How these small mound structures formed under stressed conditions represent an initial phase of mound growth can be discussed. It can be suggested that such small mounds may in a later stage coalesce to form one or several big mounds and so form a structural height that can keep up with moving sand sheets, preventing themselves from being buried. By forming bigger mounds they can go over to a mechanism whereby baffling of finer material during slack water conditions become an important giant mound growth process. The importance of tidal currents in these processes of giant mound growth can not be neglected, as they might provide the necessary alternation between quiet periods where fine sedimentation prevails and periods characterized by high current speeds to supply nutrients for the cold-water corals and so enhance cold-water coral growth. As fine sediments are more cohesive and so more difficult to erode than sands these quiet phases are necessary for the stabilization and consolidation of giant mounds. The fact that the Moira Mound build-ups do not make it nowadays to go over to a stage of giant mound growth can be the lack of the deposition of fine, cohesive sediments, a crucial factor in mound stabilization. It should be mentioned that the sediments recovered at the base of Challenger Mound lack a distinctive sandy facies or a facies comparable to that encountered in the Moira Mounds nowadays (Huvenne et al. 2006). This suggests that for Challenger Mound an initial phase of mound build-up explained by the coalescence of small Moira-like mounds is rather unlikely.

It can be concluded that current speeds, sediment transport (and deposition) processes and tidal currents are crucial factors in the competition between cold-water coral growth and sedimentation to build up mounded structures. Small mounded structures can be formed by the interaction between cold-water coral growth and sediment baffling as a positive feedback mechanism. However, such small mound

build-ups seems to represent rather a way of mound formation under stressed conditions than an initial phase of extensive mound growth. On the other hand, it can not be excluded that such small mound patches may coalesce in a later phase to form one or several bigger mounds. Once the mounds gained a certain height they can become elevated above the benthic boundary layer, allowing them to go over to a process of giant mound development under a tidal current regime whereby finer sediments are deposited in between the corals during slack water and whereby the peak tidal currents are responsible for enough food supply. However, modelling these processes of initial mound build up and giant mound development in well-defined and controlled lab-environments is necessary to understand the initial and fundamental processes of mound build-up.

7.4.2 "Dead" Mounds Next to "Live" Mounds?

One of the most obvious observations is that erosive features with gravel patches, evidencing N-ward directed coarse-grained sediment transport, are dominating the seabed around the eastern ridge of "dead" mounds or better expressed as mounds covered with mainly dead cold-water coral rubble and eroded cold-water coral fragments. Active sediment transport is also occurring around the western ridge of "live" mounds (or mounds covered with live coral framework) but seems to be dominated by sand transport and the creation of associated sandwaves, evidencing lower erosive currents than observed in the neighbourhood of the eastern ridge. However, the number of "dead" mounds is dominating on the amount of "live" mounds in the Belgica Mound Province. The more, also in the environment of the "live" mounds, corals seem to occur in a sediment-stressed environment (Sect. 7.4.1). The high amount of gravel occurring between the mounds can be explained as deposited during the last glacial period when ice-sheets where probably reaching the shelf edge of the Porcupine Seabight (Sejrup et al. 2005).

As discussed in Sect. 5.5.4, extensive contourite drift sedimentation is characterizing the off-mound areas since the last 0.5 Ma. The strong contour currents, responsible for extensive drift sedimentation have a dual impact on the coral mounds by burying their eastern flanks through the deposition of thick sediment sequences and by eroding their western flanks. Such extensive contourite sedimentation and the associated high contour currents have thus probably a negative effect on mound growth. However, the western flanks and the summits of the "live" mounds belonging to the western mound ridge may form a kind of shelter, where cold-water corals are protected against the N-ward directed contour currents. In these "sheltered" areas the impact of tidal currents seems to be important, as evidenced by the N-S directed sediment waves encountered at the lower eastern flank of the live Galway Mound (Sect. 7.3.2). Such tidal currents provide the cold-water corals enough nutrients and organic particulate matter to survive during peak tides and enough quietness to allow the finer material sinking down during low tides which is necessary to stabilize the mound. Hence, bottom intensified tidal currents seem to have

a positive effect on mound and cold-water coral growth. The importance of bottom intensified tidal currents by shaping the mounds in the Belgica Mound Province is evidenced by White et al. (2007). The reason why "dead" mounds are occurring next to "live" mounds is still unclear and more research, such as comparative current meter measurements on and off "dead" and "live" mounds, is necessary.

7.5 Summary

Micro-bathymetry over the Moira Mounds revealed the presence of 3 well-delineated zones, each characterized by typical sedimentary structures bearing witness of active sediment transport: (1) **regular E-W directed sandwaves**, (2) **irregular overgrown sandwaves**, and (3) **furrows** and **ridges** associated with straight-crested sandwaves. The **Moira Mounds** appear as small-mounded features, subcircular in shape, measuring 30–50 m across and up to ~5 m tall.

The evolution of the Moira Mounds can be explained as formed by the interaction between cold-water coral growth and sediment baffling through a **positive feedback mechanism**. However, such small mound build-ups seems to represent rather a way of mound formation under **stressed conditions** than an initial phase of extensive mound growth.

ROV video imagery visualized the different facies encountered on the mounds and between the mounds in the Belgica Mound Province. An **eastern ridge** of **"dead" mounds** mainly covered with sediment clogged dead cold-water coral rubble and dead cold-water coral fragments is observed. Just a few "live" mounds are present in the study area, clustered in a **western ridge** of **"live" mounds** and covered with live coral framework. **Bottom intensified diurnal tidal currents** have an important and **positive impact** on the western ridge of "live" mounds. Such tidal currents can provide the cold-water corals enough nutrients and organic particulate matter to survive during peak tides and enough quietness to allow the finer material sinking down during low tides which is necessary to stabilize the mound.

A new method is presented and successfully tested for the **quantitative analysis** of ROV video imagery by **video mosaicing** and their integration in **GIS**-based environments.

Chapter 8
Carbonate Mounds in the Gulf of Cadiz

An exploratory cruise of R/V Belgica in 2002 off Larache (Morocco) has led to the discovery of small mounds topping ridges and structural heights (respectively on Pen Duick Escarpment, Renard Ridge, Vernadsky Ridge and Al Idrisi Ridge). These mounds are found amidst 9 giant mud volcanoes: the El Arraiche mud volcano field (Van Rensbergen et al. 2005a). They occur in a setting where focused fluid seepage is observed (Baraza and Ercilla 1996; Pinheiro et al. 2003; Somoza et al. 2003; Van Rooij et al. 2005). Because of its unique setting, the carbonate mound site on the Moroccan margin became rapidly involved in a developing stage of focused multidisciplinary research. In May 2004, a 9m-long Kasten core was recovered with R/V Marion Dufresne on top of one of the largest build-ups – 60 m high. It contained cold-water corals over its whole length, a striking similarity with the Porcupine mound cores (Foubert et al. 2007) but a very strong smell of hydrogen sulphide was reported on deck. The core featured a well-delineated zone of heavily dissolved cold-water corals and a zone of diagenetic carbonate precipitation. Pore water analyses gave evidence of a sharp sulphate-methane transition (SMT) zone at 3.5 m below the mound top. Cruises in summer 2004 and 2005 have confirmed these observations, and have expanded the exploration of this cluster of mounds.

The high amount of data, acquired recently in these new mound settings on the Moroccan margin, asks for a comprehensive review which will be presented in this chapter. These data formed the base for a new IODP Proposal 673-Pre, now admitted to the stage of a full proposal IODP 673-Full, focusing on the non-buried mounds on the Pen Duick Escarpment, off Morocco (Van Rooij et al. 2008).

8.1 General Setting

8.1.1 Geological Setting

The Gulf of Cadiz is situated west of Gibraltar between 9°W–6°45′W and 34°N–37°15′N, enclosed by the Iberian Peninsula and Morocco (Fig. 8.1A). The geological setting of the Gulf of Cadiz is complex and still under debate (Sartori et al. 1994; Maldonado et al. 1999; Gutscher et al. 2002). The area is characterized by

A. Foubert, J.-P. Henriet, *Nature and Significance of the Recent Carbonate Mound Record*, Lecture Notes in Earth Sciences 126, DOI 10.1007/978-3-642-00290-8_8,

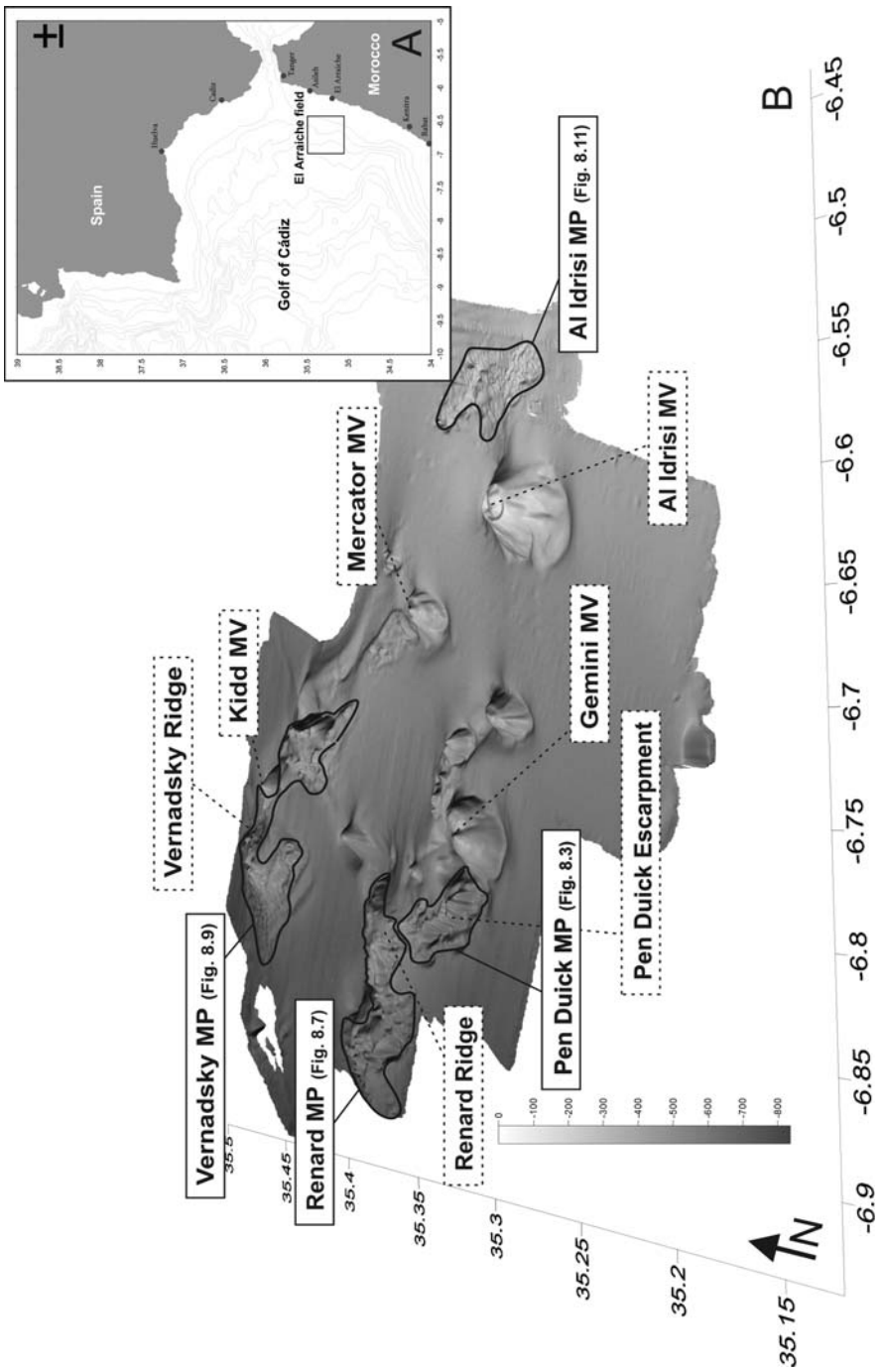

Fig. 8.1 (continued)

the presence of an accretionary wedge formed by a westward motion of the front of the Gibraltar Arc (the Betic-Rif mountain chain) during the Middle Miocene. Formation of a large olistostrome complex (allochthonous nappes) took place during the Tortonian, as a consequence of increased subsidence (Maldonado et al. 1999). The African-Eurasian convergence since the Cenozoic yields a compressional-transpressional tectonic regime, reactivating many normal faults and causing widespread diapirism in the north of the Gulf of Cadiz (Berastegui et al. 1998; Somoza et al. 2003). The main part of the olistostrome unit occupies the central part of the Gulf of Cadiz as a lobe-shaped structure, extending over 300 km into the Atlantic Ocean (Maldonado et al. 1999; Somoza et al. 2003).

The study area, El Arraiche mud volcano field, is situated 35 km offshore the north-western Moroccan margin, on top of the accretionary wedge of the Gulf of Cadiz (Van Rensbergen et al. 2005a). The bathymetry is increasing from 200 to 800 m at the north-western Moroccan continental slope. The study area is characterized by extensional tectonics, in contrast to the main part of the Gulf of Cadiz. This is expressed as large rotated blocks bound by lystric faults that created Plio-Pleistocene depocentres (Flinch 1993, 1996). In El Arraiche mud volcano field these rotated blocks are expressed at the sea-floor as two sub-parallel ridges, Vernadsky and Renard Ridges, both with steep fault escarpments, as exemplified by Pen Duick Escarpment (PDE) on Renard Ridge (Fig. 8.1B). The ridges rise up in water depths of about 700 m and stretch to the shelf edge. Eight mud volcanoes are clustered around these ridges, positioned above large normal faults that bound the rotated blocks and serve as fluid migration pathways fuelling the mud volcanoes (Van Rensbergen et al. 2005a) (Fig. 8.1B). The source of the overpressured fluids is believed to be located at the base of the accretionary wedge body since rock clasts in the mud breccia are reported to be of an age up to Early Eocene (Ovsyannikov et al. 2003). The onset of mud volcano activity in the El Arraiche mud volcano field is estimated at about 2.4 Ma. Since the Upper Pliocene, episodic expulsion of liquidized sediment created vertical piles of extruded mud up to 500 m thick (Van Rensbergen et al. 2005a).

Geophysical evidence of shallow gas and subsurface fluid flow has been reported in the Gulf of Cadiz (Baraza and Ercilla 1996; Pinheiro et al. 2003; Somoza et al. 2003). Rodrigues and Cunha (2005) described cold-seep communities in the area. The highest number of specimens in these communities has been collected in the Moroccan sector, especially on mud volcanoes that show evidence of relatively recent activity. Gas hydrates on the Moroccan margin and in the Gulf of Cadiz have only been reported from a small number of deep-water mud volcanoes (Gardner 2001; Kenyon et al. 2001; Mazurenko et al. 2003; Pinheiro et al. 2003). Depreiter et al. (2005b) observed anomalous reflections (H-event) on seismic profiles in the

Fig. 8.1 (**A**) Location of the study area "El Arraiche mud volcano field" (*rectangle*) on the Moroccan margin. (**B**) 3D bathymetric map of the study area. The *dashed lines* represent the mud volcanoes (MV) and the geomorphological structures. The *solid lines* indicate the presence of the mound provinces (MP)

shallow mud volcanoes on the Moroccan margin. This event was mapped in the Mercator mud volcano and interpreted as the base of a gas hydrate stability zone (Depreiter et al. 2005b). During the CADIPOR II cruise with the R/V Belgica in 2005, an active "brown smoker" chimney was for the first time reported on Mercator mud volcano in a water depth of about 400 m, which can be possible linked with the disintegration of a gas hydrate layer between the sea-floor and a subsurface level that is dependent on pressure and temperature (Depreiter et al. 2005b; Van Rooij et al. 2005). Stadnitskaia et al. (2006) investigated molecular and carbon isotopic variability of hydrocarbon gases from methane through butanes on deeper mud volcanoes in the Gulf of Cadiz and found that the gas groups are allochthonous to the erupted mud breccia and represent a complex of secondary migrated, mixed and microbially altered hydrocarbons. It may possibly imply the presence of hydrocarbon accumulations in the deep subsurface of the Gulf of Cadiz. Analyses of carbonate crusts and chimneys from the Moroccan continental margin demonstrate the influence of different parental fluids, including seawater, Fe-charged deep fluids and fluids derived from the destabilization of gas hydrates (De Boever 2005) as well as a wide variety of carbon sources, ranging from biogenic methane, organic matter derived carbon to marine CO_2 (Depreiter 2009).

8.1.2 Oceanographic Setting

The present-day oceanographic circulation in the Gulf of Cadiz is controlled by the exchange of water masses through the Strait of Gibraltar and by the interaction of Mediterranean Outflow Water (MOW) with the Atlantic circulation. The highly saline and warm near-bottom MOW flows into the Atlantic Ocean below the less saline, surficial Atlantic Inflow Water (AI) that enters the Mediterranean Sea (Madelain 1970; Thorpe 1976; Ochoa and Bray 1991; Baringer and Price 1999) (Fig. 8.2A).

The AI is composed of North Atlantic Superficial Water (NASW) flowing between the surface and a water depth around 100 m and North Atlantic Central Water (NACW) extending between 100 and 700 m (Caralp 1988) (Fig. 8.2A). The North Atlantic Central Waters stretch down to at least the level of minimum salinity, some 36.0 salinity units at the Gulf′s northern and eastern ends, and down to 35.6 salinity units at its southern end (Ochoa and Bray 1991; Mauritzen et al. 2001; Ambar et al. 2002). This level is located at about 300 m depth at the outflow from the strait (6.5°W) but reaches about 600–700 m in the outer and southern portions (Machin et al. 2006). The general surface circulation in the Gulf of Cadiz is anticyclonic with short-term, meteorologically induced variations in the upper layer. It must be considered in relation to the north-eastern Atlantic circulation. Recent numerical models (Johnson and Stevens 2000) indicate the significance of the Azores current, a southern branch of the Gulf Stream passing just south of the Azores, in the Gulf of Cadiz. The Azores current splits into a northern branch along 35°N, which meanders eastward towards the Gulf of Cadiz and a second branch,

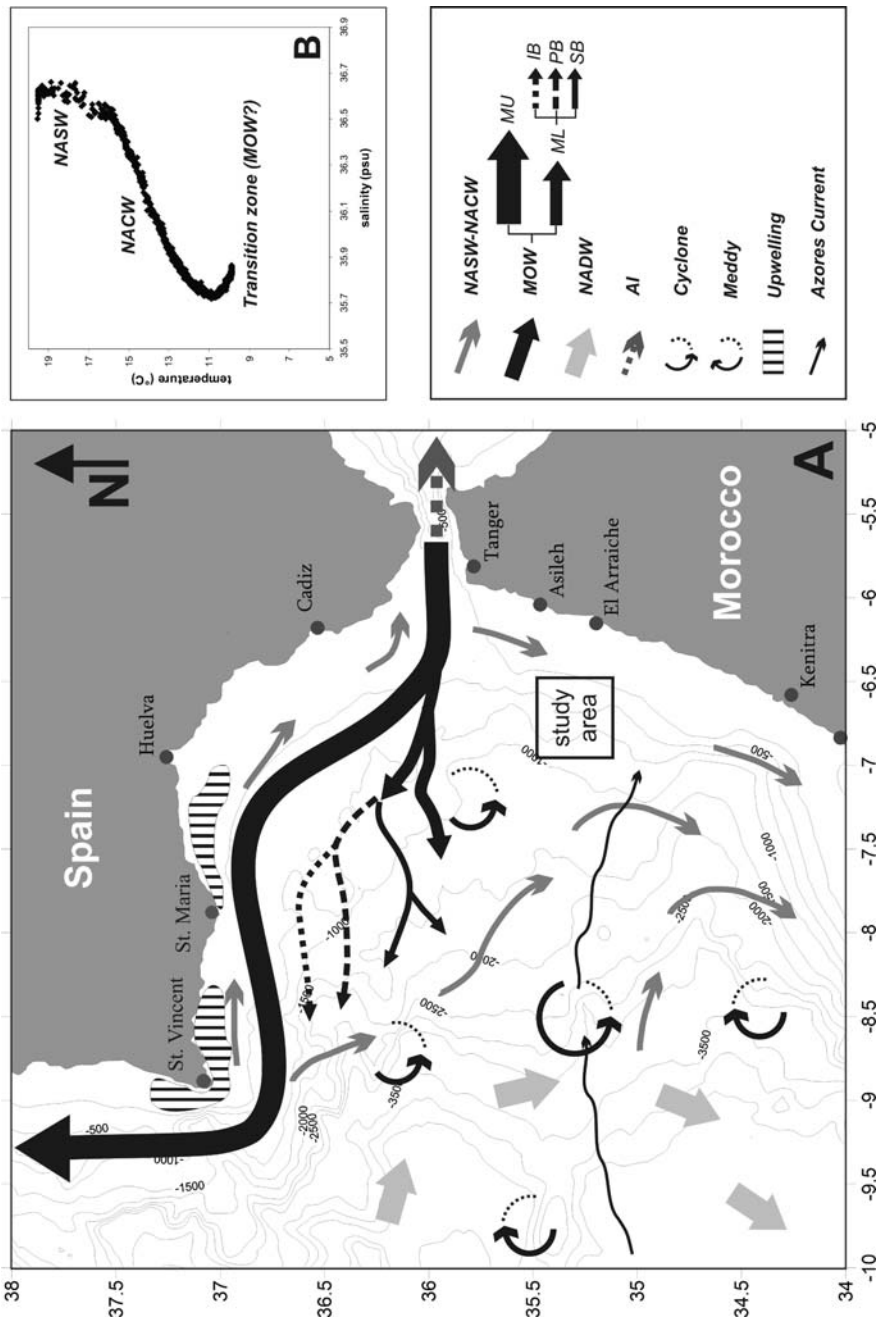

Fig. 8.2 (continued)

which continues south-eastward towards the Canary Islands. The surface circulation in the Gulf of Cadiz could be understood as the last meander of the Azores current. Mittelstaedt (1991) reviewed the eastern boundary Canary current, which flows along the coast of Africa and through the Canary archipelago. This boundary current is associated with coastal upwelling, filaments and eddies. The upwelling along the African coast in certain periods is caused by enhanced trade winds (Meincke 2002). However, Wooster et al. (1976), Nykjaer and Van Camp (1994) and Hernandez-Guerra and Nykjaer (1997) show the lack of coastal upwelling north of 33°N. The surface circulation pattern in the Gulf of Cadiz is also the direct result of local wind forcing (Garcia-Lafuente et al. 2006). Wind forcing is responsible for the presence of upwelling regions off its northern margin, with prominent filaments emanating from Capes St. Vincent and St. Maria (Ruiz and Navarro 2006) (Fig. 8.2A).

Below NACW, Mediterranean Water is present. After having passed the Strait of Gibraltar, the MOW undergoes a decrease in temperature, salinity and velocity caused by its rapid mixing with NACW. It then divides into two main cores west of 6°20′W: a Mediterranean Upper Core (MU) and a Mediterranean Lower Core (ML). The upper core is a geostrophically steered current following a northward path along the Spanish and Portuguese continental margin between 400 and 800 m water depth. The lower core is a more ageostrophical current flowing at depths between 800 and 1300 m (Zenk and Armi 1990; Baringer 1993; Bower et al. 1997). This lower core is influenced by the morphology of the slope and divided in three minor branches between the Cadiz and the Huelva meridians (6°20′–7°) (Kenyon and Belderson 1973; Melieres 1974; Nelson et al. 1999; Hernandez-Molina et al. 2003): (a) Intermediate Branch (IB), (b) Principal Branch (PB) and a (c) Southern Branch (SB) (Fig. 8.2A). It has to be mentioned that at Cape St. Vincent the undercurrents veer northwards and become unstable enough to often produce deep anticyclones, called meddies (Bower et al. 1995; Sadoux et al. 2000). Meddies, containing a core of salty and warm Mediterranean Water, are typically 20–100 km in diameter and 200–1000 m thick, centred about 1000 m depth. Richardson et al. (1989) estimated that 8–12 meddies form each year based on estimates of the numbers of coexisting meddies and there average lifetime (2–3 years), and that they may transport 25% of the salinity anomaly flux that comes through the Strait of Gibraltar. Bower et al. (1997) have estimated a meddy formation rate of 15–20 meddies per year, supporting the idea that a large portion of the zonal salinity anomaly flux (about 50%) is related to meddies. These meddies propagate south-westward from their site of generation (Zenk

Fig. 8.2 (**A**) General circulation pattern in the Gulf of Cadiz (figure modified after Thomson et al. 1999; Schönfeld and Zahn 2000; Carton et al. 2002; Hernandez-Molina et al. 2003; Vanney and Ménanteau 2004; Llave et al. 2006; Ruiz and Navarro 2006) with visualization of North Atlantic Surface Water (NASW), North Atlantic Central Water (NACW), Mediterranean Outflow Water (MOW), North Atlantic Deep Water (NADW), Azores Current, meddies, cyclones and upwelling regions. (**B**) CTD-profile (temperature versus salinity) characterizing the different water masses in the study area

et al. 1992) and can live for several years and slowly dissipate by mixing or brutally disappear by colliding with seamounts (Richardson et al. 1989, 2000). Hydrological measurements in 1999 revealed three eddies in the Gulf of Cadiz, displaying substantial interactions: two meddies (meddy Christine, S of Cape St. Vincent and meddy Isabelle close to the Moroccan margin) and a deep cyclone, which is coupled with meddy Isabelle as a baroclinic dipole (N of meddy Isabelle and SE of meddy Christine) (Carton et al. 2002) (Fig. 8.2A).

North Atlantic Deep Water (NADW) is present below the MOW at depths >1500 m (Fig. 8.2A) (Ambar et al. 2002). It flows from the Greenland-Norwegian Sea region towards the south. This low-temperature and low salinity water mass mixes partly with the saltier MOW in the Gulf of Cadiz, flowing southwards down the eastern part of the Atlantic Ocean (Knauss 1978).

Recent CTD-measurements and current measurements showed that El Arraiche Mud Volcano Field along the Moroccan margin is mainly influenced by NACW (with temperatures between 11 and 16°C and salinities between 35.6 and 36.5 psu) (Fig. 8.2B). What uniquely characterizes the NACW circulation pattern in this region is the existence of water inflow towards the coastal region (Machin et al. 2006). The typical signature of MOW is not clearly recorded in the study area but the temporarily influence of MOW by meddies can not be excluded (Fig. 8.2B). Measurements with a BOBO-Lander of the Netherlands Institute of Sea Research (NIOZ), deployed on top of Pen Duick Escarpment, showed the effect of internal waves and tidal currents resulting in temperature changes of 0.5° and salinity changes of 0.05‰ (Mienis et al. 2005). The average bottom current velocity is 10 cm/s but it reaches peak values up to 15 cm/s. Both, intermediate (250–300 m) and bottom nepheloid layers are present in the study area (Mienis et al. 2004; de Haas et al. 2005).

8.1.3 Palaeoenvironmental Setting

The circulation pattern and intensity of the MOW in the past is still under discussion and not straightforward. Most of the studies focus on the Spanish and Portuguese margins, while the Moroccan margin remains neglected. Since the middle of the Pliocene, the MOW had a strong influence on the distribution of the water masses in the whole Gulf. Cacho et al. (2000) propose an enhanced Mediterranean circulation during the Heinrich event and Glacial Maximum conditions in comparison to warmer intervals. Moreover, Baringer and Price (1999) suggest that a smaller and denser MOW, which would mix more vigorously with North Atlantic waters, prevailed during cool stages. However, the MOW volume was certainly lower during the glacial sea level lowstands (Bryden and Stommel 1984; Zahn et al. 1997; Matthiesen and Haines 1998). This setting results in a decrease in water exchange between the Mediterranean Sea and the Atlantic Ocean (Duplessy et al. 1988). On the other hand, due to the reduced exchange and a generally dryer Mediterranean Sea, the glacial MOW has a significantly higher salinity and density (Schönfeld 1997; Zahn et al. 1997; Cacho et al. 2000). So, during these times, an intensive and

deeper MOW is created (Thomson et al. 1999; Schönfeld and Zahn 2000). Llave et al. (2006) suggested a variable spatial influence of the MOW during each climatic stage: an enhancement of the lower MOW branch during climatic cooling and a stronger upper MOW branch circulation during warm intervals.

Recent studies on a core localized in the El Arraiche mud volcano field between Renard Ridge and Vernadsky Ridge have shown the impact of Late Quaternary variations in this area (Vanneste 2005; Mertens et al. 2006; Mertens 2009). A glacial and interglacial period can be clearly recognized in geochemical proxies (TOC, $CaCO_3$), XRF analysis (K, Mg, Fe) and stable isotopic analysis on planktonic and benthic foraminifera ($\delta^{18}O$, $\delta^{13}C$), but also in abundances of coccoliths and more particularly *Emiliania huxleyi* (Mertens et al. 2006). Grain size analyses show a variable trend, with finer material deposited during the Holocene (with an average sedimentation rate of 18.5 cm/ka) and coarser material characterizing the last glacial period (Foubert et al. 2005b). Clay mineralogical analyses indicate that kaolinite is the major component of the clay fraction, which can be associated with aeolian input from the North African continent and/or input under the control of currents from the Mediterranean Sea (Vanneste 2005; Mertens 2009).

8.2 Material and Methodology

The multibeam bathymetry was acquired with a SIMRAD Kongsberg EM1002, installed on board of R/V Belgica during the CADIPOR I and II cruises (Gulf of CADiz – PORcupine Seabight Comparative Study) in respectively 2002 and 2005. The data were recorded with a sailing speed of 6–7 knots and swath widths ranging from c. 500 m in deep water to 700 m in shallow water. The beam angles were generally chosen quite narrow (20–30°), in order to focus the acoustic energy towards the relatively large depth below the vessel. A spike filter of weak to medium strength was switched on during acquisition. The data were corrected and cleaned with the Kongsberg packages Merlin and Neptune. The footprint at 400 m is 15 × 15 m. In total 725 km^2 was covered.

High-resolution seismic data were acquired during the CADIPOR I and II campaigns (R/V Belgica 2002, 2005) with a 80 electrode 500 J sparker, 35 cubic inch Sodera GI gun and the Ifremer Deeptow Chirp Sonar System. The seismic profiles were digitally recorded using the Elics Delph system. Data processing (swell-filter, band pass filter, deconvolution and signal amplification) was done using Landmark Promax processing software. Interpretation and mapping was executed in the Kingdom Suite seismic interpretation software package (Seismic Micro-Technology, Inc.).

Sidescan sonar imagery (SSS) was collected with the MAK-1 M deep-towed hydro-acoustic complex on board of the R/V Logachev during the TTR-12, TTR-14, and TTR-15 cruises in 2002, 2004, and 2005. The MAK-1 M deep-towed hydroacoustic system contains a high-resolution sidescan sonar operating at a frequency of 30 kHz, with a total swath range of 2 km (1 km per side) and a subbottom profiler, operating at a frequency of 5 kHz. The fish was towed at a constant altitude

of about 100 m above the sea-floor with a speed of 1.5–2 knots. The positioning of the tow-fish was archived by using a short-based underwater navigation system. The data were recorded digitally and stored in SEG-Y format. A time-variant gain control was applied during the acquisition of the data. The processing of the collected data (slant-range-to-ground-range (SLT) correction, geometrical correction and smoothing average filtering) was carried out on board.

Video imagery was collected during the TTR12 cruise with R/V Logachev (TVAT33 and TVAT36) and during the CADIPOR II campaign with R/V Belgica (c0505-video06) by using a deep-towed frame mounted camera. The imagery was recorded on analog tapes, converted in digital format and imported in a GIS system (Adélie-GIS 8.3).

6 Hammon grabs (B05-1212, B05-1211, B05-1209, B05-1208, B05-1214, and B05-1215), 2 TV-guided grabs (AT407Gr, AT406Gr) and 1 dredge (AT574D) are used in this study to ground-truth the video material, sidescan sonar imagery and multibeam. The samples were collected respectively during the CADIPOR II cruise (R/V Belgica 2005) and the TTR-12 and TTR-15 campaigns (R/V Logachev 2002, 2005). One Kasten core (MD04-2804) was collected during the CADICOR cruise in 2004 on board of the R/V Marion Dufresne to give insight into the mound structures on PDE. The Kasten core was opened and described in detail. Bulk samples were taken each 20 cm for macro-faunal analysis. Six coral species from the top of the core were sampled for U/Th dating. ^{230}Th/U datings were measured in the Laboratoire des Sciences du Climat et de l′Environnement (LSCE) in Gif-sur-Yvette with a thermal ionization mass spectrometer (Finnigan MAT262). Five cores (AT564G, AT534G, AT570G, AT571G and AT572G) were acquired during respectively the TTR14 and TTR15 cruises with the gravity corer on board of R/V Logachev. The cores were opened and described in detail.

8.3 Data Description and Interpretation

8.3.1 Pen Duick Mound Province

8.3.1.1 Geomorphology

Extensive multibeam bathymetry and seismics along the top of PDE, a fault-bounded cliff, revealed a series of elongated mounds and mound clusters (Fig. 8.3). The mounds occur in water depths between 500 and 600 m and can measure up to 60 m in height. They are elongated in E-W direction, with a length of about half a kilometre. At the base of the cliff smaller mound patches are found, again characterized by an E-W orientation. A NW-SE oriented moat delineates the base of the escarpment. Based on the integration of bathymetry, seismic data and sidescan sonar imagery, so far 15 mound structures along the top of the cliff have been identified. The south-west facing part of the cliff has a height of 65 m above the sediments and an average slope gradient varying between 15 and 20°. The eastern edge of the cliff reaches slope gradients up to 25°.

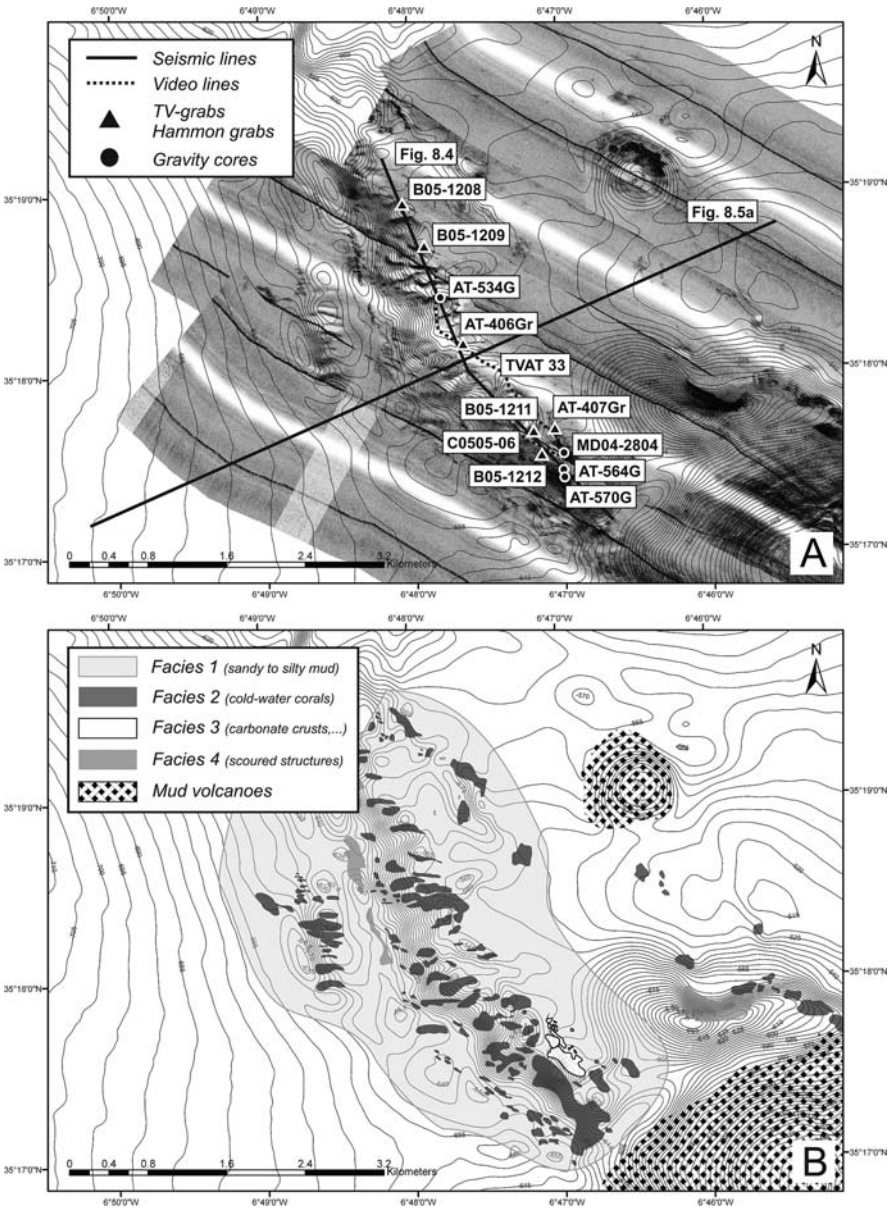

Fig. 8.3 (**A**) Bathymetry (contour spacing is 5 m), sidescan sonar imagery and location of the seismic profiles, core material and video lines in the Pen Duick Mound Province. (**B**) Interpretation of sidescan sonar imagery (MAKAT 66-68), representing the four described facies

8.3.1.2 Video Imagery and SSS

The integrated analysis of sidescan sonar (MAKAT 66-68), video imagery (TVAT 33 and c0505-video06) and ground-truthing by surface coring (AT407Gr, AT406Gr, B05-1212, B05-1211, B05-1209 and B05-1208) revealed four distinctive facies (Fig. 8.3).

Facies 1 corresponds with sandy to silty clays (Figs. 8.3 and 8.8C), characterized by an even surface with some well-delineated patches of cobble to boulder-sized stones. This facies presents the surface sediments in between the different mounds and mound patches. On sidescan sonar imagery it shows low backscatter strength with a very smooth surface. These fine-grained deposits are associated with typical soft-bottom communities (spiral anthipatharians, isidiid gorgonians and hexactinellid sponges), as well as characterized by a high amount of burrows. Noteworthy is the presence of the bamboo coral *Isidella elongata*, colonizing the soft substrate.

Facies 2 reveals cold-water corals, lying at the surface of the mounds and mound patches along the crest of PDE. Most of the mounds are covered with dead coral fragments and sediment clogged dead coral rubble, surrounded and overlaid by a layer of brownish silty mud (Fig. 8.8D). The most common observed cold-water coral fragments are classified as *Dendrophyllia* spp. *(D. alternate, D. cornucopia* and *D.* sp.*), Lophelia pertusa*, *Madrepora oculata*, *Desmophyllum cristagalli,* and *Caryophyllia calveri.* It is remarkable that at the south-eastern edge of PDE the surface units are dominated by *Dendrophyllia* spp. *(D.* sp. and *cornucopia)* and some small fragments of *Stenocyathus vermiformis,* as identified in box cores B05-1212 and B05-1211. Gravity coring (see below) shows that these upper units, built up by mainly *Dendrophyllia* spp., are further down-core replaced by *Lophelia pertusa* and *Madrepora oculata*, associated with *Desmophyllum cristagalli* and *Caryophyllia* spp. Box cores B05-1209, B05-1208 and grab AT406Gr learn that more west on Pen Duick Escarpment, the dominating coral species are *Lophelia pertusa*, *Madrepora oculata* and *Dendrophyllia alternata*. A high amount of macro-faunal and micro-faunal life is associated with the cold-water coral fragments (crinoids, bryozoans, ophiurods, gastropods, molluscs, hydroids, serpulids, gorgonians, foraminifers). Mass occurrences of crinoids are observed, using the dead skeletons of cold-water corals as substrate. The cold-water coral patches are characterized by a high backscatter strength and a clear acoustic shadow on sidescan sonar imagery.

Facies 3 consists of carbonate crusts, boulders or hard rock covered by a fine layer of hemipelagic mud (Fig. 8.8E). Boulder fields, rock outcrops and outcropping carbonate crusts are a common feature in between the mounds. Two distinct patches of carbonate slabs are observed in the eastern part of the TV-line TVAT33, respectively with a length of 11 and 20 m (Fig. 8.3B). Depreiter (2009) described these crusts as consisting of light greyish to brownish well lithified to brittle host sediments, with variable inclusions of bioclastic shells, coral fragments and bryozoans (Fig. 8.8B). The formation of the carbonate crusts on PDE occurred in equilibrium with seawater, probably under the influence of the upward migration of thermogenic hydrocarbons (Depreiter 2009). Solemyid bivalve shells,

brachiopods (*Megerlia truncata*), dendrophyllid corals, anthipatharians, sponges and calcareous tube worms (Serpulidae) were observed attached on the carbonate crusts. It should be noted that the dominating cold-water corals associated with these carbonate crusts are mainly *Dendrophyllia* spp. using fossil coral framework and carbonate crusts as substrate. The bivalve *Spondylus gussoni* is often co-occurring with these species on hard substrates.

Facies 4 is recognized on sidescan sonar imagery by its strong backscatter. It corresponds with the scoured moat at the foot of the escarpment or with a steep bank or slope, probably created by strong erosive alongslope currents leaving behind a lag deposit of coarser material or dead cold-water coral fragments.

8.3.1.3 Seismics

A very high resolution deeptow chirp seismic profile along the crest of PDE (Fig. 8.4) shows the mounds as rounded cone shaped features, with a height up to 60 m. No internal structures are observed. On some parts of the profile, mostly between 1500 and 4000 m along the distance axis, subsurface reflections are recorded. Generally, the subsurface has a low amplitude. The widely U-shaped geometry of the reflections is caused by directional changes during the acquisition of the data (Fig. 8.3A). An erosive surface below the mounds can be observed and is interpreted as the mound base.

A profile perpendicular to the PDE shows medium to high amplitude sequences, covering a low amplitude unit (Fig. 8.5A). The low amplitude body has a very steep SW dipping slope beneath the escarpment. Northwards, NE dipping reflections are observed in the low amplitude unit. The low amplitude structural acoustic basement, which is part of Renard Ridge, is eroded and crops out at the sea-floor. Diffractions at and above the outcropping basement are indicative for the occurrence of elevated mound structures.

A small mound-like low amplitude body occurs in the high amplitude sequences that cover the basement. Other profiles near the PDE also indicated the presence of small mound-like features in the sedimentary sequences (inset Fig. 8.5A). Reflections are draping the features, indicating that they are real physical structures. The small mounded features only occur upslope a set of small normal faults associated with gas blanking and bright spots. A direct relation between the two observations

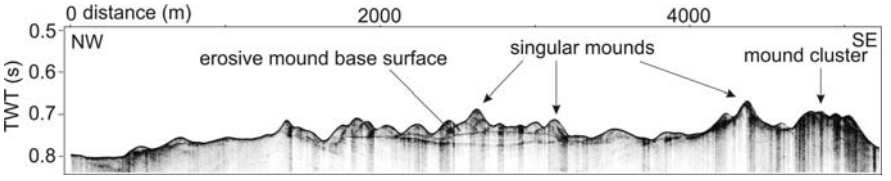

Fig. 8.4 CHIRP seismic profile (IFREMER) over Pen Duick Escarpment indicating the singular mounds topping the cliff and the erosive mound base surface (location: see Fig. 8.3A)

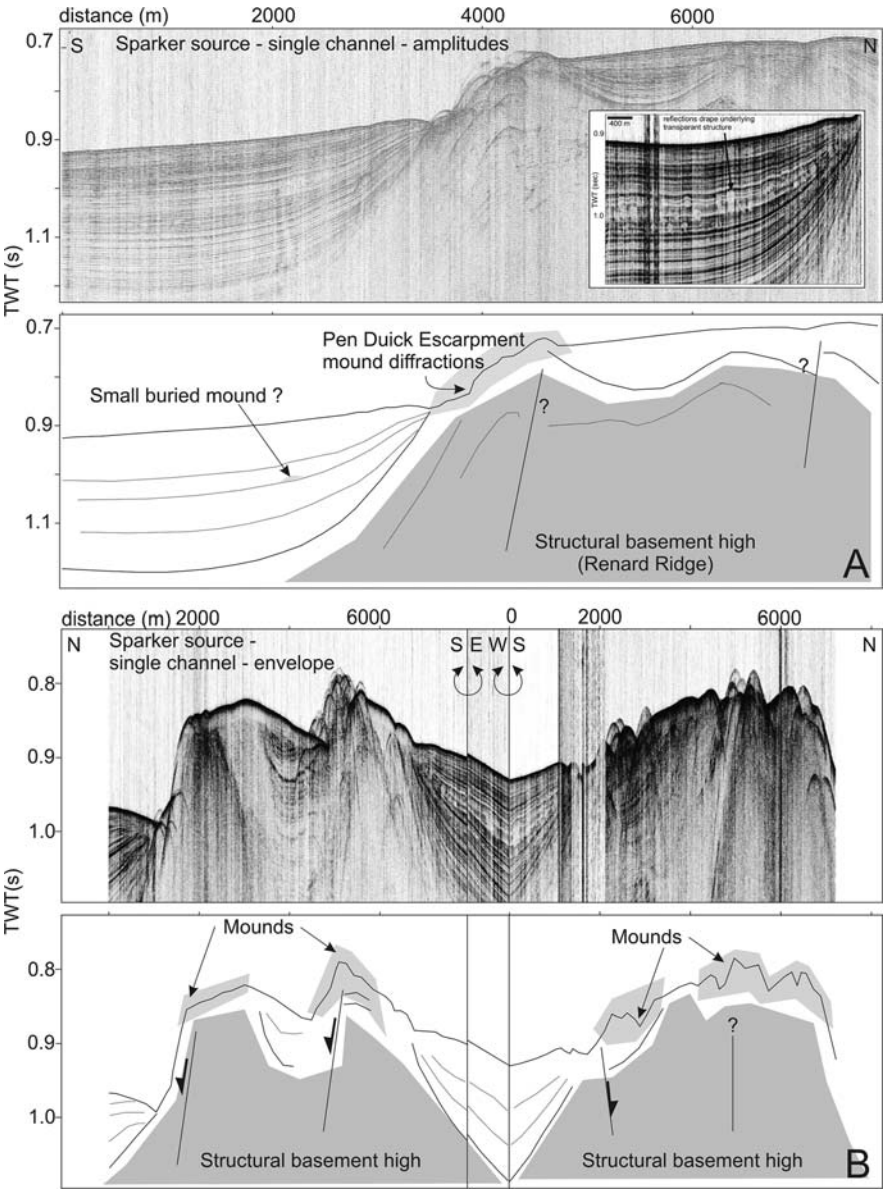

Fig. 8.5 (**A**) Sparker seismic profile perpendicular to the PDE, showing the mound diffractions on the escarpment, the structural basement high (location: see Fig. 8.3). The inset represents some small buried mounds occurring in the sediments at the foot of the escarpment. (**B**) Set of Sparker seismic profiles over Renard Ridge (location: see Fig. 8.7). The structural basement, two faults and mound structures can be recognized on the profiles

is speculative. The features may be interpreted as small buried mounds and could be an indication of the onset of mound growth in the area.

8.3.1.4 Coring

Four cores, respectively a Kasten core MD04-2804 and three gravity cores AT564G, AT534G and AT570G have been collected on PDE to give insight into the mound structures (Fig. 8.3A). The mound cores display throughout all their penetration depth a high number of reef-forming cold water scleractinians like *Lophelia pertusa*, *Madrepora oculata*, *Desmophyllum cristagalli, Dendrophyllia* spp. and *Caryophyllia* spp. in association with numerous shell-bearing invertebrates formerly inhabiting the econiches provided by the coral framework. Based on these observations, every single mound structure on PDE can be interpreted as a cold-water coral mound.

The Kasten core MD04-2804, with a core penetration of 594 cm, is located on the mound cluster at the eastern edge of PDE at a water depth of 505 m (Fig. 8.3A). The whole core is characterized by cold-water coral fragments embedded in brownish oxidized sandy silt to very fine sand in the top 10 cm grading downwards in silty clays to clayey silts (Fig. 8.6). The most common colonial cold-water coral species, *Lophelia pertusa*, *Madrepora oculata* and *Dendrophyllia* spp ., representing 90% of the total coral content, are alternating in distinctive zones. The upper part, between 0 and 60 cm, is dominated by *Dendrophyllia* spp. *(D. cornucopia* and *D.* sp.) in association with *Stenocyathus vermiformis*(forming small well-preserved (fossil) specimens up to 2 cm long and 1 to 2 mm wide). Less common in the upper part are *Lophelia pertusa* and *Madrepora oculata*. *Desmophyllum cristagalli* occurs as big fragments (up to 5–6 cm) in between the previously described species. Down-core, *Lophelia pertusa* and *Madrepora oculata* are predominating, associated with some specimens of *Desmophyllum cristagalli* and *Caryophyllia* sp. *Dendrophyllia* spp. is disappearing. As a result of bioerosion and chemical dissolution, the preservation of the coral fragments is rather poor in certain units. In between 215 and 330 cm the cold-water coral fragments are in a very bad stage of preservation mainly due to chemical dissolution (Fig. 8.6). The carbonate-content increases in the sediments below the unit where the corals start to be heavily dissolved. The density of the coral fragments is changing throughout the core.

Among the cold-water coral fragments, other invertebrate species could be identified. Most of the reported species are known to live in association with cold-water corals. Frequently occurring species were the bivalves *Lima marioni, Acesta excavata, Asperarca nodulosa, Delectopecten vitreus, Pseudamussium sulcatum, Spondylus gussoni* and *Heteranomia squamula,* the gastropods *Calliostoma* cf. *maurolici, Bursa ranelloides, Alvania tomentosa, Alvania cimicoides and Amphissa acutecostata,* the brachiopod species *Megerlia truncata* and *Terebratulina* spp. as well as several echinoderms, e.g. the echinoid *Cidaris cidaris* and mass occurrences of unidentified crinoids.

Some species of the molluscan association are indicative for an important influence of MOW in the past. The bivalve species *Lima marioni* and *Spondylus gussoni* are preferably occurring in areas with a clear influence of MOW. Molluscan

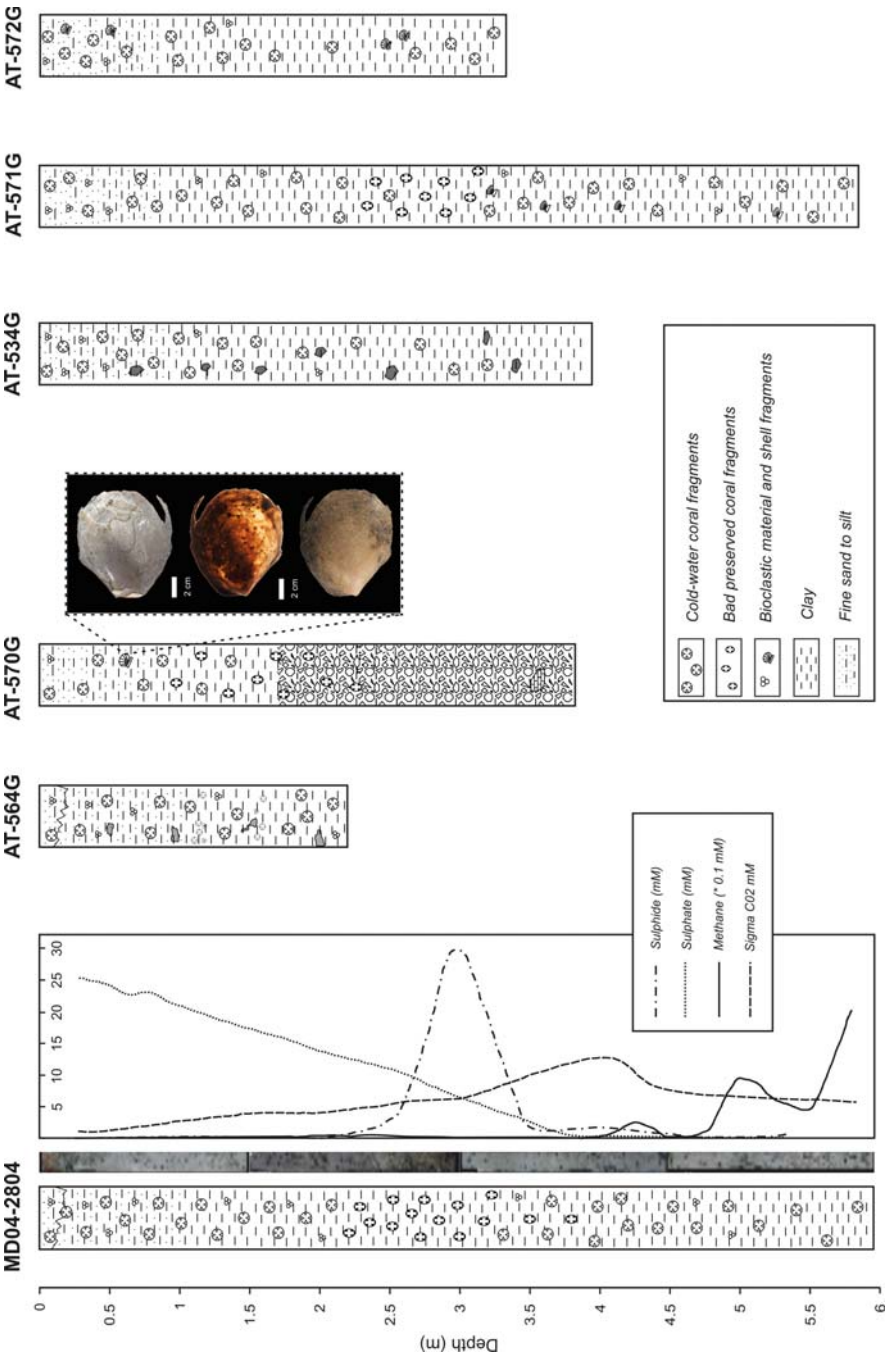

Fig. 8.6 (continued)

species such as the bivalves *Microgloma tumidula* and *Yoldiella wareni* or the gastropod species *Drilliola emendata* and *Alvania electa* are mainly occurring in areas under the influence of MOW. Another group of bivalves and gastropods occurring as associates in the cold-water coral environments of the study area are noteworthy as representatives of a local fauna not present in other cold-water coral environments further north. These species are either restricted to the Moroccan margin, at least restricted to the Gulf of Cadiz area (e.g. the gastropod species *Alvania tomentosa*, *Neptunea contraria*, *Pseudosetia amydralox, Crisilla amphiglypha* and *Bittium watsoni*) or are part of a fauna not extending further north than the southernmost Bay of Biscay (e.g. *Limopsis angusta, Bursa ranelloides*). These species are of high importance for palaeoenvironmental or palaeoceanographic reconstructions as they are not reported from any other cold-water coral site along the European continental margin. The large bivalve *Acesta exavata*, on the other hand, implies a clearly boreal influence, nowadays known to be a common and abundant associate to cold water coral reefs along the Norwegian margin.

Pore water analysis evidences a sharp sulphate-methane transition (SMT) zone at 3.5 m below the mound top, whereas the depth of no sulphate is much deeper in the surrounding sediments (Maignien et al. subm.). The horizon characterized by a strong corrosion of the coral fragments is just lying above and at the front of the recent location of the zone of anaerobic methane oxidation (AOM). The AOM horizon is associated with carbonate release into the sediments (Fig. 8.6).

Due to the alteration of the cold-water coral fragments, absolute U/Th dating should be questioned (U-series open system behaviour). However, two U/Th datings at 10 and 50 cm core depth yielded confident ages of respectively 290±20 ka and 320±36 ka. Radiocarbon dating on the bivalve *Acesta excavata*, recovered from the top of the core, yielded ages from more than 50.000 years BP (M. Lopez Correa pers. com.).

Gravity core AT564G is localized on the same mound cluster as core MD04-2804 at a water depth of 538 m and has a recovery length of 219 cm (Fig. 8.3). The top of the sediments (0–15 cm) consists of brownish water-saturated very fine sand with coral fragments (Fig. 8.6), dominated by *Dendrophyllia* spp. in association with *Lophelia pertusa* and *Madrepora oculata*. As in core MD04-2804, also *Stenocyathus vermiformis*, well-preserved *Desmophyllum cristagalli* and some *Caryophyllia* spp. fragments are reported in the upper part. The remaining part of the core is represented by a 200 cm thick horizon of silty clay to clayey silt, with a high amount of *Lophelia pertusa* in alternation with *Madrepora oculata*. *Dendrophyllia* spp. are missing again, while *Desmophyllum cristagalli* and *Caryophyllia.* spp . are still present in minor quantities. The density of the coral fragments is

Fig. 8.6 Description of Kasten core MD04-2804 and gravity cores AT564G, AT570G and AT534G located in the Pen Duick Mound Province and gravity cores AT571G and AT572G, located in the Renard Mound Province. Pore water analysis (sulphate, sulphide, methane and CO_2) and core images are shown for core MD04-2804. The picture represents an altered bivalve species (*Acesta excavata*), recovered from core AT570G

changing throughout the core. The preservation of the coral fragments is only fair but a well-delineated zone of very badly preserved coral fragments could not be detected. Throughout the succession bioturbations and burrows filled with (soupy) water-saturated clays are observed. Between 116–125 cm and 154–165 cm, an accumulation of smaller coral fragments is noted.

Another core, situated at the south-eastern flank of the same mound cluster as described before and at a water depth of 580 m, is gravity core AT570G. It has a recovery length of 385 cm (Fig. 8.3). The upper 30 cm are characterized by cold-water coral fragments (dominated by *Dendrophyllia* spp .) embedded in a brownish silty matrix (Fig. 8.6). Between 0 and 93 cm the brownish silty sediments are grading into greyish silty clays, while the embedded cold-water coral fragments become dominated by the species *Lophelia pertusa* and *Madrepora oculata*. The amount of coral debris is denser at respectively 15–25 and 41–80 cm. At 63 cm, a 10 cm big bivalve *Acesta excavata* was recovered. From 93 to 174 cm, cold-water coral fragments embedded in a grey clayey matrix become more and more dissolved (especially between 147 and 174 cm). A remarkable observation is the presence of mud breccia and mud clasts between 174 and 385 cm. From 174 to 231 cm, some coral fragments are still present between the mud breccia and the clay but they disappear completely below this zone.

Gravity core AT534G is retrieved from a mound at the western edge of PDE at a water depth of 550 m (Fig. 8.3). It has a total length of 395 cm. The presence of large cold-water coral fragments, mainly *Lophelia pertusa* associated with *Madrepora oculata* and big fragments of *Desmophyllum cristagalli* (up to 3 cm length) in a greyish brown silty matrix are characterizing the uppermost 10 cm of the core (Fig. 8.6). *Dendrophyllia* spp. (*D. cornucopia* and *D.* sp.) are not present anymore, as observed in AT564G and MD04-2804. Some fragments of *Dendrophyllia alternata* could be identified. Between 10 and 37 cm the silty sediments go over in silty clay. This silty clay is present through the whole core unit until the base, whereas the amount of coral fragments (mainly *Lophelia pertusa*) is decreasing downwards. The bottom part of the core (from 330 cm to bottom) is free of coral fragments. The preservation of the coral fragments throughout the core is rather good.

8.3.2 Renard Mound Province

8.3.2.1 Geomorphology

The western edge of Renard Ridge forms a structural high where cold-water corals probably started to build up mound-like structures (Fig. 8.7). The western part of the ridge has a height of 100 m above the sea-floor. The top of the ridge is covered with mound clusters and single mounds occurring in water depths between 550 and 700 m. Single mounds are reaching a height up to 30 m. The mounds are smaller than the mounds reported along the PDE. Cold-water coral patches are present on the sediments flanking the western and south-western sides of the ridge. The total

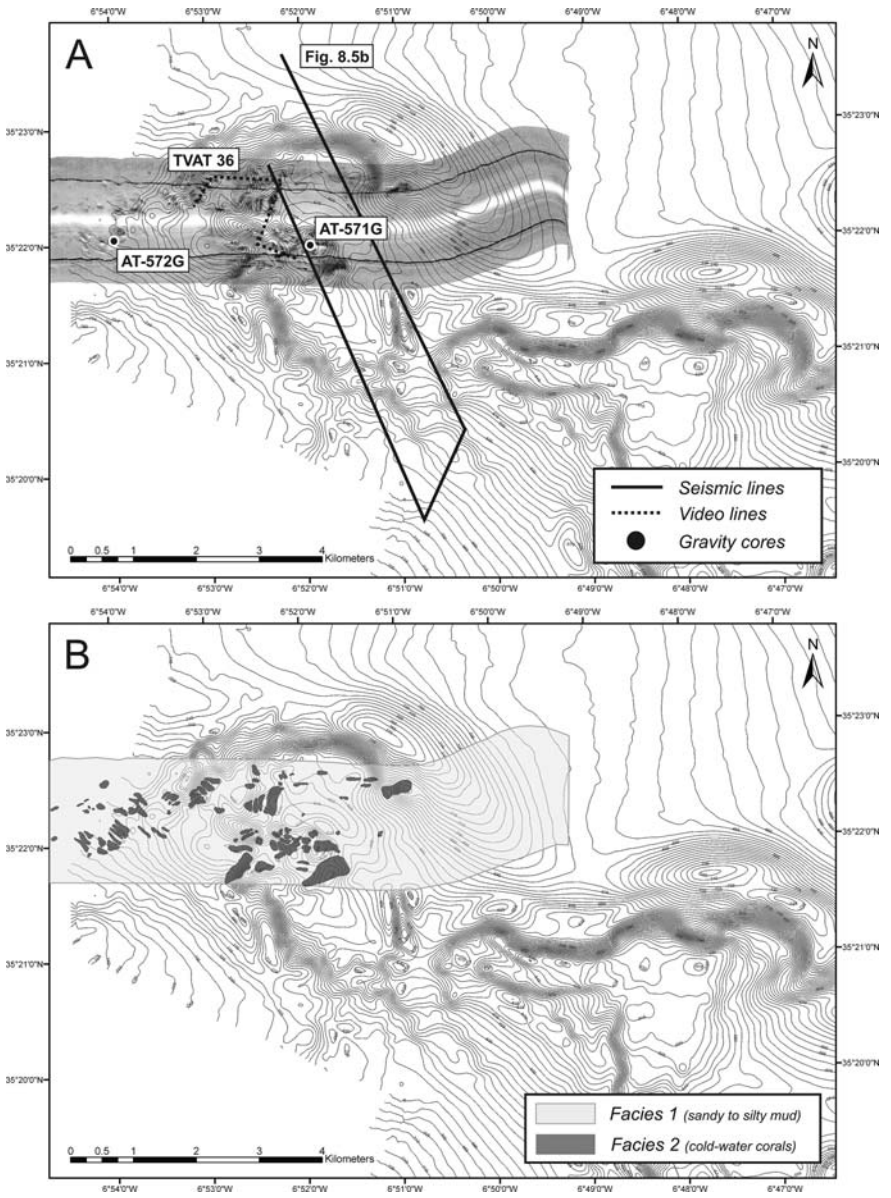

Fig. 8.7 (**A**) Bathymetry (contour spacing is 5 m), sidescan sonar imagery and location of the seismic profiles, core material and video line in the Renard Mound Province. (**B**) Interpretation of sidescan sonar imagery (MAKAT 75), representing two distinctive facies

amount of mounds and cold-water coral patches can be estimated at 65. As observed on PDE, the mounds and patches are elongated. A clear E-W oriented moat is present at the north-eastern part of the ridge which shows a slope inclination of 23°.

8.3.2.2 Video Imagery and SSS

The combination of sidescan sonar imagery (MAKAT 75) and ROV video imagery (TVAT 36) made it possible to delineate the different patches and mounds covered with mainly dead cold-water coral fragments, identified as *Lophelia pertusa*, *Madrepora oculata* and some *Dendrophyllia alternata*. It corresponds with facies 3 as described on PDE (Figs. 8.7 and 8.8). It should be noted that the corals are more densely branched and form higher frameworks in comparison to PDE, where most of the corals are present at the sea-floor as smaller fragments and branches. Anthipatharians, large reddish alcyonaceans, sponges and many crinoids use the dead cold-water coral fragments as substrate.

Facies 1, consisting of sandy to silty mud, is draped over whole the ridge and forms the main facies between the mounds and cold-water coral patches (Figs. 8.7

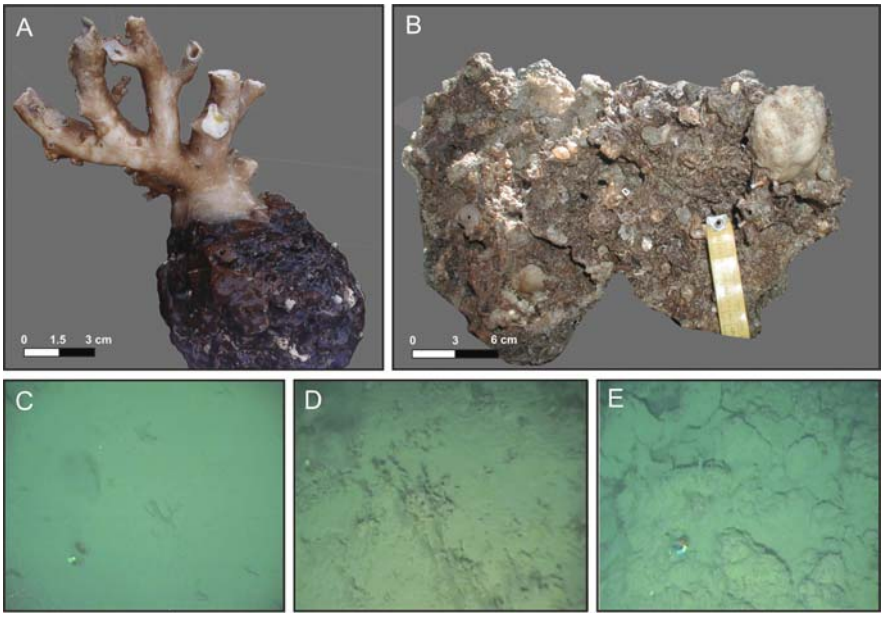

Fig. 8.8 (**A**) Cold-water coral *Dendrophyllia alternata* attached on carbonate chimney (station AT574D). (**B**) Benthic epifauna (bivalves *Spondylus gussoni*), brachiopods (*Megerlia truncata*), sponge and calcareous tube worms (Serpulidae) attached on carbonate crust (station AT407Gr). (**C**) Video image representing silty mud colonized by spiral anthipatharians and isidiid gorgonians (∼facies 1). (**D**) Sediment clogged dead cold-water coral fragments (∼facies 2). (**E**) Video image showing outcropping carbonate crusts, covered with a thin layer of silty mud (∼facies 3)

and 8.8). As on PDE, this mud layer is colonized by typical soft-bottom communities (spiral anthipatharians, isidiid gorgonians and hexactinellid sponges). Bioturbation and burrows are common. Some boulders, colonized by benthic epifauna, are present between the mounds.

8.3.2.3 Seismics

A set of seismic profiles, jointly shown in Fig. 8.5B, shows the occurrence of many mounded features at the culminations of the low-amplitude acoustic (and structural) basement. The two sides of the profile are mirrored sections of the ridge – the ends of the profile are located north, the central part of the profile south (Fig. 8.7). The presence of at least two large normal faults can be inferred from the data. A first fault occurs at the northern side of the ridge and dips towards the north. At the surface, the basement crops out. Along the ridge, elevated features are indicating the presence of mound structures. Further southwards, a second normal fault with a large offset again disrupts the sea-floor. A large set of diffractions is again interpreted as the presence of mounds on top of the outcropping basement. The height of the mounds reaches several tens of metres.

8.3.2.4 Coring

Two gravity cores have been collected at the western edge of Renard Ridge, respectively AT571G on top of a small mound on Renard Ridge and AT572G on top of a cold-water coral patch in the sediments flanking Renard Ridge (Fig. 8.7).

Gravity core AT571G has a recovery length of 581 cm and is localized on top of a small mound at a water depth of 580 m. Coral fragments are present throughout whole the core length but the density of coral fragments changes (Fig. 8.6). The main coral fragments are identified as *Lophelia pertusa* and *Madrepora oculata.* Less abundant are the species *Desmophyllum cristagalli*, *Dendrophyllia alternata* and *Caryophyllia* spp. The determined species of the coral fragments are alternating in different zones, whereby in certain units *Lophelia pertusa* seems to dominate, while in other zones *Madrepora oculata* takes the overhand. The matrix in the upper 37 cm consists of brownish sandy silt going over in silty clay becoming more compact towards the bottom. Bioclastic fragments from bivalves, gastropodes (including pteropodes), echinoids, crinoids, bryozoans, crustaceans and serpulids are present between the coral fragments. Planktonic and benthic foraminifera are common. Badly preserved and heavily dissolved coral fragments are frequently observed between 250 and 300 cm. The colour of the sediments in which the corals are embedded becomes lighter in and especially below this unit. This effect can be correlated with a higher carbonate-content as observed in Kasten core MD04-2804.

Core AT572G, with a recovery length of 333 cm, is acquired on top of a cold-water coral patch on the flank of Renard Ridge at a water depth of 712 m. Coral fragments are present in the upper 70 cm but their amount is decreasing by going downwards (Fig. 8.6). The upper brownish sandy silt (0–70 cm) grades into greyish silty clay to dark clay at the bottom. The most abundant coral species are identified

as *Madrepora oculata* and *Lophelia pertusa.* The coral fragments in the upper zone are rather well preserved.

8.3.3 Vernadsky Mound Province

8.3.3.1 Geomorphology

The northern edge of Vernadsky Ridge is densely covered by small mound-like structures while mound-like patches are found on the sediments flanking the ridge (Fig. 8.9). The mounds on top of the ridge reach heights up to 50 m and widths up to 250 m. The mounds and mound patches are elongated and seem to be lined up, following the structural height. They occur in water depths between 700 and 500 m. The south-western flank of the Vernadsky Ridge has a gentler slope than the north-eastern flank, reaching maximum slope values of 21–23°. A small NW-SE directed moat is present at the south-western flank, while deeper scoured moat structures are observed at the other side of the ridge. The total amount of mounds and cold-water coral patches on this northern edge of the Vernadsky Ridge can be estimated at 130.

The central part of the Vernadsky Ridge consists also of a topographic height, providing substrate for the settlement of benthic organisms. At the edges, mound-like structures are recognized, which can be interpreted as small NW-SE orientated mound patches. They have a similar acoustic signature on seismics and sidescan sonar imagery as the mound-like structures at the northern edge of Vernadsky Ridge (Fig. 8.9).

8.3.3.2 SSS

Sidescan sonar imagery (MAKAT 107-108) revealed similar acoustic signatures as observed on Renard Ridge and PDE (Fig. 8.9). The mound structures and mound patches are characterized by a high backscatter strength and a clear acoustic shadow, and can be interpreted as cold-water coral carbonate mounds and/or cold-water coral patches (cfr. facies 2 on PDE and Renard Ridge). In between the mound patches, a smooth surface with low backscatter intensity is observed, corresponding with sandy to silty clays (facies 1). Kidd mud volcano can be clearly delineated (Fig. 8.9). Another area with high backscatter intensity is located on top of Vernadsky Ridge. Ground-truthing using a dredge (station AT574D), revealed that this area with high backscatter corresponds with the presence of carbonate crusts and chimneys. Serpulids, Bivalvia (*Spondylus gussoni)*, bryozoans, dendrophyllid corals, etc. use the chimneys and crusts as substrate to settle on (e.g. Fig. 8.8B: *Dendrophyllia alternata* attached on chimney). Also the steep north-eastern flanks with their associated NW-SE orientated scoured moats, are characterized by higher backscatter strengths.

8.3.3.3 Seismics

Seismic profiles over the central part of the Vernadksy Ridge give insight into its structure. Figure 8.10A shows the outcropping and eroded low-amplitude acoustic

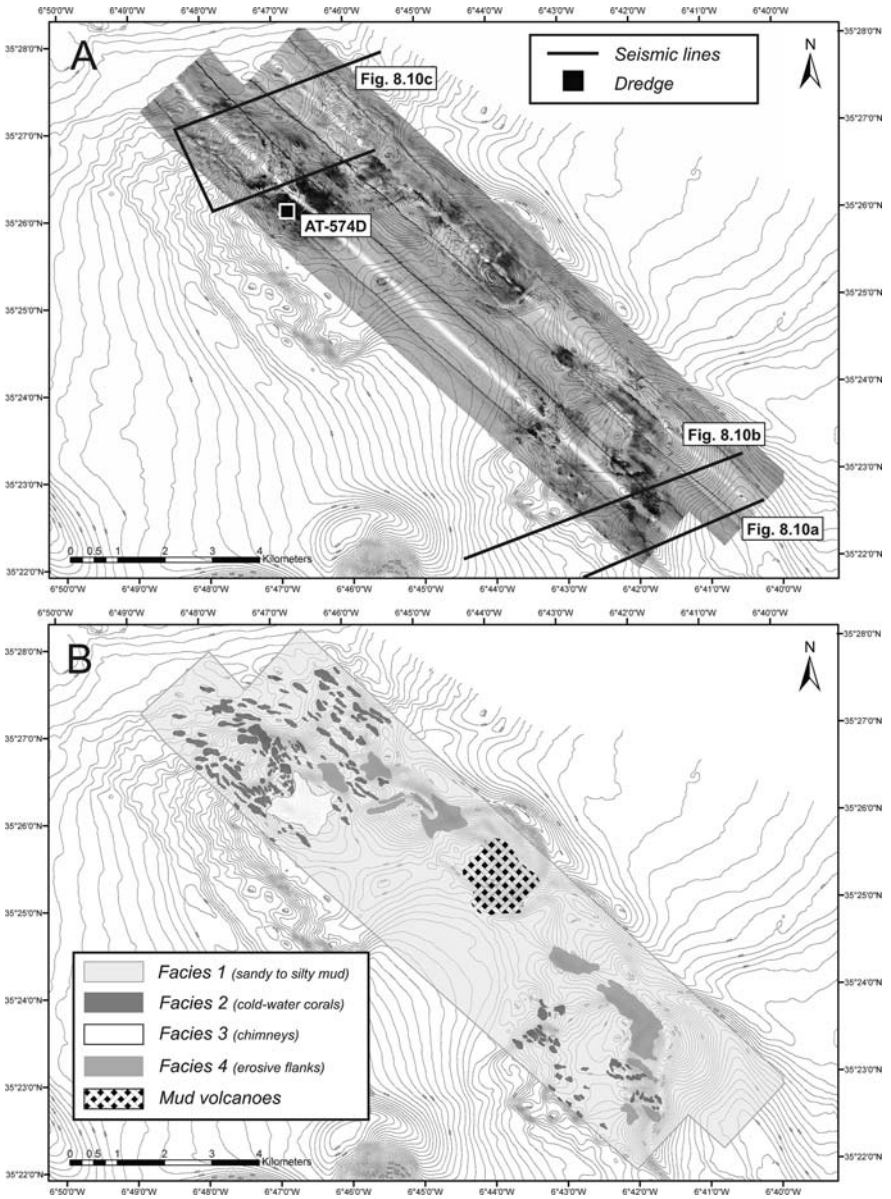

Fig. 8.9 (**A**) Bathymetry (contour spacing is 5 m), sidescan sonar imagery and location of the seismic profiles and core material in the Vernadsky Mound Province. (**B**) Interpretation of sidescan sonar imagery (MAKAT 107-108), representing four distinctive facies

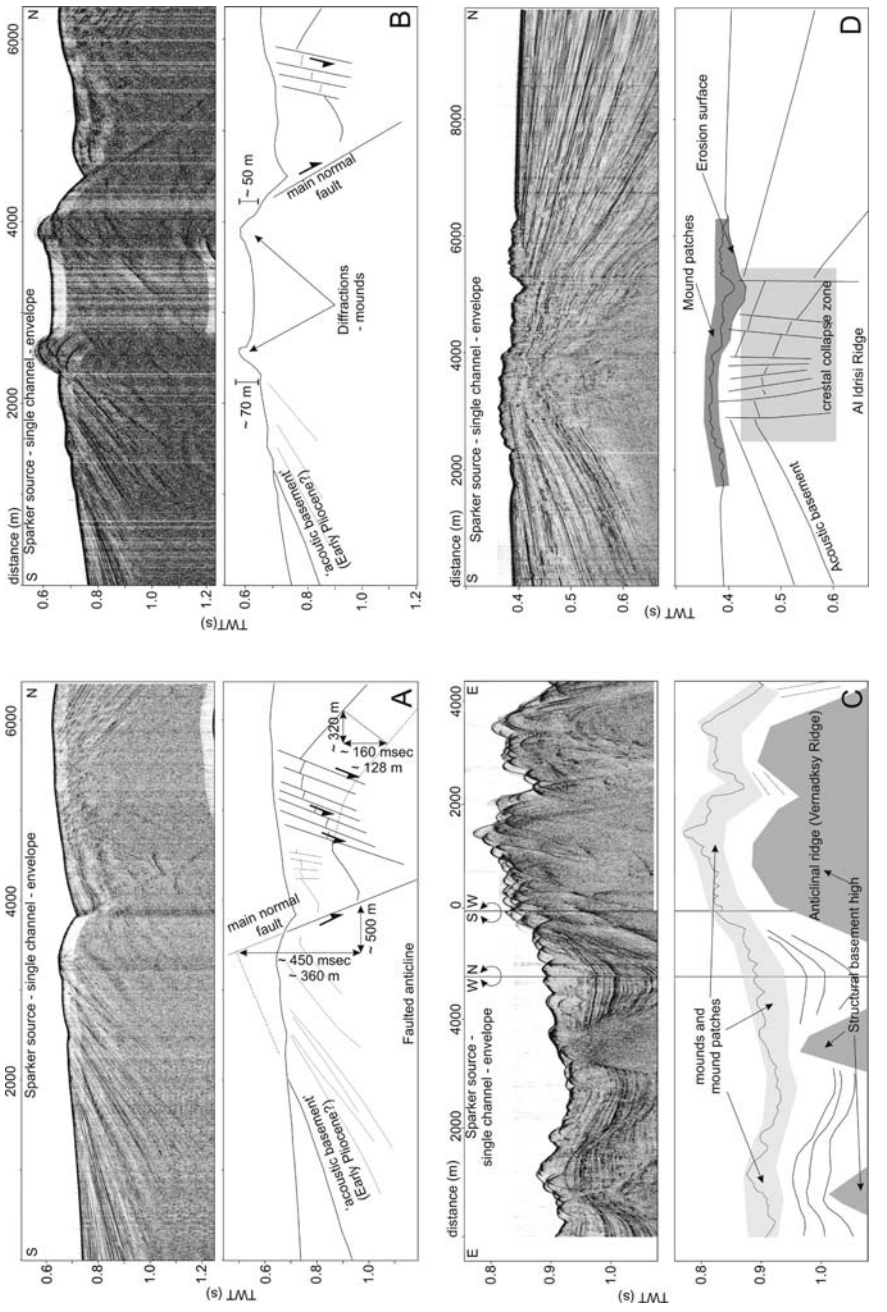

Fig. 8.10 (continued)

basement being covered by younger sequences. Correlation of the seismic data around the ridge culmination indicated that a large normal fault had been active during the past. This has created an offset of about 400 m at the ridge crest. Northwards of the large normal fault, smaller faults are found, which could either be antithetics from the main fault, or a consequence of sediment removal in the subsurface due to mud volcano activity.

In the vicinity of this structurally active place, acoustic diffractions are observed (Fig. 8.10B). Some diffractions clearly stand out above the sea-floor and thus can be interpreted as mound structures.

The seismic data retrieved at the northern part of the Vernadksy Ridge are densely populated by acoustic diffractions (Fig. 8.10C). Structural basement highs are separating small intra-ridge basins. These are likely to be fault controlled. Nearly the whole sea-floor reflection is obscured by diffractions. The diffraction height runs up to 50 m and their width up to 200 m. These diffractions are again interpreted as mound diffractions, indicating that nearly the whole seabed is covered with mound build-ups and mound patches.

8.3.4 Al Idrisi Mound Province

8.3.4.1 Geomorphology and SSS

East of mud volcano Al Idrisi, patches on a much smaller scale are observed (Fig. 8.11). They appear on multibeam bathymetry and sidescan sonar imagery as small E-W aligned mound-like features, not higher than 10 m and in rather shallow water depths (350–200 m). Ground-truthing by Hammon grabs (B05-1214 and B05-1215) revealed that the structures are covered with cold-water coral fragments, dominated nearly exclusively by *Lophelia pertusa* and *Madrepora oculata*, embedded in brownish oxidized silty clays, which grade into greyish and stiff silty clays.

8.3.4.2 Seismics

Below the Al Idrisi mud volcano, an anticline is buried below the sedimentary sequences. The crest of the low amplitude basement, culminating at less than 100 m below the sea-floor, is highly fractured and has collapsed in response to sediment

Fig. 8.10 (**A**) Sparker seismic profile over the central part of Vernadsky Ridge (location: see Fig. 8.9), showing the outcropping acoustic basement as well as a normal fault and a set of smaller faults giving insight into the structure of the ridge. (**B**) Sparker seismic profile over the central part of Vernadsky Ridge (location: see Fig. 8.9), representing a set of diffractions on top of the basement, which can be interpreted as mound structures. (**C**) Set of seismic profiles over the northern part of Vernadsky Ridge (location: see Fig. 8.9), showing the dense population of different mounds and mound patches and the structural basement highs separated by small intraridge basins. (**D**) Sparker seismic profile in Al Idrisi Mound Province (location: see Fig. 8.11), representing the Al Idrisi Ridge and a set of small mound-like features on the sediments burying the ridge

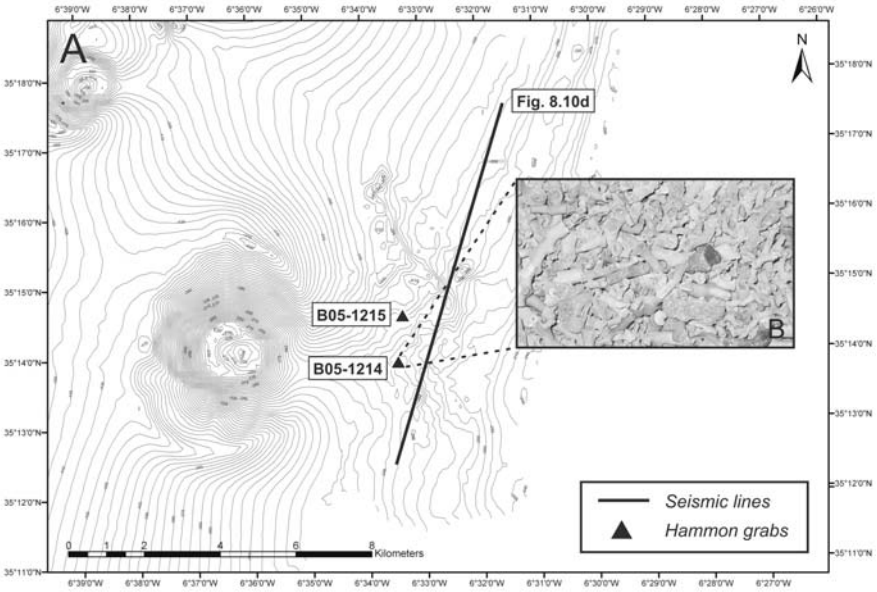

Fig. 8.11 Bathymetry (contour spacing is 5 m) and location of seismic profile and core material in the Al Idrisi Mound Province. Inset presents the dead cold-water coral fragments (mainly *Lophelia pertusa* and *Madrepora oculata*), recovered from the surface

withdrawal by mud volcano activity (Van Rensbergen et al. 2005a). Several bright spots indicate the presence of gas in the sediments at shallow positions.

Mound-like features with a low amplitude and chaotic internal facies are topping the anticline culmination area at the sea-floor. Below the chaotic facies, an erosive surface is present (Fig. 8.10D). The chaotic mounded features can be interpreted as small coral patches, what is confirmed by sampling. The erosive surface is interpreted as the base of the mounds.

8.4 Discussion

8.4.1 Initiation of Cold-Water Coral Growth (or Settlement)

As shown before seismic data reveal a close association between the anticlinal ridges and mound structures. In El Arraiche mud volcano province, cold-water coral mounds show to be closely related to the Renard, Vernadsky and Al Idrisi Ridges. While Renard and Vernadsky Ridges show nowadays outcropping basement, Al Idrisi Ridge is entirely buried, with indications of gas occurrence in the sediments above the ridge. Two main explanations for this co-occurrence between mounds and ridges seem to be possible.

1. The erosive basement surface creates a prime hard substrate for coral larvae to settle on. The more, by forming sea-floor elevations these basement ridges create enhanced currents and thus a higher food particle flux which forms the base for a highly active planktonic food chain, which is often regarded as an important factor in the process of cold-water coral growth: "the highest on the elevation, the more food" (Mortensen 2000; Freiwald et al. 2002; De Mol et al. 2002). Moreover, the effect of tidal waves, as reported on PDE by Mienis et al. (2004), may enhance seabed food supply. The external input of nutrients driving cold-water coral growth is not the only factor controlling mound build-up. Sediment input is another important factor for mound growth, whereby cold-water coral colonies on elevated structures are baffling transported sediments to build up mounds (Foubert et al. 2005a; Huvenne et al. 2005; Wheeler et al. 2005b).
2. As Al Idrisi Ridge does not show a clear topographic elevation that would have favoured cold-water coral growth as explained in scenario 1, the main reason for initial cold-water coral growth might be the presence of a suitable settling ground. Because Al Idrisi Ridge is clearly buried, with the cold-water coral build-ups not related to the basement, hardgrounds may have been an initial substrate. Hardgrounds could have been created by gas or fluid seepage cementing partly the sea-floor or by erosive effects.

8.4.2 Extinction of Cold-Water Corals

Another phenomenon is the widespread extinction of cold-water corals on the Moroccan margin, Gulf of Cadiz. So far, no extensive live frame-work building corals could be observed. In contrast, healthy living coral colonies are observed on the Norwegian margins up to the north, in the Rockall Trough and on the Rockall Bank, on the Porcupine Bank, in the Porcupine Seabight, south of the Galicia bank and in single colonies on the Seamounts off Portugal. The cold-water corals and their associated ecosystems in the Mediterranean Sea are already in a stage of retirement since the onset of the Holocene (Taviani et al. 2005). The coral fragments appearing at the surface in the southern part of the Gulf of Cadiz are rather old, reaching ages older than 300 ka (∼MIS 9) at the south-eastern edge of Pen Duick Escarpment.

However, the presence of clear mound structures built up by cold-water corals evidences that in the recent geological past, environmental and oceanographic conditions were suitable for prolific cold-water coral growth. Before the onset of the recent interglacial conditions, the Gulf of Cadiz was much more influenced by a North Atlantic regime (Vanney 2002), resulting in a descent of the polar front (until Portugal), decrease in temperatures, lowering of the general sea level (100–120 m), influence of icebergs and their associated ice rafted debris from the north (even up to south of the Gulf of Cadiz) (Heinrich events, Lebreiro et al. 1996). Under these circumstances, probably more favourable conditions for cold-water coral growth were present in the Gulf of Cadiz.

Llave et al. (2006) and Voelker et al. (2006) suggested that the lower Mediterranean branch with a significantly higher salinity and density (Schönfeld 1997; Zahn et al. 1997; Cacho et al. 2000), enhanced during climatic coolings (glacials/stadials). This lower branch of intensive and deeper MOW (Thomson et al. 1999; Schönfeld and Zahn 2000; Rogerson 2002) results in a stronger interaction with the sea-floor and higher current velocities (Llave et al. 2006). The enhancement of the lower core of MOW (mainly the Principal and Southern Branches) during previous glacial conditions can have enhanced the formation of meddies (carriers of cells of MOW with their full biological content), which have probably strongly influenced the Moroccan Margin. Several molluscan and foraminiferal species co-occurring with the cold-water corals, as observed in the Kasten core MD04-2804 and the surface box cores, belong to a Mediterranean fauna. Moreover, the study of an off-mound core (Vanneste 2005) between Renard Ridge and Vernadsky Ridge, showed the presence of coarser and more reworked material during colder periods, indicating higher currents which can be linked with the input of a more vigorous meddies and the interaction of these meddies with NACW. These meddies and the interaction of these meddies with NACW, are responsible for a fresh supply and a higher flux of nutrients, which is positive for prolific cold-water coral growth (Freiwald et al. 2002).

Nowadays, all the cold-water coral fragments and mounds are draped by a fine layer of silty mud. The off-mound core between Renard Ridge and Vernadsky Ridge is characterized by finer sediments since the onset of the Holocene and a rather high sedimentation rate (18.5 cm/ka) could be calculated for this period (Foubert et al. 2005b). Currents seem to be nowadays weaker than during colder periods. It can be postulated that a decrease in the food particle flux and higher sedimentation rates are responsible for the dead of most of the cold-water coral colonies.

It is worth to mention that the environmental and oceanographic situation described for colder periods on the Moroccan margin, can be nowadays observed in well-delineated areas of PSB, where cold-water corals are still alive (De Mol et al. 2002; Foubert et al. 2005a; Huvenne et al. 2005; Wheeler et al. 2005b; see previous Chaps.). Current regimes in Porcupine Seabight and along the Moroccan margin seem to be opposite to each other during glacial and interglacial periods (at least for the most recent ones).

8.4.3 Cold-Water Coral Dissolution and Carbonate Precipitation

In the Gulf of Cadiz on the Moroccan margin, mounds built up by cold-water corals occur in an area characterized by the presence of gas seepage and subsurface fluid flow. However it should be noted that no direct relationship could be found between cold-water coral growth and fluid or gas seepage.

The cold-water coral fragments embedded in the sediments, as observed in well-delineated parts of the studied cores, are heavily dissolved. This phenomenon is clearly observed in core MD04-2804, whereby the cold-water coral fragments are

in a rather bad stage of preservation due to dissolution just above and at the front of the recent zone of anaerobic oxidation of methane, whereas the zone of AOM corresponds with a release of carbonate in the surrounding sediments and so carbonate precipitation. This can be explained by a pure diagenetic process (resulting from the fluxes in pore water transport). Oxidation of organic matter alters the pH and the alkalinity of interstitial water and thus the diagenesis of carbonate minerals (Tribble 1993). In general, model results indicate that mineral saturation states decrease during oxic respiration (from release of carbonic acid) and increase during sulphate reduction (from increase in alkalinity) (Jorgensen 1983; Reeburg 1983). The C:N ratio of the organic matter and the degree to which sulphide precipitates as a mineral phase also affect the saturation state with respect to carbonate minerals. Tribble (1993) suggested that the aragonite saturation state initially drops but becomes oversaturated during extensive sulphate reduction. A pattern of initial aragonite dissolution followed by carbonate precipitation as a function of the extent of sulphate reduction can occur within reefs in a manner similar to that described for sediments (Tribble 1993). Throughout this process the interstitial waters keep close to equilibrium compositions with aragonite. This buffers the pH of the waters. Because interstitial water in the reef has a short residence time, the observed equilibration suggests rapid kinetics. A similar process is noted in the mounds in Porcupine Seabight SW of Ireland, where no obvious recent methane fluxes or seepage is noted but where extensive dissolution dominate on carbonate precipitation (Sect. 4.5.2). However, when a flux of methane reaches the aerobic zone, aerobic methane oxidation takes the overhand and drops the pH drastically, stimulating a net dissolution of aragonite. During coupled anaerobic methane oxidation and sulphate reduction, HCO_3^- and HS^- are released, increasing the pH and so stimulating a system that becomes oversaturated in respect to aragonite, resulting in carbonate precipitation. So, focused and alternating fluxes of methane in time can stimulate dissolution of cold-water corals in the aerobic zone and precipitation of carbonate in the anaerobic zone. The presence of such a methane flux can explain the more extensive carbonate precipitation observed in the mounds along the Moroccan margin, compared to the mounds in the Porcupine Seabight.

A positive relationship between focused fluid flow and carbonate mound distribution on the south-eastern edge of PDE is observed. This is evidenced by the rather high sulphate gradient, with a methane oxidation front at 3 m below the surface measured on core MD04-2804 (Maignien et al. subm.). Three main reasons can be invoked to explain a higher internal methane flux towards the mounds at the south-eastern edge of the ridge. First of all, a mounded feature on a scarp or a hill on the seabed subjected to rather strong peak currents will develop zones of high pressure at the lows of the slopes and low pressure areas at or near the summit (Depreiter et al. 2005a). This pressure effect would create a fluid migration from deeper layers to the top of the structure. This effect will be enhanced at the edges of a ridge, where higher pressure gradients are created. So, in this view, the pumping of fluids in carbonate mound systems is driven by external currents. Another reason is the association of the mounds with the ridges, and thus with the faults co-occurring with the ridges. Indeed, as observed on the seismics, the ridges are

partly fault-controlled. The faults can be preferable pathways for fluids, canalizing the fluids towards the mounds on top of the ridges. A third reason can be the influence by the recent eruptive activity of the neighbouring Gemini West mud volcano, focusing the extrusion of fluids towards the mud volcano crater. Van Rensbergen et al. (2005b) has shown that Gemini West mud volcano is one of the most active mud volcanoes in the region, as it lacks a hemipelagic sediment drape of fine mud (as observed over most of the mud volcanoes, mounds, carbonate slabs and covering the sea-floor in between the mounds) and it features a shallow sulphate reduction zone (as observed in the Kasten core MD04-2804). The presence of mud breccia and mud clasts in gravity core AT570G (at the south-eastern flank of a mound at the south-eastern edge of PDE), confirms the influence of the recent activity of mud volcanoes on this south-eastern edge. The mud breccia and clasts recovered in this core are similar to the mud breccia and clasts recovered from cores on the neighbouring mud volcanoes (Van Rensbergen et al. 2005b).

While cold-water coral growth has obviously nothing to do with seepage, the mounds they create by the interaction between sediment dynamics and coral framework can be affected by internally controlled fluid fluxes. The effects of coral alteration have to be further investigated in detail but the positive effect of carbonate precipitation during sulphate reduction and anaerobic methane oxidation on mound stabilization is noteworthy to mention.

8.4.4 Model for the Development of Carbonate Mounds

By combining the observations, a three-phase mound development model can be proposed for the mounds on the Moroccan margin:

1. In a first stage the cold-water corals start to colonize a suitable substrate under specific environmental and oceanographic conditions, positive for cold-water coral growth. The most important factor is the presence of a planktonic food chain, based on a high primary production and an enhanced food particle flux towards the sea-floor. Elevated positions, creating enhanced currents and so a higher nutrient flux, are preferable. Tidal currents have an additional positive effect on the availability of planktonic food particles for cold-water corals. Suitable substrates are cemented and/or eroded horizons or carbonate crusts.
2. During a second phase, the interaction between sediments, currents and cold-water corals plays an important role. As described in Porcupine Seabight, sedimentation and hydrodynamics regulated by oceanographic and climatic changes are crucial in mound development (De Mol et al. 2005; Dorschel et al. 2005; Foubert et al. 2005a; Frank et al. 2005; Huvenne et al. 2005; Rüggeberg et al. 2005, 2007; Wheeler et al. 2005b; previous Chaps.). The initial cold-water coral frameworks start to baffle sediments under certain current regimes, a crucial phase to build up **cold-water coral mounds**. In this phase, coral colony development and sediment baffling proceed in harmony. When sedimentation prevails, cold-water

corals can be buried. On the contrary, when no sediments are available the polyps can be kept sediment-free and cold-water corals can build healthy **reef frameworks (cold-water coral reefs)** up to several metres high, as observed on the Norwegian margins (Freiwald et al. 2002).

3. In a last phase, when the cold-water corals are embedded in a sediment-rich matrix and when an initial mound structure is already built, fluid seepage and fluxes in pore water transport affects the built structures by diagenetic processes, resulting in cold-water coral dissolution and/or carbonate precipitation. During this stage, it can be said that the cold-water coral mounds (characterized by cold-water corals embedded in a sediment-rich matrix) develop partly towards **carbonate mounds**, whereby the carbonate precipitation is responsible for the mound stabilization. It should be mentioned that the last phase can be concurrent with phase 2. A continuous interaction between the different phases is responsible for the final character of the mound structures.

8.5 Summary

The **mound** and **mound patches** in El Arraiche mud volcano field can be divided in four well-delineated provinces: **Pen Duick Mound Province**, **Renard Mound Province**, **Vernadsky Mound Province** and **Al Idrisi Mound Province**. The mounds are highest and most developed on PDE, while the Al Idrisi patches are just characterized by small elevated structures (up to 3 m). The Renard Mounds and Vernadsky Mounds have many similarities, whereby most of the mounds are observed on top of the ridges and fading out mound patches are colonizing the sediments burying the flanks of the ridges. The seismic data confirmed a **close association** between the **anticlinal ridges** at or below the sea-floor, and the **mound structures** built up by cold-water corals on the sea-floor.

The gravity cores, box cores and video imagery display a high number of **reef-forming cold water scleractinians** with numerous **faunal associates** formerly inhabiting the econiches provided by the coral framework. **Temporal and spatial variations** are observed in the dominance of the different cold-water coral species. Under **present interglacial** environmental and oceanographic conditions, **no healthy live coral reefs** could be observed. However, environmental and oceanographic conditions during **colder periods** (glacials/stadial) where probably **more favourable for cold-water coral growth**. Meddies, anticyclonic cells of MOW, and the interaction of these meddies with NACW, could have played hereby a major role.

Fluid seepage can affect the built mound structures by **diagenetic processes**, resulting in **cold-water coral dissolution** and **carbonate precipitation**. However, no obvious relation between cold-water coral growth and seepage is observed.

A **three-phase model** for the **mound development** on the Moroccan margin can be proposed. During a first phase the cold-water corals start to **colonize suitable**

substrates under specific environmental and oceanographic conditions positive for cold-water coral growth. In a second stage, the cold-water coral frameworks start to **baffle sediments** regulated by environmental changes and build up cold-water coral mounds. During the last phase, **fluid seepage affects the initial structures by diagenetic processes**, resulting in cold-water coral dissolution and carbonate precipitation. So, a **cold-water coral mound**, consisting of cold-water corals embedded in a sediment-rich matrix, can become a **carbonate mound** by diagenetic alteration. The continuous interaction between the last two phases, which may be concurrent, is responsible for the final character of the mounds.

Chapter 9
Conclusions and Outlook

The presented work has tried to give the reader insights in the nature of recent carbonate mounds. Challenger Mound, the first recent carbonate mound drilled in history, during IODP Expedition Leg 307, has been chosen as key site. The internal structure of Challenger Mound was studied from a visual (Chap. 3), geochemical and geophysical (Chap. 4), and magnetic (Chap. 5) viewpoint. The mound body plays a double role in the deciphering of the story of mound formation – the "Mound Challenger Code". On the one hand, the mound acts as a cyclic recorder of environmental changes. On the other hand, the mound is an early transformer which distorts a primary record into diagenetically altered signals. The significance of the carbonate mound record was examined by the study of other carbonate mound provinces along the continental margin (Chaps. 6 and 8) and by an intensive look to the role which surface processes play nowadays (Chap. 7).

In the following account, the highlights of this volume are summarized. These findings and statements are subsequently put in a "controversial" light, before topping off the present volume with a brief look-a'head.

9.1 Conclusions

9.1.1 Findings and Statements

Based on the results presented and discussed in previous chapters, the following conclusions can be highlighted:

- The internal composition of Challenger Mound can be summarized as a facies of cold-water coral fragments (mainly *Lophelia pertusa* and some minor to rare occurrences of *Madrepora oculata* and *Desmophyllum cristagalli*) and biogenic fragments embedded in an alternating biogenic (carbonate-rich) to terrigenous (siliciclastic) matrix. The terrigenous sediments are dominated by clay minerals (illite, kaolinite and chlorite) and silt-sized quartz with secondary potassium feldspar and plagioclase (albite). Western Ireland can be proposed as the

A. Foubert, J.-P. Henriet, *Nature and Significance of the Recent Carbonate Mound Record*, Lecture Notes in Earth Sciences 126, DOI 10.1007/978-3-642-00290-8_9,

primary source of terrigenous, detrital material towards the Irish shelves. The biogenic sediments are dominated by nannofossil ooze (coccoliths), evidencing that the planktic factory seem to be important in providing carbonate towards the Challenger carbonate mound system, and micro-bioclastic (bio-detrital) fragments (foraminifera, sponge spiculae, radiolarian, echinoderms, bivalves, gastropods,. . .).

- Cold-water coral fragments are present throughout the whole mound body but in changing quantities, with an average surface quantity (2D) estimated at 4.49% and an average volume quantity (3D) estimated at 7.81%.
- The porosity is mainly identified as a primary intergranular porosity in the fine muddy matrix sediments. Porous and hollow skeletons are responsible for a superimposed intragranular porosity. Dissolved cold-water coral fragments can create a secondary moldic porosity and some particular intervals seem to be sensitive to develop a kind of fracture porosity.
- The cyclic record is induced by the continuous alternation between terrigenous Fe-rich and clay-rich (siliciclastic) material and biogenic Ca-rich material, suggesting a predominantly two-component sedimentary environment. The cyclicity can be explained as driven by glacial-interglacial changes, characterizing the northern hemisphere during Quaternary periods.
- The mean carbonate content in Challenger Mound is estimated at ∼49.60%.
- Early differential diagenesis overprints the primary environmental cyclic record in particular in the Ca-rich intervals. Extensive coral dissolution and the genesis of small-scaled semi-lithified layers are the main diagenetic features observed in Challenger Mound. Low cementation rates compared to extensive aragonite dissolution are explained by an open system diagenetic model.
- A general evolution model for Challenger Mound and its surrounding environment can be proposed, mainly based on magnetostratigraphic interpretations:

1. In a first phase, identified as the pre-mound phase, the evolution of the eastern margin of the Porcupine Seabight before the onset of mound growth was studied. The mounds in the Belgica Mound Province started to grow on an erosive unconformity probably caused by a combination of uplifting of the continental margin and associated changes in bottom current regimes. A Late Burdiglan (16.70 Ma) to Late Serravalian (12.01 Ma) age is attributed to the sediments at Site U1318 immediately below the unconformity. These sediments are deposited during the Middle Miocene Climatic Optimum and a subsequent cooling phase around 13.60 Ma.
2. Challenger Mound started to grow between ∼2.70 and ∼2.50 Ma, identified as the mound initiation phase. This onset of mound growth coincides with the onset of the northern hemisphere glaciations.
3. The third phase of mound evolution occurred in two important mound growth episodes:

   – a vertical growth episode (vertical expansion of the mound) from ∼2.60 until ∼2.00 Ma

- a horizontal growth episode (lateral expansion of the mound) from ~2.00 Ma until ~1.60 Ma

Mean mound growth rates are ~13 cm/ka, with maximum growth rates up to 52.60 cm/ka in the centre of the mound during distinctive growth events. Such high peak growth rates make that carbonate mounds act as excellent recorders of palaeoenvironmental changes.

4. Different observations pointed to the fact that Challenger Mound is nowadays in a phase of mound decline. The switch towards more intense and prolonged glacial states during the Mid-Pleistocene Revolution (MPR) may have been responsible for the observed mound decline. Extensive off-mound sedimentation started around the same period, respectively at 475 ka and 550 ka at Sites U1316 and U1318. The off-mound sediments can be interpreted as drift sediments deposited mainly during the extensive glaciations after the MPR as silty muddy contourites. Sediment lofting from density currents generated from freshwater discharges can explain the laminated horizons in the glacial silty muddy contourites. Dropstones in the glacial deposits bear witness of ice rafting events. The intercalation of small coarser intervals, represent interglacial or interstadial sandy contourites deposited by vigorous bottom current conditions during warmer periods whereby Mediterranean Outflow Water (MOW) probably played an important role.

- A study of on-mound gravity cores made it possible to compare the uppermost sediments on Challenger Mound (eastern margin of the Porcupine Seabight, Belgica Mound Province) with the uppermost sediments of Mound Perseverance (northern part of the Porcupine Seabight, Magellan Mound Province). While Challenger Mound is now in a stage of mound decline with only some small reinitiating phases of cold-water coral growth during interglacials or interstadials, the record full of corals in the uppermost sediments on top of Mound Perseverance evidence a main growth phase during the Holocene resulting in mound growth rates of 85 cm/ka. Not only during present times but also in the past, both provinces, the Belgica Mound Province and the Magellan Mound Province, show clear palaeoenvironmental differences.
- Small mound build-ups are recognized in between the giant Belgica Mounds. The evolution of these Moira Mounds can be explained by the interaction between cold-water coral growth and sediment baffling through a positive feedback mechanism. It is assumed that such small mound build-ups represent rather a way of cold-water coral growth under stressed conditions than an initial phase of extensive mound growth.
- Most of the Belgica Mounds are covered with sediment-clogged dead coral rubble and dead cold-water coral fragments. Just a few “live” mounds are encountered in the study area, with their summits and western flanks covered with live coral frameworks. Bottom intensified tidal diurnal currents seem to have a positive effect on these mounds by providing the cold-water corals with enough nutrients and organic particulate matter during peak velocities in the tidal cycle,

and enough quietness to allow finer material sinking down during velocity lows, which is a factor of mound stabilization.

- A new cluster of mounds and mound patches has been discovered along the Moroccan margin in El Arraiche mud volcano field. Four well-delineated provinces are recognized: the Pen Duick Mound Province (on Pen Duick Escarpment), the Renard Mound Province (at the western edge of Renard Ridge), the Vernadsky Mound Province (on the Vernadsky Ridge), and the Al Idrisi Mound Province (above the Al Idrisi Ridge). The seismic data confirmed a close association between the anticlinal ridges at or below the sea-floor, and the mound structures built up by cold-water corals on the sea-floor. Under present conditions, no healthy live cold-water coral frameworks or mound structures covered with live cold-water corals are observed, evidencing that the mound structures are "dead" and probably relict structures of former mound growth. Fluid seepage in the mounds on Pen Duick Escarpment may have affected the built mound structures in a second phase.

9.1.2 Controversy

9.1.2.1 Recent Carbonate Mounds: Highly Productive Carbonate Factories?

It can be questioned what the role is of recent deep-water carbonate mounds in the global carbonate budget. The role of different carbonate factories was recently described by Schlager (2003) and well elucidated by Mutti and Hallock (2003) with respect to nutrient and temperature gradients. Schlager (2003) postulated a model showing that marine carbonate precipitation occurs in three basic modes: abiotic (or quasi abiotic), biotically induced, and biotically controlled. On a geological scale, these precipitation modes combine to form three benthic carbonate production systems or "factories": (1) tropical shallow-water factories, dominated by biotically controlled (mainly photo-autotrophic) and abiotic precipitates, (2) cool-water factories, dominated by biotically controlled (mainly heterotrophic) precipitates, and (3) mud mound factories, dominated by biotically induced and abiotic precipitates (Schlager 2003). The term "carbonate factory" represents the space where carbonate sediment is produced but it also represents the processes that lead to carbonate production (Tucker and Wright 1990; James and Bourque 1992). Vecsei (2004) presented a new estimate of global reefal carbonate production including the fore reefs, while Dullo (2005) focused on the growth rates of modern corals in relation to modern reefs and the impact of shallow-water reefs in the global budget of CO_3^{2-} and CO_2.

Due to the scarcity of data and measurements, deep-water carbonate mounds have been up to now excluded from any global carbonate budget calculation. However, it can be supposed that deep-water coral reef and carbonate mound systems do play an important role in the global carbonate budget. Dorschel et al. (2007b) proposed a first carbonate budget model for Propeller Mound, one of the recent carbonate mounds encountered in the Hovland Mound Province in the Porcupine

Seabight. The authors concluded that Propeller Mound has a carbonate content of >50% with the carbonate to a significant amount consisting of fragments of the cold-water corals *Lophelia pertusa* and *Madrepora oculata*. Mound growth rates between 6 and 7 cm/ka were calculated for the uppermost sediments. The effect of coral growth on the on-mound accumulation was estimated at about ∼15%. A net accumulation for the last 175 ka accounted for only 0.3 g/cm^2/ka. However, these data were only revealing carbonate estimations for the upper few metres of the mound.

Based on the combination of carbonate content estimates and coral quantifications, the potential role of a recent carbonate mound, such as Challenger Mound in the global carbonate budget can be discussed. The total carbonate content of Challenger Mound is estimated at ∼50%. Carbonate is mainly present in the mound sediments as calcite and aragonite, whereby calcite is mainly originating from nannofossil ooze (matrix sediments), whereas aragonite is mainly concentrated in the coral fragments (framework builders). Small amounts of dolomite are present and the contribution of diagenetic calcite can not be neglected. At a regional scale, it should be highlighted that the sediments encountered in the main mound body of Challenger Mound are unique. No time-equivalent sediments are encountered in the adjacent drift deposits on the margin immediately upslope and downslope of the moundbody. In this way, Challenger Mound can be seen as an unique palaeoceanographic archive. However, to evaluate the amount of calcite present in the background sediments (mainly as calcitic nannofossil ooze), time-equivalent sediments should be objectively studied. Sediments at ODP Sites 980/981 (Feni Drift, Rockall Trough) deposited in the same time interval, have an average calcium carbonate content of ∼54%, which is similar to the average amount of calcium carbonate content calculated for the Challenger Mound sediments. This suggests that the supposed high carbonate contents encountered on the mound are not extremely high when compared with similar sediments deposited during the same period. The particularity lies in the carbonate contribution by cold-water coral fragments and associated macro- and micro-bioclastic material. Such a stable cold-water coral framework is most probably responsible for the baffling of the sediments and/or the active catch or calcareous plankton in regions where normally no sedimentation takes place due to a strong hydrodynamic regime. The total amount of coral fragments is varying between 0% and 26.19%, with an average value of 7.81% based on three-dimensional X-ray computer tomographic analysis. Two-dimensional analysis on surface pictures revealed a mean coral content of 4.46%, varying between 0% and 12.12%. However, these coral quantifications are based on macro-scaled observations. Titschack et al. (2006) made an attempt to incorporate in these coral quantification estimates the amount of aragonite quantified by XRD analyses, revealing an average coral or aragonite content of ∼17%. Recent calculations of Titschack et al. (2009) show that only about 33 to 44 wt.% of the carbonate is derived from corals. So, the unique character of Challenger Mound lies in the contribution of framework builders (the cold-water corals), and the associated benthic fauna. The amount of carbonate produced by the planktic factory is of major importance but not less than observed in other sediments deposited during the same time period. The

more, the important fraction of siliciclastic material in Challenger Mound seems to lower its carbonate budget drastically and the amount of cold-water coral fragments is less than ¼ of the total mound system. However, it should be mentioned that the carbonate estimations and coral quantities presented here are mean values of the whole mound system. As discussed earlier the cyclic record is an important feature of Challenger Mound, suggesting that Challenger Mound might be in certain time intervals a real carbonate factory (as identified in the intervals rich in carbonate with values up to 70% carbonate), while during other time intervals Challenger Mound does not seem to be a specific or extra-ordinary carbonate factory at all. Recently, Titschack et al. (2009) estimated the carbonate accumulation rate of Challenger Mound at 17.3 g/cm^2/ka for the main mound body (i.e. from the moundbase until the mound hiatus). These carbonate accumulation rates are about 4 to 12% of the carbonate accumulation rates of tropical shallow water reefs (Titschack et al., 2009). However, more research is necessary to fully address this topic.

On the other hand, Roberts et al. (2006) pointed to the potential risk of ocean acidification, caused by rising atmospheric carbon dioxide levels, on cold-water corals. Current research predicts that tropical coral calcification would be reduced by up to 54% if atmospheric carbon dioxide doubled (Caldeira and Wickett 2003). There have been no studies to examine these effects on cold-water corals, but given the lowered carbonate saturation state at higher latitudes and deeper waters, these species may be even more vulnerable to ocean acidification (Roberts et al. 2006). In addition to the effect acidification could have on coral calcification, modelling studies suggest that the depth at which aragonite dissolves could shallow by several hundreds of metres, thereby raising the prospect that areas once suitable for cold-water coral growth will become inhospitable (Orr et al. 2005; Guinotte et al. 2006; Roberts et al. 2006). The effect on mound growth will probably be that the main actors responsible for the framework of the mound will be replaced once again, as observed by studies on ancient carbonate mound systems through time: “the actors change but the plays goes on”.

9.1.2.2 “Recent Carbonate Mounds” Analogues for “Ancient Mud Mounds”?

A lot of discussion is going on about the question to what extent the deep-water carbonate mounds encountered nowadays along the European and North African Atlantic continental margins, may represent analogues for ancient mud mounds. However, such a comparison is a whole study on itself and has to be undertaken with great caution. In this section, only some comments on the many attempts to compare ancient mound systems with recent systems, will be given.

Throughout this study, it became clear that recent deep-water carbonate mound and reef systems show already a wide variety in structure and composition. The main framework builders in the studied system are azooxanthellate scleractinian corals, including different dominating species. Depending on the interaction of such cold-water corals with sedimentary processes different kinds of structures can be built. Challenger Mound can be interpreted as a carbonate mound system whereby the interaction between cold-water corals and terrigenous (mainly clay minerals) and

biogenic (mainly nannofossil ooze and biodetrital fragments) sediments seem to be the main driving factor of mound growth. However, the mound is nowadays in a stage of decline. The carbonate mounds encountered in the Gulf of Cadiz are rather dead in terms of active mound growth but seem to be affected nowadays by active fluid seepage having an important effect on diagenetic pathways. On the other hand, extensive cold-water scleractinian coral reefs seem to flourish in Norwegian waters but no real mounded structures, as observed in the Porcupine Seabight, and along the Moroccan margin, are formed. One of the main objectives in future research should be to elucidate the different forms of recent deep-water "carbonate mound" and "reef" growth and to distinguish between these kinds of growth structures. Until now, no reliable classification system exists for these recent deep-water "reef" and "mound" systems and the classification systems used are adapted systems from the study of the well-known tropical reef systems and ancient mound and reef systems, complicating any attempt for comparison. It can not be excluded that deep-water reefs can develop towards deep-water carbonate mounds, hence proposing a holistic model is not straightforward. As discussed in Sect. 3.6.2, the classification system of Riding (2002) and Bourque et al. (2004) is probably a suitable approach but mainly based on the study of ancient mound and reef systems. Taking into account the basic precipitation modes, such as proposed by Schlager (2003), may be another good point of departure for the classification of these recent systems. However, it seems not always easy to draw a straight line between biotically induced, abiotic or biotically controlled precipitation (Schlager 2003). In addition, the cyclic record characterizing Challenger Mound makes adequate naming not easy, as different facies are following up each other in a rather fast way with even up to metre-scaled alternations. Moreover, it has to be mentioned that most of the studied carbonate mound systems, such as Challenger Mound and the mound systems along the Moroccan margin, seem to be in a stage of decline, suggesting that the term "recent" should be used with caution.

When making an attempt to compare Challenger Mound with Palaeozoic mud mounds, only similarities in terms of size and geometry can be highlighted. The most striking differences can be summarized as follows:

- Palaeozoic mounds are composed almost entirely of carbonate muds and skeletal material whereas Challenger Mound contains a substantial siliciclastic component.
- The micritic carbonate component of the Challenger Mound is almost entirely allochthonous nannoplankton. There is no evidence for a similar planktonic origin of micrite in Palaeozoic mud mounds.
- Palaeozoic mud mounds bear evidence of extensive early diagenetic lithification, brecciation, and marine cementation. These features seem to be less pronounced in Challenger Mound. Stromatactis-like structures as observed in Palaeozoic mounds are not present in Challenger Mound.
- The clear cyclic record encountered in Challenger Mound, is not observed in ancient Palaeozoic mud mound systems.

However, more detailed studies should be undertaken to allow comparisons between these "on first sight" different systems. Ancient systems should by restudied in view of new revelations in recent mound research, while still a lot of energy has to be spent in elucidating the early diagenetic pathways in recent mound systems in different environmental settings. Only then both paths in mound research, defined as "recent" and "ancient" mound systems, might meet once in the future.

9.2 A Look Ahead

In the present volume, a first attempt is made to look literally into a recent carbonate mound. However by debating the findings, it became clear that there is still a long way to go before the whole carbonate mound system will be fully understood. Different pathways in the jumble of mound research are still unexplored and a lot of questions remain unanswered or speculative. Particularly promising are investigations in the following directions:

- Drilling one mound in one specific environmental setting is not enough to elucidate the variety of processes playing a role in mound evolution. Other drilling actions are necessary. IODP Proposal 673-Full is a step in the right direction to drill the non-buried mounds on the Pen Duick Escarpment, off Morocco (Van Rooij et al. 2008). ESF-founded projects such as CARBONATE, will focus on the carbonate mounds in other regional settings. Only by comparing different recent mound systems in different settings, an appropriate classification system for recent deep-water carbonate mounds and reefs can be established. This step is important to allow comparison with ancient mound systems.
- Drilling Palaeozoic mud mounds over their full height is necessary to allow an adequate comparison with recent carbonate mound systems. Only similar sampling strategies will make it possible to study ancient and recent mound systems from the same viewpoint.
- Multi-disciplinary research and interaction between carbonate sedimentologists studying ancient carbonate build-ups and scientist studying recent mound development processes is necessary to understand both systems.
- Modeling studies in lab-specific environments can help in elucidating mound initiation processes. The main control on mound initiation is not yet unveiled.
- The sedimentological controls on cold-water coral growth should be modeled. The detailed processes through which the biosphere interacts with sedimentary processes might play a crucial role, whereby cold-water coral reefs can be formed in cases with low sediment-input while cold-water coral mounds seem to develop in environments with high sedimentation input. The role of sediments as limiting factor should be studied in detail.
- The role of carbonate mounds as palaeoenvironmental recorders should be checked on a global scale. As palaeoclimatic and palaeoceanographic processes

had an important influence on Challenger Mound, these processes should have left their traces on carbonate mounds on a global scale and similar cyclic records should be observed in other carbonate mounds. In this way, the cyclic record in carbonate mounds might become an important world-wide correlation tool.

- The influence of specific water masses and their effect on cold-water coral growth and mound growth, in particular for specific environments such as the Moroccan margin, should be studied in detail. The more, the impact of bottom intensified diurnal tides on mound growth should be further explored.
- During the main mound growth phase of Challenger Mound, no sediments seem to have been deposited in the off-mound regions. The reason why these off-mound sediments are not present or not preserved, contrasting sharply with the extensive mound evolution phase, is still not clear. More research, focusing on the lateral extension of the mound base, can elucidate the answer.
- More detailed research is necessary to explain the extensive dissolution versus really slow cementation processes in Challenger Mound. It has been shown that early diagenesis plays a role in Challenger Mound but the exact mechanisms are not yet understood. Such diagenetic research is necessary to evaluate the reservoir qualities of these recent carbonate mound systems.

References

Abe K (2006) Planktonic and benthic foraminifers: IODP Expedition 307. 2nd Post-cruise Meeting IODP Expedition Leg 307, Yokohama

Adams JAS, Gasparini P (1970) Gamma-ray spectrometry of rocks. Meth Geochem Geophys 10

Aitken SA, Collom CJ, Henderson CM, Johnston PA (2002) Stratigraphy, paleoecology, and origin of Lower Devonian (Emsian) carbonate mud buildups, Hamar Laghdad, eastern Anti-Atlas, Morocco, Africa. B Can Petrol Geol 50:217–243

Akhmetzhanov AM, Kenyon NH, Ivanov MK, Wheeler AJ, Shashkin PV, van Weering TCE (2003) Giant carbonate mounds and current-swept seafloors on the slope of the Southern Rockall Trough. In: Mienert J, Weaver PPE (eds) European margin sediment dynamics: side-scan sonar and seismic images. Springer-Verlag, Berlin Heidelberg, pp 203–209

Allen JRL (1982) Simple models for the shape and symmetry of tidal sand waves: (3) Dynamically stable asymmetrical equilibrium forms without flow separation. Mar Geol 48:321–336

Ambar I, Serra N, Brogueira MJ, Cabecadas G, Abrantes F, Freitas P, Goncalves C, Gonzalez N (2002) Physical, chemical and sedimentological aspects of the Mediterranean outflow off Iberia. Deep-Sea Res Pt II 49:4163–4177

ASTM (1990) Standard method for laboratory determination of water (moisture) content of soil and rock. Annual Book of ASTM Standards, D 2216-90 (revision of 2216-63, 2216-80)

Ballet O, Coey JMD, Burke KJ (1985) Magnetic properties of sheet silicates – 2-1-1 layer minerals. Phys Chem Miner 12:370–378

Baraza J, Ercilla G (1996) Gas-charged sediments and large pockmark-like features on the Gulf of Cadiz slope (SW Spain). Mar Petrol Geol 13:253–261

Baringer MO (1993) Mixing and dynamics of the mediterranean outflow. PhD thesis, Mass. Institute of Technology/Woods Hole Oceanographic Institute Joint Program

Baringer MON, Price JF (1999) A review of the physical oceanography of the Mediterranean outflow. Mar Geol 155:63–82

Beck T, Freiwald A (2005) Key species of cold-water coral-associated fauna. In: Abstract Book Third International Symposium on Deep-Sea Corals: Science and Management. IFAS, Miami, p 50

Belderson RH, Kenyon NH, Wilson JB (1973) Iceberg plough marks in the Northeast Atlantic. Palaeoclimatol Palaeogeogr Palaeoecl 13:215–224

Belderson RH, Johnson MA, Kenyon NH (1982) Bedforms. In: Stride HH (ed) Offshore tidal sands: processes and deposits. Chapman and Hall, London, pp 27–57

Belka Z (1998) Early Devonian Kess-Kess carbonate mud mounds of the eastern Anti-Atlas (Morocco), and their relation to submarine hydrothermal venting. J Sediment Res 68: 368–377

Berastegui X, Banks CJ, Puig C, Taberner C, Waltham D, Fernandez M (1998) Lateral diapiric emplacement of Triassic evaporites at the southern margin of the Guadalquivir Basin, Spain. In: Mascle A (ed) Cenozoic foreland basins of western europe. Geological Society Special Publication, London, pp 49–68

Berger A, Imbrie J, Hays J, Kukla G, Saltzman B (1984) Milankovitch and climate. Springer, New York

Berger A, Loutre MF (1991) Insolation values for the climate of the last 10000000 years. Quaternary Sci Rev 10:297–317

Bergstrom SM, Lofgren A, Grahn Y (2004) The stratigraphy of the Upper Ordovician carbonate mounds in the subsurface of Gotland. GFF 126:289–296

Berner RA (1970) Sedimentary pyrite formation. Am J Sci 267:19–42

Berner RA (1984) Sedimentary pyrite formation – An update. Geochim Cosmochim Ac 48: 605–615

Bett BJ, Billet DSM, Masson DG, Tyler PA (2001) RRS Discovery Cruise 248: A multidisciplinary study of the environment and ecology of deep-water coral ecosystems and associated seabed facies and features (the Darwin Mounds, Porcupine Bank and Porcupine Seabight). Southampton Oceanogr Cruise Rep 36

Beyer A, Schenke HW, Klenke M, Niederjasper F (2003) High resolution bathymetry of the eastern slope of the Porcupine Seabight. Mar Geol 198:27–54

Blackman RB, Tukey JW (1958) The measurement of power spectra. Dover Publ Inc., New York

Bloemendal J, Lamb B, King J (1988) Paleoenvironmental implications of rock magnetic properties of late quaternary sediment cores from the eastern equatorial Atlantic. Paleoceanography 3:61–87

Bloemendal J, King JW, Hall FR, Doh SJ (1992) Rock magnetism of late Neogene and Pleistocene deep-sea sediments – Relationship to sediment source, diagenetic processes, and sediment lithology. J Geophys Res-Sol Ea 97:4361–4375

Blum P (1997) Physical properties handbook. IODP Technical Notes

Böhme M (2003) The Miocene climatic optimum: Evidence from ectothermic vertebrates of Central Europe. Palaeogeogr Palaeocl 195:389–401

Bond G, Heinrich H, Broecker WS, Labeyrie LD, McManus J, Andrews JT, Huon S, Jantschik R, Clasen S, Simet C, Tedesco K, Klas M, Bonani G, Ivy S (1992) Evidence for massive discharges of icebergs into the North Atlantic ocean during the last glacial period. Nature 360:245–249

Borradaile GJ, Werner T (1994) Magneticanisotropy of some phyllosilicates. Tectonophysics 235:223–248

Bosence DWJ, Bridges PH (1995) A review of the origin an evolution of carbonate mud-mounds. In: Monty CLV, Bosence DWJ, Bridges PH, Pratt BR (eds) Carbonate mud-mounds: their origin and evolution. Blackwell Science, Oxford, pp 3–9

Boulvain F, Cornet P, da Silva AC, Delaite G, Demany B, Humblet M, Renard M, Coen-Aubert M (2004) Reconstructing atoll-like mounds from the Frasnian of Belgium. Facies 50: 313–326

Bourque PA, Boulvain F (1993) A model for the origin and petrogenesis of the red stromatactis limestone of paleozoic carbonate mounds. J Sediment Petrol 63:607–619

Bourque PA, Neuweiler F, Boulvain F (2004) The mud-mound system: products and processes. In: 32nd International Geological Congress. CD ROM abstracts part 2. IGC, Florence, p 1079

Boven KL, Rea DK (1998) Partitioning of eolian and hemipelagic sediment in eastern equatorial Pacific core TR 163-31B and the late Quaternary paleoclimate of the northern Andes. J Sediment Res 68:850–855

Bowen DQ (1989) The last interglacial-glacial cycle in the British Isles. Quatern Int 3/4:41–47

Bowen DQ (1991) Time and space in the glacial sediment systems of the British Isles. In: Ehlers J, Gibbard PL, Rose J (eds) Glacial deposits in great Britain and Ireland. Balkema, Rotterdam, pp 3–13

Bowen DQ, Phillips FM, McCabe AM, Knutz PC, Sykes GA (2002) New data for the last glacial maximum in great Britain and Ireland. Quaternary Sci Rev 21:89–101

Bower AS, Armi L, Ambar I (1995) Direct evidence of meddy formation off the southwestern coast of Portugal. Deep-Sea Res Pt I 42:1621–1630

Bower AS, Armi L, Ambar I (1997) Langrangian observations of meddy formation during a Mediterranean undercurrent seeding experiment. J Phys Oceanogr 27:2545–2575

Boyce RE (1976) Definitions and laboratory techniques of compressional sound velocity parameters and wet-water content, wet-bulk density, and porosity parameters by gravimetric and gamma-ray attenuation techniques. In: Schlanger SO, Jackson ED (eds) Initial Reports DSDP, 33. U.S. Government Printing Office, Washington, pp 931–958

Broad WJ (1997) The universe below: discovering the secrets of the deep sea. Simon and Schuster Trade, New York

Broecker WS, Bond G, Klas M, Clark E, McManus J (1992) Origin of the Northern Atlantic's Heinrich Events. Clim Dynam 6:265–273

Bryden HL, Stommel HM (1984) Limiting processes that determine basic features of the circulation in the Mediterranean Sea. Oceanol Acta 7:289–296

Buhl-Mortensen L, Mortensen PB (2004) Symbiosis in deep-water corals. Symbiosis 37:33–61

Burdon-Jones C, Tambs-Lyche H (1960) Observations on the fauna of the North Brattholmen stone-coral reef near Bergen. Arb Univ Bergen, Mat-Naturv Ser 4:1–24

Cacho I, Grimalt JO, Sierro FJ, Shackleton N, Canals M (2000) Evidence for enhanced Mediterranean thermohaline circulation during rapid climatic coolings. Earth Planet Sc Lett 183: 417–429

Cairns SD (1979) The deep-water Scleractinia of the Caribbean Sea and adjacent waters. Studies on the Fauna of Curaçao and other Carribean Islands 67:1–341

Cairns SD (1982) Antarctic and subantarctic Scleractinia. Antarct Res Ser 34:1–74

Cairns SD (1995) The marine fauna of New Zealand: Scleractinia (Cnidaria: Anthozoa). New Zeal Oceanogr Inst Mem 103:1–210

Caldeira K, Wickett ME (2003) Anthropogenic carbon and ocean pH. Nature 425:365–365

Cande SC, Kent DV (1992) A new geomagnetic polarity time scale for the late Cretaceous and Cenozoic. J Geophys Res-Sol Ea 97:13917–13951

Cande SC, Kent DV (1995) Revised calibration of the geomagnetic polarity timescale for the late Cretaceous and Cenozoic. J Geophys Res-Sol Ea 100:6093–6095

Caralp MH (1988) Late glacial to recent deep-sea Benthic foraminifera from the Northeastern Atlantic (Cadiz Gulf) and western mediterranean (Alboran Sea): Paleooceanographic results. Mar Micropaleontol 13:265–289

Carlson WD (2006) Three-dimensional imaging of earth and planetary materials. Earth Planet Sc Lett 249:133–147

Carton X, Cherubin L, Paillet J, Morel Y, Serpette A, Le Cann B (2002) Meddy coupling with a deep cyclone in the Gulf of Cadiz. J Marine Syst 32:13–42

Channell JET, Labs J, Raymo ME (2003) The Reunion Subchronozone at ODP site 981 (Feni Drift, north Atlantic). Earth Planet Sc Lett 215:1–12

Channell JET, Raymo ME (2003) Paleomagnetic record at ODP Site 980 (Feni Drift, Rockall) for the past 1.2 Myrs. Geochem Geophy Geosy 4:1033

Channell JET, Mazaud A, Sullivan P, Turner S, Raymo ME (2002) Geomagnetic excursions and paleointensities in the Matuyama Chron at Ocean Drilling Program Sites 983 and 984 (Iceland Basin). J Geophys Res-Sol Ea 107:2244

Cloetingh S, Gradstein FM, Kooi H, Grant AC, Kaminski M (1990) Plate re-organization – A cause of rapid late Neogene subsidence and sedimentation around the North-Atlantic. J Geol Soc London 147:495–506

Cnudde V (2006) Exploring the potential of X-ray tomography as a new non-destructive research tool in conservation studies of natural building stones. PhD thesis, University Ghent

Cnudde V, Masschaele B, Dierick M, Vlassenbroeck J, Van Hoorebeke L, Jacobs P (2006) Recent progress in X-ray CT as a geosciences tool. Appl Geo-chem 21:826–832

Colman JG, Gordon DM, Lane AP, Forde MJ, Fitzpatrick JJ (2005) Carbonate mounds off Mauretania, Northwest Africa: status of deep-water corals and implications for management of fishing and oil exploration activities. In: Freiwald A, Roberts JM (eds) Cold-water Corals and Ecosystems. Springer-Verlag, Berlin Heidelberg, pp 417–441

Conroy JJ, Brock A (1989) Gravity and magnetic studies of crustal structure across the Porcupine Basin West of Ireland. Earth Planet Sc Lett 93:371–376

Constable CG, Tauxe L, Parker RL (1998) Analysis of 11 Myr of geomagnetic intensity variation. J Geophys Res-Sol Ea 103:17735–17748

Conway KW, Krautter M, Barrie JV, Whitney F, Thomson RE, Reiswig H, Lehnert H, Mungov G, Bertram M (2005) Sponge reefs in the Queen Charlotte Basin, Canada: controls on distribution, growth and development. In: Freiwald A, Roberts JM (eds) Cold-water corals and ecosystems. Springer-Verlag, Berlin Heidelberg, pp 605–621

Cortijo E, Reynaud J-Y, Labeyrie L, Paillard D, Lehman B, Cremer M, Grousset FE (1995) Etude de la variabilité climatique à haute résolution dans des sédiments de l'Atlantique Nord. C R Acad Sci Paris, Série II a 321:231–238

Coxon P (2001) Cenozoic: Tertiary and Quaternary (until 10,000 years before present). In: Holland CH (ed) The geology of Ireland. Dunedin Academic Press, Edinburgh

Croker PF, Shannon PM (1987) The evolution and hydrocarbon prospectivity of the Porcupine Basin, Offshore Ireland. In: Brooks J, Glennie K (eds) Petroleum Geology of North West Europe. Graham and Trotman, pp 633–642

Crowhurst SJ (2002) Composite isotope sequence. The Delphi Project, www.sc.cam.ac.uk/new/v10/research/institutes/godwin/body.html

Crowley TJ (1991) Modeling Pliocene warmth. Quaternary Sci Rev 10:275–282

Da Silva AC, Boulvain F (2004) From palaeosols to carbonate mounds: facies and environments of the middle Frasnian platform in Belgium. Geol Q 48:253–265

De Boever E (2005) Integrated geophysical and petrological study of fluid expulsion features along the Moroccan Atlantic margin. MSc thesis, University Gent

De Cock K (2005) 3D-seismische studie van koraalbanken aan de oostelijke rand van het Porcupine Bekken. MSc thesis, University Gent

de Haas H, Mienis F, Scientific Crew (2005) Cold water corals and carbonate mound formation at the Pen Duick Escarpment (Gulf of Cadiz) and Rockall Bank. Cruise report R/V Pelagia cruise M2005 (640PE237). Royal Nether-lands Institute for Sea Research (NIOZ), Den Helder

de Haas H, Huvenne V, Wheeler A, Unnithan V, the shipboard scientific crew (2002) A TOBI sidescan sonar survey of cold-water coral carbonate mounds in the Rockall Trough and Porcupine Seabight. Cruise report R/V Pelagia cruise M2000 (64PE165). Royal Netherlands Institute for Sea Research (NIOZ), Den Helder

De Mol B (2002) Development of coral banks in Porcupine Seabight (SW Ireland): A multidisciplinary approach. PhD thesis, University Gent

De Mol B, Henriet JP, Canals M (2005) Development of coral banks in Porcupine Seabight: do they have Mediterranean ancestors? In: Freiwald A, Roberts JM (eds) Cold-water corals and ecosystems. Springer-Verlag, Berlin Heidelberg, pp 515–533

De Mol B, Van Rensbergen P, Pillen S, Van Herreweghe K, Van Rooij D, McDonnell A, Huvenne V, Ivanov M, Swennen R, Henriet J-P (2002) Large deep-water coral banks in the Porcupine Basin, southwest of Ireland. Mar Geol 188:193–231

De Mol B, Kozachenko M, Wheeler AJ, Alvares H, Henriet J-P, Olu-Le Roy K (2007) Thérèse Mound: A case study of coral bank development in the Belgica Mound Province, Porcupine Seabight. Int J Earth Sci 96:103–120

DeMenocal PB, Laine EP, Ciesielski PF (1988) A Magnetic Signature of Bottom Current Erosion. Phys Earth Planet In 51:326–348

Depreiter D (2009) Sources, modes and effects of seabed fluid flow. Unpublished PhD. Thesis, University Ghent

Depreiter D, Foubert A, Henriet JP (2005a) Geofluid pumping in carbonate mound systems: A factor for growth and stabilisation? In: Geosphere-Biosphere coupling processes: the TTR interdisciplinary approach towards studies of the European and North African margins. UNESCO, Marrakech, p 16

Depreiter D, Poort J, Van Rensbergen P, Henriet JP (2005b) Geophysical evidence of gas hydrates in shallow submarine mud volcanoes on the Moroccan margin. J Geophys Res 110:B10103

Dierick M, Masschaele B, Van Hoorebeke L (2004) Octopus, a fast and user-friendly tomographic reconstruction package developed in LabView (R). Meas Sci Technol 15:1366–1370

Dix GR, Mullins HT (1988) Rapid Burial Diagenesis of Deep-Water Carbonates – Exuma Sound, Bahamas. Geology 16:680–683
Dobson MR, Haynes JR, Bannister AD, Levene DG, Petrie HS, Woodbridge RA (1991) Early Tertiary palaeoenvironments and sedimentation in the NE Main Porcupine Basin (well 35/13-1), offshore western Ireland – evidence for global change in the Tertiary. First Break 3:99–117
Dons C (1944) Norges korallrev. Det Kongelige Norske Videnskabers Selskab. Forhandlinger 16:37–82
Doré AG, Lundin ER, Jensen LN, Birkeland O, Eliassen PE, Fichler C (1999) Principal tectonic events in the evolution of the northwest European Atlantic margin. In: Fleet AJ, Boldy SAR (eds) Petroleum Geology of North-west Europe: Proceedings of the 5th Conference. Geological Society, London, pp 41–61
Dorlodot HD (1909) Les faunes du Dinantien et leur signification Stratigraphique. Bull Soc Belge Géol XXIII:153–174
Dorschel B, Hebbeln D, Rüggeberg A, Dullo C, Freiwald A (2005) Growth and erosion of a cold-water coral covered carbonate mound in the Northeast Atlantic during the Late Pleistocene and Holocene. Earth Planet Sc Lett 233:33–44
Dorschel B, Hebbeln D, Foubert A, White M, Wheeler AJ (2007a) Cold-water coral carbonate mound hydrodynamics: instrumentation and model development. Mar Geol 244:184–195
Dorschel B, Hebbeln D, Ruggeberg A, Dullo C (2007b) Carbonate budget of a cold-water coral carbonate mound: Propeller Mound, Porcupine Seabight. Int J Earth Sci 96:73–83
Duineveld GCA, Lavaleye MSS, Berghuis EM (2004) Particle flux and food supply to a seamount cold-water coral community (Galicia Bank, NW Spain). Mar Ecol- Prog Ser 277:13–23
Dullo WC (2005) Coral growth and reef growth: a brief review. Facies 51:37–52
Dullo WC, Flögel S, Rüggeberg A (2008) Cold-water coral growth in relation to the hydrography of the Celtic and Nordic European continental margin. Mar Ecol Prog Ser 371:165–176
Dunham RJ (1962) Classification of carbonate rocks according to depositional texture. In: Ham WE (ed) Classification of carbonate rocks. A symposium. Amer Ass Petrol Geo Mem, pp 108–171
Duplessy JC, Shackleton NJ, Fairbanks RG, Labeyrie LD, Oppo D, Kallel N (1988) Deepwater source variations during the last climatic cycle and their impact on the global deepwater circulation. Paleoceanography 3:343–360
Durham JW (1947) Corals from the Gulf of California and the North Pacific coast of America. Mem Geol Soc Am 20:1–68
Eder W (1982) Diagenetic redistribution of carbonate, a process in forming limestone-marl alternations (Devonian and Carboniferous), Rheinische Schiefergebirge, W Germany. In: Einsele G, Seilacher A (eds) Cyclic and Event Stratification. Springer, Berlin, pp 98–112
Embry AF, Klovan JE (1971) A late Devonian reef tract on northeastern Banks Island. N.W.T. Bull. Canadian Petrol Geol 19:730–781
Enos P, Sawatsky LH (1981) Pore Networks in Holocene Carbonate Sediments. J Sediment Petrol 51:961–985
Evans D, Stoker MS, Shannon PM, Partners S (2005) The STRATAGEM project: Stratigraphic development of the glaciated European margin. Mar Petrol Geol 22:969–976
Evans HB (1965) GRAPE - a device for continuous determination of material density and porosity. In: Trans SPWLA 6th Ann. Logging Symposium. Dallas, pp B1–B25
Ewing M, Vine AC, Worzel JL (1946) Photography of the ocean bottom. J Opt Soc Am 36:307–321
Expedition 307 Scientists (2006a) Expedition 307 Summary. In: Ferdelman TG, Williams T, Kano A, Henriet JP, Scientists Exp (eds) Proceedings Integrated Ocean Drilling Program, Volume 307. Integrated Ocean Drilling Program Management International Inc., Washington, pp 1–34
Expedition 307 Scientists (2006b) Methods. In: Ferdelman TG, Williams T, Kano A, Henriet JP, Scientists Exp (eds) Proceedings Integrated Ocean Drilling Program, Volume 307. Integrated Ocean Drilling Program Management International Inc., Washington, pp 1–25
Expedition 307 Scientists (2006c) Site U1316. In: Ferdelman TG, Williams T, Kano A, Henriet JP, Scientists Exp (eds) Proceedings Integrated Ocean Drilling Program, Volume 307. Integrated Ocean Drilling Program Management International Inc., Washington, pp 1–63

Expedition 307 Scientists (2006d) Site U1317. In: Ferdelman TG, Williams T, Kano A, Henriet JP, Scientists Exp (eds) Proceedings Integrated Ocean Drilling Program, Volume 307. Integrated Ocean Drilling Program Management International Inc., Washington, pp 1–65

Expedition 307 Scientists (2006e) Site U1318. In: Ferdelman TG, Williams T, Kano A, Henriet JP, Scientists Exp (eds) Proceedings Integrated Ocean Drilling Program, Volume 307. Integrated Ocean Drilling Program Management International Inc., Washington, pp 1–57

Farrow GE, Durant GP (1985) Carbonate-basaltic sediments from Cobb Sea-mount, Northeast Pacific: zonation, bioerosion and petrology. Mar Geol 65:73–102

Ferdelman TG, Kano A, Williams T, Henriet JP, the Expedition 307 Scientists (2006) Modern Carbonate Mounds: Porcupine Drilling. Proceedings Integrated Ocean Drilling Program, Volume 307. Integrated Ocean Drilling Program Management International Inc., Washington, pp 1–65

Fernandez LP, Nose M, Fernandez-Martinez E, Mendez-Bedia I, Schroder S, Soto F (2006) Reefal and mud mound facies development in the Lower Devonian La Vid Group at the Colle outcrops (Leon province, Cantabrian Zone, NW spain). Facies 52:307–327

Ferretti P, Shackleton NJ, Rio D, Hall MA (2005) Early-Middle Pleistocene deep circulation in the western subtropical Atlantic: southern hemisphere modulation of the North Atlantic Ocean. In: Head MJ, Gibbard PL (eds) Early-middle pleistocene transitions: The land-ocean evidence. Geological Society Special Publications, London, pp 131–145

Flajs G, Vigener M, Keupp H, Meischner D, Neuweiler F, Paul J, Reitner J, Warnke K, Weller H, Dingle P, Hensen C, Schäfer P, Gautret P, Leinfelder RR, Hüssner H, Kaufmann B (1995) Mud mounds: A polygenetic spectrum of fine-grained carbonate buildups. Facies V32: 1–69

Flinch J (1993) Tectonic evolution of the Gibraltar Arc. PhD thesis, Rice University

Flinch J (1996) Accretion and extensional collapse of the external Western Rif (northern Morocco). In: Ziegler PA, Horvath F (eds) Peri-tethys memoir 2: Structure and prospects of alpine basins and forelands. Mus. Natl d'hist Nat, Paris, pp 61–86

Flood RD (1980) Deep-sea sedimentary morphology – Modeling and interpretation of echo-sounding profiles. Mar Geol 38:77–92

Flood RD (1983) Classification of sedimentary furrows and a model for furrow initiation and evolution. Geol Soc Am Bull 94:630–639

Florindo F, Roberts AP, Palmer MR (2003) Magnetite dissolution in siliceous sediments. Geochem Geophy Geosy 4:1053

Flügel E (2004) Microfacies of carbonate rocks: Analysis, Interpretation and Application. Springer-Verlag, Berlin Heidelberg

Fosså JH, Mortensen PB (1998) Artsmangfoldet på Lophelia-korallrev og metoder for kartlegging og overvåkning. Fisken og Havet 17:1–95

Fosså JH, Mortensen PB, Furevik DM (2000) *Lophelia*-korallrev langs norskekysten forekomst og tilstand. Fisken og Havet 2:1–94

Fosså JH, Lindberg B, Christensen O, Lundälv T, Svellingen I, Mortensen PB, Alvsvåg J (2005) Mapping of Lophelia reefs in Norway: Experiences and survey methods. In: Freiwald A, Roberts JM (eds) Cold-water corals and ecosystems. Springer-Verlag, Berlin Heidelberg, pp 359–391

Foubert A, Beck T, Wheeler AJ, Opderbecke J, Grehan A, Klages M, Thiede J, Henriet JP, the Polarstern ARK-XIX/3a Shipboard Party (2005a) New view of the Belgica Mounds, Porcupine Seabight, NE Atlantic: preliminary results from the Polarstern ARK-XIX/3a ROV cruise. In: Freiwald A, Roberts JM (eds) Cold-water corals and ecosystems. Springer-Verlag, Berlin Heidelberg, pp 403–415

Foubert A, Maignien L, Beck T, Depreiter D, Blamart D, Henriet JP (2005b) Pen duick escarpmant on the Moroccan margin: A new mound lab? In: Geo-sphere-Biosphere coupling processes: The TTR interdisciplinary approach towards studies of the European and North African margins. UNESCO, Marrakech, p 17

Foubert A, Depreiter D, Beck T, Maignien L, Pannemans B, Frank N, Blamart D, Henriet JP (2008) Carbonate mounds in a mud volcano province off northwest Morocco: key to processes and controls. Mar Geol 248:74–96

Foubert A, Van Rooij D, Blamart D, Henriet J-P (2007) X-ray imagery and physical core logging as a proxy of the content sediment cores in cold-water coral mound provinces: A case study from Porcupine Seabight, SW of Ireland. Int J Earth Sci 96:141–158

Francus P (2004) Image analysis, sediments and paleoenvironments. Springer, Dordrecht

Frank N, Lutringer A, Paterne M, Blamart D, Henriet J-P, Van Rooij D, Van Weering TCE (2005) Deep-water corals of the northeastern Atlantic margin: carbonate mound evolution and upper intermediate water ventilation during the Holocene. In: Freiwald A, Roberts JM (eds) Cold-water Corals and Eco-systems. Springer-Verlag, Berlin Heidelberg, pp 113–133

Frank N, Ricard E, Paque A, Blamart D, van der Land C, Colin C, Foubert A, Van Rooij D, Henriet J-P, de Haas H, van Weering T (subm.) Carbonate mound evolution on Rockall Bank and in Porcupine Seabight derived from 230 U/Th dating of deep-water corals. Mar Geol

Frederichs T, Bleil U, Däumler K, von Dobeneck T, Schmidt AM (1999) The magnetic view on the marine paleoenvironment: parameters, techniques and potentials of rock magnetic studies as a key to paleoclimatic and paleoceanographic changes. In: Fischer G, Wefer G (eds) Use of proxies in paleoceanography: examples from the South Atlantic. Springer-Verlag, Berlin Heidelberg, pp 575–599

Frederiksen R, Jensen A, Westerberg H (1992) The distribution of the scleractinian coral *Lophelia-pertusa* around the faroe Islands and the relation to internal tidal mixing. Sarsia 77:157–171

Freiwald A (1998) Geobiology of *Lophelia pertusa* (scleractinia) reefs in the North Atlantic. Habilitationsschrift, University Bremen

Freiwald A (2002) Reef-forming cold-water corals. In: Wefer G, Billett D, Hebbeln D, Jorgensen BB, Schlüter M, Van Weering T (eds) Ocean margin systems. Springer-Verlag, Berlin Heidelberg, pp 365–385

Freiwald A, Wilson JB (1998) Taphonomy of modern deep, cold-temperate water coral reefs. Hist Biol 13:37–52

Freiwald A, Roberts JM (2005) Cold-water corals and ecosystems. Springer-Verlag, Berlin Heidelberg

Freiwald A, Henrich R, Patzold J (1997) Anatomy of a deep-water coral reef mound from Stjernsund West Finnmark, northern Norway. In: James NP, Clarke JAD (eds) Cool-water carbonates. SEPM Special Publication, pp 441–162

Freiwald A, Wilson JB, Henrich R (1999) Grounding Pleistocene icebergs shape recent deep-water coral reefs. Sediment Geol 125:1–8

Freiwald A, Huhnerbach V, Lindberg B, Wilson JB, Campbell J (2002) The Sula Reef Complex, Norwegian shelf. Facies 47:179–200

Freiwald A, Fosså JH, Grehan A, Koslow T, Roberts JM (2004) Cold-water coral reefs. UNEP-WCMC, Cambridge

Fuller M, Hastedt M, Herr B (1998) Coring-induced magnetization of recovered sediments. In: Weaver PPE, Schmincke HU, Firth JH, Duffield W (eds) Proceedings ODP, Scientific Results Volume 157. Ocean Drilling Program, College Station, pp 47–56

Fuller M, Molina-Garza R, Touchard Y, Kidane T (2006) Paleomagnetic records from carbonate legs in the Southern Oceans and attendant drilling and coring related effects. Phys Earth Planet In 156:242–260

Funnell BM (1996) Plio-Pleistocene palaeogeography of the southern North Sea basin (3.75–0.60 Ma). Quaternary Sci Rev 15:391–405

Games KP (2001) Evidence of shallow gas above the Connemara oil accumulation, Block 26/28, Porcupine Basin. In: Shannon PM, Haughton P, Corcoran D (eds) The Petroleum Exploration of Ireland's Offshore Basins. Geological Society, London, pp 361–373

Garcia-Lafuente J, Delgado J, Criado-Aldeanueva F, Bruno M, del Rio J, Miguel Vargas J (2006) Water mass circulation on the continental shelf of the Gulf of Cadiz. Deep-Sea Res Pt II 53:1182–1197

Gardner JM (2001) Mud volcanoes revealed and sampled on the Western Moroccan continental margin. Geophys Res Lett 28:339–342

Glaub I (1994) Mikrobohrspuren in ausgewählten Ablagerungsräumen des europäischen Jura un der Unterkreide (Klassifikation und Palökologie). Courier Forschinst Senckenberg 174: 1–324

Gregg JM, Somerville ID, Foubert A, Doyle E, the IODP Expedition 307 Shipboard Scientific Party (2006) Neogene deepwater carbonate mud-mounds and their paleozoic counterparts – Comparisons of geometry, sedimentology, and petrology. AAPG Annual Meeting, Houston

Grehan A, Unnithan V, Wheeler A, Monteys F, Beck T, Wilson M, Guinan J, Hall-Spencer J, Foubert A, Klages M, Thiede J (2003) Evidence of major fisheries impact on cold-water corals off the Porcupine Bank, west coast of Ireland: implications for Offshore coral conservation within the European Union. Erlanger Geol Abh Sonderbd 4:42

Grousset FE, Labeyrie LD, Sinko JA, Cremer M, Bond G, Duprat J, Cortijo E, Huon S (1993) Patterns of ice-rafted detritus in the glacial North Atlantic. Paleoceanography 8:175–192

Grousset FE, Pujol C, Labeyrie L, Auffret GA, Boelaert A (2000) Were the North Atlantic Heinrich events triggered by the behavior of the European ice sheets? Geology 28:123–126

Grousset FE, Cortijo E, Huon S, Hervé L, Richter TO, Burdloff D, Duprat J, Weber O (2001) Zooming in on Heinrich layers. Paleoceanography 16:240–259

Grygier MJ (1990) *Introcornia* (Crustacea: Ascothoracida: Petrarcidae) parasitic in an ahermatypic coral from St. Paul Island, Indian Ocean. Vie et Milieu 40:313–318

Guinotte JM, Orr J, Cairns S, Freiwald A, Morgan L, George R (2006) Will human-induced changes in seawater chemistry alter the distribution of deep-sea scleractinian corals? Front Ecol Environ 4:141–146

Gutscher MA, Malod J, Rehault JP, Contrucci I, Klingelhoefer F, Mendes-Victor L, Spakman W (2002) Evidence for active subduction beneath Gibraltar. Geology 30:1071–1074

Guyodo Y, Valet JP (1999) Global changes in intensity of the Earth's magnetic field during the past 800 kyr. Nature 399:249–252

Guyodo Y, Valet JP (2006) A comparison of relative paleointensity records of the Matuyama Chron for the period 0.75–1.25 Ma. Phys Earth Planet In 156:205–212

Hardenbol J, Thierry J, Farley MB, Jacquin T, de Graciansky PC, Vail PR (1998) Cenozoic sequence biochronostratigraphy. In: de Graciensky PC, Hardenbol J, Jacquin T, Vail P (eds) Mesozoic and Cenozoic sequence strati-graphy of European basins. SEPM Special Publication, Tulsa

Haug GH, Tiedemann R (1998) Effect of the formation of the Isthmus of Panama on Atlantic Ocean thermohaline circulation. Nature 393:673–676

Haug GH, Sigman DM, Tiedemann R, Pedersen TF, Sarnthein M (1999) Onset of permanent stratification in the subarctic Pacific Ocean. Nature 401:779–782

Hausser F, O'Reilly BM, Jacob AWB, Shannon PM, Makris J, Vogt U (1995) The crustal structure of the Rockall Trough: Differential stretching without underplating. J Geophys Res 100: 4097–4116

Helmke JP, Bauch HA, Rohl U, Mazaud A (2005) Changes in sedimentation patterns of the Nordic seas region across the mid-Pleistocene. Mar Geol 215:107–122

Henrich R, Freiwald A, Wehrmann A, Schafer P, Samtleben C, Zankl H (1996) Nordic cold-water carbonates: occurences and controls. In: Reitner J, Neuweiler F, Gunkel F (eds) Global and regional controls on biogenic sedimentation. Göttinger Arb Geol Paläont, Göttingen, pp 35–52

Henriet J-P, Guidard S, the ODP "Proposal 573" Team (2002) Carbonate mounds as a Possible Example for Microbial Activity in Geological Processes. In: Wefer G, Billet DSM, Hebbeln D, Jorgensen BB, Schlüter M, van Weering TCE (eds) Ocean margin systems. Springer-Verlag, Berlin Heidelberg, pp 439–455

Henriet J-P, De Mol B, Pillen S, Vanneste M, Van Rooij D, Versteeg W, Croker PF, Shannon PM, Unnithan V, Bouriak S, Chachkine P, The Porcupine-Belgica 97 Shipboard Party (1998) Gas hydrate crystals may help build reefs. Nature 391:648–649

Henriet J-P, De Mol B, Vanneste M, Huvenne V, Van Rooij D, the "Porcupine-Belgica" '97 '98 and '99 shipboard parties (2001) Carbonate mounds and slope failures in the Porcupine Basin: A development model involving past fluid venting. In: Shannon PM, Haughton P, Corcoran D (eds) The petroleum exploration of Ireland's Offshore basins. Geological Society, London, pp 375–383

Hernandez-Guerra A, Nykjaer L (1997) Sea surface temperature variability off northwest Africa: 1981–1989. Int J Remote Sens 18:2539–2558

Hernandez-Molina FJ, Llave E, Somoza L, Fernandez M, Maestro A, Leon R, Medialdea T, Barnolas A, Garcia M, Diaz del Rio V, Fernandez-Salas LM, Gardner J (2003) Looking for clues to plaeoceanographic imprints: A diagnosis of the Gulf of Cadiz contourite depositional systems. Geology 31:19–22

Hesse R, Khodabakhsh S (2006) Significance of fine-grained sediment lofting from melt-water generated turbidity currents for the timing of glaciomarine sediment transport into the deep sea. Sediment Geol 186:1–11

Hollister CD, Southard JB, Flood RD, Lonsdale PF (1976) Flow phenomena in the benthic boundary layer and bed forms beneath deep current systems. In: McCave IN (ed) The benthic boundary layer. Plenum, New York, pp 183–204

Hoppie BW, Blum P, the Shipboard Scientific Party (1994) Natural gamma-ray measurements on ODP cores: Introduction to procedures with examples from Leg 150. In: Mountain GS, Miller KG, Blum P, et al (eds) Proceedings ODP Initial Reports, vol 150. Ocean Drilling Program, College Station, pp 51–59

Hovland M (1990) Do carbonate reefs form due to fluid seepage? Terra Nova 2:8–18

Hovland M (2008) Deep-water coral reefs. Unique biodiversity hot-spots. Springer Praxis Books

Hovland M, Thomsen E (1997) Cold-water corals – are they hydrocarbon seep related? Mar Geol 137:159–164

Hovland M, Mortensen PB (1999) Norske korallrev og prosesser i havbunnen (Norwegian coral reefs and seabed processes). John Grieg, Bergen

Hovland M, Croker PF, Martin M (1994) Fault-associated seabed mounds (carbonate knolls?) off western Ireland and north-west Australia. Mar Petrol Geol 11:232–246

Hovland M, Mortensen PB, Brattegard T, Strass P, Rokoengen K (1998) Ahermatypic coral banks off Mid-Norway: Evidence for a link with seepage of light hydrocarbons. Palaios 13:189–200

Hrouda F (1994) A technique for the measurement of thermal changes of magnetic susceptibility of weakly magnetic rocks by the Cs-2 apparatus and Kly-2 Kappabridge. Geophys J Int 118: 604–612

Huthnance JM (1986) The rockall slope current and shelf-edge processes. P Roy Soc Edinb B 88:83–101

Huvenne VAI (2003) Spatial geophysical analysis of the Magellan carbonate build-ups and the interaction with sedimentary processes: key to a genetic interpretation? PhD thesis, University Gent

Huvenne VAI, Masson DG, Wheeler AJ (2008) Sediment dynamics of a sandy contourite: the sedimentary context of the Darwin cold-water coral mounds, Northern Rockall Trough. Int J Earth Sci

Huvenne VAI, Van Rooij D, De Mol B, Thierens M, O'Donnell R, Foubert A (subm.) Sediment dynamics on and around the initial Challenger Mound, a cold-water coral carbonate mound in the Porcupine Seabight, NE Atlantic. Mar Geol

Huvenne VAI, Blondel P, Henriet J-P (2002) Textural analyses of sidescan sonar imagery from two mound provinces in the Porcupine Seabight. Mar Geol 189:323–341

Huvenne VAI, De Mol B, Henriet J-P (2003) A 3D seismic study of the morphology and spatial distribution of buried coral banks in the Porcupine Basin, SW of Ireland. Mar Geol 198:5–25

Huvenne VAI, Beyer A, de Haas H, Dekindt K, Henriet JP, Kozachenko M, Olu-Le Roy K, Wheeler AJ, the TOBI/Pelagia 197 and CARACOLE cruise participants (2005) The seabed appearance of different coral bank provinces in the Porcupine Seabight, NE Atlantic: results from sidescan sonar and ROV seabed mapping. In: Freiwald A, Roberts JM (eds) Cold-water corals and eco-systems. Springer-Verlag, Berlin Heidelberg, pp 535–569

Huvenne VAI, Bailey WR, Shannon PM, Naeth J, di Primio R, Henriet J-P, Horsfield B, de Haas H, Wheeler AJ, Olu-Le Roy K (2007) The Magellan mound province in the Porcupine Basin. Int J Earth Sci 96:85–101

Imbrie J, Berger A, Boyle EA, Clemens SC, Duffy A, Howard WR, Kukla G, Kutzbach J, Martinson DG, McIntyre A, Mix AC, Molfino B, Morley JJ, Pe-terson LC, Pisias NG, Prell WL, Raymo ME, Shackleton NJ, Toggweiler JR (1992) On the structure and origin of major glaciation cycles 1. Linear responses to Milankovitch forcing. Paleoceanography 7:701–738

Jacobs JA (1998) Variations in the intensity of the Earth's magnetic field. Surv Geophys 19: 139–187

Jacobs P, Cnudde V (2008) Applications of X-ray computed tomography in engineering geology. Engineering Geology 103:67–146

Jaffe JS, Moore KD, MvLean J, Strand MP (2001) Underwater optical imaging: status and prospects. Oceanography 14:64–75

James NP, Bourque PA (1992) Reefs and mounds. In: Walker RG, James NP (eds) Facies models. Geol Assoc Can, St Johns, pp 323–345

James NP, Clarke JAD (1997) Cool-water carbonates. SEPM Special Publication 56, Tulsa

Jansen E, Raymo ME, Blum P, et al (1996) Proceedings IODP initial reports, vol 162. Ocean Drilling Program, College Station

Jansen JHF, Van der Gaast SJ, Koster B, Vaars AJ (1998) CORTEX, a ship-board XRF-scanner for element analyses in split sediment cores. Mar Geol 151:143–153

Japsen P, Chalmers JA (2000) Neogene uplift and tectonics around the North Atlantic: Overview. Glob Planet Change 24:165–173

Jelinek V (1981) Characterization of the magnetic fabric of rocks. Tectonophysics 79:T63–T67

Jenkins WJ, Rhines PB (1980) Tritium in the deep North-Atlantic Ocean. Nature 286:877–880

Jensen A, Frederiksen R (1992) The fauna associated with the bank-forming deep-water coral *Lophelia-pertusa* (Scleractinaria) on the Faroe Shelf. Sarsia 77:53–69

Joachimski MM, Buggisch W (1999) Hydrothermal origin of Devonian conical mounds (kess-kess) of Hamar Lakhdad Ridge, Anti-Atlas, Morocco: Comment. Geology 27:863–863

Johnson H, Ritchie JD, Gatliff RW, Williamson JP, Cavill J, Bulat J (2001) Aspects of the structure of the Porcupine and Porcupine Seabight basins as revealed from gravity modelling of regional seismic transects. In: Shannon PM, Haughton PDW, Corcoran DV (eds) The petroleum exploration of Ireland's Offshore basins. Geological Society Special Publications, London, pp 265–274

Johnson H, Ritchie JD, Hitchen K, McInroy DB, Kimbell GS (2005) Aspects of Cenozoic deformational history of the northeast Faroe–Shetland Basin, Wyville–Thomson Ridge and Hatton Bank areas. In: Doré AG, Vining B (eds) Petroleum geology: Northwest Europe. Proceedings of the Sixth Petroleum Geology Conference. Geological Society, London, pp 933–1007

Johnson J, Stevens I (2000) A fine resolution model of the eastern North Atlantic between the Azores, the Canary Islands and the Gibraltar Strait. Deep-Sea Res Pt I 47:875–899

Jones SM, White N, Lovell B (2001) Cenozoic and Cretaceous transient uplift in the Pocupine Basin and its relationship to a mantle plume. In: Shannon PM, Haughton PDW, Corcoran DV (eds) The petroleum explorations of Ireland's Offshore basins. Geological Society London, pp 345–360

Jorgensen BB (1983) Processes at the sediment-water interface. In: Bolin B, Cook RB (eds) The major biogeochemical cycles and their interactions. John Wiley and Sons, pp 477–509

Joseph LH, Rea DK, van der Pluijm BA (1998) Use of grain size and magnetic fabric analyses to distinguish among depositional environments. Paleoceanography 13:491–501

Jurkiw A (2005) Variability in Pleistocene to recent sedimentation from the carbonate mound provinces in Porcupine Seabight, NE Atlantic: implications for carbonate mound growth and development. Unpublished PhD. Thesis, University Bremen

Kano A, Ferdelman TG, Williams T, Henriet JP, Ishikawa T, Kawagoe N, Ishikawa T, Kawagoe N, Takashima C, Kakizaki Y, Abe K, Sakai S, Browning E, Li X, the IODP Expedition 307 Scientists (2007) Age constraints on the origin and growth history of a deep-water coral mound in NE Atlantic drilled during IODP Expedition 307. Geology 35:1051–1054

Karlin R, Levi S (1983) Diagenesis of magnetic minerals in recent hemipelagic sediments. Nature 303:327–330

Karlin R, Levi S (1985) Geochemical and sedimentological control of the magnetic properties of hemipelagic sediments. J Geophys Res-Solid 90:373–392
Kent DV (1973) Post-depositional remanent magnetization in deep-sea sediment. Nature 246: 32–34
Kent DV (1982) Apparent correlation of paleomagnetic intensity and climatic records in deep-sea sediments. Nature 299:538–539
Kenyon N, Ivanov M, Akhmetzanov A, Akhmanov G (2001) Interdisciplinary geoscience research on the north-east Atlantic margin. In: IOC UNESCO Technical Series, vol 76. UNESCO, Paris
Kenyon NH (1987) Mass-wasting features on the continental slope of North-west Europe. Mar Geol 74:57–77
Kenyon NH, Belderson RH (1973) Bed forms of the Mediterranean undercurrent observed with side-scan sonar. Sediment Geol 9:77–79
Kenyon NH, Ivanov MK, Akhmetzhanov AM (1998) Cold water carbonate mounds and sediment transport on the north-east Atlantic margin. In: IOC UNESCO technical series. UNESCO, Paris, p 178
Kenyon NH, Akhmetzhanov AM, Wheeler AJ, van Weering TCE, de Haas H, Ivanov MK (2003) Giant carbonate mud mounds in the southern Rockall Trough. Mar Geol 195:5–30
Ketcham RA, Carlson WD (2001) Acquisition, optimization and interpretation of X-ray computed tomographic imagery: applications to the geosciences. Comput Geosci 27:381–400
Khan MA (1962) The anisotropy of magnetic susceptibility of some igneous and metamorphic rocks. J Geophys Res 95:2873–2858
Kiessling W, Flügel E, Golonka J (2002) Phanerozoic reef patterns. SEPM Special Publication Series 72, Tulsa
King JW, Banerjee SK, Marvin J (1983) A new rock-magnetic approach to selecting sediments for geomagnetic paleointensity studies – Application to paleointensity for the last 4000 years. J Geophys Res 88:5911–5921
Kirschvink JL (1980) The least-square line and plane and the analysis of paleomagnetic data. Geophys J R Astron Soc 62:699–718
Kissel C, Laj C, Mazaud A, Dokken T (1998) Magnetic anisotropy and environmental changes in two sedimentary cores from the Norwegian sea and the North Atlantic. Earth Planet Sc Lett 164:617–626
Klages M, Thiede J, Foucher JP (2004) The expedition ARKTIS XIX/3 of the research Vessel Polarstern in 2003: Reports of Legs 3a, 3b and 3c. Berichte zur Polar und Meeresforschung 488:1–355
Knauss JA (1978) Introduction to physical oceanography. Prentice-Hall, New Jersey
Knoll AH, Swett K (1990) Carbonate deposition during the Late Proterozoic Era: An example from Spitsbergen. Am J Sci 290A:104–132
Knott SD, Burchell MT, Jolley EJ, Fraser AJ (1993) Mesozoic to Cenozoic plate reconstructions of the North Atlantic and hydrocarbon plays of the Atlantic margins. In: Parker JR (ed) Petroleum geology of Northwest Europe. Proceedings of the Fourth Conference. Geological Society, London, pp 953–974
Kopaska-Merkel DC, Haywick DW (2001) Carbonate mounds: sedimentation, organismal response, and diagenesis. Sedimentology 145:3–4
Kozachenko M (2005) Present and past environments of the Belgica mounds (deep-water coral carbonate mounds), Eastern Porcupine Seabight, NE Atlantic. PhD thesis, Department of Geology and Environmental Research Institute Cork
Ku TCW, Walter LM, Coleman ML, Blake RE, Martini AM (1999) Coupling between sulfur recycling and syndepositional carbonate dissolution: Evidence from oxygen and sulfur isotope composition of pore water sulfate, South Florida Platform, USA. Geochim Cosmochim Ac 63:2529–2546
Le Danois E (1948) Les profondeurs de la mer. Payot, Paris
Le Goff-Vitry MC, Pybus OG, Rogers AD (2004) Genetic structure of the deep-sea coral *Lophelia pertusa* in the northeast Atlantic revealed by microsatellites and internal transcribed spacer techniques. Mol Ecol 13:537–549

Le Guilloux E, Olu K, Bourillet JF, Savoye B, Iglésias SP, Sibuet M (2009) First observations of deep-sea coral reefs along the Angola margin. Deep-Sea Res Pt II

Lear CH, Rosenthal Y, Wright JD (2003) The closing of a seaway: Ocean water masses and global climate change. Earth Planet Sc Lett 210:425–436

Lebreiro SM, Moreno JC, McCave IN, Weaver PPE (1996) Evidence for Heinrich layers off Portugal (Tore Seamount: 39°N, 12°W). Mar Geol 131:47–56

Ledbetter MT, Ellwood BB (1980) Spatial and temporal changes in bottom-water velocity and direction from analysis of particle-size and alignment in deep-sea sediment. Mar Geol 38: 245–261

Lees A, Miller J (1995) Waulsortian banks. In: Monty CLV, Bosence DWJ, Bridges PH, Pratt BR (eds) Carbonate mud-mounds: Their origin and evolution. Blackwell Science, Oxford, pp 191–271

Léonide P (2006) Sedimentological features of a bioclastic mound: Challenger Mound, Porcupine Seabight. 2nd Post-cruise Meeting IODP Expedition Leg 307, Yokohama

Léonide P, Floquet, M, Baudin F (2009) Bio- and lithofacies mineralogy and organic content of Challenger Mound (Porcupine Seabight, SW Ireland). In: Ferdelman TG, Kano A, Williams T, Henriet JP, and the Expedition 307 Scientists. Proceedings of the Integrated Ocean Drilling Program, Volume 30

Li HY, Zhang SH (2005) Detection of mineralogical changes in pyrite using measurements of temperature-dependence susceptibilities. Chinese J Geo-phys-Ch 48:1384–1391

Lisiecki LE, Raymo ME (2007) Plio-Pleistocene climate evolution: trends and transitions in glacial cycle dynamics. Quat Sci Rev 26:56–69

Llave E, Schonfeld J, Hernandez-Molina FJ, Mulder T, Somoza L, Diaz del Rio V, Sanchez-Almazo I (2006) High-resolution stratigraphy of the Mediterranean outflow contourite system in the Gulf of Cadiz during the late Pleistocene: The impact of Heinrich events. Mar Geol 227:241–262

Lofi J, Weber O (2001) SCOPIX – digital processing of X-ray images for the enhancements of sedimentary structures in undisturbed core slabs. Geo-Mar Lett 20:182–186

Lourens L, Hilgens F, Shackleton NJ, Laskar J, Wilson J (2004) The Neogene. In: Gradstein FM, Ogg JG, Smith AG (eds) A Geological Timescale. Cambridge University Press, Cambridge, pp 409–430

Louwye S, Foubert A, Mertens K, Van Rooij D, the IODP Exp. 307 Scientific Party (2008) Integrated palynostratigraphy and palaeoecology of the Lower and Middle Miocene of Porcupine Basin, IODP Exp. 307. Geol Mag 145:321–344

Lund S, Stoner JS, Channell JET, Acton G (2006) A summary of Brunhes paleomagnetic field variability recorded in Ocean Drilling Program cores. Phys Earth Planet In 156:194–204

Luong HQ, Philips W, Foubert A (2006) Robust video mosaicing for benthic habitat mapping. In: Proceedings of First International Conference on Computer Vision Theory and Applications.

MacDonald H, Allan PM, Lovell JPB (1987) Geology of oil accumulation in Block 26/28, Porcupine Basin, Offshore Ireland. In: Brooks J, Glennie K (eds) Petroleum geology of North West Europe. Graham and Trotman, pp 643–651

Machin F, Pelegri JL, Marrero-Diaz A, Laiz I, Ratsimandresy AW (2006) Near-surface circulation in the southern Gulf of Cadiz. Deep-Sea Res Pt II 53:1161–1181

Mackenzie GD, Shannon PM, Jacob AWB, Morewood NC, Makris J, Gaye M, Egloff F (2002) The velocity structure of the sediments in the southern Rockall Basin: results from new wide-angle seismic modelling. Mar Petrol Geol 19:989–1003

Madelain F (1970) Influence de la topographie du fond sur l'ecoulement méditerranéen entre le Détroit de Gibraltar et le Cap Saint-Vincent. Cah Oceanogr 22:43–61

Maher BA, Thompson R (1999) Quaternary climates, environments and magnetism. Cambridge University Press, Cambridge

Maignien L, Foubert A, Depreiter D, Boon N, Boeckx P, Blamart D, Verstraet W, Henriet J-P (subm.) Biogeochemical evidence for anaerobic methane oxidation in the carbonate mounds from the Gulf of Cadiz. Int J Earth Sci

Maldonado A, Somoza L, Pallares L (1999) The Betic orogen and the Iberian-African boundary in the Gulf of Cadiz: Geological evolution (central North Atlantic). Mar Geol 155:9–43

Malone MJ, Slowey NC, Henderson GM (2001) Early diagenesis of shallow-water periplatform carbonate sediments, leeward margin, Great Bahama Bank (Ocean Drilling Program Leg 166). Geol Soc Am Bull 113:881–894

Martinson DG, Pisias NG, Hays JD, Imbrie J, Moore TC, Shackleton NJ (1987) Age dating and the Orbital theory of the ice ages: Development of a high-resolution 0 to 300,000-year Chronostratigraphy. Quaternary Res 27:1–29

Maslin MA, Ridgwell AJ (2005) Mid-Pleistocene revolution and the 'eccentricity myth'. In: Head MJ, Gibbard PL (eds) Early-middle Pleistocene transitions: The Land-Ocean Evidence. Geological Society Special Publications, London, pp 19–34

Massa D, Combaz A, Manderscheid G (1965) Observations sur le Siluro–Dévonien des confines algero-marocains. Compagnie Française des Pétroles, Notes Mém 8:1–187

Masschaele B, Cnudde V, Dierick M, Jacobs P, Van Hoorebeke L, Vlassenbroeck J (2007) UGCT: New X-ray radiography and tomography facility. NIM A 580:266–269

Masson DG, Bett BJ, Billet DSM, Jacobs CL, Wheeler AJ, Wynn RB (2003) The origin of deep-water, coral-topped mounds in the northern Rockall Trough, Northeast Atlantic. Mar Geol 194:159–180

Mathys M (2001) Hoge-resolutie geofysische studie van gasmigratie in oppervlakkige mariene sedimenten ter hoogte van olie- en gasreservoirs, Porcupine Bekken (SW Ierland). MSc thesis, University Ghent

Matthiesen S, Haines K (1998) Influence of the Strait of Gibraltar on past changes in mediterranean thermohaline circulation. International Conference on Palaeoceanography, Lisbon

Mauritzen C, Morel Y, Paillet J (2001) On the influence of mediterranean water on the central waters of the North Atlantic Ocean. Deep-Sea Res Pt I 48:347–381

Mazurenko LL, Soloviev VA, Gardner JM, Ivanov MK (2003) Gas hydrates in the Ginsburg and Yuma mud volcano sediments (Moroccan Margin): results of chemical and isotopic studies of pore water. Mar Geol 195:201–210

McDonnell A (2001) Comparative Tertiary basin development in the Porcupine and Rockall Basins. PhD thesis, Department of Geology, Dublin

McDonnell A, Shannon PM (2001) Comparative Tertiary stratigraphic evolution of the Porcupine and Rockall Basins. In: Shannon PM, Haughton P, Corcoran D (eds) The Petroleum Exploration of Ireland's Offshore basins. Geological Society, London, pp 323–344

Mead GA, Tauxe L, LaBrecque JL (1986) Oligocene paleoceanography of the South Atlantic: paleoclimatic implications of sediment accummulation rates and magnetic susceptibility measurements. Paleoceanography 1:273–284

Meincke J (2002) Climate Dynamics of the North Atlantic and NW-Europe: An Observation-Based Overview. In: Wefer G, Berger WH, Behre K-E, Jansen E (eds) Climate Development and History of the North Atlantic Realm. Springer, Berlin-Heidelberg, pp 25–40

Melieres (1974) Recherches sur la dynamique sédimentaire du Gole de Cadiz (Espagne). PhD thesis, University Paris A

Melim LA, Westphal H, Swart PK, Eberli GP, Munnecke A (2002) Questioning carbonate diagenetic paradigms: evidence from the Neogene of the Baha-mas. Mar Geol 185:27–46

Mertens K, Vanneste H, Foubert A, Louwye S, Hebbeln D (2006) Biometry of late Quaternary coccoliths from the Southern Cadiz region. In: Proceedings European Geosciences Union 2006. Vienna, p 07934

Mertens K (2009) Tracing hydrological millennial-scale cycles in the late Quaternary of the Cariaco Basin and the southern Gulf of Cadiz using coccoliths and dinoflagellate cysts. PhD. Thesis, University Ghent

Messing CG, Neumann AC, Lang JC (1990) Biozonation of deep-water lithoherms and associated hardgrounds in the Northeastern Straits of Florida. Palaios 5:15–33

Michel JL, Klages M, Barriga F, Fouquet Y, Sibuet M, Sarradin PM, Siméoni P, Drogou JF (2003) Victor 6000: Design, utilization and first improvements. In: Proceedings of the International Offshore and Polar Engineering Conference 2003

Mienis F, de Haas H, Party SS (2004) The distribution, morphology, sedimentology and water mass characteristics of and around mounds in the Gulf of Cadiz and at the SW Rockall Trough Margin. Royal Netherlands Institute for Sea Research. Cruise report R.V. Pelagia cruise M2004 (640PE229). Royal Netherlands Institute for Sea Research (NIOZ), Den Helder

Mienis F, Van Weering TCE, de Stichter H, de Haas H, Richter T (2005) Near bed hydrodynamic conditions of carbonate mounds in the Northeast Atlantic Ocean. In: Proceedings European Geosciences Union. Vienna, p 04902

Mienis F, Van Weering T, De Haas H, De Stigter HC, Huvenne V, Wheeler A (2006) Carbonate mound development at the SW Rockall Trough margin based on high resolution TOBI and seismic recording. Mar Geol 233:1–19

Mienis F, de Stigter HC, White M, Duineveld G, de Haas H, van Weering TCE (2007) Hydrodynamic controls on cold-water coral growth and carbonate-mound development at the SW and SE Rockall Trough Margin, NE Atlantic Ocean. Deep Sea Res Pt I: Oceanographic Research Papers 54:1655–1674

Migeon S, Weber O, Faugères J-C, Saint-Paul J (1999) SCOPIX: A new X-ray imaging system for core analysis. Geo-Mar Lett 18:251–255

Mikkelsen N, Erlenkeuser H, Killingley JS, Berger WH (1982) Norwegian corals: radiocarbon and stable isotopes in *Lophelia pertusa*. Boreas 11:163–171

Milankovitch M (1941) Kanon der Erdbestrahlung und seine Anwendung auf das Eiszeitenproblem. Roy Serb Acad Spec Publ 133:1–633

Miller KG, Mountain GS, Browning JV, Kominz M, Sugarman PJ, Christie-Blick N, Katz ME, Wright JD (1998) Cenozoic global sea level, sequences, and the New Jersey transect: Results from coastal plain and continental slope drilling. Rev Geophys 36:569–601

Mittelstaedt E (1991) The ocean boundary along the African Coast. Circulation and oceanographic properties at the sea surface. Prog Oceanogr 26:307–355

Mohn C, Bartsch J, Meincke J (2002) Observations of the mass and flow field at Porcupine Bank. Ices J Mar Sci 59:380–392

Möller NK, Kvingan K (1988) The genesis of nodular limestones in the ordovician and silurian of the oslo region (Norway). Sedimentology 35:405–420

Monty CLV (1995) The rise and nature of carbonate mud-mounds: an introductory actualistic approach. In: Monty CLV, Bosence DWJ, Bridges PH, Pratt BR (eds) Carbonate mud-mounds: their origin and evolution. Blackwell Science, Oxford, pp 11–48

Monty CLV, Bosence DWJ, Bridges PH, Pratt BR (1995) Carbonate mud-mounds: Their origin and evolution. Blackwell Science, Oxford

Moore JG, Shannon PM (1991) Slump structures in the late Tertiary of the Porcupine Basin, Offshore Ireland. Mar Petrol Geol 8:184–197

Moore JG, Shannon PM (1992) Palaeocene-Eocene deltaic sedimentation, Porcupine Basin, Offshore Ireland - a sequence stratigraphic approach. First Break 10:461–469

Morewood NC, Shannon PM, Mackenzie GD (2004) Seismic stratigraphy of the southern Rockall Basin: a comparison between wide-angle seismic and normal incidence reflection data. Mar Petrol Geol 21:1149–1163

Morse JW, MacKenzie FT (1990) Geochemistry of sedimentary carbonates. Elsevier, Amsterdam

Mortensen PB (2000) *Lophelia pertusa* (Scleractinia) in Norwegian waters. Distribution, growth, and associated fauna. PhD thesis, University of Bergen

Mortensen PB (2001) Aquarium observations on the deep-water coral *Lophelia pertusa* (L., 1758) (Scleractinia) and selected associated invertebrates. Ophelia 54:83–104

Mortensen PB, Rapp HT (1998) Oxygen and carbon isotope ratios related to growth line patterns in skeletons of *Lophelia pertusa* (L.) (Anthozoa, Scleractinia): implications for determination of linear extension rates. Sarsia 83:433–446

Mounji D, Bourque PA, Savard MM (1998) Hydrothermal origin of Devonian conical mounds (kess-kess) of Hamar Lakhdad Ridge, Anti-Atlas, Morocco. Geology 26:1123–1126

Mount J (1985) Mixed siliciclastic and carbonate sediments – a proposed 1st-order textural and compositional classification. Sedimentology 32:435–442

Mudelsee M, Raymo ME (2005) Slow dynamics of the Northern Hemisphere glaciation. Paleoceanography 20:PA4022

Mudelsee M, Stattegger K (1997) Exploring the structure of the mid-Pleistocene revolution with advanced methods of time series analysis. Geol Rundsch 86:499–511

Mullins HT, Wise SW, Gardulski AF, Hinchey EJ, Masters PM, Siegel DI (1985) Shallow subsurface diagenesis of Pleistocene periplatform ooze – Northern Bahamas. Sedimentology 32: 473–494

Munnecke A, Samtleben C (1996) The formation of micritic limestones and the development of limestone-marl alternations in the Silurian of Gotland, Sweden. Facies 34:159–176

Munnecke A, Westphal H (2004) Shallow-water aragonite recorded in bundles of limestone-marl alternations – the Upper Jurassic of SW Germany. Sediment Geol 164:191–202

Munnecke A, Westphal H (2005) Variations in primary aragonite, calcite, and clay in fine-grained calcareous rhythmites of Cambrian to Jurassic age – an environmental archive? Facies 51: 611–626

Murray J, Renard AF (1891) Report on the scientific results of the voyage of the Challenger: Reports on Deep-Sea Deposits

Mutti M, Hallock P (2003) Carbonate systems along nutrient and temperature gradients: some sedimentological and geochemical constraints. Int J Earth Sci 92:465–475

Nadeau M-J, Schleicher M, Grootes PM, Erlenkeuser H, Gottdang A, Mous DJW, Sarnthein JM, Willkomm H (1997) The Leibniz-Labor AMS facility at the Christian-Albrechts University, Kiel, Germany. Nucl Instrum Methods Phys Res B 123(1–4):22–30

Naylor D, Shannon PM (2005) The structural framework of the Irish Atlantic Margin. In: Doré AG, Vining B (eds) Petroleum geology: North-West Europe and global perspectives – Proceedings of the 6th petroleum geology conference. Geological Society, London, pp 1009–1021

Naylor D, Shannon PM, Murphy N (1999) Irish Rockall Basin region – A standard structural nomenclature system. Petroleum Affairs Division Special Publication 1/99

Naylor D, Shannon PM, Murphy N (2002) Porcupine-Goban region – A standard structural nomenclature system. Petroleum Affairs Division Special Publication 1/02

Nelson CH, Baraza J, Maldonado A, Rodero J, Escutia C, Barber Jr JH (1999) Influence of the Atlantic inflow and Mediterranean outflow currents on Late Quaternary sedimentary facies of the Gulf of Cadiz continental margin. Mar Geol 155:99–129

Neumann AC, Kofoed JW, Keller GH (1977) Lithoherms in Straits of Florida. Geology 5:4–10

Neuweiler F, Gautret P, Thiel V, Lange R, Michaelis W, Reitner J (1999) Petrology of Lower Cretaceous carbonate mud mounds (Albian, N-Spain): insights into organomineralic deposits of the geological record. Sedimentology 46:837–859

Neuweiler F, d'Orazio V, Immenhauser A, Geipel G, Heise KH, Co-cozza C, Miano TM (2003) Fulvic acid-like organic compounds control nucleation of marine calcite under suboxic conditions. Geology 31:681–684

Noe S, Titschack J, Freiwald A, Dullo WC (2006) From sediment to rock: diagenetic processes of hardground formation in deep-water carbonate mounds of the NE Atlantic. Facies 52:183–208

Norris RD, Klaus A, Kroon D (2001) Mid-Eocene deep water, the Late Palaeocene Thermal Maximum and continental slope mass wasting during the Cretaceous–Palaeogene impact. In: Kroon D, Norris RD, Klaus A (eds) Western North Atlantic Palaeogene and Cretaceous Palaeoceanography. Geological Society, London, pp 23–48

Nykjaer L, Van Camp L (1994) Seasonal and interannual variability of coastal upwelling along northwest Africa and Portugal from 1981 to 1991. J Geophys Res 99:14197–14207

O'Reilly BM, Hauser F, Jacob AWB, Shannon PM (1996) The lithosphere below the Rockall Trough: wide-angle seismic evidence for extensive serpentinisation. Tectonophysics 255:1–23

Ochoa J, Bray NA (1991) Water mass exchange in the Gulf of Cadiz. Deep-Sea Res 38:S465–S503

Olu-Le Roy K, Caprais J-C, Crassous P, Dejonghe E, Eardly D, Freiwald A, Galeron J, Grehan A, Henriet J-P, Huvenne VAI, Lorance P, Noel P, Opder-becke J, Pitout C, Sibuet M, Unnithan V, Vacelet J, van Weering TCE, Wheeler AJ, Zibrowius H (2002) CARACOLE Cruise Report. 30/07/2001 (Cobh) – 15/08/2001 (Foynes) N/O L'Atalante & ROV VICTOR, Vols. 1&2. IFREMER, Brest

Opderbecke J, Simeoni P, Allais AG, Edy C, Bisquay H (2004) High Resolution Swath Bathymetric Sea-bed Mapping with the ROV Victor 6000. In: Proceedings of The Fourteenth International Offshore and Polar Engineering Conference. The International Society of Offshore and Polar Engineers, Tou-lon

Opdyke ND (1972) Paleomagnetism of deep-sea cores. Rev Geophys Space Ge 10:213–217

Orr JC, Fabry VJ, Aumont O, Bopp L, Doney SC, Feely RA, Gnanadesikan A, Gruber N, Ishida A, Joos F, Key RM, Lindsay K, Maier-Reimer E, Matear R, Monfray P, Mouchet A, Najjar RG, Plattner GK, Rodgers KB, Sabine CL, Sarmiento JL, Schlitzer R, Slater RD, Totterdell IJ, Weirig MF, Yamanaka Y, Yool A (2005) Anthropogenic ocean acidification over the twenty-first century and its impact on calcifying organisms. Nature 437:681–686

Ortiz J, Mix A, Harris S, O'Connell S (1999) Diffuse spectral reflectance as a proxy for percent carbonate content in North Atlantic sediments. Paleoceanography 14:171–186

Ortiz JD, Rack FR (1999) Non-invasive sediment monitoring methods: current and future tools for high-resolution climate studies. In: Abrantes F, Mix AC (eds) Reconstructing Ocean History: A Window into the Future. Kluwer Academic/Plenum Publishers, New York, pp 343–380

Ottesen D, Dowdeswell JA, Rise L, Rokoengen K, Henriksen S (2005) Large-scale morphological evidence for past ice-stream flow on the mid-Norwegian continental margin. In: Dowdeswell JA, Ocofaigh C (eds) Glacier-influenced sedimentation in high-latitude continental margins. Geological Society Special Publications, London, pp 245–258

Ovrebo LK, Haughton PDW, Shannon PM (2006) A record of fluctuating bottom currents on the slopes west of the Porcupine Bank, Offshore Ireland – implications for Late Quaternary climate forcing. Mar Geol 225:279–309

Ovsyannikov DO, Sadekov AY, Kozlova EV (2003) Rock fragments from mud volcanic deposits of the Gulf of Cadiz: an insight into the Eocene-Pliocene sedimentary succession of the basin. Mar Geol 195:211–221

Paillard D, Labeyrie L, Yiou P (1996) Macintosh program performs time-series analysis. Eos Trans AGU 77:379

Pantin HM, Evans CDR (1984) The Quaternary History of the Central and Southwestern Celtic Sea. Mar Geol 57:259–293

Patterson WP, Walter LM (1994) Depletion of C-13 in seawater Sigma-CO2 on modern carbonate platforms – Significance for the carbon isotopic record of carbonates. Geology 22:885–888

Paull CK, Neumann AC, Ende BAA, Ussler W, Rodriguez NM (2000) Lithoherms on the Florida-Hatteras slope. Mar Geol 166:83–101

Pearson I, Jenkins DG (1986) Unconformities in the Cenozoic of the North-East Atlantic. In: Summerhayes CP, Shackleton NJ (eds) North Atlantic Palaeoceanography. Geological Society, London, pp 79–86

Peckmann J, Walliser OH, Riegel W, Reitner J (1999) Signatures of hydrocarbon venting Middle Devonian carbonate mound (Hollard Mound) at the Hamar Laghdad (Antiatlas, Morocco). Facies 40:281–296

Peckmann J, Little CTS, Gill F, Reitner J (2005) Worm tube fossils from the Hollard Mound hydrocarbon-seep deposit, Middle Devonian, Morocco: Palaeozoic seep-related vestimentiferans? Palaeogeogr Palaeocl 227:242–257

Perry CT, Taylor KG (2006) Inhibition of dissolution within shallow water carbonate sediments: Impacts of terrigenous sediment input on syn-depositional carbonate diagenesis. Sedimentology 53:495–513

Pingree RD, Le Cann B (1989) Celtic and Armorican Slope and Shelf residual currents. Prog Oceanogr 23:303–338

Pingree RD, Le Cann B (1990) Structure, strength and seasonality of the slope currents in the Bay of Biscay Region. J Mar Biol Assoc UK 70:857–885

Pinheiro LM, Ivanov MK, Sautkin A, Akhmanov G, Magalhaes VH, Volkonskaya A, Monteiro JH, Somoza L, Gardner J, Hamouni N, Cunha MR (2003) Mud volcanism in the Gulf of Cadiz: Results from the TTR-10 cruise. Mar Geol 195:131–151

Pollard RT, Griffttths MJ, Cunningham SA, Read JF, Perez FF, Rios AF (1996) Vivaldi 1991 – A study of the formation, circulation and ventilation of Eastern North Atlantic Central Water. Prog Oceanogr 37:167–172

Pollitz FF (1988) Episodic North-America and Pacific Plate Motions. Tectonics 7:711–726
Potts (1987) A handbook of silicate rock analysis. Blackie, Glasgow
Praeg D, Stoker MS, Shannon PM, Ceramicola S, Hjelstuen BO, Laberg JS, Mathiesen A (2005) Episodic Cenozoic tectonism and the development of the NW European 'passive' continental margin. Mar Petrol Geol 22:1007–1030
Pratje O (1924) Korallenbänke in tiefem und kühlem Wasser. Zentralblatt für Mineralogie, Geologie und Paläontologie 1924:410–415
Pratt BR (1995) The origin, biota and evolution of deep-water mud mounds. In: Monty CLV, Bosence DWJ, Bridges PH, Pratt BR (eds) Carbonate mud-mounds: Their origin and evolution. Blackwell Science, Oxford, pp 49–123
Radtke G (1991) Die mikroendolithischen Sporenfossilien im Alt-Tertiär West-Europas und ihre palökologische bedeutung. Courier Forschinst Senckenberg 138:1–185
Raiswell R (1997) A geochemical framework for the application of stable sulphur isotopes to fossil pyritization. J Geol Soc London 154:343–356
Ramsay ATS, Smart CW, Zachos JC (1998) A model of early to middle Miocene deep ocean circulation for the Atlantic and Indian Oceans. In: Cramp A, MacLeod CJ, Lee SV, Jones EJW (eds) Geological evolution of ocean basins: Results from the Ocean Drilling program. Geological Society, London, pp 55–70
Ratmeyer V, Hebbeln D, Beck T, Belling R, Bergenthal M, Beuck L, Brakel C, Buhmann S, Dodds L, Dorschel B, Engemann G, Foubert A, Gault J, Grehan A, Hayn C, Jurkiw A, Kahl G, Kaiser J, Klar S, Lutz M, Noe S, Papstein H, Rüggeberg A, Ruhland G, Schewe F, Schmidt W, Schröder M, Seiter C, Truscheit T, Wienberg C (2006) Report and preliminary results of RV Meteor cruise M61/3. Development of carbonate mounds on the Celtic continental margin, Northeast Atlantic. Cork (Ireland)-Ponta Delgada (Portugal), 04.-21.06.2004. Berichte aus dem fachberich Geowissenschaften der Universitat Bremen, vol 247
Ravelo AC, Andreasen DH, Lyle M, Lyle AO, Wara MW (2004) Regional climate shifts caused by gradual global cooling in the Pliocene epoch. Nature 429:263–267
Raymo ME (1994) The initiation of northern-hemisphere glaciation. Annu Rev Earth Pl Sc 22: 353–383
Raymo ME, Ruddiman WF, Shackleton NJ, Oppo DW (1990) Evolution of Atlantic Pacific Delta-C-13 Gradients over the Last 2.5 My. Earth Planet Sc Lett 97:353–368
Rea DK, Hovan SA (1995) Grain-size distribution and depositional processes of the mineral component of abyssal sediments – Lessons from the North Pacific. Paleoceanography 10:251–258
Reeburg WS (1983) Rates of biogeochemical processes in anoxic sediments. Ann Rev Earth Planet Sci 11:269–298
Rees AI, Woodall WA (1975) Magnetic fabric of some laboratory-deposited sediments. Earth Planet Sc Lett 25:121–130
Reston TJ, Pennell J, Stubenrauch A, Walker I, Perez-Gussinye M (2001) Detachment faulting, mantle serpentinization, and serpentinite-mud volcanism beneath the Porcupine Basin, southwest of Ireland. Geology 29:587–590
Reston TJ, Gaw V, Pennell J, Klaeschen D, Stubenrauch A, Walker I (2004) Extreme crustal thinning in the south Porcupine Basin and the nature of the Porcupine Median High: implications for the formation of non-volcanic rifted margins. J Geol Soc London 161:783–798
Rice AL, Thurston MH, New AL (1990) Dense aggregations of a hexactinellid sponge, *Pheromena carpenteri*, in the Porcupine Seabight (northeast Atlantic Ocean), and possible causes. Prog Oceanogr 24:179–196
Rice AL, Billet DSM, Thurston MH, Lampitt RS (1991) The Institute of Oceanographic Sciences Biology programme in the Porcupine Seabight: background and general introduction. J Mar Biol Assoc UK 71:281–310
Richardson PL, Bower AS, Zenk W (2000) A census of meddies tracked by floats. Prog Oceanograpr 45:209–250
Richardson PL, Walsh D, Armi L, Schröder M, Price JF (1989) Tracking three meddies with SOFAR floats. J Phys Oceanogr 19:371–383

Richter TO, Lassen S, van Weering TCE, de Haas H (2001) Magnetic susceptibility patterns and provenance of ice-rafted material at Feni Drift, Rockall Trough: implications for the history of the British-Irish ice sheet. Mar Geol 173:37–54

Riding R (2002) Structure and composition of organic reefs and carbonate mud mounds: Concepts and categories. Earth-Sci Rev 58:163–231

Roberts AP (1995) Magnetic properties of sedimentary greigite (Fe3s4). Earth Planet Sc Lett 134:227–236

Roberts AP (2006) High-resolution magnetic analysis of sediment cores: Strengths, limitations and strategies for maximizing the value of long-core magnetic data. Phys Earth Planet In 156: 162–178

Roberts DG (1972) Slumping on the eastern margin of the Rockall Bank, North Atlantic Ocean. Mar Geol 13:225–237

Roberts JM, Wheeler AJ, Freiwald A (2006) Reefs of the deep: The biology and geology of cold-water coral ecosystems. Science 312:543–547

Roberts JM, Henry LA, Long D, Hartley JP (2008) Cold-water coral reef frameworks, megafaunal communities and evidence for coral carbonate mounds on the Hatton Bank, north east Atlantic. Facies 54:297–316

Roberts JM, Wheeler A, Freiwald A, Cairns S (2009) Cold-water corals: the biology and geology of deep-sea coral habitats. Cambridge University Press

Roberts JM, Peppe OC, Dodds LA, Mercer DJ, Thomson WT, Gage JD, Mel-drum DT (2005) Monitorint environmental variability around cold-water coral reefs: the use of a benthic photolander and the potential of seafloor observatories. In: Freiwald A, Roberts JM (eds) Cold-water corals and ecosystems. Springer-Verlag, Berlin Heidelberg, pp 483–502

Robinson SG (1986) The late pleistocene paleoclimatic record of North-Atlantic deep-sea sediments revealed by mineral-magnetic measurements. Phys Earth Planet In 42:22–47

Robinson SG, Maslin MA, McCave IN (1995) Magnetic susceptibility variations in Upper Pleistocene deep-sea sediments of the NE Atlantic: Implications for ice rafting and paleocirculation at the last glacial maximum. Paleoceanography 10:221–250

Roch E (1934) Sur des phénomènes remarquables observes dans la région d'Erfoud (confins algero-marocains du Sud). Géol Méd Oc 5:1–10

Rodrigues CF, Cunha MR (2005) Common chemosynthetic species in the Gulf of Cadiz: updated spatial distribution. In: Geosphere-Biosphere coupling processes: The TTR interdisciplinary approach towards studies of the European and North African margins. UNESCO, Marrakech, pp 26–28

Rogers AD (1999) The biology of *Lophelia pertusa* (LINNAEUS 1758) and other deep-water reef-forming corals and impacts from human activities. Int Rev Hydrobiol 84:315–406

Rogerson M (2002) Climatic influence on sediment transport in the Mediterranean outflow current (Gulf of Cadiz, Spain). Newsl Micropalaeontol 66:16–17

Röhl U, Abrams LJ (2000) High-resolution, downhole, and nondestructive core measurements from sites 999 and 1001 in the Carribean Sea: application to the Late Paleocene Thermal Maximum. In: Leckie RM, Sigurdsson H, Acton GD, Draper G (eds) Proceedings of the Ocean Drilling Program, Scientific Results, vol 164. US Government Printing Office, Washington, pp 191–203

Ruddiman WF (1977) Late Quaternary deposition of ice-rafted sand in the subpolar North Atlantic (lat 40° to 65°N). Geol Soc Am Bull 88:1813–1827

Ruddiman WF, Kidd RB, Thomas E (1987) Site 610. In: Ruddiman WF, Kidd RB, Thomas E (eds) Initial reports of the Deep Sea Drilling Project, vol. 94. US Government Printing Office, Washington, pp 351–470

Rüggeberg A, Dorschel B, dullo WC, Hebbeln D (2005) Sedimentary patterns in the vicinity of a carbonate mound in the Hovland Mound Province, northern Porcupine Seabight. In: Freiwald A, Roberts JM (eds) Cold-Water Corals and Ecosystems. Springer-Verlag, Berlin Heidelberg

Rüggeberg A, Dullo C, Dorschel B, Hebbeln D (2007) Environmental changes and growth history of a cold-water carbonate mound (Propeller Mound, Porcupine Seabight). Int J Earth Sci 96: 57–72

Ruiz J, Navarro G (2006) Upwelling spots and vertical velocities in the Gulf of Cadiz: An approach for their diagnose by combining temperature and ocean colour remote sensing. Deep-Sea Res Pt II 53:1282–1293

Russ JC (2002) The image processing handbook. CRC press, New York

Russel MI, Frank TD, Andres M (2006) Early diagenetic controls on porosity distribution in carbonate mounds. AAPG Annual Convention and Exhibition, Long Beach, CA

Rybicki F, Denis JF, Peyronnet JP (1999) POSIDONIA: Acoustic positioning system. In: Proceedings of the International Offshore and Polar Engineering Conference 1999

Sadoux S, Baey JM, Fincham A, Renouard D (2000) Experimental study of the stability of an intermediate current and its interaction with a cape. Dyn Atmos Oceans 31:165–192

Sanders D (2003) Syndepositional dissolution of calcium carbonate in neritic carbonate environments: geological recognition, processes, potential significance. J Afr Earth Sci 36:99–134

Sanders D, Baron-Szabo RC (2005) Scleractinian assemblages under sediment input: their characteristics and relation to the nutrient input concept. Palaeogeogr Palaeocl 216:139–181

Sartori R, Torelli N, Zitellini D, Peis D, Lodolo E (1994) Eastern segment of the Azores - Gibraltar line (central-eastern Atlantic): An oceanic plate boundary with diffuse compressional deformation. Geology 22

Schlager W (2003) Benthic carbonate factories of the Phanerozoic. Int J Earth Sci 92:445–464

Schönfeld J (1997) The impact of the Mediterranean Outflow Water (MOW) on the benthic foraminiferal assemblages and surface sediments at the southern Portuguese continental margin. Mar Micropaleontol 29:211–236

Schönfeld J, Zahn R (2000) Late Glacial to Holocene history of the Mediterranean Outflow. Evidence from benthic foraminiferal assemblages and stable isotopes at the Portuguese margin. Palaeogeogr Palaeocl 159:85–111

Scourse JD, Hall IR, McCave IN, Young JR, Sugdon C (2000) The origin of Heinrich layers: evidence from H2 for European precursor events. Earth Planet Sc Lett 182:187–195

Sejrup HP, Hjelstuen BO, Dahlgren KIT, Haflidason H, Kuijpers A, Nygard A, Praeg D, Stoker MS, Vorren TO (2005) Pleistocene glacial history of the NW European continental margin. Mar Petrol Geol 22:1111–1129

Serra O (1984) Fundamentals of Well-Log Interpretation. Elsevier, Amsterdam

Shackleton NJ, Hall MA (1984) Oxygen and Carbon Isotope Stratigraphy of Deep-Sea Drilling Project Hole-552a – Plio-Pleistocene Glacial History. Initial Rep Deep Sea 81:599–609

Shackleton NJ, Berger A, Peltier WR (1990) An alternative astronomical calibration of the lower Pleistocene timescale based on ODP Site 677. T Roy Soc Edin-Earth 81:251–261

Shackleton NJ, Hall MA, Pate D (1995a) Pliocene stable isotope stratigraphy of Site 846. In: Pisias NG, Janacek LA, Palmer-Julson A, Van Andel TH (eds) Proceedings of the Ocean Drilling Program, Scientific Results, volume 138. US Government Printing Office, Washington, pp 337–355

Shackleton NJ, Backman J, Zimmerman H, Kent DV, Hall MA, Roberts DG, Schnitker D, Baldauf JG, Desprairies A, Homrighausen R, Huddlestun P, Keene JB, Kaltenback AJ, Krumsiek KAO, Morton AC, Murray JW, West-Bergsmith J (1984) Oxygen isotope calibration of the onset of ice-rafting and history of glaciation in the North-Atlantic region. Nature 307:620–623

Shackleton NJ, Crowhurst S, Hagelberg T, Pisias NG, Schneider DA (1995b) A new Late Neogene time scale: Application to Leg 138 Sites. In: Pisias NG, Janacek LA, Palmer-Julson A, Van Andel TH (eds) Proceedings of the Ocean Drilling Program, Scientific Results, vol 138. US Government Printing Of-fice, Washington, pp 73–101

Shannon PM (1991) The development of Irish offshore sedimentary basins. J geol Soc London 148:181–189

Shannon PM (1992) Early Tertiary submarine fan deposits in the Porcupine Basin, offshore Ireland. In: Parnell J (ed) Basins on the Atlantic Seaboard: Petroleum geology, Sedimentology and Basin Evolution. Geological Society, London, pp 351–373

Shannon PM, McDonnell A, Bailey W (2007) The evolution of the Porcupine and Rockall Basins, offshore Ireland: The geological template for carbonate mound development. Int J Earth Sci 96:21–35

Shannon PM, Moore JG, Jacob AWB, Makris J (1993) Cretaceous and Tertiairy basin development west of Ireland Petroleum geology of Northwest Europe: proceedings of the Fourth Conference. Geological Society, London, pp 1057–1066

Shannon PM, Jacob AWB, Makris J, O'Reilly B, Hauser F, Vogt U (1994) Basin evolution in the Rockall Region, North Atlantic. First Break 12:515–522

Shannon PM, Jacob AWB, Makris J, O'Reilly B, Hauser F, Readman PW (1999) Structural setting, geological development and basin modelling in Rockall Trough. In: Fleet AJ, Boldy SAR (eds) Petroleum geology of North-west Europe: proceedings of the 5th conference. Geological Society, London, pp 421–431

Shannon PM, Stoker MS, Praeg D, Van Weering TCE, De Haas H, Nielsen T, Dahlgren KIT, Hjelstuen BO (2005) Sequence stratigraphic analysis in deep-water, underfilled NW European passive margin basins. Mar Petrol Geol 22:1185–1200

Shi CD, Zhu RX, Suchy V, Zeman A, Guo B, Pan YX (2001) Identification and origins of iron sulfides in Czech loess. Geophys Res Lett 28:3903–3906

Shipboard Scientific Party (1996) Sites 980/981. In: Jansen E, Raymo ME, Blum P, et al (eds) Proceedings ODP, Initial reports, vol 162. Ocean Drilling Program, College Station, pp 49–90

Shor AN, Kent DV, Flood RD (1984) Contourite or turbidite?: Magnetic fabric of fine-grained Quaternary sediments, Nova Scotia continental rise. In: Stow DAV, Piper DJW (eds) Fine-Grained Sediments: Deep-water Processes and Facies. Blackwell Science, Cambridge, pp 257–273

Sinclair IK, Shannon PM, Williams BPJ, Harker SD, Moore JG (1994) Tectonic control on sedimentary evolution of three North Atlantic borderland Mesozoic basins. Basin Res 6:193–218

Sivhed U, Erlstrom M, Bojesen-Koefoed JA, Lofgren A (2004) Upper Ordovician carbonate mounds on Gotland, central Baltic Sea: Distribution, composition and reservoir characteristics. J Petrol Geol 27:115–140

Skinner LC, McCave IN (2003) Analysis and modelling of gravity- and piston coring based on soil mechanics. Mar Geol 199:181–204

Snoeckx H, Grousset FE, Revel M, Boelaert A (1999) European contribution of ice-rafted sand to Heinrich layers H3 and H4. Mar Geol 158:197–208

Solan M, Germano JD, Rhoads DC, Smith C, Michaud E, Parry D, Wenzhofer F, Kennedy B, Henriques C, Battle E, Carey D, Iocco L, Valente R, Watson J, Rosenberg R (2003) Towards a greater understanding of pattern, scale and process in marine benthic systems: a picture is worth a thousand worms. J Exp Mar Biol Ecol 285:313–338

Somoza L, Diaz-del-Rio V, Leon R, Ivanov M, Fernandez-Puga MC, Gardner JM, Hernandez-Molina FJ, Pinheiro LM, Rodero J, Lobato A (2003) Seabed morphology and hydrocarbon seepage in the Gulf of Cadiz mud volcano area: Acoustic imagery, multibeam and ultra-high resolution seismic data. Mar Geol 195:153–176

Soulsby R (1997) Dynamics of marine sands. Thomas Telford Publications, London

Sparks RSJ, Bonnecaze RT, Huppert HE, Lister JR, Hallworth MA, Mader H, Phillips J (1993) Sediment-Laden Gravity Currents with Reversing Buoyancy. Earth Planet Sc Lett 114: 243–257

Spiro B, Roberts JM, Gage J, Chenery S (2000) $^{18}O/^{16}O$ and $^{13}C/^{12}C$ in an ahermatypic deep-water coral *Lophelia pertusa* from the North Atlantic: A case of disequilibrium isotope fractionation. Rapid Commun Mass Sp 14:1332–1336

Squires DF (1957) New species of caryophylliid corals from the Gulf Coast Tertiary. J Paleontol 31:992–996

Squires DF (1964) Fossil coral thickets in Wairarapa, New Zealand. J Paleon-tol 38:904–915

Stadnitskaia A, Ivanov MK, Blinova V, Kreulen R, van Weering TCE (2006) Molecular and carbon isotopic variability of hydrocarbon gases from mud volcanoes in the Gulf of Cadiz, NE Atlantic. Mar Petrol Geol 23:281–296

Stetson TR, Squires DF (1962) Coral banks occuring in deep water on the Blake Plateau. Am Mus Novit 2114:1–39

Stoker MS (1997) Mid- to late Cenozoic sedimentation on the continental margin off NW Britain J Geol Soc London 154:509–515

Stoker MS, van Weering TCE, Svaerdborg T (2001) A mid- to late Cenozoic tectonostratigraphic framework for the Rockall Trough. In: Shannon PM, Haughton P, Corcoran D (eds) Petroleum Exploration of Ireland's offshore basins. Geological Society, London, pp 411–438

Stoker MS, Praeg D, Hjelstuen BO, Laberg JS, Nielsen T, Shannon PM (2005) Neogene stratigraphy and the sedimentary and oceanographic development of the NW European Atlantic margin. Mar Petrol Geol 22:977–1005

Stow DAV (1982) Bottom currents and contourites in the North Atlantic. Bull Inst Géol Bassin d'Aquitaine 31:151–166

Stow DAV, Wetzel A (1990) Hemiturbidite: A new type of deep-water sediment. In: Cochran JR, Stow DAV (eds) Ocean Drilling Program, College Station, pp 25–33

Strømgren T (1971) Vertical and horizontal distribution of *Lophelia pertusa* (Linné) in Trondheimsfjorden on the West Coast of Norway. Det Kongelige Norske Videnskabers Selskabs Skrifter 6:1–9

Stuiver M, Reimer PJ (1993) Extended C-14 DataBase and Revised Calib 3.0 C-14 Age Calibration Program. Radiocarbon 35:215–230

Taira A, Lienert BR (1979) Comparative reliability of magnetic, photometric and microscopic methods of determining the orientations of sedimentary grains. J Sediment Petrol 49:759–771

Takashima C (2006) Diagenetic influence of lithified horizon in mound section IODP Expedition 307 2nd Post-cruise Meeting, Yokohama

Tarling DH, Hrouda F (1993) The magnetic anisotropy of rocks. Chapman and Hall, London

Tate M, White N, Conroy JJ (1993) Lithospheric extension and magmatism in the Porcupine Basin West of Ireland. J Geophys Res-Sol Ea 98:13905–13923

Tate MP, Dobson MR (1988) Syn- and post-rift igneous activity in the Porcupine Seabight and adjacent continental margin west of Ireland. In: Morton AC, Parson ML (eds) Early Tertiary volcanism and the opening of the E Atlantic. Geological Society Special Publications, London, pp 309–334

Tauxe L (1993) Sedimentary records of relative Paleointensity of the Geomagnetic Field – Theory and practice. Rev Geophys 31:319–354

Taviani M, Corselli C, Freiwald A, Malinverno E, Mastrototaro F, Remia A, Savini A, Tursi A, CORAL Shipboard Staff (2005a) Rise, decline and ressurrection of deep-coral banks in the Mediterranean Bassin: Results of 2002 Coral Mission in the Ionian Sea. In: Freiwald A, Roberts JM (eds) Cold-water Corals and Ecosystems. Springer-Verlag, Berlin Heidelberg

Taviani M, Freiwald A, Zibrowius H (2005b) Deep coral growth in the Mediterranean Sea: an overview. In: Freiwald A, Roberts JM (eds) Cold-water corals and ecosystems. Springer-Verlag, Berlin Heidelberg, pp 137–156

Teichert C (1958) Cold- and deep-water coral banks. Am Assoc Petrol Geol B 42:1064–1082

Thierens M (2005) Paleooceanografische studie van Laat-Quartaire sedimenten aan de hand van foraminiferen en coccolieten in het noorden van Porcupine Seabight, ten zuidwesten van Ierland. MSc thesis. University Gent

Thompson R, Oldfield F (1986) Environmental Magnetism. Allan and Unwin, London

Thompson R, Bloemendal J, Dearing JA, Oldfield F, Rummery TA, Stober JC, Turner GM (1980) Environmental applications of magnetic measurements. Science 207:481–486

Thomson J, Nixon S, Summerhayes CP, Schonfeld J, Zahn R, Grootes P (1999) Implications for sedimentation changes on the Iberian margin over the last two glacial/interglacial transitions from $^{230}Th_{excess})_0$ systematics. Earth Planet Sc Lett 165:255–270

Thorpe SA (1976) Variability of the Mediterranean undercurrent in the Gulf of Cadiz. Deep-Sea Res 23:711–727

Thouveny N, de Beaulieu J-L, Bonifay E, Creer KM, Guiot J, Icole M, Johnsen S, Jouzel J, Reille M, Williams T, Williamson D (1994) Climate variations in Europe over the past 140 kyr deduced from rock magnetism. Nature 371:503–506

Thouveny N, Moreno E, Delanghe D, Candon L, Lancelot Y, Shackleton NJ (2000) Rock magnetic detection of distal ice-rafted debries: clue for the identification of Heinrich layers on the Portuguese margin. Earth Planet Sc Lett 180:61–75

Titschack J, Freiwald A (2005) Growth, deposition and facies of Pleistocene bathyal coral communities from Rhodes, Greece. In: Freiwald A, Roberts JM (eds) Cold-water corals and ecosystems. Springer-Verlag, Berlin Heidelberg, pp 41–59

Titschack J, Foubert A, Freiwald A, Ferdelman TG, Kano A, Williams T, Henriet JP, IODP Expedition 307 Scientists (2006) X-ray computer tomography and image analyses as tools for coral quantification and identification in cold-water coral mounds (Challenger Mound, Porcupine Seabight, IODP Expedition 307). 17th International Sedimentological Congress, Fukuoka, Japan

Titschack J, Thierens M, Dorschel B, Schulbert C, Freiwald A, Kano A, Takashima C, Kawagoe N, Li X, IODP Expedition 307 Scientific Party (2009) Carbonate budget of a cold-water coral mound (Challenger Mound, IODP Exp. 307). Mar geol 259:36–46

Tobin KJ, Walker KR (1996) Ordovician low- to intermediate-Mg calcite marine cements from Sweden: Marine alteration and implications for oxygen isotopes in Ordovician seawater. Sedimentology 43:719–735

Tribble GW (1993) Organic matter oxidation and aragonite diagenesis in a coral reef. J Sediment Petrol 63:523–527

Tucker ME (1974) Sedimentology of Paleozoic pelagic limestones: the Devonian Griotte (southern France) and Cephalopodenkalk (Germany). In: Hsü KJ, Jenkyns HE (eds) Pelagic sediments on land and under the sea. International Association Sedimentologists Special Publication, pp 71–92

Tucker ME, Wright VP (1990) Carbonate sedimentology. Blackwell Science, Oxford

Tudhope AW, Scoffin TP (1995) Processes of sedimentation in Gollum Channel, Porcupine Seabight: Submersible observations and sediment analyses. Trans R Soc Edinb: Earth Sci 86:49–55

Unnithan V, Shannon PM, McGrane K, Readman PW, Jacob AWB, Keary R, Kenyon NH (2001) Slope instability and sediment redistribution in the Rockall Trough: constraints from GLORIA. In: Shannon PM, Haughton PDW, Corcoran D (eds) The petroleum exploration of Ireland's Offshore basins. Geological Society Special Publications, London, pp 439–454

Unnithan V, Shannon PM, Croker P, Henriet JP (2003) Frequency and distribution of carbonate mounds in the Irish Atlantic. Irish Geological Research Meeting, Belfast

Valet JP (2003) Time variations in geomagnetic intensity. Rev Geophys 41:F1004

Valet JP, Meynadier L (1993) Geomagnetic field intensity and reversals during the past 4 million years. Nature 366:234–238

van Aken HM, Becker G (1996) Hydrography and through-flow in the North-Eastern North Atlantic Ocean: the NANSEN project. Prog Oceanogr 38:297–346

Van Rensbergen P, Depreiter D, Pannemans B, Moerkerke G, Van Rooij D, Marsset B, Akhmanov G, Blinova V, Ivanov M, Rachidi M, Magalhaes V, Pinheiro L, Cunha M, Henriet JP (2005a) The El arraiche mud volcano field at the Moroccan Atlantic slope, Gulf of Cadiz. Mar Geol 219:1–17

Van Rensbergen P, Depreiter D, Pannemans B, Henriet J-P (2005b) Seafloor expression of sediment extrusion and intrusion at the El Arraiche mud volcano field, Gulf of Cadiz. J Geophys Res 110:F02010

Van Rooij D (2004) An integrated study of Quaternary sedimentary processes on the eastern slope of the Porcupine Seabight, SW of Ireland. PhD thesis, University Ghent

Van Rooij D, De Mol B, Huvenne V, Ivanov MK, Henriet J-P (2003) Seismic evidence of current-controlled sedimentation in the Belgica mound province, upper Porcupine slope, southwest of Ireland. Mar Geol 195:31–53

Van Rooij D, Depreiter D, Bouimetarhan I, De Boever E, De Rycker K, Foubert A, Huvenne V, Réveillaud J, Staelens P, Vercruysse J, Versteeg W, Henriet J-P (2005) First sighting of active fluid venting in the gulf of cadiz. Eos Trans AGU 86:509–511

Van Rooij D, Blamart D, Richter TO, Wheeler AJ, Kozachenko M, Henriet J-P (2007a) Quaternary sediment dynamics in the Belgica mound province, Porcupine Seabight: Ice rafting events and contour current processes. Int J Earth Sci 96:121–140

Van Rooij D, Blamart D, Kozachenko M, Henriet J-P (2007b) Small mounded contourite drifts associated with deep-water coral banks, Porcupine Seabight, NE Atlantic Ocean. In: Viana AR, Rebesco M (eds) Economic and Palaeoceanographic importance of contourite deposits. Geological Society, London, pp 225–244

Van Rooij D, Huvenne VAI, Foubert A, Blamart D, Staelens P, Henriet JP, Wheeler A, de Haas H (2007c) The lost Enya mounds: causal relationships with sediment drifts and/or pockmarks? Int J Earth Sci

Van Rooij D, Henriet JP, Dullo WC, McKenzie JA, van Weering TCE, Sinninghe Damsté JS, Freiwald A, Blamart D, Spezzaferri S, Swennen R, Hamoumi N, Hebbeln D (2008) Atlantic Mound Drilling 2: Morocco Margin. IODP 673 Full Proposal

van Weering TCE, de Haas H, de Stigter HC, Lykke-Andersen H, Kouvaev I (2003) Structure and development of giant carbonate mounds at the SW and SE Rockall Trough margins, NE Atlantic Ocean. Mar Geol 198:67–81

Vanneste H (2005) Een paleooceanografische studie van Laat-Quartaire sedimenten aan de hand van coccolieten en kleimineralogie langsheen de Marokkaanse continentale rand, Golf van Cadiz. MSc thesis, University Gent

Vanney J-R (2002) Géographie de l'océon Global. Gordon & Breach, Paris

Vanney JR, Ménanteau L (2004) Géographie du golfe ibéro-marocain. Instituto Hidrografico, Lisboa – Portugal

Vecsei A (2004) A new estimate of global reefal carbonate production including the fore-reefs. Glob Planet Change 43:1–18

Vennin E, Aretz M, Boulvain F, Munnecke A (2007) Facies from Palaeozoic Reefs and Bioaccumulations. Memoires du museum national d'histoire naturelle 195

Vine AC (1975) Early history of underwater photography. Oceanus 18:2–10

Vlassenbroeck J, Dierick M, Masschaele B, Cnudde V, Van Hoorebeke L, Jacobs P (2007) Software tools for quantification of X-ray microtomography at the UGCT. Nucl Instrum Meth A 580:442–445

Voelker AHL, Lebreiro SM, Schonfeld J, Cacho I, Erlenkeuser H, Abrantes F (2006) Mediterranean outflow strengthening during northern hemisphere coolings: A salt source for the glacial Atlantic? Earth Planet Sc Lett 245:39–55

Von Dobeneck T, Schmieder F (1999) Using rock-magnetic proxy records for orbital tuning and extended time series analyses into the super- and sub-Milankovitch bands. In: Fischer G, Wefer G (eds) Use of proxies in paleoceanography. Springer-Verlag, Heidelberg Berlin, pp 601–633

Waller R (2005) Deep-water Scleractinia (Cnidaria: Anthozoa): Current knowledge of reproductive processes. In: Freiwald A, Roberts JM (eds) Cold-water corals and ecosystems. Springer-Verlag, Berlin Heidelberg, pp 691–700

Walter LM, Burton EA (1990) Dissolution of recent platform carbonate sediments in marine pore fluids. Am J Sci 290:601–643

Waller R, Tyler PA (2005) The reproductive biology of two deep-water reef building scleractinians from the NE Atlantic Ocean. Coral Reefs 24:514–522

Walter LM, Bischof SA, Patterson WP, Lyons TW (1993) Dissolution and recrystallization in modern shelf carbonates – Evidence from pore-water and solid-phase chemistry. Philos T Roy Soc A 344:27–36

Warren WP, Ashley GM (1994) Origins of the Ice-Contact Stratified Ridges (Eskers) of Ireland. J Sediment Res A 64:433–449

Weaver PPE, Wynn RB, Kenyon NH, Evans J (2000) Continental margin sedimentation, with special reference to the north-east Atlantic margin. Sedimentology 47:239–256

Webster G, Blazejak A, Cragg BA, Schippers A, Sass H, Rinna J, Tang X, Mathes F, Ferdelman T, Fry JC, Weightman AJ, Parkes RJ (2009) Subsurface microbiology and biogeochemistry

of a deep, cold-water carbonate mound from the Porcupine Seabight (IODP Expedition 307). Environ Microbiol 11(1):239–257

Westphal H (2006) Limestone-marl alternations as environmental archives and the role of early diagenesis: a critical review. Int J Earth Sci 95:947–961

Westphal H, Munnecke A, Pross J, Herrle JO (2004) Multiproxy approach to understanding the origin of Cretaceous pelagic limestone-marl alternations (DSDP site 391, Blake-Bahama Basin). Sedimentology 51:109–126

Wheeler AJ, Kenyon NH, Ivanov MK, Beyer A, Cronin B, McDonnell A, Schenke HW, Akhmetzhanov AM, Satur N, Zaragosi S (2003) Canyon heads and channel architecture of the gollum channel, Porcupine Seabight. In: Mienert J, Weaver PPE (eds) European margin sediment dynamics: Side-scan sonar and seismic images. Springer-Verlag, Berlin Heidelberg, pp 183–186

Wheeler AJ, Beck T, Thiede J, Klages M, Grehan A, Monteys FX, the Polar-stern ARK XIX/3a Shipboard Party (2005a) Deep-water coral mounds on the Porcupine Bank, Irish margin: preliminary results from the Polarstern ARK-XIX/3a ROV cruise. In: Freiwald A, Roberts JM (eds) Cold-Water Corals and Ecosystems. Springer-Verlag, Berlin Heidelberg, pp 393–402

Wheeler AJ, Kozachenko M, Beyer A, Foubert A, Huvenne VAI, Klages M, Masson DG, Olu-Le Roy K, Thiede J (2005b) Sedimentary processes and carbonate mounds in the Belgica mound province, Porcupine Seabight, NE Atlantic. In: Freiwald A, Roberts JM (eds) Cold-water corals and ecosystems. Springer-Verlag, Berlin Heidelberg, pp 571–603

Wheeler AJ, Beyer A, Freiwald A, de Haas H, Huvenne VAI, Kozachenko M, Olu-Le Roy K, Opderbecke J (2007) Morphology and environment of cold-water coral carbonate mounds on the NW European margin. Int J Earth Sci 96:37–56

Wheeler AJ, Kozachenko M, Masson DG, Huvenne VAI (2008) Influence of benthic sediment transport on cold-water coral bank morphology and growth: the example of the Darwin Mounds, north-east Atlantic. Sedimentology 55:1875-1887

Wheeler AJ, Kozachenko M, Foubert A, Henry LA, de Haas H, Huvenne V, Masson DG, Olu-Le Roy K (in prep.) Small cold-water coral banks in the Porcupine Seabight, NE Atlantic: do the Moira Mounds represent giant carbonate mound formation?

White M (2001) Hydrography and physical dynamics at the NE Atlantic margin that influence the deep water cold reef ecosystem. Internal report, Dept. of Oceanography, Galway

White M (2007) Benthic dynamics at the carbonate mound regions of the Porcupine Sea Bight continental margin. Int J Earth Sci 96:1–9

White M, Mohn C, de Stigter H, Mottram G (2005) Deep-water coral development as a function of hydrodynamics and surface productivity around the submarine banks of the Rockall Trough, NE Atlantic. In: Freiwald A, Roberts JM (eds) Cold-Water Corals and Ecosystems. Springer-Verlag, Berlin Heidel-berg, pp 503–514

White M, Roberts JM, van Weering TCE (2007) Bottom intensified diurnal tidal currents shape alignment of carbonate mounds in the NE Atlantic. Geo-Marine Letters

White N, Lovell B (1997) Measuring the pulse of a plume with the sedimentary record. Nature 387:888–891

White N, Tate M, Conroy JJ (1992) Lithospheric stretching in the Porcupine Basin, west of Ireland. In: Parnell J (ed) Basins on the Atlantic Seaboard: Petroleum geology, sedimentology and basin evolution. Geological Society Special Publications, London, pp 327–331

Wienberg C, Beuck L, Heidkamp S, Hebbeln D, Freiwald A, Pfannkuche O, Monteys X (2008) Franken Mound – facies and biocoenoses on a newly-discovered carbonate mound on the western Rockall Bank, NE Atlantic. Facies 54:1–24

Wilson JB (1979a) The distribution of the coral *Lophelia pertusa* (L.) [L. prolifera] in the North-East Atlantic. J Mar Biol Assoc UK59:149–164

Wilson JB (1979b) 'Patch' development of the deep-water coral *Lophelia pertusa* (L.) on Rockall Bank. J Mar Biol Assoc UK59:165–177

Wingfield R (1990) The origin of major incisions within the pleistocene deposits of the North-Sea. Mar Geol 91:31–52

Wisshak M, Connor D, Hain S, Golding N, Freiwald A (2006) *Lophelia pertusa* in the Northeast Atlantic: The current record. HERMES-meeting, Mallorca, Spain

Wisshak M, Freiwald A, Lundälv T, Gektidis M (2005) The physical niche of the bathyal *Lophelia pertusa* in a non-bathyal setting: environmental and palaeoecological implications. In: Freiwald A, Roberts JM (eds) Cold-Water Corals and Ecosystems. Springer-Verlag, Berlin Heidelberg, pp 979–1001

Wooster WS, Bakun A, McLain DR (1976) The seasonal upwelling cycle along the eastern boundary of the North Atlantic. J Mar Res 34:131–141

Yamazaki T, Oda H (2005) A geomagnetic paleointensity stack between 0.8 and 3.0 Ma from equatorial Pacific sediment cores. Geochem Geophy Geosy 6: Q11H20

Yue L, Kershaw S (2003) Reef reconstruction after extinction events of the latest ordovician in the Yangtze platform, South China. Facies 48:269–284

Zachos J, Pagani M, Sloan L, Thomas E, Billups K (2001) Trends, rhythms, and aberrations in global climate 65 Ma to present. Science 292:686–693

Zahn R, Schönfeld J, Kudrass H-R, Park M-H, Erlenkeuser H, Grootes P (1997) Thermohaline instability in the North Atlantic during melt-water events: Stable isotope and ice-rafted detritus records from core SO75–26KL, Portuguese margin. Paleoceanography 12:696–710

Zenk W, Armi L (1990) The complex spreading pattern of Mediterranean Water off the Portuguese continental slope. Deep-Sea Res Pt A. 37:1805–1823

Zenk W, Schults-Tokos KL, Boebel O (1992) New observations of meddy movement south of the Tejo Plateau. Geophys Res Lett 12:2389–2392

Zhang C, Ogg JG (2003) An integrated paleomagnetic analysis program for stratigraphy labs and research projects. Comput Geosci 29:613–625

Zhao WZ, Yang XP, Kershaw S, Zhang BM (2006) Reservoir potential of Silurian carbonate mud mounds in the southern Sichuan Basin, Central China. Acta Geol Sin-Engl 80:684–692

Zibrowius H (1980) Les Scléractiniens de la Méditerranée et de l'Atlantique nord-oriental. Mém Inst Océanogr Monaco 11:1–284

Index